# Xenoliths as tracers of magmatic and intra-crustal processes at volcanic arcs

A thesis submitted to Keele University
for the degree of Doctor of Philosophy

June 2020

By
Sean Oliver Whitley
Keele University

# Contents

# List of Tables

# List of Figures

# Abstract

Arc magmas typically show distinct geochemical and petrographical evidence indicating a complex petrogenesis. The surface products represent a summation of the complex interplay of geodynamic magma generation processes, varied differentiation histories, and crustal interaction. Xenoliths, 'foreign rocks', are found in the deposits of most volcanoes worldwide, and represent snapshots of individual events occuring during magmatic petrogenesis. Crustal xenoliths record the interaction between magma and the surrounding wall-rock, whilst plutonic xenoliths record the magma generation and differentiation history. This work uses two case study volcanoes: Merapi in the Indonesian Sunda Arc to focus on calc-silicate crustal xenoliths, and Santorini in the central South Aegean Volcanic Arc to focus on plutonic xenoliths.

The calc-silicate xenoliths at Merapi record magma-carbonate interaction processes. Thermobarometric calculations, fluid inclusion microthermometry and newly calibrated oxybarometry based on $Fe^{3+}/\Sigma Fe$ in clinopyroxene indicate xenolith formation conditions of ~510-910 $\pm$ 45°C, $<$ 100 MPa and at an oxygen fugacity between the NNO buffer and air. Halogen, sulphur and copper-bearing minerals show magmatic brine infiltration and the early stages of economic mineral deposition. Assessment of the timescales of xenolith formation and crustal $CO_2$ liberation demonstrates that magma-carbonate interaction could affect eruption intensity, and at a larger scale, impact global carbon cycling.

The plutonic xenoliths at Santorini can be considered cumulates to the magmatic system. Their whole-rock, melt inclusion and intercumulus glass chemistry shows they are representative of the entire liquid line of descent. Thermobarometry indicates they formed over a wide temperature range between ~1100 to 750°C, at shallow to mid crustal depths ($<$ 400 MPa) from a partially differentiated deep crustal melt. These pressures are shallower than those estimated for the East and West South Aegean Arc. Early melts extracted from the cumulates produce liquids comparable to the volcanic whole-rocks, but some samples show extensive post-cumulus crystallisation, and generation of evolved trapped liquids that may only interact during cumulate remobilisation episodes.

Together, these case studies demonstrate that xenoliths are powerful tracers of individual processes that define the complex geochemical signatures occuring at arc volcanoes. Although xenoliths may not be present in all volcanic deposits of all volcanoes, the understanding gained from studies such as this are applicable worldwide.

# Acknowledgements

I would first like to thank my supervisors, Ralf "Ralf 2" Halama and Ralf "Ralf 1" Gertisser for the opportunity to study this project, and pointing me back on the right direction when I went off track. Katie Preece, Valentin Troll and Frances Deegan are thanked for their great ideas that helped expand my work beyond my often quite pessimistic view. Hazel Beaumont's advice in my second year of "start writing now" definitely made these last few weeks less stressful, as did her advice in my undergrad as a demonstrator "save every paper to your computer, you might need it in 5 years". Rachel Butterworth, my partner throughout all this, is thanked for all the adventures outside of work: the mountain days, climbing, new tricks at the skatepark, handstands, gymnastics, and suffering through many of my poorly navigated ("it's only a small hill") bike rides. Don't let PhD work stop you enjoying what you love in life.

This work would not have been possible without the help of all of the often uncredited behind the scenes technical staff that keep everything working in the background. At Keele, I thank Peter Greatbatch and David Wilde for their expert and rapid thin section preparation, Dave Emley and Adam Jeffery for all things lab related (and Dave's lunchtime nature walks), Ian Wilshaw for keeping PhD finances in check, Rich Burgess for computer support, and Vladimir Zholobenko for Raman spectrometry and a belay partner while rock climbing. John Craven and Mike Hall at the University of Edinburgh for putting in significantly longer hours at the SIMS than I did as the user, Peter Appel and Barbera Mader at Kiel University for all things EMPA and ice cream when the machine died. Thor Hansteen and Matthias Frische at GEOMAR for LA-ICP-MS help, and Torsten Vennemann at the University of Lausanne for oxygen isotope analyses. And finally Hannah Woods and Rachel Butterworth for field assistance in Santorini.

I thank Keele for funding the PhD, and the VMSG and the KPA for additional conference funding. NERC is thanked for the grant to Ralf 1 for SIMS analysis.

I would also like to thank all the people who spend their free time making open source and free software for others to use, often for no financial reward. In no specific order, all of these projects have helped immensely in this project: R, R Studio, ggplot, bookdown, Pandoc, Inkscape, GIMP, Libreoffice, LaTeX, Jabref, Linux, Wine, Nvim, Nvim-R, Termux, Tabular and Okular (taking data easily from PDFs!), MELTS.

My final thanks go to everyone that has helped provide us all with inaccessible scientific literature. We cannot stand on the shoulders of giants when their knowledge is locked away.

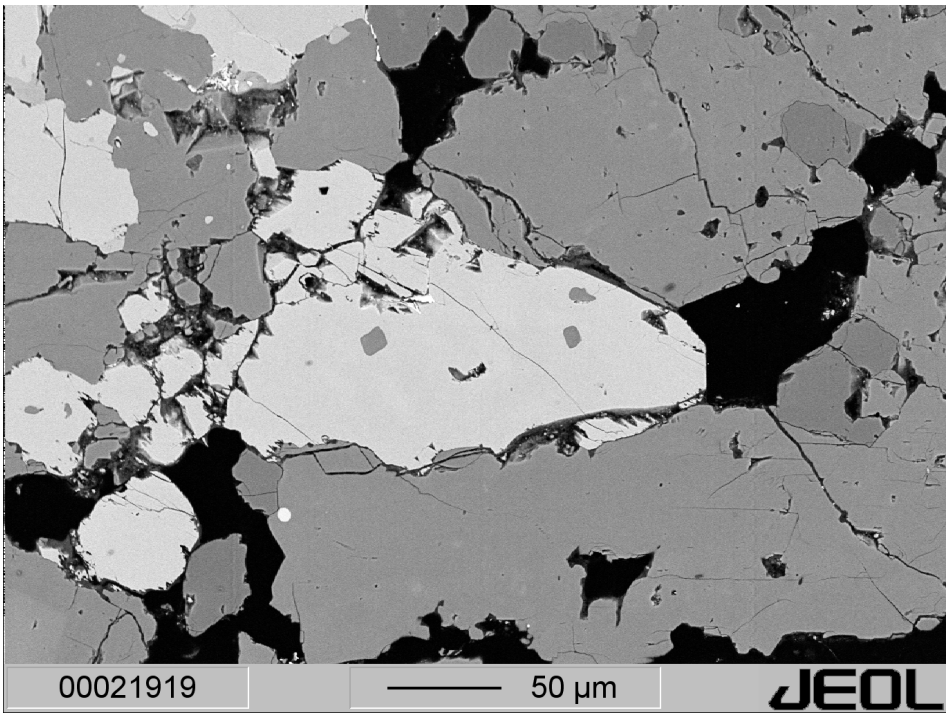


”Hey, you can do it!”

# Chapter 1

# Introduction

Arc magmas typically show distinct geochemical and petrographical evidence indicating a complex petrogenesis. The surface products represent a summation of the complex interplay of geodynamic magma generation processes, varied differentiation histories, and crustal assimilation. The formation of primitive arc magmas is generally regarded as being a result of partial melting of the mantle wedge with a contribution from slab dehydration (e.g. McBirney, 1969; Kushiro, 1990; Ulmer, 2001; Grove *et al.*, 2006, 2012). Silicic magma generation is generally now considered to be a deep crustal process involving fractionation and crustal partial melting, modified by further shallow level evolution (Hildreth and Moorbath, 1988; Annen *et al.*, 2006, 2015), with the geochemical trends influenced by 'cryptic' fractionation of phases such as amphibole and garnet at depth, which are not observed in the volcanic deposits (Cawthorn and O'Hara, 1976; Foden and Green, 1992; Davidson *et al.*, 2007; Alonso-Perez *et al.*, 2009; Smith, 2014). These arc magmas additionally carry a geochemical signature requiring involvement with continental crust (e.g. Arculus and Johnson, 1981; Pyle and Ivanovich, 1988; Thirlwall *et al.*, 1996; Davidson *et al.*, 2005). Two general models of magmatic contamination are commonly invoked: i) source contamination from the addition of subducted slab material to the mantle wedge (e.g. Hildreth and Moorbath, 1988; Davidson *et al.*, 1990; Ellam and Harmon, 1990; Gertisser and Keller, 2003a; Debaille *et al.*, 2006; Handley *et al.*, 2011), and ii) crustal contamination from assimilated crustal-derived material during magmatic ascent (e.g. DePaolo, 1981; Thompson *et al.*, 1984; Davidson, 1985; Thirlwall *et al.*, 1996; Annen *et al.*, 2006; Chadwick *et al.*, 2007).

Much of the published work about the petrogenesis of subduction magmas focuses on the lava flows, pyroclastics and intrusions, and pay relatively little attention to xenoliths, although

a near ubiquitous product of volcanic eruptions. Eruptive products generally preserve and place constraints on pre-eruptive magmatic conditions, and store radiogenic isotope evidence of mantle sources and geodynamics. Generally, little detailed evidence for the mechanisms of wall-rock interaction and plutonic processes are preserved. Geochemical and isotopic studies are commonly invoked using whole-rock xenolith compositions to give a general overview and quantify overall crustal assimilation (e.g. DePaolo, 1981). The detailed study of xenoliths however (e.g. Costa *et al.*, 2002; Chadwick *et al.*, 2007; Tollan *et al.*, 2012, 2015; Stamper *et al.*, 2014; Jolis *et al.*, 2015) can provide a unique insight and snapshot into the individual deep and shallow level magmatic processes that collectively form the distinct geochemical and petrological trends found in subduction settings.

The following section aims to highlight the role that detailed studies of xenoliths play in elucidating the processes relevant to magma formation in subduction zone settings, primarily focusing on two genetic classifications of xenoliths: crustal and cognate plutonic (cumulate), with specific references to localities in the South Aegean and Sunda arcs. Crustal xenoliths give insight into magma-crust interaction and the crustal structure of volcanic arcs, whilst cognate plutonic xenoliths give insight into the formation, fractionation history and evolution of magma during magmatic ascent from the mantle, and the subvolcanic crustal plumbing system through which the magma passes through. The following section outlines the geological settings of the two case study regions of the research project, and gives an overview of the value of studying xenoliths to understand the magmatic and intra-crustal processes occurring within subduction zones.

## 1.1 Volcanic and Tectonic Setting of the Sunda Arc and the South Aegean Volcanic Arc

### 1.1.1 South Aegean Active Volcanic Arc

The South Aegean Active Volcanic Arc (Hellenic Arc) is situated in the eastern Mediterranean Sea, and is a result of the 50-60mm $y^{-1}$ (Jackson, 1994) subduction of the African plate beneath the Aegean-Anatolian microplate, initiated ~13 Ma ago (Le Pichon and Angelier, 1979; Angelier *et al.*, 1982), with estimates extending to 16 Ma (Mercier *et al.*, 1989) (Figures 1.1, 1.2). Volcanism began in the late Pliocene (Pe-Piper *et al.*, 1983). The basement comprises late Palaeozoic/Mesozoic metapelites, metacarbonates, metabasites, metasediments, and granitoid intrusions of the Cycladic Crystalline Complex, overlying carboniferous pre-Alpine orthogneisses (Schliestedt *et al.*, 1987; Druitt *et al.*, 1999; Forster and Lister, 1999; Kilias *et al.*, 2013). The arc is considered (Pe-Piper and Piper, 2005) as comprising three distinct groups: Pliocene typical calc-alkaline andesites to dacites in the western-central sector of the arc (Aegina, Methana, Milos, early Santorini), mid to late Quaternary felsic products in the thinner, extended, central-eastern region (Milos, Santorini, Nisyros), and minor Pliocene to mid Quaternary 'marginal rhyolites' (Sousaki, Kos) restricted to the north-west and north-east margins of the arc respectively (Figure 1.1). At least three of these centres are considered active (Methana, Santorini, Nisyros), having had historic eruptions (Druitt *et al.*, 1999). Volcanic products of the arc range from basalt to rhyolite, chemically mildly tholeiitic to calc-alkaline with medium-high K contents (Druitt *et al.*, 1999). The three groups differ chemically; the variation is attributed to 'classical subduction' hydration melting of the mantle wedge and deep amphibole fractionation in the older western arc, a greater influence from an asthenospheric source in the younger eastern arc, and mid-crustal anatexis forming the minor rhyolites (Pe-Piper and Piper, 2005). Assimilation of crustal material is also observed across the arc, with Assimilation-Fractional Crystallisation (AFC DePaolo, 1981) modelling indicating assimilation to fractionation ratios of 0.1 to 0.2 throughout the arc (Pe-Piper and Piper, 2005).

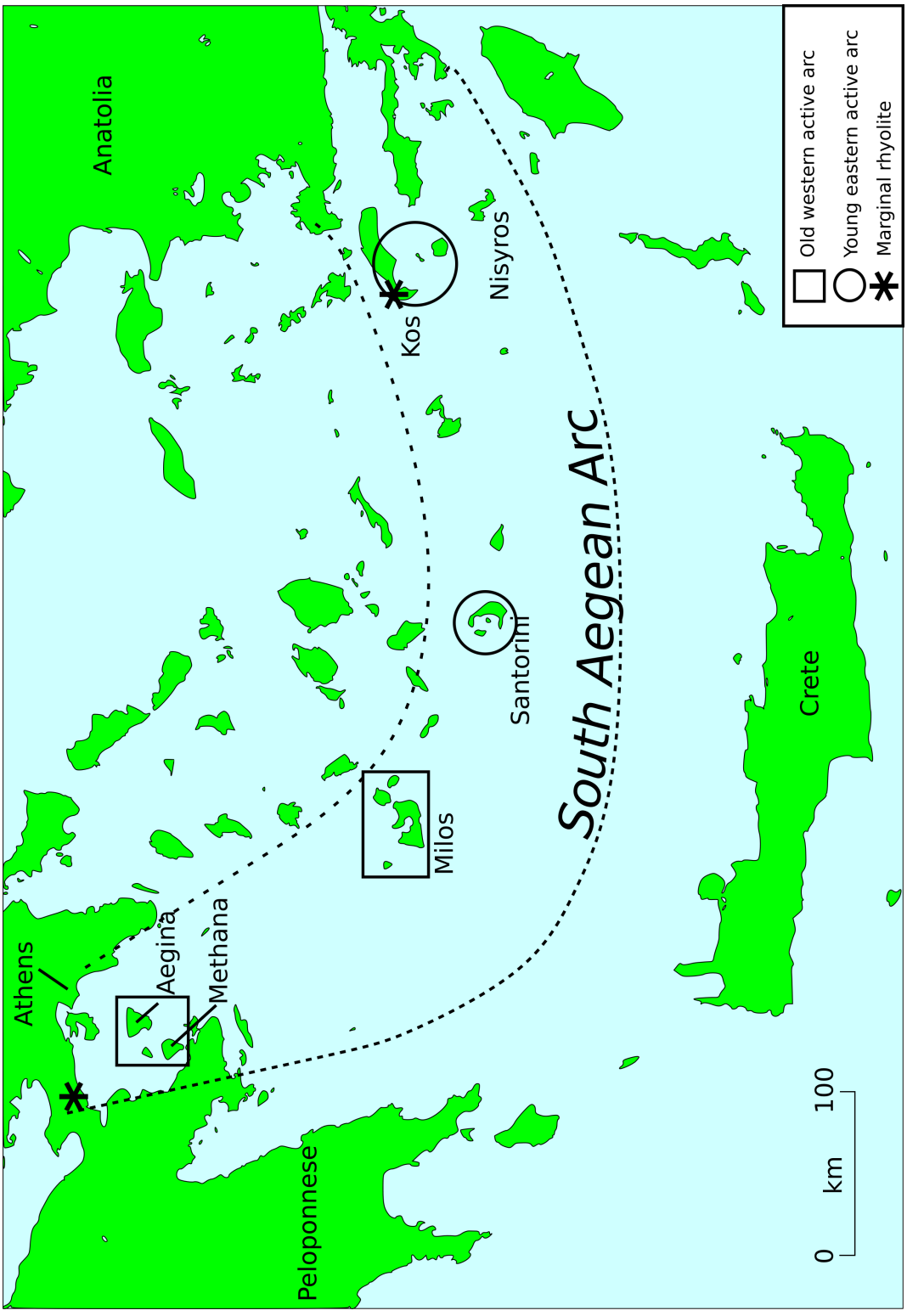


*Figure 1.1: Tectonic setting of the South Aegean Volcanic Arc showing the three groupings of volcanic centres (modified after Pe-Piper and Piper, 2005).*

Santorini is regarded as the most hazardous of the volcanic islands that comprise the South

Aegean volcanic arc. It consists of the three islands of Thera, Therasia and Aspronisi which mark the outline of a flooded caldera, and the Palaea Kameni and Nea Kameni islands situated within a flooded caldera (Figure 1.2). Pre-volcanic basement outcrops at Athinios and Mount Profitis Ilias on Thera, comprising blueschist-amphibolite grade meta-pelites, and crystalline limestones, respectively (Davis and Bastas, 1978; Skarpelis and Liati, 1990; Kilias *et al.*, 1998; Druitt *et al.*, 1999). Volcanic activity is strongly influenced by two NE-SW trending tectonic lineaments (the Kameni and Columbus lines) and began ~650 ka ago at the Akrotiri peninsula, producing amphibole-bearing silicic tuffs and lava flows (Druitt *et al.*, 1999). Twelve major plinian eruptions have occurred since ~360 Ka, occurring every ~20-30 ka, referred to as the Thera Pyroclastic Formation, of which at least four have led to caldera collapse (Druitt *et al.*, 1989, 1999; Druitt and Francaviglia, 1992). Two cycles of mafic to silicic magma evolution have been identified, each ending with significant caldera-forming eruptions: the Lower Pumice 2 and Minoan eruptions (Druitt *et al.*, 1999). Interplinian activity has included subplinian explosive activity, lava flows and extrusive edifice construction (Barton and Huijsmans, 1986; Druitt *et al.*, 1999; Vespa *et al.*, 2006; Vaggelli *et al.*, 2009). Chemically, the eruptive products of Santorini range from low- to high-K basalt to rhyodacite, with rare rhyolite, with $K_2O$ content increasing with evolution. Sr-Nd-Pb isotopic and trace element studies indicate varying contamination of Santorini magma with upper Aegean continental crust, at least some of the contamination having occurred in upper crustal reservoirs (Druitt *et al.*, 1999 and references therein). Magmatic differentiation occurs dominantly in mid to shallow level reservoirs, with little evidence for deep fractionation (Cottrell *et al.*, 1999; Druitt *et al.*, 1999, 2016; Gertisser *et al.*, 2009; Cadoux *et al.*, 2014; Andújar *et al.*, 2015, 2016).

The most recent 'Minoan' plinian eruption (Bond and Sparks, 1976; Druitt *et al.*, 1999; Druitt, 2014), $^{14}C$ dated ~1627-1600 BC (Friedrich *et al.*, 2006), is regarded to have important archaeological-environmental consequences (e.g. Luce, 1969; LaMoreaux, 1995; Pyle, 1997; Bruins *et al.*, 2008). The eruption volume has been considered to rival the 1815 eruption of Tambora (Indonesia) (Sigurdsson *et al.*, 2006), the largest known historical eruption, highlighting the importance of research into this eruption and the Santorini volcanic system. Studies

of this eruption have significance for modern day hazard assessments, notably recent diffusion profile modelling work across plagioclase phenocrysts showing that the silica-rich recharge event that triggered the Minoan eruption occurred very rapidly, within ~100 years before eruption, a significantly shorter time period than the 18 kyr period between the Minoan and the previous major caldera-forming eruption (Druitt *et al.*, 2012). Much recent research interest at Santorini has focused on the recent 2011 unrest which was not followed by an eruption (Parks *et al.*, 2012; Foumelis *et al.*, 2013; Konstantinou *et al.*, 2013; Gregg *et al.*, 2013; Saltogianni *et al.*, 2014; Browning *et al.*, 2015; Rizzo *et al.*, 2015).

Xenoliths have been long identified throughout the Santorini volcanic succession, both cumulates and calc-silicate assemblages (Fouqué, 1879; Lacroix, 1893, 1900, 1901; Kténas, 1927; Reck, 1936; Nicholls, 1971a, 1971b; Barton and Huijsmans, 1986; Druitt *et al.*, 1999; Mortazavi and Sparks, 2004; Martin *et al.*, 2006a, 2006b; Druitt, 2014), however, relatively little work has been focused on them. Xenoliths have highlighted a high $f_{O2}$ in recent lavas imposed by calc-silicate mineral breakdown (Nicholls, 1971b), magma replenishment in recent lavas (Martin *et al.*, 2006b), crustal assimilation (Druitt *et al.*, 1999), and potential cumulate remobilisation-entrainment (Gertisser *et al.*, 2009). These studies will be discussed in more detail in sections 1.4 and 1.3.

### 1.1.2 Sunda Arc

Volcanism across the Indonesian archipelago can be attributed to four principal subduction systems: the Sunda, Sangihe, Halmahera and Banda arcs (Hamilton, 1979). The Sunda arc extends 5600 km from the Andaman Islands in north-west Sumatra to the Banda arc in the east (Hamilton, 1979; Newcomb and McCann, 1987), and is a result of northward subduction of the Indo-Australian plate beneath the Eurasian plate at a rate of ~6cm $yr^{-1}$ beneath Sumatra and ~7cm $yr^{-1}$ beneath Java (Minster and Jordan, 1978; Hamilton, 1979; Jarrard, 1986; DeMets *et al.*, 1990; Tregoning *et al.*, 1994) (Figure 1.3). The age of the subducting oceanic plate varies between ~80 and 130 Ma from West to East Java respectively (Hamilton, 1979; Syracuse and Abers, 2006). The basement in Central Java is thought of as a Cretaceous imbricated

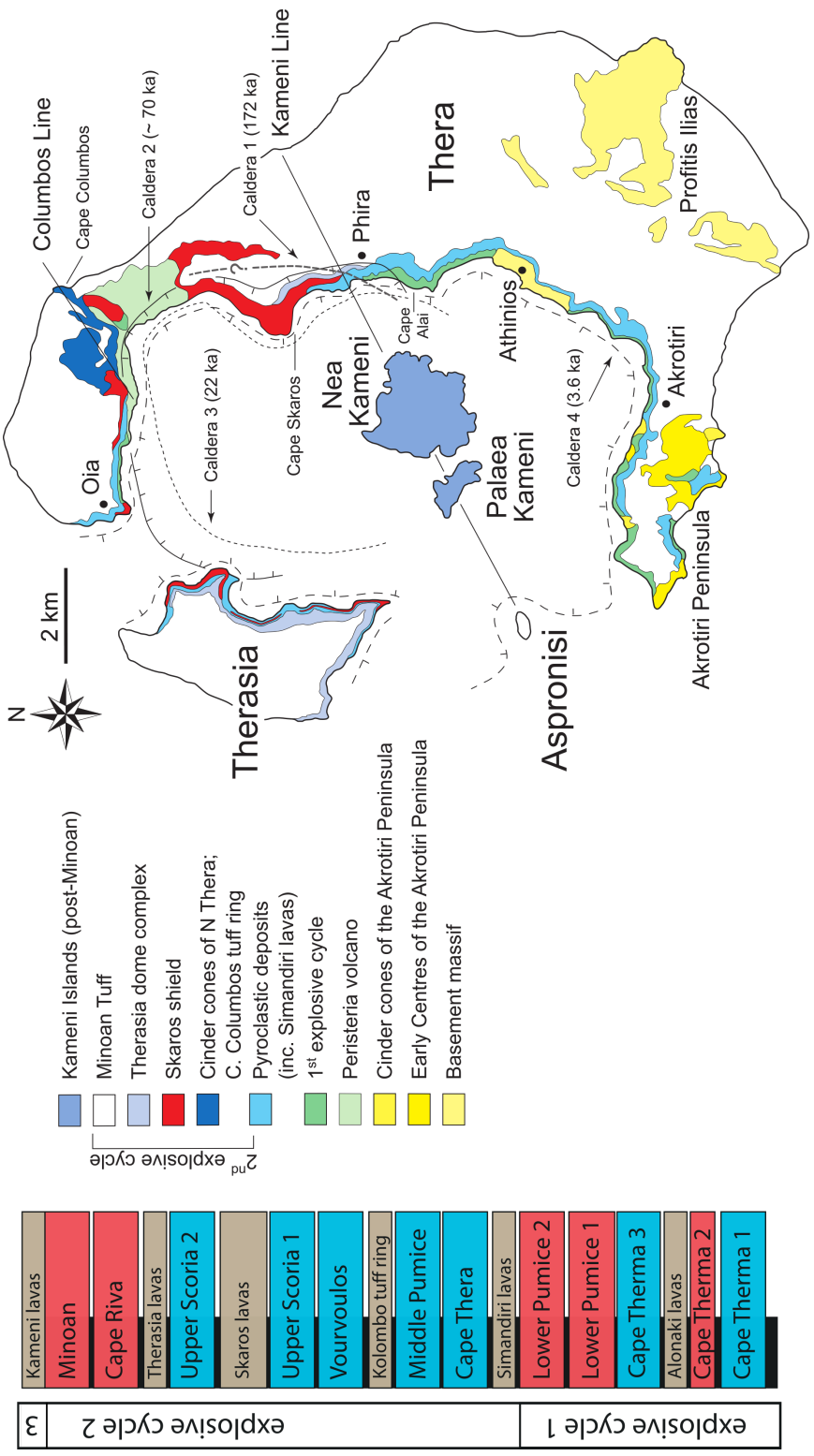


*Figure 1.2: Stratigraphy and geological map of Santorini. Straigraphic column after Druitt* et al. *(2016). Red eruptions in the stratigraphic column are dominantly silicic eruptions, and blue are intermediate in composition. Black boxes are interplinian deposits and brown boxes are prominent lava or tuff successions in the interplinian deposits (Vespa* et al.*, 2006; Druitt* et al.*, 2016).*

accretionary complex, known as the Lok Ulo Complex, which comprises ophiolitic and sedimentary rocks, crystalline schists and gneisses (van Bemmelen, 1949; Wakita and Bambang, 1994; Smyth *et al.*, 2005; Kadarusman *et al.*, 2007). Most exposed basement rocks on Java comprise Cenozoic volcanogenic turbidites and breccias, quartz-rich sandstones and limestone (van Bemmelen, 1949; Hamilton, 1979; Smyth *et al.*, 2005; Clements and Hall, 2007; Clements *et al.*, 2009).

The Sunda arc hosts numerous volcanoes, including Tambora, Kelut, Krakatau and Merapi. Of these, Merapi is considered one of Indonesia's most dangerous (Gertisser *et al.*, 2011). Merapi, situated in Central Java, overlies an upper crust of 8 km (Genevraye and Samuel, 1972) to 11 km (Untung *et al.*, 1978) thick sediments of the Kendeng basin; Cretaceous to Tertiary reworked volcaniclastic sediments are overlain by shallow marine limestones and marls, all of which overlie suspected Cretaceous arc/ophiolite basement material (van Bemmelen, 1949; Smyth *et al.*, 2005). Xenoliths of metamorphosed basement and plutonic material are abundant in Merapi lavas (Kerinec, 1982; Clocchiatti *et al.*, 1982; Camus *et al.*, 2000; Gertisser and Keller, 2003a; Chadwick *et al.*, 2007; Troll *et al.*, 2012, 2013). Recent eruptive activity is dome growth, with block-and-ash flows and associated ash fall, compositionally high-K basaltic-andesite in a restricted range between ~51-57 wt.% $SiO_2$ (Gertisser and Keller, 2003a, 2003b). Activity is near continuous, with periods of dome growth frequently interrupted by gravitational or explosive subplinian (VEI 1-4) dome collapse and associated pyroclastic density currents (Andreastuti *et al.*, 2000; Camus *et al.*, 2000; Newhall *et al.*, 2000; Voight *et al.*, 2000; Gertisser *et al.*, 2012; Surono *et al.*, 2012; Komorowski *et al.*, 2013).

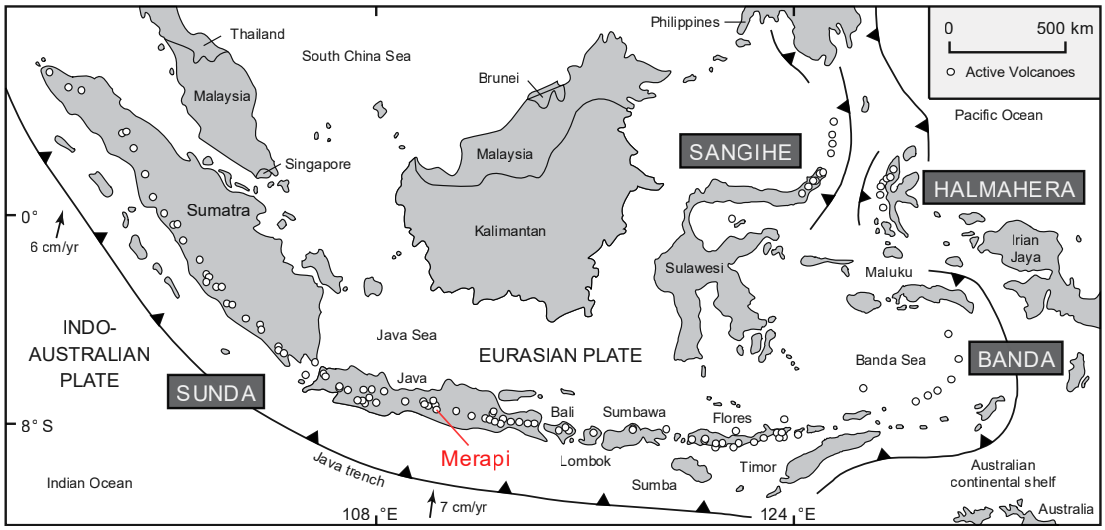


*Figure 1.3: Sunda Arc map and location of Merapi. After Gertisser and Keller (2003a)*

The recent 2010 eruption was the most explosive in over a century, killing over 400 people (Gertisser *et al.*, 2011; Surono *et al.*, 2012), prompting a special edition of the Journal of Volcanology and Geothermal Research (Vol. 261, 2013) dedicated to understanding the processes behind this and the previous explosive eruption of 2006. Whole-rock isotopic ratios indicate predominance of subducted continental material over crustal assimilation during magma genesis (Gertisser and Keller, 2003a), however much recent work has highlighted the role of crustal contamination, most notably the influence of carbonate assimilation on eruptive dynamics (Chadwick *et al.*, 2007; Troll *et al.*, 2012; Deegan *et al.*, 2010; Borisova *et al.*, 2013). Coupled with studies from Central Italy, the work on Merapi emphasises the role of carbonate assimilation on adding to the $CO_2$ budget and explosivity of volcanoes hosted within carbonate substratum (e.g. Freda *et al.*, 2008; Gaeta *et al.*, 2009; Mollo *et al.*, 2010b; Deegan *et al.*, 2010; Troll *et al.*, 2013; Jolis *et al.*, 2013, 2015). In the case of Merapi, the influence of assimilation of crustal carbonate is thought to have caused an increase in eruptive intensity of the 2006 eruption by a factor of 3 to 5 (Troll *et al.*, 2012). This also potentially played a role in influencing the explosivity of the 2010 eruption (Borisova *et al.*, 2013), although this is contested (Costa *et al.*, 2013; Handley *et al.*, 2018), highlighting the necessity of increasing our understanding of magma-crust interaction in these carbonate hosted magmatic systems.

## 1.2 Xenolith Formation and Assimilation dynamics

Xenoliths represent fragments of thermomechanically eroded magma chamber wall-rock, conduits, or surface material entrained in erupted materials during emplacement. This erosion occurs via two end-member processes: (1) thermal erosion, in which melting (partial or complete) causes disaggregation, and assimilation of country rock occurs due to magmatic heat (Furlong and Myers, 1985; Kerr, 2001), and (2) mechanical erosion, in which country rock is abrasively removed and entrained via brittle deformation, crack propagation, fragmentation and/or magma-water interaction (Macedonio *et al.*, 1994; Rubin, 1995; Valentine and Groves, 1996; Del Gaudio and Ventura, 2008). The types of crustal lithologies that can become entrained in magma is strongly dependent on the mechanical properties (tensile strength) of the specific crustal lithologies and also that of the magma (strain rate, crystalinity-viscosity), and therefore may not be representative of the substratum stratigraphy (Del Gaudio and Ventura, 2008). A basalt has higher potential to erode poor quality country rocks (such as volcaniclastic rocks compared to gneisses) whilst a crystal-rich magma has a higher potential to fragment conduit walls, which for example at Salina, Italy, causes a strong bias towards volcanic xenoliths over basement rocks (Del Gaudio and Ventura, 2008).

Once entrained, the host magma will generally be at a higher temperature than the solidus of the xenolith, therefore causing melting and subsequent assimilation into the host magma. Melting rates are rapid, with 0.1-2mm $h^{-1}$ predicted for typical continental crustal lithologies, faster for mafic and water saturated lithologies (Watson, 1982; McLeod and Sparks, 1998; Shaw, 2000), and up to 17 mm $h^{-1}$ for mafic-granulite lithologies in the lower crust (McLeod and Sparks, 1998). The assimilation of carbonate lithologies in magmatic melts has been shown experimentally to occur very rapidly, with carbonate lithologies within the experimental capsules being fully assimilated within minutes (Deegan *et al.*, 2010; Jolis *et al.*, 2013). These rapid rates suggest that xenoliths can only be preserved in rapidly chilled intrusion margins and during rapid eruptions that do not allow time for complete xenolith melting (McLeod and Sparks, 1998). Xenoliths that preserve evidence of partial melting are not uncommon

(e.g. Grapes, 1986; Grove *et al.*, 1988; Zanon and Nikogosian, 2004; Shaw, 2009; McGee *et al.*, 2015). Melts derived from xenoliths are generally not homogeneous in composition, as melting commonly occurs via preferential disequilibrium melting of low temperature phases, and can result in varied contamination of the host magma, sometimes within a single suite of xenoliths (e.g. Watson, 1982; Grove *et al.*, 1988; Peccerillo and Wu, 1992; Markl, 2005; Forni *et al.*, 2015; McGee *et al.*, 2015).

Costa and Dungan (2005) modelled assimilation of partially disaggregated mafic cumulate xenoliths and additionally propose that assimilation is rapid. They note that melting and assimilation rates which are in the order of years to decades (Dungan, 2005), exceed the rate of magma transport time through the crust, which is shorter than the repose period of arc volcanoes (Costa and Dungan, 2005), adding support to theory of crustal partial melting and assimilation influencing arc magmatic geochemical signatures. Partial disaggregation of xenoliths has been shown (McLeod and Sparks, 1998) to occur due to non-eutectic partial melting of xenoliths, forming a mush layer on the xenolith surface that can disaggregate and efficiently form xenocrysts. Disaggregation has been proposed (Clarke *et al.*, 1998; Beard *et al.*, 2005) as a model for bulk assimilation, due to the large energy constraints needed for full dissolution (Bowen, 1922; Beard *et al.*, 2005; Glazner, 2007). Partial melting (aided by dehydration melting of hydrous phases) physically weakens the xenolith, causing mixing of xenolithic melt and crystals into the host magma. Incongruent hydration crystallisation reactions (Beard *et al.*, 2004) then occur between phenocrysts and xenocrysts, forming amphiboles and micas, destroying previously preserved evidence for mixing (Beard *et al.*, 2005). Unless recharge processes buffer the magma at a constant thermal energy, the latent heat of fusion reduces the temperature of the magma, driving crystallisation. The amount of crystallisation can be significant, dramatically increasing the crystallinity and viscosity of the magma. This, coupled with the decrease in thermal energy of the magma, self-limits the assimilation of further material to a few tens of percent, suggesting that magma mixing may be a more significant mechanism for large scale magmatic contamination than crustal assimilation (Glazner, 2007).

Xenoliths that evade full dissolution or disaggregation into the host magma commonly show

evidence of thermal alteration and contact metamorphism, coined 'pyrometamorphism' when occurring at very high (magmatic) temperatures in shallow, low pressure conditions, producing 'sanidinite' facies assemblages (Brauns, 1912a, 1912b; Tyrrell, 1926; Grapes, 2010). The core of a 2 metre thick marble xenolith has been shown to reach near magmatic temperatures within a few weeks (Lovering, 1937), and weeks to months for a 4 m diameter sphere or infinite slab metabasaltic xenolith (Brandriss *et al.*, 1996), implying the (pyro)metamorphic xenolithic mineral assemblages can equal magmatic temperatures (Grapes, 2010). Specific examples of thermally altered xenoliths will be discussed with their implications in the following sections.

Many numerical, geochemical and thermodynamical methods have been developed to aid quantification and modelling of magmatic evolution processes, including the influence of assimilation, such as linear least squares mass balance (Bryan *et al.*, 1969; Stormer and Nicholls, 1978), assimilation-fractional crystallisation (AFC DePaolo (1981); Aitcheson and Forrest (1994)], MELTS thermodynamical software (Ghiorso and Sack, 1995; Asimow and Ghiorso, 1998; Gualda *et al.*, 2012), and Energy-Constrained Assimilation Fractional Crystallisation (EC-AFC Spera and Bohrson (2001)]. EC-AFC is an advancement of the AFC model of DePaolo (1981) and takes into account the thermodynamical energy constraints on partial melting and assimilation.

## 1.3 Plutonic xenoliths

This thesis considers plutonic xenoliths to be fragments of coarse grained igneous material co-egenetic to the current magmatic system, generally considered cumulates (the instantaneous solid material Morse, 1976) or complete crystallisation of a volume of magma (total solid composition, Morse, 1976). Plutonic mafic and ultramafic cumulate rocks are found in many arc volcanic rocks (e.g. Arculus and Wills, 1980; Beard, 1986; Costa *et al.*, 2002; Laiolo and Cigolini, 2006; Troll *et al.*, 2013; Stamper *et al.*, 2014), and preserve evidence of differentiation histories, magmatic ascent, and crustal structure that cannot be directly observed in extrusive rocks. Beard (1986) proposed a generalised classification of cumulate xenolith suites found in arcs: Type 1 suites consisting primarily of olivine gabbro, subordinate olivine and clinopyroxene rich ultramafic rocks, and olivine-free gabbronorite, type 2 suites lacking coexisting olivine and

plagioclase, dominated by olivine-bearing ultramafic rocks and olivine-free gabbronorite, and type 3 suites, where amphibole is a cumulus phase, comprising of hornblende olivine gabbro, hornblende gabbro and amphibole-rich ultramafic rocks. Beard (1986) additionally highlighted the association of calcic $An_{85\text{-}100}$ plagioclase and moderately Fe-rich $Fo_{60\text{-}80}$ olivine as being distinctive of arc settings, attributed to higher water contents of arc magmas suppressing the plagioclase solid solution (e.g. Arculus and Wills, 1980; Sisson and Grove, 1993; Müntener *et al.*, 2001; Tollan *et al.*, 2012; Stamper *et al.*, 2014).

The term 'cumulate' has provoked debate since the nomenclature was proposed by Wager *et al.* (1960). Cumulate textures were originally attributed to density-controlled crystal settling, an accumulation of crystals (Wager *et al.*, 1960; Jackson, 1967). Work has since argued against this (Bottinga and Weill, 1970; Campbell, 1978; McBirney and Noyes, 1979), favouring in-situ crystallisation (Jackson, 1961; McBirney and Noyes, 1979) over crystal settling. Irvine (1982) proposed that the original cumulate nomenclature is still valuable if the genetic connotation is disregarded, and cumulates are simply to be regarded as igneous rocks comprising a framework of touching mineral crystals, concentrated via fractional crystallisation. Processes such as textural re-equilibration, recrystallisation, compaction and mineral reactions can affect the cumulate pile after mineral precipitation (e.g. Sparks *et al.*, 1985; Hunter, 1996; Holness *et al.*, 2005a), further emphasising that a detailed study of cumulate textures are required before any genetic process for formation can be implied. This project will consider cumulates as proposed by Irvine (1982) and Hunter (1996), as a textural description, with no implication of a genetic process.

### 1.3.1 Fractionation History and Crustal Formation

The continental crust is considered to be formed of a felsic upper crust overlying a dominantly mafic lower crust (Christensen and Mooney, 1995; Ducea *et al.*, 2003; Rudnick and Gao, 2003); a density contrast thought by early workers to influence melt stagnation and evolution via neutral buoyancy (Herzberg *et al.*, 1983; Ryan, 1987; Glazner and Ussler, 1988). Andesites and dacites form a significant proportion of the products of convergent arc magmatism, however

the processes that form compositionally intermediate bulk continental crust is widely debated (e.g. Gill, 1981; Hildreth and Moorbath, 1988; Rudnick and Fountain, 1995; Annen *et al.*, 2006; Blatter *et al.*, 2017; Klaver *et al.*, 2018). Cumulates, and cognate plutonic xenoliths thereof, are found in several arc settings (Beard, 1986) and have been long considered evidence for crystal fractionation as a process for formation of more silicic melts in subduction settings (e.g. Stern, 1979), predominantly thought of as a shallow crustal process (e.g. Glazner, 1994). Recent work (e.g. Annen *et al.*, 2006, 2015; Jagoutz, 2014; Cashman *et al.*, 2017) has proposed an alternative model, in which differentiation occurs primarily in 'deep crustal hot zones', to explain the lack of observed shallow level crustal mafic cumulates that should form contemporaneously with voluminous silicic melts. This model proposes a succession of lower crustal emplaced sills generating a hot zone where partial crystallisation and anatexis of crustal rocks produces characteristic $H_2O$-rich differentiated melts. These melts then ascend and can undergo multiple stages of evolution at different stages throughout the crust (Cashman *et al.*, 2017)

Cumulate xenoliths indicate an important role of fractionation of certain phases at depth, specifically amphibole, in controlling the liquid line of descent and subsequently producing the calc-alkaline differentiation trend and andesitic magmatic compositions characteristic of arcs. Compared to the relative abundance in cumulate xenoliths in volcanic suites, amphibole is found in lesser modal abundance in arc lavas (e.g. Arculus and Wills, 1980; Costa *et al.*, 2002) leading to hypotheses of fractionation of amphibole at depth ('cryptic fractionation') and the 'amphibole sponge', where these deep hydrous cumulates can create a potential water reservoir (Davidson *et al.*, 2007; Smith, 2014). Coupled with the xenolithic and exposed batholithic cumulate evidence for deep amphibole fractionation, arc magmas commonly show rare earth element patterns consistent with amphibole fractionation (increasing La/Yb and decreasing Dy/Yb with evolution). The lower $SiO_2$ concentration in amphibole compared to basalt allows basaltic compositions to evolve to andesitic with fractionation of a lower crustal cumulate assemblage of amphibole, clinopyroxene, plagiclase and olivine, or by mixing of basalt with a fractionated silicic end member (Foden and Green, 1992; Davidson *et al.*, 2007; Otamendi *et al.*, 2016; Klaver *et al.*, 2018). This is in accordance with experimental studies showing amphibole

as a crystallising phase in arc magmas, with stability favoured at higher pressures over garnet with increased $H_2O$ content in the melt (e.g. Foden and Green, 1992; Sisson and Grove, 1993; Alonso-Perez *et al.*, 2009).

Detailed studies of cumulate xenoliths can highlight the role of amphibole fractionation in arc magma generation. Amphibole itself can be used as a geothermobarometer, such as the amphibole-plagioclase geothermometer of Holland and Blundy (1994) and amphibole geothermobarometers of Ridolfi and Renzulli (2012) and Putirka (2016). Hydrogen in plagioclase and plagioclase-melt equilibria can indicate the water content of the melt (Housh and Luhr, 1991; Putirka, 2008; Lange *et al.*, 2009; Hamada *et al.*, 2013; Waters and Lange, 2015) and many clinopyroxene thermobarometers are known (e.g. Nimis, 1995, 1999; Nimis and Ulmer, 1998; Putirka, 2008; Neave and Putirka, 2017). Geothermometric and geohygrometric calculations applied to the amphibole-bearing xenoliths and cognate silicic host lavas at Akrotiri, Santorini coupled with geochemistry and petrology indicate a multistage magma genesis for these early deposits (Mortazavi and Sparks, 2004). Hydrous mantle derived partial melts stalled in the lower crust and fractionated olivine, spinel and clinopyroxene, and late stage plagioclase and amphibole to form cooler wet basaltic melts. Low Y, MREE and HREE in the silicic rocks indicate amphibole fractionation in the lower crust played a major role in their genesis. Silicic melts ascended and were later remobilised by wet mafic melts in the upper crust, evidenced by mingling and quench textures in the xenoliths. Mass balance calculations using the gabbroic xenoliths and lava compositions post-Akrotiri Santorini deposits indicate that crystal fractionation in shallow chambers plays a more dominant role in the genesis of younger magmas at Santorini (Druitt *et al.*, 1999). The presence of and textural studies of amphibole-rich xenoliths at Merapi point to deep (>11 km, potentially 35 km) crystallisation and fractionation of clinopyroxene, plagioclase and amphibole. These melts then rise to shallower levels and experience magma mixing, fractionation and crustal assimilation (van der Zwan *et al.*, 2013). Chemically, the basaltic-andesite compositions erupted at Merapi have been attributed to amphibole fractionation (Chadwick *et al.*, 2010). Amphibole fractionation is observed worldwide, for example the Washington Cascades (Dessimoz *et al.*, 2012), Tibet (Xu *et al.*, 2015), Sunda

arc (Foden and Green, 1992; Chadwick *et al.*, 2010) Andes (Costa *et al.*, 2002; Otamendi *et al.*, 2016), Aegean (Elburg *et al.*, 2014; Klaver *et al.*, 2017, 2018), and Japan (Tiepolo *et al.*, 2012). Xu *et al.* (2015) studied the intrusive gabbroic rocks of the Gangdese belt, Tibet and highlighted the role of amphibole fractionation from geochemistry, outcrop and amphibole-rich xenolith evidence, and additionally that amphibole fractionation may have driven magmatic compositions towards adakite-like signatures ($>$ 56 wt. % $SiO_2$, high Sr/Y and La/Yb). This supports previous workers proposing a fractionation dominated adakite petrogenesis over slab derived partial melts (see review by Castillo, 2012)

The mechanism of amphibole fractionation has been studied using xenoliths, showing that fractionation can occur as the result of cumulus-melt interaction at depth, not traditional crystal precipitation and fractionation. Costa *et al.* (2002) showed that magmatic differentiation trends observed and amphiboles with high-$Cr_2O_3$ concentration found in Andean gabbroic xenoliths are not a result of early amphibole crystallisation, but later multistage reactions between melt and olivine, Cr-spinel, pyroxenes or plagioclase, forming substantial quantities of and fractionation of amphibole. A study of the cumulate xenoliths and lava phenocrysts from Savo volcano, Solomon Islands (Smith, 2014), show clinopyroxene-hornblende reaction-replacement textures in the xenoliths and trace element evidence of amphibole fractionation in the lavas, showing 'cryptic' decoupling of deep clinopyroxene-amphibole replacement-fractionation in the lower crustal 'hot zones' and production of largely crystal-free andesitic melt. Otamendi *et al.* (2016) further demonstrated the formation of amphibole via melt - olivine+plagioclase±orthopyroxene cumulate reaction in the Famatinian Arc, Andes. The silica content of melts extracted from these 'hot zones' are a function of the amount of amphibole formed, and form a silicic mixing endmember for production of intermediate arc magmas (Klaver *et al.*, 2018).

Plutonic xenoliths additionally give insight into shallow level differentiation processes. Pressure estimates based on P-$H_2O$ ranges that cumulate xenolith plagioclase compositions observed at St. Vincent (Lesser Antilles) would be in equilibrium with hornblende-hosted melt inclusions indicate shallow level (170 MPa, $<\tilde{}$ 7 km) differentiation (Tollan *et al.*, 2012). A primitive melt fractionating olivine + Cr spinel ± clinopyroxene produces hydrous $Al_2O_3$ and CaO-rich

melts, which ascend into the lower crust. $H_2O$ saturation during ascent leads to precipitation of plagioclase, resulting in the high $An_{86\text{-}96}$ plagioclase and low $Fo_{70\text{-}80}$ olivine characteristic of arcs, followed by later precipitation of hornblende ± clinopyroxene after further cooling (Tollan *et al.*, 2012). Parental magma varies laterally in the Lesser Antilles arc, and is expressed in plutonic xenoliths from Grenada, 140km south-west of St. Vincent. A higher melt $H_2O$ content (~7 wt.%) is inferred due to later stage plagioclase saturation than observed at St. Vincent, and small fluctuations in source chemistry and storage conditions impose distinct chemical and mineralogical variations within the xenolith suite (Stamper *et al.*, 2014). Cumulates at Grenada formed deeper than at St. Vincent (200-500 MPa, ~8-20 km), a result of thickened oceanic lithosphere due to Grenada's proximity to the South American continental margin (Stamper *et al.*, 2014).

### 1.3.2 Remobilisation

The generation of generally aphyric silicic melts in the absence of abundant erupted andesite has received attention in the recent literature, and a crystal mush extraction model has been proposed (Bachmann and Bergantz, 2004; Hildreth, 2004) as an alternative to evolution dominated by assimilation and fractional crystallisation. This model proposes that intermediate composition magmas evolve and crystallise, producing rhyolitic interstitial melts within a forming crystal mush. At around 50% crystallinity the crystal mush-liquid system starts behaving as a solid framework, impeding convection and turnover (Marsh, 1981, 1988a; Vigneresse *et al.*, 1996). At these intermediate crystallinities, aphyric rhyolitic melt can escape the interstitial porosity (such as assisted by a viscosity decrease in the presence of volatiles: e.g. Sisson and Bacon, 1999; Pistone *et al.*, 2015) and accumulate above the crystal mush, where it can eventually erupt. This model has been shown to not fit all rhyolitic volcanic suites (e.g. Streck, 2014). Petrological and geochemical evidence from both lavas and xenoliths from many regions worldwide have recently highlighted the role of cumulate melting and remobilisation as an important process in silicic melt generation (Macdonald *et al.*, 2008; Deering *et al.*, 2011; Pamukcu *et al.*, 2013; Bachmann *et al.*, 2014; Ellis *et al.*, 2014; Sliwinski *et al.*, 2015; Wolff *et al.*, 2015). The

majority of these studies are focused on large zoned continental ignimbrites, but this process has also been identified in arc setting from xenolithic and enclave evidence. Cumulate fragments in the rhyolites from Lipari show resorption of low-temperature phases (biotite and sanidine), reacted Fo-rich olivine, and strong Sr and Ba enrichment in plagioclase, interpreted as evidence for mafic recharge into the crystal mush (Forni *et al.*, 2015). Approximately ~60% fractionation from intermediate compositions leaves a cumulate mush, which is partially resorbed following mafic injection. Melts then locally enriched in K, Sr, and Ba recrystalise to form Sr-Ba enriched plagioclase and impose a high $K_2O$ concentration on the enclaves (Forni *et al.*, 2015). Similar cumulates found in the rhyolites from Vulcano lead Forni *et al.* (2015) to propose cumulate remobilisation may be common process across the Aeolian Islands. At a larger, arc wide scale, cumulate remobilisation has been identified in a few studies as influencing the chemical characteristics of arc magmas, in particular the assimilation of the amphibole-rich cumulates in the lower arc crust (formation of such cumulates is discussed in the previous section). Partial assimilation and recycling of the plutonic roots of the Tatara-San Pedro complex, Andes, is proposed to explain the variable isotopic and trace element signatures, and the presence of cumulate microxenoliths within the lavas that are inconsistent with assimilation of continental crust (Dungan and Davidson, 2004). Davidson *et al.* (2007) propose that amphibole-bearing cumulate recycling may act as a 'sponge', allowing large amounts of fluid to be liberated, enhancing crustal melting, and metal solute transport enabling the formation of ore deposits. Other examples of cumulate recycling and remobilisation affecting the arc magmatic evolution are found in Japan (Tiepolo *et al.*, 2012), and Papua New Guinea (Zhang *et al.*, 2015).

### 1.3.3 Textural History and Post-Cumulus Processes

Detailed studies of textures and dihedral angles at clinopyroxene-clinopyroxene-plagioclase grain boundaries can give insights into the late stage evolution and thermal history of cumulates. Crystallisation of the residual pore material can lie between two distinguishable end-members: impingement (crystal face growth) and textural equilibrium (minimisation of internal energies) (Holness *et al.*, 2005a). Recognition of these textures have been used on the cumulates of

the Rum Layered Intrusion to distinguish between units formed by crystal accumulation, units intruded by picritic sills, and replenishment events (Holness *et al.*, 2005b, 2007), and with the mafic enclaves in the Kameni lavas of Santorini to recognise texturally the role of $H_2O$ in replenishment eruption dynamics (Holness *et al.*, 2005b), and high permeability in near solidified crystal mushes (Holness *et al.*, 2007).

Crystal size distribution (CSD) analysis uses the profiles of density distributions of binned crystal size populations to infer crystallisation histories, including nucleation and growth rates, kinetic processes and physical processes such as fractionation, accumulation and mixing (Marsh, 1988b, 1998; Higgins, 2000, 2006). Application of CSD theory to the mafic enclaves in the Kameni lavas of Santorini elicited the reconstruction of the magmatic system beneath Santorini during 1925 and 1950, evidence for which is not preserved in the lavas (Martin *et al.*, 2006a). Filter pressed (interstitial liquid release by pressure) andesitic liquids derived from a crystal mush replenished the chamber several times, and some of these liquids entrained and recycled older crystal populations.

Crystallisation of magma produces boundary layers of varying crystallinity. At 25-50 % crystallinity, the mush stage, residual melt can escape, producing silica-rich melts (Marsh, 1996). At the critical crystallinity of ~50% crystals (Marsh, 1981, 1988a, 1996; Vigneresse *et al.*, 1996), it locks up and melt is unable to escape. In the absence of remobilisation, this can continue to crystallise in an essentially closed system. These trapped melt pockets will exhibit extreme post-cumulus fractional crystallisation and incompatible element enrichment influencing the mineral compositions (e.g. Bédard, 1994; Bernstein, 2006; Borghini and Rampone, 2007; Krause *et al.*, 2007). This melt can also re-equilibrate with the cumulus mineral phases, making reconstruction of original magmatic mineral compositions more difficult (Barnes, 1986; Bédard, 1994). Reconstruction can also be complicated when the system is not a closed system, such as during remobilisation, or in the presence of an infiltrative fluid flux that can modifying the cumulate chemistry (Borghini and Rampone, 2007). This highlights the complexity of cumulate processes and care that must be taken when studying these rocks.

### 1.3.4 Plutonic Xenoliths Summary

Plutonic xenoliths preserve detailed information regarding the processes responsible for the petrogenesis of primitive magmas and subsequent silicic magma generation in arc systems. The role of high water contents and amphibole fractionation on influencing the distinctive arc magma compositions has been demonstrated. Geothermobarometry of common cumulus phases is a powerful tool for placing constraints on magmatic conditions during magma genesis. Infiltration into and remobilisation of the cumulate pile has recently been demonstrated to have an important role in the generation of silicic magmas. Textural studies can further help constrain the processes occurring within the cumulate pile of magmatic systems.

## 1.4 Crustal xenoliths

Crustal xenoliths are fragments of country rock entrained in magmatic flow. They can comprise any crustal lithology, and in this thesis we consider crustal xenoliths to be dominantly comprising upper crustal sedimentary lithologies. These lithologies are often overprinted with a thermal metamorphic assemblage which can preserve evidence for many magmatic processes, discussed in this section.

### 1.4.1 Carbonate: Skarns and Assimilation

Several notable volcanic systems lie within carbonate substratum, for example Merapi in Indonesia (e.g. van Bemmelen, 1949; Allard, 1983; Chadwick *et al.*, 2007; Troll *et al.*, 2012), Vesuvius, Etna and the Alban Hills in Italy (e.g. Scacchi, 1887; Zambonini, 1910; Rittmann, 1933; Clocchiatti *et al.*, 1986; Michaud, 1995; Fulignati *et al.*, 2004; Gaeta *et al.*, 2009; Jolis *et al.*, 2015), Popocatépetl in Mexico (e.g. Goff *et al.*, 2001), Nisyros in Greece (Spandler *et al.*, 2012), Lascar in Chile (Matthews *et al.*, 1996) and Yellowstone in the USA (e.g. Werner and Brantley, 2003). The role of carbonate assimilation in producing pronounced geochemical trends, adding to the global $CO_2$ budget, and influencing eruptive explosivity via volatile exsolution has received a large amount of attention within the past decade, and will be discussed in this section.

**Metamorphic reactions**

Metamorphism of carbonate country rock or a xenolith by magma produces a characteristic Ca-Fe-Mg-rich calc-silicate metamorphic phase assemblage. These 'skarn' rocks can be classified by metasomatic reactions within the carbonate wall-rock (exoskarn) or rocks formed by melt-carbonate wall-rock interaction processes such as diffusion and carbonate assimilation (endoskarn). Phase assemblages and zoning produced during thermal metamorphism vary based on the carbonate protolith composition, extent of Mg, Al and alkali diffusion and/or infiltration from the magma to form mono/multimineralic zones (Thompson, 1959; Korzhiniskii, 1970; Kerrick, 1977), metamorphic P-T conditions, and $X_{CO2}$ of the fluid (e.g. Figure 1.4). Examples of mineral phases found in skarns at magmatic temperatures are shown in Figure 1.5.

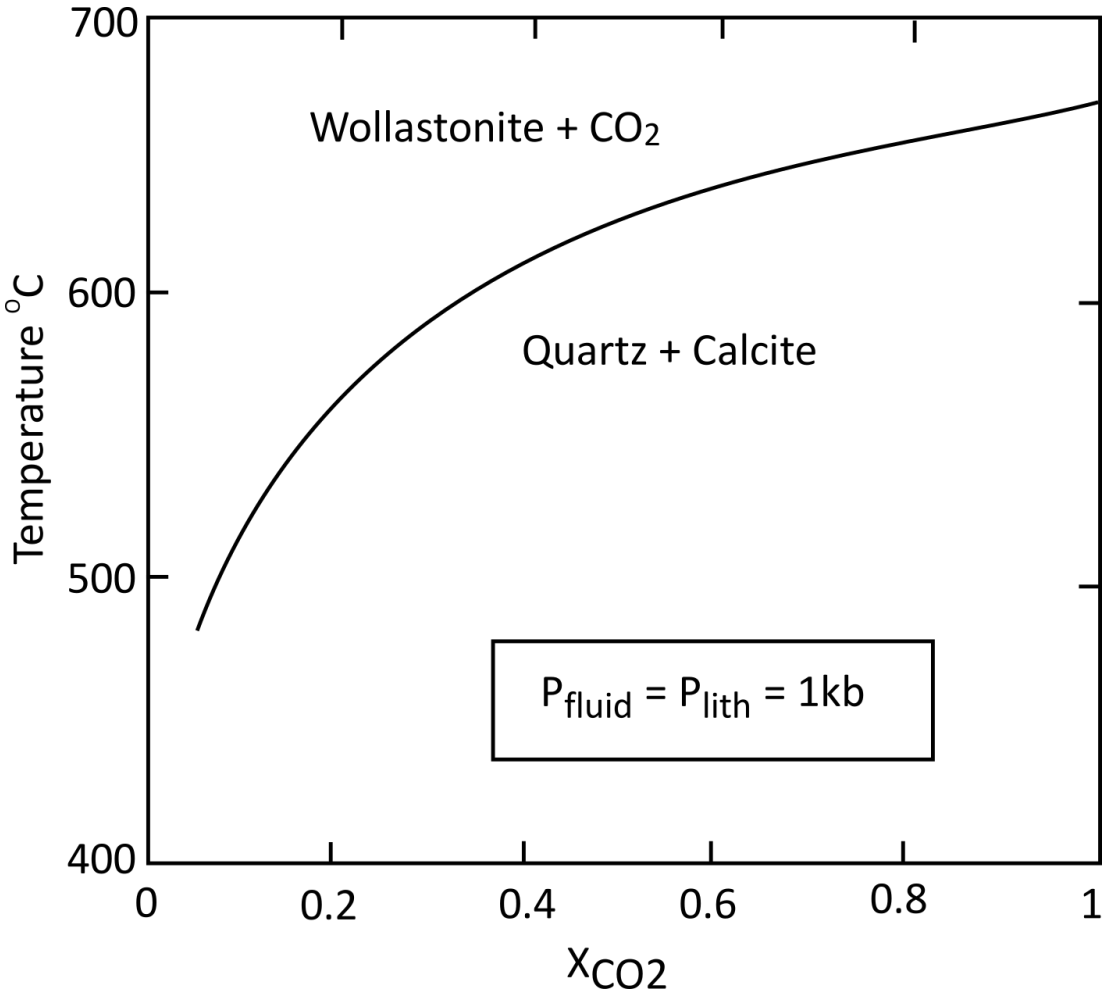


*Figure 1.4: Fluid composition ($CO_2$ - $H_2O$) influence on reaction temperature (after Greenwood, 1967).*

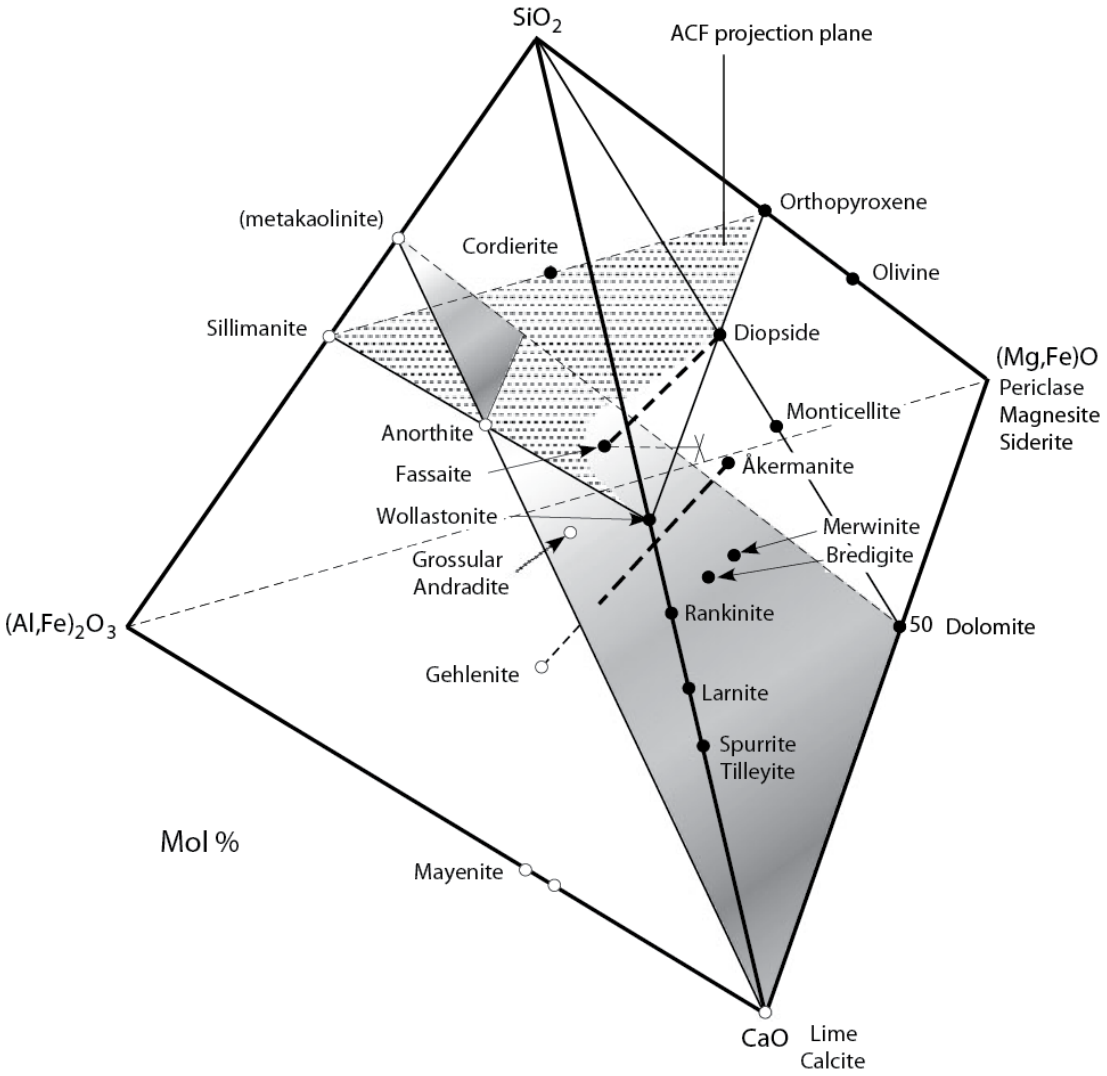


*Figure 1.5: Calc-silicate phases found in metamorphosed carbonate sediments (after Grapes, 2010)*

$H_2O$ is significantly more soluble than $CO_2$ in magma (Burnham, 1979; Holloway and Blank, 1994; Botcharnikov *et al.*, 2005), therefore any additional $CO_2$ release from decarbonation reactions will not be incorporated into the magma, and instead will increase the $X_{CO2}$ of the fluid phase, influencing the phase assemblages formed. For example, the temperature of wollastonite formation is strongly controlled by the $X_{CO2}$ during the decarbonation reaction: calcite + quartz -> wollastonite + carbon dioxide (Figure 1.4). The partial pressure of $CO_2$ formed during the decarbonation reaction being usually higher than that of the magmatic fluid, coupled with rapid degassing and volume loss from $CO_2$ release, generally inhibits magmatic $H_2O$ infiltration and retrograde assemblage formation. However, a lag between volatile loss and compaction, or $H_2O$

infiltration through cracks can form retrograde assemblages in calc-silicate skarns and xenoliths (Grapes, 2010).

**Evidence and Mechanisms for Magma-carbonate Interaction**

Xenoliths of thermally metamorphosed carbonate and skarns are commonly found at volcanoes such as Merapi (e.g. Clocchiatti *et al.*, 1982; Camus *et al.*, 2000; Chadwick *et al.*, 2007) and Vesuvius (e.g. Scacchi, 1887; Zambonini, 1910; Fulignati *et al.*, 2004; Jolis *et al.*, 2015) giving clear indication of subvolcanic magma-crust interaction. Studies of volcanic degassing at Popacatépetl (Goff *et al.*, 2001) volcano have indicated large short-duration bursts of 32000t $day^{-1}$ $CO_2$ attributed to assimilation of limestone. Isotopic gas studies at Etna (Chiodini *et al.*, 2011) have indicated systematic increase of $\delta^{13}C$, possibly a result of carbonate assimilation. Isotopic gas studies at Merapi have indicated carbonate interaction (Allard, 1983). During the 2006 eruption, Troll *et al.* (2012) showed an increase in $\delta^{13}C_{CO2}$ from an average baseline -4.1 $\pm$ 0.3‰, attributed to subducted sediment and mantle wedge derived $CO_2$, to -2.4 $\pm$ 0.2‰, consistent with considerable crustal $CO_2$ input.

Petrographically and geochemically, there is abundant evidence for carbonate interaction in carbonate-hosted volcanic systems. Elevated $\delta^{18}O$ ratios in clinopyroxene from the Alban Hills with variably enriched in calcium Tschermak components are attributed to crustal interaction (Dallai *et al.*, 2004; Mollo and Vona, 2014). Ca-Tschermak ('fassaite') ($CaAlAlSiO_6$), Ca-Fe-Tschermak ('esseneite') ($CaFe^{3+}AlSiO_6$), and Ca-Ti-Tschermak ($CaTiAl_2O_6$) clinopyroxene are not naturally occurring end-members, and compositions with a significant Ca-Tschermak component are generally restricted to meteorites (e.g. Mason, 1974; Kimura *et al.*, 2009; Ma *et al.*, 2009), high pressure metamorphic rocks (e.g. Lovering and White, 1969; Macgregor and Carter, 1970; Thompson, 1974), and skarns (e.g. Tilley and Harwood, 1931; Tilley and Vincent, 1938; Baker and Black, 1980; Pascal *et al.*, 2005). High pressure clinopyroxenes tend to have elevated Na content due to increasing jadeite substitution with pressure (e.g. Irving, 1974; Thompson, 1974; Upton *et al.*, 2001), whilst the concentration of REE-Th-Zr-Y in carbonate-related clinopyroxenes is elevated with increasing $Al^{IV}$ concentration (Blundy and Dalton, 2000;

Hill *et al.*, 2000; Dallai *et al.*, 2004; Francis and Minarik, 2008), aiding identification of skarn vs. high pressure genesis. Ca-$Fe^{3+}$-Ti-Al clinopyroxene formation is highly dependent on $fO_2$. $CO_2$ fluxing from carbonate breakdown and the subsequent $X_{CO2}$ increase elevates the $fO_2$ of the magma (e.g. $CO_2^{fluid} + 2FeO^{melt} = CO^{fluid} + Fe_2O_3^{melt}$) (Wenzel *et al.*, 2002; Simakin *et al.*, 2012; Spandler *et al.*, 2012), increasing the $Fe^{3+}$ content of precipitated clinopyroxene, promoting increased $Al^{IV}$ substitution into the tetrahedral site, and additional Ti incorporation to balance charge imbalances (Carbonin *et al.*, 1991; Mollo and Vona, 2014).

Whole-rock $^{87}Sr/^{86}Sr$ ratios have been shown at Vesuvius and the Alban Hills to be ineffective at identifying magma-carbonate interaction, as the $^{87}Sr/^{86}Sr$ ratios of the carbonate platform are almost identical to those of the lavas (e.g. Vollmer, 1975; Gilg *et al.*, 2001; Gaeta *et al.*, 2006). In-situ mineral analyses however, are often more insightful. Isotopic analyses of zoned plagioclase phenocrysts from lavas and calc-silicate xenoliths at Merapi show notably elevated An mol% and $^{87}Sr/^{86}Sr$ ratios in the crystal cores, requiring a Ca-rich, low Mg-Fe melt. This is strong evidence for carbonate interaction, which is masked in whole rock studies (Chadwick *et al.*, 2007). Later experimental studies (Deegan *et al.*, 2010) reproduced the results of Chadwick *et al.* (2007), confirming this interpretation. Carbonate assimilation is further supported by elevated $\delta^{18}O$ values in feldspar and clinopyroxene phenocrysts, attributed to a carbonate component (Troll *et al.*, 2013; Deegan *et al.*, 2016b). Although calc-silicate xenoliths in the 2010 Merapi eruption deposits are very minor by volume (« 0.1 vol%; Erdmann *et al.*, 2016), evidence for carbonate interaction is shown by $An_{94\text{-}97}$ plagioclase cores, whole rock ($^{87}Sr/^{86}Sr$ 0.70571–0.70598) and anorthite core (6.5‰ $\delta^{18}O$) isotopic enrichment (Borisova *et al.*, 2013; Troll *et al.*, 2013), $CO_2$-rich groundmass glass (higher than reasonably soluble in the melt), and carbonate grains in the volcanic ash (Genareau *et al.*, 2015).

Mg-rich skarn xenoliths with very low CaO (<0.3 wt.%) in the Loko-Dovyren intrusion (Russia) were shown to be the residue of dolomite partial melts (Wenzel *et al.*, 2002). Assimilation of the released Ca-rich melts and resultant increased $a$CaO and/or reduced $a SiO_2$ in the melt changed the phase relations, precipitating CaO-rich (<=1.67 wt % CaO) $Fo_{99\text{-}98}$ cumulus olivine and CaTs clinopyroxene. High $fO_2$ from metamorphic $CO_2$ liberation caused precipitation of

very Mg-rich olivine and Cr-poor spinel around the xenoliths. The Hortavær intrusion, Norway (Barnes *et al.*, 2005), records carbonate interaction through the abundance of Ca-rich minerals, calcite with a non-magmatic $\delta^{13}C$ signature in textural equilibrium with igneous silicates, absence of olivine and low whole rock Sc contents suggesting liquidus clinopyroxene over olivine (cf. Tilley, 1952), and strong evolution towards alkaline silica-undersaturated compositions.

Daly (1910) was first to propose that addition of CaO from carbonate dissolution will promote precipitation of Ca-bearing phases, notably Ca-pyroxene, which fractionation of said phases could lead to considerable desilication of the melt and alkali enrichment. Early workers proposed this process in Italy to occur at Vesuvius (Rittmann, 1933), and recent work at the ultra-potassic silica-undersaturated Alban Hills volcanic district, Italy (Trigila, 1995) has shown validity to this hypothesis. Carbonate xenoliths have been long identified at Alban Hills (e.g. Fornaseri and Turi, 1969), along with ultramafic xenoliths with high-MgO high-CaO olivine (Federico *et al.*, 1994), and high $fO_2$ conditions during xenolith crystallisation (Gaeta *et al.*, 2000), all indicating magma-carbonate interaction. Gaeta *et al.* (2006) proposed that clinopyroxene fractionation has a strong influence on the liquid line of descent, supported by later experimental studies (Iacono-Marziano *et al.*, 2007, 2008; Freda *et al.*, 2008; Mollo *et al.*, 2010b). Addition of CaO to the melt from carbonate breakdown increases the stability field of clinopyroxene on the liquidus over olivine, precipitation of which consumes silica and desilicates the melt more strongly than can be attributed solely to a dilution effect.

Detailed analysis of xenoliths from the Alban Hills and Vesuvius (Gaeta *et al.*, 2009; Di Rocco *et al.*, 2012; Jolis *et al.*, 2015), and additional experimental work (Mollo *et al.*, 2010b), have shed light on the mechanism of carbonate reaction. Three types of xenoliths attributed to carbonate interaction are identified at the Alban Hills (Gaeta *et al.*, 2009; Di Rocco *et al.*, 2012): $\tilde{}Fo_{90}$ olivine-bearing cumulates precipitated at CaO-bearing rock-magma interface, Ca-Tschermak clinopyroxene-bearing endoskarns precipitated due to carbonate assimilation, and exoskarns formed as a result of carbonate wall rock thermo-metamorphism. The cumulates comprise dominantly clinopyroxene with partially resorbed disequilibrium high-Ca (0.4-0.87 wt. %) olivine. They are characterized by relatively high CaO content in the interstitial glass, the

presence of calcite, and high $\delta^{18}O$ values in clinopyroxene and olivine (6.2 to 8.4 ‰ for both). The skarns contain calcite as inclusions within minerals or as interstitial crystals, CaO enriched interstitial glass, CaO enriched olivine and Ca-Tschermak clinopyroxene, and show high $\delta^{18}O$ in clinopyroxene and olivine (Di Rocco *et al.*, 2012). Magmatic contamination occurs via the simultaneous dissolution and assimilation of both solid crustal material (carbonate wall rock and exoskarn recycling), and CaO-rich partial crustal melts (Gaeta *et al.*, 2009; Di Rocco *et al.*, 2012; Jolis *et al.*, 2015) (Figure 1.6) in the reaction (accounting for the strong $fO_2$ influence on phase composition identified by Mollo and Vona (2014)):

$$2\overset{calcite}{CaCO_3} + 2\overset{magma}{Al_2O_3} + TiO_2 + \overset{clinopyroxene}{CaFeSi_2O_6} + Mg_2Si_2O_6 =$$
$$\overset{clinopyroxene}{CaAlAlSiO_6} + \overset{clinopyroxene}{CaFeAlSiO_6} + CaTiAlSiO_6 + \overset{olivine}{Mg_2SiO_4} + 2\overset{fluid}{CO_2}$$

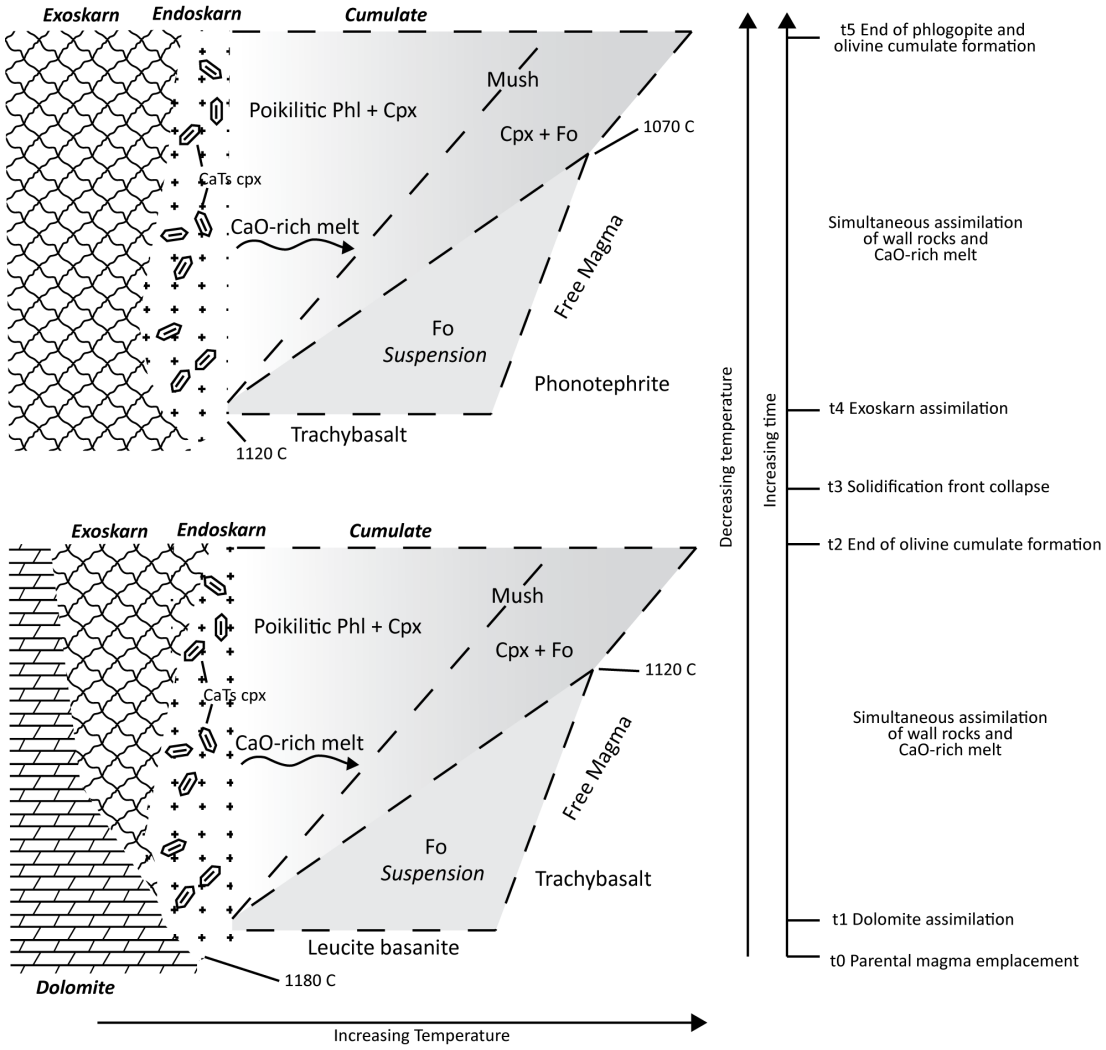


*Figure 1.6: Skarn formation beneath the Alban Hills (after Di Rocco* et al.*, 2012).*

Formation of CaO-rich melts and cumulate endoskarns is not specific to alkaline magmas, and is also observed for example in the Ioko-Dovyren intrusion, Russia. Here, calcite melt mixed with mafic magmas to form a dunite cumulate with olivine containing up to 1.67 wt% CaO (Wenzel *et al.*, 2002). Clinopyroxenite xenoliths and associated lavas from the Kanafià Synthem, Nisyros (Aegean Arc, Greece) show elevated Sr, MREE/HREE and $MgO/Fe_2O_3$ compared to the other eruptive products, and the xenoliths have been interpreted (Spandler *et al.*, 2012) as having a non-mantle nor cumulate origin, instead resembling the Ca-Tschermak endoskarns described from the Alban Hills. The xenoliths are in disequilibrium with the host magma and comprise Ca-Tschermak pyroxene. Desilication is not observed at Nisyros, and excluding Sr enrichment, carbonate assimilation here has resulted in little noticeable change in the melt composition, attributed to the more evolved basaltic-andesitic initial composition of the Kanafià Synthem magma compared to that of the Alban Hills (Spandler *et al.*, 2012). Spandler *et al.* (2012) suggest that unrecognised carbonate assimilation may be more common in arc magmas, with consequences for incorrect modelling of $CO_2$ fluxes in arc systems, in addition to the increased partitioning of REE and other trace elements into aluminous clinopyroxene (Blundy and Dalton, 2000; Hill *et al.*, 2000; Dallai *et al.*, 2004; Francis and Minarik, 2008) leading to erroneous interpretations of trace element ratios in arc magma genesis. Carbonate xenoliths and skarns have been identified in the deposits of Santorini (Druitt *et al.*, 1999; Druitt, 2014), and crustal assimilation has been demonstrated isotopically (Druitt *et al.*, 1999; Zellmer *et al.*, 2000, 2005; Elburg *et al.*, 2014), however any influence of carbonate assimilation specifically on the magmatic system has not yet been fully quantified. Calc-silicate mineral assemblages in xenoliths found in the historic lavas of Santorini have been attributed to considerable $fO_2$ increase from thermal breakdown of carbonates, high enough to stabilise anhydrite (Nicholls, 1971b).

Skarn xenoliths have been used in a few studies to reconstruct the skarn environment and metasomatic fluid composition beneath volcanoes. Vesuvius skarn xenoliths are shown to preserve the full prograde metamorphic to magmatic endoskarn transitional processes and reactions

occurring during several eruptions, including evidence for multiple types of immiscible metasomatic fluids (Del Moro *et al.*, 2001; Gilg *et al.*, 2001; Fulignati *et al.*, 2000, 2001, 2004, 2005). A similar approach has been applied at Lascar volcano, Andes, to reconstruct the skarn environment and additionally isotopically identify the basement protolith formation from the regional geology (Matthews *et al.*, 1996).

### $CO_2$ Liberation and Implications

The generalised carbonate breakdown reaction ($CaCO_3 \rightarrow CaO + CO_2$) suggests that carbonate breakdown adds to the volatile budget of the magmatic system, and due to the low solubility of $CO_2$ in silicate melts (Holloway and Blank, 1994; Botcharnikov *et al.*, 2005), will often form a fluid phase. $CO_2$ is present as a magmatic fluid, and determining the source of $CO_2$ released is important. Volcanoes emitting crustal $CO_2$ can be identified by elevated $CO_2/S$, $\delta^{13}C$, and $^3He/^4He$ in emitted gases (Troll *et al.*, 2012, 2013; Lee *et al.*, 2013; Aiuppa *et al.*, 2017; Mason *et al.*, 2017), and mineral chemical evidence such as elevated oxygen isotopes in mineral phases discussed previously (Dallai *et al.*, 2004; Borisova *et al.*, 2013). Carbonate assimilation and decarbonation reactions have been shown experimentally to occur very rapidly, in the order of hours to days (Deegan *et al.*, 2010; Jolis *et al.*, 2013), indicating that the effects of carbonate interaction may have consequences for eruption dynamics and triggering. Deegan *et al.* (2010), Troll *et al.* (2012) and Carr *et al.* (2018) suggest that the 2006 Yogyakarta earthquake may have fractured the crustal limestone beneath Merapi, increasing the surface area in contact with magma and thus promoting decarbonation, enhancing the intensity of the 2006 eruptive activity, and/or $CO_2$ release may have lubricated fault planes (e.g. Miller *et al.*, 2004), triggering the earthquake in a positive feedback loop. $CO_2$ liberation is also suggested to have influenced the paroxysmal 2010 eruption (Borisova *et al.*, 2013), however the main trigger is attributed to influx of a deeper, hotter, more volatile-rich magma (Surono *et al.*, 2012; Costa *et al.*, 2013; Jousset *et al.*, 2013; Preece *et al.*, 2014). Estimates of crustal $CO_2$ addition at Vesuvius suggest that crustal $CO_2$ addition outweighs magmatic $CO_2$ by greater than factor of 7 in the Pompeii and Pollena eruptions, and may have been an eruption trigger (Jolis *et al.*, 2015). Some

examples of explosive mafic eruptions have additionally been attributed to decarbonation. For example, the Pozzolane Rosse eruption at the Alban Hills is attributed to a high fluid $X_{CO2}$ and depressurisation driving leucite crystallisation, which increased the magmatic viscosity and volatile pressurisation, ultimately leading to an explosive eruption (Freda *et al.*, 2011).

The rate of breakdown and influence on the outgassing and/or overpressuring of the system caused by carbonate assimilation is dependent on the liberated $CO_2$ being permitted to migrate from the reaction site (Barnes *et al.*, 2005, 2009; Mollo *et al.*, 2012, 2013; Heap *et al.*, 2013; Blythe *et al.*, 2015). Inhibition of $CO_2$ migration in a closed system decarbonation reaction favours the reactants, ultimately causing the decarbonation reaction to stop at any pressure/temperature (Mollo *et al.*, 2013). Thermal fracturing however is considered to drive initially closed systems to open system within time, allowing decarbonation to proceed and chemically weaken the host rock (for example calcite to weaker portlandite in metasomatic skarns), promoting volcanic edifice instability (Mollo *et al.*, 2012, 2013). Melt viscosity has also been experimentally shown to exert a control on exsolved $CO_2$ migration, therefore influencing assimilation rates and eruption dynamics. High viscosity melt experiments (simulating Merapi-type melts) are shown to inhibit $CO_2$ migration and cause localised volatile over-pressurisation (explosivity) compared to lower viscosity runs, which allow $CO_2$ to migrate freely, allowing decarbonation and assimilation reactions to occur unhindered which may drive sustained $CO_2$ driven eruptions (Blythe *et al.*, 2015).

Any crustal $CO_2$ liberated has implications for $CO_2$ cycling, which is often generally considered to be derived from subducted sediment source contamination and mantle sources. This additional reservoir of $CO_2$ has received attention recently as it may dwarf the $CO_2$ released from source contamination (Aiuppa *et al.*, 2017; Mason *et al.*, 2017). This has implications for the present day $CO_2$ budget, and also past climatic periods, where increased temperatures have been attributed to increased marine carbonate production, increased volcanism, and therefore increased crustal $CO_2$ release (Carter and Dasgupta, 2016, 2018; Mason *et al.*, 2017; Chu *et al.*, 2019).

### 1.4.2 Non-Carbonate Crustal Assimilation

Assimilation of crustal material and anatectic melts is a common process in arc volcanic systems. Isotopic studies and modelling (e.g. DePaolo, 1981) of the Aeolian arc volcanic rocks has shown that crustal assimilation occurs across the arc to varying extents (Ellam and Harmon, 1990; Peccerillo and Wu, 1992; Clocchiatti *et al.*, 1994; Del Moro *et al.*, 1998; Calanchi *et al.*, 2002; Santo *et al.*, 2004; Peccerillo *et al.*, 2013). Positive $^{87}Sr/^{86}Sr$ and $\delta^{18}O‰$ correlations with $SiO_2$ are shown for many islands (Ellam and Harmon, 1990), with contamination having increased $\delta^{18}O$ values as high as +8.5, but having a lesser effect on Sr ratios. Decreasing $^{87}Sr/^{86}Sr$ with $SiO_2$ at Alicudi is interpreted as contamination occurring most readily in the deeper hotter basaltic systems (Peccerillo and Wu, 1992; Peccerillo *et al.*, 2004), and has been less clearly identified at Filicudi (Santo and Peccerillo, 2008; Lucchi *et al.*, 2013). Crustal assimilation is also identified isotopically through the South Aegean volcanic arc (Francalanci *et al.*, 1995; Druitt *et al.*, 1999; Buettner *et al.*, 2005), Sunda arc (Gasparon and Varne, 1998; Dempsey, 2013; Handley *et al.*, 2014; Jeffery *et al.*, 2013) and in many other worldwide arcs (e.g. Hildreth and Moorbath, 1988; Thirlwall *et al.*, 1996). These studies commonly use the isotopic compositions of crustal xenoliths as model contaminants, or in fewer cases an average crustal composition (e.g. Francalanci *et al.*, 1995).

#### Anatexis Recorded in Crustal Xenoliths

High-silica xenoliths are found across the Aeolian arc in the mafic lavas. These xenoliths are interpreted as restites from high degrees of partial melting of the Calabro-Peloritano metamorphic basement on the basis of (1) consisting almost exclusively of quartz, (2) containing glassy intergranular films, (3) the scarcity of quartzite lithologies in the basement, and (4) having incompatible trace elements an order of magnitude lower than the basement lithologies (Honnorez and Keller, 1968; Peccerillo and Wu, 1992; Renzulli *et al.*, 2001; Vaggelli *et al.*, 2003; Zanon *et al.*, 2003; Bonelli *et al.*, 2004; Frezzotti *et al.*, 2004; Zanon and Nikogosian, 2004). Potassic melt inclusions within these xenoliths (Frezzotti *et al.*, 2004; Zanon and Nikogosian,

2004) are considered as crustal partial melts and potential contaminant liquids that may influence the potassic character of the Aeolian Arc. Incompatible trace element concentrations in these inclusions however preclude contamination by these liquids as the cause of calc-alkaline to potassic magmatism observed across the arc. Quartzite xenoliths are also found at Etna, indicating assimilation of crustal partial melts that may influence the magmatic composition (Mollo *et al.*, 2017).

The island of Lipari hosts unusual cordierite-bearing lavas, comprising up to 20-30% metapelitic and gabbroic xenoliths (Bergeat, 1910; Honnorez and Keller, 1968; Barker, 1987; Di Martino *et al.*, 2011). Study of the lavas and metapelitic xenoliths (Di Martino *et al.*, 2011) indicate that lower crustal dehydration-melting of the metasedimentary country rock results in contamination by anatectic melt assimilation, and formation of cordierite by the following peritectic reactions:

(1) Biotite + Aluminosilicate + Quartz + Albite = Garnet + Cordierite + K-feldspar + Melt

(2) Biotite + Garnet + Quartz = Orthopyroxene + Cordierite + K-feldspar + Melt

In addition to the high-silica quartz xenoliths and cordierite-bearing lavas, the presence of buchites (partial to almost exclusively glass, with high-temperature low-pressure phase assemblages) (Salvioli-Mariani *et al.*, 2005; Del Moro *et al.*, 2011) and incipient melting textures in high grade cordierite-anorthoclase hornfels (Renzulli *et al.*, 2003; Harlov *et al.*, 2006) at Stromboli show further evidence that crustal melting and assimilation is prevalent in the Aeolian arc. Assimilation of crustal melts has also be demonstrated worldwide at arcs (e.g. Beard *et al.*, 1993; Ducea and Saleeby, 1998), and may be difficult to recognise due to their melting and assimilation dynamics (Burchardt *et al.*, 2016).

**Crustal Structure, Barometry and Magmatic Ascent**

Fluid inclusion studies of xenoliths (e.g. Roedder, 1984; Hansteen and Klügel, 2008) have been used successfully to infer magma ponding depths and ascent paths from the mantle, and have also been used in many other studies (e.g. Hildner *et al.*, 2012; Levresse *et al.*, 2016) to complement mineral equilibration thermobarometry (e.g. Putirka, 2008). The density of the trapped

fluid directly relates to the trapping (and/or re-equilibration) temperature and pressure, following an isochore during ascent and decompression, assuming no volumetric re-equilibration (Bodnar, 2003) occurs. An estimate of the minimum trapping pressure can be derived if an independent estimate of temperature (for example from melt inclusion rehomogenisation or mineral equilibration thermobarometry) is provided. Re-equilibration and resetting of fluid inclusion densities can be incomplete within a sample, varying with residence time, mineralogy, inclusion size, and fluid composition (Bodnar, 2003), potentially providing evidence for several short-lived ponding depths (e.g. Hansteen *et al.*, 1998; Zanon *et al.*, 2003). Fluid inclusion studies from quartz-rich xenoliths across the Aeolian Islands (Clocchiatti *et al.*, 1994; Frezzotti *et al.*, 2003; Vaggelli *et al.*, 2003; Zanon *et al.*, 2003; Bonelli *et al.*, 2004; Zanon and Nikogosian, 2004; Di Martino *et al.*, 2010) consistently show a bimodal density distribution, showing a fairly high ascent speed between two distinct magma ponding regions at ~25-12km and ~6-1km, where anatexis and xenolith formation mainly occurs in the deeper reservoirs, and magmatic evolution mainly occurring in the shallower reservoirs. Generation of lower crustal felsic anatectic melts is interpreted at Lipari to create density barriers which inhibit ascent of mafic magmas, and additionally generate the unusual cordierite bearing lavas (Di Martino *et al.*, 2010, 2010, 2011).

Although this thesis defines crustal xenoliths as sedimentary upper crustal lithologies, the crust contains almost all lithologies, therefore crustal xenoliths can include for example older igneous material. In this broader definition, crustal xenoliths have been used to place constraints on crustal growth processes and the composition of the lower crust at other arcs worldwide. Hornblende dominant crustal xenoliths from the northern Andes have metamorphic assemblages characteristic of lower crustal origin, with an oceanic basalt character, and lack chemical characteristics indicative of cumulate or restite origin, indicating crustal growth by subduction-accretion and dehydration, potentially melting, of this material to form more refractory rocks (Hickey-Vargas *et al.*, 1995; Weber *et al.*, 2002). Mafic and ultramafic xenoliths from the Taupo Volcanic Zone, New Zealand, show mantle derived magmatic underplating of the lower crust, and a lower crust formed of cumulate and restite lithologies (Price *et al.*, 2015). As discussed in the previous plutonic xenolith section, xenoliths collected from across the Lesser Antilles arc

exhibit along arc variations (e.g. Arculus and Wills, 1980; Tollan *et al.*, 2012; Stamper *et al.*, 2014; Cooper *et al.*, 2016; Melekhova *et al.*, 2017; Camejo-Harry *et al.*, 2018), and have helped compliment geophysical studies reconstruct the along arc crustal structure (Melekhova *et al.*, 2019). These studies have also helped reconstruct lateral variations in magmatic differentiation, with implications worldwide for deep amphibole fraction, which is discussed in the next section.

#### Crustal Xenoliths Summary

Studies of crustal xenoliths have been shown to provide a powerful tool for understanding magma-crust interactions and contamination. The role of carbonate assimilation in influencing shallow level magmatic differentiation and eruption dynamics has been demonstrated at several volcanic systems. Mineral equilibria and fluid inclusion geothermobarometry has placed constraints on the P-T conditions these interactions have occurred. Isotopic studies have demonstrated that crustal contamination is a widespread process occurring in arc systems and is not always simple to identify, and additionally distinguish from source contamination. Crustal anatexis is shown to be a process for magma contamination in some arc volcanoes.

## 1.5 Rationale and Thesis Outline

This thesis investigates the petrogenesis of xenoliths at volcanic arcs, and the implications these petrogenetic processes have on the host magmatic systems. This work focuses on both crustal xenoliths, their metamorphic history and assimilation into the host magma, and plutonic xenoliths, their intensive variables and their role in magma genesis. Crustal xenoliths are investigated using Merapi volcano in Indonesia as the case study system due to ubiquitous calc-silicate crustal xenoliths in the deposits, and the hazard it poses to the neighbouring city of Yogyakarta. Plutonic xenoliths are investigated using Santorini volcano in Greece as the case study system, due to the excellent outcrop exposure, well constrained stratigraphy, and abundant plutonic xenoliths spanning the stratigraphy.

**Aim**: Use crustal and cognate plutonic xenoliths to place constraints and develop models for the complex magmatic and intra-crustal processes occurring within subduction zones, utilising

case studies from the Aegean and Sunda volcanic arcs.

**Santorini - Magmatic differentiation and cumulus processes**

1) Determine P-T-X-$fO_2$ conditions of magmatic cumulate formation, and utilise these to place constraints on the plumbing system depths, and the role of cumulate formation and magma differentiation processes during the evolution of Santorini magmas.

2) Assess the role of cumulus and post-cumulus processes recorded in the plutonic xenoliths using trace element geochemistry.

3) Combine major element, trace element and oxygen isotope data to develop a model for the evolution of the plumbing system and magma differentiation at Santorini.

**Merapi – Shallow Crustal Assimilation Processes**

4) Determine the reactions occurring within the Merapi calc-silicate xenoliths and evaluate their relevance for volatile release, element transfer, and compositional effects on the host magma.

5) Determine P-T-X-$fO_2$ conditions of xenolith formation and evaluate this in context with the host magmatic system.

6) Develop a model of magma-crust interaction at Merapi and implications for these processes occuring at other carbonate-hosted volcanoes.

These aims and objectives are fulfilled in the thesis chapters outlined below:

Chapter 1 provides the general introduction to the thesis, background, literature review and the rationale.

Chapter 2 presents a detailed petrological study of the plutonic xenoliths found at Santorini. This chapter aims to determine the pressure and temperature conditions of cumulate processes occurring, and use these to establish magma differentiation depths. The second aim is to evaluate the cumulate, post-cumulus and melt separation processes during the magmatic differentiation. This chapter is in preparation for submission for publication.

Chapter 3 presents a detailed petrological study of the calc-silicate xenoliths collected in the 1994 to 2010 deposits of Merapi. This chapter aims to constrain the intensive variables of xenolith petrogenesis, and use these in turn to constrain these parameters for the magmatic system. The chapter then aims to evaluate the effects of carbonate assimilation at Merapi on the magmatic system. This chapter has been submitted for publication and is under review at the Journal of Petrology.

Chapter 4 presents a detailed petrological and oxygen isotope study of the different textural types of calcite present in the Merapi calc-silicate xenoliths discussed in Chapter 3. This chapter aims to identify the processes occurring during metamorphism of wall-rock limestone into calc-silicate assemblages, and quantify the $CO_2$ release into the atmosphere from decarbonation reactions. This chapter has been published in Nature Scientific Reports: Whitley, S., Gertisser, R., Halama, R., Preece, K., Troll, V.R. and Deegan, F.M., 2019. Crustal CO 2 contribution to subduction zone degassing recorded through calc-silicate xenoliths in arc lavas. *Scientific Reports*, 9(1), p.8803. `https://doi.org/10.1038/s41598-019-44929-2`

Chapter 5 is a synthesis and discussion of the work presented in this thesis and places it in a wider context. This chapter concludes with the main conclusions of the thesis.

The thesis concludes with appendices and all geochemical data collected as an online supplement to the thesis.

# Chapter 2

# Plutonic xenoliths from Santorini, Greece: Magmatic differentiation and post-cumulus processes

This chapter is in preparation for submission and publication, in collaboration with the project supervisors Ralf Gertisser and Ralf Halama, Thor Hansteen and Matthias Frische (GEOMAR) and Torsten Venneman (University of Lausanne). This chapter was written by myself with input from Gertisser and Halama. Hansteen and Frische provided analytical time and assistance with LA-ICP-MS analysis, and Venneman provided oxygen isotope analyses.

## 2.1 Introduction

Arc magmas typically show distinct geochemical and petrographical evidence indicating a complex petrogenesis. The magmas represent a summation of the interplay of magma generation processes, magmatic differentiation during ascent and crustal assimilation. Much of the published work about the petrogenesis of arc magmas focuses on the extrusive rocks, and pays relatively little attention to plutonic xenoliths, although these are found in the deposits of many volcanoes (e.g. Arculus and Wills, 1980; Beard, 1986; Druitt *et al.*, 1999; Stamper *et al.*, 2014; Cooper *et al.*, 2016; Klaver *et al.*, 2017; Yanagida *et al.*, 2018). Eruptive products generally preserve and place constraints on pre-eruptive magmatic conditions and record geochemical and isotopic evidence of magma source composition and differentiation, whilst plutonic cumulate xenoliths can additionally provide a direct insight into the early differentiation history and individual deep and shallow level magmatic processes that collectively determine the distinct geochemical and petrological trends found in subduction settings. These plutonic xenolith studies have focused on reactive melt flow in the lower crust and its role in amphibole fractionation (Costa *et al.*, 2002; Cooper *et al.*, 2016; Klaver *et al.*, 2017), cumulate oxygen isotopic equilibration conditions (Tollan *et al.*, 2012), polybaric differentiation of cumulus and phenocryst phases (Stamper *et al.*, 2014; Klaver *et al.*, 2017), and magma differentiation trends (Druitt *et al.*, 1999; Stamper *et al.*, 2014).

This study focuses on the plutonic xenoliths found at Santorini volcano in the South Aegean Volcanic Arc (Greece) to elucidate the role of crystal mush and cumulus processes on the magmatic evolution of Santorini, which is difficult to constrain using volcanic deposits alone. Santorini is notable for several significant explosive eruptions, and a well-constrained stratigraphy to study these eruptions (Druitt *et al.*, 1999). Many deposits contain abundant plutonic xenoliths. These range from microcumulate fragments at thin section scale to fist-sized nodules. Santorini is characterised by early (pre-530 ka) hydrous amphibole bearing magma, and modern (post-530 ka) magmatic differentiation dominated by an almost entirely anhydrous phase assemblage and trace element geochemistry (Nicholls, 1971c; Huijsmans *et al.*, 1988; Dietrich *et*

*al.*, 1998; Druitt *et al.*, 1999, 2019; Elburg *et al.*, 2014), in contrast to many arc volcanoes that show phenocryst or geochemical evidence for pervasive amphibole fractionation during their petrogenesis (e.g. Davidson *et al.*, 2007). Recent petrological work at Santorini has focused on constraining pre-eruptive magmatic conditions derived from experimental petrology (Cottrell *et al.*, 1999; Cadoux *et al.*, 2014; Andújar *et al.*, 2015, 2016), volatile solubility (Druitt *et al.*, 2016) and diffusion modelling (Druitt *et al.*, 2012; Fabbro *et al.*, 2018; Flaherty *et al.*, 2018) of the eruptive products, which forms the framework for this study. Previous studies of the plutonic xenoliths by Druitt *et al.* (1999) and Michaud *et al.* (2000) have estimated temperatures of cumulus phase formation and later re-equilibration temperatures, and highlighted the role of shallow crustal magma differentiation in andesite/dacite genesis. In this study we use mineral chemistry, *in situ* LA-ICP-MS trace element data for minerals, melt inclusions and interstitial glasses coupled with oxygen isotopes of mineral separates to place constraints on pressure and temperature conditions of plutonic xenolith formation, post-cumulus processes, the plumbing system at Santorini, and magmatic differentiation processes at Santorini. The plutonic xenoliths record crystallisation, and therefore magma differentiation at Santorini, dominantly at shallow crustal depths ($<$ 350 MPa). Oxygen isotopes show that only limited amounts of crystal assimilation occurred during magma genesis and differentiation. LA-ICP-MS analyses show that while the major element chemistry of the xenolith minerals are generally comparable to the volcanic phenocrysts, strong incompatible element enrichment in some samples record crystallisation or equilibration with trapped intercumulus melts. This produces volumetrically small uneruptable melts with up to 82 wt% $SiO_2$, and mineral phases (K-feldspar, quartz) that are rare to absent in the volcanic record. These melts may mix with the magmatic system during cumulate remobilisation periods, evidenced by mush fragments in the deposits of some eruptions.

## 2.2 Geological Setting

Santorini is located in the South Aegean Volcanic Arc approximately 120 km north of Crete. The South Aegean Volcanic Arc is situated in the eastern Mediterranean Sea, and is a result of the

50-60 mm $y^{-1}$ (Jackson, 1994) subduction of the African plate beneath the Aegean Anatolian microplate, initiated ~13-16 Ma ago (Le Pichon and Angelier, 1979; Angelier *et al.*, 1982; Mercier *et al.*, 1989; Papazachos, 2019; Francalanci and Zellmer, 2019; Vougioukalakis *et al.*, 2019). Volcanism commenced in the late Pliocene (Pe-Piper *et al.*, 1983).

Santorini consists of the three islands Thera, Therasia and Aspronisi, which mark the outline of a flooded caldera. The post-caldera Palaea Kameni and Nea Kameni islands are situated within this caldera (Figure 2.1). Pre-volcanic Triassic to Palaeocene basement outcrops at Athinios and Mount Profitis Ilias on Thera, comprising blueschist to amphibolite facies metapelites and crystalline limestones (Davis and Bastas, 1978; Skarpelis and Liati, 1990; Kilias *et al.*, 1998; Druitt *et al.*, 1999). Volcanic activity is strongly influenced by two NE-SW trending tectonic lineaments (the Kameni and Columbos lines) (Druitt *et al.*, 1999; Klaver *et al.*, 2016; Nomikou *et al.*, 2019) and the earliest preserved volcanic activity commenced ~650 ka ago at the Akrotiri peninsula, producing amphibole-bearing silicic tuffs and lava flows (Dietrich *et al.*, 1998; Davis *et al.*, 1998; Druitt *et al.*, 1999; Mortazavi and Sparks, 2004). This is followed by eruption of magmas bearing dominantly anhydrous phases, starting with the Peristeria volcano (530-430 ka) (Figure 2.1). Twelve major plinian eruptions have occurred since ~360 ka, occurring every ~20-40 ky, forming the Thera Pyroclastic Formation (Druitt *et al.*, 1989, 1999). Two cycles of mafic to silicic magma evolution have been identified in the post 360 ka deposits, each ending with large magnitude caldera forming eruptions: the 172 ka Lower Pumice 2 and 3.6 ka Minoan eruptions (e.g. Druitt *et al.*, 1999; Gertisser *et al.*, 2009; Druitt, 2014). Another caldera existed at around 67 ka and an additional caldera collapse occurred at 22 ka (Druitt *et al.*, 1999).Interplinian activity included strombolian and subplinian explosive activity, lava flows and extrusive edifice construction (e.g. Barton and Huijsmans, 1986; Huijsmans and Barton, 1989; Edwards, 1994; Druitt *et al.*, 1999; Vespa *et al.*, 2006; Vaggelli *et al.*, 2009; Fabbro *et al.*, 2013; Karátson *et al.*, 2018). Chemically, the eruptive products of Santorini range from low- to high-K basalt to rhyodacite, transitional tholeiitic to calc-alkaline (Huijsmans *et al.*, 1988; Druitt *et al.*, 1999). Sr-Nd-Pb isotopic and trace element studies indicate varying (~10%)

contamination of Santorini magma with upper Aegean continental crust during fractional crystallisation, with at least some of the contamination having occurred in upper crustal reservoirs (Druitt *et al.*, 1999 and references therein). Phase equilibria (Cadoux *et al.*, 2014; Andújar *et al.*, 2015, 2016) and fluid saturation studies (Druitt *et al.*, 2016) have shown differentiation of parental basalts (50 wt% $SiO_2$, 7 wt% MgO, 1-4 wt% $H_2O$) to andesite at ~400 MPa (~16 km depth), and to silicic compositions around 200-400 MPa (~8-16 km), before storage and eruption from reservoirs at shallow depths of a few km. Xenoliths have been long identified throughout the Santorini volcanic succession, including basement fragments, plutonic cumulates, and calc-silicate assemblages metamorphosed by their host magma (e.g. Fouqué, 1879; Lacroix, 1900; Nicholls, 1971b; Barton and Huijsmans, 1986; Druitt *et al.*, 1999; Druitt, 2014). Amphibole-bearing mafic inclusions from the early Akrotiri centre have been covered in Mortazavi and Sparks (2004), highlighting different magmatic conditions during the petrogenesis of early Santorini magmas.

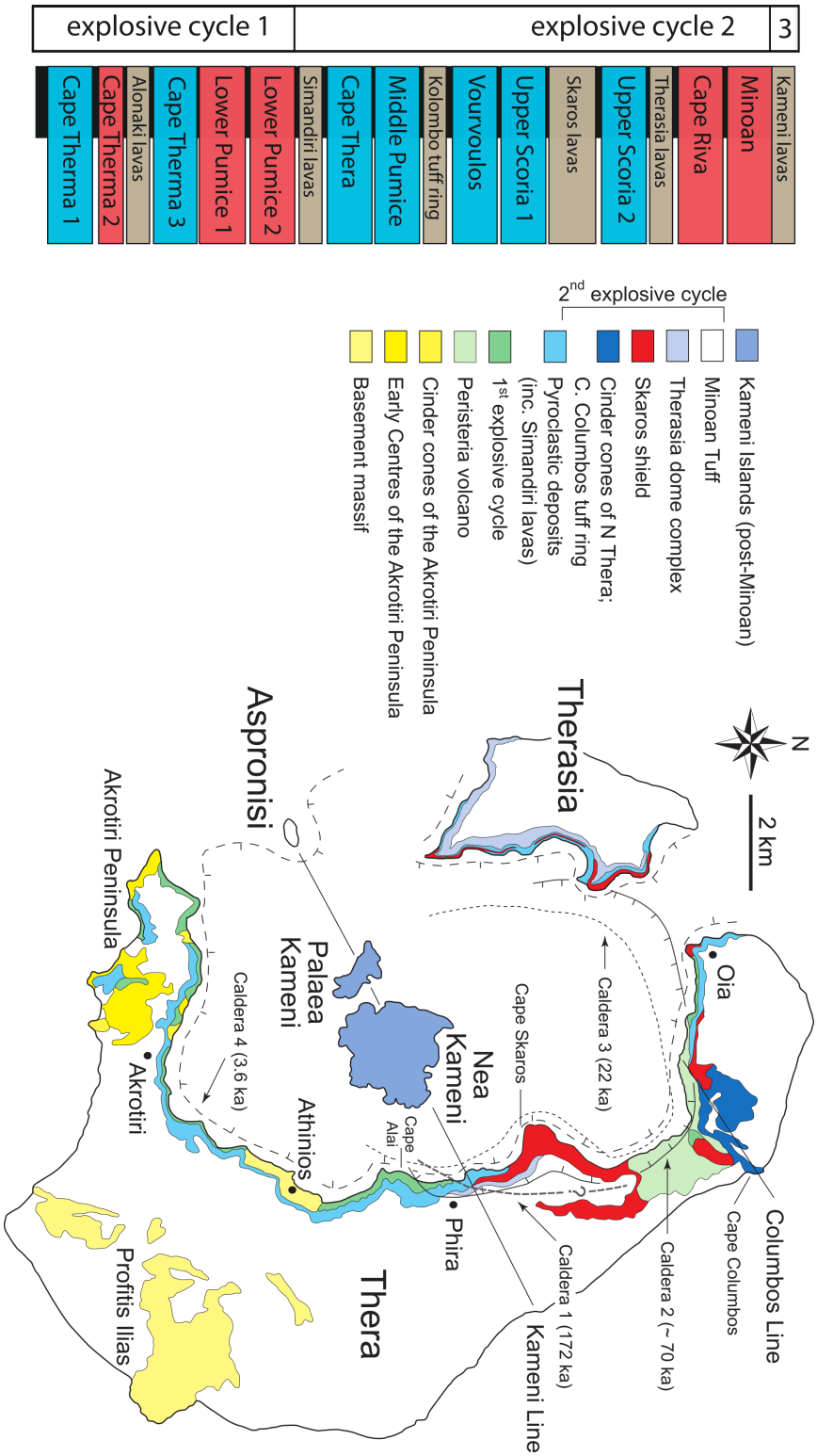


*Figure 2.1: Stratigraphy and geological map of Santorini (after Druitt* et al.*, 2016). Red eruptions in the stratigraphic column are dominantly silicic eruptions, and blue are intermediate in composition. Black boxes are interplinian deposits and brown boxes are prominent lava or tuff successions in the interplinian deposits (Vespa* et al.*, 2006; Druitt* et al.*, 2016). See Table 2.2 for details of eruptions sampled.*

## 2.3 Methods

### 2.3.1 Analytical Methods

#### Electron Microprobe

Major element concentrations in minerals, and major element, chlorine and sulphur concentrations in interstitial glasses and melt inclusions were determined with a JXA 8900 electron microprobe at the University of Kiel, Germany. Silicate and oxide minerals were analysed with a 2 µm micrometre beam diameter, 15 kV accelerating voltage and 15 nA beam current. Glasses were measured with a 5 micrometre defocused beam at 15 kV accelerating voltage and a 12 nA beam current. Na was measured first to minimise Na-loss. Measurement times were 15 s peak and 7 s background, excluding S, Cl, and P, which were measured for 60 s peak and 30 s background. Natural mineral standards (topaz, rutile, baryte, tugtupite, fayalite, forsterite, mica, anorthite, wollastonite, apatite, tephroit) were used for calibration and Smithsonian basaltic glass A-99, forsterite 83 (USNM 2566), plagioclase (USNM 115900), garnet RV2 (USNM 87375), and obsidian ASTIMEX Block SPGLASS7 were used as secondary within-run standards to assess accuracy and precision. Relative accuracy and precision are smaller than 5% for major elements and 10% for minor elements. A CITZAF matrix correction was applied.

All Mg# values are calculated assuming all Fe as $Fe^{2+}$ using $Mg\# = \frac{Mg}{Mg+Fe_{total}}$. $Fe^{3+}$ was estimated for clinopyroxene from stoichiometry using Droop (1987). Components for clinopyroxene thermobarometry were calculated following Putirka *et al.* (1996).

#### LA-ICP-MS

Trace elements in minerals and glass were analysed at the GEOMAR Helmholtz Centre for Ocean Research Kiel using a Nu Instruments ATTOM HR-ICP-MS connected to a Coherent Lambda Physics GEOLAS pro 193 nm excimer laser ablation system. Measurements were made using a 5 mJ/cm$^2$ energy density for 300 pulses at a laser repetition rate of 10 Hz with a 44 $\mu$m spot diameter for silicate minerals and a 24 $\mu$m spot diameter for glasses, and a 50s flush time. Measurements were made on the same polished sections used for EMPA to provide a robust

internal standard using the sum of $^{29}$Si and $^{43}$Ca for normalisation. Calibration was undertaken on a NIST 610 reference glass and repeat measurements of basaltic glasses USGS BCR-2G and USGS BHVO-2G as secondary standards were carried out throughout each analytical session to check accuracy and precision. Measurements were made in blocks of 8 to minimise the effects of drift. Full details of the instrument setup is provided in Fietzke and Frische (2016). Measurement errors are shown in Table 2.1

$\frac{Eu}{Eu^*}$ is calculated as $\frac{Eu}{Eu^*} = \frac{Eu_N}{\sqrt{Sm_N * Gd_n}}$ (Taylor and McLennan, 1985)

### Whole-rock Geochemistry

Samples were powdered at Keele University after washing and removal of surface altered material, using a jaw crusher followed by an agate mill. Whole rock analyses were carried out for 8 samples at Acmelabs, Canada by XRF. Due to sample size constraints, whole-rock compositions for an additional 8 samples were determined by point counting (1000-2000 points). Averaged mineral and glass chemistry was used with the phase volumes counted, corrected for varying mineral and glass densities using mineral densities from Deer *et al.* (1997). The bulk compositions were obtained using the Rock-Maker spreadsheet (Büttner, 2012), which generates bulk whole rock compositions from phase volumes and densities. All calculated compositions are presented in the appendix online spreadsheet.

*Table 2.1: Relative standard deviation (RSE) and percentage offset from reference standard values for the LA-ICP-MS sessions.*

| Isotope | Standard (BCR-2G) | Average | SD | RSD% | Offset% | Standard (BHVO-2G) | Average | SD | RSD% | Offset% |
|---|---|---|---|---|---|---|---|---|---|---|
| *n=19* | | | | | | | | | | |
| $^{7}$Li | 9.00 | 10.17 | 0.90 | 8.81 | 13.02 | 4.80 | 4.66 | 0.61 | 13.18 | -2.99 |
| $^{45}$Sc | 33.00 | 34.82 | 0.58 | 1.67 | 5.53 | 32.00 | 32.36 | 0.93 | 2.89 | 1.13 |
| $^{49}$Ti | 13500.00 | 14099.81 | 235.97 | 1.67 | 4.44 | 16300.00 | 16658.00 | 385.41 | 2.31 | 2.20 |
| $^{51}$V | 416.00 | 468.16 | 5.79 | 1.24 | 12.54 | 317.00 | 347.10 | 4.85 | 1.40 | 9.49 |
| $^{53}$Cr | 18.00 | 16.63 | 1.29 | 7.75 | -7.61 | 280.00 | 312.08 | 7.91 | 2.53 | 11.46 |
| $^{55}$Mn | 1520.00 | 1702.13 | 24.66 | 1.45 | 11.98 | 1317.83 | 1436.08 | 18.98 | 1.32 | 8.97 |
| $^{59}$Co | 37.00 | 41.18 | 0.45 | 1.10 | 11.30 | 45.00 | 49.28 | 0.82 | 1.67 | 9.50 |
| $^{61}$Ni | 13.00 | 24.06 | 7.17 | 29.78 | 85.11 | 119.00 | 142.79 | 19.97 | 13.98 | 19.99 |
| $^{65}$Cu | 21.00 | 19.11 | 1.53 | 7.99 | -8.98 | 127.00 | 141.57 | 3.45 | 2.44 | 11.47 |
| $^{66}$Zn | 127.00 | 174.62 | 9.27 | 5.31 | 37.49 | 103.00 | 135.52 | 8.22 | 6.07 | 31.58 |
| $^{85}$Rb | 46.90 | 52.87 | 1.07 | 2.02 | 12.74 | 9.11 | 10.15 | 0.41 | 4.07 | 11.46 |
| $^{86}$Sr | 340.00 | 360.21 | 8.25 | 2.29 | 5.94 | 396.00 | 411.12 | 10.52 | 2.56 | 3.82 |
| $^{88}$Sr | 340.00 | 358.76 | 5.82 | 1.62 | 5.52 | 396.00 | 408.41 | 8.22 | 2.01 | 3.13 |
| $^{89}$Y | 37.00 | 34.95 | 0.93 | 2.67 | -5.55 | 26.00 | 24.83 | 0.78 | 3.16 | -4.48 |
| $^{90}$Zr | 184.00 | 188.27 | 3.51 | 1.86 | 2.32 | 172.00 | 168.37 | 4.13 | 2.45 | -2.11 |
| $^{93}$Nb | 12.60 | 12.50 | 0.36 | 2.86 | -0.76 | 18.10 | 18.09 | 0.46 | 2.53 | -0.07 |
| $^{133}$Cs | 1.10 | 1.26 | 0.13 | 10.63 | 14.26 | 0.10 | 0.13 | 0.05 | 40.23 | 33.94 |
| $^{137}$Ba | 677.00 | 721.73 | 18.76 | 2.60 | 6.61 | 131.00 | 137.41 | 5.25 | 3.82 | 4.90 |
| $^{139}$La | 24.90 | 26.12 | 0.52 | 1.99 | 4.91 | 15.25 | 15.47 | 0.66 | 4.28 | 1.43 |
| $^{140}$Ce | 52.90 | 54.79 | 0.95 | 1.73 | 3.58 | 37.84 | 37.90 | 1.11 | 2.93 | 0.15 |
| $^{141}$Pr | 6.70 | 6.77 | 0.20 | 2.94 | 1.08 | 5.35 | 5.25 | 0.17 | 3.30 | -1.79 |
| $^{146}$Nd | 28.70 | 29.13 | 1.04 | 3.58 | 1.50 | 24.39 | 24.43 | 1.04 | 4.25 | 0.16 |
| $^{147}$Sm | 6.58 | 6.84 | 0.42 | 6.21 | 3.91 | 6.03 | 6.33 | 0.50 | 7.85 | 4.91 |
| $^{153}$Eu | 1.96 | 2.02 | 0.13 | 6.30 | 3.23 | 2.07 | 2.07 | 0.12 | 5.79 | 0.09 |
| $^{157}$Gd | 6.75 | 6.88 | 0.39 | 5.67 | 1.98 | 6.23 | 6.32 | 0.38 | 6.06 | 1.42 |
| $^{159}$Tb | 1.07 | 1.03 | 0.07 | 6.76 | -4.03 | 0.92 | 0.90 | 0.06 | 7.13 | -2.44 |
| $^{163}$Dy | 6.41 | 6.59 | 0.49 | 7.48 | 2.76 | 5.30 | 5.47 | 0.39 | 7.11 | 3.24 |
| $^{165}$Ho | 1.28 | 1.31 | 0.09 | 6.83 | 2.10 | 0.98 | 0.97 | 0.10 | 10.18 | -0.74 |
| $^{166}$Er | 3.88 | 3.73 | 0.25 | 6.63 | -3.99 | 2.55 | 2.55 | 0.20 | 7.71 | 0.20 |
| $^{169}$Tm | 0.54 | 0.51 | 0.06 | 11.24 | -4.82 | 0.33 | 0.32 | 0.05 | 14.64 | -2.02 |
| $^{172}$Yb | 3.38 | 3.52 | 0.29 | 8.21 | 4.10 | 1.96 | 2.09 | 0.29 | 14.00 | 6.73 |
| $^{175}$Lu | 0.50 | 0.51 | 0.05 | 9.72 | 2.09 | 0.27 | 0.28 | 0.03 | 12.21 | 2.07 |
| $^{178}$Hf | 4.90 | 5.15 | 0.32 | 6.20 | 5.08 | 4.36 | 4.54 | 0.27 | 6.01 | 4.12 |
| $^{181}$Ta | 0.74 | 0.71 | 0.08 | 11.30 | -3.75 | 1.14 | 1.10 | 0.08 | 7.05 | -3.74 |
| $^{208}$Pb | 11.00 | 11.73 | 0.39 | 3.34 | 6.64 | 1.60 | 2.02 | 0.15 | 7.39 | 26.18 |
| $^{232}$Th | 5.70 | 6.17 | 0.14 | 2.27 | 8.23 | 1.22 | 1.23 | 0.05 | 3.93 | 1.19 |
| $^{238}$U | 1.69 | 1.84 | 0.08 | 4.56 | 8.85 | 0.40 | 0.45 | 0.03 | 5.93 | 10.80 |
| Average | | | | 5.58 | 6.74 | | | | 6.66 | 5.55 |

**Mineral Oxygen Isotopes**

Minerals were picked from sieved grain size fractions (125 and 63 micron) of powered rocks at Keele University, using magnetic separation to remove minerals with magnetite inclusions. Minerals were then washed in acid. Oxygen isotope analyses were carried out by the Isotope Laboratory of the University of Lausanne using a $CO_2$-laser extraction line and fluorination linked to a MAT 253 and Nu-Instruments Perspective mass spectrometer (detailed in Lacroix and Vennemann, 2015). The measurement uncertainty on the Ls-1 quartz standard (accepted value of 18.1 ‰) is 0.1-0.16 ‰.

### 2.3.2 Post Entrapment Crystallisation (PEC)

Melt inclusion compositions can be modified by post entrapment processes such as diffusive equilibration and crystallisation on the melt-crystal interface (e.g. Danyushevsky *et al.*, 2000).

Melt inclusion major element data have been corrected for post entrapment crystallisation using the methodologies outlined in the appendix. As is common in plutonic material, many samples contain melt inclusions that show clear textural evidence for post-entrapment modification, such as significant dusting and crystallisation within the inclusion, which varies strongly with host phase and sample. Only melt inclusions with a clear glassy appearance were selected for analysis.

### 2.3.3 Thermobarometry

Several mineral-only and mineral-melt thermobarometers were applied to the xenoliths to place constraints on the temperature and pressure of xenolith formation. As the intercumulus liquids found within the xenoliths are often too felsic to be in equilibrium with the coexisting minerals, and some xenoliths may not be cogenetic with the eruptions they are found within, several mineral melt equilibria models were used to determine a range of plausible equilibrium liquids from known Santorini liquid compositions. An extensive database of Santorini whole rock, melt inclusion and groundmass glass analyses from the literature ($n$=1226) and this study ($n$=118) were paired with each mineral phase and plausible pairs were filtered via equilibrium tests (c.f. Winpenny and Maclennan, 2011; Neave *et al.*, 2013; Neave and Putirka, 2017; equilibrium tests of Putirka, 1999, 2008; Mollo *et al.*, 2013). Clinopyroxene, orthopyroxene and plagioclase were paired with plausible liquids using this method and thermobarometers were solved iteratively; barometers are paired to thermometers. Appendix A.2 contains a detailed assessment of the equilibrium tests, effect of iterative calculations and applicability of the thermobarometers to Santorini compositions. A new plagioclase liquid equilibrium test is derived from a large experimental dataset including Santorini experiments (Cadoux *et al.*, 2014; Andújar *et al.*, 2015, 2016) based on $X^{Si}_{liquid}$ (Appendix A.2.2) and is used here instead the two temperature bracketed test of Putirka (2008).

$$ln(KD^{Ab-An}_{Plagioclase-Liquid}) \pm 0.4541 = 1.26954 - 5.38702X^{Si}_{liquid}$$

Olivine-melt thermometry was conducted both using equations 21 and 22 of Putirka 2008 on post entrapment crystallisation corrected (PETROLOG: Danyushevsky and Plechov, 2011) (Appendix A.1) melt inclusion compositions and paired with equilibrium melts as described above. A pressure of 300 MPa is assumed based on thermobarometry and literature pressure estimates. Changing this pressure results in an insignificant 5°C variation per 100 MPa. Thermobarometric results are presented here as the mean and one standard deviation of the model output. As the thermobarometric models require a $H_2O$ estimate, the $H_2O$ is estimated from a

linear regression of $H_2O$ vs $SiO_2$, as outlined in Appendix A.2.

### 2.3.4 Trace Element Partition Coefficients

Partition coefficients for mineral-melt calculations were calculated from the following sources: plagioclase (Bédard, 2006), clinopyroxene (Bédard, 2014), and orthopyroxene (Bédard, 2007). These models use regressions through extensive experimental databases and observed natural partitioning values to calculate partition coefficients based on mineral and/or melt variables (Figure A.11). These were chosen over the lattice strain model (Blundy and Wood, 1994) and recent models built upon this (e.g. Hill *et al.*, 2011; Sun and Liang, 2012; Sun *et al.*, 2017) as the Bédard models are calibrated over a wider range of mineral compositions, melt compositions and temperature, applicable for the large variations seen within the xenoliths. For example, the Sun and Liang (2012) model is calibrated with up to 57 wt% $SiO_2$, whilst the Bédard (2014) calibration dataset extends to >75 wt% $SiO_2$. Clinopyroxene compositions in the gabbronorites for example indicate equilibration with evolved melts with up to 70 wt% $SiO_2$ (see discussion). For clinopyroxene rare earth element partition coefficients, nearest neighbour parameterisations were used based on an initial calculation of LnD Sm, as recommended by Bédard (2014). Each neighbour element is predicted with an $R^2 > 0.95$ from this initial partition coefficient. Plagioclase partition coefficient calculation results take the form $RTlnD$, therefore temperature is estimated using plagioclase molar An content (Druitt *et al.*, 2012; Fabbro *et al.*, 2018), consistent with our temperatures calculated from plagioclase-melt thermobarometry using the equation from Druitt *et al.* (2012):

$$T(K) = 1128 + 200\frac{X_{An} - 0.4}{0.4}$$

## 2.4 Results

### 2.4.1 Xenolith Petrography

Xenoliths are found in abundance in many of the eruptive units (Figure 2.2. Figure 2.3. 18 plutonic xenoliths have been chosen for detailed study, in addition to extra data collected from some of the other volcanic components at Santorini for comparison (Table 2.2, see Table A.1 for the full sample list) covering the range of lithologies observed, prioritising sample freshness. 144 thin sections from the full stratigraphy show five dominant lithologies based on the classification of Streckeisen (1974): troctolite (glomerocrysts), olivine gabbro, gabbro, gabbronorite and

diorite (Figures 2.4, 2.5, 2.6). The xenoliths are classified as diorite instead of gabbro or gabbronorite when the composition of the feldspar cores are dominantly less than $An_{50}$. Santorini magmas are characteristically amphibole free post 530 ka (Druitt *et al.*, 1999), therefore the name diorite is purely based on feldspar composition (Streckeisen, 1974), and does not imply a dominance of amphibole over clinopyroxene as the main ferromagnesian mafic mineral phase.

The plutonic xenolith mineralogy primarily comprises clinopyroxene and plagioclase, with olivine and orthopyroxene occurring within the more primitive and evolved xenoliths, respectively (Figure 2.4). Texturally many xenoliths have a cumulate texture of generally interlocking euhedral to subhedral cumulus crystals of plagioclase and clinopyroxene, with compositionally more evolved mineral contents including graphic intergrowth of orthoclase and quartz, trace amphibole and additionally residual glass in the interstitial areas (Figures 2.5, 2.6). Amphibole is very rarely observed in the Santorini post-Akrotiri early centres ($<$ 530 ka), and is almost exclusively found as a replacement phase in the xenoliths replacing clinopyroxene crystal rims and fractures, occurring together with replacement biotite, Fe-Ti oxides (magnetite, ilmenite) and rutile. The studied samples appear texturally homogeneous, with conspicuous layering of plagioclase occurring only in one gabbroic sample from the Lower Pumice 2 eruption (SAN 9-1-5, Figure 2.6A). Cumulus crystal sizes reach up to several millimetres. There is a large variety of textures, from partially equilibrated samples with triple junctions, ophitic samples (2.6B) to samples with strongly zoned mineral phases and distinct crystal size bimodality. As there is no clear relationship between xenolith type and stratigraphy, and as they may not necessarily be cogenetic to the eruption they are from (see discussion), the rock types will be discussed by lithology in the following section.

*Figure 2.2: Gabbro xenolith in the deposits of Cape Therma 3*

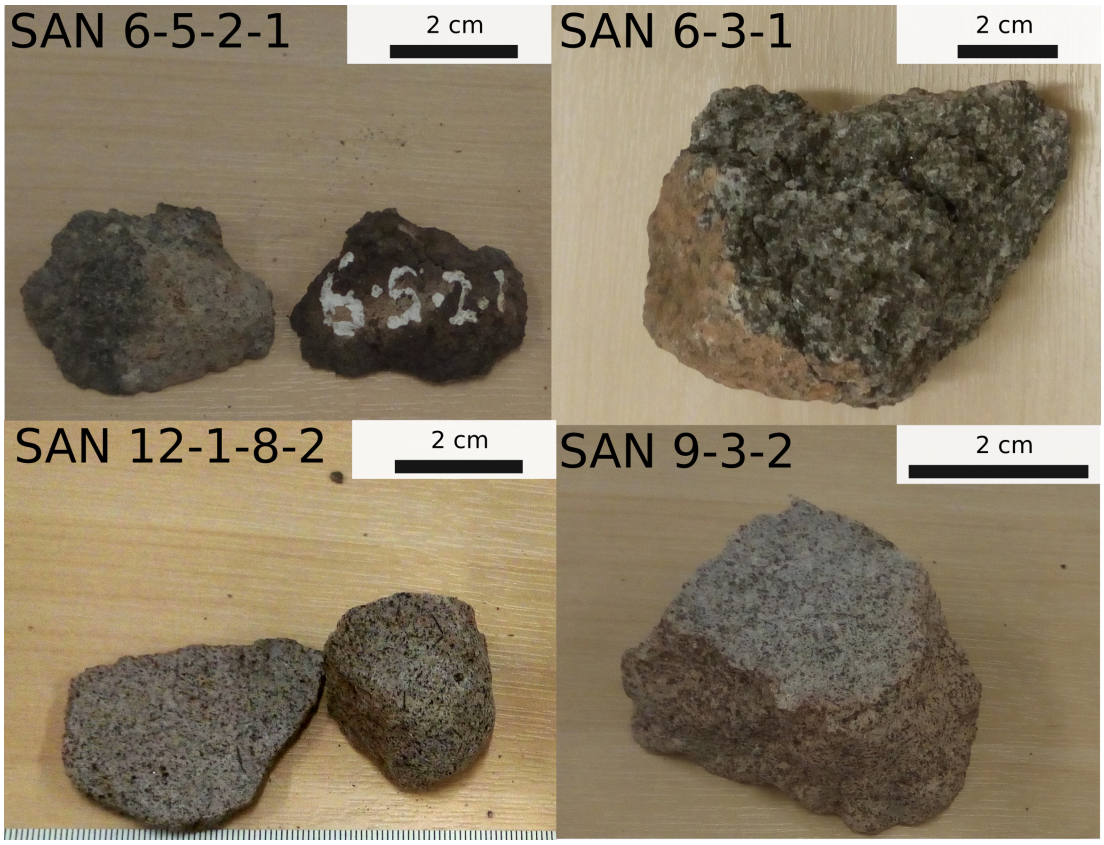


*Figure 2.3: Hand specimen photos of the Santorini xenoliths. See Table 2.2 for details of classification and eruption.*

*Table 2.2: Eruptions and samples analysed in this study. P.R. Pumice is the phenocryst-rich pumice found in the Minoan Eruption. See Table A.1 for the full sample list.*

| Eruption | Sample | Type |
|---|---|---|
| Nea Kameni | SAN 11-2-1-6 | Gabbro |
| Nea Kameni | SAN 11-2-1-6 | Host Lava |
| Nea Kameni | SAN 5-2-1u | Troctolite |
| Nea Kameni | SAN 5-2-1u | Host Lava |
| Minoan | 1-2-3 | P.R. Pumice |
| Minoan | 1-2 | Mafic Bleb |
| Minoan | 2-1 | Pumice |
| Minoan | SAN 4-4c | Gabbro |
| Minoan | SAN 9-3-2 | Gabbronorite |
| Cape Riva | SAN 12-1-5 | Gabbronorite |
| Cape Riva | SAN 5-3-4 (3) | Diorite |
| Upper Scoria 2 | SAN 12-1-8-2 | Diorite |
| Upper Scoria 2 | SAN 14-1-1-3 | Gabbronorite |
| Upper Scoria 1 | SAN 12-2-2 | Gabbronorite |
| Middle Pumice | SAN 6-5-2-1 | Olivine Gabbro |
| Middle Pumice | SAN 6-5-3 | Diorite |
| Middle Pumice | SAN 9-2-2 | Gabbro |
| Lower Pumice 2 | 20 | Pumice |
| Lower Pumice 2 | 24D | Olivine Gabbro |
| Lower Pumice 2 | 28D | Diorite |
| Lower Pumice 2 | SAN 9-1-1-3 | Gabbronorite |
| Lower Pumice 2 | SAN 9-1-8-3 | Gabbro |
| Lower Pumice 1 | SAN 6-4-2 | Gabbro |
| Cape Therma 3 | SAN 6-3-1 | Gabbro |

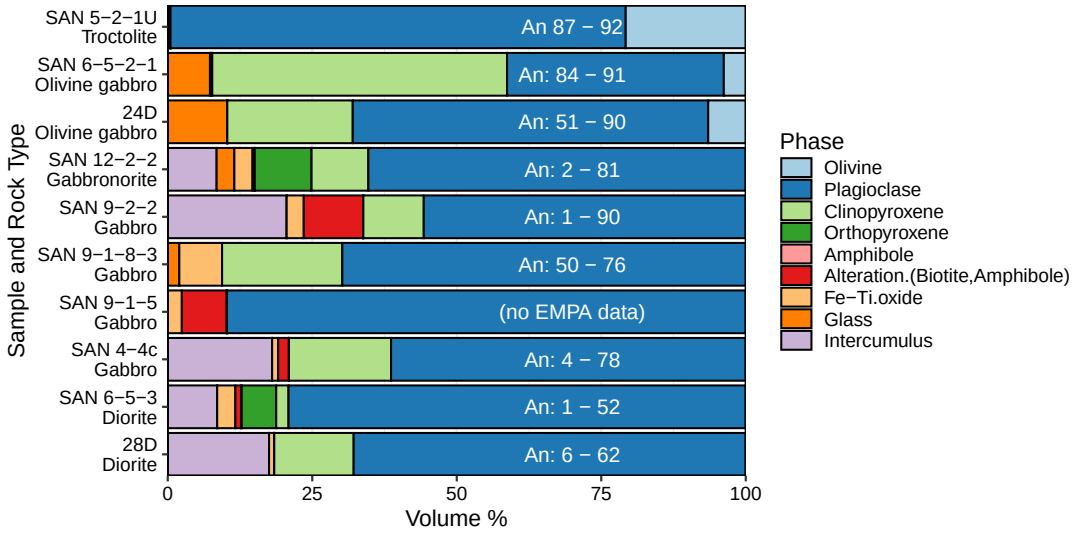


*Figure 2.4: Modal mineralogy of representative xenoliths. Alteration products are generally biotite/amphibole (Bt,Amph) replacing clinopyroxene. Texturally, the majority of hydrous phases in the samples are a result of secondary alteration. Anorthite number includes rims and intercumulus. Glass in the olivine gabbros contains microlites of plagioclase, clinopyroxene, olivine and amphibole. The intercumulus assemblage in the gabbro and gabbronorites is generally quartz ± orthoclase ± glass*

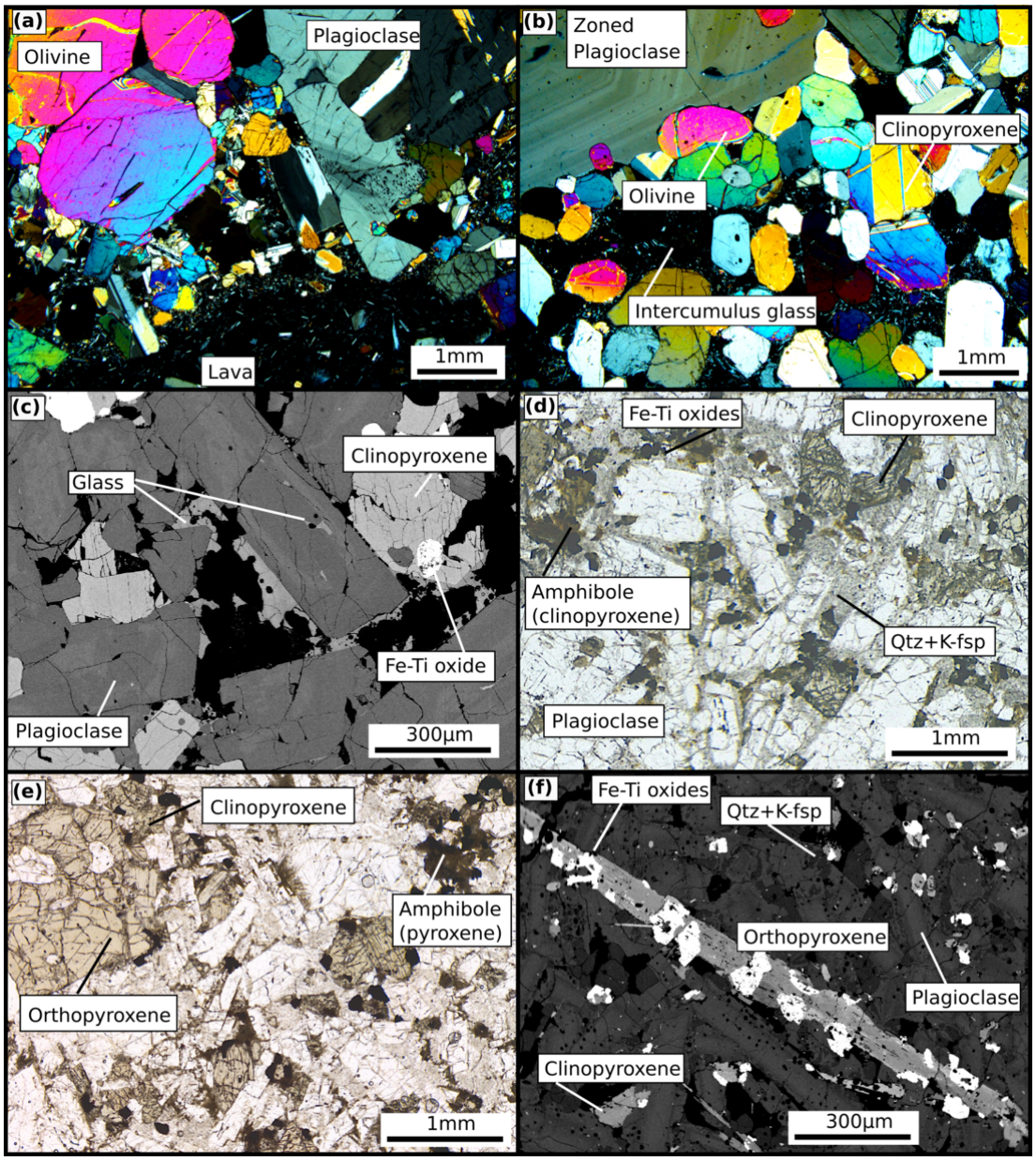


*Figure 2.5: Petrography of the xenoliths. A) Troctolitic glomerocryst assemblage with clinopyroxene-rich rim at the lava contact. Sample SAN 5-2-1U from Nea Kameni. B) Olivine gabbro with intercumulus glass. Sample 24D from Lower Pumice 2. C) Mafic glass-bearing gabbro with patchy zoned plagioclase. Sample SAN 9-1-8-3 from Lower Pumice 2. D) Intermediate holocrystalline gabbro. Sample SAN 9-2-2 from the Middle Pumice. E) Coarse grained gabbronorite. Sample SAN 14-1-3-3 from Upper Scoriae 2. F) Fine grained diorite with acicular pyroxene crystals. Sample SAN 6-5-3 from the Middle Pumice. Many gabbronorite samples are texturally indistinguishable from this sample. A), B) and D), E) are thin section microphotographs in cross-polarized and plane polarized light, respectively; C) and F) are back-scattered electron images.*

**Troctolite Glomerocrysts**

Centimetre-sized angular troctolitic glomerocrysts are found in some of the lavas sampled ex-situ on Nea Kameni (Figure 2.5A). Although not strictly xenoliths, they are discussed in this thesis as they contain information about the plumbing and mush system at Santorini. They comprise small (˜300 µm) rounded olivine grains (<25 vol%, Figure 2.4) enclosed in large millimetre sized weakly zoned plagioclase crystals. The plagioclase are often surrounded by a rim of clinopyroxenes and/or glass lacking the devitrified microlitic texture of the lavas at the lava contact, and this glass infiltrates the fragments. Strained plagioclase twins are present. These samples are similar to the gabbroic and troctolitic cumulate glomerocrysts previously described by Martin (2006a, 2007).

**Olivine Gabbro**

Olivine-gabbro cumulates in hand specimen are up to a centimetre in size, coarse grained and rounded, found rarely in the deposits of Lower Pumice 2 and Middle Pumice. They comprise up to 2 mm sized cumulus crystal assemblage of olivine (5-10 vol%), clinopyroxene and plagioclase, with abundant intercumulus glass, plagioclase and clinopyroxene microlites, and trace intercumulus amphibole (Figures 2.4, 2.5B). IInfrequent micrometre sized magnetite is restricted to clinopyroxene and olivine grain-glass boundaries, excluding sample 27D (Lower Pumice 2) in which they occur up to 500 microns in size, spread throughout the sample. Crystal forms are generally euhedral to subhedral, however, sample 25D-2 from the Lower Pumice 2 eruption shows partial equilibration and grain boundary triple junctions. Plagioclase texturally appears to be the first crystallising phase, followed by clinopyroxene and olivine, especially evident in the ophitic sample 21D (Figure 2.6B). Plagioclase has different textural forms: unzoned phenocrysts, very weakly oscillatory zoned, and crystals with strongly resorbed cores (Figure 2.6C) containing glass, clinopyroxene and magnetite microlites. Rare plagioclase crystals exhibiting these textures have been described in the pyroclastics of the Lower Pumice 2 eruption as antecrysts from these cumulates (Gertisser *et al.*, 2009). Sample 29D shows some deformation of the plagioclase twin planes. In contrast to the more common gabbroic lithologies, olivine gabbro samples show relatively good preservation and freshness. Olivine exhibits partial iddingsitisation on the rims and along fractures. All cumulus crystals show a distinct few micrometre thick overgrowth rim at contacts with the interstitial glass. Melt inclusions are exceptionally abundant within clinopyroxene and plagioclase in several samples, however depending on the sample and host phase, these melt inclusions often contain numerous daughter

crystals and/or alteration, showing evidence of significant post-entrapment modification (Appendix A.1). Olivine-hosted melt inclusions are rarer but show less evidence of modification.

**Gabbro**

The gabbros hand specimens range in size from centimetre sized pieces to fist sized blocks, in rounded to sub-angular pieces. They comprise dominantly coarse-grained (up to 2 mm) clinopyroxene and plagioclase with minor interstitial glass, Fe-Ti oxides and apatite (Figure 2.5C, D). The clinopyroxenes are commonly unzoned, however some samples show irregular zoning and a sharp rim. Plagioclase is strongly zoned, with a distinct contact between a core, and a more gradual mantle to rim profile. The cores can be patchy, and on rare occasions more sodic than the mantle and rims. The intercumulus assemblage comprises dominantly plagioclase ± quartz ± orthoclase, with rare intercumulus glass. This glass is most common in sample SAN 9-1-8-3, which lacks the more evolved quartz and orthoclase interstitial assemblage common in other gabbro samples. Clinopyroxene is commonly rimmed or fully replaced by actinolite and biotite, with minor titanite, ilmenite and rutile. Fe-Ti oxides commonly exhibit exsolution lamellae of ilmenite in titanomagnetite. Only one gabbro sample has any preferred textural orientation, sample SAN 9-1-5 from the Lower Pumice 2 eruption which exhibits preferential plagioclase orientation.

**Gabbronorite**

Gabbronorite hand specimens are up to 5 cm in size, and rounded to sub-angular pieces. They comprise clinopyroxene, orthopyroxene, strongly zoned plagioclase, Fe-Ti oxides, trace amphibole, apatite and interstitial glass in finer-grained (~<0.5 mm crystals) and coarse grained varieties (<2 mm crystal sizes) (Figure 2.5E, F). In finer-grained xenoliths the pyroxenes show acicular needle-like habits, changing from clinopyroxene to orthopyroxene along their length, but lacking clear exsolution lamellae. Fe-Ti oxides and apatite are present in both coarse and fine grained textural types. Rare olivine with two-pyroxene-bearing reaction rims are found in two samples (<1 vol%). Plagioclase often has a distinct weakly zoned core and more pronounced zonation towards the rims. Clinopyroxene and orthopyroxene are commonly unzoned and have a distinct rim at the contact with the plagioclase, orthoclase and rare glass interstitial assemblage. Fe-Ti oxides often show exsolution lamellae, and alteration of pyroxene to amphibole and biotite is common in both textural types.

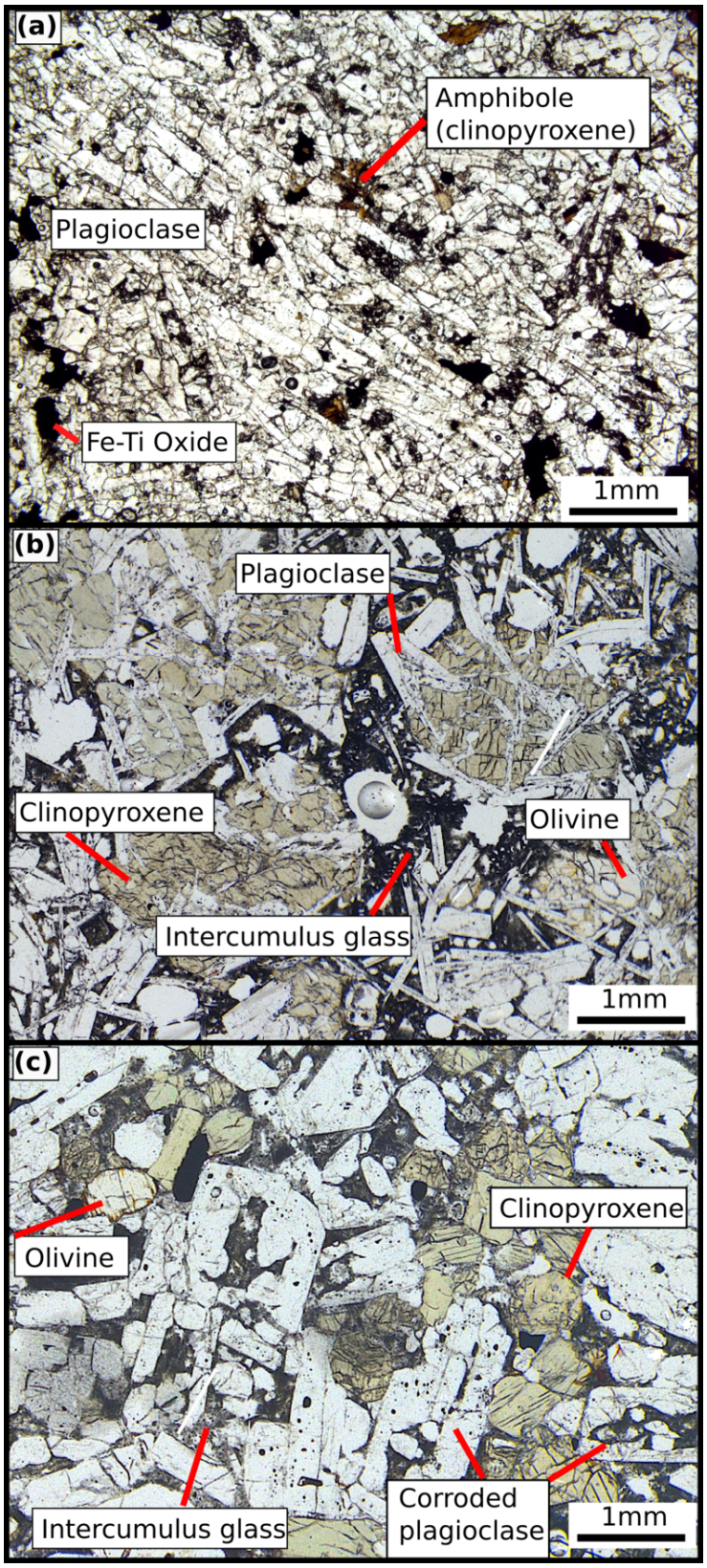


*Figure 2.6: Additional xenolith textures from the Lower Pumice 2 eruption. Plane polarised light photographs. A) Layering of plagioclase in sample SAN 9-1-5. B) Ophitic texture in olivine gabbro sample 23D. C) Corroded plagioclase with glass filled cores in sample 27D.*

#### Diorite

Diorites comprise clinopyroxene, strongly zoned plagioclase, orthopyroxene in some samples, Fe-Ti oxides, trace amphibole and interstitial glass (Figure 2.5F). They are texturally very similar to some of the more evolved gabbro and gabbronorite samples, additionally containing an interstitial assemblage of albite-rich plagioclase, orthoclase and rare interstitial glass.

#### Pumice, Mafic Blebs and Phenocryst-rich Pumice

In addition to the dominantly gabbroic plutonic xenoliths, we made limited analyses on other components of the Santorini eruptive products to compare to the xenolith mineral compositions. Detailed descriptions of these are found in the respective papers referenced below. The eruptions of Lower Pumice 2 and the Minoan contain abundant cauliform mafic 'blebs' interpreted to be quenched intruding mafic magmas (Gertisser *et al.*, 2009; Druitt *et al.*, 2012), of which we analysed one Minoan sample to supplement the Lower Pumice 2 bleb dataset of Gertisser et al. (2009). Analyses were made from one pumice clast each from the Lower Pumice 2 and the Minoan eruptions. Finally, analyses were made from a single phenocryst-rich pumice (P.R. Pumice) clast from the Minoan eruption (Druitt *et al.*, 2012) to compare to our xenolith sample from the same eruption. These phenocryst-rich pumice clasts are interpretted to be derived from an intrusion geochemically distinct to the post-530 ka magma series at Santorini (Druitt *et al.*, 1999; Druitt, 2014).

### 2.4.2 Mineral Chemistry

#### Olivine

Troctolitic glomerocryst olivine in sample SAN 5-2-1u is the most primitive and least altered in our study, with $Fo_{77\text{-}84}$ and CaO = 0.14-0.21 wt% (Figure 2.7, Table 2.3). These are more evolved than compositions reported by Martin *et al.* (2006a) for their Nea Kameni cumulate fragments ($Fo_{85\text{-}93}$). In the olivine gabbros each sample contains compositionally homogeneous olivine, with <2 mol% Fo variation per sample ($Fo_{74\text{-}78}$ CaO = 0.16-0.23 wt%), except for small intercumulus olivines in the glass ($Fo_{65\text{-}75}$ CaO = 0.19-0.43 wt%). Gabbronorite olivine is significantly less primitive $Fo_{47\text{-}69}$ CaO = 0.01-0.23 wt% and always surrounded by a rim of clinopyroxene or orthopyroxene. The samples with Fo < 60 are from sample SAN 12-1-5, which only contains this olivine composition. CaO is weakly correlated with Fo content. Transition metals are the only dominant detectable trace elements present (Co 202-206 ppm, Zn 137-175

ppm, Ni 442-608 ppm, Cu 2.6-4.1 ppm). REE concentrations are very low (∑REE 0.07 ppm) with a weak relative enrichment in HREE, and LREE typically below the detection limit.

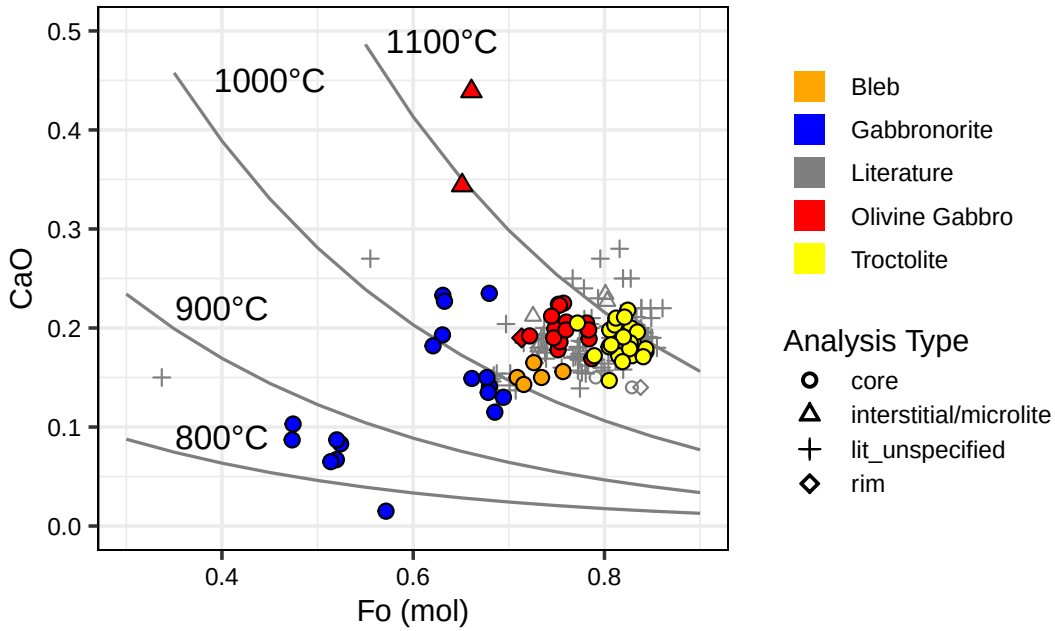


*Figure 2.7: Olivine chemistry. Isothermal contours of CaO vs Fo calculated from Shejwalkar and Coogan (2013). Although used outside the model calibration range for olivines with Fo less than 70, the contoured temperatures are consistent with the 960 to 796°C temperatures estimated from mineral-melt thermometry (see thermobarometry section in the discussion). Literature data (light grey) from Druitt (1983), Cabato (2007), Gertisser* et al. *(2009), Druitt* et al. *(2016)*

### Clinopyroxene

Crystal core Mg# generally decreases from the olivine gabbros (Mg# 76-86), through gabbros (Mg# 60-82), diorites (Mg# 68-71) to gabbronorite (Mg# 55-80) (Figure 2.8, Table 2.4). Clinopyroxene in the rim around the troctolitic glomerocryst and as small crystals within has Mg# 58-72, much lower than the olivine $Fo_{79\text{-}84}$, and generally overlapping the Mg# of the clinopyroxenes in the host lava within this sample (Mg# 70-82). Clinopyroxene crystals across the xenoliths are commonly unzoned, with some samples exhibiting a fine 5-15 $\mu$m rim with a lower Mg# in contact with the intercumulus assemblage. Olivine gabbro clinopyroxenes have little compositional variation within samples (<4 mol% Mg#) but exhibit the distinct sharp Fe-rich rim (Mg# 64-73) at the contact with intercumulus glass, and Fe-rich microlites within the glass (Mg# 59-65). Clinopyroxene within the gabbros, gabbronorites and diorites shows a wider compositional variation within samples and the crystals within some samples show patchy

*Table 2.3: Average olivine major element and trace element compositions*

| | Troctolite | $\sigma$ | Olivine Gabbro | $\sigma$ | Gabbronorite | $\sigma$ | Bleb | $\sigma$ |
|---|---|---|---|---|---|---|---|---|
| $n$ | 23 | | 19 | | 18 | | 5 | |
| $SiO_2$ | 39.35 | 0.81 | 38.96 | 0.48 | 36.05 | 1.35 | 38.19 | 0.47 |
| $TiO_2$ | 0.02 | 0.03 | 0.02 | 0.03 | 0.01 | 0.02 | 0.03 | 0.04 |
| $Al_2O_3$ | 0.03 | 0.01 | 0.06 | 0.09 | 0.03 | 0.01 | 0.02 | 0.01 |
| $Cr_2O_3$ | 0.01 | 0.01 | 0.01 | 0.01 | 0.01 | 0.02 | 0.01 | 0.01 |
| FeO | 16.72 | 1.68 | 22.92 | 2.85 | 33.94 | 5.90 | 24.37 | 1.53 |
| MnO | 0.29 | 0.04 | 0.42 | 0.07 | 0.66 | 0.12 | 0.45 | 0.05 |
| MgO | 42.28 | 1.23 | 38.10 | 2.67 | 29.23 | 4.49 | 36.65 | 1.20 |
| CaO | 0.19 | 0.02 | 0.22 | 0.06 | 0.13 | 0.06 | 0.15 | 0.01 |
| Total | 98.89 | 2.54 | 100.74 | 0.48 | 100.06 | 0.64 | 99.91 | 0.68 |
| **Cations based on 4 oxygens** | | | | | | | | |
| Si | 1.029 | 0.104 | 1.034 | 0.116 | 0.995 | 0.013 | 1.407 | 0.227 |
| Ti | 0.000 | 0.001 | 0.000 | 0.001 | 0.000 | 0.000 | 0.001 | 0.001 |
| Al | 0.001 | 0.000 | 0.002 | 0.003 | 0.001 | 0.000 | 0.001 | 0.000 |
| Cr | 0.000 | 0.000 | 0.000 | 0.000 | 0.000 | 0.000 | 0.000 | 0.000 |
| Fe | 0.366 | 0.057 | 0.508 | 0.075 | 0.788 | 0.160 | 0.747 | 0.105 |
| Mn | 0.006 | 0.001 | 0.009 | 0.002 | 0.015 | 0.003 | 0.014 | 0.002 |
| Mg | 1.648 | 0.166 | 1.509 | 0.211 | 1.199 | 0.153 | 2.015 | 0.345 |
| Ca | 0.005 | 0.001 | 0.006 | 0.002 | 0.004 | 0.002 | 0.006 | 0.001 |
| **Endmembers (mol)** | | | | | | | | |
| Fo | 0.82 | 0.02 | 0.75 | 0.04 | 0.60 | 0.08 | 0.73 | 0.02 |
| **LA-ICP-MS trace elements (ppm)** | | | | | | | | |
| Li | | | 2.47 | 0.54 | | | | |
| Sc | | | 7.08 | 0.34 | | | | |
| Ti | | | 49.09 | 10.43 | | | | |
| V | | | 6.30 | 0.43 | | | | |
| Cr | | | 14.25 | 12.28 | | | | |
| Co | | | 203.91 | 2.22 | | | | |
| Ni | | | 512.91 | 74.25 | | | | |
| Cu | | | 3.39 | 0.62 | | | | |
| Zn | | | 156.49 | 21.31 | | | | |

zonation unrelated to growth zones. Clinopyroxene inclusions within feldspars in the gabbros have a relatively low Mg# (Mg# 65-67) with respect to the overall population. $Al_2O_3$ concentrations in clinopyroxene are higher and fall into a more restricted range in the olivine gabbros (core 2.7-3.8 wt%, rim and intercumulus: 5.1-7.8 wt%) than in the gabbros and gabbronorites (<3.8wt%, with the majority below 2.5wt%). $Fe^{3+}/\sum Fe$ calculated from stoichiometry (Droop, 1987) falls predominantly below 0.3, but reaching a maximum of 0.64, with no correlation with Mg#. Olivine gabbros have an overall higher $Fe^{3+}/\sum Fe$ than the gabbronorites and diorites, with gabbros covering the entire range. Clinopyroxene compositions generally overlap compositions of phenocrysts from the explosive deposits, but some gabbro, diorite and gabbronorite samples distinctly fall away with low Al, Ti and Mn concentrations (Figure 2.8). These compositions do not match any of the experimentally produced clinopyroxenes from Cadoux *et al.*

(2014) or Andujar (2015, 2016) on Santorini liquid compositions, but however overlap the compositions of many hydrothermally altered clinopyroxenes in the literature (Manning and Bird, 1986; Rose and Bird, 1994; Good *et al.*, 1997; Martinez-Serrano, 2002; Marks *et al.*, 2010). In contrast to the low Ti-Al cluster, diorite samples SAN 6-5-3 and SAN 12-1-8-2 have elevated TiO2 and $Al^{IV}$ relative to the volcanic field.

Clinopyroxene REE profiles are generally curved with moderate MREE and HREE enrichment relative to the LREE ($(La/Sm)_N$ = 0.21-0.75, $(Gd/Lu)_N$ = 0.94-2.17, Figure 2.9 ,Table 2.5). Overall REE enrichment generally correlates with the xenolith type, with olivine gabbros showing up to 10x enrichment relative to chondrite, and gabbronorite clinopyroxene showing up to 500x enrichment. Five samples do not follow these profiles, and exhibit flatter or negative profiles with high La/Yb = 0.99-3.45 (Figure 2.9B,C). Some of these samples additionally fall into the low Ti-Al major element group (Figure 2.8). These profiles exhibit a similar negative slope and slight LREE enrichment to the few amphibole analyses made (Figure 2.9B). There is no clear correlation between REE profile slope and clinopyroxene major element composition (Ti, $Al^{IV}$, Mg#, Na), indicating crystal major element chemistry is not controlling these anomalous slopes. Multiple analyses from the same sample having similar profiles indicates inclusions are likely not the cause either. Most xenolith samples show a negative Eu anomaly that correlates with differentiation indices such as decreasing Mg# and increasing La (Figure 2.9D), but show no correlation with some other incompatible trace elements (e.g. Zr).

Clinopyroxene incompatible trace elements concentrations also show a large variation across samples, generally correlated to rock type (Figure 2.10). Similarly to the REE, profiles are generally correlated to rock type and increase/decrease with how evolved the xenolith is. Pb and Li have negative anomalies in olivine gabbros, through flat in gabbros to positive anomalies in gabbronorites and diorites.

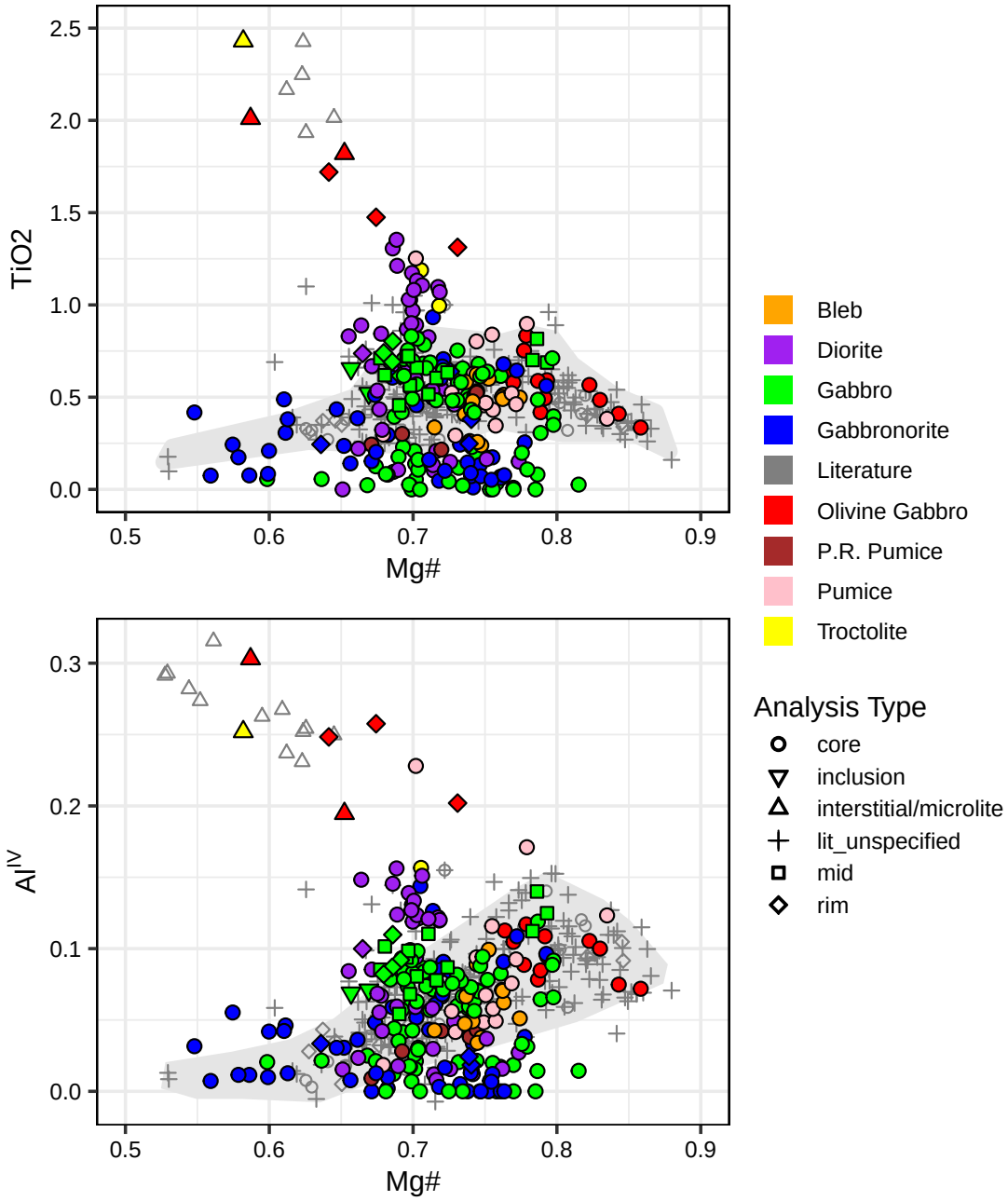


*Figure 2.8: Xenolith clinopyroxene chemistry. Grey fields show the general trend of published volcanic clinopyroxene compositions. A) $TiO_2$ versus Mg#. B) $Al^{IV}$ vs Mg#. Xenolith clinopyroxene broadly follow the volcanic trend. Notably a low Ti-Al cluster forms at intermediate Mg# compositions. Diorite samples show the inverse of this, and show increasing $TiO_2$-$Al^{IV}$ at near constant Mg#. Interstitial and microlite samples with increasing $TiO_2$-$Al^{IV}$ at low Mg# can be attributed to rapid element uptake during rapid cooling (Mollo* et al.*, 2010a). Literature data from Druitt (1983), Huijsmans (1985), Barton and Huijsmans (1986), Cottrell* et al. *(1999), Cabato (2007), Gertisser* et al. *(2009), Vaggelli* et al. *(2009), Panienka (2012), Cadoux* et al. *(2014), Andújar* et al. *(2015) and Druitt* et al. *(2016)*

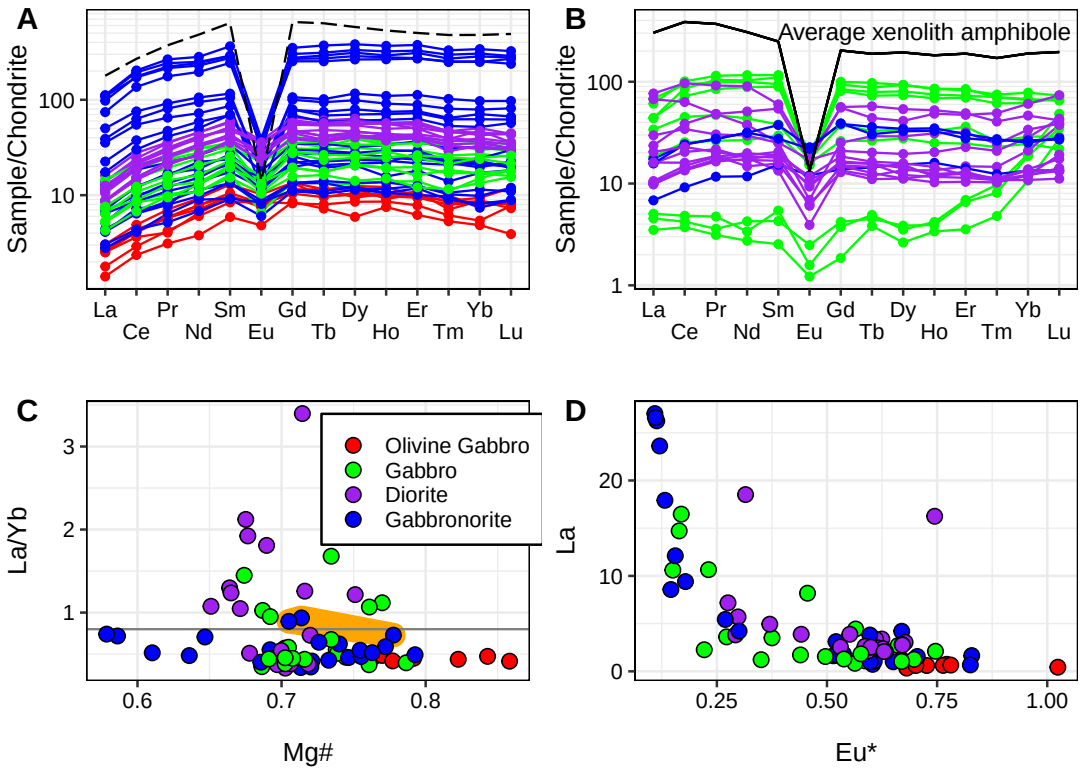


*Figure 2.9: Clinopyroxene trace elements. Normalisation values from Palme* et al. *(2014). A) Rare earth element (REE) profiles. The black dashed line represents the composition of a clinopyroxene crystallising from the final stage of closed system crystallisation of a mafic cumulate (see discussion). B) REE profiles for samples with anomalous profiles. A black line showing the average REE compositions of xenolith amphibole (typically secondary alteration) is included for comparison. These clinopyroxene have a slight enrichment in LREE and MREE compared to HREE similar to the amphibole profile. C) La/Yb vs Mg# showing the normal clinopyroxene slopes (below the line) compared to anomalous slopes. Sample SAN 9-3-2 is highlighted in orange, representing a non-cogenetic Minoan eruption xenolith (see discussion and Druitt, 2014). D) La vs Eu anomaly showing a good correlation, excluding two outlier points, indicating a strong role in fractional crystallisation influencing clinopyroxene REE enrichment (see discussion).*

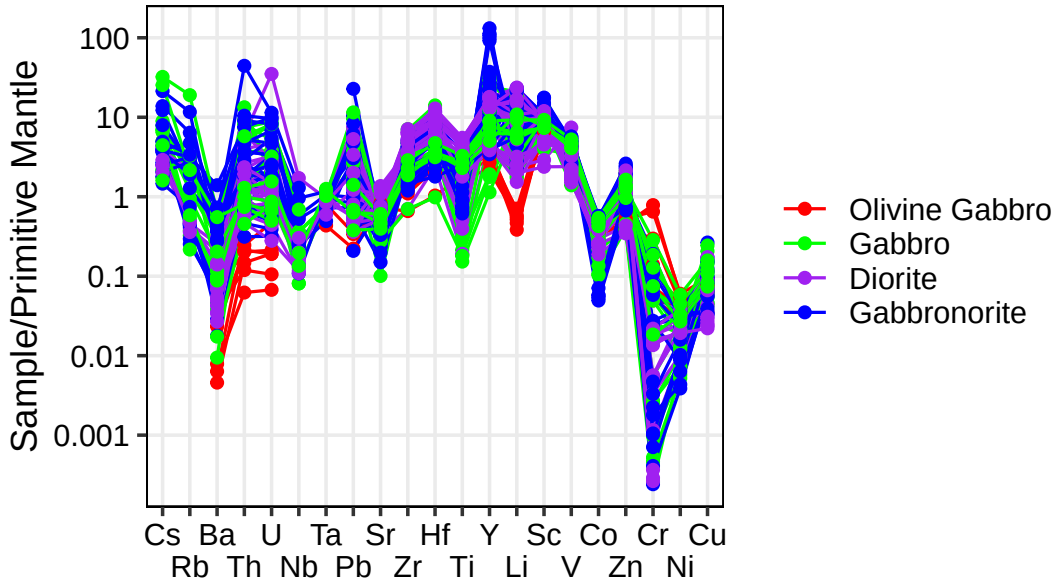


*Figure 2.10: Incompatible trace element concentrations in xenolith clinopyroxene. Normalisation values from Palme* et al. *(2014)*

*Table 2.4: Average clinopyroxene major element compositions. $Fe^{3+}$ estimated using Droop (1987).*

| | Troctolite | $\sigma$ | Olivine Gabbro | $\sigma$ | Gabbro | $\sigma$ | Diorite | $\sigma$ | Gabbronorite | $\sigma$ | P.R. Pumice | $\sigma$ | Pumice | $\sigma$ | Bleb | $\sigma$ |
|---|---|---|---|---|---|---|---|---|---|---|---|---|---|---|---|---|
| $n$ | 3 | | 17 | | 95 | | 42 | | 53 | | 5 | | 16 | | 12 | |
| $SiO_2$ | 48.60 | 2.20 | 50.38 | 2.46 | 51.70 | 1.32 | 50.76 | 1.68 | 52.13 | 1.30 | 52.50 | 0.29 | 51.32 | 1.54 | 51.99 | 0.66 |
| $TiO_2$ | 1.54 | 0.78 | 0.88 | 0.55 | 0.42 | 0.27 | 0.67 | 0.40 | 0.32 | 0.24 | 0.31 | 0.12 | 0.56 | 0.26 | 0.46 | 0.13 |
| $Al_2O_3$ | 4.79 | 1.43 | 4.06 | 1.66 | 1.62 | 0.95 | 2.06 | 1.19 | 1.21 | 0.94 | 1.28 | 0.41 | 2.54 | 1.38 | 1.88 | 0.55 |
| $Cr_2O_3$ | 0.01 | 0.02 | 0.08 | 0.11 | 0.02 | 0.03 | 0.01 | 0.01 | 0.01 | 0.02 | 0.00 | 0.00 | 0.02 | 0.04 | 0.01 | 0.01 |
| FeO | 10.74 | 1.56 | 8.43 | 3.16 | 9.77 | 1.54 | 10.27 | 0.96 | 10.84 | 2.34 | 10.01 | 1.11 | 8.74 | 1.21 | 8.96 | 0.54 |
| MnO | 0.30 | 0.04 | 0.22 | 0.06 | 0.32 | 0.13 | 0.38 | 0.14 | 0.43 | 0.11 | 0.49 | 0.15 | 0.35 | 0.12 | 0.39 | 0.09 |
| MgO | 12.36 | 2.25 | 14.62 | 1.19 | 14.20 | 1.07 | 13.49 | 0.92 | 13.70 | 1.25 | 13.97 | 0.60 | 14.61 | 0.70 | 14.94 | 0.55 |
| CaO | 21.17 | 0.81 | 21.18 | 1.41 | 20.51 | 1.97 | 20.70 | 1.88 | 20.42 | 1.38 | 20.77 | 0.25 | 20.91 | 0.55 | 20.52 | 0.55 |
| $Na_2O$ | 0.42 | 0.16 | 0.30 | 0.05 | 0.46 | 0.31 | 0.42 | 0.15 | 0.37 | 0.11 | 0.30 | 0.05 | 0.34 | 0.05 | 0.29 | 0.04 |
| Total | 99.92 | 0.24 | 100.15 | 0.69 | 99.03 | 1.07 | 98.76 | 1.09 | 99.43 | 1.04 | 99.65 | 0.36 | 99.40 | 0.64 | 99.43 | 0.45 |
| **Cations based on 6 oxygens, 4 cations** | | | | | | | | | | | | | | | | |
| Si | 1.824 | 0.068 | 1.862 | 0.073 | 1.943 | 0.035 | 1.920 | 0.047 | 1.963 | 0.038 | 1.968 | 0.014 | 1.915 | 0.053 | 1.940 | 0.020 |
| Ti | 0.044 | 0.022 | 0.025 | 0.016 | 0.012 | 0.008 | 0.019 | 0.012 | 0.009 | 0.007 | 0.009 | 0.004 | 0.016 | 0.007 | 0.013 | 0.004 |
| $Al^{IV}$ | 0.176 | 0.068 | 0.138 | 0.073 | 0.057 | 0.034 | 0.080 | 0.047 | 0.038 | 0.037 | 0.032 | 0.014 | 0.085 | 0.053 | 0.060 | 0.020 |
| $Al^{VI}$ | 0.036 | 0.003 | 0.048 | 0.024 | 0.015 | 0.016 | 0.014 | 0.012 | 0.016 | 0.011 | 0.024 | 0.005 | 0.027 | 0.013 | 0.023 | 0.007 |
| Cr | 0.000 | 0.001 | 0.002 | 0.003 | 0.001 | 0.001 | 0.000 | 0.000 | 0.000 | 0.001 | 0.000 | 0.000 | 0.001 | 0.001 | 0.000 | 0.000 |
| $Fe^{2+}$ | 0.254 | 0.020 | 0.193 | 0.045 | 0.256 | 0.056 | 0.266 | 0.038 | 0.311 | 0.081 | 0.300 | 0.039 | 0.222 | 0.062 | 0.247 | 0.022 |
| $Fe^{3+}$ | 0.083 | 0.038 | 0.069 | 0.079 | 0.052 | 0.027 | 0.060 | 0.027 | 0.031 | 0.025 | 0.013 | 0.013 | 0.051 | 0.037 | 0.033 | 0.013 |
| Mn | 0.010 | 0.001 | 0.007 | 0.002 | 0.010 | 0.004 | 0.012 | 0.005 | 0.014 | 0.004 | 0.016 | 0.005 | 0.011 | 0.004 | 0.012 | 0.003 |
| Mg | 0.691 | 0.121 | 0.805 | 0.059 | 0.796 | 0.061 | 0.761 | 0.052 | 0.768 | 0.063 | 0.781 | 0.030 | 0.813 | 0.034 | 0.831 | 0.028 |
| Ca | 0.852 | 0.039 | 0.838 | 0.048 | 0.826 | 0.073 | 0.839 | 0.071 | 0.823 | 0.050 | 0.834 | 0.007 | 0.836 | 0.019 | 0.820 | 0.023 |
| Na | 0.031 | 0.012 | 0.021 | 0.004 | 0.033 | 0.023 | 0.031 | 0.011 | 0.027 | 0.008 | 0.022 | 0.004 | 0.024 | 0.004 | 0.021 | 0.003 |
| **Endmembers (mol)** | | | | | | | | | | | | | | | | |
| Mg# | 0.67 | 0.08 | 0.76 | 0.08 | 0.72 | 0.04 | 0.70 | 0.03 | 0.69 | 0.06 | 0.71 | 0.03 | 0.75 | 0.03 | 0.75 | 0.02 |
| Wo | 0.45 | 0.03 | 0.44 | 0.03 | 0.43 | 0.04 | 0.43 | 0.03 | 0.42 | 0.03 | 0.43 | 0.00 | 0.43 | 0.01 | 0.42 | 0.01 |
| En | 0.36 | 0.06 | 0.42 | 0.03 | 0.41 | 0.03 | 0.39 | 0.03 | 0.39 | 0.03 | 0.40 | 0.02 | 0.42 | 0.02 | 0.43 | 0.01 |
| Fs | 0.18 | 0.03 | 0.14 | 0.05 | 0.16 | 0.03 | 0.17 | 0.02 | 0.18 | 0.04 | 0.17 | 0.02 | 0.15 | 0.02 | 0.15 | 0.01 |

*Table 2.5: Average clinopyroxene trace element compositions.*

| | Olivine Gabbro | $\sigma$ | Gabbro | $\sigma$ | Diorite | $\sigma$ | Gabbronorite | $\sigma$ |
|---|---|---|---|---|---|---|---|---|
| *n* | 7 | | 21 | | 22 | | 24 | |
| *ppm* | | | | | | | | |
| Li | 0.89 | 0.18 | 14.74 | 10.01 | 13.59 | 12.03 | 14.60 | 10.11 |
| Sc | 121.66 | 14.92 | 134.60 | 34.69 | 129.40 | 47.60 | 171.42 | 47.64 |
| V | 364.04 | 39.60 | 284.33 | 115.08 | 255.08 | 121.75 | 373.50 | 78.00 |
| Cr | 735.84 | 769.16 | 120.16 | 182.74 | 14.12 | 18.84 | 86.82 | 135.06 |
| Co | 40.38 | 3.45 | 36.41 | 13.87 | 31.37 | 8.64 | 40.02 | 18.56 |
| Ni | 82.36 | 19.77 | 35.15 | 29.39 | 18.84 | 23.71 | 28.93 | 28.82 |
| Cu | 1.46 | 0.24 | 1.73 | 1.23 | 0.99 | 0.86 | 1.68 | 1.28 |
| Zn | 33.00 | 8.41 | 68.86 | 33.11 | 71.15 | 27.84 | 75.54 | 32.66 |
| Rb | 0.00 | 0.00 | 0.95 | 2.48 | 0.18 | 0.38 | 1.15 | 1.64 |
| Sr | 16.07 | 1.24 | 9.76 | 3.75 | 15.46 | 6.33 | 10.11 | 3.95 |
| Y | 13.34 | 2.56 | 49.26 | 36.03 | 48.46 | 23.80 | 135.36 | 170.08 |
| Zr | 13.26 | 3.58 | 35.68 | 16.40 | 49.08 | 18.34 | 29.49 | 13.28 |
| Nb | 0.00 | 0.00 | 0.08 | 0.11 | 0.10 | 0.22 | 0.13 | 0.20 |
| Cs | 0.00 | 0.00 | 0.10 | 0.15 | 0.03 | 0.03 | 0.06 | 0.10 |
| Ba | 0.15 | 0.17 | 1.14 | 1.21 | 0.70 | 0.89 | 1.88 | 2.31 |
| La | 0.57 | 0.14 | 4.47 | 4.73 | 4.58 | 4.35 | 7.76 | 9.27 |
| Ce | 2.34 | 0.54 | 17.92 | 19.41 | 16.02 | 11.99 | 33.55 | 41.84 |
| Pr | 0.48 | 0.13 | 3.15 | 3.29 | 2.79 | 1.55 | 6.42 | 8.08 |
| Nd | 3.28 | 0.82 | 16.82 | 16.54 | 15.54 | 7.94 | 35.89 | 43.00 |
| Sm | 1.46 | 0.33 | 5.94 | 5.20 | 5.52 | 2.45 | 14.04 | 16.98 |
| Eu | 0.46 | 0.09 | 0.77 | 0.39 | 1.19 | 0.65 | 1.09 | 0.54 |
| Gd | 2.25 | 0.44 | 7.61 | 5.99 | 7.74 | 3.84 | 19.00 | 22.45 |
| Tb | 0.38 | 0.07 | 1.31 | 1.03 | 1.34 | 0.67 | 3.49 | 4.31 |
| Dy | 2.51 | 0.55 | 9.11 | 6.99 | 9.14 | 4.70 | 24.63 | 30.63 |
| Ho | 0.55 | 0.08 | 1.90 | 1.40 | 1.95 | 1.01 | 5.26 | 6.50 |
| Er | 1.51 | 0.26 | 5.54 | 4.02 | 5.66 | 2.83 | 15.67 | 19.55 |
| Tm | 0.20 | 0.04 | 0.80 | 0.55 | 0.77 | 0.38 | 2.20 | 2.77 |
| Yb | 1.27 | 0.29 | 5.52 | 3.30 | 5.41 | 2.50 | 14.44 | 18.39 |
| Lu | 0.20 | 0.06 | 0.93 | 0.48 | 0.83 | 0.37 | 2.12 | 2.64 |
| Hf | 0.69 | 0.23 | 1.78 | 0.87 | 2.46 | 0.91 | 1.60 | 0.69 |
| Ta | 0.01 | 0.01 | 0.01 | 0.02 | 0.01 | 0.02 | 0.01 | 0.02 |
| Pb | 0.04 | 0.03 | 0.54 | 0.56 | 0.47 | 0.54 | 0.62 | 0.90 |
| Th | 0.02 | 0.01 | 0.31 | 0.32 | 0.17 | 0.13 | 0.39 | 0.76 |
| U | 0.00 | 0.00 | 0.07 | 0.06 | 0.07 | 0.17 | 0.08 | 0.08 |
| Eu* | 0.78 | 0.11 | 0.45 | 0.19 | 0.54 | 0.14 | 0.44 | 0.25 |

**Orthopyroxene**

Mg# ranges between 46-76, and crystals commonly have a rim of Mg# = 46-55 (Table 2.6). $Al_2O_3$ concentrations are <3.5 wt%, with the bulk of orthopyroxenes containing <2 wt%, increasing with Mg#. Excluding three outliers reaching 9 mol%, Wo content ranges from 1.3 to 4.6 mol%. As with the clinopyroxenes, most samples fall within the range of eruptive compositions found in the literature, however two gabbronorite samples plot distinctly away, having high Ti-low Mg# (SAN 12-1-5) and low Ti-high Mg# populations (SAN 9-1-1-3) (Figure 2.11A). REE concentrations are low ($\sum$REE = 4.94-28.85 ppm, Table 2.7) and profiles show a steep

enrichment of MREE and HREE relative to chondrite ($(La/Yb)_N$ = 0.003-0.259, Figure 2.11B) with varying negative Eu anomalies (0.08-0.87) that have no systematic correlation with Mg#.

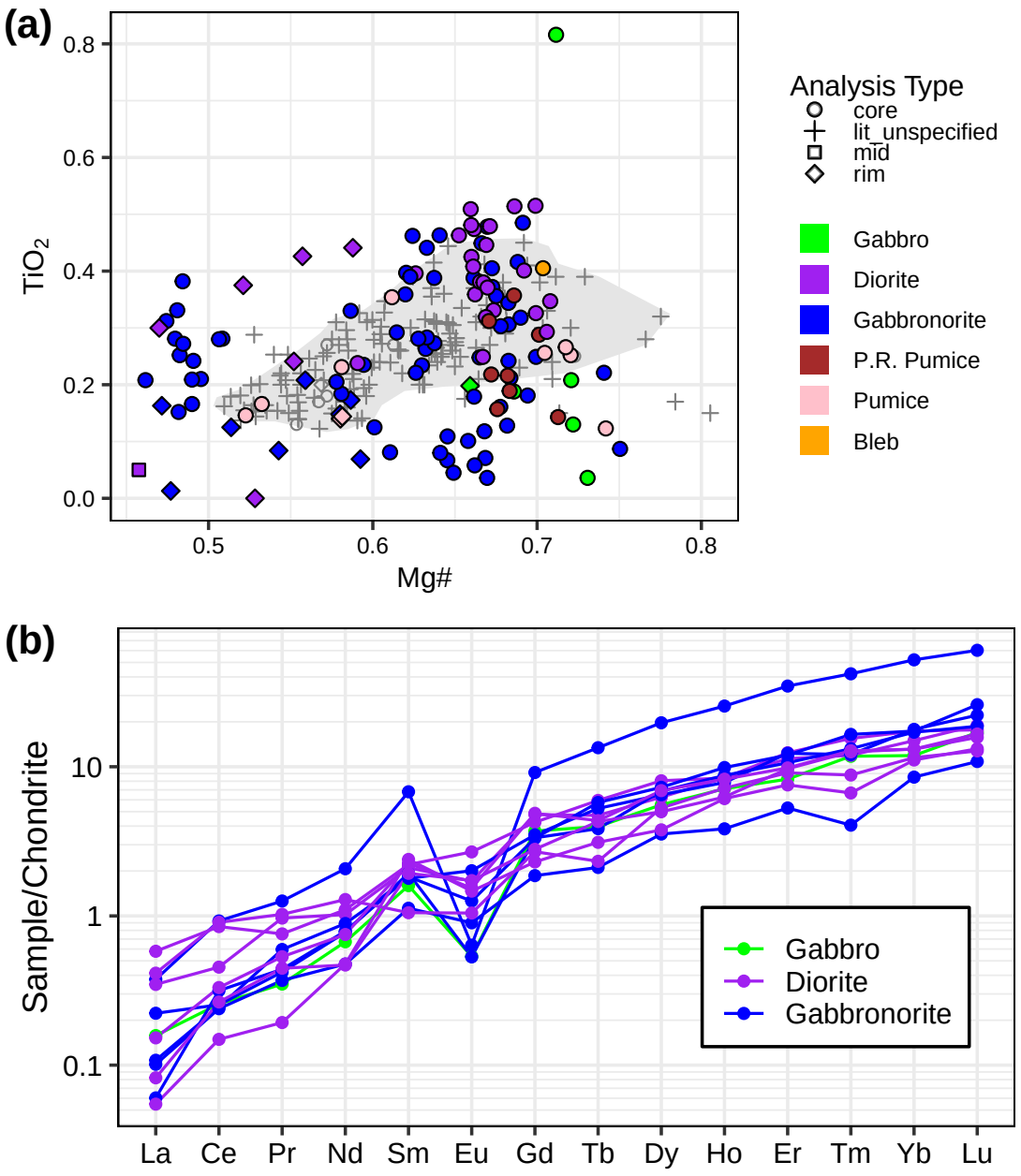


*Figure 2.11: Orthopyroxene chemistry. A) Major element chemistry. $TiO_2$ vs Mg# showing a wide spread of data compared to literature volcanic data. B) REE profiles. Literature data (light grey) from Druitt (1983), Huijsmans (1985), Cabato (2007), Gertisser* et al. *(2009), Panienka (2012) and Druitt* et al. *(2016)*

*Table 2.6: Average orthopyroxene major element compositions.*

| | Gabbro | $\sigma$ | Diorite | $\sigma$ | Gabbronorite | $\sigma$ | P.R. Pumice | $\sigma$ | Pumice | $\sigma$ | Bleb |
|---|---|---|---|---|---|---|---|---|---|---|---|
| $n$ | 6 | | 30 | | 73 | | 8 | | 10 | | 1 |
| $SiO_2$ | 53.42 | 1.05 | 52.14 | 0.93 | 52.37 | 1.29 | 53.70 | 0.32 | 52.73 | 1.18 | 53.28 |
| $TiO_2$ | 0.26 | 0.28 | 0.36 | 0.12 | 0.24 | 0.12 | 0.24 | 0.08 | 0.21 | 0.08 | 0.40 |
| $Al_2O_3$ | 1.26 | 1.07 | 1.12 | 0.50 | 0.76 | 0.51 | 1.14 | 0.29 | 0.92 | 0.49 | 1.18 |
| $Cr_2O_3$ | 0.03 | 0.04 | 0.01 | 0.01 | 0.01 | 0.01 | 0.01 | 0.02 | 0.01 | 0.01 | 0.00 |
| FeO | 18.09 | 1.73 | 21.52 | 3.55 | 23.33 | 4.06 | 19.19 | 0.88 | 22.06 | 4.49 | 17.95 |
| MnO | 0.59 | 0.10 | 0.95 | 0.42 | 0.78 | 0.23 | 0.61 | 0.05 | 1.03 | 0.46 | 0.66 |
| MgO | 24.27 | 1.57 | 21.13 | 2.69 | 20.54 | 3.06 | 23.45 | 0.55 | 21.17 | 3.30 | 23.90 |
| CaO | 1.58 | 0.99 | 1.71 | 0.27 | 1.60 | 0.56 | 1.34 | 0.12 | 1.40 | 0.09 | 1.41 |
| $Na_2O$ | 0.14 | 0.25 | 0.04 | 0.02 | 0.04 | 0.02 | 0.04 | 0.02 | 0.03 | 0.02 | 0.02 |
| Total | 99.70 | 0.36 | 98.98 | 0.62 | 99.68 | 0.60 | 99.72 | 0.39 | 99.56 | 0.61 | 98.81 |
| **Cations based on 6 oxygens, 4 cations** | | | | | | | | | | | |
| Si | 1.961 | 0.037 | 1.969 | 0.023 | 1.975 | 0.025 | 1.984 | 0.009 | 1.982 | 0.017 | 1.978 |
| Ti | 0.007 | 0.008 | 0.010 | 0.003 | 0.007 | 0.003 | 0.007 | 0.002 | 0.006 | 0.002 | 0.011 |
| $Al^{IV}$ | 0.039 | 0.037 | 0.031 | 0.023 | 0.025 | 0.025 | 0.016 | 0.009 | 0.018 | 0.017 | 0.022 |
| $Al^{VI}$ | 0.017 | 0.018 | 0.019 | 0.015 | 0.013 | 0.014 | 0.033 | 0.007 | 0.023 | 0.013 | 0.030 |
| Cr | 0.001 | 0.001 | 0.000 | 0.000 | 0.000 | 0.000 | 0.000 | 0.001 | 0.000 | 0.000 | 0.000 |
| $Fe^{2+}$ | 0.528 | 0.066 | 0.671 | 0.132 | 0.721 | 0.144 | 0.593 | 0.028 | 0.694 | 0.155 | 0.557 |
| $Fe^{3+}$ | 0.028 | 0.032 | 0.011 | 0.016 | 0.018 | 0.022 | 0.000 | 0.000 | 0.002 | 0.003 | 0.000 |
| Mn | 0.018 | 0.003 | 0.031 | 0.014 | 0.025 | 0.008 | 0.019 | 0.001 | 0.033 | 0.015 | 0.021 |
| Mg | 1.328 | 0.081 | 1.187 | 0.132 | 1.152 | 0.151 | 1.292 | 0.028 | 1.183 | 0.159 | 1.323 |
| Ca | 0.062 | 0.039 | 0.069 | 0.011 | 0.065 | 0.023 | 0.053 | 0.005 | 0.056 | 0.004 | 0.056 |
| Na | 0.010 | 0.017 | 0.003 | 0.001 | 0.003 | 0.002 | 0.003 | 0.001 | 0.002 | 0.002 | 0.001 |
| **Endmembers (mol)** | | | | | | | | | | | |
| Mg# | 0.71 | 0.03 | 0.64 | 0.07 | 0.61 | 0.08 | 0.69 | 0.01 | 0.63 | 0.08 | 0.70 |
| Wo | 0.03 | 0.02 | 0.04 | 0.01 | 0.03 | 0.01 | 0.03 | 0.00 | 0.03 | 0.00 | 0.03 |
| En | 0.68 | 0.03 | 0.60 | 0.07 | 0.58 | 0.08 | 0.66 | 0.01 | 0.60 | 0.08 | 0.68 |
| Fs | 0.29 | 0.03 | 0.36 | 0.07 | 0.39 | 0.07 | 0.31 | 0.01 | 0.37 | 0.08 | 0.30 |

### Feldspar

Feldspar, dominantly zoned plagioclase, is present in every sample. A bimodal distribution of feldspar compositions is observed in the literature dataset ($An_{93\text{-}70}$,$An_{65\text{-}30}$) and this is also observed in the xenolith dataset (Figure 2.12A-B, Table 2.8). The troctolitic glomerocrysts and olivine gabbros show the least zonation, containing weakly oscillatory zoned plagioclase with $An_{93\text{-}86}$ in the troctolitic glomerocrysts and $An_{91\text{-}84}$ in the olivine gabbros, with <5% An variation within samples regardless of crystal texture (sieve or homogeneous). These are within the range of $An_{95\text{-}85}$ identified in the Nea Kameni cumulate xenoliths of Martin *et al.* (2006a). Feldspar has a higher An than the coexisting olivine ($Fo_{78\text{-}74}$), as is commonly observed in arcs (e.g. Arculus and Wills, 1980; Sisson and Grove, 1993; Tollan *et al.*, 2012). Although the interiors of the plagioclase crystals in the olivine gabbro are essentially unzoned, they possess a very distinct sharp rim of $An_{65\text{-}62}$ in contact with the interstitial glass. Plagioclase within the gabbros, diorites and gabbronorites is significantly more variable, with cores and mantle covering the range $An_{90\text{-}25}$, and commonly very strong normal zoning to $An_1Ab_{99}Or_6$ at the rims in contact with the intercumulus assemblage, occasionally rimmed by K-feldspar with up to 58 mol% orthoclase. K-feldspar is also found as a graphic intercumulus assemblage with up to 79 mol% orthoclase. FeO concentrations reach 1.32 wt% in interstitial or microlite feldspar,

*Table 2.7: Average orthopyroxene trace element compositions*

| | Gabbro | Diorite | $\sigma$ | Gabbronorite | $\sigma$ |
|---|---|---|---|---|---|
| *n* | 1 | 6 | | 7 | |
| *ppm* | | | | | |
| Li | 3.16 | 16.45 | 3.64 | 12.26 | 6.31 |
| Sc | 54.42 | 66.28 | 5.05 | 55.77 | 5.04 |
| V | 75.66 | 66.93 | 15.37 | 100.91 | 30.53 |
| Cr | 0.82 | 0.42 | 0.59 | 13.50 | 32.07 |
| Co | 72.07 | 48.24 | 2.33 | 88.65 | 6.06 |
| Ni | 0.00 | 3.31 | 8.12 | 34.10 | 29.30 |
| Cu | 1.55 | 1.24 | 0.34 | 0.78 | 1.09 |
| Zn | 306.22 | 274.73 | 30.24 | 298.07 | 67.34 |
| Rb | 0.00 | 0.33 | 0.64 | 0.06 | 0.11 |
| Sr | 2.68 | 0.57 | 0.63 | 0.26 | 0.45 |
| Y | 10.21 | 11.04 | 2.07 | 15.18 | 10.99 |
| Zr | 4.67 | 5.60 | 1.20 | 3.82 | 1.07 |
| Nb | 0.20 | 0.00 | 0.00 | 0.00 | 0.00 |
| Cs | 0.06 | 0.07 | 0.12 | 0.01 | 0.01 |
| Ba | 0.69 | 0.66 | 1.11 | 0.12 | 0.13 |
| La | 0.04 | 0.07 | 0.05 | 0.20 | 0.36 |
| Ce | 0.16 | 0.30 | 0.19 | 0.58 | 0.83 |
| Pr | 0.03 | 0.06 | 0.03 | 0.10 | 0.11 |
| Nd | 0.32 | 0.40 | 0.16 | 0.61 | 0.42 |
| Sm | 0.25 | 0.31 | 0.07 | 0.43 | 0.31 |
| Eu | 0.03 | 0.10 | 0.03 | 0.06 | 0.03 |
| Gd | 0.77 | 0.75 | 0.24 | 0.81 | 0.51 |
| Tb | 0.15 | 0.16 | 0.05 | 0.22 | 0.14 |
| Dy | 1.42 | 1.50 | 0.39 | 2.03 | 1.39 |
| Ho | 0.40 | 0.42 | 0.06 | 0.56 | 0.41 |
| Er | 1.37 | 1.65 | 0.28 | 2.20 | 1.64 |
| Tm | 0.31 | 0.30 | 0.08 | 0.40 | 0.32 |
| Yb | 2.00 | 2.28 | 0.39 | 3.36 | 2.47 |
| Lu | 0.42 | 0.40 | 0.06 | 0.61 | 0.42 |
| Hf | 0.25 | 0.30 | 0.12 | 0.15 | 0.05 |
| Ta | 0.00 | 0.01 | 0.01 | 0.00 | 0.00 |
| Pb | 0.84 | 0.38 | 0.56 | 0.06 | 0.11 |
| Th | 0.00 | 0.03 | 0.04 | 0.05 | 0.10 |
| U | 0.00 | 0.00 | 0.00 | 0.02 | 0.02 |
| Eu* | 0.22 | 0.64 | 0.15 | 0.42 | 0.25 |

however the majority of analyses are less than 1 wt%, and FeO is weakly positively correlated to An content, generally overlapping published phenocryst data. Plagioclase zoning can be weakly oscillatory, distinctly patchy or radially diffuse across the crystal. The crystal cores commonly comprise a high An zone with a strong resorption texture. However, some gabbro and gabbronorite samples have cores with lower An contents than the normal zoned mantle to rim zones (Figure 2.12C).

Ba and Sr are weakly inversely correlated with An content. REE concentrations are low $\sum$REE 0.42-31.35 ppm and show a LREE enrichment compared to MREE and HREE

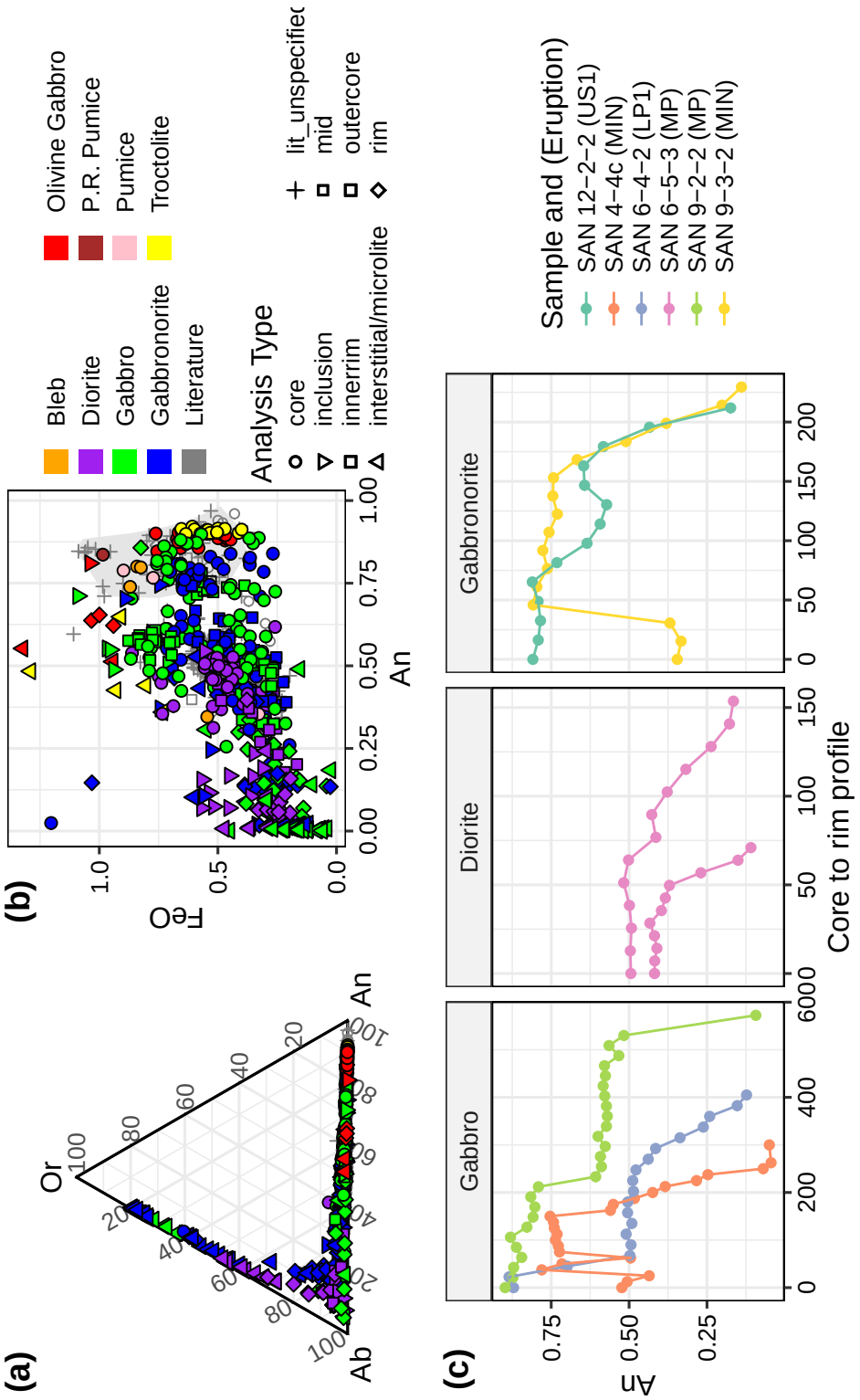


*Figure 2.12: Feldspar compositions. A) Ternary feldspar compositions. B) An vs FeO plot. C) Selected core to rim traverses for xenolith types that show strong compositional zoning of feldspars. Fields show the general trend of literature volcanic feldspar, highlighting the bimodal distribution of compositions. Literature data from Druitt (1983), Cabato (2007), Panienka (2012), Druitt* et al. *(2012) and Druitt* et al. *(2016)*

($(La/Yb)_N$ 5-114) with a strong positive Eu anomaly inversely correlated to An mole fraction (Table 2.9). Crystal rims show up to two times enrichment in incompatible elements relative to cores (Figure 2.13).

### Amphibole and Biotite

Amphiboles are classified using the classification scheme of Hawthorne *et al.* (2012) using the classification spreadsheet of Locock (2014). Amphibole microlites within the olivine gabbro intercumulus glass are magnesio-ferri-hornblende. Primary intercumulus amphibole within the gabbronorite are magnesio-ferri-hornblende and pargasite. Phenocryst-rich pumices are found in the Minoan eruption contain primary Ti-rich pargasite (see also Druitt *et al.*, 1999; Druitt, 2014). Actinolite is the dominant amphibole form, found as a secondary replacement phase. Xenolith amphibole, whether primary or replacing, predominantly has lower $Al^{IV}$ ($< 1.4$) than the microlite amphibole found in Lower Pumice 2 (Gertisser *et al.*, 2009) or Akrotiri phenocrysts (Mortazavi and Sparks, 2004) (Figure 2.14). REE slopes for a limited number of amphibole analyses ($n$=5) are generally negative, with $La/Yb_N$ between 0.91 to 1.89. Biotite is present as a replacement phase replacing clinopyroxene, with Mg# between 0.49 and 0.77, and $Al_2O_3$ between 9.34 and 14.18 wt%.

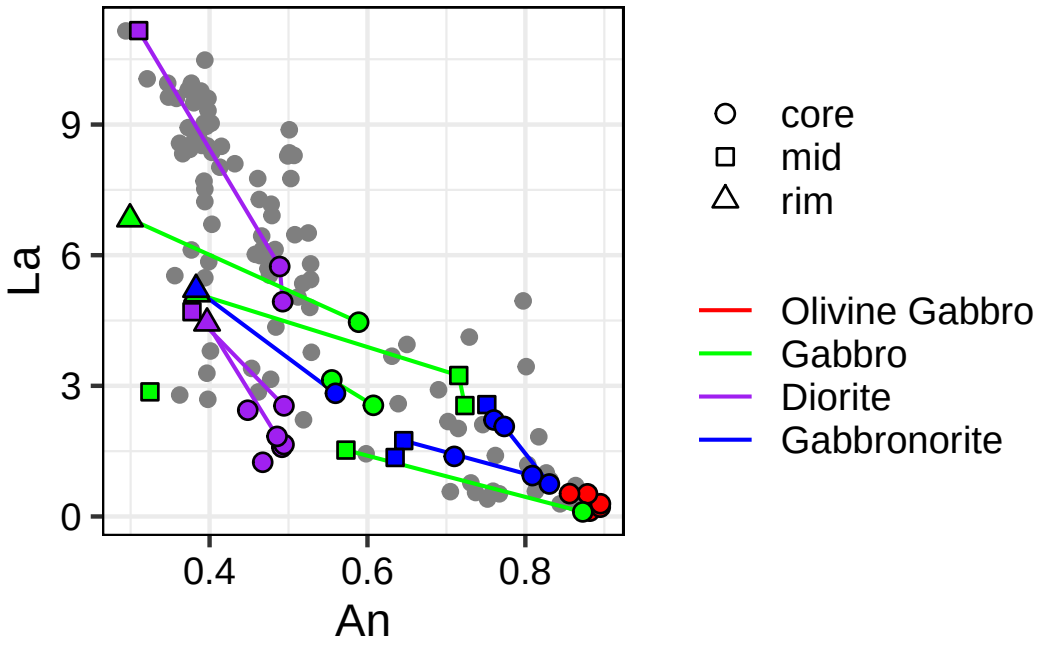


*Figure 2.13: Xenolith feldspar La vs An (mol) showing core to rim incompatible trace element enrichment. Literature pumice data in grey from Santo (2005), Druitt* et al. *(2012) and Fabbro* et al. *(2018).*

*Table 2.8: Feldspar major element compositions.*

| | Troctolite | $\sigma$ | Olivine Gabbro | $\sigma$ | Gabbro | $\sigma$ | Diorite | $\sigma$ | Gabbronorite | $\sigma$ | P.R. Pumice | $\sigma$ | Pumice | $\sigma$ | Bleb | $\sigma$ |
|---|---|---|---|---|---|---|---|---|---|---|---|---|---|---|---|---|
| $n$ | 26 | | 25 | | 168 | | 109 | | 147 | | 1 | | 3 | | 4 | |
| $SiO_2$ | 47.61 | 4.35 | 47.68 | 2.92 | 55.45 | 6.11 | 59.97 | 4.85 | 56.87 | 6.21 | 46.83 | | 51.71 | 5.82 | 51.32 | 5.91 |
| $TiO_2$ | 0.02 | 0.05 | 0.05 | 0.04 | 0.00 | 0.01 | 0.00 | 0.01 | 0.00 | 0.00 | 0.10 | | 0.03 | 0.03 | 0.04 | 0.03 |
| $Al_2O_3$ | 32.89 | 3.38 | 33.81 | 2.39 | 27.76 | 4.50 | 24.32 | 3.50 | 26.10 | 4.62 | 33.27 | | 29.63 | 3.95 | 30.26 | 3.95 |
| FeO | 0.63 | 0.19 | 0.71 | 0.22 | 0.47 | 0.24 | 0.39 | 0.14 | 0.42 | 0.19 | 0.98 | | 0.67 | 0.30 | 0.77 | 0.15 |
| MgO | 0.02 | 0.05 | 0.13 | 0.03 | 0.01 | 0.04 | 0.01 | 0.05 | 0.00 | 0.00 | 0.04 | | 0.06 | 0.03 | 0.08 | 0.02 |
| CaO | 16.98 | 3.59 | 16.73 | 2.36 | 10.12 | 5.12 | 6.36 | 3.93 | 8.88 | 5.34 | 17.26 | | 13.17 | 4.78 | 14.02 | 4.44 |
| $Na_2O$ | 2.03 | 2.05 | 2.03 | 1.33 | 5.12 | 2.43 | 7.53 | 1.72 | 5.44 | 2.16 | 1.85 | | 4.14 | 2.91 | 3.75 | 2.52 |
| $K_2O$ | 0.06 | 0.12 | 0.04 | 0.05 | 1.57 | 3.88 | 1.35 | 2.22 | 1.97 | 3.61 | 0.02 | | 0.18 | 0.15 | 0.14 | 0.16 |
| Total | 100.27 | 0.82 | 101.04 | 0.36 | 100.50 | 0.69 | 99.93 | 1.72 | 99.68 | 0.95 | 100.53 | | 99.69 | 0.77 | 100.49 | 0.11 |
| **Cations based on 8 oxygens** | | | | | | | | | | | | | | | | |
| Si | 2.185 | 0.181 | 2.171 | 0.125 | 2.501 | 0.253 | 2.690 | 0.194 | 2.579 | 0.262 | 2.152 | | 2.363 | 0.236 | 2.331 | 0.233 |
| Ti | 0.001 | 0.002 | 0.000 | 0.001 | 0.000 | 0.000 | 0.000 | 0.000 | 0.000 | 0.000 | 0.003 | | 0.001 | 0.001 | 0.001 | 0.001 |
| Al | 1.781 | 0.193 | 1.814 | 0.134 | 1.479 | 0.252 | 1.288 | 0.194 | 1.398 | 0.258 | 1.802 | | 1.599 | 0.230 | 1.624 | 0.231 |
| Fe | 0.024 | 0.007 | 0.027 | 0.008 | 0.018 | 0.009 | 0.015 | 0.005 | 0.016 | 0.007 | 0.038 | | 0.026 | 0.012 | 0.029 | 0.006 |
| Mg | 0.002 | 0.003 | 0.001 | 0.003 | 0.000 | 0.003 | 0.000 | 0.004 | 0.000 | 0.000 | 0.003 | | 0.004 | 0.002 | 0.005 | 0.001 |
| Ca | 0.837 | 0.181 | 0.816 | 0.117 | 0.492 | 0.253 | 0.307 | 0.191 | 0.434 | 0.264 | 0.850 | | 0.647 | 0.240 | 0.685 | 0.223 |
| Na | 0.180 | 0.178 | 0.179 | 0.117 | 0.445 | 0.205 | 0.654 | 0.144 | 0.476 | 0.184 | 0.165 | | 0.365 | 0.252 | 0.329 | 0.215 |
| K | 0.004 | 0.007 | 0.002 | 0.003 | 0.091 | 0.225 | 0.077 | 0.127 | 0.114 | 0.211 | 0.001 | | 0.010 | 0.009 | 0.008 | 0.009 |
| **Endmembers (mol)** | | | | | | | | | | | | | | | | |
| An | 0.82 | 0.18 | 0.82 | 0.12 | 0.48 | 0.25 | 0.30 | 0.19 | 0.42 | 0.26 | 0.84 | | 0.64 | 0.24 | 0.67 | 0.22 |
| Ab | 0.18 | 0.17 | 0.18 | 0.12 | 0.43 | 0.19 | 0.63 | 0.13 | 0.46 | 0.18 | 0.16 | | 0.35 | 0.24 | 0.32 | 0.21 |
| Or | 0.00 | 0.01 | 0.00 | 0.00 | 0.09 | 0.22 | 0.07 | 0.12 | 0.11 | 0.21 | 0.00 | | 0.01 | 0.01 | 0.01 | 0.01 |

*Table 2.9: Average feldspar trace element compositions*

| | Olivine Gabbro | $\sigma$ | Gabbro | $\sigma$ | Diorite | $\sigma$ | Gabbronorite | $\sigma$ |
|---|---|---|---|---|---|---|---|---|
| $n$ | 6 | | 10 | | 11 | | 10 | |
| *ppm* | | | | | | | | |
| Li | 1.70 | 0.99 | 4.86 | 6.24 | 12.13 | 9.02 | 6.56 | 5.52 |
| Sc | 0.45 | 0.20 | 0.41 | 0.34 | 0.46 | 0.26 | 0.46 | 0.50 |
| Ti | 84.53 | 20.86 | 198.95 | 85.34 | 241.61 | 62.66 | 191.40 | 68.14 |
| V | 1.81 | 0.47 | 1.33 | 0.67 | 0.60 | 0.45 | 2.01 | 1.23 |
| Cr | 0.00 | 0.00 | 1.09 | 1.01 | 0.13 | 0.39 | 0.36 | 0.71 |
| Mn | 36.47 | 4.69 | 41.54 | 15.65 | 30.35 | 11.72 | 41.69 | 12.14 |
| Co | 0.37 | 0.26 | 0.43 | 0.29 | 0.35 | 0.25 | 0.22 | 0.27 |
| Ni | 5.27 | 12.90 | 5.74 | 10.64 | 8.99 | 14.61 | 12.23 | 18.63 |
| Cu | 1.88 | 0.94 | 0.37 | 0.90 | 0.21 | 0.42 | 1.28 | 1.65 |
| Zn | 2.29 | 0.29 | 6.89 | 2.79 | 6.78 | 2.32 | 7.01 | 3.19 |
| Rb | 0.20 | 0.23 | 0.69 | 0.65 | 0.85 | 0.60 | 1.06 | 1.79 |
| Sr | 322.58 | 13.80 | 436.73 | 92.15 | 481.61 | 72.45 | 386.61 | 74.93 |
| Y | 0.07 | 0.12 | 0.49 | 0.32 | 0.31 | 0.29 | 0.58 | 0.41 |
| Zr | 0.06 | 0.15 | 0.11 | 0.24 | 0.08 | 0.17 | 0.16 | 0.20 |
| Nb | 0.05 | 0.08 | 0.06 | 0.10 | 0.05 | 0.10 | 0.09 | 0.12 |
| Cs | 0.03 | 0.04 | 0.00 | 0.00 | 0.02 | 0.06 | 0.09 | 0.11 |
| Ba | 11.69 | 3.53 | 107.03 | 67.66 | 173.86 | 165.15 | 73.33 | 52.36 |
| La | 0.31 | 0.17 | 3.24 | 1.88 | 3.84 | 2.89 | 2.11 | 1.28 |
| Ce | 0.56 | 0.28 | 5.09 | 2.73 | 5.42 | 3.41 | 3.18 | 1.86 |
| Pr | 0.07 | 0.04 | 0.49 | 0.27 | 0.48 | 0.25 | 0.30 | 0.17 |
| Nd | 0.21 | 0.12 | 1.82 | 0.91 | 1.60 | 0.72 | 1.13 | 0.51 |
| Sm | 0.05 | 0.06 | 0.29 | 0.18 | 0.30 | 0.20 | 0.16 | 0.13 |
| Eu | 0.12 | 0.10 | 0.85 | 0.48 | 1.21 | 0.86 | 0.71 | 0.63 |
| Gd | 0.00 | 0.00 | 0.23 | 0.16 | 0.18 | 0.21 | 0.07 | 0.12 |
| Tb | 0.03 | 0.04 | 0.03 | 0.02 | 0.01 | 0.02 | 0.02 | 0.03 |
| Dy | 0.04 | 0.04 | 0.13 | 0.06 | 0.07 | 0.09 | 0.10 | 0.09 |
| Ho | 0.01 | 0.01 | 0.02 | 0.02 | 0.01 | 0.02 | 0.04 | 0.06 |
| Er | 0.05 | 0.10 | 0.06 | 0.04 | 0.04 | 0.06 | 0.07 | 0.13 |
| Tm | 0.02 | 0.03 | 0.02 | 0.03 | 0.02 | 0.03 | 0.03 | 0.04 |
| Yb | 0.02 | 0.04 | 0.06 | 0.07 | 0.03 | 0.04 | 0.03 | 0.07 |
| Lu | 0.01 | 0.02 | 0.03 | 0.03 | 0.01 | 0.01 | 0.01 | 0.02 |
| Hf | 0.01 | 0.01 | 0.01 | 0.02 | 0.01 | 0.02 | 0.00 | 0.00 |
| Ta | 0.01 | 0.02 | 0.01 | 0.04 | 0.03 | 0.05 | 0.00 | 0.00 |
| Pb | 0.29 | 0.16 | 3.18 | 2.21 | 2.52 | 1.36 | 2.60 | 2.04 |
| Th | 0.01 | 0.02 | 0.02 | 0.03 | 0.02 | 0.02 | 0.01 | 0.02 |
| U | 0.01 | 0.02 | 0.01 | 0.01 | 0.01 | 0.02 | 0.01 | 0.02 |
| Eu* | | | 9.71 | 6.53 | 19.73 | 19.79 | 17.80 | 16.03 |

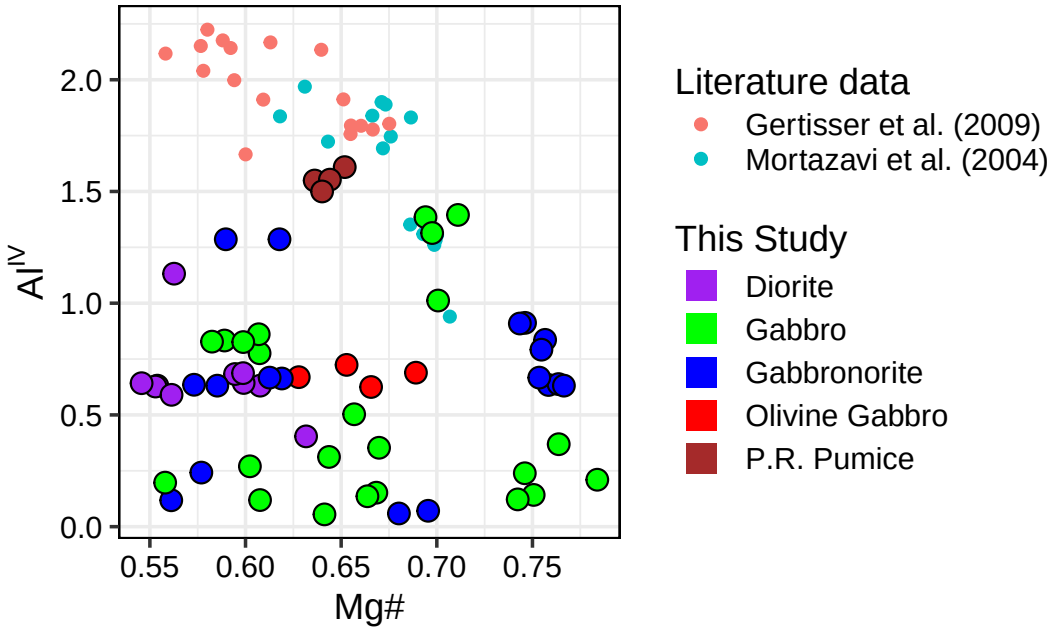


*Figure 2.14: Amphibole compositions in the xenoliths and published volcanic data. Literature data are pre-530 ka Akrotiri amphiboles from Mortazavi and Sparks (2004), and phenocryst + post-entrapment melt inclusion amphiboles from Lower Pumice 2 (Gertisser* et al.*, 2009). There is clear compositional difference between Akrotiri amphibole and the potentially related phenocryst-rich pumice (Druitt* et al.*, 2012) and the xenolith amphibole, even when not related to sample alteration, e.g. intercumulus microlite amphibole in the olivine gabbros.*

### Fe-Ti Oxides

Both magnetite and ilmenite are present across the xenoliths, but not always coexisting. Evidence of exsolution of ilmenite lamellae is common and additionally secondary alteration in some samples is shown by red oxidised rims. Compositions lie on the spinel-magnetite exchange vector (Figure 2.15A). $TiO_2$ in magnetite ranges from 0.03 to 17 wt% (Figure 2.15B). $Cr_2O_3$ is predominantly less than 0.2 wt%, with one analysis reaching 1.4 wt%.

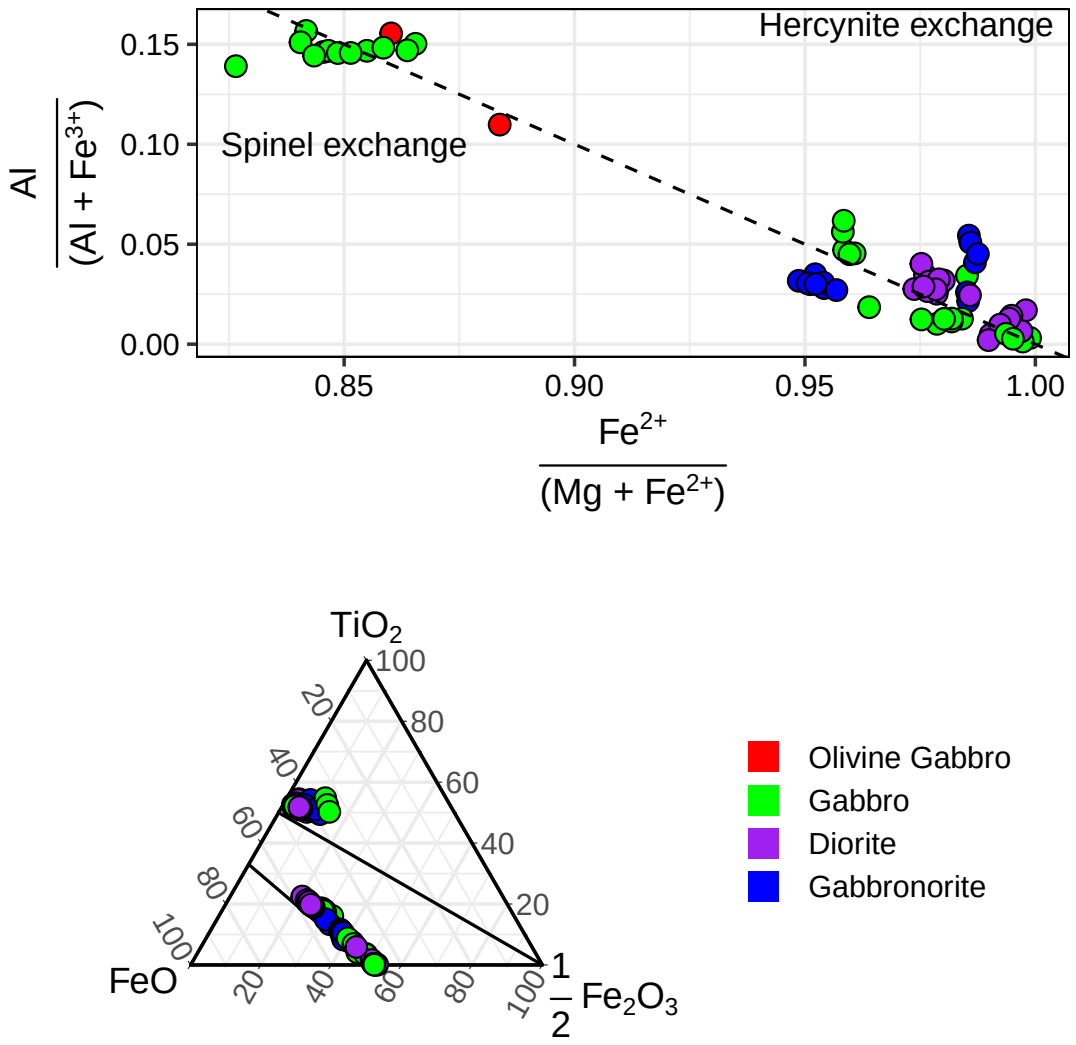


*Figure 2.15: Fe-Ti oxide chemistry.*

### 2.4.3 Whole-Rock and Glass Chemistry

Xenolith whole rock compositions (calculated from point counting and measured) broadly follow the liquid line of descent for Santorini, with a few that fall off the trend for various elements (Figure 2.16). $SiO_2$ concentrations range from 46 to 65 wt%. The olivine gabbros and intermediate glass-bearing gabbro are mafic ($SiO_2$ 46-49 wt%) whilst the gabbros and gabbronorites are dominantly intermediate, both spanning a range from 52 to 65 wt% $SiO_2$. The high $TiO_2$ in the most $SiO_2$ poor xenolith (SAN 9-1-8-3) is due to a large modal (7.4 vol%) proportion of titanomagnetite. A low $K_2O$ diverging trend is formed from samples almost entirely composed of clinopyroxene and plagioclase, similar to three gabbroic xenoliths analysed in Druitt *et al.* (1999). Six olivine gabbro and gabbro xenoliths have systematically ~3-5 wt% lower FeO

concentrations than the liquid line of descent, but gabbronorites and diorites sit on the trend. Four gabbro xenoliths have $Na_2O$ concentrations up to 3 wt% higher than equivalent $SiO_2$ lava whole rocks, lying at an extension of an inflection in $Na_2O$ in the literature data and xenolith glass analyses.

Melt inclusion and interstitial glass analyses from the xenoliths (44-82 wt% $SiO_2$) overlap almost the entire compositional range of published whole rock, melt inclusion and glass analyses for the Santorini deposits (40-79 wt% $SiO_2$)(see 2.16 for data references), with only melt inclusions from gabbroic inclusions at Nea Kameni (Michaud *et al.*, 2000) extending to lower $SiO_2$ (Table 2.10, 2.11). Xenolith glass compositions extend to higher $SiO_2$ concentrations however, reaching 82 wt% $SiO_2$ in the intercumulus glass and in melt inclusions in the gabbronorites. Some deviations from the eruptive liquid line of descent are observed. Intermediate glass compositions found in the olivine gabbros show an enrichment in FeO at lower $SiO_2$ concentrations and enrichment in $TiO_2$, MnO and $P_2O_5$.

Sulphur and chlorine concentrations negatively and positively correlate with $SiO_2$ respectively (<LOD to 641 ppm S, 810-6050 ppm Cl), generally falling within values from the extrusives from the literature (see Figure 2.16 for references). A few andesitic to dacitic glass and melt inclusions have up to 2000 ppm enrichment in chlorine relative to equivalent $SiO_2$ literature lava glass and melt inclusion analyses.

Concentrations of trace elements including the REEs in melt inclusions and intercumulus glass from the olivine gabbros and a glass-rich gabbro (SAN 9-1-8-3, LP2 eruption) fall within almost the entire range of literature whole-rock analyses (Figure 2.17). The data presented are not corrected for PEC. Melt inclusions have distinctly lower REE concentrations than intercumulus glasses. Intercumulus glass and melt inclusions were too small in the gabbronorites for reliable analysis, but it is expected these would have strong enrichments in trace elements, based on their high $SiO_2$ and strong mineral trace element concentrations (Figure 2.9A). REE profile slopes ($La/Lu_N$ = 0.99-5.18) become more negative due to a relative LREE enrichment over HREE in more felsic glass compositions, a feature additionally noted by Elburg *et al.* (2014). Trace element data show profiles that are more primative than the bulk of the literature dataset (Figure 2.9B).

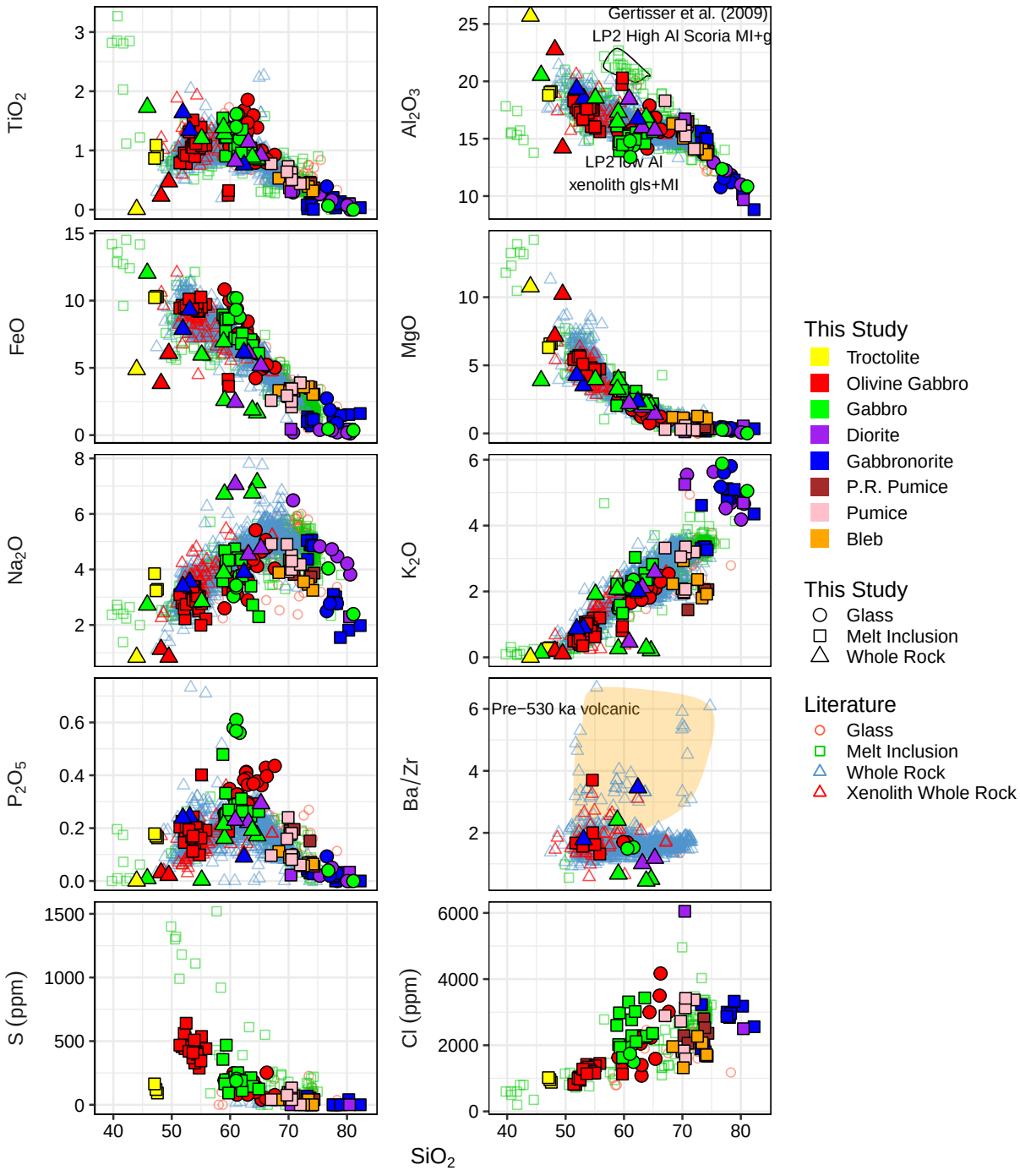


*Figure 2.16: Whole rock, interstitial glass and melt inclusion compositional data for xenoliths and extrusives from the literature (GEOROC accessed 2017; Druitt, 1983; Druitt* et al.*, 1999; Michaud* et al.*, 2000; Gertisser* et al.*, 2009 unpublished; Bailey* et al.*, 2009; Panienka, 2012; Fabbro* et al.*, 2013; Elburg* et al.*, 2014; Simmons* et al.*, 2017). Field of pre-530 ka volcanic deposits (Akrotiri) shown on Ba/Zr plot (see discussion). Melt inclusion data comprise olivine, plagioclase and clinopyroxene hosted inclusions, and compositions shown are corrected for post entrapment modification, as discussed in Appendix A.1. All major element values are normalised to 100 wt% volatile free.*

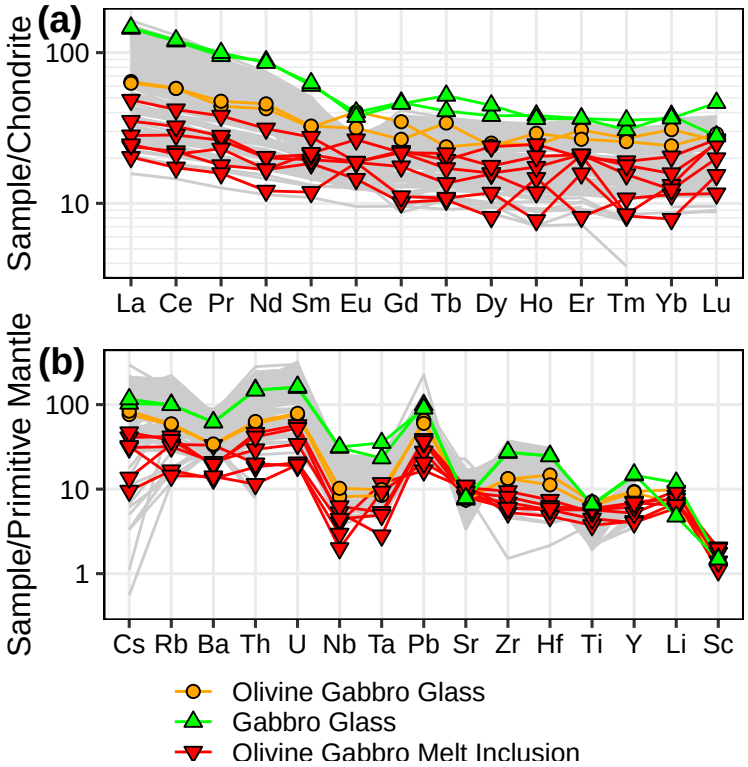


*Figure 2.17: Glass and melt inclusion trace and REE data. The light grey lines are literature data for the volcanic deposits from GEOROC (accessed 2017), Druitt* et al. *(1999), Bailey* et al. *(2009), Panienka (2012), Fabbro* et al. *(2013), Elburg* et al. *(2014) and Simmons* et al. *(2017). Normalisation values from Palme* et al. *(2014).*

*Table 2.10: Average melt inclusion compositions of PEC corrected inclusions. See supplementary data for individual raw data and corrected analyses*

| | Troctolite | $\sigma$ | Olivine Gabbro | $\sigma$ | Gabbro | $\sigma$ | Diorite | $\sigma$ | Gabbronorite | $\sigma$ |
|---|---|---|---|---|---|---|---|---|---|---|
| $n$ | 3 | | 28 | | 13 | | 2 | | 13 | |
| $SiO_2$ | 47.24 | 1.05 | 51.36 | 1.76 | 59.69 | 1.60 | 74.73 | 7.14 | 75.10 | 2.45 |
| $TiO_2$ | 0.96 | 0.13 | 0.98 | 0.27 | 1.09 | 0.21 | 0.20 | 0.14 | 0.08 | 0.05 |
| $Al_2O_3$ | 18.95 | 0.50 | 16.63 | 0.87 | 14.62 | 0.48 | 13.07 | 4.92 | 12.66 | 2.39 |
| $Cr_2O_3$ | 0.00 | 0.00 | 0.01 | 0.01 | 0.01 | 0.01 | 0.00 | 0.00 | 0.00 | 0.00 |
| FeO | 10.26 | 0.24 | 8.73 | 1.46 | 7.50 | 0.96 | 0.44 | 0.00 | 1.24 | 0.27 |
| MnO | 0.08 | 0.02 | 0.19 | 0.04 | 0.24 | 0.03 | 0.02 | 0.03 | 0.04 | 0.03 |
| MgO | 6.48 | 0.28 | 4.38 | 0.73 | 2.73 | 0.55 | 0.33 | 0.30 | 0.32 | 0.07 |
| CaO | 11.99 | 0.16 | 8.95 | 0.74 | 5.44 | 1.00 | 2.05 | 0.45 | 0.99 | 0.24 |
| $Na_2O$ | 3.44 | 0.28 | 2.78 | 0.38 | 3.84 | 0.76 | 3.29 | 1.43 | 3.49 | 1.33 |
| $K_2O$ | 0.28 | 0.02 | 0.77 | 0.24 | 2.09 | 0.47 | 4.92 | 0.39 | 4.17 | 0.76 |
| $P_2O_5$ | 0.17 | 0.01 | 0.18 | 0.05 | 0.28 | 0.06 | 0.03 | 0.01 | 0.03 | 0.02 |
| Cl | 0.10 | 0.01 | 0.12 | 0.02 | 0.25 | 0.06 | 0.43 | 0.25 | 0.25 | 0.06 |
| $SO_3$ | 0.03 | 0.01 | 0.10 | 0.02 | 0.05 | 0.03 | 0.00 | 0.00 | 0.00 | 0.01 |
| Total | 99.85 | 1.83 | 94.96 | 0.63 | 97.53 | 1.10 | 99.08 | 0.16 | 98.12 | 1.04 |
| **LA-ICP-MS trace elements (ppm)** | | | | | | | | | | |
| Li | | | 11.95 | 2.10 | | | | | | |
| Sc | | | 28.01 | 6.33 | | | | | | |
| V | | | 330.23 | 56.03 | | | | | | |
| Cr | | | 7.46 | 3.81 | | | | | | |
| Co | | | 22.36 | 7.34 | | | | | | |
| Ni | | | 37.18 | | | | | | | |
| Cu | | | 53.60 | 37.09 | | | | | | |
| Zn | | | 104.11 | 25.42 | | | | | | |
| Rb | | | 17.80 | 6.87 | | | | | | |
| Sr | | | 209.79 | 26.35 | | | | | | |
| Y | | | 23.07 | 5.49 | | | | | | |
| Zr | | | 71.49 | 16.04 | | | | | | |
| Nb | | | 2.47 | 0.92 | | | | | | |
| Cs | | | 0.52 | 0.27 | | | | | | |
| Ba | | | 136.73 | 48.86 | | | | | | |
| La | | | 7.26 | 2.50 | | | | | | |
| Ce | | | 16.85 | 5.58 | | | | | | |
| Pr | | | 2.33 | 0.75 | | | | | | |
| Nd | | | 9.25 | 3.06 | | | | | | |
| Sm | | | 3.07 | 0.78 | | | | | | |
| Eu | | | 1.14 | 0.23 | | | | | | |
| Gd | | | 3.60 | 1.14 | | | | | | |
| Tb | | | 0.59 | 0.17 | | | | | | |
| Dy | | | 3.96 | 1.37 | | | | | | |
| Ho | | | 0.91 | 0.34 | | | | | | |
| Er | | | 2.95 | 0.86 | | | | | | |
| Tm | | | 0.35 | 0.12 | | | | | | |
| Yb | | | 2.28 | 0.72 | | | | | | |
| Lu | | | 0.52 | 0.15 | | | | | | |
| Hf | | | 1.80 | 0.26 | | | | | | |
| Ta | | | 0.29 | 0.16 | | | | | | |
| Pb | | | 5.44 | 1.72 | | | | | | |
| Th | | | 2.36 | 1.17 | | | | | | |
| U | | | 0.77 | 0.40 | | | | | | |

*Table 2.11: Average glass compositions*

| | Olivine Gabbro | $\sigma$ | Gabbro | $\sigma$ |
|---|---|---|---|---|
| $n$ | 19 | | 4 | |
| $SiO_2$ | 61.76 | 2.01 | 59.21 | 1.06 |
| $TiO_2$ | 1.25 | 0.31 | 1.35 | 0.15 |
| $Al_2O_3$ | 15.18 | 0.84 | 13.81 | 0.62 |
| $Cr_2O_3$ | 0.01 | 0.01 | 0.01 | 0.01 |
| FeO | 7.10 | 1.84 | 9.31 | 0.66 |
| MnO | 0.21 | 0.04 | 0.27 | 0.02 |
| MgO | 1.53 | 0.53 | 2.25 | 0.19 |
| CaO | 4.53 | 0.95 | 4.75 | 0.09 |
| $Na_2O$ | 3.99 | 0.73 | 3.29 | 0.31 |
| $K_2O$ | 1.88 | 0.27 | 2.12 | 0.13 |
| $P_2O_5$ | 0.35 | 0.05 | 0.56 | 0.02 |
| Cl | 0.22 | 0.08 | 0.18 | 0.02 |
| $SO_3$ | 0.03 | 0.02 | 0.05 | 0.00 |
| Total | 97.79 | 1.32 | 96.94 | 1.44 |
| **LA-ICP-MS trace elements (ppm)** | | | | |
| Li | 13.13 | 3.71 | 13.35 | 8.13 |
| Sc | 22.52 | 0.94 | 24.56 | 0.42 |
| V | 257.11 | 46.99 | 138.56 | 2.21 |
| Cr | 3.55 | | 3.81 | 2.65 |
| Co | 25.84 | 0.84 | 15.95 | 0.17 |
| Ni | | | | |
| Cu | 81.11 | 1.94 | 39.06 | 20.04 |
| Zn | 172.06 | 15.15 | 167.23 | 8.23 |
| Rb | 35.29 | 0.80 | 60.23 | 0.38 |
| Sr | 169.04 | 7.67 | 169.44 | 4.92 |
| Y | 38.36 | 0.42 | 61.04 | 1.09 |
| Zr | 136.22 | 1.76 | 280.25 | 3.91 |
| Nb | 5.46 | 0.89 | 18.57 | 0.23 |
| Cs | 1.44 | 0.10 | 1.97 | 0.17 |
| Ba | 231.06 | 4.25 | 423.85 | 1.79 |
| La | 15.32 | 0.29 | 35.11 | 0.41 |
| Ce | 35.86 | 0.05 | 74.23 | 0.83 |
| Pr | 4.30 | 0.23 | 9.14 | 0.30 |
| Nd | 20.88 | 1.08 | 41.08 | 0.72 |
| Sm | 4.95 | 0.07 | 9.46 | 0.26 |
| Eu | 2.12 | 0.37 | 2.29 | 0.11 |
| Gd | 6.35 | 1.20 | 9.57 | 0.13 |
| Tb | 1.10 | 0.28 | 1.76 | 0.29 |
| Dy | 6.27 | 0.21 | 10.58 | 1.19 |
| Ho | 1.51 | 0.19 | 2.11 | 0.08 |
| Er | 4.74 | 0.47 | 6.05 | 0.01 |
| Tm | 0.69 | 0.03 | 0.86 | 0.09 |
| Yb | 4.63 | 0.81 | 6.31 | 0.18 |
| Lu | 0.69 | 0.05 | 0.93 | 0.33 |
| Hf | 3.90 | 0.73 | 7.45 | 0.07 |
| Ta | 0.39 | 0.04 | 1.26 | 0.37 |
| Pb | 11.58 | 0.68 | 17.45 | 1.12 |
| Th | 5.20 | 0.22 | 12.61 | 0.18 |
| U | 1.78 | 0.04 | 3.68 | 0.08 |

### 2.4.4 Oxygen Isotopes

Oxygen isotope analyses were made on the freshest samples from the most abundant rock types with sufficient sample material (olivine gabbro, gabbro and gabbronorite) (Figure 2.18A, Table 2.12). In olivine gabbros, plagioclase ($n$=3) has a $\delta^{18}O$ of +6.3 to +6.4 ‰ (SMOW), clinopyroxene ($n$=3) between +5.9 to +6.0 ‰, and olivine ($n$=2) between +5.4 to +5.6 ‰. In gabbro, plagioclase ($n$=2) ranges between +6.6 and +7.2 ‰ and clinopyroxene ($n$=1) is +5.9 ‰. In gabbronorite, plagioclase ($n$=2) ranges between 6.4 and 6.5 ‰ and the pyroxenes (undifferentiated due to similar oxygen isotope fraction factors: $\Delta_{cpx\text{-}opx} < 0.1$ Kyser *et al.*, 1981; Zheng, 1993) ($n$=2) are +5.9 to +6.1 ‰. The xenolith plagioclase compositions fall within the range of plagioclase analysed by Druitt *et al.* (1999) ($\delta^{18}O$ = +5.7 to +7.5 ‰, Figure 2.18A).

The $\delta^{18}O$ composition of melts in equilibrium with the xenolith mineral phases were calculated assuming the following fractionation factors: $\Delta_{ol\text{-}melt}$ = -0.7, $\Delta_{plag\text{-}melt}$ = 0.2, and $\Delta_{pyx\text{-}melt}$ = -0.3 (Kyser *et al.*, 1981; Kalamarides, 1986; Harris *et al.*, 2004). These calculated melts range between 6.1 and 7.0 ‰. These values are higher than typical MORB basalts (~5.7 ± 0.3 Ito *et al.*, 1987; Harmon and Hoefs, 1995).

Oxygen isotope thermometry (Figure 2.18B) is discussed in section 2.5.4.

*Table 2.12: Oxygen isotope compositions of the xenolith mineral phases. Gabbronorite pyroxnes are undifferentiationed ortho and clinopyroxenes. All other pyroxenes are clinopyroxene. All units are δ.*

| Sample | Rock Type | Plag | Olv | Px |
|---|---|---|---|---|
| SAN 9-1-8-2 | Olivine Gabbro | 6.3 | 5.6 | 6.0 |
| SAN 9-1-8-1 | Olivine Gabbro | 6.3 | 5.4 | 5.9 |
| SAN 14-1-3-3 | Gabbronorite | 6.4 | | 6.0 |
| SAN 12-1-5 | Gabbronorite | 6.5 | | 5.9 |
| SAN 9-2-2 | Gabbro | 6.6 | | 5.9 |
| SAN 6-3-1 | Gabbro | 7.2 | | |

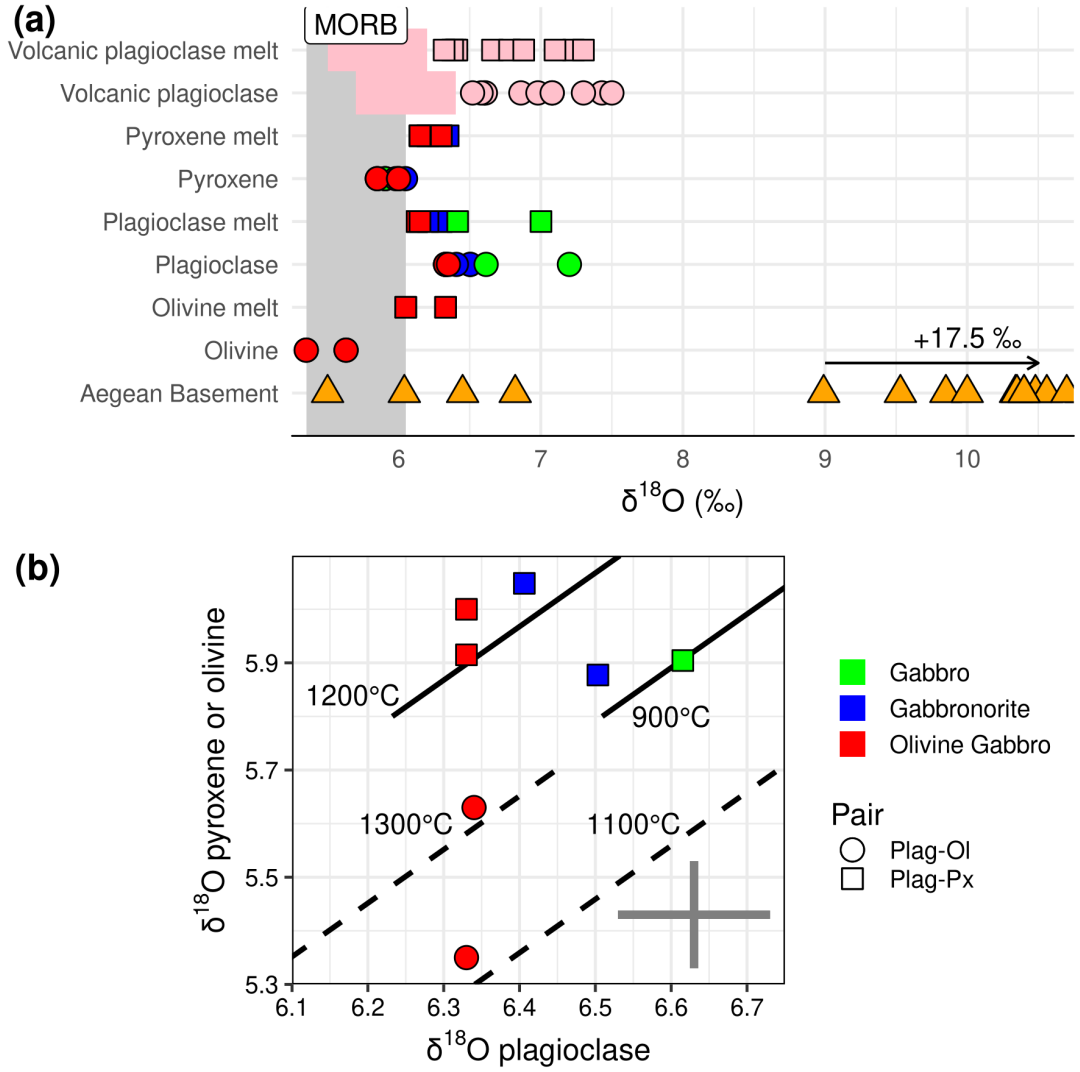


*Figure 2.18: Oxygen isotopic compositions of xenolith mineral phases. (A) $\delta^{18}O$ compositions of the xenolith mineral phases, volcanic plagioclase and Aegean basement. The volcanic plagioclase points are pumice plagioclase phenocrysts from Druitt* et al. *(1999). The fields are lava plagioclase phenocrysts from Wyers (1987). Aegean basement lithologies from Matthews and Schliestedt (1984), McGrath* et al. *(2017), Putlitz* et al. *(2000), Bröcker* et al. *(1993) that may be considered potential contaminants of Santorini magmas. Calculated $\delta^{18}O$ of melts in equilibrium with the mineral phases are shown (see text for more detail) for comparison with typical MORB compositions (Ito* et al.*, 1987). The xenolith rock types are coloured as in panel B. Symbols are used to highlight calculated melts from analyses, and are not the same as in panel B. (B) $\delta^{18}O$ of xenolith pyroxene or olivine against coexisting plagioclase to assess mineral equilibration temperatures. Solid lines show isotherms of equilibrium pyroxene-plagioclase fractionation, and dashed lines show equilibrium isotherms of olivine-plagioclase fractionation. Circle symbols are pyroxene-plagioclase pairs and square symbols are olivine-plagioclase pairs. The cross indicates typical analytical uncertainty.*

## 2.5 Discussion

In the following discussion we will focus on variations between the geochemistry of the xenoliths and the volcanic rocks to understand magma differentiation processes at Santorini. This is combined with thermobarometry and oxygen isotopes to understand the intensive variables of magma differentiation, and this is compared to other Aegean volcanic systems.

### 2.5.1 Comparison between the Plutonic Xenoliths and Santorini Volcanic Deposits

Major element whole-rock, melt inclusion and glass analyses from the xenoliths overlap almost the entire compositional range of Santorini volcanic deposits for all major elements, generally following the well defined liquid line of descent (Figure 2.16). Many xenolith whole-rock analyses fall off the liquid line of descent, indicating a subtractive assemblage/cumulate origin (e.g. Morse, 1976; Cooper *et al.*, 2016; Melekhova *et al.*, 2017). The olivine gabbros and troctolitic glomerocrysts plot at generally lower $SiO_2$ (46-49 wt%) than the liquid line of descent (>50 wt%), and are therefore considered to be the crystal fractionates that drive magmatic differentiation until ~58 wt% $SiO_2$ (Figure 2.16). The abundance of vesicular glass within these xenoliths indicate super-solidus conditions, and therefore these xenoliths are likely fragments of an entrained crystal mush (e.g. Hermes and Cornell, 1981; Passmore *et al.*, 2012; Cooper *et al.*, 2016). At 58 wt% $SiO_2$ Ti-magnetite joins the liquidus, recorded in cumulate gabbro sample SAN 9-1-8-3 by elevated $TiO_2$ and low $SiO_2$ concentrations compared to the liquid line of descent. Xenoliths with high $Na_2O$ (> 6.5 wt%) between 59 and 65 wt% $SiO_2$ record the Na-rich plagioclase assemblage that drives inflection and differentiation to low $Na_2O$ contents at greater than 68 wt% $SiO_2$ (Figure 2.16). The xenolith samples that overlap the liquid line of descent (2 gabbronorite, 2 diorite, 1 gabbro), in contrast to those previously discussed, can also be considered cumulates based on their texture, and the Mg-rich nature of xenolith orthopyroxene, which cannot be formed from *in situ* crystallisation of a typical orthopyroxene-bearing andesitic to dacitic Santorini magma (Druitt *et al.*, 1999).

Two distinct melt compositions have been identified at Santorini: pre-530 ka melts characterised by low Zr and high Ba that formed the Akrotiri volcanic deposits, and the post-530 ka melts, characterised by high Zr and low Ba. Xenoliths that contain the low Zr, high Ba signature of the Akrotiri volcanic deposits are found in the deposits of the 3.6 ka Minoan eruption ("hornblende diorites" of Druitt, 2014), attributed to entrainment of fragments of an intrusion compositionally distinct to modern erupted magmas (Druitt *et al.*, 1999; Druitt, 2014). To test

if any of the xenoliths from this study are derived from magmas different from their post-530 ka parental deposits we compared the Ba/Zr against $SiO_2$ (Figure 2.16) of whole rock and glass analyses, and Ba against Zr of whole rock, glass and calculated melts in equilibrium with the mineral phases in the xenoliths (Figure 2.19). Sample SAN 9-3-2 from the Minoan deposit in this study falls within the field of low Zr, high Ba Akrotiri volcanic deposits, following the xenoliths of Druitt (2014). The remaining samples overlap the post-530 ka literature data, or lie below due to their cumulate origin (Figure 2.19). This additionally includes gabbro sample SAN 4-4c, also from the Minoan eruption, which does not exhibit the Akrotiri geochemical signature, suggesting it may be cogenetic to the Minoan eruption. Although propagated uncertainty is substantial due to poorly constrained partition coefficients for Ba and Zr (~30% relative Bédard, 2006, 2007, 2014), melts in equilibrium with a small subset of crystals exhibiting a high Ba and low Zr character are found as individual crystals in some samples. These isolated high Ba clinopyroxene crystals in the non-Minoan samples may tentatively represent xenocrysts inherited from the older Akrotiri volcanic deposits. The whole-rock plutonic xenolith dataset of Druitt *et al.* (1999) shows two xenoliths from the Cape Therma 3 eruption containing a high Ba, low Zr character that is possibly derived from older material, supporting that pre-530 ka material may exist in eruptions other than the Minoan. Dominantly however, the xenoliths in this study represent material derived from the post-530 ka magmas.

### 2.5.2 The Role of Intercumulus Melts in Crystallisation and Re-equilibration

The diverse range of glass and melt inclusion compositions (47-82 wt% $SiO_2$) within the xenoliths record trapping of melts encompassing almost the entire magmatic history of Santorini (Figure 2.16). These compositions however do not always closely overlap the liquid line of descent at Santorini, and this variation between whole rock, melt inclusion and intercumulus glasses within individual samples raises the question whether the intercumulus melts represent eruptable Santorini melts, or closed system fractionated uneruptable melts?

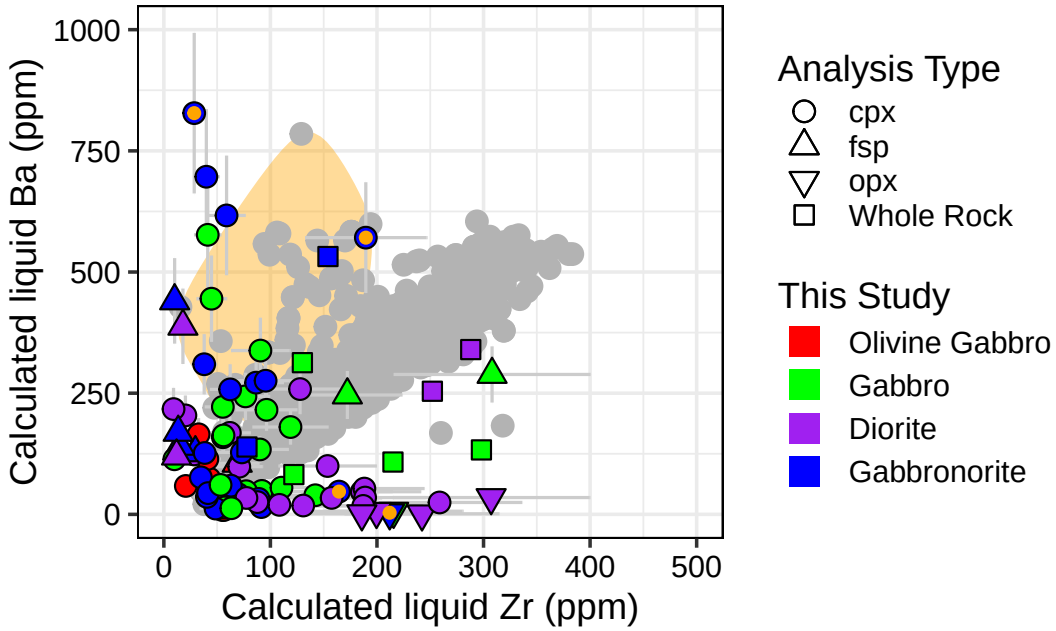


*Figure 2.19: Ba vs Zr plot highlighting the geochemical difference between the early Akrotiri volcanic deposits (orange field and points within) and later <530 ka volcanic deposits (grey points). Literature data sources as in Figure 2.17. Melts calculated in equilibrium with xenolith clinopyroxene, orthopyroxene and plagioclase are shown (partition coefficients from Bédard, 2006, 2007, 2014), as well as xenolith whole rock data. Orange points represent melts in equilibrium with the Minoan gabbronorite (hornblende-diorite of Druitt, 2014). Equilibrium melt calculations introduce an uncertainty of ~30%, as indicated by the error bars.*

Mafic and intermediate (<65 wt% $SiO_2$) xenolith intercumulus glass compositions fall outside of the literature volcanic defined liquid line of descent for many elements such as $Al_2O_3$, FeO, $TiO_2$, and $P_2O_5$ (Figure 2.16), suggesting these may represent trapped intercumulus melts not expressed by the volcanic products. Although the increase in $P_2O_5$ could be explained by analysing boundary layer glasses, that are enriched in slow diffusing incompatible elements like $P_2O_5$ (Baker, 2008), these glasses define trends of continued fractionation that do not exhibit the inflection caused by Fe-Ti oxide and apatite saturation at ~55 wt% and 60 wt% $SiO_2$ respectively. They instead follow a trend produced by continued fractionation of plagioclase, with olivine and clinopyroxene, lowering the melt $Al_2O_3$ to slightly lower than the liquid line of descent. These samples are dominantly from the Lower Pumice 2 eruption. Interestingly, in contrast, Lower Pumice 2 mafic scoria interstitial glass and melt inclusion data from Gertisser *et al.* (2009) show the opposite trend, with compositions that contain significantly higher $Al_2O_3$ concentrations (Figure 2.16 circled $Al_2O_3$ data) than the liquid line of descent. Although post-entrapment crystallisation will increase the $Al_2O_3$ concentrations of melt inclusions hosted in ferro-magnesian minerals (Figure A.1), it is not thought these high $Al_2O_3$ inclusions in mafic

scoria (Gertisser *et al.*, 2009) are a result of this as they are overlapped by two interstitial glass analyses in their study, and two corrected clinopyroxene hosted inclusions in this study. This tentatively suggests that the low $Al_2O_3$ melts in the cumulates may somehow be linked to the high $Al_2O_3$ melts in the mafic scoria, and this decoupling is unique to the Lower Pumice 2 eruption, or the cumulates evolve on a different path to the mafic magma. High $Al_2O_3$ may indicate a process supressing plagioclase saturation in the mafic intruding magma, but this is outside the scope of this discussion.

The intercumulus glasses are usually more silicic than the melt inclusions within the same samples, and are often out of equilibrium with the ferro-magnesian phases, based on mineral-melt partition coefficients (e.g. $KD_{Fe-Mg}^{cpx-melt} = 0.23 - 0.28 \pm 0.06$ Bédard, 2010; Putirka, 2008) (Figure 2.20). This is additionally shown by regressing the Santorini liquid line of descent Fe/Mg values against $SiO_2$ ($R^2 = 0.75$), and using $KD_{Fe-Mg}^{cpx-melt} = 0.23 - 0.28 \pm 0.06$ to estimate the $SiO_2$ of melts that would be in equilibrium with clinopyroxene. The maximum melt $SiO_2$ in equilibrium with xenolith clinopyroxene is ~$70 \pm 3$ wt% $SiO_2$, lower than the values of up to 82 wt% $SiO_2$ in the interstitial glasses. This indicates continued fractional crystallisation within the cumulate.

The effects of continuing fractional crystallisation can be evaluated using clinopyroxene trace element compositions and the calculated melts in equilibrium with the clinopyroxenes. The equilibrium calculated melt trace element profiles (Figure 2.21) generally overlap volcanic whole-rock concentrations, and the range of melt inclusion and interstitial glass compositions from the olivine gabbros (Figure 2.17), indicating the bulk of clinopyroxene crystallisation is from a mafic to intermediate melt. For those rocks, there is little evidence for significantly prolonged fractional crystallisation recorded in the clinopyroxene trace element chemistry alone, although this may be sampling bias from mostly crystal core analyses. For example, gabbronorite SAN 12-2-2 show the progressive enrichment of trace element concentrations in clinopyroxene with increasing crystallisation of the intercumulus melt (Figure 2.21B) over a range of Mg# from 79 to 56. Trace element enrichment correlated with declining Mg# indicates the enrichment is controlled by fractional crystallisation of the intercumulus melt. Plagioclase is the dominant intercumulus mineral phase, and it is often strongly normal zoned to albite (Figure 2.12C). The role of feldspar and fractional crystallisation on enriching the trace element concentrations is clearly reflected in the Eu anomaly in clinopyroxene, which is strongly correlated to enrichment in REEs such as La (Figure 2.9D). Gabbronorite SAN 9-1-1-3 has a restricted Mg# range between 76 and 72, yet the highest trace element enrichment of any xenolith and the largest

Eu anomaly (Figures 2.9, 2.21B). This indicates clinopyroxene crystallisation occured after significant feldspar fractionation, perhaps under different P-T-$fO_2$-$H_2O$ conditions to the other xenoliths, suppressing early clinopyroxene fractionation.

This *in situ* trapped interstitial melt crystallisation, or post-cumulus crystallisation, has been recognised in layered intrusions and plutons to significantly influence the chemistry, including increasing incompatible trace element concentrations, of minerals that crystallise from or reequilibrate with these late stage melts (e.g. Barnes, 1986; Bédard, 1994; Borghini and Rampone, 2007). To test if the clinopyroxene REE compositions and equilibrium melts can be produced from closed system fractional crystallisation of a Santorini melt we modelled the REE concentrations during equilibrium crystallisation of a Santorini basalt (Bailey *et al.*, 2009 sample MVD-T 00-10) over 3 steps (c.f. Borghini and Rampone, 2007). The bulk partition coefficient (D) was estimated as 0.05 for the entire crystallisation, approximating a fractionating assemblage comprising plagioclase and pyroxenes (Bédard, 2006, 2007, 2014; Sun and Liang, 2012; Sun *et al.*, 2017), and a bulk D of 0.5 for Eu, based on the high modal proportion of plagioclase and large Eu anomalies in the xenolith mineral phases. 0.05 was chosen for each element partition coefficient because although $D_{REE}$ decreases with ionic radius in the pyroxenes (Bédard, 2006, 2014; Sun and Liang, 2012), it increases in plagioclase (Bédard, 2007; Sun *et al.*, 2017), essentially cancelling out the differences. For example, increasing the bulk D by 0.01 for each step from La to Lu produces strongly negative profile slopes,not observed in the xenolith clinopyroxene (Figure 2.9). This simplified model does not account for the weak amphibole fractionation signature in the more evolved REE profiles at Santorini (discussed below) and a changing mineral assemblage during differentiation (olivine in most primitive stages, Fe-Ti oxides and apatite later), however as a first order estimation, complete equilibrium closed system crystallisation of a mafic cumulate comprising plagioclase and pyroxenes and a trapped intercumulus melt can produce the full range of clinopyroxene REE compositions (Figure 2.9A) and equilibrium melts (Figure 2.21) observed in the xenoliths. The final fractionating assemblage in most gabbros, diorites and gabbronorites is extremely albite-rich plagioclase, with sometimes K-feldspar and quartz. Pyroxenes are not stable in this final evolved melt, and are last stable in melts with a maximum of ~70 wt% $SiO_2$, as discussed above. This clinopyroxene-absent assemblage would push the bulk D of the fractionating final assemblage to lower values (Bédard, 2006, 2014; Sun *et al.*, 2017), resulting in even stronger enrichment in incompatible elements in the intercumulus melts. For example, a small change from D = 0.05 to 0.04 over the final 25% of crystallisation increases calculated melt La concentration from 1475 ppm to 1844 ppm, which

further supports *in situ* fractional crystallisation as a process driving trace element enrichment.

An alternate explanation for the highly enriched clinopyroxene trace element compositions is re-equilibration with the crystallising intercumulus melt. This 'trapped liquid shift' (Barnes, 1986) drives ferromagnesian mineral compositions to iron enrichment and lower Mg# values, and diffusive homogenisation of these mineral phases. As both crystallisation from a trace element enriched melt and reequilibration with this melt will ultimately produce a similar end result of trace element enriched mineral phases, it is difficult to establish the the exact process occuring. Re-equilibration is apparent however in some gabbronorite samples that contain rare olivine. This olivine ($Fo_{47-69}$) has a reaction rim and Fo values that lower than mafic equilibrium olivine gabbro and troctolitic glomerocrysts values ($Fo_{74-84}$) and lava phenocrysts ($Fo_{68-93}$, Figure 2.7). Temperature estimated from Ca in olivine (Shejwalkar and Coogan, 2013, Figure 2.7) and mineral-melt thermometry (Figure 2.24) show re-equilibration at temperatures as low as ~800°C, either with the intercumulus melt or with the cumulus clinopyroxene and orthopyroxene in the same samples. Whichever the process, equilibration is incomplete in these samples, evidenced by the reaction rims around the olivine. REE diffusion is slow in clinopyroxene (Van Orman *et al.*, 2001), so although the major element chemistry may have been influenced by equilibration with the crystallising intercumulus melt, clinopyroxene should retain REE zonation from post-cumulus overgrowth crystallisation. This is shown in sample SAN 12-2-2 (Figure 2.21B), demonstrating enrichment of clinopyroxene rims relative to cores due to trapped melt crystallisation and subsequent REE enrichment.

In summary, many xenoliths show evidence that the trapped intercumulus melts may not be the direct melts that when extracted produce the Santorini liquid line of descent. Extraction of melts at earlier stages of cumulate evolution may be able to produce compositions comparable to the erupted Santorini magma (c.f. Flaherty *et al.*, 2018), shown by melt inclusion compositions across the xenolith types generally overlapping the liquid line of descent. Further cooling and crystallisation from this point would cause the cumulate mush to eventually reach the critical crystallinity of ~50%, where rheological lock-up occurs (Marsh, 1981, 1988a, 1996; Vigneresse *et al.*, 1996) and melts cannot be extracted. rhyoliteMELTS (version 1.2; Gualda *et al.*, 2012; Ghiorso, 2016) modelling of a Santorini Lower Pumice 2 rhyodacite (Cadoux *et al.*, 2014) at 200 MPa indicates this lock-up occurs at around 750°C (Figure 2.22), consistent with thermometry of plagioclase crystal rims and intercumulus crystals in the gabbronorites (see thermobarometry below). Further fractionation from this point in the Santorini xenoliths can continue in a closed system, producing unique xenolith intercumulus melt and mineral compositions in some

samples. Recharge of mafic magma into silicic mush (e.g. Andújar *et al.*, 2016) would result in stagnation of the mafic magma due to the density and rheological contrast, causing it to cool, crystallise and reach volatile saturation. Release of these volatiles into the silicic mush enables efficient heat transfer and remobilisation of the silicic mush (Huber *et al.*, 2010), enabling the evolved intercumulus melts and/or cumulus crystals to mix with the main magma body. Evidence of cumulate remobilisation processes is shown for example by the presence of the troctolitic glomerocrysts in the Nea Kameni lavas, and the Lower Pumice 2 pumice containing the corroded core plagioclase found in the olivine gabbros (see Gertisser *et al.*, 2009). This may also produce in part some of the mixed melt compositions shown on the liquid line of descent (Figure 2.16). Recognition and quantification of the extent of mixing with these trapped melts, or antemelts, is difficult (e.g. Bragagni *et al.*, 2014) and requires further study.

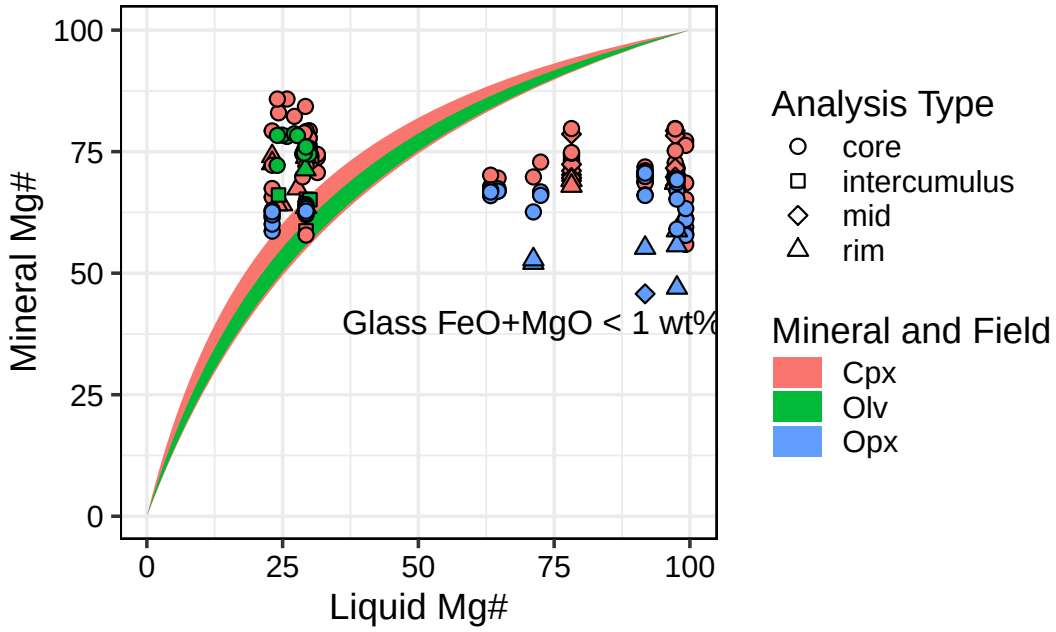


*Figure 2.20: Evaluation of equilibrium between ferromagnesian minerals and intercumulus melt.*

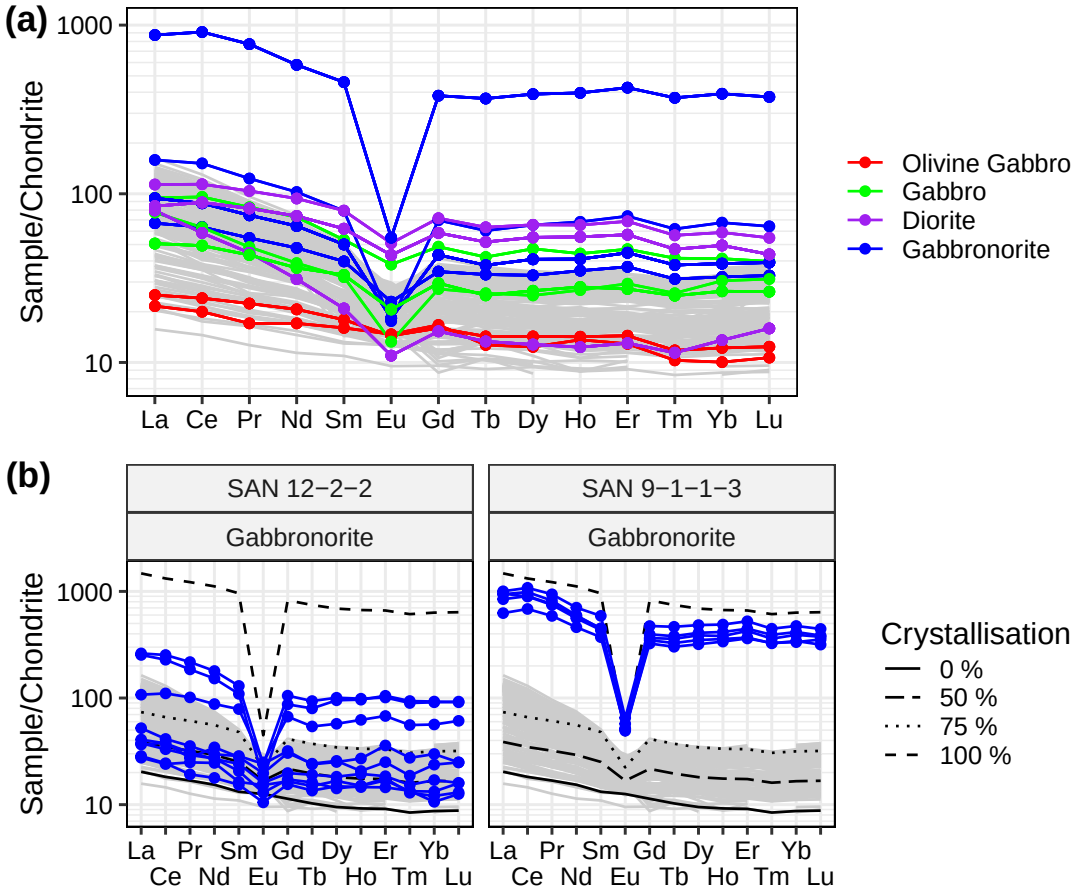


*Figure 2.21: Calculated melts in equilibrium with xenolith clinopyroxene compared to literature volcanic whole-rocks (light grey). A) Average calculated melts in equilibrium with xenolith clinopyroxene in each sample. See the text for discussion on the choice of partition coefficients. B) Two selected samples that show either a wide range of REE concentrations (SAN 12-2-2) or highly enriched compositions (SAN 9-1-1-3)*

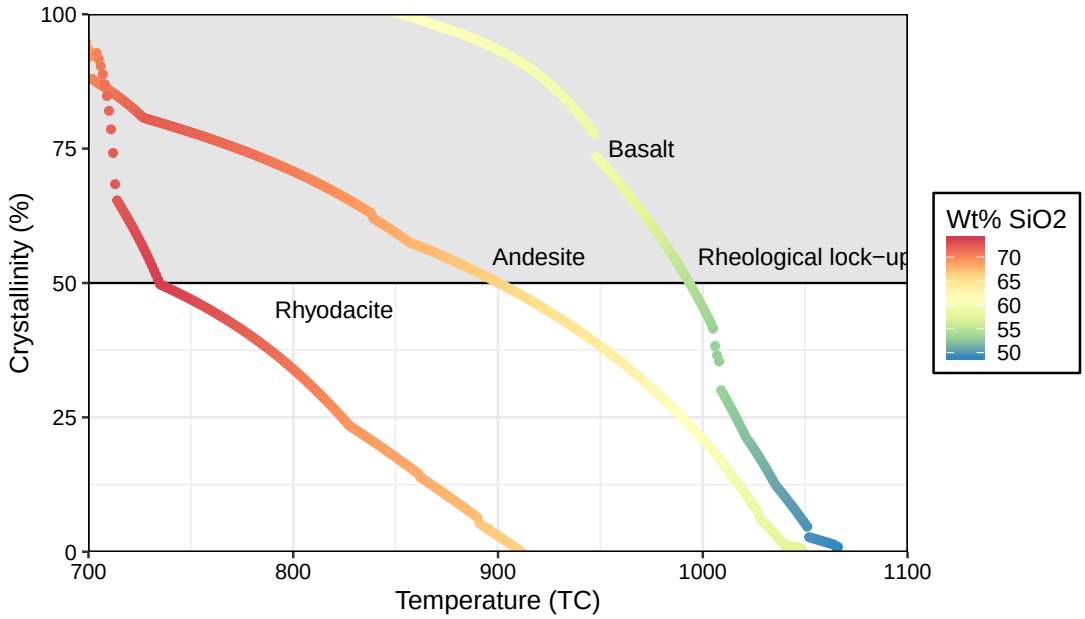


*Figure 2.22: RhyoliteMELTS (version 1.2; Gualda* et al.*, 2012; Ghiorso, 2016) modelling of three compositions of Santorini magmas: Basalt (Balos lava, Andújar* et al.*, 2015), Andesite (Upper Scoria 2, Andújar* et al.*, 2016) and rhyodacite (Lower Pumice 2, Cadoux* et al.*, 2014), showing the temperatures a crystal mush would reach the rheological lock-up crystallinity of ~50% (Marsh, 1981). All models were run at 200 MPa and at the QFM oxygen fugacity buffer.*

### 2.5.3 Evidence for Cogenetic and Non-cogenetic Xenoliths

Mineral compositions across the plutonic xenoliths generally overlap those of the volcanic deposits (Figures 2.7, 2.8, 2.11, 2.12), but also extend to lower values values in key compositional parameters (An in plagioclase, Mg# in pyroxenes, Fo in olivine) that demonstrate significant magmatic differentiation. There is insufficient published mineral chemical data on an eruption by eruption basis to conclusively test if the xenoliths are cogenetic to the deposits they are found in (Appendix Figures A.12, A.13), but the presence of glass in some xenoliths indicates super-solidus conditions and entrainment of crystal mush (e.g. Hermes and Cornell, 1981; Passmore *et al.*, 2012; Cooper *et al.*, 2016), and therefore at least some xenoliths are likely to be cogenetic. The Lower Pumice 2 eruption has a wide variety of xenoliths, and a comparison between volcanic and xenolith materials is possible using chemical data from minerals in the pumice deposits (Gertisser *et al.*, 2009).

Clinopyroxene chemistry from the Lower Pumice 2 xenoliths and volcanic deposits (Gertisser *et al.*, 2009) are shown in Figure 2.23. The clinopyroxene of the olivine gabbros compositionally overlap the quenched blebs of intruding mafic magma found within the Lower Pumice 2 rhyodacitic pumice, suggesting they are cogenetic. Plagioclase with resorbtion textures and

melt-infiltrated cores are present in the olivine gabbro xenoliths, and antecrysts of these are also found in the pumice, indicating they are cogenetic (Figure 2.6C, also Figure 4c of Gertisser *et al.*, 2009). The gabbro xenolith clinopyroxene overlaps the chemistry of clinopyroxene found within the pumice, and similarly the presence of xenolith glass indicates sampling of a cogenetically crystallising cumulate.

The diorite and gabbronorite samples plot below the expected compositional trend between the pumice and pumice groundmass, and plot within the low Ti-Al clinopyroxene compositional group observed in xenoliths sampled from many eruptions (Figure 2.8). This compositional group is not matched by any experimental clinopyroxenes synthesised from Santorini compositions (Cadoux *et al.*, 2014; Andújar *et al.*, 2015, 2016). Instead, they are best matched by major element compositions ($Al_2O_3$, $TiO_2$, CaO, Figure 2.23) of some hydrothermally altered clinopyroxenes (Manning and Bird, 1986; Rose and Bird, 1994; Good *et al.*, 1997; Martinez-Serrano, 2002; Marks *et al.*, 2010), suggesting low Ti and Al as a way to identify hydrothermally altered clinopyroxenes. Hydrothermal alteration is pervasive in many xenoliths and although the freshest samples were chosen for analysis, alteration may have modified the crystal chemistry without changing the pyroxenes fully to amphibole (Figure 2.9B, C). Not every sample with evidence of alteration has anomalous chemistry however, and some samples with low Ti-Al have clinopyroxene REE profiles consistent with unaltered samples. In the case of Lower Pumice 2, the presence of fresh glass-bearing olivine gabbros and gabbros with chemistry that match the volcanic deposits, and altered gabbronorites and diorites within the same deposit indicate that the gabbronorites and diorites may be entrained fragments of previously altered cumulates from a previous eruption or intrusion (c.f. Druitt *et al.*, 1999), whilst the olivine gabbro and gabbros are samples from a crystallising Lower Pumice 2 crystal mush. This has implications for work that is based on interpreting individual eruptions, as this indicates that not only a percentage of the lithic cargo in the eruptions may be derived from earlier non-cogenetic material, individual crystals could become entrained from older cumulate and mixed into the magmatic system. Identification of low Ti-Al clinopyroxenes only serves to highlight crystals derived from altered older material, which may not always be the case. Relict mineral cores are a common feature in the Santorini volcanic deposits, and detailed studies (e.g. Fabbro *et al.*, 2018) are required to assess their provenance.

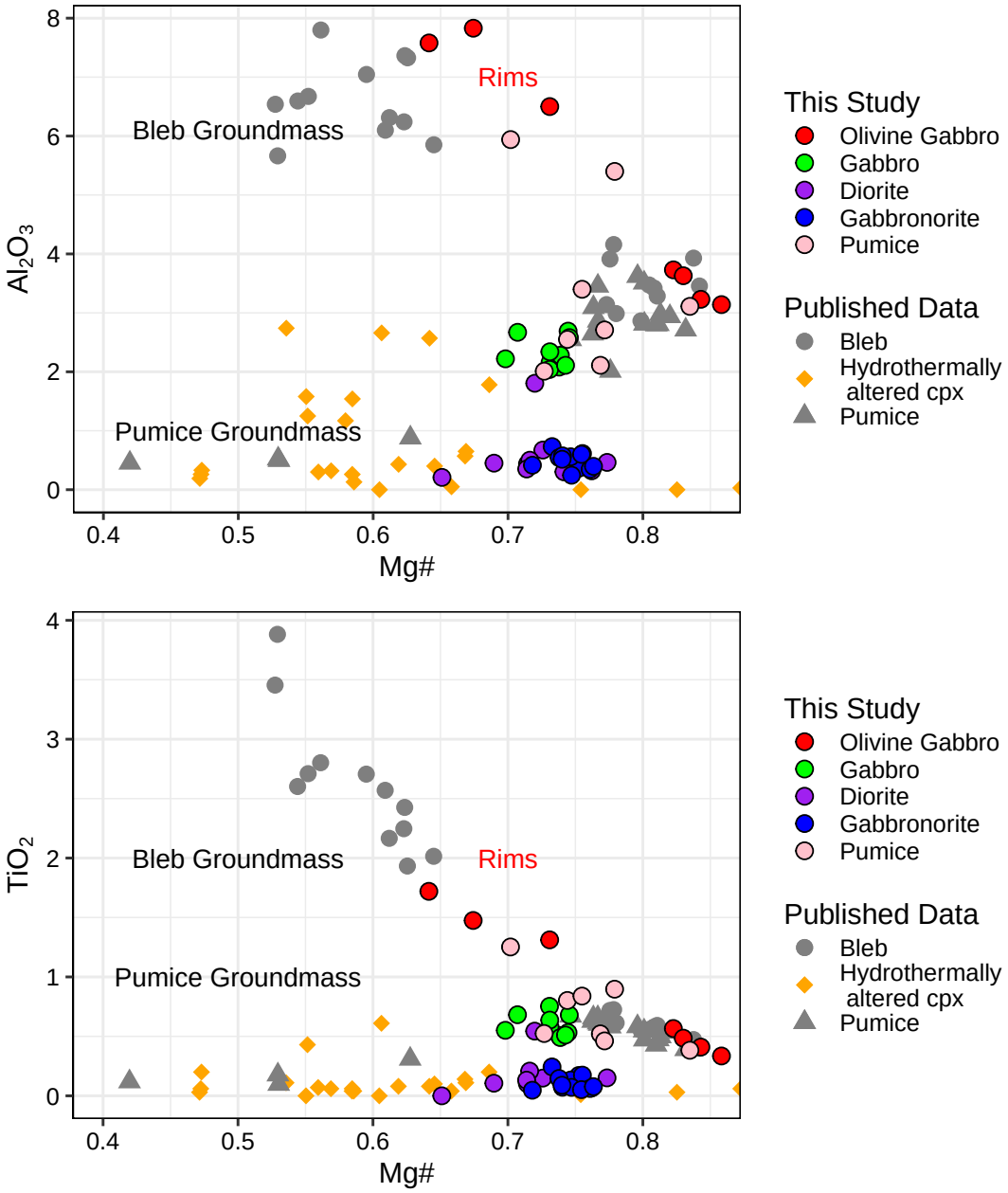


*Figure 2.23: Comparison of Lower Pumice 2 phenocryst and xenolith clinopyroxene compositions. Published and unpublished volcanic data from Gertisser* et al. *(2009), Cadoux* et al. *(2014) and Druitt* et al. *(2016). Hydrothermal clinopyroxene compositions from Manning and Bird (1986), Rose and Bird (1994), Good* et al. *(1997), Martinez-Serrano (2002) and Marks* et al. *(2010).*

### 2.5.4 Xenolith Intensive Variables and Magma Plumbing.

To place constraints on the formation conditions of the xenoliths, we utilised thermobarometric models (as outlined in the methods and Appendix A.2) and comparison between xenolith minerals and experimental data (Cadoux *et al.*, 2014; Andújar *et al.*, 2015, 2016). Olivine, plagioclase,

orthopyroxene and clinopyroxene thermobarometric models indicate the entire xenolith suite is formed at pressures approximately <350 MPa (±~100 MPa model uncertainty), corresponding to depths of approximately <11 km when assuming a Santorini crustal density of 2640 kg $m^{-3}$ (Konstantinou, 2010) (Figure 2.24). The pressure estimates cover a range of pressures from 0 to 350 MPa, and it is difficult to differentiate rock types based on pressures due to relatively large model errors. Olivine gabbro mineral cores record pressures of less than 200 ± 100 MPa, whilst the other lithologies span the full pressure range. Temperature and pressure estimates are generally positively correlated. Some clinopyroxene rim analyses produce higher pressure estimates than the cores. We believe these to be spurious results caused by rapid element uptake during cooling (Mollo *et al.*, 2010a) and therefore are not shown.

There is no accurate barometer for the troctolitic glomerocryst sample (c.f. Putirka, 2008), however, clinopyroxene in the rim around the sample and interstitial within produce pressures of 250 ± 100 MPa. Based on the estimated temperature of 936 ± 55°C and their occurrence as a reaction rim around the xenolith or texturally infiltrate crystals, we interpret these as estimates of a later stage reservoir, and not that of the pressure of original formation of the troctolitic cumulates.

Temperature estimates range from 1124 ± 55°C for plagioclase crystallisation in the troctolitic glomerocryst to 731 ± 33°C for rim and intercumulus plagioclase in the gabbronorites. Individual samples can record 200°C variation between mineral core and rim/intercumulus temperatures. The olivine gabbros and troctolitic glomerocryst record the highest temperatures, and the gabbros, gabbronorites and diorites generally overlap at lower temperature ranges. There are temperature variations between thermometric results based on the different mineral phases. Plagioclase temperatures record crystallisation throughout the entire differentiation history, consistent with petrography and major element geochemistry, from 1124 to 731°C. Clinopyroxene crystallises over the 1063 to 893°C temperature range, orthopyroxene between 1015 and 871°C. Olivine crystallises between 1105 and 1010°C, and is found as texturally partially re-equilibrated rare xenocrysts in gabbronorites, recording temperatures between 960 and 796°C. These lower re-equilibration temperatures estimated from mineral-melt thermometry are additionally consistent with Ca-in-olivine thermometry (Shejwalkar and Coogan, 2013, Figure 2.7), although using the model outside its calibration range (1170 to 1322°C c.f. Melekhova *et al.*, 2017; Camejo-Harry *et al.*, 2018).

Temperatures estimated from oxygen isotope fractionation (Zheng, 1993) between the xenolith mineral phases is in broad agreement with the mineral-melt derived temperatures (Figure 2.18), indicating oxygen isotope equilibration at magmatic temperatures. Olivine gabbro temperatures range between 935 and 1304°C (Ol-plag, cpx-plag), gabbronorite temperatures between 805 and 1184°C (px-plag), and 899°C (cpx-plag) for the gabbro. Gabbronorite sample SAN 14-1-1-3 however has a calculated plagioclase-pyroxene temperature of 1309°C, which is higher than predicted from mineral-melt thermometry and expected from the relatively evolved mineral compositions. This indicates disequilibrium between the plagioclase and pyroxenes in the sample. Although potential accidental incorporation of albite-rich rim and intercumulus plagioclase would result in higher estimated temperatures (Zheng, 1993), this alone cannot produce such high calculated temperatures, and disequilibria is required.

A comparison between measured mineral compositions and compositions produced experimentally under controlled P-T conditions are useful to evaluate the results of the thermobarometric calculations and constrain crystallisation conditions. Comparisons of the mineral chemistry of the olivine gabbro mineral assemblage to experimental data of Andújar *et al.* (2015) match the 200-400 MPa 1040°C experiments, consistent with the mineral-melt thermobarometry above. Andújar *et al.* (2016) found that Santorini melt FeO/MgO is controlled by the depth of crystallisation, and found this parameter can be used as a geobarometer. A comparison beween olivine gabbro and gabbro glass and melt inclusion FeO/MgO vs $SiO_2$ compositions to the experimental data of Andújar *et al.* (2015) and Andújar *et al.* (2016) additionally indicates 200-400 MPa formation pressures. Gabbronorite melt inclusions match experimental melts produced in experiments at 100-200 MPa experiments. The mineral assemblage olivine, plagioclase, clinopyroxene and orthopyroxene found in three gabbronorite samples are matched by 400 MPa experiments, however the olivines in these gabbronorite xenoliths is likely xenolithic due to presence of reaction rims.

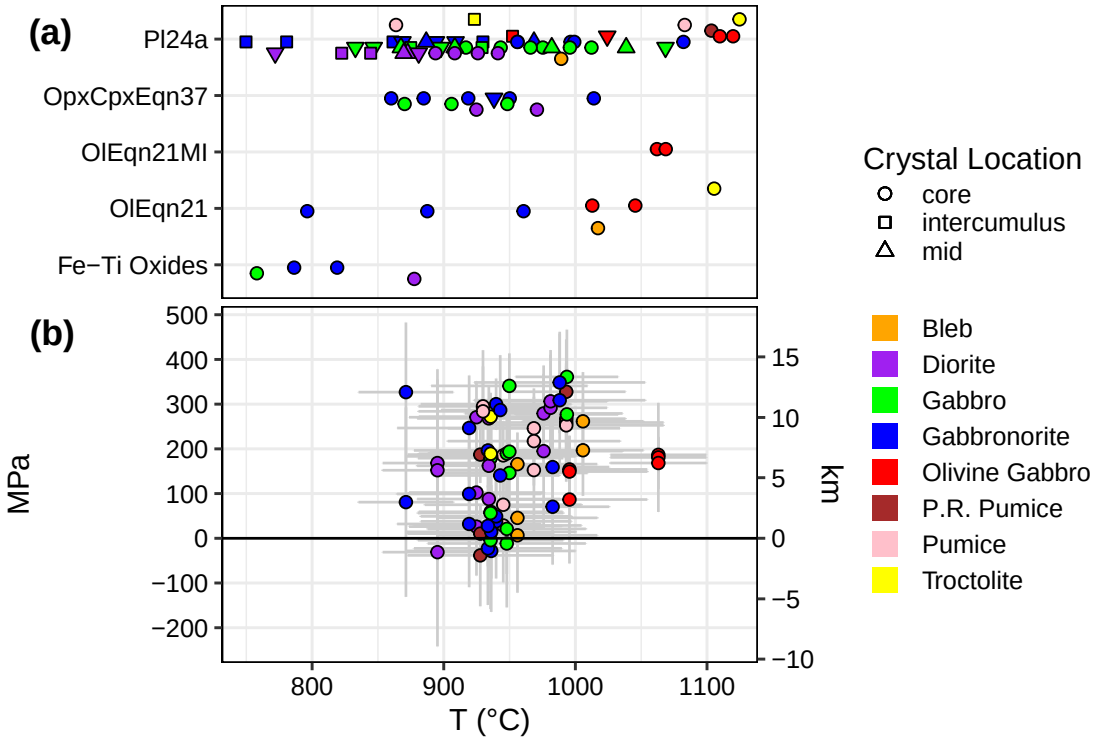


*Figure 2.24: Thermobarometry of the Santorini xenoliths. As discussed in the Appendix A.2, some models have been corrected to account for systematic overestimation at low pressure. Model uncertainty bars are 1 standard deviation of the mean pressure or temperature calculated, which is generally less than the model uncertainty (c.f. Putirka, 2008). (a) the results from thermometric models that lack a reliable paired barometric equation. A pressure of 200 MPa is assumed. Temperatures vary <10°C/100 MPa, which is insignificant in the 0 to 350 MPa range estimated from barometric models. (b) the results from Putirka (2008) equations clinopyroxene 31, 33 and 32b, orthopyroxene 29a and 29b, and the Neave and Putirka (2017) clinopyroxene barometer. Pressures estimated from crystal rims are not shown due to anomalously high (>600 MPa) and low < -200 MPa) estimates. These anomalous pressures may be due to disequilibria in the crystal rims from fast cooling, which promotes uptake of certain elements such as Al and Ti (Mollo* et al.*, 2010a). Additionally pressure estimates from the low Ti-Al clinopyroxene/orthopyroxene samples are not shown due to the negative pressures estimated. Temperature estimates from Fe-Ti oxides are from 2.25.*

The olivine gabbro xenoliths generally lack Fe-Ti oxides, excluding micrometre sized crystals of magnetite attached to the crystal rims at the contact with the intercumulus glass for estimating oxygen fugacity and temperature using two-oxide models. However, $fO_2$ can be estimated using the clinopyroxene-plagioclase-melt oxybarometer of France *et al.* (2010). We have not used the France *et al.* (2010) model on more evolved lithologies as the interstitial glasses are not in equilibrium with the clinopyroxene (see intercumulus glass discussion above, Figure 2.20). Pairings of mineral cores with melt inclusions, and rims with intercumulus glass in the olivine gabbros and the glass-rich gabbro SAN 9-1-8-3 give a range of values between NNO+1 to NNO+1.9 ($1\sigma$ uncertainty on individual estimates is 0.7-2.28, $1\sigma$ uncertainty per sample

is ±0.5) with no significant difference between core-melt inclusion and rim-intercumulus glass. These estimates are close to the experimental estimates (NNO+1) for Upper Scoria 1 andesitic magma (Andújar *et al.*, 2016) and two oxide estimates for rhyodacitic magma (~NNO + 0.5 Cottrell *et al.*, 1999), although higher than previously determined for mafic magmas from two oxide oxybarometry and experimental constraints (~QFM Gertisser *et al.*, 2009; Andújar *et al.*, 2015). Oxygen fugacity estimates for gabbros and gabbronorites based on two oxide oxybarometry (ILMAT Lepage, 2003) indicate conditions of NNO -1 to +2 (Figure 2.25). Temperatures range from 903°C to 605°C. The lower values in this range of temperatures, combined with the high estimated oxygen fugacities, are likely a combination of both subsolidus storage of the xenoliths and/or hydrothermal alteration of some of the xenoliths.

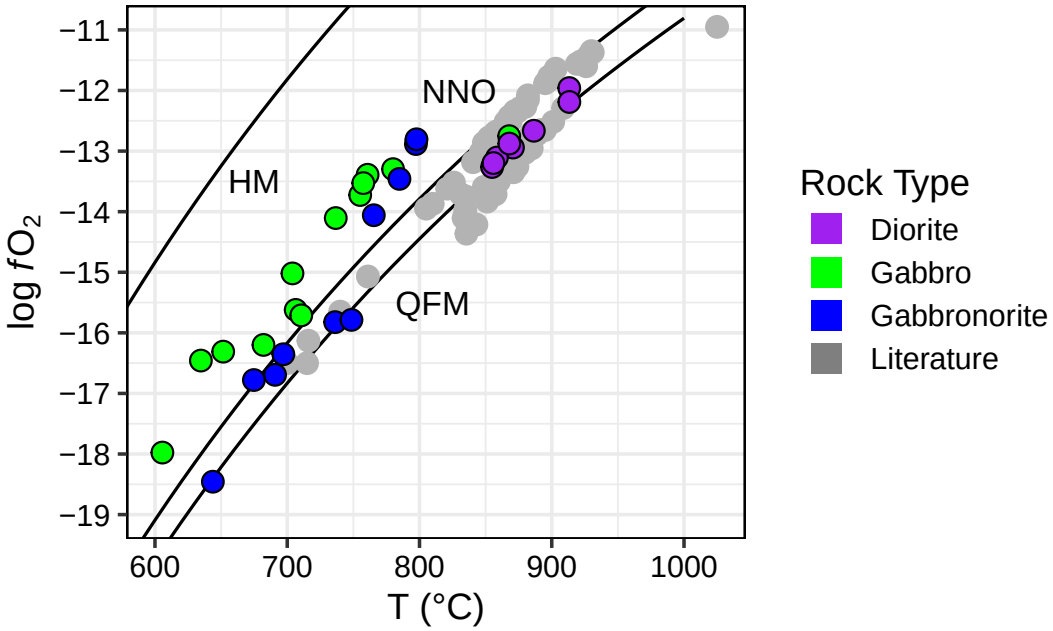


*Figure 2.25: Temperatures and oxygen fugacity estimated from coexisting magnetite and ilmenite pairs. Light grey literature values are Kameni dacite and diorite nodule values from Druitt (2014), Lower Pumice 2 pumice and mafic bleb values from Gertisser* et al. *(2009), pumice values from Cadoux* et al. *(2014) (Lower Pumice 1, Lower Pumice 2, Cape Riva, Minoan), and Minoan pumice values from Panienka (2012).*

Water contents estimated from plagioclase-melt hygrometry (Putirka, 2008) range between 2 to 7 wt%. The lowest water contents are estimated for the troctolite crystal clot sample with 2 wt% $H_2O$, Olivine gabbro water contents are 2.4 (crystal core) to 4.4 wt% (microlites), gabbro 3.5 to 5.9 wt%, gabbronorite 3.1 to 6.9 wt% and diorite 4.7 to 7 wt%. These are comparable to the measured values from mafic to felsic volcanic products at Santorini (Panienka, 2012; Cadoux *et al.*, 2014; Druitt *et al.*, 2016).

**Implications for the Santorini Plumbing System from Plutonic Xenoliths**

Pressures estimated from mineral-melt thermobarometry and comparison with experimental mineral and glass compositions indicate formation at pressures less than 400 MPa for the entire xenolith suite analysed, over a temperature range from 1124 to 749°C (excluding Fe-Ti oxide temperatures) at a $fO_2$ of ~NNO -1 to +2 and 2 to 7 wt% $H_2O$. This shows a dominant role of upper to mid crustal magmatic differentiation. A weak trend of decreasing pressure with increasing magmatic evolution and decreasing temperature can be noted overall and within individual model results, however large uncertainty with condensed phase barometry and variation between different barometric models preclude more precise interpretation. Overlap between cumulate mineral compositions and volcanic phenocrysts indicate both form at shallow to mid crystal depths from already partially differentiated mantle melts. These results are however in agreement with previous work (Druitt *et al.*, 2016 and references within) indicating significant differentiation of mafic melts at Santorini occurs in the mid to upper crust. The weak shallowing trend is consistent with experimental work (Andújar *et al.*, 2015, 2016) and core-to-rim pressure decreases in Minoan phenocrysts showing deeper (~320 MPa) magma generation and later shallow temporary (100-200 MPa) storage depth (Cottrell *et al.*, 1999; Druitt *et al.*, 2016). Ultramafic cumulates from the lower crust related to the parental mantle-derived melts have not yet been found at Santorini.

### 2.5.5 Volatile Behaviour: Inferences from Plutonic Xenoliths

The S and Cl concentrations in the xenolith melt inclusion and glasses (Figure 2.16) closely follow the trends defined by the literature data from basalt to rhyolitic compositions, with S decreasing and Cl increasing with increasing $SiO_2$. Pyrrhotite, although present in Santorini magmas (Gertisser *et al.*, 2009; Cadoux *et al.*, 2014; Druitt *et al.*, 2016), is not present in large enough quantities in the magma (« 1 vol%) to affect the melt S concentrations significantly (Druitt *et al.*, 2016). Pyrrhotite has additionally not been observed in the xenoliths. It follows that removal of S from the xenolith cumulate melts occurs instead via open system exsolution into a free vapour phase, as demonstrated for melt inclusions and glasses trapped in the volcanic deposits (Michaud *et al.*, 2000; Gertisser *et al.*, 2009; Cadoux *et al.*, 2014; Druitt *et al.*, 2016). Cl behaves incompatibly during differentiation at Santorini (Figure 2.16), and the few plutonic xenolith samples that show enrichment in Cl compared to the literature volcanic values may be a result of intercumulus melt crystallisation, which enriches this melt in incompatible elements, discussed previously.

### 2.5.6 Crustal Contamination Contraints from the Plutonic Xenoliths

The range of oxygen isotopic compositions in both the xenoliths (this study) and volcanic deposits (Wyers, 1987; Druitt *et al.*, 1999), and their calculated equilibrium melts (xenolith: $\delta^{18}O$ = 6.1-7.0 ‰, volcanic deposits 5.5-7.3 ‰) generally exceed that expected from crystallisation from an uncontaminated mantle-derived magma (~5.7 ± 0.3 Ito *et al.*, 1987; Harmon and Hoefs, 1995, Figure 2.18). Closed system differentiation of a MORB composition to silicic compositions (75 wt%) would increase the $\delta^{18}O$ by only <~ 0.5 ‰ (Eiler, 2001; Bindeman, 2008). The range of xenolith whole-rock and trapped glass major element chemistry (Figure 2.16) show that the xenoliths are formed throughout the differentiation history of Santorini magmas, and therefore much of the xenolith oxygen isotope variability can be explained by fractional crystallisation (c.f. Druitt *et al.*, 1999). Higher values of melts with up to $\delta^{18}O = 7.0$ ‰ require small amounts of crustal assimilation. Taking a mean value of the potential contaminent basement lithologies in Figure 2.18 as 11.2 ‰ requires 10-20% crustal contamination to produce the elevated $\delta^{18}O$ melts in the xenoliths. This is consistent with the results from radiogenic isotopic systems for the volcanic deposits by Druitt *et al.* (1999).

### 2.5.7 Comparison with Aegean Plutonic Xenoliths

Plutonic xenoliths are not exclusive to Santorini, and are additionally present at Nisyros (Di Paola, 1974; Klaver *et al.*, 2017, 2018), situated towards the eastern end of the South Aegean Volcanic Arc. The xenolith suite at Nisyros has a richer variety of cumulates than Santorini, containing gabbros and olivine gabbros from upper crustal reservoirs, similar to Santorini, and additional deep crustal cumulates such as hornblende-wehrlites. Deep crustal amphibole-bearing cumulates are additionally characteristic of many other worldwide arcs, such as the Lesser Antilles (Arculus and Wills, 1980; Tollan *et al.*, 2012; Stamper *et al.*, 2014; Cooper *et al.*, 2016; Camejo-Harry *et al.*, 2018), Andes (Costa *et al.*, 2002), Japan (Tiepolo *et al.*, 2012) and Solomon Islands (Smith, 2014). Primary amphibole is rare however at Santorini, only found as microlites within the olivine gabbro glass and rare intercumulus crystals in the more evolved xenoliths (c.f. Druitt *et al.*, 1999), showing limited amphibole stability in shallow, lower temperature intermediate Santorini melts. Pressures estimated from these amphiboles are 90 to 250 MPa (using Ridolfi and Renzulli, 2012; Putirka, 2016), consistent with the upper to mid-crustal pressures estimated from clinopyroxene barometry, also consistent with rare amphibole in the Lower Pumice 2 eruption (430 MPa estimated in Gertisser *et al.*, 2009; P=~200

MPa when using Ridolfi and Renzulli, 2012). Post-Akrotiri magmas at Santorini (< 530 ka) are characteristically amphibole free, and they do not show clear geochemical tracers of amphibole fractionation (Davidson *et al.*, 2007), such as low to near constant Y or decreasing Dy/Yb during differentiation (Elburg *et al.*, 2014) (Figure 2.26). Plutonic xenolith whole-rock compositions, glasses, melt inclusions and mineral chemistry additionally follow the amphibole-free differentiation trend, consistent with their anhydrous mineral assemblage. Gabbronorite sample SAN 9-3-2 (Minoan eruption) falls within the amphibole-bearing differentiation trend, consistent with previous discussion showing it to be a xenolith derived from earlier high Ba, low Zr Akrotiri volcanic deposits or an unerupted intrusion compositionally similar to the Akrotiri deposits (Druitt *et al.*, 1999; Druitt, 2014). The late stage intercumulus amphibole in the xenoliths has a limited effect on the geochemical signature of Santorini magmas, and reflected in the weak inflection in Figure 2.26 to flatter profiles (c.f. Elburg *et al.*, 2014). The differing role of amphibole in the geochemical signatures at Santorini compared to Nisyros (and additionally Methana in the western arc segment) can be related to the differing depths of primitive magmatic differentiation (< 400 MPa at Santorini, both ~200 MPa and > 500 MPa at Nisyros), and the composition of the source magmas (Druitt *et al.*, 1999; Elburg *et al.*, 2014; Andújar *et al.*, 2015; Klaver *et al.*, 2017, 2018).

## 2.6 Conclusions

Plutonic xenoliths collected from across the stratigraphy of Santorini are troctolite, olivine gabbro, gabbro, diorite and gabbronorites. Texturally and chemically they can be considered cumulates to the volcanic succession. Mineral chemistry generally overlaps that of the volcanic phenocrysts but also extends to differentiation indices that demonstrate a higher degree of differentiation (low Fo, An, Mg#) in the intercumulus. Oxygen isotopes show a small influence of crustal assimilation during magmatic differentiation (<20%). Significant mineral trace element enrichment is observed in some samples, related to post-cumulus crystallisation of or equilibration with trapped intercumulus melts. Cumulate remobilisation processes may cause these cumulus crystals and trapped melts to mix into the magmatic system. Thermobarometry shows the entire xenolith suite is formed over a wide temperature range between ~1100 to 750°C, at shallow to mid crustal depths (< 400 MPa) from a partially differentiated deep crustal primitive mantle melt. This shallow magma differentiation at Santorini inhibits significant amphibole fractionation, in contrast to Nisyros and Methana to the east and west of the South Aegean Volcanic Arc respectively. Although plutonic xenoliths may not be common in

all volcanic deposits of all volcanoes, the understanding of the processes occuring during arc magma petrogenesis and cumulate mush generation gained from studying them is applicable worldwide, and warrants further study.

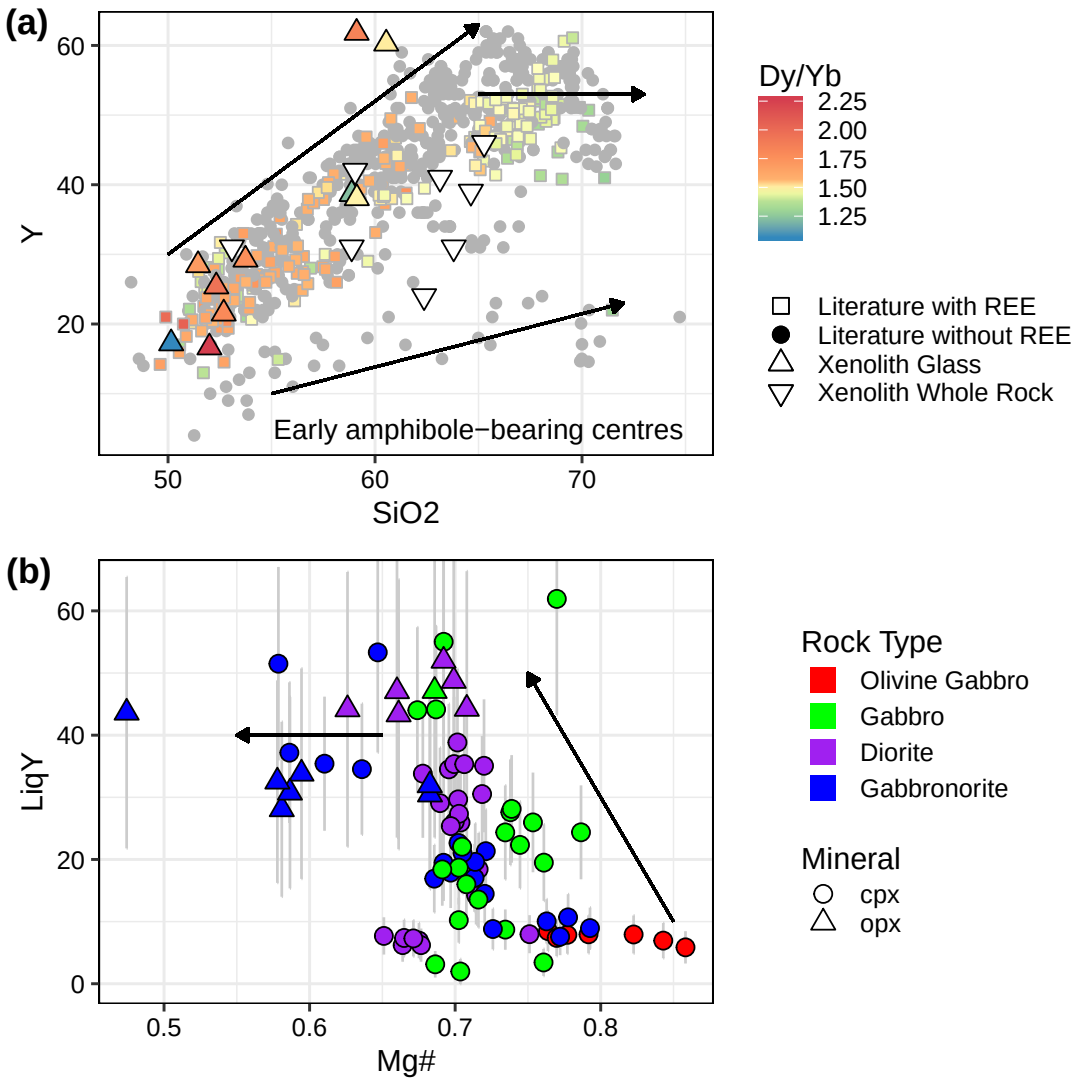


*Figure 2.26: Geochemical tracers of amphibole fractionation applied to Santorini plutonic xenoliths. A) Y vs SiO2 variation at Santorini. Xenolith melt inclusion and intercumulus glass (upwards triangles, coloured by Dy/Yb) and whole rock (downwards triangles) for comparison with literature volcanic data. The influence of amphibole (flat Y with differentiation, decreasing Dy/Yb) is only clear at Akrotiri and at >65 wt% $SiO_2$later. B) Calculated melt Y in equilibrium with clinopyroxene and orthopyroxene against Mg# as a differentiation index. A similar trend to the Y vs $SiO_2$ is shown, with increasing Y until an inflection at higher differentiation (lower Mg#). Uncertainty in Y equilibrium melt calculations are ~30% and ~ 50% for cpx and opx relative respectively (Bédard, 2007, 2014).*

# Chapter 3

# Magmatic and metasomatic effects of magma-carbonate interaction recorded in calc-silicate xenoliths from Merapi volcano (Indonesia)

This chapter has completed first revision for publication at the Journal of Petrology. The work was reviewed positively by Massimo D'Antonio and Anastassia Borisova. This work is in collaboration with the PhD supervisors Ralf Halama and Ralf Gertisser, Katie Preece (University of Swansea), Valentin Troll and Frances Deegan (Uppsala University). The samples were collected by Gertisser, Preece, and Troll. Electron microprobe data was collected myself with an additional dataset provided by Deegan. This manuscript was written by myself with input from all authors at various stages.

## 3.1 Introduction

Calc-silicate (skarn) xenoliths are found within the deposits of many hazardous arc volcanoes worldwide, including Popocatépetl (e.g. Goff *et al.*, 2001), Vesuvius (e.g. Fulignati *et al.*, 2001), Merapi (e.g. Chadwick *et al.*, 2007), Colli Albani (e.g. Di Rocco *et al.*, 2012) and Nisyros (Spandler *et al.*, 2012). Formed as a result of interaction between crustal carbonate and the host magmatic system, these xenoliths preserve evidence of complex reaction processes that can have profound impact on the host magmatic system, including altering magmatic differentiation paths (e.g. Iacono-Marziano *et al.*, 2008), influencing eruptive dynamics (e.g. Freda *et al.*, 2011; Troll *et al.*, 2012; Carr *et al.*, 2018), and liberating large volumes of crustal $CO_2$ into the atmosphere (e.g. Mason *et al.*, 2017).

Much of the knowledge about crustal magma-carbonate interaction processes is derived from diverse approaches. Isotope mass balance calculations (e.g. Troll *et al.*, 2012, 2013; Jolis *et al.*, 2015) have shown that large volumes of crustal carbonate, up to 30%, are incorporated into some volcanic systems, and *in situ* stable isotopes have demonstrated decarbonation is highly efficient in magmatic systems (Whitley *et al.*, 2019, Chapter 4). Experimental magma-carbonate studies (e.g. Iacono-Marziano *et al.*, 2008; Deegan *et al.*, 2010; Jolis *et al.*, 2013; Blythe *et al.*, 2015; Carter and Dasgupta, 2016) have further demonstrated how magmatic melt differentiation paths are modified towards silica undersaturation in mafic melts, and that magma-carbonate interaction may be extremely rapid (syn-magmatic), operating on the order of minutes to hours. Moreover, detailed petrographical and geochemical studies of the individual xenoliths have provided insights into the architecture of subvolcanic skarn contact aureoles (Matthews *et al.*, 1996; Fulignati *et al.*, 2004), the depth of magma-carbonate interaction from fluid inclusions (Clocchiatti *et al.*, 1982), xenocryst incorporation into the magma and skarn recycling (Chadwick *et al.*, 2007; Jolis *et al.*, 2015), changes in magmatic redox conditions and phase equilibria (Wenzel *et al.*, 2002), and the economic metallogenic potential of magmatic fluids that interact with the country rock (Fulignati *et al.*, 2013).

In this study we present a detailed analysis of the petrography, mineralogy and geochemistry of calc-silicate xenoliths from the 1994-2010 eruptions of Merapi volcano, Indonesia. We demonstrate that these xenoliths represent fragments of either complete replacement of carbonate wall rock to calc-silicate mineral assemblages around the magma reservoir margins, or are transient fragments of entrained carbonate which is caught in the process of being metamorphosed within the magma itself. The xenoliths record evidence of interaction with a magmatic-derived halogen-bearing fluid that produced exotic halogen-bearing mineral phases, whilst enriching

the xenoliths in economically important metals such as copper and iron, and by analogy the more extensive skarn system below Merapi. We also show that traditional mineral-melt thermobarometry and fluid inclusion analysis can be applied to some of the xenoliths, and we present a new calibration of a single clinopyroxene crystal oxybarometer to determine intensive variables (T, P, $fO_2$) during xenolith formation.

## 3.2 Geological Background

Merapi is the most active of Indonesia's volcanoes, and is considered one of the Sunda arc's most dangerous (Gertisser *et al.*, 2011, 2012). Activity is near continuous, with periods of dome growth frequently interrupted by gravitational dome collapse and associated pyroclastic density current emission (Andreastuti *et al.*, 2000; Camus *et al.*, 2000; Newhall *et al.*, 2000; Voight *et al.*, 2000; Gertisser *et al.*, 2012). Larger explosive vulcanian and subplinian eruptions occur at longer ~100 year time-scales, such as the 2010 VEI 4 eruption which killed close to 400 people (Surono *et al.*, 2012). Compositionally, the erupted material is medium to high-K basalt to basaltic andesite with a restricted range of ~49 to 58 wt% $SiO_2$ (Gertisser and Keller, 2003a, 2003b). Early work at Merapi suggested a significant subducted sediment contamination component to the Merapi magmas (Gertisser and Keller, 2003b), while subsequent work also highlighted an influence from crustal carbonate on magma genesis (e.g. Chadwick *et al.*, 2007; Troll *et al.*, 2013; Aiuppa *et al.*, 2017). Merapi overlies an upper crust of 8 to 11 km thick sediments of the Kendeng basin, where Cretaceous to Cenozoic volcaniclastic sediments are overlain by shallow marine limestones and marls, all of which overlie inferred Cretaceous arc and ophiolite basement rocks (van Bemmelen, 1949; Smyth *et al.*, 2005). Fragments of the sedimentary basement are frequently found as thermally metamorphosed xenoliths within the eruptive deposits (Brouwer, 1928; Clocchiatti *et al.*, 1982; Camus *et al.*, 2000; Gertisser and Keller, 2003b; Chadwick *et al.*, 2007; Troll *et al.*, 2012, 2013). These xenoliths testify to prevalent magma-carbonate interaction [Chadwick *et al.* (2007); Troll *et al.* (2013); Whitley *et al.* (2019); Chapter 4], a process that is ongoing and occurs at rapid syn-magmatic eruptive timescales (Deegan *et al.*, 2010, 2011; Troll *et al.*, 2012; Reagan *et al.*, 2017). Radiogenic ($^{87}Sr/^{86}Sr$) and stable ($\delta^{13}C$, $\delta^{18}O$) isotope analysis of bulk xenoliths and mineral separates of calc-silicate mineral phases (wollastonite, diopside, calcite), have been used to demonstrate up to 30% crustal carbonate assimilation during the genesis of Merapi magmas [Chadwick *et al.* (2007); Troll *et al.* (2013); Whitley *et al.* (2019); Chapter 4]. Liberation of large volumes of crustal $CO_2$ during syn-magmatic activity has additionally been linked to enhancing eruptive

explosivity at Merapi (e.g. Troll *et al.*, 2012, 2013; Borisova *et al.*, 2013; Carr *et al.*, 2018). The available evidence thus indicates that magma-carbonate interaction at Merapi may have wide-ranging implications for the magmatic evolution and volcanic hazard potential at Merapi.

## 3.3 Methods

### 3.3.1 Scanning Electron Microscopy and Raman Spectroscopy

Scanning electron microscopy was undertaken at Keele University, UK using a Hitachi TM3000 scanning electron microscope with an EDS attachment. The EDS was used to aid sample exploration due to the relatively high uncertainty (1-2 wt% on major elements), and therefore analyses presented in this work are from the electron microprobe. A rare unknown mineral found in sample MX1, compositionally similar to wadalite, was analysed with Raman spectroscopy at Keele University using a confocal Thermo Scientific DXR Raman spectrometer with a 532 nm laser, a 50x objective, and a standard 30 µm uncovered polished thin section.

### 3.3.2 Microthermometry

Microthermometry was carried out at Keele University using a Linkam THMS600 freezing-heating stage. Thermocouples were calibrated at –56.6°C, 0.0°C and +374.1°C using synthetic fluid inclusions provided by Linkam. The precision of temperature measurements at -56.6°C is ±0.1°C, and ±2°C at 374.1°C. Measurements were made on ~100 µm thick double polished wafer fragments.

### 3.3.3 Electron Microprobe Analysis

Major element concentrations in minerals, and major element, chlorine and sulphur concentrations in groundmass glasses and melt inclusions were determined with a JXA 8900R Electron Probe Microanalyser at the University of Kiel, Germany. Silicate and oxide minerals were analysed with a 15 kV accelerating voltage, a 15 nA beam current and a 2 µm beam diameter. Calcite was measured with a 7 µm beam diameter at 15 kV accelerating voltage and a 10 nA beam current. Glasses were measured with a 5 µm beam at 15 kV accelerating voltage and a 12 nA beam current. Measurement times were 15 s at the peak and 7 s on the background, excluding S, Cl, P which were measured for 30 s at the peak and 10s on the background. Extended counting times of 30 s peak and 10 s background for Fe, Mg and Mn, and 60 s peak

and 30 s background for Ba and Sr were applied during calcite analyses. Na was measured first to minimise alkali migration. Natural mineral standards (topaz, rutile, baryte, tugtupite, fayalite, forsterite, mica, anorthite, wollastonite, apatite, tephroit) were used for calibration and Smithsonian basaltic glass A-99, forsterite 83 USNM2566, plagioclase USNM115900, garnet RV2 USNM 87375, and obsidian ASTIMEX Block SPGLASS7 were used as secondary within run standards to assess accuracy and precision, presented in the supplementary spreadsheet.

This chapter additionally includes microprobe data from Dr. Ralf Gertisser (initial exploratory dataset, see Gertisser, 2001 for methods) and Dr. Frances Deegan (Uppsala University, see Deegan *et al.*, 2010 for methods and samples analysed).

All Mg# values were calculated assuming all Fe as $Fe^{2+}$ using $Mg\# = 100\frac{Mg}{Mg+Fe_{total}}$. Ternary clinopyroxene components are calculated assuming all Fe as $Fe^{2+}$ e.g. $Fs = 100\frac{Fe_{total}}{Mg+Fe_{total}+Ca}$. $Fe^{3+}$ was estimated for clinopyroxene from stoichiometry using Droop (1987). $Al^{IV}$ was calculated as 2-Si, and any remaining Al was allocated as $Al^{VI}$. Components for clinopyroxene thermobarometry were calculated using Putirka *et al.* (1996). Garnet end member mole fractions and $Fe^{3+}$ were estimated using the Arai (2010) R script implementation of the Muhling and Griffin (1991) calculation scheme, which provides a more accurate $Fe^{3+}$ estimate for garnet than Droop (1987). Melilite mole fractions were calculated considering 4 end members by firstly allocating Na to the Na-melilite end member, and then the remaining cations, minus the Al required for Na-melilite, were allocated between gehlenite, åkermanite and Fe-åkermanite. These mole fractions were calculated as follows (abbreviations as in Table 3.2):

$$\text{Na-Mel} = \frac{Na}{Na+Ca-1}$$

$$\text{Geh} = (1 - \text{Na-Mel}) \cdot \frac{\frac{Al-2Na}{2}}{\frac{Al-2Na}{2}+Fe+Mg}$$

$$\text{Ak} = (1 - \text{Na-Mel}) \cdot \frac{Mg}{\frac{Al-2Na}{2}+Fe+Mg}$$

$$\text{Fe-Ak} = (1 - \text{Na-Mel}) \cdot \frac{Fe}{\frac{Al-2Na}{2}+Fe+Mg}$$

### 3.3.4 Whole-rock Geochemistry

Due to the small size of most xenoliths combined with the textural and mineralogical uniqueness of each sample, whole-rock compositions and compositions of individual zones for six representative xenoliths were determined by point counting (1000-2000 points). Averaged mineral and glass chemistry was used with the phase volumes counted, corrected for varying mineral and glass densities using mineral densities from Deer *et al.* (1997). The bulk compositions were obtained using the Rock-Maker spreadsheet (Büttner, 2012), which generates bulk whole rock compositions from phase volumes and densities. All calculated compositions are presented in

the appendix online spreadsheet.

### 3.3.5 Thermodynamic Modelling

Theriak-Domino software (build date 3-1-2012, de Capitani and Petrakakis, 2010) was used for thermodynamic modelling, using calculated whole-rock compositions (see above) in the system Si-Al-Fe-Mg-Ca-C for samples MX99-5s and MX99-3s. The database used (Holland and Powell, 1998, version 5.5) lacks solid solution models that include the CaTs component in clinopyroxene, and mixing between gehlenite and åkermanite. Therefore, ideal mixing was assumed for these two solid solutions (Charlu *et al.*, 1981; Povoden *et al.*, 2002). Implementing a CaTs-Di-Hd ideal mixing model for clinopyroxene over the default database model however has little effect on the calculated phase boundaries of the system. For example, this clinopyroxene model produce only a ~20°C variation in melilite-garnet phase boundaries, which is relevant to the xenoliths.

## 3.4 Petrography

Calc-silicate xenoliths (*n=33*) collected from the 1994 to 2010 eruption deposits at Merapi can be subdivided into three distinct groups (magmatic skarn *n=25*, exoskarn *n=5* and buchite *n=3*) on the basis of their dominant mineralogy, modal zonation, and the presence of glass. 12 xenoliths that best represent the three groups, and which highlight the mineralogical and textural variety of the xenoliths were chosen for detailed study (see Table 3.1) and Appendix Table B.1 for full sample list). The xenoliths are generally centimetre to tens of centimetre in size, and texturally complex variations in mineralogy and zonation can be seen at hand specimen scale (Figure 3.1). Contacts with host basaltic-andesite are vesicular, and texturally the xenoliths can often be seen mingling with the host lava. Magmatic skarn xenoliths are commonly layered with reaction rims parallel to the host basaltic andesite up to a few centimeters thick, whilst exoskarn xenoliths often exhibit sharper contacts. No magmatic skarn-exoskarn contacts are found in the samples, presumably due to different formation processes and mechanical properties, similar to that observed by other workers on skarn xenoliths (e.g. Matthews *et al.*, 1996; Fulignati *et al.*, 2004; Gaeta *et al.*, 2009). The detailed petrography of the xenolith types are discussed below. Volcaniclastic and metasedimentary xenoliths are additionally present at Merapi but not discussed in this paper (see Chadwick *et al.*, 2007). A summary of the mineral phases identified in this study and their formulas are presented in Table 3.2.

*Table 3.1: Merapi xenolith sample list and data collected. Samples MXCS and MXCS-1 and data from these were provided by Frances Deegan. Samples with - as a type are not calc-silicate*

| Sample | Type | SEM study | EMPA | LA-ICP-MS (calcites) | SIMS O-C isotopes (calcites) | Microthermometry | Raman |
|---|---|---|---|---|---|---|---|
| CS-1 | Magmatic Skarn | | | | | | |
| CS-2 | Magmatic Skarn | X | X | | | | |
| CS 3 | Magmatic Skarn | | | | | | |
| CS-4 | - | | | | | | |
| CS-5 | Magmatic Skarn | | | | | | |
| CS-6 | Magmatic Skarn | | | | | | |
| CS-7 | Magmatic Skarn | | | | | | |
| CS-8 | Magmatic Skarn | | | | | | |
| CS-9 | Magmatic Skarn | X | | | | | |
| CS-10 | Buchite | | | | | | |
| CS-11 | Exoskarn | X | X | X | X | | |
| CS-12 | - | | | | | | |
| CS-13 | - | | | | | | |
| CS 14 | Buchite | X | | | | | |
| CS-15 | - | | | | | | |
| CS-16 | Magmatic Skarn | X | X | | | | |
| CS-17 | Magmatic Skarn | | | | X | | |
| CS-18 | Magmatic Skarn | | | | | | |
| CS-19 | Magmatic Skarn | X | | | | | |
| MX-1 | Magmatic Skarn | X | X | | | | X |
| MX-2 | - | X | | | | | |
| MX-3 | Magmatic Skarn | X | X | | X | X | |
| MX-4 | Magmatic Skarn | | | | | | |
| MX-5 | Magmatic Skarn | X | | | X | X | |
| MX-6 | Exoskarn | | | | | | |
| MX99-3s | Exoskarn B | X | X | | | | |
| MX99-4s | Magmatic Skarn | X | X | | | X | |
| MX99-5s | Exoskarn | X | X | | | | |
| M13-24G | Magmatic Skarn | X | | | | | |
| M13-24G1 | Magmatic Skarn | X | X | | | | |
| M13-04C | Buchite | X | | | | | |
| M13-30 | Magmatic Skarn | | | | | | |
| M13-10 | Magmatic Skarn | X | | | | | |
| M11-34 | Magmatic Skarn | | | | | | |
| M13-02 | Exoskarn | X | X | | X | | |
| MXCS | Exoskarn | | X | | | | |
| MXCS-1 | Magmatic Skarn | | X | | | | |

*Table 3.2: Mineral phases identified within the Merapi calc-silicate xenoliths in this study, and abbreviations used throughout the text. The minerals are ordered as they appear within this manuscript.*

| Mineral | Abbreviation | Formula | Mag | Exo A | Exo B |
|---|---|---|---|---|---|
| **Rock-forming and their endmembers** | | | | | |
| Plagioclase | Pl | $(Ca,Na)(Al,Si)_4O_8$ | M | M | m |
| –Anorthite | An | $CaAl_2Si_2O_8$ | M | M | m |
| Clinopyroxene | Cpx | $Ca(Fe,Mg)Si_2O_6$ | M | | |
| –Calcium Tschermak's Pyroxene | CaTs | $CaAlAlSiO_6$ | m | M | M |
| –Esseneite (Clinopyroxene) | Ess | $CaMgSi_2$ | m | M | M |
| Wollastonite | Wo | | M | M | m |
| –Ferrobustamite | Bst | $CaFeSi_2$ | m | m | |
| Garnet | Grt | | m | M | M |
| –Andradite | Adr | $CaFe^{3+}AlSiO_6$ | m | M | m |
| –Grossular | Grs | $CaSiO_3$ | m | M | M |
| –Schorlomite | Sch | $Ca(Fe^{2+},Ca,Mn^{2+})Si_2O_6$ | m | | |
| Melilite | | $Ca_3(Fe^{3+},Al,Ti)_2Si_3O_{12}$ | | | |
| –Åkermanite | Åk | $Ca_3Fe^{3+}{}_2Si_3O_{12}$ | m | m | M |
| –Fe-Åkermanite | Fe-Åk | $Ca_3Al_2Si_3O_{12}$ | m | m | M |
| –Gehlenite | Gh | $Ca_3Ti_2Si_3O_{12}$ | m | m | M |
| –Na-Melilite | Na-Mel | | | | |
| **Sulphur and Halogen-bearing** | | | | | |
| Pyrrhotite | Po | $Ca_2FeSi_2O_7$ | m | m | |
| Anhydrite | Anh | $Ca_2Al_2SiO_7$ | m | m | |
| Cubanite | Cu | $CaNaAl_2SiO_7$ | m | | |
| Cuspidine | Cusp | | m | m | |
| Spurrite | Spu | $Fe_{1-x}S$ (x=0-0.2) | | m | |
| Larnite | Lrn | $CaSO_4$ | | m | |
| Fluorite | Fl | $CuFe_2S_3$ | m | | |
| Apatite | Ap | $Ca_4Si_2O_7(F,OH)_2$ | m | | |
| Ellestadite | El | $Ca_5Si_2O_8CO_3$ | | m | m |
| Baryte | Ba | $Ca_2SiO_4$ | m | | |
| Cotunnite | Cot | $CaF_2$ | m | | |
| Wadalite† | Wad | $Ca_5(PO_4)_3(OH,F,Cl)$ | m | | |
| **Oxides, Other Silicates, and Accessory Minerals** | | | | | |
| Magnetite | Mgt | $BaSO_4$ | M | m | |
| Ilmenite | Ilm | $PbCl_2$ | m | | |
| Hematite | Hm | $Ca_{12}Al_{10}Si_4O_{32}Cl_6$ | | m | |
| Perovskite | Psk | | m | | |
| Ca-Zr-Ti oxide | CaZrTi | $Fe^{2+}Fe^{3+}{}_2O_4$ | m | | |
| Titanite | Ttn | $FeTiO_3$ | m | m | |
| Spinel | Sp | $Fe_2O_3$ | | | M |
| Monazite | Mo | $CaTiO_3$ | | m | |
| Xenotime | Xe | Ca-Zr-Ti | | m | |
| Calcite | Cal | $CaTiSiO_4$ | m | M | |
| Cebollite† | Ce | $(Fe,Mg)Al_2O_4$ | | m | |
| Chromite | Chr | $(Ce,La)PO_4$ | m | | |
| Quartz | Qtz | $YPO_4$ | M | m | |

Mag: Magmatic skarn. Exo A: Exoskarn type A. Exo B: Exoskarn type B
M: Major rock forming mineral. m: Minor to accessory (<1 vol%) mineral
† Identification Uncertain

### 3.4.1 Magmatic Skarn xenoliths

The most abundant calc-silicate xenolith type ($n$=25) is the one we term 'magmatic skarn' (c.f. Fulignati *et al.*, 2004) based on the abundance of Ca-enriched magmatic glass, melt inclusions in the newly formed calc-silicate skarn minerals, and pronounced reaction zones at contacts with the host lava. Attempting to explain the variety of xenoliths in this group, the magmatic skarn xenoliths are subdivided into a series of idealised mineralogical/textural zones, such as a series of reaction zones and a core zone (Figures 3.2, 3.3). The lava contact (R1) is represented by a zone of coarse (100-300 μm) pale green clinopyroxene and a concentration of magnetite (Figure 3.3A). This is followed by a finer grained (up to 100 μm) zone (R2) of plagioclase + clinopyroxene ± glass (Figure 3.3A), with rare amphibole also present in sample MX1. This zone grades into a zone of coarse dark green/yellow pleochroic clinopyroxene (R3) separating R2 from a zone of vesicular glass (R4) (Figure 3.3A-B). The glass zone typically contains strongly irregularly Fe-Mg zoned (see mineral chemistry), colourless to deep green/yellow pleochroic diopsidic clinopyroxene crystals (Figure 3.3B). These clinopyroxene crystals are similar to those of zone R3, and often appear to be incorporated from zone R3. Plagioclase and wollastonite microlites are additionally present within the glass. Sample MX5 has comparatively large quartz and plagioclase crystals (~100 μm) within the glass zone, and sample MX3 shows this zone to be almost fully crystallised to quartz and plagioclase, with scarce melt inclusions within the quartz crystals. The xenolith core (Figure 3.3C) has a sharp contact to decussate wollastonite, but occasionally the core is a mixture of wollastonite, clinopyroxene, and accessory garnet. Additionally, glass is often present within the core of these xenoliths. At glass-wollastonite contacts, a thin rim of semi-dendritic ferrobustamite often forms. The samples have a vesicular texture across all zones.

The described zonation is idealised, and variations naturally occur. Samples MX1 and M13-10, for instance show no glass zone (R4) separating the wollastonite-dominant core from R3 and R2. In this case, a pale yellow clinopyroxene and garnet zone formed instead of the coarse clinopyroxene of zone R3, which we call R3b (Figures 3.2, 3.3D). This clinopyroxene is optically and chemically distinct (CaTs: $CaAlAlSiO_6$ rich, see section Mineral Chemistry) from any others in the Merapi magmatic skarn xenoliths. In sample MX1, one half of the xenolith shows the common zonation (with glass zone R4 present), whilst the other half has no glass and instead has the zone R3b CaTs clinopyroxene and garnet zone (Figure 3.2). Rare patches of garnet are found interstitial to wollastonite in the MX1 core, and also together with wollastonite and CaTs clinopyroxene in sample CS16.

Accessory phases are generally restricted to the xenolith cores, and include calcite, titanite, chromite, gehlenite, a wadalite-like Si-Al-Fe-Ca-O-Cl mineral, perovskite, a Ca-Zr-Ti-O mineral, cotunnite, sulphates (anhydrite and baryte) and sulphides (pyrrhotite and cubanite)(Table 3.2). Titanite is also present within the glass in zone R4 and ilmenite is exclusively found in sample MX3 in zone R2. Calcite is present as four distinct textural types: 1) globular crystals within the glass R4 zone, 2) interstitial to wollastonite in the cores, 3) inclusions in wollastonite and garnet, and 4) a melt-like infiltrative texture containing rare Cl-F rich phases such as fluorite, cuspidine and the wadalite-like mineral within regions where the calcite pools (Figure 3.4A-B). These calcites are discussed in detail in Whitley *et al.* (2019) and Chapter 4.

Many crystals contain significant quantities of melt inclusions (Figure 3.4C-G), exceeding 80 in a single 600 µm long wollastonite crystal. Melt inclusions are also present in clinopyroxene of zones R3-4, plagioclase in zone R4 and titanite within the xenolith cores. The inclusions are most commonly glassy and have a single shrinkage bubble, but, in rare cases they can contain daughter crystals and multiple bubbles. The daughter crystals are found either in the glass or in the bubble, and are most commonly Fe-bearing phases (pyrrhotite, cubanite, magnetite) and occasionally apatite. Vapour-rich $CO_2$ fluid inclusions are also common in wollastonite (Figure B.2).

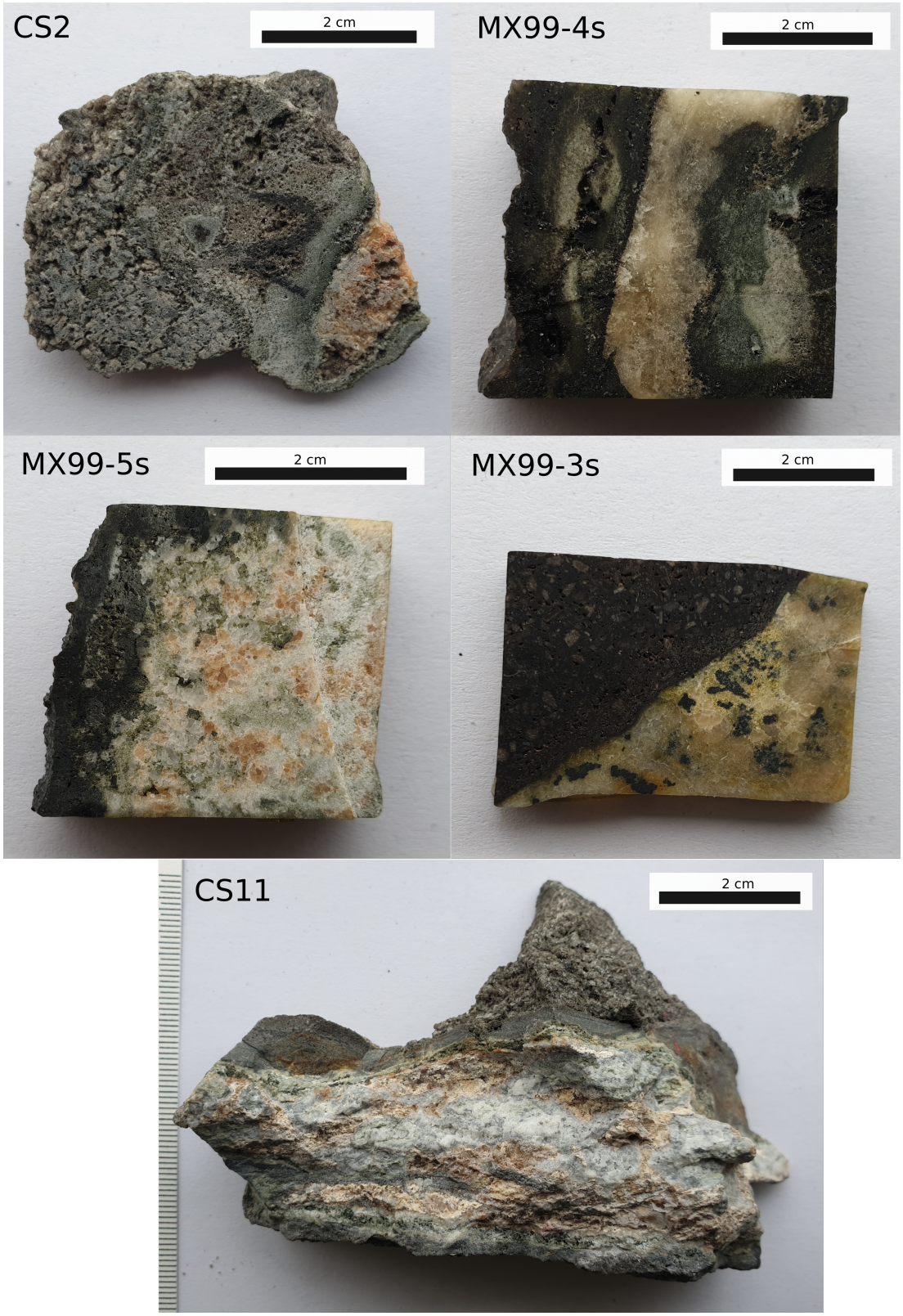


*Figure 3.1: Hand specimen photos of the Merapi xenoliths. CS2 (xenolith to bottom right) and MX99-4s (xenolith centered): magmatic skarn xenoliths. MX99-5s: exoskarn type A xenolith. Note the lack of layering at the lava (left) and xenolith (right) contact. MX99-3s: exoskarn type B xenolith. Note the lack of layering at the lava (top left) and xenolith (bottom right) contact. CS11: exoskarn xenolith. Small piece of host basaltic andesite in the top right.*

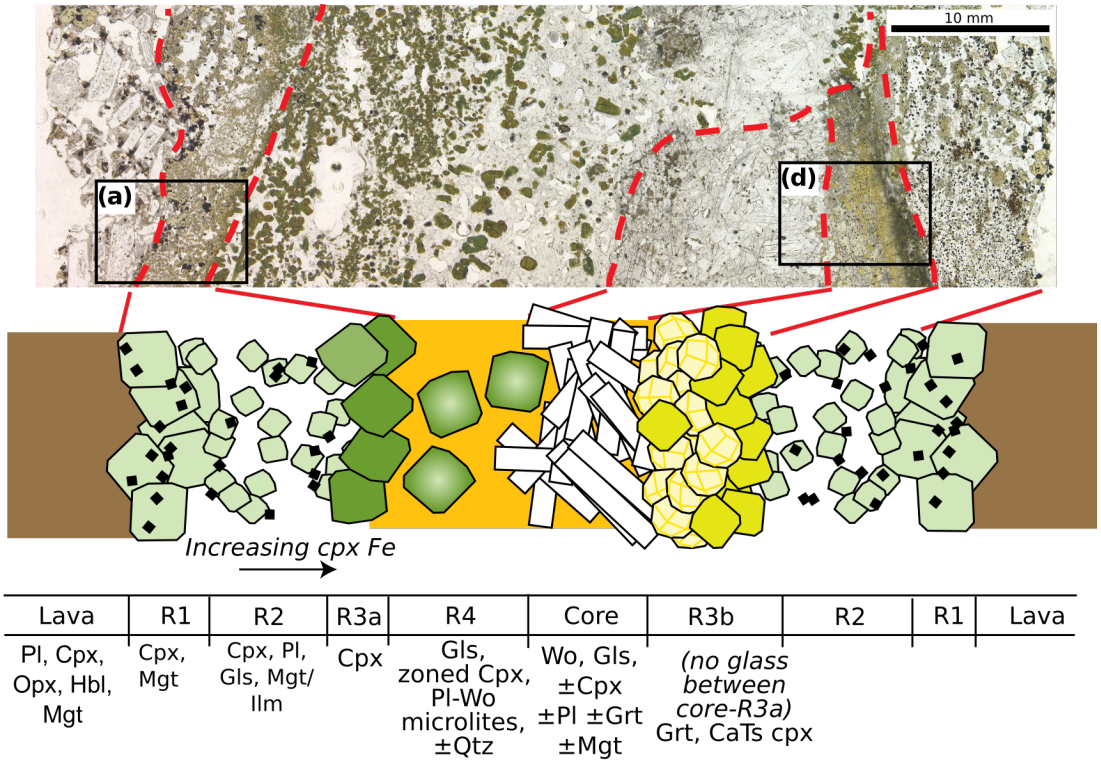


*Figure 3.2: Zoning in sample MX1 (thin section) and idealised diagram for zoning patterns in the magmatic skarn xenoliths. Highlighted zones (a) and (d) correspond to the respective panels in Figure 3.3. See Table 3.2 for all mineral abbreviations used. Gls: interstitial Ca-rich glass.*

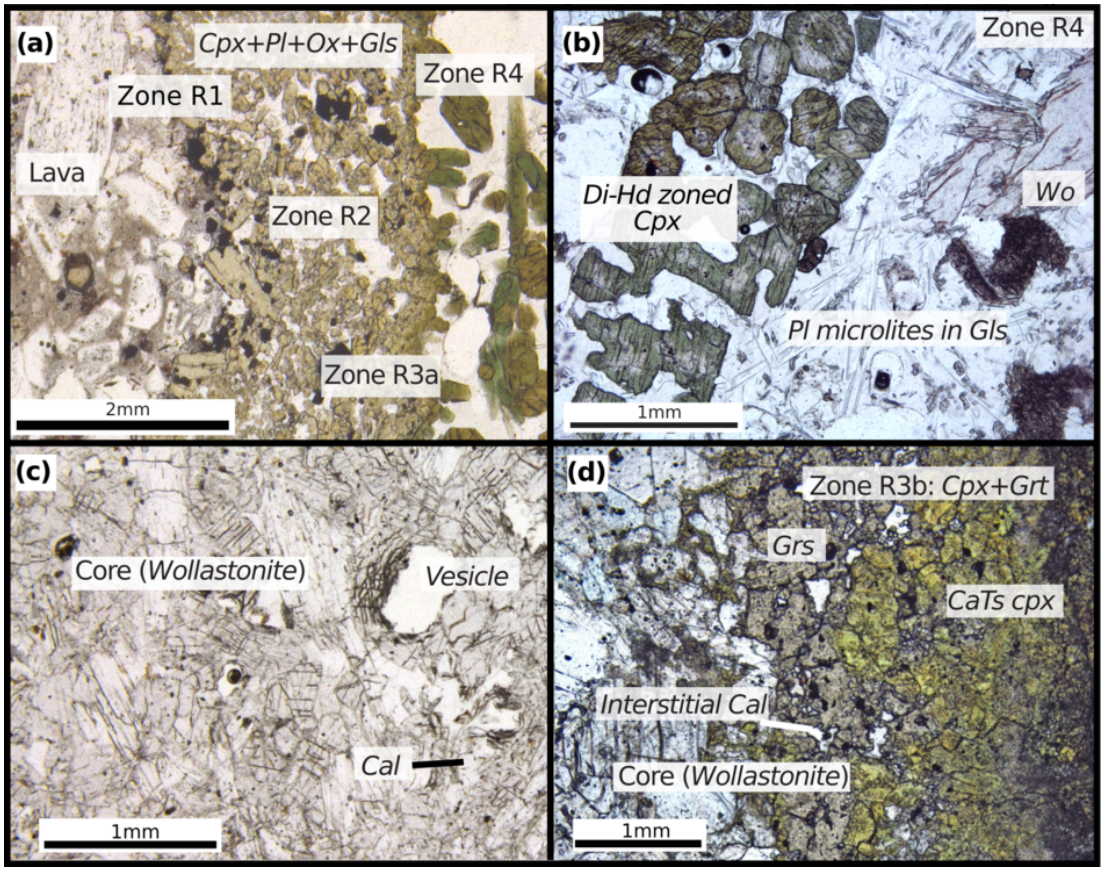


*Figure 3.3: Examples of the respective zones in magmatic skarn xenoliths. A) Host lava contact and zones R1 to R4. Note the progressive darkening of the clinopyroxene colour due to changing composition to iron enrichment. Sample MX1. B) Normally zoned diopside-hedenbergite clinopyroxene within glass dominant zone R4. Also present are plagioclase microlites and wollastonite. Sample CS2. C) Wollastonite-dominant xenolith core with vesicles and accessory calcite. Sample MX5. D) Zone R3b, showing garnet + CaTs clinopyroxene formation where there is no glass zone R4 between the core and zone R2. Sample MX1. See Table 3.2 for mineral abbreviations.*

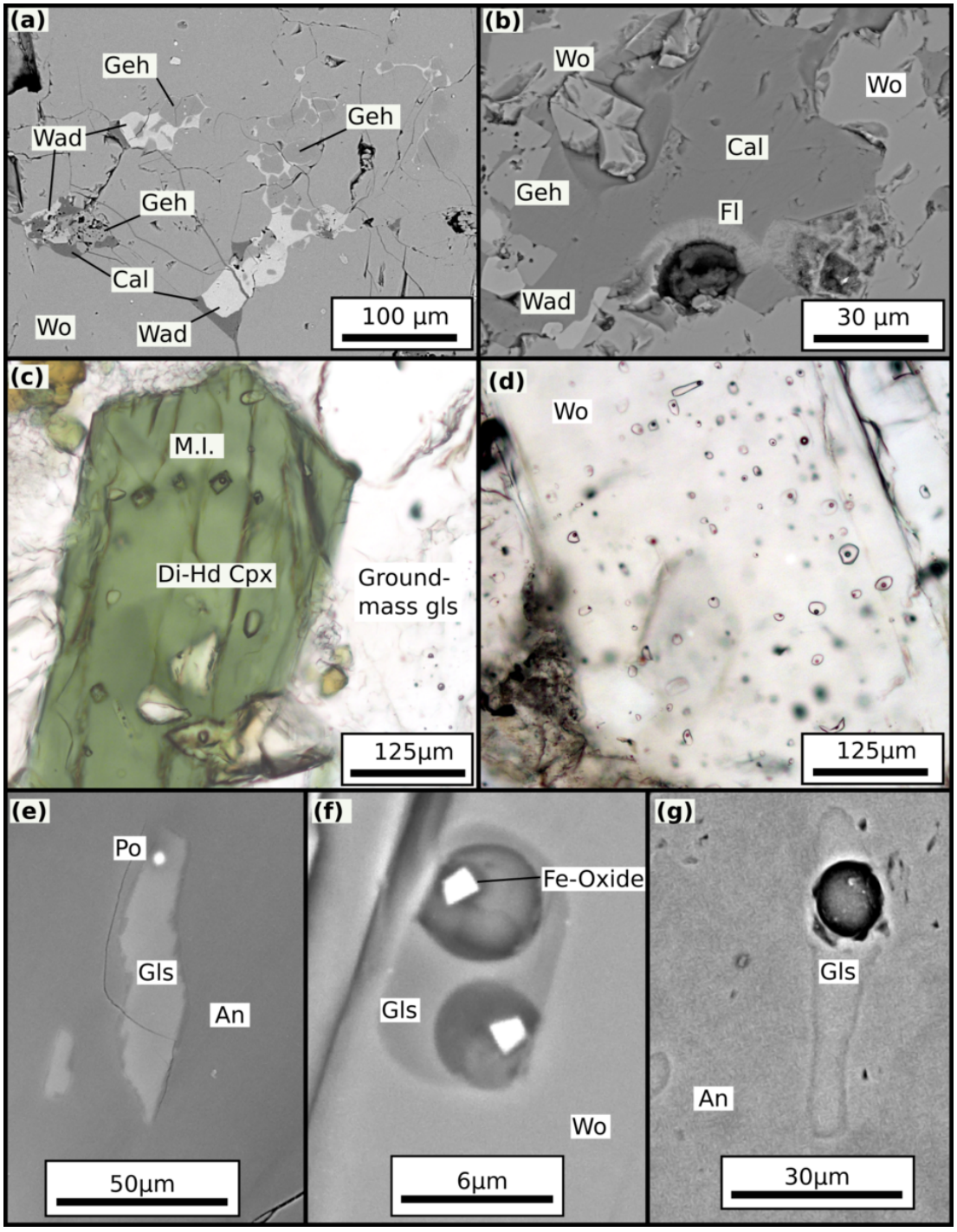


*Figure 3.4: Magmatic skarn accessory minerals and melt inclusions. All images are from sample MX1, apart from panels E and G, which are from sample CS16. A-B) Accessory gehlenite, fluorite, calcite and the wadalite-like mineral in the xenolith core. C-G) Examples of wollastonite, clinopyroxene and plagioclase-hosted melt inclusions, showing variable abundance and textural forms. Abbreviations as in Table 3.2*

### 3.4.2 Exoskarn Xenoliths

Exoskarn xenoliths are distinct from the magmatic skarn xenoliths by having a different mineralogy, lacking mineralogical zonation, and by almost entirely lacking glass. On the basis of their mineral assemblages resembling typical high temperature skarns worldwide (e.g. Meinert, 1992), and the lack of glass, which indicates formation by subsolidus reactions, we classify these xenoliths as exoskarns (c.f. Fulignati *et al.*, 2004, see also discussion). These xenoliths comprise two distinct skarn mineral assemblages (A and B), often with a rim of clinopyroxene and plagioclase at the host lava contact. The most common assemblage (A) is wollastonite + garnet + plagioclase ± CaTs clinopyroxene ± quartz ± calcite with a granoblastic texture (Figure 3.5A). Some clinopyroxenes and garnets exhibit weak patchy zonation. Accessory S, Cl, and F-bearing phases such as cuspidine, ellestadite, anhydrite and pyrrhotite are additionally present, and also unidentified Ca-Al-Si-Cl-F minerals that are distinct from the wadalite-like mineral in the magmatic skarn xenoliths. No hydrous phases that can often occur in skarns, such as epidote and vesuvianite (c.f. Meinert, 1992), have been identified in this study, although epidote and prehnite have been identified in earlier descriptions of Merapi xenoliths (Kerinec, 1982; Camus *et al.*, 2000). Garnet often contains inclusions of plagioclase and wollastonite. Calcite is present as either rare inclusions within garnet crystals or as large mm-sized crystals, surrounded by complex reaction rims that contain larnite, spurrite, and Ca-Si-rich S-Cl-F-bearing phases including fluorite, cuspidine, ellestadite, anhydrite, and many additional unidentified phases (Ca-Si-O, Ca-Al-Si-O, Ca-Al-Si-P-O Table 3.9, Figure 3.5B). Xenotime and monazite form accessory inclusions within these calcites.

The second assemblage (B), only found in one sample (MX99-3s), comprises gehlenite + grossular garnet + CaTs clinopyroxene + spinel + wollastonite + plagioclase, with trace amounts of ellestadite (Figure 3.5C). This sample shows evidence for disequilibrium, such as patchy compositional zoning of garnets, and spinel with rims of gehlenite followed by an outer rim of CaTs clinopyroxene. Patches of localised equilibrium are shown by granular ~120° triple junctions in the gehlenite-dominant areas of the sample.

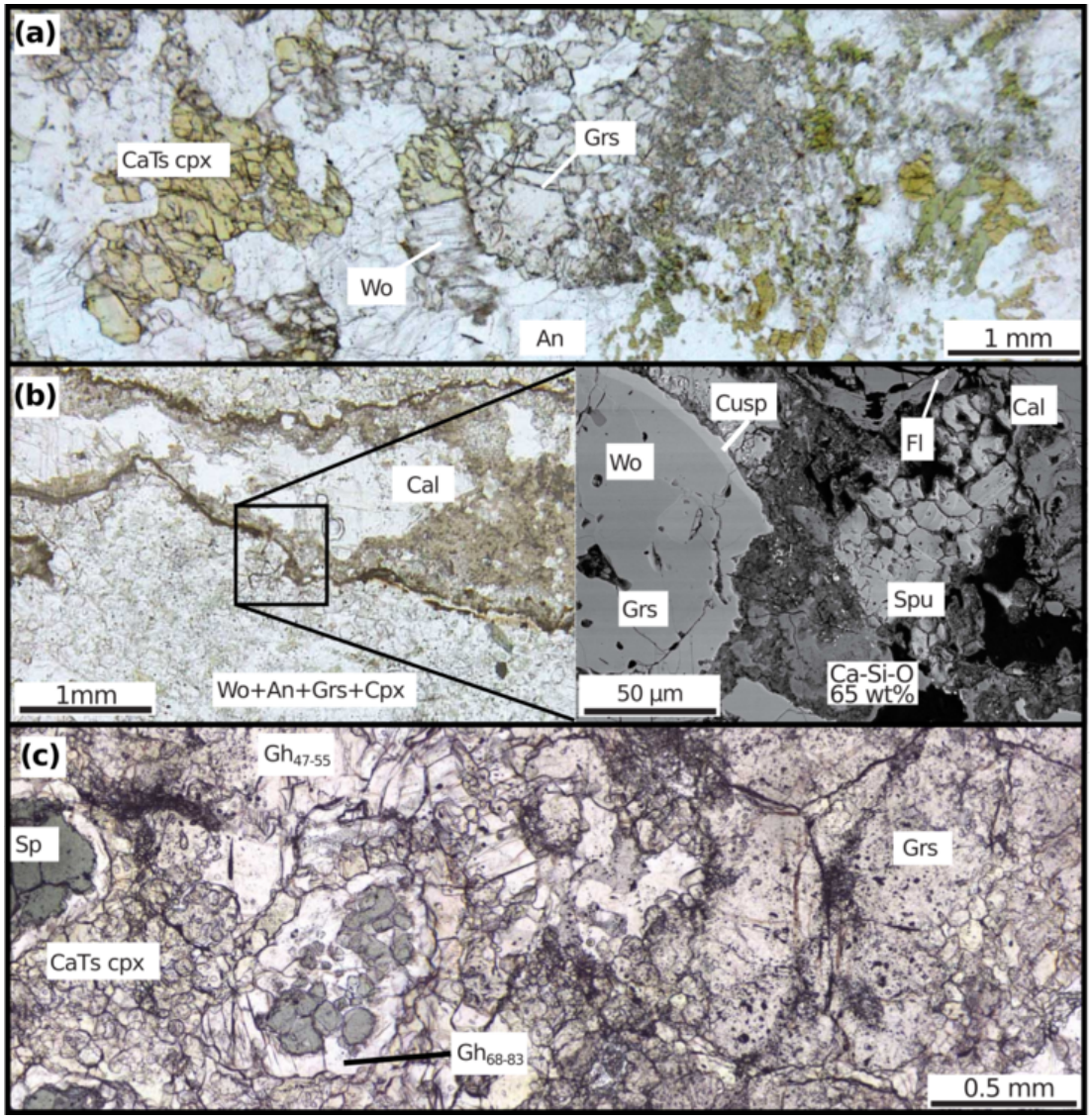


*Figure 3.5: Typical textures in exoskarn xenoliths. A) CaTs-cpx + Wo + An + Grs in exoskarn type A xenolith MX99-5s. B) Large residual calcite crystals in exoskarn type A xenolith CS11. Expanded image shows the complex decarbonation textures and reactions occurring influenced by a F-rich fluid. A Ca-Si-O phase is present with low analytical totals (~65 wt%). C) Exoskarn B xenolith MX99-3s shows a unique assemblage of spinel, gehlenite, CaTs-cpx, grossular, with accessory wollastonite and anorthite. Spinel is rimmed by gehlenite followed by CaTs-cpx. For mineral abbreviations, see Table 3.2.*

### 3.4.3 Buchite

These rare xenoliths (samples M13-04C, CS14, CS10) contain abundant (>70 vol%) quartz (or $SiO_2$ polymorphs) with interstitial glass around the crystal borders, and minor small interstitial clinopyroxene, plagioclase and wollastonite (Appendix Figure B.1). Patches of clinopyroxene-rich glass are present, similar to zone R4 of the magmatic skarn xenoliths. We have classified these samples as buchites (pyrometamorphic glass-rich rocks), following the classification by

Matthews *et al.* (1996) of texturally similar xenoliths at Lascar volcano, Chile. Similar quartz-rich, partially melted xenoliths have also been described at the Aeolian islands (e.g. Frezzotti *et al.*, 2004; Zanon and Nikogosian, 2004; Del Moro *et al.*, 2011), Etna (Mollo *et al.*, 2017) and the Central Apennines [Melluso2003]. Although the quartz-rich assemblage could be derived from a volcaniclastic protolith, the presence of wollastonite suggests a carbonate or marl component. The rounded shape of the quartz crystals, separated by interstitial glass, indicates that partial melting has occurred. The dissolution of quartz xenocrysts in arc magmas was observed in products of the 1991 Pinatubo eruption, where highly silicic glass (~80-85 wt.% $SiO_2$) formed in reaction zones around the xenocrysts, pointing to possible compositional modifications of the melt, at least on a micrometre scale (Borisova *et al.*, 2014). However, the buchite xenoliths have not been studied in detail and are briefly mentioned for completeness, and thus will not be discussed further.

## 3.5 Results

### 3.5.1 Whole-Rock Major Element Chemistry

Calculated major element compositions of individual zones in magmatic xenoliths are compared for two selected samples to evaluate chemical changes (Figure 3.6). There are distinct differences between the zones and some systematic variations from the lava contact towards the xenolith cores point to a progressive change from magmatic to calcic compositions (Figure 3.6A, Appendix Figures B.3, B.4) (c.f. Troll *et al.*, 2012). CaO contents are lowest in the lavas and highest in the xenolith cores, whereas $Al_2O_3$ contents show exactly the opposite behaviour. One xenolith (sample MX-1) shows a systematic increase in CaO from the contact towards the core, except for glass zone R4 that creates a distinct anomaly in the element profiles, having higher $SiO_2$ and lower CaO than the adjacent zones. FeO is relatively enriched in zone R1, decreasing towards the core, whereas $SiO_2$ is lowest in this zone. MgO shows only limited variation and has the lowest contents in the innermost zone (R4) and in the core.

In terms of whole rock major element composition (Figure 3.6B), magmatic skarn xenoliths fall within the range of xenoliths analysed by Chadwick *et al.* (2007) (which we believe classify as magmatic skarn xenoliths in our grouping), forming diverging trends from basaltic-andesite compositions. Magmatic skarn xenoliths have lower $Al_2O_3$ contents than lavas (<16 wt%), while exoskarn xenoliths display $Al_2O_3$ contents comparable to lava values (18 to 25 wt%), although at a much lower $SiO_2$ content (33 to 45 wt%). All xenoliths have much higher CaO

than the lavas, up to 36 wt%, but lower $TiO_2$ and $K_2O$ contents. FeO and MgO span the range of lava values, with FeO up to 10.0 wt%, and MgO up to 6.6 wt%. Exoskarn xenoliths generally plot distinct from magmatic skarn xenoliths when considered with the Chadwick *et al.* (2007) data (Figure 3.6B). For instance, the exoskarn xenoliths have low $SiO_2$, $TiO_2$ and FeO, relative to the magmatic skarn xenoliths, but form a linear trend of decreasing $TiO_2$ and FeO with increasing $SiO_2$.

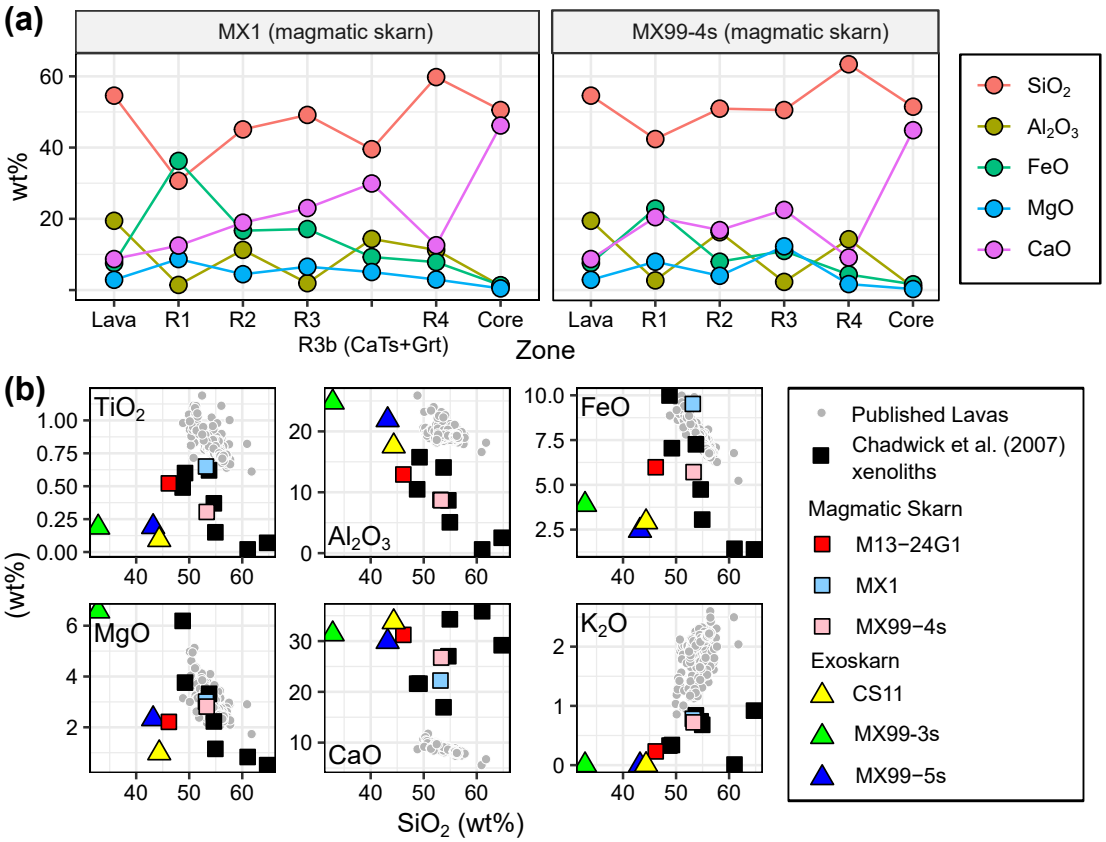


*Figure 3.6: Xenolith whole-rock geochemistry (calculated from mineral modes and mineral chemistry, corrected for mineral densities using data from Deer* et al. *(1997) and the Rock-Maker spreadsheet (Büttner, 2012)). A) Profiles through the distinct zones of two magmatic xenoliths. B) Calculated whole-rock compositions of bulk xenoliths compared to published lava and xenolith data. Published lava data from Gertisser (2001), Gertisser* et al. *(2012), Nadeau* et al. *(2013b), Borisova* et al. *(2013), Costa* et al. *(2013), Innocenti* et al. *(2013), Preece* et al. *(2014) and the GEOROC database (`http://georoc.mpch-mainz.gwdg.de/georoc/`). Published Merapi calc-silicate xenoliths from Chadwick* et al. *(2007)*

### 3.5.2 Mineral Chemistry

#### Feldspar

Feldspar compositions in the Merapi calc-silicate xenoliths are entirely plagioclase, but spanning a wide compositional range ($An_{46\text{-}100}$, Table 3.3). In magmatic skarn xenoliths, anorthite content

progressively increases towards the xenolith cores (Figure 3.7A). Zoning is relatively insignificant compared to the differences between zones. Magmatic skarn xenolith plagioclase comprises both microlites ($An_{46-59}$) within the interstitial glass in zone R4, and interstitial plagioclase in the high-An cores ($An_{73-100}$). Where analyses of the host lava attached to the xenolith were possible ($An_{29-81}$), plagioclase in zones R2 and R4 overlap magmatic plagioclase compositions, including the previously published data (Gertisser, 2001; Preece, 2014; Erdmann *et al.*, 2016). In An-FeO space, xenolith core plagioclase compositions generally fall within and extend the high FeO-An compositional ellipse of Merapi xenolith plagioclase from Chadwick *et al.* (2007) (Figure 3.7B). Plagioclase microlites within the zone R4 glass have strong FeO enrichment (up to 1.7 wt% FeO), as is observed with the strong FeO enrichment of both clinopyroxene and ferrobustamite overgrowths on wollastonite within this glass zone (see below). Exoskarn plagioclase is essentially pure anorthite, with lower anorthite contents restricted to the lava contact. FeO concentrations in exoskarn anorthite are characteristically lower than those of magmatic plagioclase and the majority of the magmatic skarn plagioclase data.

*Table 3.3: Average plagioclase compositions for the zones in the magmatic skarn xenoliths and the exoskarn xenoliths. All analyses normalised to 8 oxygens. Lava analyses are where the xenolith section had a small rind of lava still attached. Analyses are reported as the mean and one standard deviation. Plagioclase components: An = anorthite, Ab = albite, Or = orthoclase.*

| | Host Lava | $\sigma$ | R2 | $\sigma$ | R4 | $\sigma$ | Core | $\sigma$ | Exo A | $\sigma$ | Exo B | $\sigma$ |
|---|---|---|---|---|---|---|---|---|---|---|---|---|
| $n$ | 8 | | 49 | | 27 | | 76 | | 63 | | 7 | |
| $SiO_2$ | 53.61 | 4.03 | 48.91 | 4.42 | 52.91 | 4.28 | 45.21 | 2.80 | 44.43 | 3.50 | 42.51 | 0.51 |
| $TiO_2$ | 0.02 | 0.03 | 0.01 | 0.02 | 0.04 | 0.08 | 0.01 | 0.02 | 0.02 | 0.03 | | |
| $Al_2O_3$ | 28.10 | 2.94 | 31.73 | 3.31 | 28.68 | 3.00 | 33.98 | 2.03 | 34.90 | 2.48 | 36.55 | 0.37 |
| FeO | 0.72 | 0.34 | 0.58 | 0.16 | 0.94 | 0.33 | 0.65 | 0.22 | 0.33 | 0.33 | 0.24 | 0.02 |
| MgO | 0.06 | 0.07 | 0.02 | 0.02 | 0.02 | 0.03 | 0.01 | 0.02 | 0.02 | 0.02 | | |
| CaO | 11.12 | 3.28 | 15.05 | 3.72 | 12.25 | 2.99 | 17.82 | 2.18 | 19.09 | 2.63 | 20.17 | 0.26 |
| $Na_2O$ | 5.06 | 1.70 | 3.01 | 2.12 | 4.25 | 1.65 | 1.34 | 1.23 | 0.78 | 1.45 | 0.08 | 0.03 |
| $K_2O$ | 0.68 | 0.52 | 0.23 | 0.20 | 0.53 | 0.44 | 0.10 | 0.14 | 0.07 | 0.17 | 0.02 | 0.01 |
| Total | 99.47 | 0.64 | 99.56 | 0.87 | 99.76 | 1.20 | 99.12 | 1.09 | 99.75 | 1.01 | 99.56 | 1.06 |
| **Cations based on 8 oxygens** | | | | | | | | | | | | |
| Si | 2.449 | 0.166 | 2.252 | 0.188 | 2.416 | 0.168 | 2.108 | 0.113 | 2.063 | 0.138 | 1.983 | 0.009 |
| Ti | 0.001 | 0.001 | 0.000 | 0.001 | 0.001 | 0.002 | 0.000 | 0.001 | 0.001 | 0.001 | 0.000 | 0.000 |
| Al | 1.515 | 0.168 | 1.724 | 0.191 | 1.546 | 0.178 | 1.869 | 0.118 | 1.912 | 0.146 | 2.009 | 0.009 |
| Fe | 0.028 | 0.013 | 0.022 | 0.006 | 0.036 | 0.013 | 0.025 | 0.009 | 0.013 | 0.013 | 0.009 | 0.001 |
| Mg | 0.004 | 0.005 | 0.001 | 0.001 | 0.001 | 0.002 | 0.000 | 0.001 | 0.001 | 0.001 | 0.000 | 0.000 |
| Ca | 0.546 | 0.165 | 0.744 | 0.189 | 0.601 | 0.154 | 0.891 | 0.114 | 0.951 | 0.135 | 1.008 | 0.006 |
| Na | 0.448 | 0.147 | 0.267 | 0.188 | 0.375 | 0.143 | 0.120 | 0.109 | 0.069 | 0.126 | 0.007 | 0.003 |
| K | 0.039 | 0.030 | 0.013 | 0.012 | 0.030 | 0.025 | 0.006 | 0.008 | 0.004 | 0.010 | 0.001 | 0.000 |
| **Endmembers (mol%)** | | | | | | | | | | | | |
| An | 52.9 | 16.2 | 72.8 | 19.1 | 59.8 | 15.5 | 87.6 | 11.1 | 92.9 | 13.1 | 99.2 | 0.3 |
| Ab | 43.3 | 14.0 | 25.9 | 18.1 | 37.2 | 14.1 | 11.8 | 10.7 | 6.7 | 12.2 | 0.7 | 0.3 |
| Or | 3.8 | 2.9 | 1.3 | 1.1 | 3.1 | 2.7 | 0.6 | 0.8 | 0.4 | 0.9 | 0.1 | 0.0 |

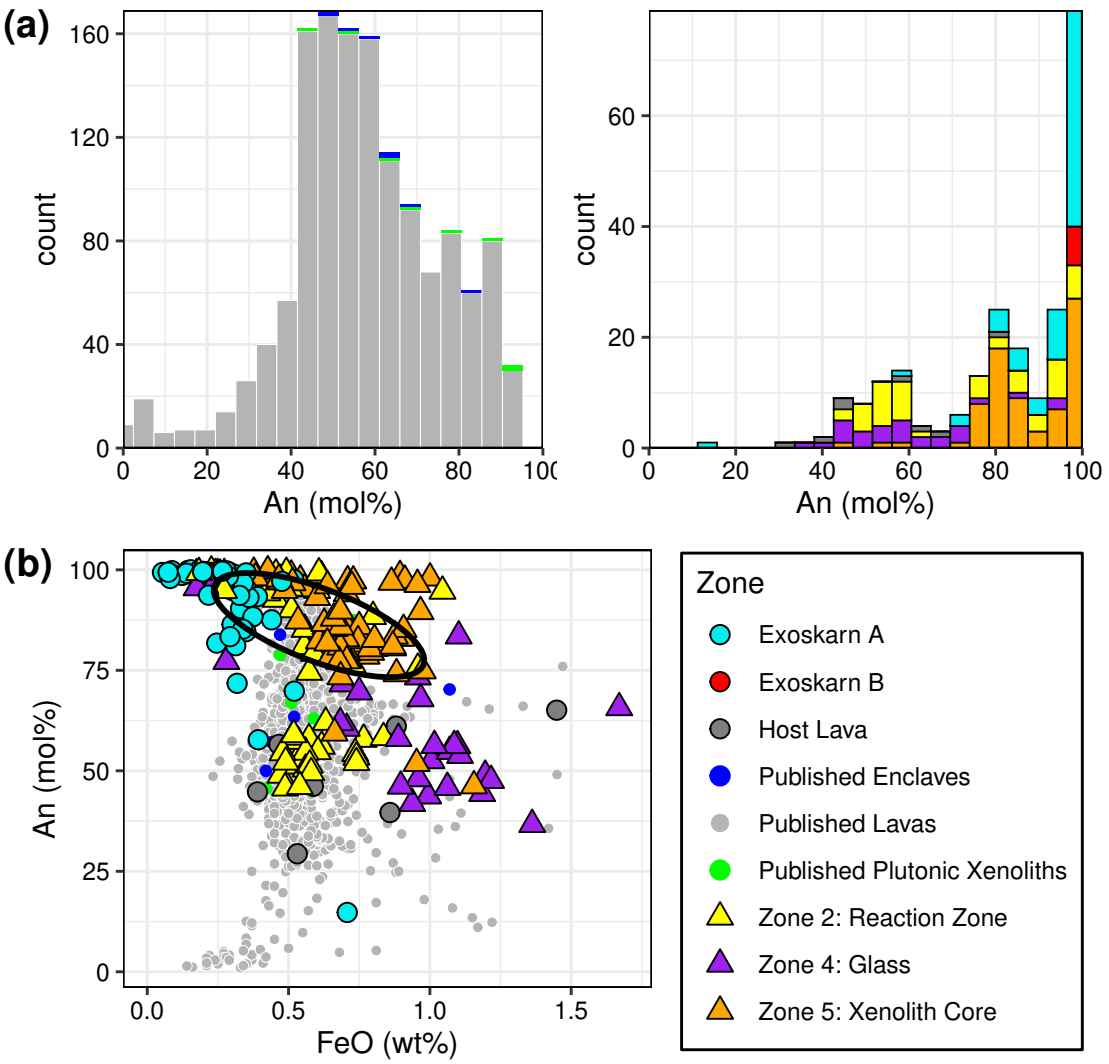


*Figure 3.7: Merapi xenolith and magmatic feldspar compositions. A) Anorthite content histograms showing (left) published data from Merapi lavas (grey), enclaves (dark blue) and plutonic xenoliths (green) for comparison with xenolith and host lava feldspar data (right, key below). B) An vs FeO plot showing the different xenolith plagioclase compositions compared to Merapi lava plagioclase. Ellipse of xenolith and xenocryst plagioclase compositions from Chadwick* et al. *(2007). Notably, plagioclase from zones R1 and R2 overlaps with the lava compositions, although they are formed from magma-carbonate interaction. Published lava feldspar data from Gertisser (2001), Preece (2014) and Erdmann* et al. *(2016). Enclave and plutonic xenolith data from Chadwick* et al. *(2013).*

**Clinopyroxene**

Clinopyroxene compositions range from quadrilateral diopside-hedenbergite (Di-Hd) (Morimoto, 1988) to high-Al diopside. These high Al clinopyroxenes are enriched both in esseneite ($CaFe^{3+}AlSiO_6$) and Calcium-Tschermak's (CaTs: $CaAlAlSiO_6$) components (Table 3.4), demonstrated by the strong correlation between $Fe^{3+}$ and $Al^{IV}$ ($R^2$=0.88, Figure 3.8A), and $Al^{IV}$ with $Al^{VI}$ ($R^2$=0.81, not shown) across all analysed crystals. Incorporation of $Al^{IV}$ is accommodated by a strong reduction of Si in the tetrahedral site. These clinopyroxenes are commonly generalised as fassaite [$Ca(Mg,Fe^{3+},Al)(Si,Al)_2O_6$] where $Al^{IV} > 0.25$; Deer *et al.* (1997)]. As this is not a formal name (Morimoto, 1988) and the clinopyroxenes show an enrichment in the CaTs component, we refer to these clinopyroxenes as CaTs-clinopyroxene in this manuscript.

In magmatic skarn xenoliths, the clinopyroxene compositions are generally comparable to Merapi magmatic clinopyroxenes in zone R1 (Figure 3.8A-C), and progressively become more Ca/wollastonite-rich until sitting along the diopside-hedenbergite (Di-Hd) join ($Wo_{50}$) in zones R3, R4 and in the core (Figure 3.8C). There is a sharp compositional change at zone R4 and within the core, where the clinopyroxenes closely follow the Di-Hd join and progressively become more Hd-rich (Figure 3.8C). Xenolith core clinopyroxenes can also be enriched in $Al_2O_3$ (up to 11.57 wt%, corresponding to 18 mol% CaTs), bringing compositions above the DiHd join in the traditional clinopyroxene composition ternary diagrams, although this is uncommon and only observed in sample CS16. These Al-rich clinopyroxenes are strongly zoned, from this Al-rich core to weakly oscillatory Di-Hd zoned mantle and rim zones (Figure 3.8E). Commonly however, magmatic skarn xenolith clinopyroxene zonation is restricted to the Di-Hd join (Figure 3.8C), with patchy, highly irregular resorption surfaces (Figure 3.8F). Titanium is correlated well with $Al^{IV}$ across the magmatic skarn xenolith zones, excluding zone 3b, where CaTs-rich clinopyroxenes form with low Ti, comparable to the compositionally distinct exoskarn xenolith clinopyroxene (Figure 3.8B).

Exoskarn clinopyroxenes are highly Al enriched (Figure 3.8A, B, D), containing up to 22.3 wt% $Al_2O_3$, approaching the highest natural terrestrial values known to the authors (24.0 wt% in gehlenite-rich skarns from the Carpathians, Romania; Pascal *et al.*, 2005). $Fe^{3+}/\sum Fe$ (calculated following Droop, 1987) approaches unity (Figure 3.8A). Clinopyroxene compositions at the exoskarn xenolith rim overlap magmatic compositions, but then immediately jump to highly Al-rich compositions, usually lacking the gradual progression observed in the magmatic skarn xenoliths (Figure 3.8A-C).

*Table 3.4: Average clinopyroxene compositions for each zone in the magmatic skarn xenoliths and exoskarns. Average compositions across all samples for wollastonite and ferrobustamite are additionally shown, as there is very little compositional variability for the pyroxenoids. $Fe^{3+}$ calculated using Droop (1987). Analyses are reported as the mean and one standard deviation. Clinopyroxene components: Wo = wollastonite, En = enstatite, Fs = ferrosilite*

| | Clinopyroxene | | | | | | | | | | | | | | | | | Bustamite | | Wollastonite | |
|---|---|---|---|---|---|---|---|---|---|---|---|---|---|---|---|---|---|---|---|---|---|
| | Host Lava | $\sigma$ | R1 | $\sigma$ | R2 | $\sigma$ | R3 | $\sigma$ | R3b | $\sigma$ | R4 | $\sigma$ | Core | $\sigma$ | Exo A | $\sigma$ | Exo B | $\sigma$ | All | $\sigma$ | All | $\sigma$ |
| $n$ | 7 | | 19 | | 43 | | 44 | | 18 | | 71 | | 112 | | 40 | | 18 | | 16 | | 94 | |
| $SiO_2$ | 51.13 | 0.72 | 50.11 | 1.54 | 50.37 | 0.94 | 49.89 | 1.41 | 40.89 | 0.46 | 49.83 | 1.70 | 46.26 | 1.94 | 43.24 | 2.67 | 40.52 | 1.87 | 49.81 | 0.52 | 50.70 | 0.69 |
| $TiO_2$ | 0.50 | 0.11 | 0.49 | 0.10 | 0.45 | 0.16 | 0.42 | 0.10 | 0.57 | 0.10 | 0.37 | 0.23 | 0.67 | 0.27 | 0.53 | 0.36 | 0.36 | 0.27 | 0.06 | 0.04 | 0.04 | 0.05 |
| $Al_2O_3$ | 2.63 | 0.43 | 2.71 | 1.56 | 2.09 | 0.64 | 2.37 | 0.59 | 14.64 | 0.40 | 2.08 | 0.96 | 5.76 | 2.89 | 13.93 | 5.95 | 18.19 | 1.97 | 0.02 | 0.02 | 0.07 | 0.08 |
| $Cr_2O_3$ | 0.00 | 0.01 | 0.02 | 0.02 | 0.02 | 0.02 | 0.02 | 0.02 | 0.01 | 0.01 | 0.01 | 0.02 | 0.02 | 0.02 | 0.01 | 0.01 | 0.02 | 0.02 | 0.01 | 0.01 | 0.01 | 0.01 |
| FeO | 8.85 | 0.12 | 12.38 | 5.99 | 10.62 | 1.85 | 12.58 | 2.84 | 8.58 | 0.47 | 13.46 | 4.14 | 11.26 | 3.03 | 7.96 | 6.72 | 5.65 | 1.15 | 10.81 | 0.97 | 1.31 | 0.80 |
| MnO | 0.56 | 0.11 | 0.57 | 0.19 | 0.55 | 0.11 | 0.48 | 0.10 | 0.32 | 0.02 | 0.50 | 0.16 | 0.21 | 0.10 | 0.24 | 0.32 | 0.08 | 0.03 | 1.13 | 0.19 | 0.37 | 0.16 |
| MgO | 14.43 | 0.43 | 11.38 | 4.68 | 11.74 | 1.77 | 10.82 | 2.83 | 9.07 | 0.52 | 9.45 | 2.73 | 9.66 | 1.41 | 8.59 | 2.25 | 9.57 | 1.12 | 0.70 | 0.22 | 0.22 | 0.08 |
| CaO | 21.20 | 0.66 | 22.06 | 1.27 | 22.62 | 0.68 | 22.72 | 1.12 | 25.18 | 0.17 | 23.90 | 0.77 | 23.76 | 0.70 | 25.04 | 0.84 | 25.88 | 0.47 | 38.08 | 1.48 | 47.09 | 0.92 |
| $Na_2O$ | 0.43 | 0.04 | 0.34 | 0.12 | 0.41 | 0.08 | 0.38 | 0.07 | 0.02 | 0.02 | 0.29 | 0.14 | 0.33 | 0.15 | 0.07 | 0.07 | 0.04 | 0.02 | 0.04 | 0.03 | 0.02 | 0.02 |
| Total | 99.75 | 0.50 | 100.08 | 0.81 | 98.87 | 0.71 | 99.67 | 0.82 | 99.28 | 0.64 | 99.93 | 0.60 | 97.92 | 0.70 | 99.62 | 1.24 | 100.31 | 0.81 | 100.80 | 1.40 | 99.93 | 0.88 |
| **Cations based on 6 oxygens, 4 cations** | | | | | | | | | | | | | | | | | | | | | | |
| Si | 1.901 | 0.021 | 1.895 | 0.059 | 1.918 | 0.028 | 1.898 | 0.024 | 1.535 | 0.013 | 1.906 | 0.040 | 1.786 | 0.086 | 1.624 | 0.136 | 1.485 | 0.065 | 1.956 | 0.038 | 1.967 | 0.025 |
| Ti | 0.014 | 0.003 | 0.014 | 0.003 | 0.013 | 0.005 | 0.012 | 0.003 | 0.016 | 0.003 | 0.011 | 0.006 | 0.019 | 0.008 | 0.015 | 0.011 | 0.010 | 0.008 | 0.002 | 0.001 | 0.001 | 0.001 |
| $Al^{IV}$ | 0.099 | 0.021 | 0.105 | 0.059 | 0.082 | 0.028 | 0.102 | 0.024 | 0.465 | 0.013 | 0.094 | 0.040 | 0.214 | 0.086 | 0.376 | 0.136 | 0.515 | 0.065 | 0.044 | 0.038 | 0.033 | 0.025 |
| $Al^{VI}$ | 0.018 | 0.013 | 0.018 | 0.021 | 0.013 | 0.009 | 0.006 | 0.008 | 0.183 | 0.013 | 0.007 | 0.018 | 0.047 | 0.047 | 0.238 | 0.117 | 0.271 | 0.036 | 0.000 | 0.000 | 0.000 | 0.000 |
| Cr | 0.000 | 0.000 | 0.000 | 0.001 | 0.001 | 0.001 | 0.000 | 0.001 | 0.000 | 0.000 | 0.000 | 0.001 | 0.000 | 0.001 | 0.000 | 0.000 | 0.000 | 0.001 | 0.000 | 0.000 | 0.000 | 0.000 |
| $Fe^{2+}$ | 0.190 | 0.032 | 0.309 | 0.241 | 0.264 | 0.071 | 0.300 | 0.087 | 0.019 | 0.022 | 0.339 | 0.122 | 0.212 | 0.106 | 0.138 | 0.230 | 0.000 | 0.002 | 0.269 | 0.076 | 0.010 | 0.018 |
| $Fe^{3+}$ | 0.086 | 0.033 | 0.088 | 0.060 | 0.075 | 0.031 | 0.102 | 0.024 | 0.251 | 0.014 | 0.094 | 0.041 | 0.153 | 0.038 | 0.117 | 0.051 | 0.173 | 0.037 | 0.086 | 0.075 | 0.033 | 0.023 |
| Mn | 0.017 | 0.004 | 0.018 | 0.007 | 0.018 | 0.004 | 0.015 | 0.003 | 0.010 | 0.001 | 0.016 | 0.005 | 0.007 | 0.003 | 0.008 | 0.011 | 0.002 | 0.001 | 0.038 | 0.006 | 0.012 | 0.005 |
| Mg | 0.800 | 0.021 | 0.635 | 0.255 | 0.665 | 0.092 | 0.611 | 0.148 | 0.507 | 0.027 | 0.536 | 0.143 | 0.555 | 0.072 | 0.478 | 0.118 | 0.523 | 0.058 | 0.041 | 0.013 | 0.013 | 0.005 |
| Ca | 0.844 | 0.028 | 0.895 | 0.064 | 0.923 | 0.037 | 0.927 | 0.060 | 1.013 | 0.006 | 0.980 | 0.022 | 0.982 | 0.014 | 1.006 | 0.016 | 1.017 | 0.008 | 1.601 | 0.043 | 1.957 | 0.033 |
| Na | 0.031 | 0.003 | 0.024 | 0.009 | 0.030 | 0.006 | 0.028 | 0.005 | 0.002 | 0.001 | 0.022 | 0.010 | 0.025 | 0.012 | 0.005 | 0.005 | 0.003 | 0.001 | 0.003 | 0.002 | 0.002 | 0.001 |
| **Endmembers (mol%)** | | | | | | | | | | | | | | | | | | | | | | |
| Mg# | 74.4 | 0.6 | 60.6 | 22.7 | 66.1 | 7.3 | 59.8 | 11.3 | 65.3 | 2.5 | 55.3 | 14.2 | 60.7 | 9.9 | 68.3 | 21.5 | 75.0 | 5.8 | 10.4 | 3.0 | 27.5 | 14.1 |
| Wo | 43.6 | 1.2 | 46.0 | 3.3 | 47.5 | 1.9 | 47.4 | 3.0 | 56.3 | 0.6 | 49.8 | 0.8 | 51.5 | 1.7 | 57.9 | 3.9 | 59.3 | 1.3 | 78.7 | 1.5 | 96.7 | 1.5 |
| En | 41.3 | 1.1 | 32.7 | 13.1 | 34.2 | 4.7 | 31.3 | 7.6 | 28.2 | 1.4 | 27.3 | 7.1 | 29.1 | 4.1 | 27.8 | 7.8 | 30.4 | 2.9 | 2.0 | 0.6 | 0.6 | 0.2 |
| Fs | 15.1 | 0.3 | 21.3 | 10.8 | 18.3 | 3.2 | 21.3 | 4.8 | 15.5 | 0.9 | 22.9 | 7.1 | 19.4 | 5.3 | 14.3 | 11.4 | 10.3 | 2.3 | 19.3 | 1.5 | 2.7 | 1.4 |

### Pyroxenoids

Wollastonite, present in all xenoliths, ranges from essentially pure $CaSiO_3$ to 5 mol% $FeSiO_3$ with $<$ 1.5 mol% $MnSiO_3$ (Figure 3.9A). Wollastonite compositions from 17 to 21 mol% $FeSiO_3$ are attributed to the ferrobustamite member of the wollastonite group rather than iron-rich wollastonite, as bustamite is the stable crystal structure above ~12 mol% FeSiO3 (Rutstein, 1971; Rutstein and White, 1971). The ferrobustamite crystals are found as overgrowth crystals on wollastonite in the glass-bearing magmatic skarn xenoliths, in rare inclusions in wollastonite in magmatic skarn xenoliths, and in accessory phases in the calcite reaction rims in large calcite-bearing exoskarn xenoliths.

### Garnet

Garnet is found predominantly in the exoskarn xenoliths as a main rock forming mineral, with magmatic skarn xenolith garnet restricted to small interstitial patches in the cores or in zone R3b (Figures 3.2,3.3B). Garnet compositions across all xenolith types closely follow the grossular-andradite join, with only schorlomite ($Ca_3Ti_2SiFe^{3+}{}_2O_{12}$) being a notable additional component (Figure 3.9B), increasing with andradite content ($Sch_{0\text{-}76}$). Pyrope and almandine end members combined are $<$ 6 mol%.

Magmatic skarn xenolith garnets exhibit a wide compositional range ($Grs_{0\text{-}66}Adr_{24\text{-}75}Sch_{0\text{-}76}$). In zone R3b, these garnets are compositionally distinct ($Grs_{60\text{-}66}Adr_{31\text{-}37}Sch_{1\text{-}2}$) from interstitial garnets within the wollastonite core ($Grs_{0\text{-}66}Adr_{24\text{-}75}Sch_{1\text{-}76}$). The interstitial garnets, in close spatial association with calcite, cuspidine, gehlenite and a wadalite-like phase (see below), have inclusions of this wadalite-like phase, possibly a result of similarities between the crystal structure between hydrogarnet and wadalite-mayenite (e.g. Glasser, 1995; Grew *et al.*,

*Figure 3.8 (following page): Clinopyroxene compositions. A) $Fe^{3+}/Fe_{total}$ versus $Al^{IV}$ plot showing a good correlation ($R^2$=0.88). The fassaitic boundary ($Al^{IV} > 0.25$) is from Deer* et al. *(1997). B) Ti versus $Al^{IV}$ plot. Exoskarn clinopyroxene plot distinct from magmatic skarn clinopyroxenes. Zone 3b plots with the exoskarn data, showing a metamorphic character to this zone. C) Ternary Wo-En-Fs components for magmatic skarn clinopyroxene. Two partial ternary diagrams shown for clarity, with ternary location shown on inset figure. Clinopyroxenes in zones 1 to 3 progressively become more Wo-rich, diverging from magmatic compositions. The remaining zones follow the Di-Hd join or plot above due to the large amount of Al. D) Partial ternary Wo-En-Fs components for exoskarn clinopyroxenes. E) Al and Mg# traverse along a magmatic skarn clinopyroxene (sample CS16). Al and Mg-rich cores progressively grade to low Al-high Fe compositions. F) Al and Mg# traverse in magmatic skarn clinopyroxene from sample CS2. These crystals do not have an Al-rich core, and compositions instead follow the Di-Hd join. Published data sources as in Figure 3.7 and additionally Deegan* et al. *(2016b).*

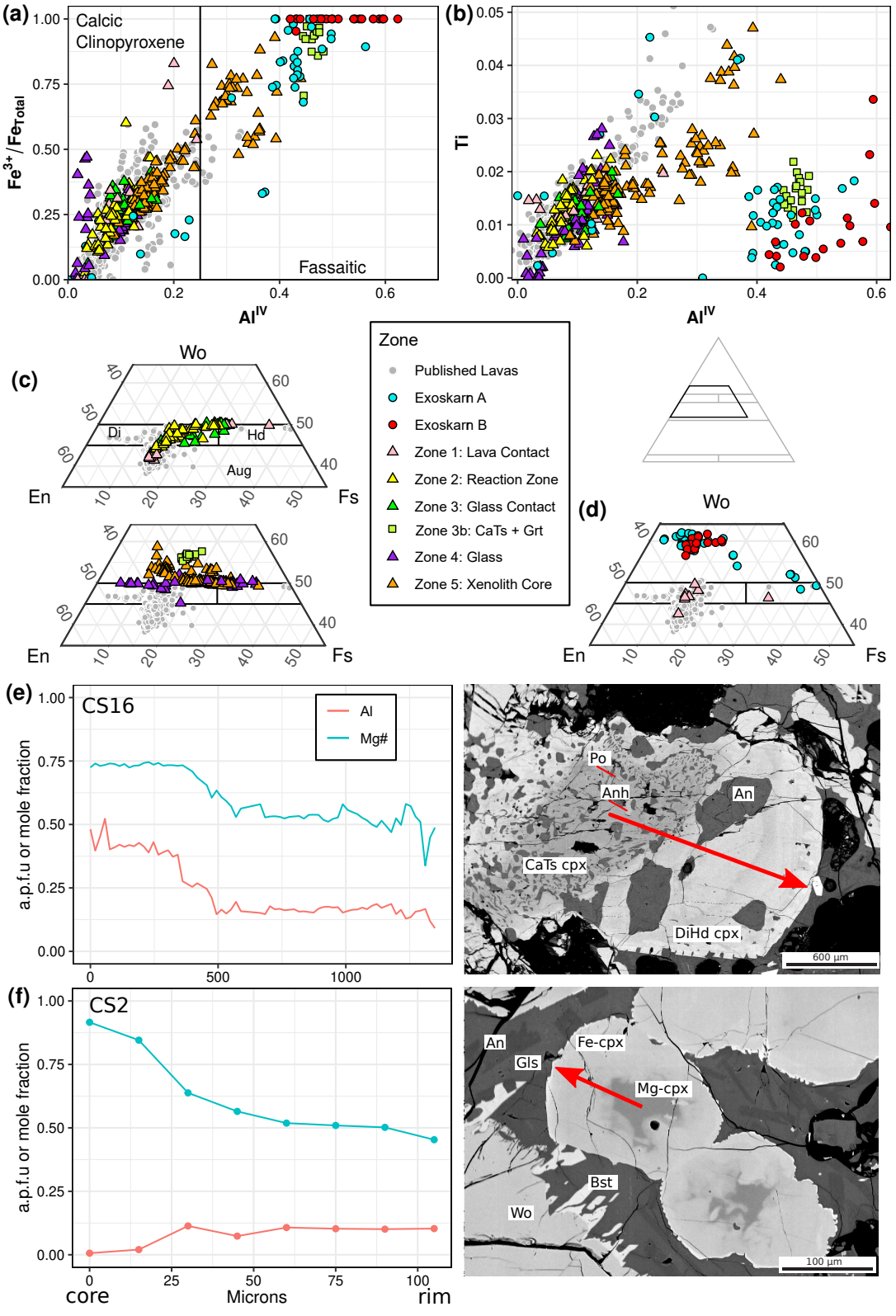
(a)
Calcic Clinopyroxene
Fassaitic
$Fe^{3+}/Fe_{Total}$
$Al^{IV}$
(b)
Ti
$Al^{IV}$
(c)
Wo
En
Fs
Di
Hd
Aug
Zone
Published Lavas
Exoskarn A
Exoskarn B
Zone 1: Lava Contact
Zone 2: Reaction Zone
Zone 3: Glass Contact
Zone 3b: CaTs + Grt
Zone 4: Glass
Zone 5: Xenolith Core
(d)
Wo
En
Fs
(e)
CS16
Al
Mg#
a.p.f.u or mole fraction
Po
Anh
An
CaTs cpx
DiHd cpx
600 µm
(f)
CS2
a.p.f.u or mole fraction
core
Microns
rim
An
Gls
Fe-cpx
Mg-cpx
Bst
Wo
100 µm

2013). Garnets with 76 mol% schorlomite [$Ca_{3.0}(Ti_{1.5}Fe^{2+}{}_{0.1}Fe^{3+}{}_{0.2}Mg_{0.1})(Si_{1.8}Al_{0.6}Fe^{3+}{}_{0.6})O_{12}$] are found as rims around titanite, in close association with perovskite. Ti gradients are found across rare wadalite-like phase-bearing garnet crystals ($Sch_{3\text{-}21}$).

Exoskarn xenolith garnets have a more restricted compositional range, limited to higher grossular contents ($Grs_{73\text{-}97}Adr_{3\text{-}24}Sch_{0\text{-}2}$, Table 3.5). The highest grossular contents, up to $Grs_{97}$ are found exclusively within exoskarn A type xenoliths, around residual calcite crystals and their spurrite ± larnite-rich reaction rims. One garnet analysis from this reaction rim matches hydrogarnet/katoite (42.8% Katoite) when assuming 10.5 wt% water to bring the analytical total to 100 wt% ($Ca_{2.9}Al_{2.0}Fe_{0.2}Si_{1.6}O_{6.7}OH_{4.6}$).

*Table 3.5: Average garnet compositions for the zones in the magmatic skarn xenoliths and the exoskarn xenoliths. Abbreviations as in Table 3.2. Additional garnet abbreviations: Prp - pyrope, Alm - almandine, Sp - spessartite, Uv - uvarovite. See Methods section for end-member calculation details. $Fe^{3+}$ calculated using Arai (2010). Analyses are reported as the mean and one standard deviation.*

| | R3b | $\sigma$ | Core | $\sigma$ | Exo A | $\sigma$ | Exo B | $\sigma$ |
|---|---|---|---|---|---|---|---|---|
| *n* | 10 | | 65 | | 47 | | 10 | |
| $SiO_2$ | 38.27 | 0.23 | 35.01 | 2.93 | 39.27 | 0.55 | 38.94 | 0.30 |
| $TiO_2$ | 0.76 | 0.24 | 3.45 | 3.73 | 0.23 | 0.20 | 0.29 | 0.19 |
| $Al_2O_3$ | 14.24 | 0.50 | 9.64 | 3.16 | 20.37 | 1.68 | 18.88 | 1.02 |
| $Cr_2O_3$ | | | 0.02 | 0.03 | 0.01 | 0.02 | 0.01 | 0.02 |
| FeO | 10.14 | 0.49 | 15.25 | 3.60 | 3.26 | 1.88 | 4.66 | 1.11 |
| MnO | 0.47 | 0.05 | 0.26 | 0.09 | 0.72 | 0.68 | 0.15 | 0.03 |
| MgO | 0.57 | 0.04 | 0.49 | 0.19 | 0.42 | 0.17 | 0.74 | 0.10 |
| CaO | 35.13 | 0.26 | 33.75 | 0.78 | 35.86 | 0.78 | 36.68 | 0.54 |
| Total | 99.59 | 0.29 | 97.86 | 0.98 | 100.23 | 0.92 | 100.35 | 0.65 |
| **Cations based on 12 oxygens, 8 cations** | | | | | | | | |
| Si | 2.972 | 0.013 | 2.831 | 0.196 | 2.966 | 0.026 | 2.944 | 0.032 |
| Ti | 0.044 | 0.014 | 0.214 | 0.243 | 0.013 | 0.012 | 0.016 | 0.011 |
| Al | 1.304 | 0.043 | 0.913 | 0.281 | 1.813 | 0.139 | 1.681 | 0.077 |
| Cr | 0.000 | 0.000 | 0.001 | 0.002 | 0.000 | 0.001 | 0.001 | 0.001 |
| $Fe^{2+}$ | 0.007 | 0.017 | 0.042 | 0.042 | 0.013 | 0.024 | 0.000 | 0.000 |
| $Fe^{3+}$ | 0.652 | 0.038 | 0.995 | 0.247 | 0.194 | 0.120 | 0.295 | 0.073 |
| Mn | 0.031 | 0.003 | 0.018 | 0.007 | 0.046 | 0.043 | 0.010 | 0.002 |
| Mg | 0.066 | 0.004 | 0.059 | 0.023 | 0.047 | 0.019 | 0.083 | 0.011 |
| Ca | 2.923 | 0.023 | 2.926 | 0.039 | 2.902 | 0.064 | 2.970 | 0.024 |
| **Endmembers (mol%)** | | | | | | | | |
| Grs | 64.3 | 1.7 | 37.5 | 17.2 | 87.7 | 6.6 | 83.9 | 4.0 |
| Adr | 33.5 | 1.9 | 52.0 | 14.4 | 9.6 | 6.4 | 15.1 | 3.7 |
| Sch | 1.4 | 0.6 | 9.3 | 12.7 | 0.4 | 0.4 | 0.7 | 0.4 |
| Alm | 0.0 | 0.2 | 0.2 | 0.5 | 0.4 | 0.7 | 0.0 | 0.0 |
| Prp | 0.7 | 0.8 | 0.8 | 0.9 | 0.7 | 0.8 | 0.3 | 0.6 |
| Sp | 0.1 | 0.4 | 0.1 | 0.3 | 1.2 | 1.7 | 0.0 | 0.0 |
| Uv | 0.0 | 0.0 | 0.0 | 0.1 | 0.0 | 0.0 | 0.0 | 0.0 |

### Melilite

Melilite is only found in non-trace quantities in exoskarn assemblage B xenoliths. Melilite compositions are gehlenite-rich, closely following the gehlenite-åkermanite join, with $< 8$ mol% Na-melilite and $< 10$ mol% Fe-åkermanite ($Gh_{43\text{-}91}Ak_{2\text{-}45}Na\text{-}Mel_{0\text{-}8}$) (Figure 3.9C, Table 3.6). In exoskarn type B xenoliths, melilite has three textural forms: surrounding spinel, intergrown with CaTs-clinopyroxene, and locally texturally equilibrated with 120° grain boundaries (Figure 3.5C). Melilite in association with spinel is richer in gehlenite ($Gh_{68\text{-}83}$) than the clinopyroxene intergrowths ($Gh_{57\text{-}58}$) and well equilibrated types ($Gh_{47\text{-}50}$).

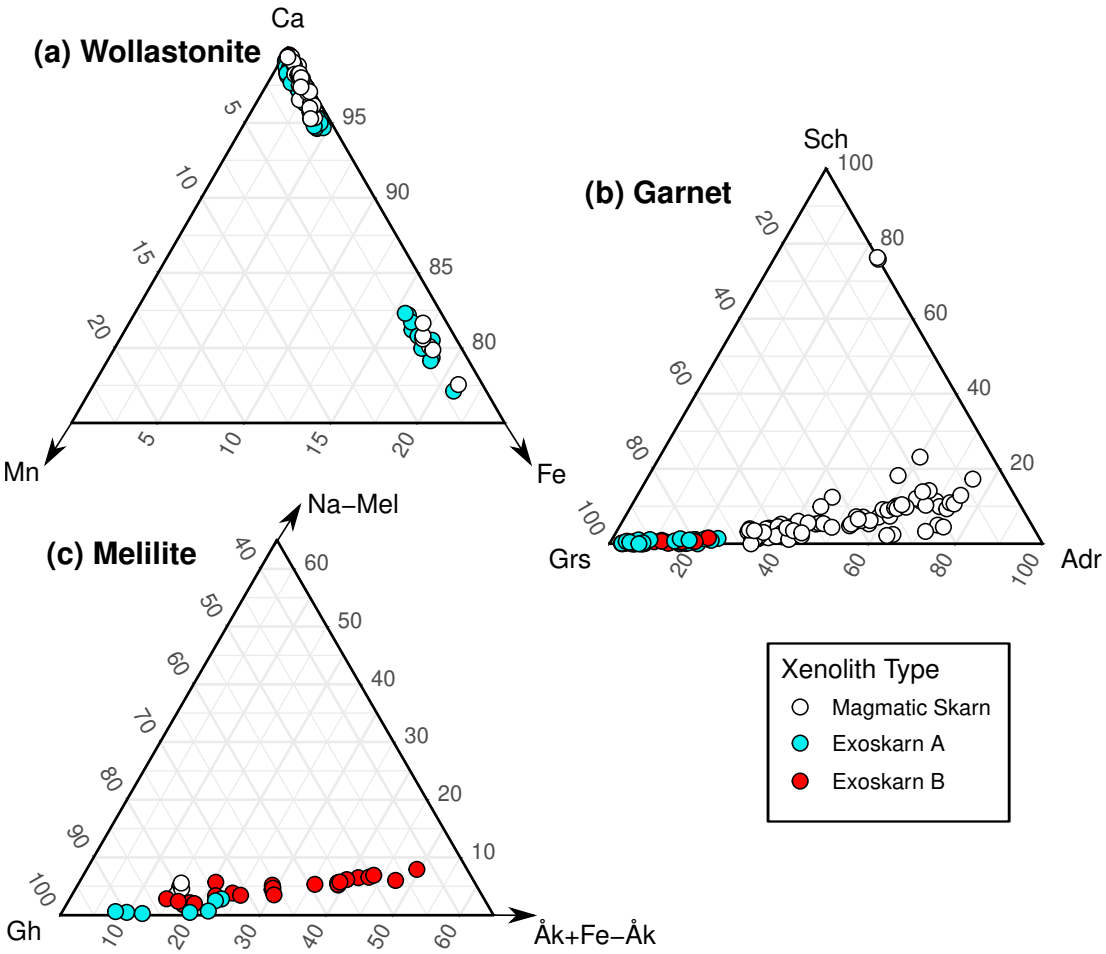


*Figure 3.9: Additional rock-forming mineral compositions. A) Wollastonite and ferrobustamite. B) Garnet. C) Melilite. Note the different ternary scales for each plot. Arrows indicate truncated scales. Mineral abbreviations as in Table 3.2.*

*Table 3.6: Average melilite compositions for the magmatic skarn xenolith core and the exoskarn xenoliths. All analyses are normalised to 7 oxygens. See Methods section for details about the calculation of mole fractions of end-member compositions. Analyses are reported as the mean and one standard deviation.*

| | Core | $\sigma$ | Exo A | $\sigma$ | Exo B | $\sigma$ |
|---|---|---|---|---|---|---|
| $n$ | 4 | | 7 | | 26 | |
| $SiO_2$ | 24.72 | 0.43 | 25.29 | 1.80 | 29.06 | 3.01 |
| $TiO_2$ | 0.01 | 0.02 | 0.01 | 0.02 | 0.01 | 0.02 |
| $Al_2O_3$ | 29.87 | 0.47 | 28.92 | 2.03 | 25.09 | 4.37 |
| $Cr_2O_3$ | 0.02 | 0.01 | 0.02 | 0.01 | 0.01 | 0.01 |
| FeO | 2.66 | 0.07 | 1.87 | 0.97 | 0.93 | 0.18 |
| MnO | 0.10 | 0.02 | 0.35 | 0.24 | 0.05 | 0.03 |
| MgO | 0.69 | 0.03 | 1.22 | 1.05 | 3.74 | 1.43 |
| CaO | 39.56 | 0.16 | 40.60 | 0.43 | 40.56 | 0.95 |
| $Na_2O$ | 0.54 | 0.10 | 0.13 | 0.12 | 0.52 | 0.21 |
| Total | 98.17 | 0.88 | 98.55 | 0.93 | 99.99 | 1.09 |
| **Cations based on 8 oxygens** | | | | | | |
| Si | 1.165 | 0.013 | 1.186 | 0.074 | 1.331 | 0.136 |
| Ti | 0.000 | 0.001 | 0.000 | 0.001 | 0.000 | 0.001 |
| Al | 1.659 | 0.012 | 1.600 | 0.120 | 1.354 | 0.237 |
| Cr | 0.001 | 0.000 | 0.001 | 0.001 | 0.000 | 0.000 |
| Fe | 0.105 | 0.002 | 0.074 | 0.038 | 0.036 | 0.007 |
| Mn | 0.004 | 0.001 | 0.014 | 0.010 | 0.002 | 0.001 |
| Mg | 0.048 | 0.002 | 0.085 | 0.072 | 0.255 | 0.097 |
| Ca | 1.998 | 0.021 | 2.042 | 0.032 | 1.990 | 0.036 |
| Na | 0.049 | 0.009 | 0.012 | 0.011 | 0.046 | 0.018 |
| **Endmembers (mol%)** | | | | | | |
| Gh | 79.7 | 0.7 | 82.3 | 7.1 | 65.2 | 12.5 |
| Åk | 4.9 | 0.2 | 8.9 | 7.6 | 26.6 | 10.5 |
| Fe Åk | 10.7 | 0.2 | 7.7 | 3.9 | 3.7 | 0.7 |
| Na Mel | 4.7 | 0.8 | 1.1 | 1.1 | 4.5 | 1.8 |

### Sulphur and Halogen-bearing Phases

Pyrrhotite is found in both magmatic and exoskarn xenoliths, often touching or rimmed by anhydrite. In magmatic skarn xenoliths, pyrrhotite is found in zone R2, as accessory inclusions in wollastonite and CaTs-clinopyroxene, and as rare inclusions in melt inclusions in the core. Fe/S ranges from 83 to 85%, and Cu concentrations range from 0.06 to 0.59 wt%. Pyrrhotite is sometimes found with near stoichiometric cubanite (Table 3.7). The associated anhydrite is pure, with $< 0.04$ wt% BaO and $< 0.1$ wt% SrO.

*Table 3.7: Cu-bearing mineral compositions. Cubanite has only been found in magmatic skarn xenoliths, whilst pyrrhotite is found across all xenolith types, with little chemical variation between xenolith types. Analyses are reported as the mean and one standard deviation.*

| | Po | | Cub | |
|---|---|---|---|---|
| *n* | *10* | | *5* | |
| Fe | 58.44 | 0.49 | 38.70 | 1.12 |
| S | 39.83 | 0.24 | 35.08 | 0.67 |
| Co | 0.20 | 0.02 | 0.12 | 0.03 |
| Ni | 0.48 | 0.11 | 0.06 | 0.05 |
| Cu | 0.30 | 0.17 | 24.26 | 1.51 |
| Zn | 0.03 | 0.02 | 0.09 | 0.05 |
| Total | 99.28 | 0.6 | 98.30 | 0.57 |
| | | | | |
| Sulphurs | 1 | | 3 | |
| | | | | |
| Fe | 0.842 | 0.007 | 1.899 | 0.036 |
| Co | 0.003 | 0.000 | 0.005 | 0.001 |
| Ni | 0.007 | 0.002 | 0.003 | 0.002 |
| Cu | 0.004 | 0.002 | 1.048 | 0.082 |
| Zn | 0.000 | 0.000 | 0.004 | 0.002 |
| Total | 0.856 | 0.007 | 2.959 | 0.072 |
| | | | | |
| Fe/S | 0.84 | 0.01 | | |

Cuspidine is found as crystals within calcite (magmatic skarn xenoliths) or forming within the reaction rim around calcite (exoskarn xenoliths) associated with stoichiometric spurrite ± larnite and an unidentified Ca-Si-Al-O phase. Fluorine a.p.f.u. approach the ideal 2 (1.937-2.035) indicating negligible OH (Table 3.8). Fluorite is a fine grained (<20 μm) accessory phase replacing calcite in both xenolith types, and evidently nucleated at crystal borders or forming fine halos around vesicles in calcite.

Apatite is found in magmatic skarn xenolith zone R4, and contains 0.7 to 0.8 wt% Cl and no detectable $SO_3$. Ellestadite is found as an accessory phase in exoskarn xenoliths with 7.2 to 10.0 wt% $SO_3$ and 0.7 to 1.2 wt% Cl (Table 3.8. F was not analysed with EMPA, however ~2 wt% F was identified using SEM-EDS, indicating that OH is minimal. Stoichiometric ellestadite (undetectable $P_2O_5$) with ~1.9 wt% Cl was determined with SEM-EDS coexisting with anhydrite in sample M13-02, within the reaction rim around large remnant calcite crystals.

Qualitative EDS analyses have identified trace quantities of small (<5 μm) baryte crystals in both magmatic and exoskarn xenoliths, and additionally a crystal of cotunnite ($PbCl_2$) is present in the magmatic skarn xenoliths.

There are unidentified Cl-bearing minerals, which tentatively may be new minerals. Skarn

*Table 3.8: Selected analyses of halogen and sulphur-bearing minerals. Wad-1, Wad-2 are the wadalite-like phase, found in sample MX1. The last two columns are the unknown volatile-bearing minerals in samples CS11 and MXCS-b respectively. SEM-EDS analysis shows the presence of Cl and F in these latter two minerals. Normalisation cations for the unknown volatile-bearing minerals are chosen to produce plausible formula units, and are not to represent any currently known minerals. Analyses are reported as the mean with one standard deviation.*

| | Cuspidine | | Ellestadite | | Wad | | Wad | | CS11 CaAlSi | | M-XCS b CaAlSi | |
|---|---|---|---|---|---|---|---|---|---|---|---|---|
| | All | $\sigma$ | All | $\sigma$ | Core | $\sigma$ | Core | $\sigma$ | Exo A | $\sigma$ | Exo A | $\sigma$ |
| *n* | 5 | | 4 | | 11 | | 2 | | 2 | | 2 | |
| $SiO_2$ | 32.70 | 0.42 | 8.37 | 1.27 | 17.63 | 0.41 | 24.98 | 1.99 | 26.70 | 0.05 | 23.33 | 0.44 |
| $TiO_2$ | 0.19 | 0.15 | 0.02 | 0.03 | 0.38 | 0.17 | 0.56 | 0.29 | 0.00 | 0.00 | 0.01 | 0.02 |
| $Al_2O_3$ | 0.02 | 0.01 | 0.03 | 0.02 | 23.85 | 1.05 | 19.59 | 0.98 | 14.47 | 0.42 | 12.98 | 0.02 |
| $Cr_2O_3$ | 0.02 | 0.02 | 0.00 | 0.00 | 0.01 | 0.02 | 0.00 | 0.01 | 0.00 | 0.00 | 0.00 | 0.00 |
| FeO | 0.14 | 0.08 | 0.08 | 0.03 | 5.63 | 1.21 | 6.26 | 2.60 | 1.52 | 0.37 | 0.71 | 0.15 |
| MnO | 0.08 | 0.02 | 0.03 | 0.01 | 0.18 | 0.05 | 0.24 | 0.15 | 0.26 | 0.10 | 0.07 | 0.06 |
| MgO | 0.07 | 0.07 | 0.05 | 0.02 | 0.60 | 0.08 | 0.43 | 0.09 | 0.24 | 0.01 | 0.01 | 0.01 |
| CaO | 60.20 | 0.24 | 54.16 | 1.19 | 40.18 | 0.43 | 39.67 | 3.09 | 52.48 | 0.13 | 56.23 | 0.26 |
| $Na_2O$ | 0.02 | 0.02 | 0.01 | 0.02 | 0.17 | 0.16 | 0.09 | 0.04 | 0.00 | 0.00 | 0.01 | 0.02 |
| $K_2O$ | 0.01 | 0.01 | 0.00 | 0.00 | 0.00 | 0.01 | 0.02 | 0.00 | 0.00 | 0.00 | 0.01 | 0.01 |
| $P_2O_5$ | 0.00 | 0.00 | 24.03 | 3.25 | 0.13 | 0.13 | 0.13 | 0.18 | | | 0.04 | 0.02 |
| $SO_3$ | 0.00 | 0.00 | 8.12 | 1.42 | 0.01 | 0.01 | 0.00 | 0.00 | | | 0.02 | 0.01 |
| Cl | 0.01 | 0.00 | 1.04 | 0.22 | 12.91 | 0.17 | 8.87 | 2.74 | | | 2.12 | 0.00 |
| F | 10.26 | 0.14 | | | 0.02 | 0.02 | 0.00 | | | | 4.90 | 0.00 |
| Total | 103.70 | 0.40 | 95.94 | 0.81 | 101.69 | 0.56 | 100.85 | 2.08 | 95.67 | 0.12 | 100.61 | 0.10 |
| O=($F_2$,$Cl_2$) | -4.32 | 0.06 | -0.23 | 0.05 | -2.92 | 0.04 | -2.00 | 0.62 | 0.00 | 0.00 | -2.54 | 0.00 |
| Total | 99.38 | 0.44 | 95.71 | 0.78 | 98.77 | 0.53 | 98.85 | 1.46 | 95.67 | 0.12 | 98.07 | 0.10 |
| **Cations based on x cations** | | | | | | | | | | | | |
| *Cations* | *6* | *6* | *8* | *8* | *26* | *26* | *26* | *26* | *9* | *9* | *16* | *16* |
| Si | 2.002 | 0.009 | 0.701 | 0.106 | 4.753 | 0.092 | 6.168 | 0.277 | 2.337 | 0.006 | 4.042 | 0.058 |
| Ti | 0.009 | 0.007 | 0.002 | 0.002 | 0.078 | 0.034 | 0.103 | 0.051 | 0.000 | 0.000 | 0.001 | 0.002 |
| Al | 0.001 | 0.001 | 0.003 | 0.002 | 7.578 | 0.297 | 5.713 | 0.484 | 1.493 | 0.037 | 2.649 | 0.009 |
| Cr | 0.001 | 0.001 | 0.000 | 0.000 | 0.003 | 0.003 | 0.001 | 0.001 | 0.000 | 0.000 | 0.000 | 0.000 |
| Fe | 0.007 | 0.004 | 0.006 | 0.002 | 1.270 | 0.277 | 1.285 | 0.493 | 0.112 | 0.028 | 0.103 | 0.022 |
| Mn | 0.004 | 0.001 | 0.002 | 0.001 | 0.042 | 0.012 | 0.050 | 0.030 | 0.019 | 0.008 | 0.011 | 0.008 |
| Mg | 0.007 | 0.006 | 0.007 | 0.003 | 0.240 | 0.032 | 0.159 | 0.039 | 0.031 | 0.001 | 0.002 | 0.002 |
| Ca | 3.949 | 0.026 | 4.858 | 0.102 | 11.610 | 0.160 | 10.524 | 1.187 | 4.923 | 0.008 | 10.436 | 0.096 |
| Na | 0.002 | 0.002 | 0.001 | 0.003 | 0.087 | 0.083 | 0.045 | 0.022 | 0.000 | 0.000 | 0.004 | 0.005 |
| K | 0.001 | 0.001 | 0.000 | 0.000 | 0.002 | 0.003 | 0.007 | 0.000 | 0.000 | 0.000 | 0.002 | 0.002 |
| P | 0.000 | 0.000 | 1.704 | 0.230 | 0.031 | 0.029 | 0.027 | 0.038 | 0.000 | 0.000 | 0.006 | 0.003 |
| S | 0.000 | 0.000 | 0.510 | 0.089 | 0.001 | 0.003 | 0.000 | 0.000 | 0.000 | 0.000 | 0.002 | 0.001 |
| Cl | 0.001 | 0.000 | 0.147 | 0.031 | 5.903 | 0.087 | 3.735 | 1.277 | 0.000 | 0.000 | 0.622 | 0.003 |
| F | 1.986 | 0.044 | 0.000 | 0.000 | 0.006 | 0.011 | 0.000 | 0.000 | 0.000 | 0.000 | 2.684 | 0.012 |

xenoliths, such as those from the Upper Chegem caldera, Russia, can be host to numerous new minerals (e.g. Galuskin *et al.*, 2013), and this may additionally be the case at Merapi. A wadalite-like Ca-Al-Fe-Si-Cl mineral compositionally similar to the wadalite-eltyubyuite mayenite solid solution (when normalised to 26 cations) is found in association with calcite, cuspidine, garnet and gehlenite in magmatic skarn xenolith MX1 (Table 3.8). These crystals however have compositions with Si a.p.f.u. 4.6-5.5 (Table 3.8, higher than the ideal Si 4, and lack sufficient Mg to balance this increase in Si in wadalite (c.f. Galuskin *et al.*, 2015). Raman spectra of this phase are included as Appendix Figure B.5.

A Ca-Al-Si-Cl-F mineral is found in exoskarn xenoliths CS11 and M-XCS in the rim around areas where larnite and spurrite have replaced calcite. Concentrations of Cl and F in this

mineral have only been determined by SEM-EDS, and as it contains 10 wt% more CaO than the wadalite-like mineral, and lower volatile contents (~7 wt%) we believe it to be a different mineral (Table 3.8.

**Oxides, Other Silicates, and Accessory Minerals**

The dominant Fe-Ti oxide in the magmatic skarn xenoliths is magnetite, with 0.3 to 11.5 wt% $TiO_2$. Magnetite within the xenolith cores is distinct (<0.3 wt% $TiO_2$) from magnetite in the other zones (8.9-11.5 wt% $TiO_2$). Ilmenite is present in zone R2 of one xenolith. Qualitative EDS analysis has identified micrometre sized chromite in the xenolith cores. Hematite is the dominant oxide found in the exoskarn xenoliths, with rare magnetite present as well. Perovskite is found as a 50 µm vermicular cluster intergrown with wollastonite and plagioclase in one magmatic skarn xenolith (sample MX1) and is essentially stoichiometric $CaTiO_3$. A Ca-Zr-Ti-O mineral (calzirtite?) is found in the same magmatic skarn xenolith. Titanite across all xenolith types contains 1.04 to 2.51 wt% $Al_2O_3$ and 0.73 to 2.86 wt% FeO. An unidentified Ca-Al-Si-P mineral is found in exoskarn A samples CS11 and MXCS, approximating the formula $Si_{3.1}Ti_{0.1}Al_{2.9}Ca_{3.0}P_{0.9}O_{16}$ when assuming 16 oxygens. Xenotime and monazite are very rare calcite inclusions in exoskarn A xenoliths. Spinel ($Sp_{83\text{-}89}Her_{11\text{-}17}$) is found exclusively in the gehlenite-garnet-CaTs clinopyroxene-spinel exoskarn B xenolith (MX99-3s). These mineral analyses are given in Table 3.9.

Transition metal alloys occur as trace <5 µm inclusions in wollastonite and garnet crystals in the magmatic skarn xenoliths. Data for a ~2 µm CuZn alloy approximates tongxinite $Cu_2Zn$. There is a small chance these may be contamination from the grinding plate, although plausible for this mineral to occur in pyrrhotite and cubanite-bearing xenoliths, therefore is not discussed further. A Cu-Zn-Pb phase has additionally been identified.

### 3.5.3 Glass Chemistry

Melt inclusions and interstitial glass are almost entirely restricted to magmatic skarn xenoliths, with melt inclusions and glass only found in the exoskarn xenoliths within the clinopyroxene-rich reaction rim at the host lava contact. Xenolith interstitial (zones R1, R2, R4 and core) and melt inclusion (zones R1, R3, R4 and core) glass compositions show strong deviation from lava groundmass glass and melt inclusion compositions, and also show compositional differences between zones (Figure 3.10, Table 3.10). Melt inclusions are compositionally more diverse than the interstitial glass. CaO concentrations in intersitital glass and melt inclusions from zone R1

*Table 3.9: Average analyses of oxides and other silicate minerals found in the Merapi xenoliths. Analyses are reported as the mean with one standard deviation.*

| | CaSiAlP | ox-hem | $\sigma$ | ox-ilm | ox-mag | $\sigma$ | psk | $\sigma$ | sp | $\sigma$ | ttn | $\sigma$ |
|---|---|---|---|---|---|---|---|---|---|---|---|---|
| $n$ | 1 | 4 | | 1 | 27 | | 3 | | 8 | | 8 | |
| $SiO_2$ | 33.30 | 0.31 | 0.15 | 5.92 | 0.14 | 0.10 | 1.13 | 0.83 | 0.01 | 0.01 | 30.91 | 1.13 |
| $TiO_2$ | 1.19 | 0.15 | 0.20 | 43.22 | 9.91 | 5.16 | 54.75 | 0.63 | 0.01 | 0.01 | 36.28 | 2.33 |
| $Al_2O_3$ | 26.28 | 0.59 | 1.14 | 1.10 | 2.66 | 1.15 | 0.43 | 0.16 | 66.59 | 0.58 | 1.70 | 0.51 |
| $Cr_2O_3$ | 0.00 | 0.02 | 0.02 | 0.19 | 0.18 | 0.20 | 0.01 | 0.01 | 0.10 | 0.07 | 0.03 | 0.03 |
| FeO | 0.28 | 86.61 | 2.79 | 42.16 | 78.73 | 4.81 | 0.80 | 0.15 | 8.48 | 1.41 | 1.31 | 0.70 |
| MnO | 0.00 | 0.13 | 0.14 | 0.87 | 0.89 | 0.30 | 0.04 | 0.03 | 0.38 | 0.08 | 0.08 | 0.07 |
| MgO | 0.00 | 0.35 | 0.58 | 1.54 | 1.78 | 0.55 | 0.01 | 0.01 | 22.69 | 0.77 | 0.12 | 0.29 |
| CaO | 29.53 | 0.47 | 0.19 | 1.74 | 0.17 | 0.21 | 40.71 | 0.47 | 0.01 | 0.00 | 28.13 | 1.04 |
| $Na_2O$ | 0.46 | 0.06 | 0.04 | 0.40 | 0.05 | 0.05 | 0.02 | 0.02 | 0.00 | 0.00 | 0.02 | 0.01 |
| Total | 102.40 | 88.70 | 1.67 | 97.37 | 94.51 | 1.37 | 97.92 | 0.45 | 98.27 | 0.68 | 98.66 | 2.18 |
| **Cations based on x oxygens** | | | | | | | | | | | | |
| Oxygens | 16 | 3 | 3 | 3 | 4 | 4 | 3 | 3 | 4 | 4 | 5 | 5 |
| Si | 3.098 | 0.006 | 0.005 | 0.146 | 0.005 | 0.004 | 0.026 | 0.019 | 0.000 | 0.000 | 1.010 | 0.034 |
| Ti | 0.083 | 0.001 | 0.001 | 0.802 | 0.280 | 0.153 | 0.944 | 0.008 | 0.000 | 0.000 | 0.892 | 0.053 |
| Al | 2.881 | 0.001 | 0.001 | 0.032 | 0.117 | 0.048 | 0.012 | 0.004 | 1.965 | 0.012 | 0.065 | 0.019 |
| Cr | 0.000 | 0.000 | 0.000 | 0.004 | 0.005 | 0.006 | 0.000 | 0.000 | 0.002 | 0.001 | 0.001 | 0.001 |
| $Fe^{2+}$ | 0.000 | 0.000 | 0.000 | 0.774 | 1.145 | 0.181 | 0.000 | 0.000 | 0.145 | 0.023 | 0.002 | 0.007 |
| $Fe^{3+}$ | 0.022 | 1.478 | 0.985 | 0.095 | 1.311 | 0.288 | 0.015 | 0.003 | 0.033 | 0.013 | 0.033 | 0.022 |
| Mn | 0.000 | 0.001 | 0.001 | 0.018 | 0.028 | 0.009 | 0.001 | 0.000 | 0.008 | 0.002 | 0.002 | 0.002 |
| Mg | 0.000 | 0.002 | 0.002 | 0.057 | 0.098 | 0.029 | 0.000 | 0.000 | 0.847 | 0.024 | 0.006 | 0.014 |
| Ca | 2.943 | 0.009 | 0.007 | 0.046 | 0.006 | 0.008 | 1.000 | 0.014 | 0.000 | 0.000 | 0.985 | 0.033 |
| Na | 0.083 | 0.003 | 0.002 | 0.019 | 0.003 | 0.004 | 0.001 | 0.001 | 0.000 | 0.000 | 0.001 | 0.001 |

and some R2 analyses overlap lava glass CaO values (0.2 to 3.8 wt%). CaO concentrations in the interstitial glass (0.9-6.5 wt%) and in melt inclusions (0.5-11.3 wt%) within the xenolith zones R3, R4 and the core are elevated by up to ~4 wt% in the interstitial glasses in relation to magmatic values and by up to 10 wt% in the melt inclusions. These glasses, especially the melt inclusions, are also characterised by low $Al_2O_3$ and $K_2O$ relative to lava glasses (Figure 3.10), and smaller variations from the lavas are observed in all other major and minor elements. $Al_2O_3$ concentrations are up to 5 wt% lower than in the lavas, and up to 2 wt% lower in $K_2O$. Xenolith glass volatile concentrations are broadly comparable to the lava glasses, with only a few analyses exceeding that of the lavas. Sulphur exceeds lava groundmass concentrations in some zone R1 and zone R4 analyses, containing up to 510 ppm sulphur. Chlorine is typically within lava groundmass glass concentrations, and only exceeds lava glass values in plagioclase-hosted melt inclusions in sample CS16 and interstitial glasses in MX99-4s. The few analyses for F (0 to 1110 ppm) show that concentrations are within lava values (0 to 2637 ppm). Although the melt inclusion analyses for MX1 show negligible F, localised patches of cuspidine and fluorite have been observed.

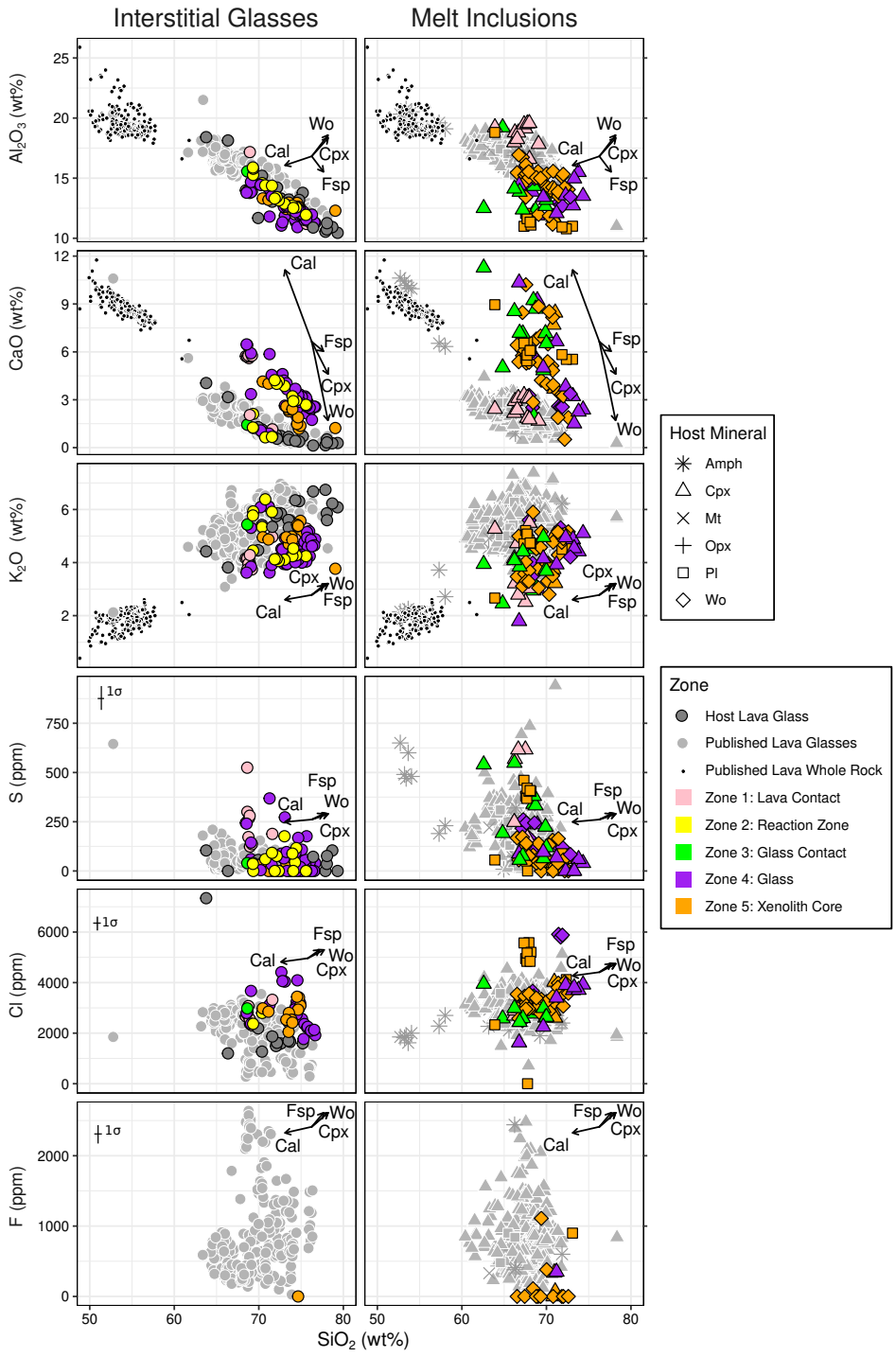


*Figure 3.10: Interstitial and melt inclusion glass compositions. All values are normalised to 100 wt% volatile free. Published data for whole rock, glass and melt inclusions at Merapi shown for comparison. Published data from Gertisser (2001), Schwarzkopf* et al. *(2001), Gertisser* et al. *(2012), Nadeau* et al. *(2013b), Borisova* et al. *(2013), Costa* et al. *(2013), Innocenti* et al. *(2013), Preece* et al. *(2014) and the GEOROC database. Arrows show the effect of adding 10% calcite, and subtracting 10% clinopyroxene, wollastonite or plagioclase. Mineral abbreviations as in Table 3.2. See Figure B.6 for the major element oxides not shown in this figure.*

*Table 3.10: Average interstitial glass and melt inclusion compositions for the zones in the magmatic skarn xenoliths. Analyses are reported as the mean with one standard deviation.*

| | Intersititial Glass | | | | | | | | | Melt Inclusion | | | |
|---|---|---|---|---|---|---|---|---|---|---|---|---|---|
| | Host Lava | $\sigma$ | R1 | $\sigma$ | R2 | $\sigma$ | R4 | $\sigma$ | Core | $\sigma$ | R1 | $\sigma$ | R4 | $\sigma$ |
| $n$ | 15 | | 11 | | 15 | | 48 | | 12 | | 12 | | 70 | |
| $SiO_2$ | 70.45 | 3.36 | 69.02 | 2.54 | 71.07 | 2.76 | 73.23 | 2.21 | 73.32 | 1.78 | 63.99 | 3.03 | 67.38 | 3.72 |
| $TiO_2$ | 0.42 | 0.11 | 0.37 | 0.10 | 0.31 | 0.14 | 0.35 | 0.13 | 0.32 | 0.09 | 0.44 | 0.05 | 0.40 | 0.19 |
| $Al_2O_3$ | 13.75 | 1.83 | 13.29 | 0.95 | 13.47 | 1.17 | 12.00 | 0.88 | 12.60 | 0.38 | 17.55 | 0.82 | 13.33 | 1.97 |
| $Cr_2O_3$ | 0.01 | 0.01 | 0.01 | 0.01 | 0.01 | 0.01 | 0.01 | 0.01 | 0.00 | 0.01 | 0.02 | 0.02 | 0.01 | 0.01 |
| FeO | 2.59 | 0.79 | 3.03 | 0.15 | 2.52 | 0.28 | 2.22 | 0.46 | 2.22 | 0.56 | 2.55 | 0.56 | 2.84 | 1.31 |
| MnO | 0.12 | 0.08 | 0.13 | 0.05 | 0.10 | 0.04 | 0.07 | 0.03 | 0.05 | 0.03 | 0.13 | 0.04 | 0.09 | 0.06 |
| MgO | 0.40 | 0.57 | 0.12 | 0.09 | 0.12 | 0.12 | 0.06 | 0.06 | 0.07 | 0.04 | 0.33 | 0.22 | 0.35 | 0.90 |
| CaO | 1.05 | 1.04 | 4.71 | 1.79 | 2.49 | 1.29 | 3.04 | 1.15 | 2.26 | 0.97 | 2.44 | 0.52 | 5.87 | 3.47 |
| $Na_2O$ | 3.89 | 1.15 | 3.41 | 0.46 | 3.59 | 0.46 | 3.22 | 0.37 | 3.32 | 0.53 | 4.01 | 0.90 | 3.43 | 0.74 |
| $K_2O$ | 5.28 | 0.72 | 4.20 | 0.52 | 4.71 | 0.80 | 4.51 | 0.56 | 4.92 | 0.50 | 3.82 | 1.03 | 4.00 | 0.99 |
| $P_2O_5$ | 0.12 | 0.12 | 0.08 | 0.05 | 0.07 | 0.08 | 0.09 | 0.36 | 0.04 | 0.02 | 0.23 | 0.08 | 0.08 | 0.04 |
| $SO_3$ | 0.01 | 0.01 | 0.06 | 0.03 | 0.01 | 0.01 | 0.02 | 0.02 | 0.00 | 0.01 | 0.11 | 0.05 | 0.03 | 0.03 |
| Cl | 0.21 | 0.16 | 0.27 | 0.03 | 0.26 | 0.03 | 0.29 | 0.07 | 0.28 | 0.04 | 0.29 | 0.02 | 0.34 | 0.11 |
| Total | 98.26 | 1.38 | 98.63 | 0.83 | 98.73 | 1.56 | 99.09 | 0.92 | 99.39 | 1.12 | 95.53 | 3.48 | 98.14 | 1.97 |

### 3.5.4 Fluid Inclusions

Fluid inclusions in the magmatic skarn xenoliths (*n=28*) are two phase vapour-rich inclusions in wollastonite. The dominant fluid composition is $CO_2$, confirmed by instantaneous melting at -57.3 to -56.1°C. The slight deviation from ideal melting at -56.6°C indicates the presence of a small percentage other dissolved gases such as $SO_2$, $N_2$, which are not thought to have a significant effect on pressure estimates (Frezzotti *et al.*, 2002). No $H_2O$ is observed either as ice or clathrate. Homogenisation is to the vapour phase at 12.9 to 29.9°C. These temperatures correspond to densities of 0.15 to 0.35 g/cm$^3$, indicating trapping pressures of 33 to 92 MPa, when assuming a formation temperature of 850°C (see discussion), utilising the Hansteen and Klügel (2008) spreadsheet implementation of Sterner and Pitzer (1994) and Span and Wagner (1996) density and equation of state models. An extreme temperature estimate increase to 1200°C only increases pressure estimates by ˜30 MPa. No inclusions for barometry with resolvable homogenisation were found in the exoskarn xenoliths, but $CO_2$ melting was observed in some inclusions.

## 3.6 Discussion

In this section we discuss the processes during formation of the xenoliths, and the pressure, temperature and $fO_2$ conditions that can be determined from the recorded mineral assemblages. We also discuss the implications for the magmatic system at Merapi, such as magmatic

contamination by xenolith phases, metal transport and the $CO_2$ output by decarbonation reactions. Accurate determination of temperature in the magmatic skarn xenoliths requires accurate estimates of the melt composition during xenolith formation; therefore we first discuss the implications for any modification of melt inclusion compositions.

### 3.6.1 Post-entrapment Modification of Melt Inclusions

The abundance of melt inclusions in the magmatic skarn xenoliths allows for constraining the original composition of the melt present during xenolith formation, and potentially application of thermobarometric models (discussed below). Post-entrapment modification of melt inclusion compositions however is a well-documented phenomenon, occurring via diffusive exchange of elements, crystallisation of a host mineral boundary layer, or from crystallisation of daughter crystals (e.g. Nakamura and Shimakita, 1998; Danyushevsky *et al.*, 2000; Nielsen, 2011). Therefore, assessment of these effects is required before interpreting the inclusion compositions. Melt inclusions are found within clinopyroxene, plagioclase and wollastonite hosts in the magmatic skarn xenoliths, all of which have no universally accepted way to back-calculate the original composition. The interstitial glass within the xenoliths provides a first order constraint on the original melt composition, showing that it is strongly elevated in CaO compared to lava glass compositions (Figure 3.10). We have not attempted correction of our melt inclusions, and consider the wollastonite-hosted melt inclusions to be the best estimates of melt CaO concentrations for the following reasons.

Examples of correcting for inclusion modification in clinopyroxene hosts include adding the host clinopyroxene to the inclusion (e.g. Bali *et al.*, 2018) until Fe-Mg partitioning between the inclusion and clinopyroxene ($KD^{cpx-MI}_{Fe-Mg}$) approaches the widely accepted equilibrium value of 0.28 $\pm$ 0.08 (Putirka, 2008), and adding calculated equilibrium clinopyroxene back to the melt inclusion until the calculated clinopyroxene has the same Mg# as the host (e.g. Preece *et al.*, 2014). A compilation of magma-carbonate (both limestone and dolomite) interaction experimental data shows that $KD^{cpx-melt}_{Fe-Mg}$ in carbonate-contaminated systems may strongly diverge from the magmatic-derived 0.28 $\pm$ 0.08 (Putirka, 2008) (Figure 3.11A), suggesting that $KD^{cpx-melt}_{Fe-Mg}$ is redox-sensitive (see oxybarometry discussion below) and an Fe-Mg partitioning equilibrium-based correction is not appropriate.

The difference between observed and predicted clinopyroxene diopside-hedenbergite (DiHd) components ($\Delta$DiHd: Putirka, 1999, 2008; Mollo *et al.*, 2013; Neave and Putirka, 2017) is more accurate at predicting equilibrium (Figure 3.11B), with 68% of magma-carbonate experimental

equilibrium clinopyroxene-melt pairs predicted to fall within model error (± 0.07 Mollo *et al.*, 2013). Applied to the Merapi xenoliths, clinopyroxene-hosted melt inclusions within zones R3 and R4 have irregular embayed forms, suggesting some sidewall crystal growth, and ΔDiHd values $> 0.07$, indicating some potential modification of trapped melt compositions. Melt inclusion-clinopyroxene pairs from zones R1 and R2 have ΔDiHd values from 0 to 0.14, with an average of 0.05, indicating some may represent unmodified melt values. These compositions overlap lava glass compositions, consistent with their proximity to the lava contact, indicating a magmatic character.

An example of plagioclase-hosted melt inclusion correction is regressing the magmatic liquid line of descent in $TiO_2$-$Al_2O_3$ space, and adding plagioclase back until the inclusions lie on the liquid line of descent (Bali *et al.*, 2018). This cannot be applied here as our measured xenolith melt inclusion compositions, evidenced by elevated CaO in xenolith interstitial glass compositions, are contaminated and are not closed system magmatic values (see below), and therefore cannot be assumed to lie on a regression line through the magmatic liquid line of descent. Moreover, a micron thick rim of Ab-rich plagioclase is observed around the inclusion walls (Figure 3.4E, G) and suggests some modification of plagioclase inclusion compositions occurred as well.

Wollastonite-hosted melt inclusions are generally well formed and equant with a single shrinkage bubble, and lack textural evidence of sidewall crystallisation and modification (Figure 3.4D). Although Fe and Mn are weakly compatible in wollastonite, traverses from inclusion contact to 20 µm into the crystal do not show any resolvable chemical gradients that would indicate diffusion and melt inclusion alteration. Therefore, wollastonite-hosted inclusions are likely the best inclusions to represent original compositions.

The effect of post-entrapment crystallisation of a melt inclusion can be tested graphically. Fractionation vectors in Figure 3.10 show the effect of 10% subtraction (crystallisation) of clinopyroxene, plagioclase and wollastonite on glass compositions. Taking the fractionation vectors for the CaO vs $SiO_2$ plot, Figure 3.10 shows that that any post-entrapment crystallisation of the respective host phase would lower the CaO concentration of the trapped melt, therefore our analyses must reflect minimum original CaO estimates, regardless of inclusion sidewall crystallisation. Melt inclusion compositions instead follow the vector for addition of calcite to the published melt compositions. Where the Cal addition vector is not followed perfectly, such as for $Al_2O_3$, increasing CaO of the melt may have triggered precipitation of other mineral phases, such as An-rich plagioclase (present in the xenolith glass), causing the data to

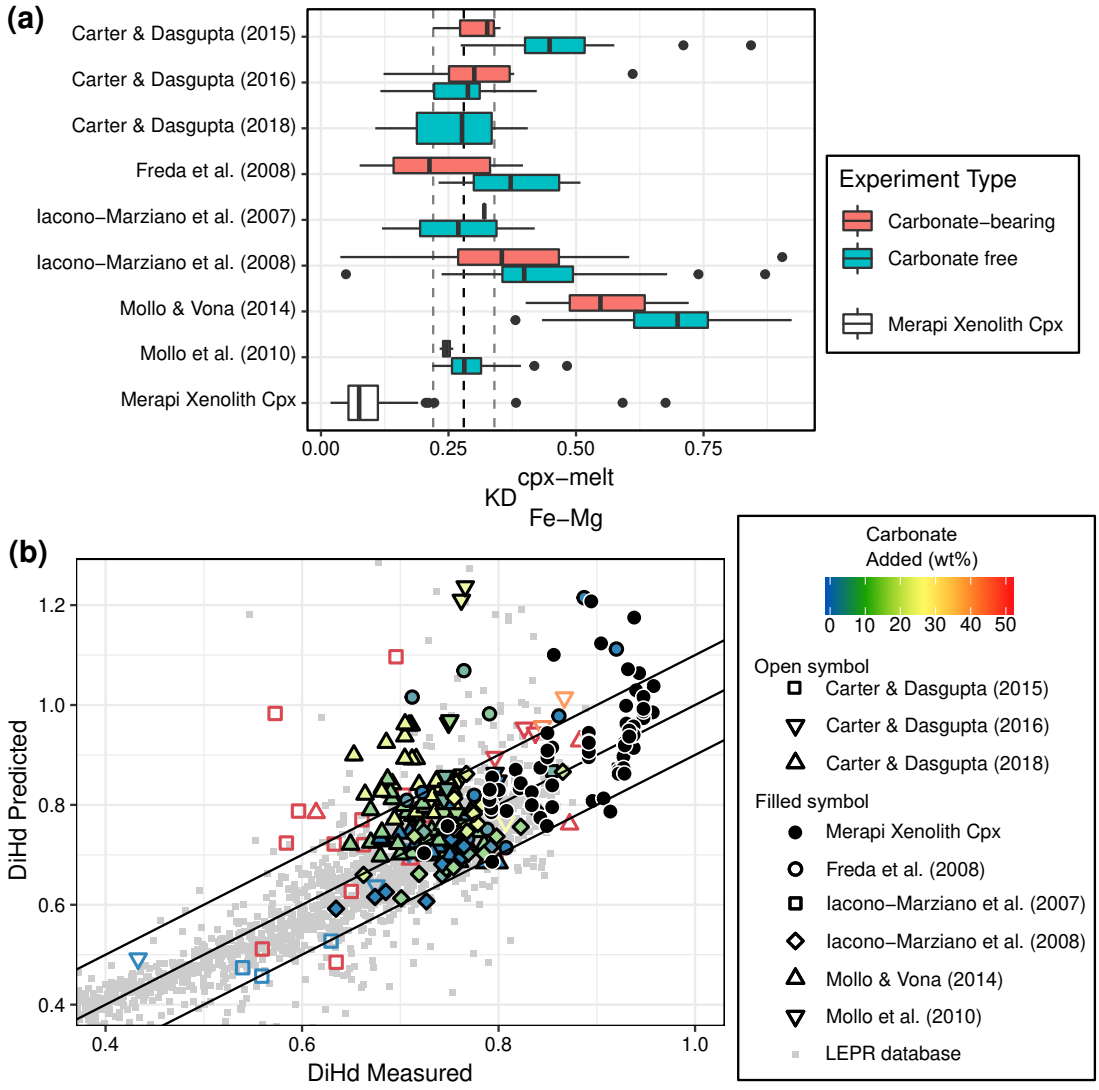


*Figure 3.11: A) Box plots of $KD_{Fe-Mg}^{cpx-melt}$ values from carbonate assimilation experiments. Black circles represent outliers calculated as 1.5 x interquartile range from the third quartile. Experiments with carbonate added have a general increase in $KD_{Fe-Mg}^{cpx-melt}$ values. Experiments by Carter and Dasgupta (2016) and Carter and Dasgupta (2018) use more evolved andesite and dacite compositions, compared to the remaining basaltic experiments, which were less affected by carbonate interaction. The extremely high values from Mollo and Vona (2014) are likely the result of very high experimental $fO_2$ conditions (up to air), which would strongly affect $Fe^{2+}/Fe^{3+}$ partitioning between clinopyroxene and melt. B) Comparison between measured clinopyroxene DiHd components and predicted ones, using the iterative approach of Neave and Putirka (2017). Light grey data are calculated from clinopyroxenes in the Library of Experimental Phase Relations database.*

follow a Cal+Fsp vector. A decrease in $K_2O$ is likely just a dilution effect, not removal of $K_2O$ in any significant proportion in any mineral phases, as no $K_2O$-rich minerals are found at Merapi or in the xenoliths. As the current methods of correcting for post entrapment crystallisation are not suitable for these compositions, no attempt has been made to account for the effects of melt inclusion modification. Additionally, these compositions overlap the compositions of Ca-contaminated interstitial glasses, and high CaO is present regardless of the host mineral phase. This shows that although post-entrapment modification may have occurred, the very high CaO values may reasonably represent minimum estimates of original melt compositions.

### 3.6.2 Intensive Variables

#### Magmatic Skarn Xenolith Thermobarometry

The abundance of glass and common mineral phases (clinopyroxene, plagioclase) allows for the application of thermobarometric models to the xenoliths. On the basis of the uncertainty in mineral-melt equilibrium testing previously discussed and the results of testing thermobarometric models with experimental carbonate assimilation data (see Appendix B.5 and Appendix Figure B.8) we apply the glass-only equation 34 (Putirka, 2008) to the clinopyroxene-saturated interstitial glasses of the magmatic skarn xenoliths, with water contents estimated by difference from 100 wt% (Anderson, 1973, 1974; Devine *et al.*, 1995), provide a temperature of 829 ± 45°C ($n$=89)(Figure 3.12). Melt inclusions, in turn, reflect a slightly higher temperature of 876 ± 49°C ($n$=88). These temperatures are consistent with the presence of ferrobustamite overgrowths on the coexisting wollastonite, which is thought stable between ~800-880°C (Rutstein, 1971). A pressure of 50 MPa was assumed for thermometry, consistent with the results of fluid inclusion barometry (our results: 34-92 MPa, and those of Clocchiatti *et al.* (1982): 67-109 MPa), and the results of equation 32b (27 ± 244 MPa). Temperature estimates are lowered by a negligible 5°C per 100 MPa. Temperatures estimated for glasses within any lava attached to the xenolith, and lava interstitial glasses from the literature (with an assumed pressure of 200 MPa: Preece *et al.*, 2014; Erdmann *et al.*, 2016) are higher than that of the xenolith glasses, at 937 ± 43°C. Phase equilibria estimates of pre-eruptive temperatures for Merapi are 925-950°C (Erdmann *et al.*, 2016), which supports the higher lava glass temperature from our glass thermometry.

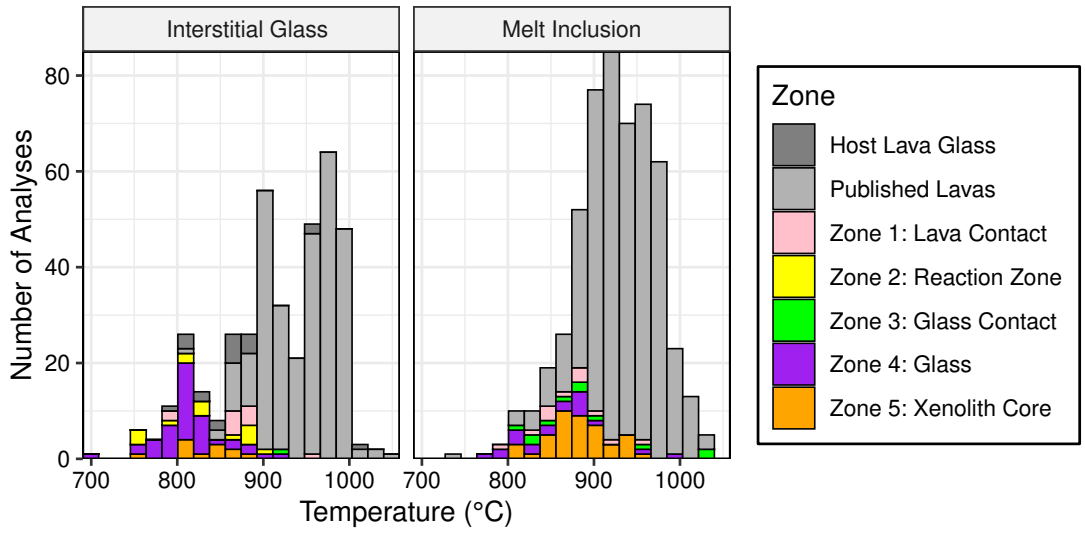


*Figure 3.12: Stacked histogram results of thermometry estimates for the magmatic skarn xenoliths and host lava glasses using Putirka (2008) equation 34. Xenolith glasses produce temperatures of 829 ± 45°C (n=89). Melt inclusions have a slightly higher temperature of 876 ± 49°C (n=89). These temperatures are slightly below the thermometry estimates for published lava glass analyses, at 937 ± 43°C*

Additional constraints can be gained from comparison with experimental phase equilibria. The small interstitial patches of garnet, plagioclase and wollastonite in sample MX1 are stable between ~510-890°C, with an $XCO_2 < 0.6$ at 100 to 200 MPa (Gordon and Greenwood, 1971; Tracy and Frost, 1991), consistent with temperatures from the glass thermometry. The R3b zone in sample MX1, comprising coexisting grossular-andradite garnet ($Adr_{0.3}$) and CaTs-clinopyroxene ($CaTs_{0.23}$) indicates temperatures of 900-950°C based on experimental phase equilibria (Huckenholz *et al.*, 1974; Gustafson, 1974).

### Exoskarn T-$XCO_2$

Although the exoskarn xenoliths lack glass, many phases and assemblages in the exoskarn xenoliths can help constrain temperatures by comparison with experimental data and thermodynamic modelling. Spurrite + cuspidine ± larnite-bearing reaction rims between calcite and wollastonite + grossular + anorthite in samples CS11 and MXCS-0 allow temperature constraints, while additionally demonstrating the progressive interaction along a $CaO$-$SiO_2$-$CO_2$ system (e.g. Zharikov, 1969). The presence of spurrite and absence of evidence for lower temperature tilleyite-forming reactions indicate spurrite formation by either interaction between wollastonite and calcite

$$3\overset{calcite}{CaCO_3} + \overset{wollastonite}{2CaSiO_3} = \overset{spurrite}{Ca_5(SiO_4)_2CO_3} + 2CO_2$$

or calcite directly with $SiO_2$

$$5\overset{calcite}{CaCO_3} + 2\overset{silica}{SiO_2} = Ca_5(\overset{spurrite}{SiO_4})_2CO_3 + 4CO_2$$

The former reaction indicates temperatures of ~700-1000°C (Tuttle and Harker, 1957). Spurrite is stable as low as 430°C at low $CO_2$ partial pressure (Henmi and Henmi, 1978), but the proximity of tens of microns to a decarbonating calcite crystal and a significant proportion of voids suggests a high $CO_2$ partial pressure. The latter reaction occurs at 910°C at 1 atm when in the presence of chlorine or fluorine (Bolio-Arceo and Glasser, 1990). Cuspidine and fluorite are found within tens of microns of the spurrite, confirming a reaction occurred with a fluorine-bearing fluid.

Larnite forms further from the calcite near the wollastonite contact (Deegan *et al.*, 2010 Figure 10b) in sample MXCS-0, indicating temperatures of >850°C (Wyllie and Haas Jr, 1965; Joesten, 1974; Treiman and Essene, 1983), following the potential reactions:

$$\overset{wollastonite}{CaSiO_3} + Ca_5(\overset{spurrite}{SiO_4})_2CO_3 = 3\overset{larnite}{Ca_2(SiO_4)} + CO_2$$

$$\overset{spurrite}{Ca_5(SiO_4)_2CO_3} = 2\overset{larnite}{Ca_2(SiO_4)} + CaO + CO_2$$

$$2\overset{calcite}{CaCO_3} + \overset{silica}{SiO_2} = 2\overset{larnite}{Ca_2(SiO_4)} + CO_2$$

The dominant mineral assemblage in these large calcite-bearing xenoliths can be described in the $SiO_2$-$Al_2O_3$-CaO system, comprising grossular garnet ($Grs_{78\text{-}96}$), wollastonite and anorthite. This assemblage is stable between ~510-890°C at 50-200 MPa, with an increasingly restricted $XCO_2$ with pressure, varying from > ~0.2 to 1 at 50 MPa, and from ~0.2 to 0.4 at 200 MPa (Gordon and Greenwood, 1971; Tracy and Frost, 1991). Grossular with inclusions of calcite, wollastonite and anorthite is additionally found in the CaTs-clinopyroxene bearing xenoliths, suggesting the following reaction has occured:

$$\overset{calcite}{CaCO_3} + \overset{wollastonite}{CaSiO_3} + \overset{anorthite}{CaAl_2Si_2O_8} = \overset{grossular}{Ca_3Al_2Si_3O_{12}} + CO_2$$

The equilibration temperature of CaTs-clinopyroxene and grossular-andradite-bearing exoskarn xenoliths is estimated as 900-950°C based on experimental data (Huckenholz *et al.*, 1974). Reactions involving these phases were further investigated using Theriak-Domino software (build date 3-1-2012, de Capitani and Petrakakis, 2010) using calculated whole-rock compositions in the system Si-Al-Fe-Mg-Ca-C. An upper limit of temperature for the exoskarn xenoliths is ~910°C at 100 MPa, which represents the limit of garnet stability (Figure 3.13). Garnet reacts out just after melilite becomes stable at ~900°C. Exoskarn type A xenoliths contain abundant garnet and trace amounts of gehlenite, constraining the temperature to this narrow field between 900 and 910°C. The calculated high (30 mol%) CaTs contents at the melilite-in boundary are in agreement with the high (up to 38 mol%) CaTs contents observed in these xenoliths, as are modelled gehlenite contents (>70 mol%) compared to the observed

ones (74-94 mol%). The mineral assemblage of the exoskarn type B xenolith is constrained by a slightly lower maximum temperature as garnet becomes unstable at 860°C (Figure (3.13). A minimum temperature estimate is given as ~780°C from high clinopyroxene CaTs component (22-39 mol%). Conditions are further constrained to $a_{CO2} < 0.5$ for both xenolith types by the absence of meionite and calcite. The results closely match the temperatures from previously cited experimental studies. These temperature estimates are similar to those estimated for the magmatic skarn xenoliths by thermobarometry.

In summary, the comparison with experimental studies and results from modelling indicate exoskarn formation temperatures up to ~910°C, with a lower limit at around 780°C for xenoliths with CaTs clinopyroxene and 510°C for xenoliths without CaTs clinopyroxene. There is no evidence for low temperature retrograde overprint, and these temperatures overlap the temperatures estimates for the magmatic skarn xenoliths (~850°C). These temperature estimates extending to as low as 510°C, combined with the petrological differences described above, indicates a metasomatic origin for the exoskarn xenoliths instead of a magmatic crystallisation for the magmatic skarn/endoskarn xenoliths.

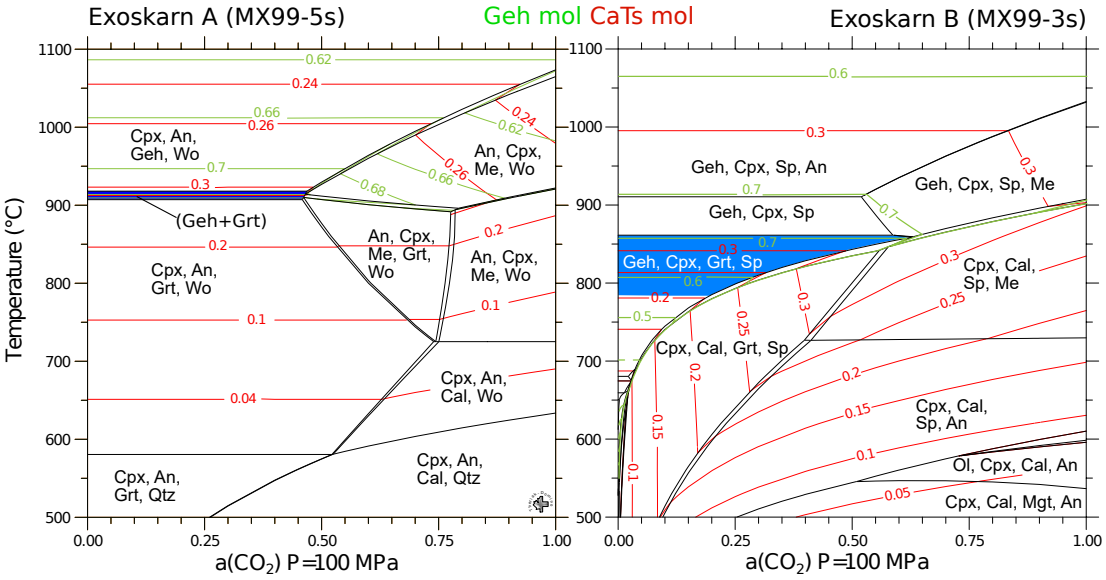


*Figure 3.13: Theriak-Domino (de Capitani and Petrakakis, 2010) T-$XCO_2$ modelling of exoskarn xenoliths. Isobaric sections at 100 MPa. Green contours show the gehlenite mole fraction. Red contours show the CaTs mole fractions. The exoskarn A xenolith (MX99-5s) formed in a narrow temperature range between ~900 to 910°C, and $XCO_2$ < 0.5. The exoskarn B xenolith (MX99-3s) mineral assemblage records temperatures between 680 and 860°C at a $XCO_2$ <~ 0.5. Abbreviations as in Table 3.2. Additional abbreviations: Grt - garnet (andradite-grossular), Me - meionite, Ol - olivine*

**Oxygen Fugacity**

Estimates of oxygen fugacity ($fO_2$) are difficult due to the lack of mineral assemblages commonly used to determine this variable. A first order estimate is obtained from the presence of magnetite in magmatic skarn xenoliths compared to hematite in the exoskarn xenoliths, indicating more oxidising conditions in the latter. Two single crystal clinopyroxene oxybarometers exist that use $Fe^{3+}$ concentrations in clinopyroxene to estimate oxygen fugacity (Cortés *et al.*, 2006; Simakin *et al.*, 2012). Although $Fe^{3+}$ concentrations in clinopyroxenes calculated by stoichiometry (e.g. Lindsley, 1983; Droop, 1987) have been shown in some studies to have a weak correlation to measured clinopyroxene $Fe^{3+}$ concentrations (e.g. Sobolev *et al.*, 1999), a positive correlation between clinopyroxene $Fe^{3+}/Fe^{total}$ and $fO_2$ has been demonstrated from experimental data by Cortés *et al.* (2006) and Simakin *et al.* (2012). When taking a much larger dataset (the Library of Experimental Phase Relations, Hirschmann *et al.*, 2008), with high $fO_2$ experiments such as those from Mollo and Vona (2014) and Sugawara (2001) and normalise in the data to the NNO (nickel-nickel oxide) buffer (c.f. Cortés *et al.*, 2006) using buffer equations from Frost (1991), then a broad positive correlation is still observed, although with a large scatter ($R^2$=0.44). $Fe^{3+}/Fe_{total}$ falls short of unity at an $fO_2$ of air, and all Fe is $Fe^{2+}$ at ~ΔNNO-2. When applied to this large experimental dataset, the oxybarometer of Cortés *et al.* (2006) strongly overestimates $fO_2$ conditions, whilst Simakin *et al.* (2012) fails to recover experiments performed in air (Figure 3.14).

We use a selection of data from experiments that span a wide fO2 range to calibrate a new oxybarometer that recovers high fO2 conditions more accurately. We use the datasets of Whitaker *et al.* (2007), Freise *et al.* (2009), Feig *et al.* (2006), Feig *et al.* (2010), and Mollo and Vona (2014) (excluding Mollo and Vona's relatively high $Fe^{3+}/Fe_{total}$ ΔNNO experiments). This calibration dataset spans a $fO_2$ between ΔNNO-5 to air, temperatures between 900 to 1280°C, 0 to 5 wt% $H_2O$, and 50-68 wt% $SiO_2$ and has a high coefficient of determination ($R^2$ = 0.80). Although the dataset of Sugawara (2001) spans the widest $fO_2$ range known to the authors (~13 log units), calculated $Fe^3/Fe_{total}$ values have larger scatter than those from other datasets, therefore we exclude these from the regression. Additionally, although $Al^{IV}$ increases in clinopyroxene with increasing $fO_2$ (e.g. Mollo and Vona, 2014), adding $Al^{IV}$ to the models shows no significant improvement on the model, therefore we only use $Fe^3/Fe_{total}$ for prediction. There is also no significant improvement in $R^2$ or the standard error when using a polynomial fit over a linear model, however we use a polynomial fit to marginally improve the estimates at low $fO_2$, as was shown by Simakin *et al.* (2012). We additionally considered constructing a

similar oxybarometer based on $Fe^{3+}$ in garnet as $Fe^{3+}$ can be estimated accurately for garnet (Arai, 2010), however there is an insufficient range of oxygen fugacity controlled experiments in the Library of Experimental Phase Relations (LEPR Hirschmann *et al.*, 2008) database to attempt building a similar single crystal oxybarometer for garnet.

For testing, we filtered the entire experimental database to clinopyroxenes equilibrated $<$ 1 GPa, with Si a.p.f.u. $< 2$, Ca $> 0.5$ a.p.f.u., cation totals between 3.98 and 4.1, and $Na_2O$ $< 1$ wt%. Our models recover the calibration dataset with a residual standard error of 1.5 log units, the global database and additional experimental data to 1.8 log units, compared to 2.1 for Cortés *et al.* (2006) and Simakin *et al.* (2012). The improvements in the error are small, in part due to a lack of high $fO_2$ experiments and potential variable data quality of the individual experiments in the LEPR database. However, the accuracy at high $fO_2$ is improved, which is most relevant to our Merapi xenoliths. We obtain the following equation:

$$\Delta NNO = 22.705\left(\frac{Fe^{3+}}{\sum Fe}\right)^3 - 32.400\left(\frac{Fe^{3+}}{\sum Fe}\right)^2 + 21.799\left(\frac{Fe^{3+}}{\sum Fe}\right) - 3.066$$

where $Fe^{3+}$ and $\sum$Fe are Fe a.p.f.u. estimated from stoichiometry (e.g. Lindsley, 1983; Droop, 1987) and ΔNNO is the deviation from the nickel nickel oxide oxygen fugacity buffer in log units.

Application of our oxybarometric model shows a wide spread of $fO_2$ values for the xenoliths (Figure 3.15A). Magmatic skarn xenolith clinopyroxenes at the lava contact zone R1 and in zones R2, R3 and R4, have values similar to the magmatic values both predicted by our model and published estimates (ΔNNO-0.2 to +1.6 Gertisser, 2001; Erdmann *et al.*, 2014). Touching pyrrhotite and anhydrite crystals in zone R2 in a small subset of magmatic skarn xenolith samples additionally indicate a near-magmatic $fO_2$ range between ΔNNO+0.5 to +2.5 (Luhr, 2008; Parat *et al.*, 2011), consistent with other estimates. The R3b zone in sample MX1 records higher oxygen fugacity conditions than the CaTs clinopyroxene + garnet absent samples, at ΔNNO $>$ +5. Xenolith core clinopyroxenes are formed through a large range of oxygen fugacity conditions. The higher values come from the CaTs-rich clinopyroxene cores of sample CS16 (Figure 3.15B). Anhydrite crystals within these clinopyroxene cores (stable at $>$ ΔNNO+1 Carroll and Rutherford, 1987) provide further evidence for a relatively high $fO_2$ during early clinopyroxene formation. Exoskarn xenolith clinopyroxene indicates formation under higher $fO_2$ than magmatic skarn xenoliths, approaching that of air (~ΔNNO + 8). While exoskarn type A xenoliths record a large range from ΔNNO -1 to +8, the exoskarn type B xenolith uniquely records conditions of exclusively $>$ ΔNNO + 5. The high $fO_2$ conditions recorded in the exoskarns are similar to that recorded in zone R3b of magmatic skarn xenolith MX1.

High $fO_2$ in skarn systems is a result of $CO_2$ release from carbonate, and this $CO_2$ can impose a $fO_2$ equal to or greater than the HM buffer (e.g. Nicholls, 1971b; Wenzel *et al.*, 2002). The magnitude of $fO_2$ increase is proportional to the freedom $CO_2$ has to leave the system. An open system continuous flux of $CO_2$ increases $fO_2$ higher than that of a closed system (Ganino *et al.*, 2008). The generally higher $fO_2$ observed in the exoskarn xenoliths may thus be a result of prolonged open system flux of $CO_2$, whereas the syn-magmatic magmatic skarn xenoliths were rapidly processed within the magma. Magmatic skarn xenolith zone R3b however records a high $fO_2$, comparable to the exoskarns, and additionally mineral phases in there, such as clinopyroxene, compositionally overlap exoskarn mineral compositions (Figure 3.8). These compositions may be in part due to a lack of glass in this region of the magmatic skarn xenolith, restricting $SiO_2$ availability, and producing as a result silica-undersaturated mineral compositions such as CaTs clinopyroxene.

### 3.6.3 Xenolith Petrogenesis

#### Protolith

An absence of Mg-rich skarn minerals within the xenoliths (olivine, periclase, merwenite, åkermanite) and the abundance of wollastonite instead suggests a calcite-limestone protolith for the xenoliths. The Merapi xenoliths do not match any mineral assemblages produced during magma-dolomite interaction experiments, instead they closely resemble the results of magma-limestone experiments (e.g Zarayskiy *et al.*, 1987: wollastonite, clinopyroxene, garnet). Electron microprobe analyses of calcites [Whitley *et al.* (2019); Chapter 4] are pure calcites with $<0.2$ wt% MgO + FeO + SrO, which additionally indicates a pure limestone protolith in the absence of Mg-rich skarn minerals. Furthermore, local carbonate sampled from Parangtritis (50 km south of Merapi) is limestone. The progressive chemical zonation within the xenoliths from "magmatic" to calcic compositions (Figure 3.6) shows that the Mg-Fe-Al-bearing phases source these elements from the host magma, not from a dolomite or marl.

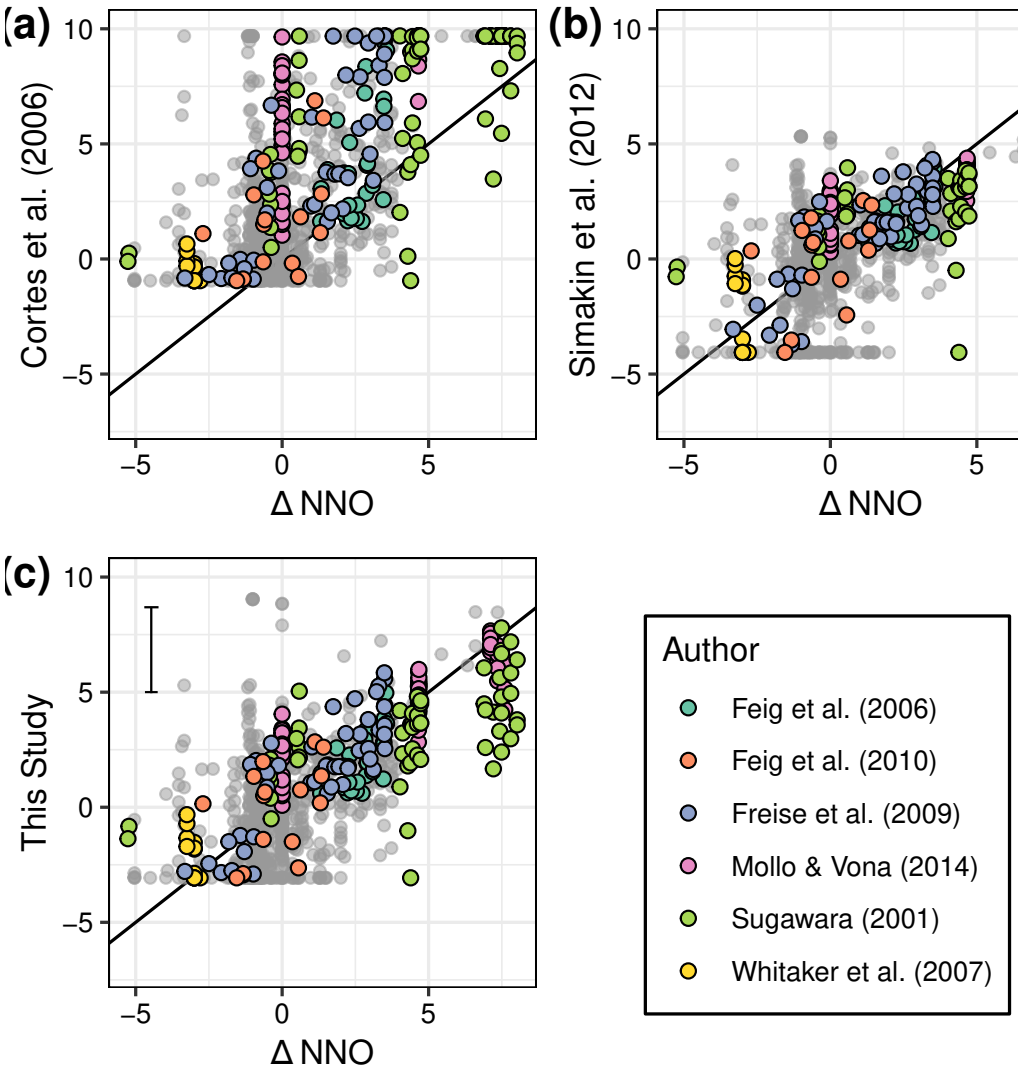


*Figure 3.14: Clinopyroxene-only single crystal oxybarometer model testing. Experiments used for the calibration of the new oxybarometer are highlighted (Feig* et al.*, 2006, 2010; Berndt* et al.*, 2005; Whitaker* et al.*, 2007; Mollo and Vona, 2014). Sugawara (2001)'s experiments which cover 13 log units, and the results of applying the oxybarometers to the filtered Library of Experimental Phase Relations (LEPR Hirschmann* et al.*, 2008) are also shown. A) Results of the Cortés* et al. *(2006) oxybarometer applied to the experimental clinopyroxenes. B) Results of the Simakin* et al. *(2012) oxybarometer applied to the experimental clinopyroxenes. C) Results of the model calibrated in this study applied to the experimental clinopyroxenes. The model error is shown in the top left.*

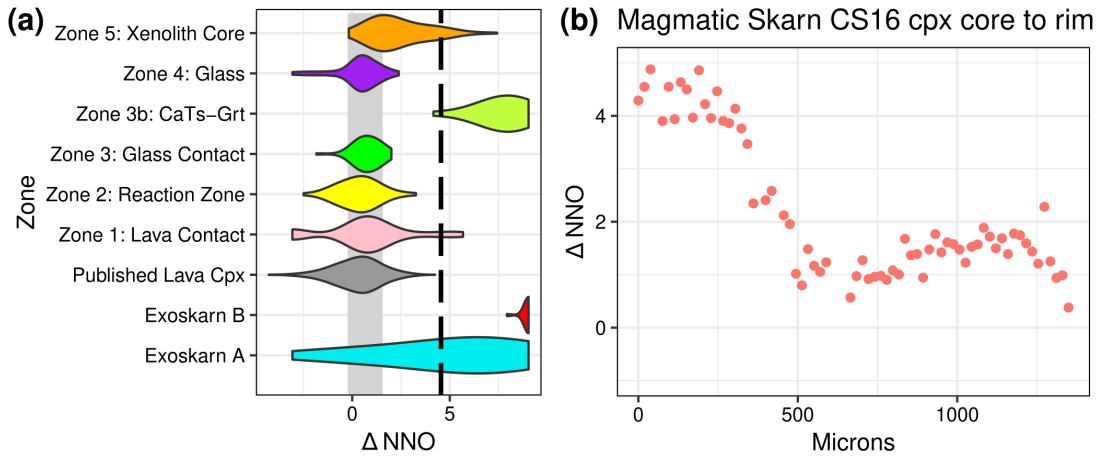


*Figure 3.15:* $fO_2$ *estimates from clinopyroxenes across all zones and traverses. A) Violin density plots of oxygen fugacity estimates for xenolith clinopyroxenes. The model error has been applied as the smoothing bandwidth. The light grey field shows published estimates of Merapi magma* $fO_2$ *from other independent methods (ΔNNO -0.2 to 1.6. Gertisser, 2001; Erdmann* et al.*, 2014). Application of our model to the literature clinopyroxene dataset detailed in Figure 3.8 is shown for comparison to past literature estimates. The solid dashed line is the magnetite-hematite oxygen fugacity buffer. The results show xenolith rims (zones R1-3) formed in* $fO_2$ *similar to magmatic conditions, whilst the cores and exoskarn xenoliths formed at much higher* $fO_2$*, up to that of air. B) Results of application of the oxybarometer to the core to rim calculated* $fO_2$ *traverse of the same clinopyroxene from sample CS16 as shown in Figure 3.8E. The results show an initial period of high fO2 during initial clinopyroxene formation and vigorous carbonate-magma interaction, then a progressive decline as the carbonate-contaminated melt precipitates mineral phases and* $CO_2$ *migrates from the reaction zone.*

### Magmatic Skarn Xenoliths

The abundance of Ca-rich melt inclusions and Ca-rich groundmass glass (Figure 3.4) indicate crystallisation of the main skarn mineralogy of clinopyroxene, plagioclase and wollastonite from a Ca-contaminated magmatic melt, produced from dissolution of the carbonate protolith (Figure 3.10) (c.f. Deegan *et al.*, 2010). Calcic melt inclusions and matrix glasses were also described from volcanic products of the 2010 eruption of Merapi (Borisova *et al.*, 2013). Thermodynamic modelling suggests formation of Ca-rich melts via a peritectic reaction of grossular-bearing calc-silicate material with the magma (Borisova *et al.*, 2016). These Ca-rich melt inclusions are spread randomly throughout their host crystals, or less commonly, along crystal growth zones, showing a primary origin (Roedder, 1984; Goldstein, 2003). Clinopyroxene compositions in these xenoliths are compositionally distinct from those in the exoskarn xenoliths, most notably those from the glass zone R4 (Figure 3.8), supporting formation from the Ca-rich melt instead of an origin as incorporated xenocrysts from partially melted exoskarns. Fe-rich ferro-bustamite growths on some wollastonite crystals is also consistent with crystallisation from this melt, as the

glass and core zones are characterised by FeO-enrichment (Figures 3.7, 3.8). Melt inclusions in wollastonite are not exclusively comprising CaO and $SiO_2$, but also contain other major element oxides such as $K_2O$, which can only be derived from the magmatic melt as there no K-bearing phases found in any of the xenoliths studied. The composition of these melt inclusions cannot be explained by dissolution of wollastonite but supports the idea that wollastonite crystallized from a Ca-enriched melt. Experimental work at Merapi has shown the contaminated melt takes up Sr and B from the carbonate protolith (Chadwick *et al.*, 2007; Deegan *et al.*, 2016a).

The arrows in Figure 3.10 show the addition of 10% CaO to the melt, indicating that the melt inclusions record crystallisation from a melt with up to 20% CaO added. The groundmass glasses retain evidence for up to 10% added CaO, after crystallisation of wollastonite and other minerals. Although whole-rock compositions at Merapi are basaltic to basaltic-andesite, the lava groundmass glasses, the melt compositions in contact with the carbonate, and xenolith glasses, are distinctly more felsic (60-76 wt% $SiO_2$). The melt inclusion CaO concentrations observed in our study (Figure 3.10) far exceed (up to 11.3 wt% CaO) those observed in glasses from calcite-saturated dacite-carbonate experiments of Carter and Dasgupta (2016) (<4.3 wt%), confirming their hypothesis that natural systems may be able to assimilate more carbonate than their closed system experiments indicated.

Skarn minerals that contain melt inclusions and show evidence for crystallisation from a carbonate contaminated magmatic melt, instead of through metasomatic transfer, is a rare but increasingly recognised phenomenon (e.g. Fulignati *et al.*, 2001; Gaeta *et al.*, 2009; Di Rocco *et al.*, 2012; Bin and Jin-song, 2016). Homogenisation temperatures of these melt inclusions in the literature (Fulignati *et al.*, 2001; Bin and Jin-song, 2016) indicate temperatures of 860-1200°C, which are in excess of those typically experienced during metasomatic skarn formation in contact metamorphic aureoles (<=800°C; Meinert, 1992), indicating direct interaction between a magmatic melt and carbonate. Trapping of melt inclusions in skarn minerals precipitated from a calcite contaminated quartz diorite melt has been experimentally confirmed (Bin and Jin-song, 2016), and dacite-carbonate interaction experiments (Carter and Dasgupta, 2016) have been shown to crystallise wollastonite, in contrast to producing dominantly Ca-rich melt in experiments with mafic melt compositions (Deegan *et al.*, 2010; Carter and Dasgupta, 2015).

As well as this rare and unique evidence for skarn mineral formation from carbonate contaminated melts, and therefore exoskarn formation by this process, the magmatic skarn xenoliths also provide insights into the morphology and cumulate-forming processes at the wall-rock

contact at Merapi. Carbonate assimilation has been shown to form and/or influence the mineralogy of cumulate assemblages; for example, changes to the mineral chemistry of dunites at the Ioko-Dovyren Intrusion, Russia (Wenzel *et al.*, 2002), formation of clinopyroxenite xenoliths at Nisyros, Greece (Spandler *et al.*, 2012), and olivine+clinopyroxene+spinel cumulate xenoliths at Colli Albani (Gaeta *et al.*, 2009; Di Rocco *et al.*, 2012). Reaction between carbonate and magmatic melt increases the stability of clinopyroxene and in more evolved melts, plagioclase also (e.g. Mollo *et al.*, 2010b). This results in a wallrock grading from a cumulate zone adjacent to the magma body (endoskarn), to skarn assemblages at the limestone contact (exoskarn). Skarn-derived Ca-rich melts are inferred (Wenzel *et al.*, 2002; Gaeta *et al.*, 2009) to be the main source of carbonate components contaminating the magmatic melt. Our magmatic skarn xenoliths are perfect examples of these processes. Zones R1 to R3 comprise the cumulate zone formed under the influence of carbonate assimilation. Similar to the cumulates at Ioko-Dovyren (Wenzel *et al.*, 2002) and Colli Albani (Gaeta *et al.*, 2009), clinopyroxenes and plagioclase in these zones only show relatively subtle variations in mineral chemistry from magmatic-derived mineral compositions that reveal their carbonate contamination origin. The CaO-enriched glass-rich zone R4 captures the carbonate process of the magmatic melt contamination, and the xenolith cores in some samples preserve very rare instances of the actual calcite carbonate melt [see Whitley *et al.* (2019); Chapter 4]. This carbonate melt has since only been inferred to occur during other instances of carbonate assimilation (Wenzel *et al.*, 2002; Barnes *et al.*, 2005; Gaeta *et al.*, 2009), whilst the magmatic skarns at Merapi preserve and demonstrate direct evidence for its existance.

A syn-magmatic origin for these xenoliths, i.e. formation by direct magma-carbonate contact during magmatic events such as eruptive periods, is consistent with the presence of glass and additionally the low pressures of 37-93 MPa (corresponding to <3.5 km) estimated from fluid inclusion barometry. These pressures are similar to some pressure estimates derived from re-equilibrated melt inclusions in magmatic clinopyroxenes at Merapi (Nadeau *et al.*, 2013b; Preece *et al.*, 2014), and they are lower than pressures estimated for the main pre-eruptive magma chamber or reservoir at Merapi (100-400 MPa, corresponding to depths of ~4-15 km; Commer *et al.*, 2006; Chadwick *et al.*, 2013; Costa *et al.*, 2013; Preece *et al.*, 2014; Erdmann *et al.*, 2016; Deegan *et al.*, 2016b). This indicates that the fluid inclusions have re-equilibrated during ascent, or have been formed at very shallow crustal pressures. A lack of 're-equilibration tail' (Hansteen and Klügel, 2008) and no evidence for pressures > 100 MPa in our fluid inclusion dataset suggests re-equilibration is unlikely, and instead suggests formation in small ephemeral

pre-eruptive reservoirs or during magmatic ascent during eruptive periods.

Patchy zoned clinopyroxenes with prominent irregular resorption surfaces (Figure 3.8) show that this syn-magmatic carbonate interaction is a dynamic process, under temporarily variable imposed oxygen fugacity conditions caused by rapid $CO_2$ release (Figure 3.15) (c.f. Mollo *et al.*, 2010b). Variations in the ability of this $CO_2$ to migrate from the reaction site (Ganino *et al.*, 2008; Blythe *et al.*, 2015) may cause the variation in oxygen fugacity across texturally similar samples, and even within xenolith zones. Al, $Fe^{3+}$-rich clinopyroxene cores and andraditic-rich garnet indicate high initial oxygen fugacity conditions (Figures 3.8,3.15; Meinert, 2005; Mollo and Vona, 2014), whilst diopside-rich cores indicate high initial carbonate-derived Ca activity in the melt (Zarayskiy *et al.*, 1987). Increasing $CO_2$ release causes clinopyroxene Fe-enrichment in the mantle and rims (Zarayskiy *et al.*, 1987) to higher than observed in magmatic clinopyroxenes in later stages of xenolith formation (Figure 3.8). Fe is additionally concentrated in plagioclase as An concentrations decrease (Figure 3.7).

Although we propose the magmatic skarn xenoliths reflect crystallisation from a Ca-contaminated melt, it is interesting to note that their mineralogical zonation still bears strong resemblance to contact metamorphic zoned bimetasomatic skarns and experimental reconstructions of these, such as produced during granodiorite-calcite interaction experiments (Zarayskiy *et al.*, 1987). Magmatic skarn xenolith samples with a garnet + CaTs clinopyroxene zone (zone R3b in Figure 3.2) represent the exo/endoskarn transition in natural skarns, where carbonate-derived elements are transferred to the magmatic system (clinopyroxene + plagioclase endoskarns, zones R1-R3). In turn, certain magma-derived elements are transferred to the carbonate protolith forming garnet + wollastonite + Di-Hd/CaTs clinopyroxene exoskarns (zone R3b and the xenolith cores), reflected also in the chemistry of the individual zones (Figure 3.6).

Dissolution of carbonate in high temperature mafic magmatic melts has been experimentally confirmed to operate on the order of hours (Deegan *et al.*, 2010; Jolis *et al.*, 2013), but mineral equilibration is slower (c.f. Carter and Dasgupta, 2016). First order constraints on the timescales of carbonate interaction at Merapi can be tentiatively placed using the growth rate of xenolith mineral phases such as clinopyroxenes. Experimental and measured growth rates for euhedral clinopyroxenes in basaltic to andesitic magmatic systems are in the order of $10^9$ to $10^7$ cm/s (e.g. Kouchi *et al.*, 1983; Simakin *et al.*, 2003; Orlando *et al.*, 2008; Kilgour *et al.*, 2014). Assuming similar growth rates for the clinopyroxenes in the xenoliths, a typical 300 µm clinopyroxene in zone R4, which has an entirely different composition to the Merapi magmatic clinopyroxenes (Figure 3.8) and therefore formed uniquely during magma-carbonate

interaction, could have formed in 3.5 to 347 days. Measurements of the growth rate of skarn formation between granodiorite and calcite, and quartz and brucite marble, in experiments of Zarayskiy *et al.* (1987) indicate similar timescales. Although clinopyroxene growth rates are poorly constrained, especially in magma-carbonate systems, it is conceivable that the xenoliths could have formed on shorter timescales, e.g. in the lead up to and during eruptive periods, such as perhaps the ~ 1 month duration prior to the 2010 eruption (Komorowski *et al.*, 2013; Surono *et al.*, 2012). The associated $CO_2$ release may then be able to influence eruption dynamics (c.f. Troll *et al.*, 2012). Future work utilising diffusive timescales would potentially increase the accuracy of these timescale estimates and aid risk assessment at Merapi.

In summary, we propose that the magmatic skarn xenoliths are syn-magmatic in origin, forming as a result of limestone dissolution into a magmatic melt, from which skarn minerals precipitate (Figure 3.16). Localised changes in oxygen fugacity caused by the $CO_2$ released to the fluid phase influenced the composition of the minerals formed. Variable transfer of Ca from limestone, and magma-derived elements, form zonations similar to those observed in metasomatic skarns, but at above solidus temperatures. The composition of the zones is controlled by element transfer between magma and limestone and the stability and abundance of the major minerals that form in the respective zones. Our evidence of syn-magmatic magma-carbonate interaction is in agreement with previous studies on Merapi magma-carbonate interaction (Deegan *et al.*, 2010, 2016a; Troll *et al.*, 2012), at Vesuvius (Blythe *et al.*, 2015; Jolis *et al.*, 2015) and at Colli Albani (Iacono-Marziano *et al.*, 2007; Freda *et al.*, 2011), which all note the likely very rapid, syn-eruptive timescales of carbonate dissolution and $CO_2$ liberation. If correct, this process has the potential to enhance eruption explosivity due to external $CO_2$ additions.

**Exoskarn Xenoliths**

Exoskarn xenoliths contain dominantly Al+Si+Ca-bearing phases, and $<$ 10 wt% FeO+MgO based on calculated whole rock compositions. Although the high Al could be indicative of a marl protolith, we believe these samples come from a calcite-bearing protolith with input from magmatically derived elements, on the basis of calcite oxygen isotopes showing evidence of interaction with magmatic fluids [Whitley *et al.* (2019); Chapter 4], and the presence of F-Cl-S-rich phases most likely derived from magmatic volatiles.

The exoskarn xenoliths lack the interstitial glass, melt inclusions and mineralogical zonation of the magmatic skarn xenoliths, with only a clinopyroxene ± plagioclase reaction rim at the lava contact. Melt inclusion compositions within these rim clinopyroxenes are indistinguishable from

the lava groundmass glasses (Figure 3.10). The core assemblage (garnet + CaTs clinopyroxene + wollastonite + anorthite ± gehlenite) is distinct from the magmatic skarn xenoliths (wollastonite ± glass ± DiHd clinopyroxene ± garnet ± anorthite). The much higher $fO_2$ conditions recorded in the clinopyroxenes (Figure 3.15) indicate that these xenoliths experienced a longer period of $CO_2$ flushing than the magmatic skarn xenoliths (c.f. Ganino *et al.*, 2008). This, coupled with the distinct mineralogy, a lack of glass and a lack of mineralogical zonation, suggests that the exoskarn xenoliths originate from a contact metamorphic aureole (exoskarn) around the upper crustal Merapi magma reservoir system (Figure 3.16). The dominance of high temperature anhydrous mineral assemblages indicates that they are sourced proximal to the magma reservoir. Contact metamorphic aureoles can be extensive in size (Aarnes *et al.*, 2010), therefore we expect low-temperature distal skarn assemblages to be present at Merapi, but these may not have been frequently sampled during this study, possibly because of the high temperature 'skarn shell' (c.f. Fulignati *et al.*, 2001; Jolis *et al.*, 2015) being overrepresented in our dataset.

The presence of spinel, as observed in one of our samples (MX99-3s), has been noted in several case studies on magma-carbonate interaction (e.g. Wenzel *et al.*, 2002; Gaeta *et al.*, 2009; Spandler *et al.*, 2012). For instance, hercynitic spinel is widespread in skarns from the Italian volcanic provinces. Skarns from the Colli Albani Volcanic District (Italy) contain Al-rich spinel in textural equilibrium with glass, which was interpreted to reflect melting of calcite and mixing of this melt with the host magma (Gaeta *et al.*, 2009). Metasomatic development through leaching was invoked to explain the occurrence of banded forsterite-spinel skarns in ejecta from the 1631 Vesuvius eruption (Pascal *et al.*, 2009). Experimental work on magma-carbonate interaction with andesitic (Carter and Dasgupta, 2016) and basanitic (Conte *et al.*, 2009) magmas also produced aluminous spinel. Clearly, the presence of aluminous spinel is a common characteristic of carbonate assimilation. None of these studies, however, shows the unique texture and association with gehlenite as in sample MX99-3s, and we classify this sample as exoskarn (type B) based on the lack of glass and the mineralogical differences to the more common magmatic skarns at Merapi.

### 3.6.4 Volatiles and Metal Transport

The numerous F-Cl-S phases identified in the xenoliths record evidence of interaction with a magmatic-derived volatile phase (MVP; c.f. Nadeau *et al.*, 2010; Preece *et al.*, 2014) during formation of the xenoliths. Although F-Cl-S-bearing phases indicate the presence of an aqueous fluid, there is no clear evidence of the role of $H_2O$ during xenolith formation. Silicate magma

has a limited capacity to dissolve the excess liberated crustal-derived $CO_2$ and any increase in melt $CO_2$ would strongly reduce the solubility of $H_2O$ [e.g. Tamic2001], increasing the free $H_2O$ available during magma-carbonate interaction. The xenoliths however contain anhydrous mineral assemblages, and fluid inclusions within are two phase liquid $CO_2$ + vapour $CO_2$ (Figure B.2) with only very rare small fluid inclusions containing unidentified daughter crystals. Nonetheless, the presence of water will promote skarn mineral formation (in place of or coupled with $CO_2$ migration from the reaction site), even if not hydrous mineral formation, as excess $CO_2$ in the magma causes the typical wollastonite-forming reaction $SiO_2$ + $CaCO_3$ -> $CaSiO_3$ + $CO_2$ to favour the reactants.

F-Cl-S-bearing phases are found within both magmatic and exoskarn xenoliths, however they are not found in every magmatic skarn xenolith sample. In the magmatic skarn xenoliths, they are found in zone R2 (anhydrite surrounding pyrrhotite ± cubanite), zone R3b (ellestadite) and as interstitial patches the wollastonite-dominant cores. These patches contain cuspidine, fluorite and the wadalite-like mineral, whilst anhydrite, apatite, and cotunnite ($PbCl_2$) are found as accessory phases elsewhere in the cores. Pyrrhotite, cubanite, Fe-oxides and apatite are sometimes found as daughter crystals in melt inclusions. The presence of fluorine-bearing phases in sample MX1 is closely related to calcite with a melt-like texture, consistent with fluorine lowering the melting temperature of calcite (Jago and Gittins, 1991; Gorzkowska *et al.*, 1988a, 1988b; see Whitley *et al.*, 2019 and Chapter 4 for more detail). Chlorine and limited data for F in the Ca-rich xenolith core interstitial glass and melt inclusions do not show elevated concentrations compared to the lavas. This suggests that the volatile-rich minerals are unlikely to have precipitated directly from the melt, like the wollastonite, clinopyroxene and plagioclase, but are instead the result of interaction with this magmatic-derived volatile phase. In sample MX1, the melt-like calcite is in places replaced by the wadalite-like mineral, which retains the calcite texture (Figure 3.4). Instances where garnet is replaced by this wadalite-like phase may be from reaction with magmatic HCl (e.g. Fujita *et al.*, 2001). Calcite additionally reacts with fluorine to form fluorite as distinct crystal phases, and as radial growths around a vesicle touching calcite (Figure 3.4A-B), suggesting fluorine is a key component of the vapour phase.

The exoskarn xenoliths additionally contain phases enriched in magmatic-derived volatiles. For instance, ellestadite is found throughout the xenoliths, and rare pyrrhotite and anhydrite are present in some samples, but the majority of volatile-rich phases (cuspidine, anhydrite, ellestadite, fluorite, spurrite) are concentrated in the reaction rims around residual large calcite crystals. A magmatic fluid source for these mineral phases is evidenced by calcite oxygen

isotopic shifts towards magmatic values [Whitley *et al.* (2019); Chapter 4] and elevated trace element LREE/HREE in these calcites compared to marine limestone (Appendix Figure B.7, Appendix Table B.2).

The presence of the magmatic-derived volatile phase within the xenoliths indicates potential for economic metal mineralisation beneath Merapi and similar carbonate-hosted arc volcanoes in the region. Oxidised silicic calc-alkaline arc intrusions are frequently associated with porphyry Cu, Zn, Pb and Fe deposits (Meinert, 2005). Ubiquitous calc-silicate xenoliths at Merapi evidence skarn formation, and garnet and clinopyroxene compositions in these xenoliths overlap those characteristic of Cu, Zn and Fe skarns (Meinert, 1992). Although these economic metals are rare in our studied xenoliths, our data suggest that ongoing mineralisation may occur at depth beneath Merapi within the upper part of the plumbing system, during the later stages of magmatic evolution at Merapi.

Sulphur-bearing arc magmas are important sources of Cu, and Cu transport has been noted across the Sunda arc (Nadeau *et al.*, 2010, 2013a; Agangi and Reddy, 2016). Globules of Cu-rich sulphide melt are found in the Merapi lavas recording evidence of Cu-rich sulphide melts exsolving from primitive magma, which are later dissolved in the magmatic-derived volatile phase and distributed through more evolved magmas, and potentially into the host-rock system (Nadeau *et al.*, 2010, 2013a). As previously discussed, the xenoliths evidence interaction between this Cu-S-enriched fluid phase and carbonate. In the magmatic skarn xenoliths, Cu is found as cubanite and as a minor constituent in pyrrhotite in zone R2, which are generally surrounded by anhydrite. Disproportionation of $SO_2$ into sulphide and sulphate is a potential mineralisation process in carbonate and calcium-bearing rocks, and can occur in the timescale of hours (Mavrogenes and Blundy, 2017), and may have formed the coexisting pyrrhotite + cubanite + anhydrite in the xenoliths. Within the magmatic skarn xenolith cores, Cu is rare, only found as a cubanite inclusion in a plagioclase hosted melt inclusion, and as a minor constituent in pyrrhotite inclusions within CaTs-rich clinopyroxene cores. The relative abundance of Cu in zone R2 compared to the core (and exoskarn xenoliths) shows limited transfer of the magmatic-derived volatile phase into the xenolith cores, and/or conditions unfavourable for Cu deposition. Oxygen fugacity is estimated to be similar to typical oxidised arc magma conditions in zone R2 ($\sim\Delta$NNO + 1), producing favourable conditions for sulphur transport and deposition (e.g. Hattori, 2018). The higher oxygen fugacity estimated in some xenolith cores by the presence of anhydrite and CaTs clinopyroxene cores ($<=$ $\Delta$NNO + 4) is potentially too high for Cu transfer, as an upper limit to mineralisation at the hematite-magnetite ($\sim\Delta$NNO + 4)

buffer may exist for porphyry copper deposition (Sun *et al.*, 2013). The large volumes of $CO_2$ released during decarbonation of the original carbonate which causes this $fO_2$ increase, combined with magmatic $CO_2$, strongly reduces Cu solubility in the fluid phase (van Hinsberg *et al.*, 2016; Kokh *et al.*, 2017). Vesicles are found within zones proximal to the host lava and the core, suggesting that a high $XCO_2$ in zone R2 may promote the deposition of Cu before it can be transferred fully into the xenolith core. Xenolith formation temperatures are additionally higher than those estimated for the bulk of Cu and Au deposition in copper porphyry systems (starting $< 700$°C and dominantly $< 400$°C) where fluid immiscibility produces coexisting vapour-rich and saline fluid inclusions (Sillitoe, 2010), which are not observed in the xenoliths studied here.

Our model, where carbonate is assimilated into a melt from which skarn minerals precipitate (magmatic skarns), has been discussed as a process occurring in many Chinese Cu-Fe-Au-deposits (e.g. Bin and Jin-song, 2016). The xenoliths of this study demonstrate that Cu-Fe sulphides can be formed during this process, and may be capable, at least in part, of producing metal sulphide deposits. Magnetite, hematite and Fe-enrichment in some silicate phases may additionally indicate iron oxide ore potential. Whilst we only have xenoliths that show Cu deposition proximal to the Merapi magma reservoir (no low temperature hydrous skarn phases observed), Cu deposition may occur at greater distances into the contact aureole. Percolation of a Cu-bearing magmatic volatile phase through the carbonate over a longer period of time, on cooling when large amounts of magmatic fluids are released, has potential to promote sulphide and Fe-oxide deposition, enhancing ore forming potential such as observed in copper porphyry systems (e.g. Landtwing *et al.*, 2005; Sillitoe, 2010).

### 3.6.5 Implications of Carbonate Interaction for the Merapi Magmatic System

#### Xenocryst Cargo

Calc-silicate xenoliths are ubiquitous in Merapi eruptive deposits, showing that magma-carbonate interaction is an on-going process at Merapi. The amount of interaction is debated in the literature, with estimates of mixing up to 40% in some samples on the basis of isotopic modelling (Troll *et al.*, 2013; Borisova *et al.*, 2013, 2016). Although our study cannot elaborate on estimating the volume of carbonate that interacts with Merapi magmas, our data suggests that calc-silicate derived crystals (xenocrysts) may be more difficult to recognise in erupted magmatic deposits than previously appreciated, as we discuss below.

Incorporation of skarn-derived minerals into the Merapi magmatic system has been shown previously (Chadwick *et al.*, 2007; Deegan *et al.*, 2010, 2016b; Borisova *et al.*, 2013, 2016). Chadwick *et al.* (2007) suggested that 6 to 12 % of crystalline material at Merapi may be crustal derived based on elevated $^{87}Sr/^{86}Sr$ plagioclase compositions and distinct major element plagioclase chemistry. Similarly, thermodynamic-geochemical models for the 2010 Merapi eruption are consistent with the incorporation of 18% of crustal calc-silicate material (Borisova *et al.*, 2016). Based on a detailed oxygen isotope study, Borisova *et al.* (2016) were even able to distinguish two stages of magma-crust interaction, resulting in distinct xenocryst plagioclase $\delta^{18}O$ values related to either high-T altered crustal rocks depleted in $^{18}O$ or $^{18}O$-enriched assimilated carbonate material. Our data show that both plagioclase and clinopyroxene compositions are produced during magma carbonate interaction in zones R1 and R2 that completely overlap magmatic compositions in respect to major elements (Figures 3.8, 3.7). These minerals are formed as a result of Ca transfer from carbonate to the melt, such as occurs within endoskarns. Increased stability of clinopyroxene and plagioclase in carbonate contaminated melts has been experimentally confirmed across a range of magmatic compositions (e.g. Iacono-Marziano *et al.*, 2007; Mollo *et al.*, 2010b; Carter and Dasgupta, 2016), and with rhyoliteMELTS (version 1.2; Gualda *et al.*, 2012; Ghiorso, 2016) which successfully reproduced Ca-contaminated xenolith glass and basaltic andesite compositions. Mineral compositions that are distinct from those found in the magma occur from zone R3 to the xenolith core, but to our knowledge, no highly CaTs-enriched, skarn derived clinopyroxenes have yet been detected in the magmatic products. Although Al-rich clinopyroxenes (up to 8 wt%) are discussed in Costa *et al.* (2013), and were attributed to higher pressure magmatic crystallisation, we have found none in our literature data synthesis that compositionally match our specific skarn clinopyroxenes. Clinopyroxene compositions matching zones R3 and R4, which lie on the DiHd join and are volumetrically more abundant, are also exceedingly rare in the lavas, with only 3 out of 431 analyses reported in Preece (2014) overlapping these compositions. A lack of these compositions may be due to a combination of a volumetrically smaller amount of 'exotic' compositions in the xenolith cores compared to magmatic-type compositions in the xenolith endoskarn rims. Alternatively, dissolution into the magma, and/or re-equilibration with the magma might also be an option. Indeed, Carter and Dasgupta (2016) showed that in carbonate assimilation experiments, within 48 hours, initially compositionally variable clinopyroxenes had equilibrated to a diopsidic composition. Some crystals that are a result of magma-carbonate interaction may therefore be 'cryptic' and distinguishable from magmatic crystals only on the basis of their isotope or trace

element chemistry. Another consequence of this finding is that clinopyroxene thermobarometry may include carbonate-interaction pressures and temperatures in their output. Although oxygen isotope evidence for magma-carbonate interaction in clinopyroxene shows limited crustal additions to the bulk of the crystals (Deegan *et al.*, 2016b), analyses of other *in situ* isotopic systems such as Sr (Chadwick *et al.*, 2007) and oxygen in plagioclase (Borisova *et al.*, 2016) have demonstrated the presence of xenocrysts and contaminated zones, consistent with the usually shallow crystallisation of intermediate plagioclase (e.g. Chadwick *et al.*, 2013). Whilst our plagioclase data for the glass-rich zone R4 have high-FeO that overlaps some literature values for plagioclase in lavas, and therefore may suggest that high-FeO plagioclase in lavas might be xenocrystic, this is more likely to be a result of disequilibria due to quenching of the xenolith glass. For example, FeO in plagioclase increases with cooling rate, producing plagioclase with up to 2.33 wt% FeO in 15°C/min experiments (Mollo *et al.*, 2011). The zone R4 plagioclase crystals contain up to 1.7 wt% FeO, and similarly wollastonite crystals in zone R4 have thin Fe-rich ferro-bustamite overgrowths, indicating that cooling rate may have the more pronounced impact on Fe-rich mineral rims in the xenoliths.

**Magma Composition**

Much of the experimental work on magma-carbonate interaction focuses on reproducing the highly potassic, silica-undersaturated compositions erupted at e.g. Vesuvius and Colli Albani (e.g. Iacono-Marziano *et al.*, 2007; Mollo *et al.*, 2010b; Jolis *et al.*, 2013). High-K compositions are observed at Merapi, and there is some variation in K between the Javanese volcanoes that may be attributed to carbonate assimilation, however this does not have a dominant control on major element evolution (Handley *et al.*, 2014). Strong silica-undersaturation from carbonate assimilation in Italian volcanoes is a result of the increased stability of clinopyroxene taking up $SiO_2$, coupled with the redissolution of olivine, which drives melts towards silica undersaturation (e.g. Mollo *et al.*, 2010b). Recent Merapi lava whole rock compositions range from ~50 to 68 wt% $SiO_2$, and the interstitial glasses within these record pre-eruptive melts with 60-75 wt% $SiO_2$ (Figure 3.10). These would not be driven to silica-undersaturation by an increase in clinopyroxene or plagioclase precipitation due to these minerals containing lower $SiO_2$ concentrations. Whole-rock compositions instead traverse a differentiation vector defined by that of the typical arc magma plagioclase and clinopyroxene differentiation assemblage (Figure 3.10, c.f. Handley *et al.*, 2014), although at a slightly elevated CaO. It is interesting to note however, that while the overall major element chemistry at Merapi is not dominated by a

carbonate assimilation signature, very rare, highly localised phonolitic leucite-bearing silica-undersaturated melts have been identified in some Merapi calc-silicate xenoliths by Brouwer (1928, 1945). These demonstrate that these exotic compositions can be formed at Merapi during very localised periods of extremely high levels of carbonate interaction, but the quantities of melt generated are volumetrically negligible.

In addition to the effects of crystal fractionation on the major element chemistry, lower temperature, high-$SiO_2$ melts such as those represented by the groundmass lava glass compositions at Merapi have a lower capacity to assimilate material than hotter mafic melts (e.g. Wenzel *et al.*, 2002; Barnes *et al.*, 2005; Gaeta *et al.*, 2009; Jolis *et al.*, 2015), and instead favour formation of skarn minerals (e.g. wollastonite) that cause only small apparent changes to melt compositions (Spandler *et al.*, 2012; Carter and Dasgupta, 2016). These minerals may become trapped as a cumulate or exoskarn layer (see above, e.g. Gaeta *et al.*, 2009; Di Rocco *et al.*, 2012) at the wall rock contact, and only have a small impact on the melt composition during skarn recycling and xenocryst incorporation (e.g. Di Rocco *et al.*, 2012; Jolis *et al.*, 2015). A discrepancy between limited whole-rock major element evidence for magma-carbonate interaction (c.f. Costa *et al.*, 2013; Handley *et al.*, 2014) and high levels of interaction recorded in multiple isotope systems (Chadwick *et al.*, 2007; Troll *et al.*, 2013; Borisova *et al.*, 2013, 2016), may thus be due a combination of the lower capacity of the magmatic melt to incorporate carbonate material, and a relatively limited mobility of Ca in these relatively low temperature, high $SiO_2$ Merapi pre-eruptive melts compared to the higher mobilities usually displayed by isotopes of trace elements (e.g. Sr, B). This decoupling has been observed in high temperature (1200°C) carbonate interaction experiments (Deegan *et al.*, 2010, 2016a; Blythe *et al.*, 2015). Moreover, quantitative modelling of magma-carbonate interaction demonstrated that low-to-moderate amounts of carbonate assimilation cause only limited changes to the major element chemistry of the magma (Spandler *et al.*, 2012). Whereas there is no doubt that magma-carbonate interaction is an important petrogenetic process at Merapi, the degree of major element compositional change may not be prominent enough to distinguish the modified magma from the overall spectrum of Merapi magmas (c.f. Spandler *et al.*, 2012).

#### Merapi Volatile Budget

Carbonate assimilation at Merapi has been shown to have a strong impact on the composition of the gases released to the atmosphere. Release of crustal derived $CO_2$ has been proposed by identification of elevated $\delta^{13}C$ and He isotopes in fumarole gases (Troll *et al.*, 2012, 2013

and references therein). An increase in these isotopic tracers has additionally been observed during eruptive periods, attributed to a positive feedback loop of wall rock fracturing during eruption, and increased $CO_2$ liberation from magma-carbonate interaction on this increased surface area (Deegan *et al.*, 2011; Troll *et al.*, 2012; Carr *et al.*, 2018). Our work shows that the magmatic skarn xenoliths may represent snapshots of this syn-magmatic carbonate interaction, and therefore eruptive flare-ups could potentially be influenced by temporal increases in carbonate interaction (c.f. Troll *et al.*, 2012; Carr *et al.*, 2018). The 2010 eruption was preceeded by an influx of hotter volatile-rich magma that exceeded the capacity of the shallow storage system (Costa *et al.*, 2013; Carr *et al.*, 2020). This increased heat and volume would cause both increased thermal decarbonation, and fracturing, that could penetrate deeper into the bedrock. A positive feedback occurs, where increased decarbonation promotes a decrease in water solubility, producing bubbles and more explosive behaviour, promoting more fracturing, resulting in temporal increases in carbonate interaction (Troll *et al.*, 2012, p.:@Carr2018; Carr *et al.*, 2020). Dome instability from weakened fractured/altered wall-rock could also produce magmatic overpressure, increasing fracturing and surface area of the carbonate available to react (Mollo *et al.*, 2012). In the magmatic skarn xenoliths, residual calcite is only present in trace quantities, and the $\delta^{13}C$ composition of these calcites are exceptionally negative (down to -29 ‰), demonstrating extremely efficient decarbonation in the magmatic skarn xenoliths [Whitley *et al.* (2019); Chapter 4]. It is unlikely that this is exclusive to Merapi, and indeed, temporal increases in carbonate assimilation increasing explosivity has been proposed elsewhere e.g. at Colli Albani (Freda *et al.*, 2011) and Vesuvius (Jolis *et al.*, 2015). $CO_2$ release is not restricted to just syn-magmatic carbonate interaction, and decarbonation reactions in the exoskarn additionally add to the $CO_2$ budget. The current $CO_2$ output at Merapi compared to estimated contact metamorphic aureole volumes around a Merapi reservoir demonstrate that this $CO_2$ release is rapid, on the timescales of just thousands of years [Whitley *et al.* (2019); Chapter 4]. When considering volcanoes that interacted with crustal carbonate, at present and in the geological past (c.f. Mason *et al.*, 2017; Carter and Dasgupta, 2018; Chu *et al.*, 2019), $CO_2$ release such as evidenced at Merapi may have the potential to modify long term climatic trends.

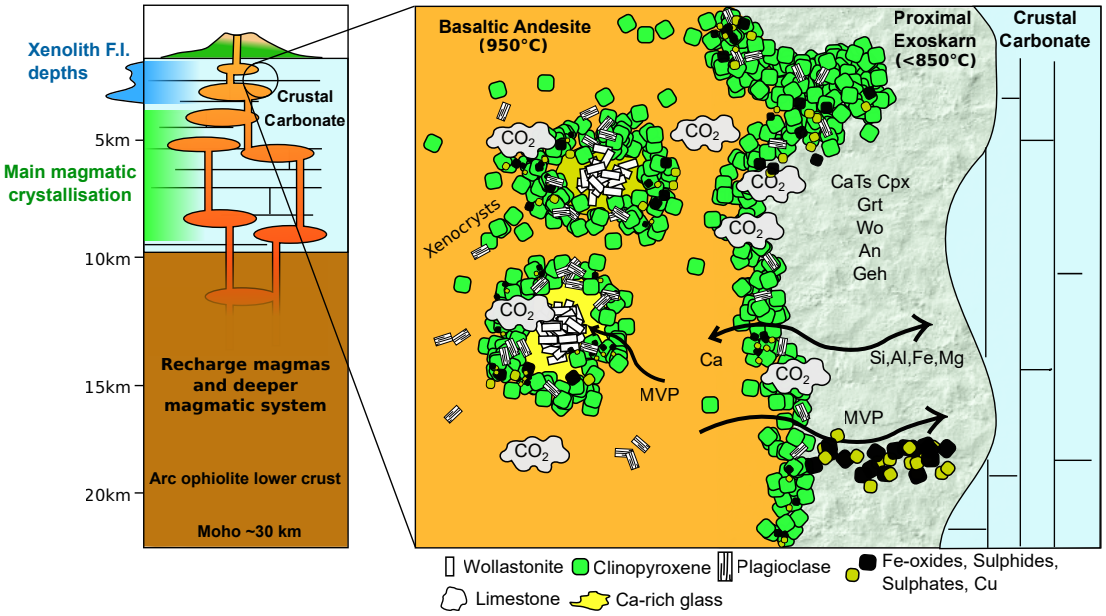


*Figure 3.16: Summary of the processes occurring during magma carbonate interaction at Merapi. Carbonate is rapidly digested forming a Ca-rich contaminated melt, from which wollastonite and other phases precipitate, forming the magmatic skarn xenoliths. Proximal to the magmatic melt, clinopyroxene and plagioclase form from Ca transfer to the melt from the carbonate. The abundance of melt in the xenoliths allows disaggregation and disperses xenolith crystals into the magma (e.g. Deegan* et al.*, 2010). The magmatic volatile phase (MVP c.f. Nadeau* et al.*, 2010; Preece* et al.*, 2014) infiltrates the xenoliths forming rare halogen and sulphur-bearing minerals. At the wall-rock contact, abundant clinopyroxene forms, partially insulating the carbonate and skarn. Magma-derived elements are transferred to the wall-rock, influenced by the increasing oxygen fugacity caused by $CO_2$ flushing, forming the exoskarn mineralogy. Regions of main magma crystallisation from Chadwick* et al. *(2013), Preece* et al. *(2014) and Erdmann* et al. *(2016). Moho from Wölbern and Rümpker (2016). Description of the lower crust from van Bemmelen (1949).*

## 3.7 Conclusions

A detailed mineralogical, petrological and geochemical study of a range of calc-silicate (skarn-type) xenoliths from Merapi volcano shows that two distinct types of xenoliths are present: 1) magmatic skarns, that are formed from eruptive timescale syn-magmatic magma-carbonate interaction that preserves abundant CaO-rich glass, and 2) fragments of the metasomatic exoskarn aureole around the Merapi magma reservoir. Thermobarometry indicates that the CaO-rich glass-bearing magmatic skarn xenoliths formed at ~850°C. Fluid inclusions record shallow pressures of $<$ 100 MPa, corresponding to depths $<$ 3.7 km. These xenoliths are the physical representation of carbonate entrained during eruptive events, which we interpret to increase eruption intensity during rapid decarbonation. The disaggregated nature of some of these xenoliths, and the similarity in the geochemistry of lava and some xenolith minerals, indicate that

skarn-derived xenocrysts may be difficult to recognise at Merapi. Experimental comparisons and thermodynamic modelling indicates formation temperatures of 510 to 910°C for the range of mineralogies shown in the metasomatic exoskarn xenoliths. A newly developed oxybarometric model indicates a wide range of $fO_2$ conditions during xenolith formation. Magmatic skarn xenoliths are predominantly formed around the NNO buffer, similar to magmatic values, whilst the cores of these xenoliths can reach values above the HM buffer in the presence of an increased amount of newly released $CO_2$. Protracted periods of $CO_2$ flushing caused predominantly conditions above the NNO buffer during exoskarn formation, possibly approaching the oxygen fugacity of air. High $fO_2$ in both xenolith types promoted formation of andradite garnet and highly aluminous clinopyroxene compositions. A magmatic volatile phase present at Merapi reacts with the xenoliths to form rare Ca-Al-Si-F-Cl phases such as cuspidine, ellestadite and wadalite-like phases. Evidence of xenolith formation during eruptive timescales demonstrates that magma-carbonate interaction and subsequent $CO_2$ release could affect eruption intensity, as recently suggested for Merapi and similar carbonate-hosted volcanoes elsewhere. In addition, copper and occasionally Fe (and likely other associated elements of economic value such as Zn) are carried within this fluid and are found concentrated in the outer shells of some of the xenoliths, indicating potential for ongoing skarn-type mineralisation at depth beneath Merapi and similar volcanoes within carbonate basement worldwide.

# Chapter 4

# Crustal $CO_2$ degassing recorded in stable isotopes of calcites in Merapi calc-silicate xenoliths.

This chapter has been published in its entirety in Nature *Scientific reports*.

Whitley, S., Gertisser, R., Halama, R., Preece, K., Troll, V.R. and Deegan, F.M., 2019. Crustal $CO_2$ contribution to subduction zone degassing recorded through calc-silicate xenoliths in arc lavas. *Scientific Reports*, 9(1), p.8803. https://doi.org/10.1038/s41598-019-44929-2

The manuscript was written by myself with input from all authors. Gertisser, Preece and Troll collected the samples. I performed the SIMS analyses with the assistance of the EIMF. I performed the electron microprobe analyses, with a small dataset of additional analyses from earlier work provided by Gertisser (as previously described in Chapter 3). Halama helped with the isotopic modelling. This work was funded by NERC grant IMF620/0517 to Gertisser.

## 4.1 Introduction

Crustal magma-carbonate interaction has been suggested as a process that may dominate the $CO_2$ output in several volcanic arcs (Aiuppa *et al.*, 2017; Mason *et al.*, 2017) and a possible source of magmatic carbonate melts (Lentz, 1999; Fulignati *et al.*, 2001; Gozzi *et al.*, 2014). Direct evidence for this process often remains elusive, but the occurrence of calc-silicate (skarn) xenoliths in the eruptive products of some active volcanoes (e.g. Vesuvius, Nisyros; Colli Albani, Merapi Fulignati *et al.*, 2004; Chadwick *et al.*, 2007; Di Rocco *et al.*, 2012; Spandler *et al.*, 2012) provide a unique opportunity to study high temperature magma-carbonate interaction, and the subsequent effects on the host magmatic system. Recent work on such xenoliths has additionally linked magma-carbonate interaction to influencing eruptive dynamics via volatile exsolution (Goff *et al.*, 2001; Chadwick *et al.*, 2007; Deegan *et al.*, 2010; Troll *et al.*, 2012), and driving magmatic differentiation trends towards highly desilicated potassic compositions (Daly, 1910; Iacono-Marziano *et al.*, 2008).

Carbon and oxygen isotopes are powerful tracers of fluid-rock interaction processes during contact metamorphism of carbonates, where skarn rocks form via reactions between magmatic fluids and carbonate country rocks (Valley, 1986; Bowman, 1998; Matthews *et al.*, 1996; Fulignati *et al.*, 2005). Sedimentary carbonates are isotopically distinct from mantle-derived igneous rocks (Valley, 1986), allowing for quantification of chemical exchange during magma-carbonate interaction. Decarbonation reactions release $CO_2$ that is enriched in $^{13}C$ and $^{18}O$ into the magmatic system (Chacko *et al.*, 1991), depleting the carbonate protolith in these isotopes, following batch or Rayleigh fractionation trends (Valley, 1986). However, some skarns show additional isotopic modifications that cannot result from equilibrium decarbonation reactions alone, but instead require mixing with magmatic fluids to produce values in near-exchange equilibrium with the adjacent magmatic system (Taylor and Bucher-Nurminen, 1986; Bowman, 1998; Shin and Lee, 2003; Jolis *et al.*, 2015). The degree of decarbonation and $CO_2$ released into the magmatic system and ultimately the atmosphere, and the extent of fluid modification of the isotopic signature, can be quantified utilising coupled carbon and oxygen isotopes. In addition, interaction with meteoric water and secondary alteration can usually be distinguished using this approach (Bowman, 1998).

Merapi is Indonesia's most active volcano, characterised by periods of lava dome growth punctuated by dome failure producing pyroclastic density currents, and intermittent explosive events (Gertisser *et al.*, 2012). Compositionally the eruptive products are restricted to high-K basalt to basaltic andesite (Gertisser *et al.*, 2012). The upper crust underlying Merapi consists

of a 8-11 km thick unit of Cretaceous to Cenozoic limestones, marls and volcaniclastic deposits (van Bemmelen, 1949, Appendix Figure C.1), and is found as thermally metamorphosed xenoliths within the eruptive deposits (Gertisser and Keller, 2003b; Chadwick *et al.*, 2007; Troll *et al.*, 2012, 2013). These xenoliths testify to prevalent magma-carbonate interaction (Chadwick *et al.*, 2007; Troll *et al.*, 2013), a process that is ongoing and occurs at rapid syn-magmatic timescales (Deegan *et al.*, 2010; Troll *et al.*, 2012). Previous work at Merapi has focused on radiogenic ($^{87}Sr/^{86}Sr$) and stable ($\delta^{13}C$, $\delta^{18}O$) isotope analysis of bulk xenoliths and mineral separates of the most abundant calc-silicate mineral phases (wollastonite, diopside)(Gertisser and Keller, 2003b; Chadwick *et al.*, 2007; Troll *et al.*, 2012, 2013), highlighting the significance of crustal contamination in the genesis of Merapi magmas, and a role of magma-carbonate interaction for enhancing eruption explosivity (Troll *et al.*, 2012, 2013; Borisova *et al.*, 2013; Carr *et al.*, 2018). Some of these Merapi xenoliths retain remnant calcite with distinct textural types, which provide an exceptional opportunity to gain novel insights into magma-crustal interaction processes. Our micro-analytical approach allows, for the first time, a detailed assessment of the roles of decarbonation, interaction between carbonates and magmatic fluids, carbonate melt generation, and crustal volatile release. We demonstrate that highly efficient decarbonation of carbonate wallrock at Merapi produces extremely negative calcite $\delta^{13}C$ values during skarn formation in some xenoliths, whereas others bear contrasting evidence of interaction between carbonate and magmatic fluids. This combination of documents fast and highly efficient liberation of crustal $CO_2$ into the atmosphere.

## 4.2 Methods

### 4.2.1 Secondary Ion Mass Spectrometry (SIMS) Analysis

Sample preparation and in-situ isotopic data were acquired at the Edinburgh Ion Microprobe Facility at the University of Edinburgh. The samples were prepared as 3mm micro-drilled thin section cores pressed into indium, preserving their original textural configuration. A calcite standard (UWC-1) was mounted in epoxy and pressed into the centre of each mount. Thin section MX1 was cut into a 1 inch diameter section with the calcite standard mounted into a hole drilled into the centre of the section. To minimise instrumental bias relative to sample position, each core was mounted to ensure all analyses were within 5 mm of the centre of the mount. All samples were polished after pressing and gold coated.

Oxygen isotope data were acquired with a Cameca ims 1270 ion microprobe, using a ~4 nA

primary $^{133}Cs^{+}$ beam. Secondary ions were extracted at 10 kV, and $^{16}O^{-}$ (~4.0 x$10^{9}$ cps) and $^{18}O^{-}$ (~7.0 x$10^{6}$ cps) were monitored simultaneously on dual Faraday cups (L'2 and H'2). Each analysis involved a pre-sputtering time of 60 seconds, followed by automatic secondary beam and entrance slit centering and finally data collection in 10 cycles, amounting to a total count time of 40 seconds.

Carbon isotope data were acquired using a ~4 nA beam. Secondary ions were extracted at 10 kV, and $^{12}C^{-}$ (~1.0 x$10^{7}$ cps) and $^{13}C^{-}$ (~1.0 x$10^{5}$ cps) were monitored on Faraday cup (L'1) and electron multiplier (EMO). Each analysis involved a pre-sputtering time of 60 seconds, followed by automatic secondary beam and entrance slit centering and finally data collection in 40 cycles, amounting to a total count time of 160 seconds.

To correct for instrumental mass fractionation (IMF), all data were normalised to an internal standard (UWC-1 $\delta^{18}O_{SMOW}$ 23.3 ‰, $\delta^{13}C_{PDB}$ -2.14 ‰), which was repeatedly measured throughout the analytical sessions. Analyses were made in blocks of 10 followed by 3 to 5 analyses of the standard. The internal precision of each analysis is +/- 0.02 ‰. The average precision for a typical standard bracket is 0.26 ‰ for oxygen, and 0.70 ‰ for carbon ($2\sigma$). Each pit was imaged using a scanning electron microscope at Keele University following analysis. Analyses from pits that showed irregularities such as fractures, cavities and mineral overlap were discarded. Instrumental bias due to variations in calcite composition were not considered important as calcite non-CaO concentrations of all samples were $<$ 0.30 wt%. All data are reported in standard δ-notation ( $= 1000(\frac{R_{sample}}{R_{standard}} - 1)$ where for example $R = \frac{^{18}O}{^{16}O}$) relative to SMOW for oxygen and PDB for carbon. 69 paired carbon and oxygen isotope analyses were made, and 8 carbon or oxygen isotope analyses where the calcite was too small for two spots. 75 oxygen and 56 carbon isotope standard analyses were made.

## 4.3 Results

### 4.3.1 Petrography of calc-silicate xenoliths and calcite types

Calc-silicate xenoliths are ubiquitous in the studied 1994 to 2010 Merapi dome lavas and can be divided into two groups on the basis of distinct textures and mineralogical assemblages: magmatic skarns and metamorphic exoskarns (c.f. Fulignati *et al.*, 2004); Table 4.1). These xenolith types are discussed in detail in Chapter 3, and are summarised again here. Magmatic skarn xenoliths contain abundant glass that is CaO-enriched (1 to 12 wt%) relative to host lava dacite groundmass glasses, and dominantly comprise wollastonite which contains numerous

CaO-enriched melt inclusions compositionally similar to the contaminated groundmass glass. These wollastonite-hosted melt inclusions and additional Fe-rich growth rims on wollastonite crystals testify to crystallisation from a melt that has assimilated a significant quantity of CaO (c.f. Bin and Jin-song, 2016). These xenoliths typically show a general rim-core zoning sequence (idealised): lava - clinopyroxene - plagioclase + clinopyroxene - clinopyroxene - glass - wollastonite core, with additional glass found in varying quantities in each zone. Vapour-rich $CO_2$ fluid inclusions are common within wollastonite crystals. Metamorphic exoskarn xenoliths are holocrystalline, granular, and primarily composed of Ca-Tschermak's component ($CaAlAlSiO_6$) enriched clinopyroxene (fassaite), wollastonite, plagioclase and grossular-andradite garnet, resembling typical skarn assemblages associated with metasomatic alteration (Meinert, 1992). They lack the magmatic xenolith zoning sequence, having only a rim of clinopyroxene at the lava contact.

*Table 4.1: Phases identified within the magmatic and exoskarn xenoliths at Merapi. See Chapter 3 for more details.*

| Magmatic Skarns | Exoskarns |
|---|---|
| *Rock-Forming Phases* | |
| Wollastonite | Wollastonite |
| Clinopyroxene (diopside-hedenbergite) | Clinopyroxene (Ca-Tschermaks) |
| Anorthite | Anorthite |
| Glass | Grossular-Andradite Garnet |
| | ± Gehlenite |
| | ± Spinel |
| | ± Quartz |
| | ± Calcite |
| *Accessory Phases* | |
| Calcite | |
| Clinopyroxene (Ca-Tschermaks) | Anhydrite |
| Grossular-andradite-schorlomite garnet | Pyrrhotite |
| Wadalite-like phase | Ellestadite |
| Cuspidine | Cuspidine |
| Gehlenite | Spurrite |
| Pyrrhotite | Larnite |
| Cubanite | Xenotime |
| Baryte | Hematite |
| Anhydrite | Monazite |
| Apatite | |
| Ellestadite | |
| Ferro-bustamite | |
| Titanite | |
| Perovskite | |
| Magnetite | |

We distinguish five textural types of calcite across both of these xenolith groups (Figure 4.1). Each textural type represents a specific process, or combination of processes, operating during magma-carbonate interaction, which C-O isotopes provide a means to quantify. Four calcite types are found within the magmatic skarn xenoliths (types A, B, C, D), and two within the exoskarn xenoliths (types D, E). Type D calcites were only analysed in wollastonite in the magmatic skarn xenoliths due to crystal size constraints. Type A calcites consist of rounded globular calcite grains within the glass-rich xenolith textural zone (Figure 4.1A). Type B calcites occur as subhedral crystals (50-100 µm in size) that are found interstitial to wollastonite, and as fractured crystals at vesicle borders within wollastonite-dominant cores (Figure 4.1B). Type C calcites are anhedral interstitial crystals (50-100 µm in size) exhibiting a melt-like, infiltrative texture between wollastonite crystals. They are found as thin interconnected veins with a rim of quartz at the wollastonite contact (Figure 4.1C-D). These veins form rare ~50 µm pools

of calcite, with occasional fluorite crystals nucleating at the edges and around calcite-hosted vesicles. Type D calcites occur as rounded inclusions (<50 µm) in wollastonite and garnet (Figure 4.1E). Type E calcites occur exclusively within exoskarn xenoliths as millimetre-sized crystals with vesiculated reaction rims containing spurrite and sulphur and fluorine-enriched phases (Figure 4.1F). These calcites contain occasional vesicles and trace amounts of phosphates. The rims are anhedral and intermingle with the void-rich reaction rim.

### 4.3.2 Geochemistry of calcite types

The calcites analysed in this study are almost pure $CaCO_3$, with MnO, FeO and MgO < 0.17 wt% across all xenoliths (Table 4.2). By contrast, calcite isotopic compositions cover a large range in $\delta^{13}C$-$\delta^{18}O$ values (Table 4.3, Figure 4.2), with different textural groups being compositionally distinct. Assuming a typical marine carbonate protolith ($\delta^{13}C$ -3 to +3 ‰, $\delta^{18}O$ >25 ‰ (Veizer and Hoefs, 1976)) or local Merapi limestone ($\delta^{13}C$ -5 to -1 ‰, $\delta^{18}O$ +18 to +25 ‰ (Gertisser and Keller, 2003b; Troll *et al.*, 2012, 2013)) as the starting composition, two compositional trends are defined: (1) a trend towards low $\delta^{13}C$-$\delta^{18}O$ compositions, approaching those of bulk xenolith core/rim mineral separates (Troll *et al.*, 2012, 2013), and (2) a trend towards low $\delta^{13}C$ with little $\delta^{18}O$ variation (Figure 4.2). The highest $\delta^{13}C$-$\delta^{18}O$ calcites are type A glass-hosted calcites, forming a compositionally tight cluster with $\delta^{13}C$ between -4.2 and +1.8 ‰, and $\delta^{18}O$ ranging from +21.4 to +24 ‰. Type B interstitial calcites have the largest $\delta^{13}C$ variation, but a restricted $\delta^{18}O$ range ($\delta^{13}C$ -29.3 to -0.6 ‰, $\delta^{18}O$ +20.5 to +25.6 ‰). Type C melt-like calcites have the widest $\delta^{18}O$ variation, between +9.9 and +23.1 ‰, and a large $\delta^{13}C$ variation, ranging from -18.5 to +3.5 ‰. Data for Type D calcite inclusions within wollastonite are few, but show a similar compositional range of $\delta^{13}C$ (-14.9 to -4.4 ‰), and $\delta^{18}O$ (+14.6 to +17.9 ‰) to the type E calcites. Type E-residual calcites in the exoskarn xenoliths, define a tight compositional cluster between $\delta^{13}C$ of -14 to -4.6 ‰ and $\delta^{18}O$ of +13.9 to +19 ‰.

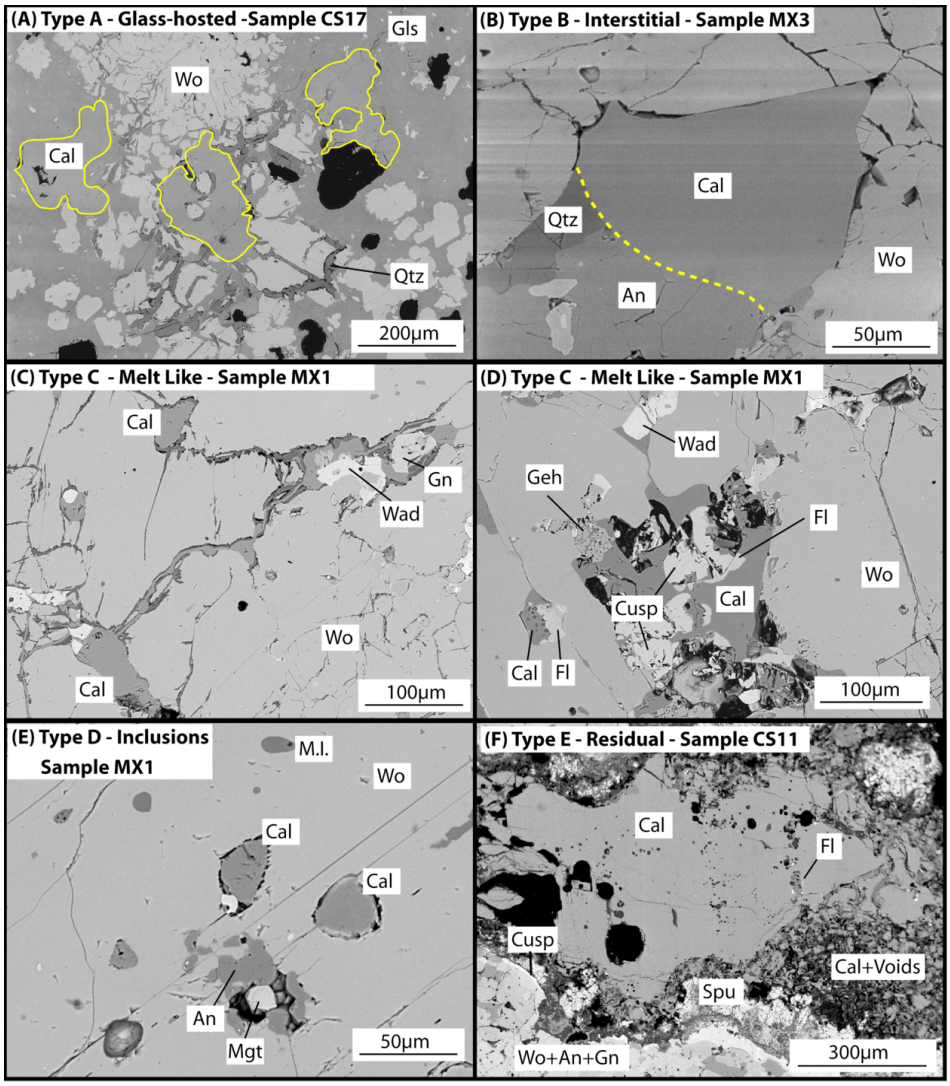


*Figure 4.1: Calcite textural types. Types A-D are from magmatic xenoliths, type E is from exoskarn xenoliths. A) Type A calcites found within the glass band of magmatic skarn xenoliths. Yellow lines highlight the glass-calcite boundary due to poor backscatter contrast. B) Type B interstitial calcite; small crystals within a decussate wollastonite-dominant xenolith core. C) Type C calcite showing pools of calcite joined by veinlets, with garnet and a phase compositionally similar to wadalite ($Ca_{12}Al_{10}Si_4O_{32}Cl_6$) closely associated. D) Type C calcites showing the close association with F bearing phases fluorite, cuspidine ($Ca_4Si_2O_7F_2$) and the wadalite-like phase. E) Type D calcite inclusions within wollastonite. Note the presence of melt inclusions (M.I.) in wollastonite. F) Type E residual calcite showing the zoned reaction rim, with disaggregated calcite and voids, spurrite, then cuspidine and the wollastonite + anorthite + grossular garnet xenolith assemblage. Accessory fluorite is present at some calcite contacts, and very rare micron-sized xenotime and monazite crystals are present within the calcite. Abbreviations: An - anorthite, Cal - calcite, Cusp - cuspidine, Fl - fluorite, Geh - gehlenite, Gls - glass, Mgt - magnetite, M.I. - melt inclusion, Qtz - quartz, Spu - spurrite, Wad - wadalite-like phase, Wo - wollastonite.*

*Table 4.2: Electron microprobe major element analyses of texturally distinct calcite types within the calc-silicate xenoliths. Type A - glass-hosted calcites were not analysed by microprobe, but show negligible concentrations of major elements excluding CaO in SEM-EDS analysis. Results are reported as averages with standard deviation in parentheses.*

| | Type B-Interstitial | Type C-Melt-like | Type D-Inclusions | Type E-Residual |
|---|---|---|---|---|
| wt% | (n=1) | (n=5) | (n=2) | (n=10) |
| FeO | 0.02 | 0.06 (0.04) | 0.17 (0.08) | 0.07 (0.06) |
| MnO | 0 | 0.12 (0.08) | 0.08 (0.18) | 0.12 (0.09) |
| MgO | 0.05 | 0.06 (0.03) | 0.05 (0.01) | 0.05 (0.02) |
| CaO | 58.68 | 55.1 (0.59) | 54.54 (0.17) | 55.48 (0.64) |
| SrO | n.d | 0.02 (0.01) | 0 (0) | 0.06 (0.01) |
| BaO | n.d | 0.01 (0.02) | 0.02 (0.03) | 0.01 (0.01) |
| Total | 58.75 | 55.37 (0.52) | 54.76 (0.25) | 55.79 (0.53) |

*Table 4.3: Summary of C-O isotopic data for the calcite textural types. The full dataset can be found in Appendix Table C.1. 2$\sigma$ errors are typically 0.4 ‰ for oxygen and 0.8 ‰ for carbon.*

| Calcite Type | Xenolith Type | $\delta^{18}O$ (‰) | $\delta^{13}C$ (‰) |
|---|---|---|---|
| A – Glass-hosted | Magmatic | +21.4 to +24.0 | -4.2 to +1.8 |
| B – Interstitial | Magmatic | +20.5 to +25.6 | -29.3 to -0.6 |
| C – Melt-like | Magmatic | +9.9 to +23.1 | -18.5 to +3.5 |
| D – Inclusions | Magmatic | +14.6 to +17.9 | -14.9 to -4.4 |
| E – Residual | Exoskarn | +13.9 to +19.0 | -14 to -4.6 |

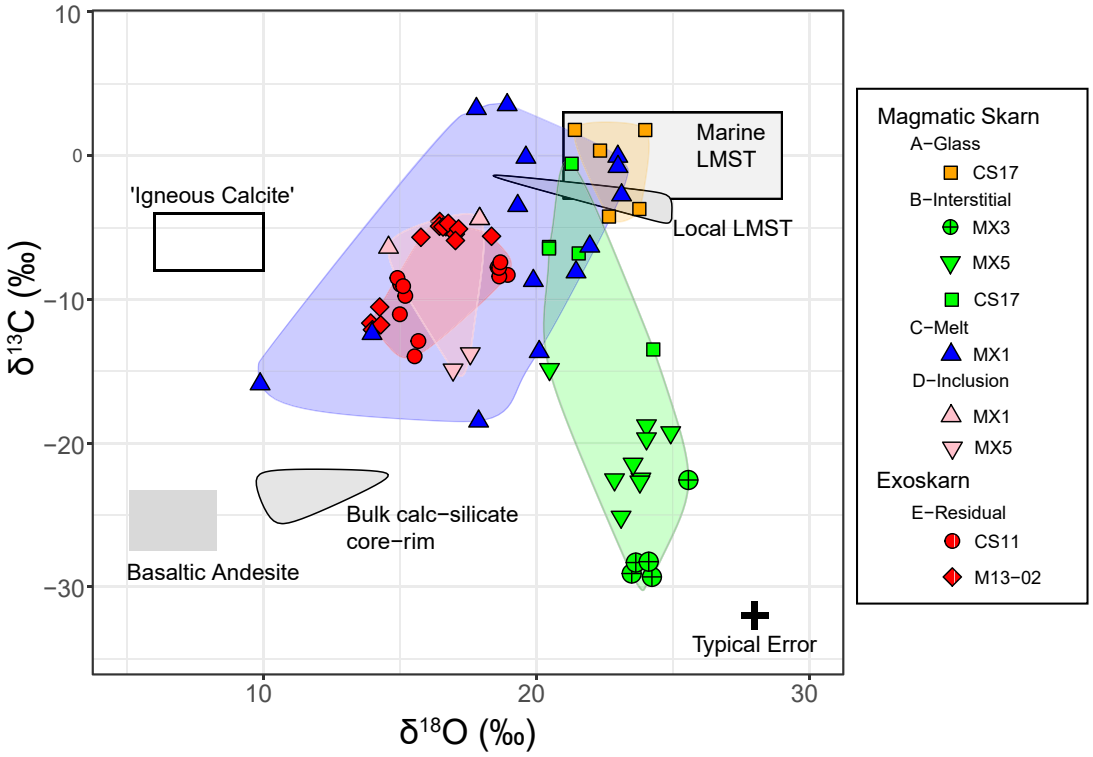


*Figure 4.2: Calcite C-O isotopic compositions. Extra data: Primary 'igneous' calcite (calcite in equilibrium with the mantle) field (Taylor, 1967). Cretaceous to Cenozoic marine limestone (Merapi limestone)(van Bemmelen, 1949; Veizer and Hoefs, 1976). Bulk calc-silicate and basaltic andesite (Troll* et al.*, 2012, 2013). Local limestone field (Gertisser and Keller, 2003b; Troll* et al.*, 2012, 2013). Typical error is 2σ*

## 4.4 Discussion

### 4.4.1 Origin of the calcite

Calcite is a common secondary alteration product in a range of rock types, therefore we first consider the origin of the calcite. We consider the xenolith calcite to be primary relics of calcite, as opposed to secondary hydrothermal calcites, for the following reasons:

Firstly, the analysed xenoliths are exceptionally fresh, with minor red oxidation of Fe-Ti oxides observed in sample CS11 only. Hydrous phases, either primary or as secondary replacement, are not observed in any of the samples studied, implying that fluid overprint was not a factor. Glass within the xenoliths is optically clear, lacking any devitrification or alteration. Typically void-filling, low-temperature secondary phases such as zeolites are not observed. Calcite is, in turn, only found within the xenolith cores, except for type A calcites in sample

CS17 where calcite can be present in glass-hosted vesicles surrounding the wollastonite dominated core zone. These latter calcite crystals do not demonstrate a geode-like internally zoned texture that would suggest secondary infill of vesicles (e.g. Lavoie, 1995), but instead have a globular habit, more indicative of a quenched previously molten calcite (c.f. Lucido *et al.*, 1980; Bailey and Kearns, 2012). In addition, secondary calcite precipitation would be expected to distribute calcite throughout the sample, wherever there may be vesicles or fractures. Type C-melt like calcite does not follow fractures or cleavage, and does not crosscut minerals, but follows the crystal boundaries.

The mineral assemblages in the xenoliths exclusively indicate high magmatic or metamorphic temperatures (>400°C) and are inconsistent with a low-temperature or hydrothermal overprint. Wollastonite is unstable below ~400°C (Greenwood, 1967), therefore interaction with meteoric water or hydrothermal fluids would be expected to cause alteration, which is not observed. Melt-like calcite (Type C) is consistent with a high temperature origin due to the equilibrium assemblage containing fluorite and cuspidine ($Ca_4Si_2O_7F_2$). Fluorine and fluorite can increase the stability of molten calcite down to 880°C (Jago and Gittins, 1991), similar to temperatures estimated from the interstitial xenolith glass (755-917°C) using the glass thermometer equation 34 (Putirka, 2008). Type E calcites are surrounded by a prominent reaction rim containing high temperature mineral assemblages; Spurrite ($Ca_5(SiO_4)_2CO_3$) is stable above 430°C at low $CO_2$ partial pressures (Henmi and Henmi, 1978), and 700-1000°C at higher $XCO_2$ (Tuttle and Harker, 1957). Wollastonite, grossular and plagioclase found on the outer edge of the reaction rim are stable between ~510-890°C (Tracy and Frost, 1991).

Chemically, significant $\delta^{13}C$ depletions can occur from contamination by organic material, as has likely occurred on the surface of some Merapi basaltic andesite whole-rock samples that interacted with burning surface vegetation (Donoghue *et al.*, 2009; Troll *et al.*, 2012). Measuring these fresh calcites *in-situ* avoids possible surface contamination.

Finally, the remote possibility that the investigated calcites represent a carbonatite magma (i.e. mantle derived carbonate melt) is also unlikely due to the high $\delta^{18}O$ values greatly exceeding mantle values, instead overlapping marine carbonate values. They additionally lack

the high SrO interpreted to represent primary carbonatite calcite (Barker, 2007), having SrO concentrations (<=0.08 wt%) closer to local limestone near to Merapi (0.01 wt%; (Chadwick, 2008)). We therefore conclude the calcites to be derived from sedimentary carbonate in the direct basement to Merapi volcano.

### 4.4.2 Oxygen isotope diversity in the calcites

We focus this remainder of the discussion on the processes that produce the compositionally and texturally diverse calcites, and the implications for the Merapi magmatic system and subsequent crustal $CO_2$ liberation to the atmosphere. To explain the C-O isotopic variations in calcite from the investigated xenoliths, we consider two distinct end-member processes: (1) decarbonation (devolatilisation) of the originally sedimentary carbonate and/or (2) magmatic fluid-carbonate interaction. We have performed Rayleigh fractionation and fluid mixing modelling, detailed below.

#### Decarbonation Reactions

Decarbonation of carbonates produces a decrease in $\delta^{18}O$ and $\delta^{13}C$ in the restitic carbonate as heavier isotopes are preferentially removed in the released $CO_2$, following the Rayleigh fractionation law (Valley, 1986):

$\delta_f - \delta_i = 1000(F^{(\alpha-1)} - 1)$

where $\delta_f$ and $\delta_i$ are final and initial isotopic values, F is the fraction of calcite remaining, and $\alpha$ is the calcite-$CO_2$ fractionation factor.

The $\delta^{13}C$ decrease can be significant, covering more than 10 $\delta$ units, but the effect on $\delta^{18}O$ is less pronounced due to the 'calc-silicate limit' (Valley, 1986), a result of newly created silicate minerals representing the major oxygen reservoir. All carbon is released as $CO_2$ whilst only ~40% of the oxygen is removed (therefore $F_{oxygen} \approx 0.4F_{carbon} + 0.6$). A typical reaction that exemplifies this is $\overset{calcite}{CaCO_3} + \overset{silica}{SiO_2} = \overset{wollastonite}{CaSiO_3} + CO_2$. A Rayleigh decarbonation curve following calc-silicate decarbonation at 850°C is shown in Figure 4.3A. This temperature is consistent with the clinopyroxene saturation temperatures calculated from the magmatic

xenolith glasses (755-917°C, Equation 34 (Putirka, 2008)). This thermometer reproduces experimental low temperature 900°C carbonate assimilation data (Carter and Dasgupta, 2016) within the published error of 45°C. Varying temperatures (e.g. ± 200°C) produces a negligible 1 ‰ variation on the calculated $\delta^{18}O$ fractionation curves, and a 3 ‰ difference $\delta^{13}C$ at 99% decarbonation (F=0.01). At 850°C, the carbon and oxygen isotopic composition of the released $CO_2$ are ~3 and 3.5‰ higher than the calcite (Chacko *et al.*, 1991), resulting in lowering of calcite isotopic values with increasing decarbonation. The initial calcite C-O isotopic composition is chosen as the highest $\delta^{13}C$ and $\delta^{18}O$ values for local limestone (Gertisser and Keller, 2003b; Troll *et al.*, 2012, 2013) and additionally an average of the type A calcite compositions, which likely represent unmodified calcite. Decarbonation can alternatively occur via the silicate-absent reaction $\overset{calcite}{CaCO_3}=\overset{lime}{CaO}+CO_2$ (Figure 4.3A) which we have additionally modelled (where $F_{oxygen} \approx 0.67F_{carbon} + 0.33$).

Type A - glass-hosted calcites have the highest $\delta^{13}C$ and $\delta^{18}O$ values (Figure 4.2), overlapping marine carbonate compositions, and therefore are the most likely calcites to represent unmodified carbonate compositions at Merapi. The limestones sampled local to Merapi (Gertisser and Keller, 2003b; Troll *et al.*, 2012) have a slightly lighter $\delta^{13}C$ composition, therefore we modelled two Rayleigh fractionation curves with both these starting compositions (Figure 4.3A). Type B interstitial calcites from two of the magmatic skarn xenoliths (samples MX3 and MX5) follow the decarbonation model closely, showing very high levels of decarbonation (Figure 4.3A). The fraction of calcite remaining falls between 0.01 and 0.0001 (Figure 4.3A), consistent with the very low (<1 vol%) modal calcite content in these xenoliths. All interstitial type B calcites are in close association with a wollastonite-dominant mineral assemblage (Figure 4.1), indicating that the formation of wollastonite by the reaction $\overset{calcite}{CaCO_3} + \overset{silica}{SiO_2}= \overset{wollastonite}{CaSiO_3} +CO_2$ is likely to be the key process causing the observed depletions in $\delta^{13}C$. Decarbonation can also occur via the silicate-absent reaction $\overset{calcite}{CaCO_3}=\overset{lime}{CaO}+CO_2$. No lime is observed, but the CaO may have transferred to the melt (c.f. Deegan *et al.*, 2010), producing the CaO-enriched xenolith glass from which wollastonite precipitated, trapping the observed abundant melt inclusions. The modelled curve for silicate-absent decarbonation (Figure 4.3A) is approximately two $\delta^{18}O$

units lower than most of the values for the interstitial calcite in the magmatic skarns. However, if a higher $\delta^{18}O$ for the protolith is chosen, this curve could equally well reproduce the calcite C-O isotope compositions in samples MX5 and MX3. A protolith with a higher $\delta^{18}O$ is not observed in the local literature limestone data, but it is plausible based on marine carbonate rocks having a wide range of $\delta^{18}O$ values (Veizer and Hoefs, 1976), exceeding +30 ‰ in some limestones (e.g. Matthews *et al.*, 1996; Jolis *et al.*, 2015). Therefore, we cannot conclusively distinguish between the two processes given the potential isotopic variability in the marine carbonate protolith. The degree of decarbonation is however shown to be extremely high independent of the exact process, as demonstrated by the very low $\delta^{13}C$ values down to -29.3 ‰, more than 20 $\delta^{13}C$ units below the presumed protolith. Hence, the fraction of calcite remaining in these xenoliths is less than 1% and possibly as small as 0.01%. This, in turn, shows that decarbonation is very efficient in the Merapi magmas.

**Fluid Mixing Processes**

The remaining calcites (Types C, D, E) show significant deviation from modelled decarbonation curves (Figure 4.3A). Various studies have shown that the C-O isotopic compositions of carbonates in skarns typically cannot be explained fully by decarbonation, and often requires interaction with magmatic fluids, causing shifts towards magmatic C-O isotopic values (Valley, 1986).

This trend is modelled in Figure 4.3B, using the mass balance equation of Taylor and Bucher-Nurminen (1986):

*Figure 4.3 (following page): Calcite C-O isotopic variations. A) Calcite types dominated by decarbonation. B) Calcite types dominated by fluid interaction and decarbonation. C) Literature calcite and skarn data. Fields for primary 'igneous' calcite (calcite in equilibrium with the mantle) from Taylor (1967). Field of Cretaceous to Cenozoic marine limestone (van Bemmelen, 1949) from Veizer and Hoefs (1976). Isotope fractionation factors from Chacko* et al. *(1991) and Zheng (2011). Wollastonite oxygen isotope data from Troll* et al. *(2013) and Borisova* et al. *(2016). Data from skarn xenoliths from Matthews* et al. *(1996), Gilg* et al. *(2001), Fulignati* et al. *(2005), Di Rocco* et al. *(2012), Gozzi* et al. *(2014) and Jolis* et al. *(2015). Skarn data from Shimazaki* et al. *(1986), Bowman* et al. *(1994), Shin and Lee (2003), Taylor and Bucher-Nurminen (1986) and unpublished data from Dunn and Bowman (2003).*

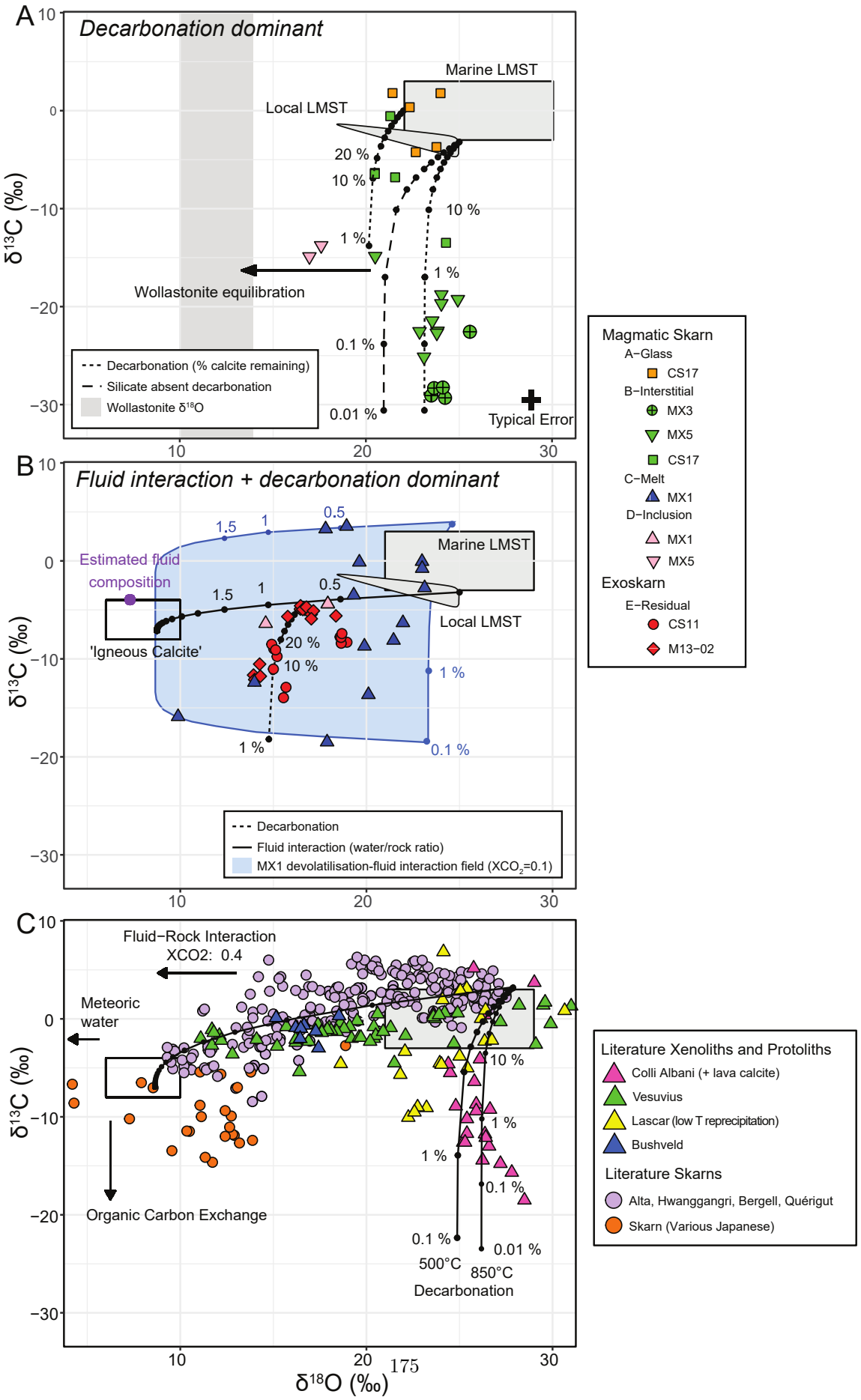
A
Decarbonation dominant
Marine LMST
Local LMST
20 %
10 %
10 %
1 %
1 %
Wollastonite equilibration
0.1 %
0.01 %
Typical Error
Decarbonation (% calcite remaining)
Silicate absent decarbonation
Wollastonite δ18O
δ13C (‰)
B
Fluid interaction + decarbonation dominant
Estimated fluid composition
'Igneous Calcite'
Marine LMST
Local LMST
1.5
1
0.5
20 %
10 %
1 %
0.1 %
Decarbonation
Fluid interaction (water/rock ratio)
MX1 devolatilisation-fluid interaction field (XCO2=0.1)
C
Fluid−Rock Interaction
XCO2: 0.4
Meteoric water
Organic Carbon Exchange
10 %
1 %
1 %
0.1 %
0.1 %
0.01 %
500°C
850°C
Decarbonation
δ18O (‰)
Magmatic Skarn
A−Glass
CS17
B−Interstitial
MX3
MX5
CS17
C−Melt
MX1
D−Inclusion
MX1
MX5
Exoskarn
E−Residual
CS11
M13−02
Literature Xenoliths and Protoliths
Colli Albani (+ lava calcite)
Vesuvius
Lascar (low T reprecipitation)
Bushveld
Literature Skarns
Alta, Hwanggangri, Bergell, Quérigut
Skarn (Various Japanese)

$$X_{CO_2} \cdot w/r = ln\left(\frac{^{13}C^i_{CO_2}+(\Delta-^{13}C^i_{cc})}{^{13}C^i_{CO_2}-(^{13}C^f_{cc}-\Delta)}\right)$$

where $X_{CO_2}$ is the mole fraction of $CO_2$ and $H_2O$ in the fluid phase, $w/r$ is the fluid/rock ratio, $^{13}C^i_{CO_2}$ is the initial fluid composition, $^{13}C^i_{cc}$ is the initial calcite composition, $^{13}C^f_{cc}$ is the final calcite composition, and $\Delta$ is the equilibrium isotope fraction between calcite and $CO_2$. Oxygen is modelled using the equivalent formula that lacks the $X_{CO_2}$ term.

The assumed fluid composition is based on the carbon isotope composition of the baseline Merapi fumarole gases (-4.1‰, (Troll *et al.*, 2012)), and oxygen isotopic composition from the estimated primary Merapi magma composition (+6.1‰ (Deegan *et al.*, 2016b)), coupled with the basalt rock-water fractionation factor of $\alpha = 0.9988114$ (Zhao and Zheng, 2003). Although this baseline value may reflect ongoing carbonate interaction at Merapi, using estimated carbon isotope Indonesian mantle values from Krakatau of -6.72 and -6.4 ‰ (Blythe *et al.*, 2012), or elevated values during eruptive periods of -2.2 to -2.6‰, does not change the overall interpretation of a magmatic fluid presence. We used a $XCO_2$ of 0.4, which affects the curvature of the models (concave to straight at unity). We chose this value because of the presence of $CO_2$ fluid inclusions and the highly vesicular nature of the xenoliths which is evidence of a strong presence of $CO_2$. Interstitial xenolith glasses are Ca-contaminated magmatic glasses, representing a melt that originally contained up to 6 wt % $H_2O$ (Preece *et al.*, 2014; Weis *et al.*, 2016), allowing for a reduction in $XCO_2$. Additionally, the mineral assemblage wollastonite + garnet + anorthite, found in both magmatic skarn sample MX1 and exoskarn sample CS11, require an $XCO_2 <\tilde{}\, 0.6$ at 100 MPa (Tracy and Frost, 1991). This pressure is consistent with the pressure estimated from microthermometry of wollastonite-hosted fluid inclusions (34-94 MPa, see Chapter 3.5.4).

Regardless of the exact modelling parameters used, a simple magma-carbonate fluid mixing curve cannot reproduce the bulk of our data, in contrast to many worldwide skarns (Valley, 1986; Jolis *et al.*, 2015, Figure 4.3B-C). The Type C melt-like calcites (Figure 4.3B) have a significant spread of data, and show a complex mixing-decarbonation history. A magmatic fluid is required to produce the strong $\delta^{18}O$ depletions, which is evidenced directly in this sample by the presence of localised areas containing calcite, the F-bearing phases fluorite and cuspidine, and a Cl-bearing phase compositionally similar to wadalite. The presence of a high temperature

magmatic brine at Merapi has been previously identified (Nadeau *et al.*, 2013b; Preece *et al.*, 2014), which has interacted with some of the xenoliths. Depletion in $^{13}C$ requires decarbonation, which may occur during carbonate melting, releasing $CO_2$ whilst producing a Ca-rich melt (Durand *et al.*, 2015), and/or during the formation of wollastonite via decarbonation reactions. The entire spectrum of type C calcite compositions can then be modelled by a single decarbonation curve and subsequent mixing with a magmatic fluid, or vice versa (Figure 4.3B).

Type D wollastonite-hosted calcite inclusions in samples MX5 and MX1 (Figure 4.3A,B) can be modelled by a combination of decarbonation followed by interaction with either a fluid, or diffusive equilibration between the calcite inclusion and the host wollastonite crystal. Host wollastonites have $\delta^{18}O$ values of +10 to +14 ‰ (Troll *et al.*, 2013; Borisova *et al.*, 2016), and any equilibration between wollastonite and calcite would cause a large reduction in calcite $\delta^{18}O$ values ($\Delta^{18}O_{\text{calcite-wollastonite}}$ at 850°C = 2.2 (Zheng, 1993)).

Residual type E calcites (Figure 4.3B) within the exoskarn xenoliths can be modelled by fluid mixing followed by decarbonation from a local limestone initial composition. Due to the absence of glass, the relatively lower temperatures compared to the magmatic xenoliths constrained from the phase assemblage (<800°C, Tracy and Frost, 1991), and the presence of magmatic volatile-bearing phases (apatite-ellestadite, cuspidine, fluorite, anhydrite), these xenoliths likely represent samples from a greater distance into a zoned carbonate alteration zone around the magma (e.g. Matthews *et al.*, 1996; Fulignati *et al.*, 2004). This scenario is similar to zoned contact metamorphic aureoles and exoskarns, where interaction with fluid released from a cooling magma may have a stronger influence than the dominant thermal metamorphic influence adjacent to the magma. Our xenoliths must, however, still be close enough to the magma contact to prevent the formation of hydrous skarn minerals (such as vesuvianite). The second stage decarbonation trend may have been produced as the sample is entrained in the melt during ascent, as decarbonation is shown to be dominant in the syn-magmatic xenolith samples MX3 and MX5.

In summary, the isotopic variations between calcite types can be attributed to whether a magmatic fluid phase was present during xenolith formation. Type A calcites represent nearly

unmodified calcite compositions. C-O isotope systematics of interstitial calcites (type B) in magmatic skarn samples can be explained by decarbonation reactions alone (Figure 4.3A). The calcites were affected dominantly by the heat of the magmatic melt. The liberated CaO from decarbonation reacted with the melt $SiO_2$ to produce wollastonite, containing abundant melt inclusions and $CO_2$-rich fluid inclusions. Type C melt-like calcites show evidence for the presence of a F+Cl-bearing magmatic fluid phase. This magmatic fluid facilitated calcite melting and oxygen isotope exchange. Simultaneous decarbonation reactions occurred forming wollastonite, similar to Type B calcites (Figure 4.3A). Wollastonite-hosted calcite inclusions (type D) represent equilibration with their host phase, lowering their $\delta^{18}O$ values. Type E calcites in the exoskarn xenoliths (samples CS11 and M13-02) lack a silicate glass phase, and have a distinct mineral assemblage, indicating they are located from within an aureole alteration zone around the magma body. Pure thermal decarbonation is likely a less prominent isotopic modification process, and instead a stronger influence of magmatic fluid interaction is recorded (as in skarns (Valley, 1986)). These exoskarns therefore record a pronounced lowering in their calcite $\delta^{18}O$ values (+13.9 to +19 ‰) and only moderate changes in their $\delta^{13}C$ values (Figure 4.3B).

### 4.4.3 Comparison with other worldwide skarn xenoliths and skarns

This variety of processes at Merapi contrasts with other reported skarn and skarn xenoliths. Figure 4.3C shows a selection of oxygen and carbon isotope data from skarn deposits and skarn xenolith suites. Skarns that form in carbonate country rocks adjacent to granitoid intrusions typically show dominantly fluid mixing trends (Figure 4.3C, Valley, 1986 Figure 6; Bowman, 1998 Figure 13), with variation in $\delta^{13}C$ attributed to a smaller degree of decarbonation. Significant depletions in $\delta^{13}C$ to below mantle values are often attributed to interaction with organic material such as graphite-bearing wall rocks or a $CH_4$-rich fluid (e.g. Shimazaki *et al.*, 1986; Bowman, 1998). Skarn xenoliths from active volcanoes and volcanic areas often exhibit two distinct trends in C-O isotope space. Calcite from Vesuvius (Gilg *et al.*, 2001; Fulignati *et al.*, 2005; Jolis *et al.*, 2015) and Bushveld (Buick *et al.*, 2000) skarn xenoliths follow the typical

skarn trend, with compositions defining a trajectory towards mantle and carbonatite C-O isotope compositions. Xenoliths and groundmass calcite within lavas from Colli Albani (Di Rocco *et al.*, 2012; Gozzi *et al.*, 2014), however, show a pure decarbonation trend, with negligible magmatic influence. At Merapi, our type B interstitial calcites show a dominant decarbonation trend, similar to Colli Albani (Figure 4.3C), however the extremely low $\delta^{13}C$ values observed at Merapi (down to $\delta^{13}C$ = -29.3 ‰) suggest more extreme degrees of decarbonation. To the best of our knowledge, these calcites record the lowest carbonate $\delta^{13}C$ values reported from skarns, approaching that of organic carbon. Our data, and the literature whole-rock data (Troll *et al.*, 2012), show that low $\delta^{13}C$ values can be achieved by high temperature decarbonation reactions alone. In the absence of other geological evidence for organic material interaction, this could indicate that other depleted skarns in the literature may reflect similar processes, without the need to involve organic carbon sources. The exoskarn xenoliths from Merapi lack the definitive skarn-like trend shown by Vesuvius and the various skarns associated with granitoid intrusions. Instead, they demonstrate a combination of both trends, lowering $\delta^{13}C$ values to below typical igneous values, which we interpret as the combined action of decarbonation and interaction with magmatic fluids. Contrasting processes of pure decarbonation and fluid infiltrative isotopic modification have been only rarely described from individual contact metamorphic aureoles, such as the Bufa Del Diente alkali syenite intrusion (Heinrich *et al.*, 1995) and Quérigut magmatic complex (Durand *et al.*, 2006). Merapi is now the first case where the contrasting processes of near-complete decarbonation and carbonate-magmatic fluid interaction can be demonstrated in xenoliths from an active volcano. This may be due to the rapid timescales of carbonate assimilation (e.g. Deegan *et al.*, 2010; Jolis *et al.*, 2013) which would hinder preservation of high temperature thermal decarbonation in typical contact aureoles, but are preserved in the xenoliths that record transient snapshots of magma-crust interaction processes. These xenoliths additionally lack evidence for slow cooling and overprint by low-T assemblages, which is commmon in *in situ* contact aureoles. Granitic intrusions typically intrude at lower temperatures than basaltic-andesite magmas, therefore the country rock is likely

to experience less intense thermal effects, and therefore less decarbonation, compared to Merapi country rock xenoliths that experience temperatures upwards of 925°C (Erdmann *et al.*, 2016). Furthermore, a cooling granitic body would release large quantities of fluid as magmatic crystallisation progresses, producing a fluid-dominant isotopic signal in the aureole. Indeed, in the Merapi xenoliths, samples that exhibit evidence for a brine phase during formation (i.e. F, Cl and S-rich mineral phases), are the samples that show a shift towards magmatic isotopic values, confirming the presence of a fluid that influenced the xenolith's isotopic composition.

In addition to modifying the isotopic composition of the calcites, the fluids facilitated carbonate melting, and therefore our xenolith samples provide new evidence that carbonate melts can be produced by interaction between magmas and crustal carbonate (c.f. Lentz, 1999; Fulignati *et al.*, 2001; Gozzi *et al.*, 2014). Our textural evidence shows calcite with typical melt-like structures that we interpret as having formed from a carbonate melt. A crustal source is evidenced by the calcite isotopic compositions overlapping those of marine carbonates. Some of the analysed melt-like calcites approach the C-O isotope values typical of magmatic mantle derived carbonates, which demonstrates interaction of the crustal carbonate with magmatic fluids (Figure 4.3B). The carbonate melts formed in the xenoliths are volumetrically small, as formation of skarn minerals via decarbonation reactions is the dominant process of magma-carbonate interaction at Merapi, and the carbonate melts require a F-rich fluid (Jago and Gittins, 1991) and a Ca-rich contaminated magmatic melt to stabilise the carbonate melt within the xenoliths. This restricts the melt locally to the xenoliths as to our knowledge, no carbonate is found within the basaltic-andesite lavas. This is in contrast to examples such as Colli Albani (Di Rocco *et al.*, 2012; Gozzi *et al.*, 2014) and the Hortavær igneous complex in central Norway (Barnes *et al.*, 2005), where carbonate derived from country rock assimilation is frequently found in the igneous materials. The xenolith Ca-rich melts are isolated from the host magma by a rim of clinopyroxene and plagioclase, however the low viscosity of carbonate and Ca-contaminated melts (e.g. Genge *et al.*, 1995; Deegan *et al.*, 2010) may allow release from the xenoliths into the Merapi magma via filter pressing or through xenolith disaggregation. These melts alone are likely to have a limited effect on the bulk magmatic composition due to the small volumes

of carbonate melt produced, relative to usage of magmatic elements to form the skarn mineral assemblages. Regardless of the exact mechanism of magma-carbonate interaction (mixing with carbonate melts, skarnification, bulk dissolution), a strong magma-crustal carbonate interaction signature at Merapi is demonstrated by isotopic (C, O, Sr, He, Gertisser and Keller, 2003b; Chadwick *et al.*, 2007; Troll *et al.*, 2012, 2013; Borisova *et al.*, 2013, 2016) and trace element ($CO_2$/S Aiuppa *et al.*, 2017) studies, indicating up to 30% contamination with crustal carbonate components.

### 4.4.4 Implications for Crustal Volatile Release

Our modelling results, and the general paucity of relict calcite in the xenoliths, demonstrate that magma-carbonate interaction at Merapi is very efficient at remobilising crustal $CO_2$ into the magmatic system and ultimately the atmosphere. Crustal carbonate assimilation has been shown to be an important contributor to $CO_2$ output at Merapi (e.g. Deegan *et al.*, 2010; Troll *et al.*, 2012; Carter and Dasgupta, 2016) and a widespread occurrence in arc volcanoes, which may even dwarf contributions from source contamination (Aiuppa *et al.*, 2017; Mason *et al.*, 2017).

We have used a mass balance model (Iacono-Marziano *et al.*, 2009) to place constraints on the amount of crustal $CO_2$ produced at Merapi:

$$\%carbonate = 100\frac{\delta^{13}C_{fumarole}-\delta^{13}C_{mantle}}{\delta^{13}C_{carbonate}-\delta^{13}C_{mantle}}$$

A mantle carbon isotope value of $\delta^{13}$C = -6.5 ‰ is chosen, based on measurements from nearby Krakatau (-6.7 and 6.4 ‰) which likely represents a primary Indonesian mantle value (Blythe *et al.*, 2012). To constrain the crustal carbon output at Merapi, both the averaged Merapi baseline and the 2006 syn-eruptive fumarole $\delta^{13}$C values (-4.1 ‰ and -2.4 ‰ respectively (Troll *et al.*, 2012)) are employed in our modelling. Although a $\delta^{13}$C value of -4.1 is within some commonly used uncontaminated MORB mantle ranges (e.g. -6 ± 2 Mason *et al.*, 2017), gas He isotopes indicate that the Merapi gas baseline during quiescence has a crustal carbonate overprint (Troll *et al.*, 2013). For this reason, we use -6.5 ‰ as the primary mantle $\delta^{13}$C value. To approximate the $\delta^{13}$C values of the carbonate crust underlying Merapi, a range of values

are utilised, from -2.2 ‰ (Troll *et al.*, 2012) to +3.5 ‰ (this study). The source of the $CO_2$ is assumed to be dominantly crustal and not from subducted sediment on the basis of elevated $CO_2/S_T$ measurements (Aiuppa *et al.*, 2017). From this modelling, we find that 24-56% of $CO_2$ emissions are crustal derived during periods of volcanic quiescence, and 41-95% during eruptive periods.

Contributions to crustal $CO_2$ release come from direct carbonate assimilation into magma, thermal carbonate breakdown, and metasomatic alteration of the wall rock. To calculate the mass of $CO_2$ released by a magma reservoir below Merapi, we followed the calculations of Jolis *et al.* (2015), which estimate the amount of $CO_2$ released from the aureole around a magma reservoir for a specified reservoir volume, aureole thickness, and decarbonation efficiency. The size of the pre-eruptive magma reservoir below Merapi is poorly constrained, but is known to reside within the carbonate substrata (Preece *et al.*, 2014; Erdmann *et al.*, 2016, see Chapter 3.5.4). Using the erupted volume from the 2010 paroxysmal eruption of 0.02 to 0.05 $km^3$ (Surono *et al.*, 2012) and an average intrusive:extrusive ratio of 5:1 (White *et al.*, 2006; c.f. Carter and Dasgupta, 2018), we assume an estimated reservoir size of 0.1 to 0.25 $km^3$. Thermal and metasomatic aureoles can be extensive in size (e.g. Aarnes *et al.*, 2010), so we calculate a range of aureole thicknesses from 5 to 30% of the reservoir width. Aureoles are thermally and chemically gradational, with proximal thermally-affected fully decarbonated and/or assimilated rocks, through metasomatic rocks, to distal marbles, therefore we use a conservative 50% decarbonation efficiency as an average for our aureole calculations. This is in line with a lack of olivine, periclase and other magnesian phases in the xenoliths, which implies the carbonate protolith at Merapi is highly likely to be limestone, which has a lower decarbonation efficiency than dolomite (c.f. Carter and Dasgupta, 2018).

Modelling the $CO_2$ released from the contact aureole outlined above indicates that 9.5 x $10^9$ to 1.8 x $10^{11}$ kg of crustal $CO_2$ could be released from the limestone surrounding the reservoir. Merapi degases approximately 4-4.6 x $10^5$ kg of $CO_2$ per day (Toutain *et al.*, 2009), of which we calculate 24-56% may be crustal derived during quiescence (see above). This means that the total $CO_2$ that could be released from the aureole of a reservoir similar in size to that of

the 2010 eruption could occur rapidly over 119 to 4960 years. This timescale may be shortened by punctuated periods of eruptive activity that increase magma-carbonate interaction [Troll *et al.* (2012);Carr *et al.* (2018); Chapter 3]. To simulate a maximum $CO_2$ output over the lifespan of Merapi, we can consider multiple reservoirs intruded into the carbonate at variable depths, which will cause much larger volumes of $CO_2$ to be released. Fully decarbonating a vertical limestone cylinder from the surface to the base of the limestone at ~10 km (van Bemmelen, 1949) with a 1 km radius, corresponding to the estimated 2010 eruption reservoir width +50%, shows that up to 3.8 x $10^{13}$kg of $CO_2$ could be released. Although Merapi is currently considered a relatively low global $CO_2$ emitter (Burton *et al.*, 2013), our calculations, and documented strongly degassed syn-magmatic xenoliths, show that crustal $CO_2$ liberation can be temporarily variable with potentially large amounts released during eruptive episodes compared to periods of overall quiescence (c.f. Deegan *et al.*, 2010; Troll *et al.*, 2012). We assume that carbonate-interacting arc systems follow similar patterns worldwide, and probably over geological time too.

Periods of global warming in the Earth's past, such as the Cretaceous hothouse and the Paleocene-Eocene Thermal Maximum (PETM) have been discussed in the context of excess atmospheric carbon originating from either organic carbon release (Svensen *et al.*, 2004), intense volcanism (Gutjahr *et al.*, 2017) and/or increased magma-crustal carbonate interaction at volcanic arcs (Carter and Dasgupta, 2018; Chu *et al.*, 2019). Some periods of global warming in the Earth's past, notably the PETM, are accompanied by negative $\delta^{13}C$ excursions of several per mil in the rock record, which could be explained by either massive volcanism (Gutjahr *et al.*, 2017) and/or organic carbon release (permafrost and/or methane hydrates) (Svensen *et al.*, 2004). Although our data show highly negative calcite $\delta^{13}C$ values, and therefore imply the release of $CO_2$ with commensurate highly negative $\delta^{13}C$, the bulk gas released from carbonate interaction will always range between the initial carbonate value and the initial carbonate + the $CO_2$-calcite fractionation factor (e.g. $\Delta^{13}C_{CO2\text{-}calcite}$ = 3.7 to 2.7 ‰ at 500-1000°C, (Chacko *et al.*, 1991)), thus driving the $\delta^{13}C$ of released $CO_2$ at volcanoes to relatively high values. A

suggested increased volume of crustal carbonate $CO_2$ release during PETM (Carter and Dasgupta, 2018) would therefore increase the $\delta^{13}C$ composition of the global volcanic $CO_2$ output above typical mantle values (c.f. Lee *et al.*, 2013; Mason *et al.*, 2017). Accepting carbonate assimilation in arcs as a contributing factor during past climate perturbations, carbon cycling models would require a much higher input of light carbon than previously thought to balance the isotopically heavier limestone-derived volcanic volatiles and still explain past negative carbon isotope excursions. Although further discussion of carbon cycling modelling is beyond the scope of this paper, we note that the increasingly recognised contribution of limestone-derived carbon to volcanic carbon budgets warrants consideration in carbon cycling models throughout Earth history.

## 4.5 Conclusions

We present the first *in-situ* carbon and oxygen isotope study of five texturally distinct calcite types within Merapi skarn xenoliths. The calcites encompass a wide range of C-O isotope compositional space ($\delta^{13}C$ –29.3 to +3.5 ‰, $\delta^{18}O$ +9.9 to +25.6 ‰), distinct from xenolith bulk-rock analyses presented in the literature ($\delta^{13}C$ -22.4 to -24.9 ‰, $\delta^{18}O$ 10.4 to 14.1 ‰). The different calcite types can be attributed to distinct C-O isotopic trends. Interstitial and glass-hosted calcites show a dominant influence of decarbonation, leading to extremely negative $\delta^{13}C$ values (up to -29.3 ‰). By contrast, melt-like and residual calcites show a mixed influence of magmatic isotopic exchange and decarbonation. Magmatic isotopic exchange is facilitated by the presence of a magmatic fluid phase percolating during xenolith metasomatism, demonstrated by the presence of F and Cl bearing-phases, which are present in the samples with decarbonation-dominant interstitial calcite. This fluid phase further contributed to carbonate melting and mobilisation. The observed melt-like calcites with clear isotopic evidence for a crustal origin show that carbonate melts can be produced by interaction of magmatic fluids with crustal carbonate. Our modelling results combined with the general paucity of remnant calcite in the xenoliths, demonstrate that magma-carbonate interaction at Merapi is very efficient at remobilising crustal $CO_2$. 24-95% of the $CO_2$ released at Merapi may be crustal derived,

and release of this additional crustal $CO_2$ from the aureoles around magma reservoirs occurs rapidly over geologically short timescales of only thousands of years. Magma-crustal carbonate interaction processes throughout Earth's past likely follow similar patterns, with the potential to release large volumes of $CO_2$ rapidly, and may require additional consideration in carbon cycling models.

# Chapter 5

# Xenoliths as Tracers of Processes in Volcanic Arcs

The preceding chapters presented a detailed study of two types of xenoliths from two case study locations. Xenoliths however are found worldwide and span a vast range of lithologies, therefore this chapter discusses how these results fit into the wider understanding of the magmatic differentiation and crustal contamination processes occurring at volcanic arcs.

## 5.1 Magma Differentiation at Volcanic Arcs

From primitive magma genesis to the production of andesite and silicic evolved products, there is still debate as to the best model to produce the complex magmas found at volcanic arcs. The high MgO, basaltic partial melts of the peridotite mantle wedge are not commonly found in arcs, and instead the volcanic products are dominated by more evolved magmas, requiring significant differentiation to occur within the crust (Taylor and McLennan, 1985; Carmichael, 2002; Lee and Bachmann, 2014; Melekhova *et al.*, 2015; Müntener and Ulmer, 2018).

### 5.1.1 Transcrustal Differentiation

Recent advances in our understanding of magmatic arcs focus on the concept of transcrustal magma differentiation, where differentiation occurs at various stages throughout the crust, and not occurring entirely in geophysically implausible large aphyric shallow magma reservoirs (Cashman *et al.*, 2017). Melt within this transcrustal system is found within, and percolates through, vertically extensive crystal mushes (crystal-rich systems kept at super-solidus conditions). Melts can be extracted and segregate (Bachmann and Huber, 2018; Gualda *et al.*, 2019), erupt (Marsh, 1996; Bachmann and Huber, 2018), react with crystals to form different

mineral phases (Davidson *et al.*, 2007; Smith, 2014; Cooper *et al.*, 2016; Otamendi *et al.*, 2016), replenish and remobilise parts of the mush system (Nakamura, 1995; Murphy *et al.*, 2000; Szymanowski *et al.*, 2017; Bachmann and Huber, 2018), and also become trapped and crystallise along paths out of equilibrium with the main magmatic system (Bernstein, 2006; Borghini and Rampone, 2007; Krause *et al.*, 2007). Plutonic xenoliths record processes occurring at steps within this mush column (e.g. Foden and Green, 1992; Upton *et al.*, 2000; Smith, 2014; Forni *et al.*, 2015; Perinelli *et al.*, 2016; Bertolett *et al.*, 2019).

This work has shown that at Santorini, magmatic differentiation of mafic to silicic melts occurs in the upper to mid crust. The plutonic xenoliths record melt compositions spanning the entirety of those observed in the volcanic rocks, showing evolution of Santorini magmas dominantly by fractional crystallisation, consistent with results from the volcanic rocks (e.g. Druitt *et al.*, 1999, 2016; Cadoux *et al.*, 2014; Andújar *et al.*, 2016) and arc systems in general (e.g. Annen *et al.*, 2006; Cashman *et al.*, 2017). Although our mineral-melt barometry has inherent large uncertainty, the broad shallowing trend with differentiation is consistent with arc magma genesis models showing that mafic and andesitic melts are generated at deeper depths, and fractionate to dacite and rhyolitic compositions and pond in the shallower crust. Our oxygen isotope results, and prior radiogenic isotope work at Santorini (e.g. Druitt *et al.*, 1999) show the role of ~10 to 20% crustal assimilation influencing the geochemical signature of the magmas during differentiation, which is a typical characteristic of arc magmas (see section 5.2 below, section 1.4 and chapters 3 and 4).

Cumulates, and cumulate xenoliths, provide insights into crystal mush processes occuring (e.g. Holness *et al.*, 2005a; Borghini and Rampone, 2007; Smith, 2014; Cooper *et al.*, 2016; Sliwinski *et al.*, 2015; Wolff *et al.*, 2015; Forni *et al.*, 2015). Xenoliths from this study show both sampling from the crystallising mush of the silicic eruptions, and record frozen mush and the closed system differentiation occuring in trapped melt pockets. Cumulate remobilisation is evidenced in the Lower Pumice 2 eruption, with texturally distinct corroded plagioclase from the cumulate found in the pyroclastic deposits. Cumulate remobilisation from magma replenishment is likely not restricted to this eruption, being a common process in forming

large silicic eruptions (Wolff *et al.*, 2015; Sliwinski *et al.*, 2017; Bachmann and Huber, 2018; Forni *et al.*, 2018), and replenishment and mixing events are identified in several Santorini eruptions (Druitt *et al.*, 1999, 2012; Fabbro *et al.*, 2018) indicating mixing of mush (Fabbro *et al.*, 2018). Future work is needed to assess the origin of phenocrysts across the eruptive sequence (e.g. Kinman and Neal, 2006; Druitt *et al.*, 2012; Fabbro *et al.*, 2018).

Reactive melt flow through a lower crustal mush can produce large volumes of amphibole, which modifies the geochemical signature of fractionating magmas and can produce large volumes of silicic melt in the deep crust (Davidson *et al.*, 2007; Klaver *et al.*, 2018). This has been evidenced in plutonic xenoliths from many arcs (e.g. Foden and Green, 1992; Costa *et al.*, 2002; Smith, 2014; Tiepolo *et al.*, 2012; Cooper *et al.*, 2016) including the Aegean (Elburg *et al.*, 2014; Klaver *et al.*, 2017, 2018). In Santorini however, amphibole is only found as a late stage intercumulus phase, or as hydrothermal alteration of clinopyroxene. This reflects shallower crustal differentiation at Santorini, compared to rhyodacitic magmas from Nisyros in the west end of the South Aegean Volcanic Arc. The Nisyros rhyodacites in contrast to Santorini lack evidence for shallow crustal differentiation and mixing processes, formed entirely by lower crustal differentiation (Klaver *et al.*, 2017, 2018), but the later andesitic Nisyros eruptive units are more comparable to Santorini, showing only shallow crustal differentiation processes (Klaver *et al.*, 2017). This highlights the complexity of arc magma genesis, where distinct batches of magma can form at individual volcanic centres (e.g. Akrotiri vs post 530-ka magma at Santorini, older rhyodacitic vs newer andesitic magma at Nisyros), and also along arcs (e.g. Aegean: Elburg *et al.*, 2014; Sunda: Handley *et al.*, 2014; Aeolian: Pe-Piper and Piper, 2005; Lesser Antilles: Melekhova *et al.*, 2019; Aleutians: Kelemen *et al.*, 2004; Mariana: Parman *et al.*, 2010).

Future work at Santorini should focus on the plutonic xenoliths from the lava sequences. Rare gabbroic xenoliths were sampled from the Skaros and Therassia lavas during this study, but proved too altered or small to study. The xenoliths in this study can be considered the cumulate to the explosive silicic eruptions, which although the most hazardous eruptive style, are only a part of the full magmatic evolution at Santorini. The lava flows of Nea Kameni are considered potentially the start of a third eruptive cycle (Druitt *et al.*, 2016), therefore understanding the

full magmatic history is crucial for understanding the risk posed in the future.

## 5.2 Crustal Contribution to Arc Magmas

Magmas passing from the mantle through the crust in arc settings rarely occurs without mass transfer and crustal contamination (e.g. Arculus and Johnson, 1981; Pyle and Ivanovich, 1988; Thirlwall *et al.*, 1996; Davidson *et al.*, 2005). The thermal influence of this melt causes chemical transfer between magma and wall rock via many different processes including diffusion, metasomatism, bulk assimilation, and recycling of metamorphosed crust (e.g. Patchett, 1980; Beard *et al.*, 1993; Reiners *et al.*, 1995; Ducea and Saleeby, 1998; Dungan and Davidson, 2004; Jolis *et al.*, 2015). This section discusses the mechanisms of crustal contamination elucidated from skarn xenolith studies, and the role this study has on advancing the understanding of these processes.

### 5.2.1 Prograde Skarn Forming Processes

Elemental transfer between wall-rock and magma produces strong chemical gradients, forming mineralogical and chemical zonation (Kerrick, 1977; Zarayskiy *et al.*, 1987). This occurs at all scales, from fine grained rapidly quenched contacts to metres long zonation across slow-cooled pluton contact aureoles. In carbonates skarn systems, two environments are identified, the endoskarn/magmatic skarn, where carbonate elements have transferred to the magma, and exoskarn, where magmatic elements have modified the original carbonate. This is identified both in studies of skarn deposits and reconstruction of skarns below active volcanoes (Kerrick, 1977; Zarayskiy *et al.*, 1987; Matthews *et al.*, 1996; Gaeta *et al.*, 2009; Di Rocco *et al.*, 2012). The endoskarns can be difficult to recognise, sometimes resembling a magmatic cumulate, requiring geochemical tracers to reveal their origin, and a piecemeal approach using different lithologies to reconstruct the skarn system morphology (Wenzel *et al.*, 2002; Barnes *et al.*, 2005; Fulignati *et al.*, 2005; Gaeta *et al.*, 2009; Di Rocco *et al.*, 2012; Spandler *et al.*, 2012). The work in Chapter 3 clearly reveals that these cumulate rocks can be formed from magma-carbonate interaction, validating interpretations of previous workers, and provide natural analogues to

experiments (e.g. Zarayskiy *et al.*, 1987). The Merapi magmatic skarn samples especially show remarkably well the effects of the chemical gradient from endo to exoskarn at thin section scale, with a cumulate-like assemblage of clinopyroxene and plagioclase at the magma contact, to wollastonite and garnet skarn assemblages towards the limestone-derived xenolith core. The geochemical compositions of the cumulate-like clinopyroxene and plagioclase overlap that of magmatic clinopyroxene and plagioclase, therefore this 'gabbroic' assemblage, if found without coexisting obvious evidence for carbonate assimilation, could be overlooked at volcanoes where carbonate assimilation is not as pervasive or apparent as at Merapi.

Our work additionally shows a rarely recognised mechanism of skarn formation, by which dissolution of carbonate into the host magma occurs followed by precipitation of calc-silicate skarn minerals from the Ca-enriched melt. This is in contrast to typical skarn formation by thermal metamorphism and metasomatism from magmatic fluids and/or diffusion (Kerrick, 1977; Zarayskiy *et al.*, 1987; Meinert, 1992). Although the zonation in the Merapi magmatic skarn xenoliths resembles metasomatic skarns, the xenoliths contain the Ca-enriched glass, skarn minerals with Ca-rich melt inclusions, and irregular zonation indicating crystallisation from a Ca-contaminated magmatic melt. Occurrences of this process of skarn formation are rare, for example identified at Vesuvius (e.g. Fulignati *et al.*, 2001) and in some skarn deposits at locations across China (Bin and Jin-song, 2016 and references therein). It likely this mechanism produces skarn rocks elsewhere, and this work at Merapi can help aid recognition elsewhere.

Liberated $CO_2$ from decarbonation reactions increases the oxygen fugacity, influencing the mineral phases produced and compositions of these (Nicholls, 1971b; Wenzel *et al.*, 2002; Mollo and Vona, 2014). Clinopyroxene increases in Ca-Tschermak ($CaAlAlSiO_6$), Ca-Fe-Tschermak ('esseneite' $CaFe^{3+}AlSiO_6$), and Ca-Ti-Tschermak ($CaTiAl_2O_6$) components due to the oxidation of Fe to $Fe^{3+}$ (Mollo and Vona, 2014). Oxygen fugacity is difficult to constrain in many skarn systems, due to the lack of coexisting Fe-Ti oxides. In this work, we built upon the existing single crystal oxybarometers of Cortés *et al.* (2006) and Simakin *et al.* (2012), to expand the calibration to oxygen fugacities and clinopyroxene compositions found in skarns. Estimation of clinopyroxene $Fe^{3+}$ from electron microprobe data uses calculation schemes (Droop, 1987;

Lindsley, 1983) that are prone to large uncertainty when determinations of the other cations are inaccurate. For this reason, calibration of oxybarometers based on measurement of $Fe^{3+}$ from methods such as Mössbauer spectroscopy may be able to improve the accuracy. $Fe^{3+}$ can be reasonably accurately estimated in garnets with the microprobe (Arai, 2010), and $Fe^{3+}$ is strongly incorporated into the crystal structure via the andradite component, therefore calibration of a garnet oxybarometer may be possible with more high-$fO_2$ experiments. High oxygen fugacity during skarn formation causing $Fe^{3+}$ incorporation into clinopyroxene drives $Al_2O_3$ enrichment. This is additionally promoted at higher temperatures (Huckenholz *et al.*, 1974; Pascal *et al.*, 2005) producing extremely enriched compositions with up to 24 wt% $Al_2O_3$. Our study provides another natural example of extreme Al enrichment, with up 22.3 wt% $Al_2O_3$.

As well as the exotic clinopyroxene compositions, many other rare minerals have been identified in this study. More work is required on the wadalite-like and other similar Ca-Al-Si±Cl,F phases for identification. Detailed microanalytical work on skarn xenoliths such as those from the Upper Chegem caldera, Russia, have found an abundance of new minerals in recent years (e.g. Galuskin *et al.*, 2013), and this may additionally be the case at Merapi.

### 5.2.2 Interaction with Non-Carbonate Crust

Whilst this study focused dominantly on the readily assimilated carbonate crust at Merapi, the other xenoliths found both at Merapi and other volcanoes may provide insights into mechanisms of elemental transfer from wall rock to magma. At Merapi, volcaniclastic xenoliths are also present, which are unlikely to have been entrained without some modification to their chemistry. Quartz-rich partially melted xenoliths additionally identified in this study at Merapi (Section 3.4.3, Appendix Figure B.1) indicate that crustal melting and assimilation of other crustal lithologies is ongoing at Merapi, and requires study. Work on similar xenoliths at the Aeolian Islands and Etna have been used to rule out these crustal melts in influencing the major element geochemistry of the magmas (Frezzotti *et al.*, 2004), constrained the effects of trace element mineral-melt partitioning during assimilation, and have additionally used these xenoliths as

geobarometers for magma stagnation depths (Zanon *et al.*, 2003). This study also found quartz-rich xenoliths in the deposits of Nea Kameni at Santorini. A rim of clinopyroxene shows they are not in equilibrium with the host dacite, and likely also represent partially melted crust. The processes and affects of assimilation of other non-carbonate lithologies requires further study.

### 5.2.3 Composition of Contaminated Magmas

Carbonate interaction has long been proposed (e.g Daly, 1910) as a process that can influence the composition of magma, notably increasing the alkalis and depleting melts in silica. This has been experimentally verified recently (e.g. Iacono-Marziano *et al.*, 2007; Mollo *et al.*, 2010b). While true for mafic melts interacting with carbonate, the effects of this are less apparent when the magmas are more evolved and cooler (Spandler *et al.*, 2012; Carter and Dasgupta, 2016, 2018). Merapi can be considered an example of this, that while producing basaltic to basaltic andesite lavas, the melts (interstitial glasses) in the system are dacitic to rhyolitic, compared to the basaltic glasses in the K-rich silica undersaturated Italian volcanic rocks (e.g. Gaeta *et al.*, 2006). As the Merapi xenoliths have shown, much of the mineralogy produced during magma-carbonate interaction at Merapi, and therefore more differentiated systems, produces clinopyroxene and plagioclase similar to the phenocryst assemblage. This is in contrast to mafic systems where clinopyroxene forms at the expense of olivine, which results in a stronger influence on the melt geochemistry (Iacono-Marziano *et al.*, 2007; Mollo *et al.*, 2010b). Merapi is similar to Nisyros (Spandler *et al.*, 2012) where carbonate assimilation does not have a strong control on major element geochemistry (Handley *et al.*, 2014). Isotopic evidence for carbonate assimilation is stronger, and shows that either the bulk major element chemistry changes little with carbonate assimilation due to the phases produced as discussed above, or a decoupling of isotopic element transfer and major element transfer during carbonate interaction (Deegan *et al.*, 2010), producing a strong isotopic signal for assimilation at only small amounts of actual bulk assimilation. Further work is needed to assess this properly.

### 5.2.4 Volatile Budgets

Magma-carbonate interaction releases $CO_2$ as the carbonate is progressively changed into a calc-silicate mineral assemblage. This study presents the first *in situ* study of texturally distinct remant calcites from the carbonate protolith using carbon and oxygen isotopes. The five distinct textural types show distinct chemistry as a result of mixed processes: 1) highly efficient decarbonation, and 2) influx of magmatic volatiles that facilitated carbonate melting. Carbonate melt is rarely observed (Lentz, 1999; Fulignati *et al.*, 2001; Gozzi *et al.*, 2014) and often attributed to carbonatites (e.g. Barker, 2007), but conclusively shown to be derivable from crustal rocks in magma-carbonate systems in this study.

The extremely low calcite $\delta^{13}C$ and paucity of residual calcite in the xenoliths shows highly efficient decarbonation. The low solubility of $CO_2$ in silicate melts (Holloway and Blank, 1994; Botcharnikov *et al.*, 2005) means that this $CO_2$ is unlikely to be retained in the magma, and will either passively escape through fractures or cause overpressurisation of the magmatic system depending on the rate of $CO_2$ release (Freda *et al.*, 2011; Troll *et al.*, 2012; Ghiorso, 2016; Carr *et al.*, 2018). At Merapi, this extra $CO_2$ is thought to potentially increase the pressure and enhance the explosivity of some eruptions, even occurring at syn-magmatic timescales (Troll *et al.*, 2012; Carr *et al.*, 2018). This work further supports that this may be possible. Experimental work has shown decarbonation is rapid in high temperature basaltic melts at Merapi and Vesuvius (Deegan *et al.*, 2010; Jolis *et al.*, 2013). The experiments were performed at higher temperatures than those estimated from the intercumulus glass and melt inclusions in this study, but this work also shows rapid, syn-eruptive carbonate interaction occurring at lower ~850°C temperatures. The magmatic skarn xenoliths are by definition products of rapid carbonate interaction, before the Ca-enriched melts can mingle into the magmatic system and the disaggregated crystals can be dissolved and/or re-equilibrated with the Merapi magmas. Timescales of magmatic skarn xenolith formation estimated in this study show that additional crustal $CO_2$ can be released in the time frames up to and during eruptions, potentially increasing explosivity. The timescales in this work are based on crystal growth rates, but these timescales could be much more accurately constrained by utilising diffusion modelling of the strongly zoned

xenolith clinopyroxene and plagioclase crystals.

Decarbonation occurs in the metamorphic aureole around the magma reservoir (Jolis *et al.*, 2015; Carter and Dasgupta, 2018), and in this study we have shown that this decarbonation is additionally rapid, in the order of 100 to a few thousand years at Merapi. In systems where the magmatic plumbing is considered a series of small reservoirs throughout the crust (e.g. Chadwick *et al.*, 2013; Cashman *et al.*, 2017), this has potential to release large volumes of crustal $CO_2$ to the atmosphere. Crustal carbonate $CO_2$ output at volcanic arcs is an increasingly widespread recognised occurrence, which may dwarf contributions from subducted source contamination (Lee *et al.*, 2013; Carter and Dasgupta, 2016, 2018; Aiuppa *et al.*, 2017; Mason *et al.*, 2017; Chu *et al.*, 2019). Resolving the impact of this $CO_2$ release on modern and past climate budgets is a key area of work that needs more research.

## 5.3 Concluding Remarks

This thesis has used detailed petrography and analytical methods to study crustal xenoliths found at Merapi, and plutonic xenoliths found at Santorini. This work, and the referenced work within, has shown the value of using xenoliths to understand the individual processes that collectively produce complex arc magmas. Future work on these xenoliths from other locations will inevitably benefit our understanding of arc magma petrogenesis. During this study we also sampled from across the Aeolian islands, where a wide variety of both crustal (calc-silicates, quartzites, basement) and plutonic (ultramafics, gabbros, diorites) xenoliths can be found. The island of Salina for example hosts both crustal and plutonic xenoliths within the same eruptive deposits, potentially allowing for the roles of crustal contamination vs differentiation processes on a single eruption to be established. The rich variety of xenoliths, coupled with the hazards posed by populations on the flanks of the Aeolian island volcanoes, makes them a desirable target for future research.

## 5.4 Main Thesis Conclusions

Plutonic xenoliths from Santorini are dominated by anhydrous gabbroic assemblages representing shallow to mid crustal (<400 MPa) storage and differentiation. Whole-rock and mineral geochemistry shows they are the complementary cumulate to the silicic eruptions, however not necessarily cogenetic to the eruption deposits that they are found within. The xenolith mineral chemistry overlaps that of the volcanic phenocrysts but also extends to differentiation indices that demonstrate a higher degree of differentiation (low Fo, An, Mg#) in intercumulus phases. This is also shown by low estimated crystallisation temperatures, and strong trace element enrichment in some samples, showing either post-cumulus growth from a heavily fractionated melt or equilibration of cumulus phases with this melt.

Cabonate assimilation at Merapi occurs by two dominant processes: 1) Dissolution of carbonate into the host magma and subsequent precipitation of calc-silicate skarn minerals, and 2) *in situ* metasomatic modification of the wall-rock. Clinopyroxene and plagioclase produced from the former precipitation process can be indistinguishable from the magmatic mineral phases on the basis of major element geochemistry, and may affect geochemical models based on mineral-melt equilibria of 'magmatic' mineral phases. Magma-carbonate interaction at Merapi can occur in the presence of a magmatic volatile-rich brine. This facilitates formation of rare halogen and metal-bearing minerals that show the initial stages of economic mineral deposit formation, which is of interest to economic geologists that often study rocks where the prograde stage of ore formation is overprinted by retrograde processes.

Significant $CO_2$ release is demonstrated by the paucity of calcite in the xenoliths, and the extremely low $\delta^{13}C$ of the texturally and geochemically distinct residual calcites. Timescales of magma carbonate interaction at Merapi are extremely rapid, capable of releasing additional $CO_2$ during eruptive periods and influencing explosivity, and fully decarbonating the wall-rock around the magma reservoir in only hundreds to a few thousand years. In systems where the plumbing is considered a series of small reservoirs throughout the crust, this has potential to release large volumes of crustal $CO_2$ to the atmosphere.

# References


Aarnes, I., Svensen, H., Connolly, J.A.D., Podladchikov, Y.Y., 2010. How contact metamorphism can trigger global climate changes: Modelling gas generation around igneous sills in sedimentary basins. *Geochimica et Cosmochimica Acta* **74**, 7179–7195.

Agangi, A., Reddy, S.M., 2016. Open-system behaviour of magmatic fluid phase and transport of copper in arc magmas at Krakatau and Batur volcanoes, Indonesia. *Journal of Volcanology and Geothermal Research* **327**, 669–686.

Aitcheson, S.J., Forrest, A.H., 1994. Quantification of crustal contamination in open magmatic systems. *Journal of Petrology* **35**, 461–488.

Aiuppa, A., Fischer, T.P., Plank, T., Robidoux, P., Di Napoli, R., 2017. Along-arc, inter-arc and arc-to-arc variations in volcanic gas $CO_2/S_T$ ratios reveal dual source of carbon in arc volcanism. *Earth-Science Reviews* **168**, 24–47.

Allard, P., 1983. The origin of hydrogen, carbon, sulphur, nitrogen and rare gases in volcanic exhalations: evidence from isotope geochemistry, in: Tazieff, H., Sabroux, J. (Eds.), Forecasting Volcanic Events. Elsevier Amsterdam, pp. 337–386.

Alonso-Perez, R., Müntener, O., Ulmer, P., 2009. Igneous garnet and amphibole fractionation in the roots of island arcs: experimental constraints on andesitic liquids. *Contributions to Mineralogy and Petrology* **157**, 541–558.

Anderson, A., 1973. The before-eruption water content of some high-alumina magmas. *Bulletin Volcanologique* **37**, 530–552.

Anderson, A.T., 1974. Evidence for a picritic, volatile-rich magma beneath Mt. Shasta, California. *Journal of Petrology* **15**, 243–267.

Andreastuti, S., Alloway, B., Smith, I., 2000. A detailed tephrostratigraphic framework at Merapi Volcano, Central Java, Indonesia: implications for eruption predictions and hazard assessment. *Journal of Volcanology and Geothermal Research* **100**, 51–67.

Andújar, J., Scaillet, B., Pichavant, M., Druitt, T.H., 2016. Generation Conditions of Dacite and Rhyodacite via the Crystallization of an Andesitic Magma. Implications for the Plumbing System at Santorini (Greece) and the Origin of Tholeiitic or Calc-alkaline Differentiation Trends in Arc Magmas. *Journal of Petrology* **57**, 1887–1920.

Andújar, J., Scaillet, B., Pichavant, M., Druitt, T.H., 2015. Differentiation conditions of a basaltic magma from Santorini, and its bearing on the production of andesite in arc settings. *Journal of Petrology* **56**, 765–794.

Angelier, J., Lybéris, N., Le Pichon, X., Barrier, E., Huchon, P., 1982. The tectonic development of the Hellenic arc and the Sea of Crete: a synthesis. *Tectonophysics* **86**, 159–196.

Annen, C., Blundy, J.D., Leuthold, J., Sparks, R.S.J., 2015. Construction and evolution of igneous bodies: Towards an integrated perspective of crustal magmatism. *Lithos* **230**, 206–221.

Annen, C., Blundy, J., Sparks, R., 2006. The genesis of intermediate and silicic magmas in deep crustal hot zones. *Journal of Petrology* **47**, 505–539.

Arai, H., 2010. Short Note: A function for the R programming language to recast garnet analyses into end-members: Revision and porting of Muhling and Griffin's method. *Computers & Geosciences* **36**, 406–409.

Arculus, R.J., Johnson, R.W., 1981. Island-arc magma sources: A geochemical assessment of the roles of slab-derived components and crustal contamination. *Geochemical Journal* **15**, 109–133.

Arculus, R.J., Wills, K.J., 1980. The petrology of plutonic blocks and inclusions from the Lesser Antilles island arc. *Journal of Petrology* **21**, 743–799.

Asimow, P.D., Ghiorso, M.S., 1998. Algorithmic modifications extending MELTS to calculate subsolidus phase relations. *American Mineralogist* **83**, 1127–1132.

Bachmann, O., Bergantz, G.W., 2004. On the origin of crystal-poor rhyolites: extracted from batholithic crystal mushes. *Journal of Petrology* **45**, 1565–1582.

Bachmann, O., Deering, C.D., Lipman, P.W., Plummer, C., 2014. Building zoned ignimbrites by recycling silicic cumulates: insight from the 1,000 km3 Carpenter Ridge Tuff, CO. *Contributions to Mineralogy and Petrology* **167**, 1–13.

Bachmann, O., Huber, C., 2018. The inner workings of crustal distillation columns; the physical mechanisms and rates controlling phase separation in silicic magma reservoirs. *Journal of Petrology* **60**, 3–18.

Bailey, D.K., Kearns, S., 2012. New forms of abundant carbonatite–silicate volcanism: recognition criteria and further target locations. *Mineralogical Magazine* **76**, 271–284.

Bailey, J.C., Jensen, E., Hansen, A., Kann, A., Kann, K., 2009. Formation of heterogeneous magmatic series beneath North Santorini, South Aegean island arc. *Lithos* **110**, 20–36.

Baker, C., Black, P.M., 1980. Assimilation and metamorphism at a basalt-limestone contact, Tokatoka, New Zealand. *Mineralogical Magazine* **43**, 797–807.

Baker, D.R., 2008. The fidelity of melt inclusions as records of melt composition. *Contributions to Mineralogy and Petrology* **156**, 377–395.

Bali, E., Hartley, M.E., Maclennan, J., Neave, D.A., Halldórsson, S.A., 2018. Melt inclusion constraints on petrogenesis of the 2014–2015 Holuhraun eruption, Iceland. *Contributions to Mineralogy and Petrology* **173**, 1.

Barker, D.S., 2007. Origin of cementing calcite in "carbonatite" tuffs. *Geology* **35**, 371–374.

Barker, D.S., 1987. Rhyolites contaminated with metapelite and gabbro, Lipari, Aeolian Islands, Italy: products of lower crustal fusion or of assimilation plus fractional crystallization? *Contributions to Mineralogy and Petrology* **97**, 460–472.

Barnes, C.G., Prestvik, T., Li, Y., McCulloch, L., Yoshinobu, A.S., Frost, C.D., 2009. Growth and zoning of the Hortavær intrusive complex, a layered alkaline pluton in the Norwegian Caledonides. *Geosphere* **5**, 286–301.

Barnes, C.G., Prestvik, T., Sundvoll, B., Surratt, D., 2005. Pervasive assimilation of carbonate and silicate rocks in the Hortavær igneous complex, north-central Norway. *Lithos* **80**, 179–199.

Barnes, S.J., 1986. The effect of trapped liquid crystallization on cumulus mineral compositions in layered intrusions. *Contributions to Mineralogy and Petrology* **93**, 524–531.

Barton, M., Huijsmans, J.P., 1986. Post-caldera dacites from the Santorini volcanic complex, Aegean Sea, Greece: an example of the eruption of lavas of near-constant composition over a 2,200 year period. *Contributions to Mineralogy and Petrology* **94**, 472–495.

Beard, J.S., 1986. Characteristic mineralogy of arc-related cumulate gabbros: implications for the tectonic setting of gabbroic plutons and for andesite genesis. *Geology* **14**, 848–851.

Beard, J.S., Abitz, R.J., Lofgren, G.E., 1993. Experimental melting of crustal xenoliths from Kilbourne Hole, New Mexico and implications for the contamination and genesis of magmas. *Contributions to Mineralogy and Petrology* **115**, 88–102.

Beard, J.S., Ragland, P.C., Crawford, M.L., 2005. Reactive bulk assimilation: A model for crust-mantle mixing in silicic magmas. *Geology* **33**, 681–684.

Beard, J.S., Ragland, P.C., Rushmer, T., 2004. Hydration crystallization reactions between anhydrous minerals and hydrous melt to yield amphibole and biotite in igneous rocks: description and implications. *The Journal of Geology* **112**, 617–621.

Bergeat, A., 1910. Der Cordieritandesit von Lipari, seine andalusitführenden Einschlüsse und die genetischen Beziehungen zwischen dem Andalusit, Sillimanit, Biotit, Cordierit, Orthoklas und Spinell in den letzteren. *Neues Jahrbuch fur Mineralogie, Abhandlungen* **30**, 575–627.

Berndt, J., Koepke, J., Holtz, F., 2005. An experimental investigation of the influence of water and oxygen fugacity on differentiation of MORB at 200 MPa. *Journal of Petrology* **46**, 135–167.

Bernstein, S., 2006. In situ fractional crystallization of a mafic pluton: Microanalytical study of a Palaeogene gabbronorite plug in East Greenland. *Lithos* **92**, 222–237.

Bertolett, E.M., Prior, D.J., Gravley, D.M., Hampton, S.J., Kennedy, B.M., 2019. Compacted cumulates revealed by electron backscatter diffraction analysis of plutonic lithics. *Geology* **47**, 445–448.

Bédard, J., 2007. Trace element partitioning coefficients between silicate melts and orthopyroxene: parameterizations of D variations. *Chemical Geology* **244**, 263–303.

Bédard, J.H., 2014. Parameterizations of calcic clinopyroxene—Melt trace element partition coefficients. *Geochemistry, Geophysics, Geosystems* **15**, 303–336.

Bédard, J.H., 2010. Parameterization of the Fe= Mg exchange coefficient (Kd) between clinopyroxene and silicate melts. *Chemical Geology* **274**, 169–176.

Bédard, J.H., 2006. Trace element partitioning in plagioclase feldspar. *Geochimica et Cosmochimica Acta* **70**, 3717–3742.

Bédard, J.H., 1994. A procedure for calculating the equilibrium distribution of trace elements among the minerals of cumulate rocks, and the concentration of trace elements in the coexisting liquids. *Chemical Geology* **118**, 143–153.

Bin, Z., Jin-song, Z., 2016. The main features of magmatic skarns and their formation mechanism. *AshEse Journal of Engineering* **2**, 22–65.

Bindeman, I., 2008. Oxygen isotopes in mantle and crustal magmas as revealed by single crystal analysis. *Reviews in Mineralogy and Geochemistry* **69**, 445–478.

Blatter, D.L., Sisson, T.W., Hankins, W.B., 2017. Voluminous arc dacites as amphibole reaction-boundary liquids. *Contributions to Mineralogy and Petrology* **172**, 1.

Blundy, J., Dalton, J., 2000. Experimental comparison of trace element partitioning between clinopyroxene and melt in carbonate and silicate systems, and implications for mantle metasomatism. *Contributions to Mineralogy and Petrology* **139**, 356–371.

Blundy, J., Wood, B., 1994. Prediction of crystal–melt partition coefficients from elastic moduli. *Nature* **372**, 452–454.

Blythe, L.S., Deegan, F.M., Freda, C., Jolis, E.M., Masotta, M., Misiti, V., Taddeucci, J., Troll, V.R., 2015. $CO_2$ bubble generation and migration during magma–carbonate interaction. *Contributions to Mineralogy and Petrology* **169**, 1–16.

Blythe, L., Troll, V., Hilton, D., Schwarzkopf, L., 2012. Understanding Crustal Volatiles: Provenance, Processes and Implications (PhD thesis). Uppsala University.

Bodnar, R.J., 2003. Reequilibration of fluid inclusions. *Fluid inclusions: Analysis and interpretation* **32**, 213–230.

Bolio-Arceo, H., Glasser, F.P., 1990. Formation of spurrite, $Ca_5(SiO_4)_2CO_3$. *Cement and Concrete Research* **20**, 301–307.

Bond, A., Sparks, R.S.J., 1976. The Minoan eruption of Santorini, Greece. *Journal of the Geological Society* **132**, 1–16.

Bonelli, R., Frezzotti, M.L., Zanon, V., Peccerillo, A., 2004. Evolution of the volcanic plumbing system of Alicudi (Aeolian Islands–Italy): evidence from fluid and melt inclusions in quartz xenoliths. *Annales Geophysicae* **47**, 1409–1422.

Borghini, G., Rampone, E., 2007. Postcumulus processes in oceanic-type olivine-rich cumulates: The role of trapped melt crystallization versus melt/rock interaction. *Contributions to Mineralogy and Petrology* **154**, 619–633.

Borisova, A.Y., Gurenko, A.A., Martel, C., Kouzmanov, K., Cathala, A., Bohrson, W.A., Pratomo, I., Sumarti, S., 2016. Oxygen isotope heterogeneity of arc magma recorded in plagioclase from the 2010 Merapi eruption (Central Java, Indonesia). *Geochimica et Cosmochimica Acta* **190**, 13–34.

Borisova, A.Y., Martel, C., Gouy, S., Pratomo, I., Sumarti, S., Toutain, J.-P., Bindeman, I.N., de Parseval, P., Métaxian, J.-P., 2013. Highly explosive 2010 Merapi eruption: evidence for shallow-level crustal assimilation and hybrid fluid. *Journal of Volcanology and Geothermal Research* **261**, 193–208.

Borisova, A.Y., Toutain, J.-P., Dubessy, J., Pallister, J., Zwick, A., Salvi, S., 2014. H2O-CO2-S fluid triggering the 1991 Mount Pinatubo climactic eruption (Philippines). *Bulletin of Volcanology* **76**, 800.

Botcharnikov, R.E., Almeev, R.R., Koepke, J., Holtz, F., 2008. Phase relations and liquid lines of descent in hydrous ferrobasalt-implications for the Skaergaard intrusion and Columbia River flood basalts. *Journal of Petrology* **49**, 1687–1727.

Botcharnikov, R., Freise, M., Holtz, F., Behrens, H., 2005. Solubility of COH mixturesin natural melts: new experimental data and application range of recent models. *Annals*

*of Geophysics.*

Bottinga, Y., Weill, D.F., 1970. Densities of liquid silicate systems calculated from partial molar volumes of oxide components. *American Journal of Science* **269**, 169–182.

Bowen, N.L., 1922. The behavior of inclusions in igneous magmas. *The Journal of Geology* 513–570.

Bowman, J.R., 1998. Stable-isotope systematics of skarns, in: Mineralized Intrusion-Related Skarn Systems. Mineralogical Association of Canada, pp. 99–145.

Bowman, J.R., Willett, S.D., Cook, S.J., 1994. Oxygen isotopic transport and exchange during fluid flow: One-dimensional models and applications. *American Journal of Science* **294**, 1–55.

Bragagni, A., Avanzinelli, R., Freymuth, H., Francalanci, L., 2014. Recycling of crystal mush-derived melts and short magma residence times revealed by U-series disequilibria at Stromboli volcano. *Earth and Planetary Science Letters* **404**, 206–219.

Brandriss, M.E., Bird, D.K., O'Neil, J.R., Cullers, R.L., 1996. Dehydration, partial melting, and assimilation of metabasaltic xenoliths in gabbros of the Kap Edvard Holm Complex, East Greenland. *American Journal of Science* **296**, 333–393.

Brauns, R., 1912a. Die kristallinen Schiefer des Laacher Seegebietes und ihre Umbildung zu Sanidinit. E. Schweizerbart'sche Verlagsbuchhandlung, Nägele & dr. Sproesser.

Brauns, R., 1912b. Die chemische Zusammensetzung granatführender kristalliner Schiefer usw. aus dem Laacher-Seegebiet. *Neues Jahrbuch fur Mineralogie, Abhandlungen* **34**, 85–175.

Brouwer, H., 1928. Production of Trachyte and Phonolite from Pyroxene Andesitic Magma Associated with Limestone. *The Journal of Geology* **36**, 545–548.

Brouwer, H.A., 1945. The association of alkali rocks and metamorphic limestone in a block ejected by the volcano Merapi (Java). Koninklijke Nederlandse Akademie van Wetenschappen.

Browning, J., Drymoni, K., Gudmundsson, A., 2015. Forecasting magma-chamber rupture at Santorini volcano, Greece. *Scientific Reports* **5**, 15785.

Bröcker, M., Kreuzer, H., Matthews, A., Okrusch, M., 1993. 40Ar/39Ar and oxygen isotope studies of polymetamorphism from Tinos Island, Cycladic blueschist belt, Greece. *Journal of metamorphic Geology* **11**, 223–240.

Bruins, H.J., MacGillivray, J.A., Synolakis, C.E., Benjamini, C., Keller, J., Kisch, H.J., Klügel, A., Plicht, J.V.D., 2008. Geoarchaeological tsunami deposits at Palaikastro (Crete) and the Late Minoan IA eruption of Santorini. *Journal of Archaeological Science* **35**, 191–212.

Bryan, W.B., Finger, L.W., Chayes, F., 1969. Estimating proportions in petrographic mixing equations by least-squares approximation. *Science (New York, N.Y.)* **163**, 926–927.

Buettner, A., Kleinhanns, I., Rufer, D., Hunziker, J., Villa, I., 2005. Magma generation at the easternmost section of the Hellenic arc: Hf, Nd, Pb and Sr isotope geochemistry of Nisyros and Yali volcanoes (Greece). *Lithos* **83**, 29–46.

Buick, I.S., Gibson, R.L., Cartwright, I., Maas, R., Wallmach, T., Uken, R., 2000. Fluid flow in metacarbonates associated with emplacement of the Bushveld Complex, South Africa. *Journal of Geochemical Exploration* **69**, 391–395.

Burchardt, S., Troll, V.R., Schmeling, H., Koyi, H., Blythe, L., 2016. Erupted frothy xenoliths may explain lack of country-rock fragments in plutons. *Scientific Reports* **6**, 34566.

Burnham, C., 1979. Magmas and Hydrothermal Fluids: in HL Barnes, ed.. Geochemistry of Hydrothermal Ore Deposits (2nd Edit.).

Burton, M.R., Sawyer, G.M., Granieri, D., 2013. Deep carbon emissions from volcanoes. *Reviews in Mineralogy and Geochemistry* **75**, 323–354.

Büttner, S.H., 2012. Rock Maker: an MS Excel™ spreadsheet for the calculation of rock compositions from proportional whole rock analyses, mineral compositions, and modal abundance. *Mineralogy and Petrology* **104**, 129–135.

Cabato, E.J.A., 2007. Abundances of Lithium, Beryllium and Boron in Phenocrysts from Santorini Volcano (Greece): Implications on Magma Genesis and Eruption Mechanisms (PhD thesis). University of Heidelberg.

Cadoux, A., Scaillet, B., Druitt, T.H., Deloule, E., 2014. Magma storage conditions of large Plinian eruptions of Santorini Volcano (Greece). *Journal of Petrology* **55**, 1129–1171.

Calanchi, N., Peccerillo, A., Tranne, C., Lucchini, F., Rossi, P., Kempton, P., Barbieri, M., Wu, T., 2002. Petrology and geochemistry of volcanic rocks from the island of Panarea: implications for mantle evolution beneath the Aeolian island arc (southern Tyrrhenian sea). *Journal of Volcanology and Geothermal Research* **115**, 367–395.

Camejo-Harry, M., Melekhova, E., Blundy, J., Attridge, W., Robertson, R., Christopher, T., 2018. Magma evolution beneath Bequia, Lesser Antilles, deduced from petrology of lavas and plutonic xenoliths. *Contributions to Mineralogy and Petrology* **173**, 77.

Campbell, I., 1978. Some problems with the cumulus theory. *Lithos* **11**, 311–323.

Camus, G., Gourgaud, A., Mossand-Berthommier, P.-C., Vincent, P.-M., 2000. Merapi (Central Java, Indonesia): an outline of the structural and magmatological evolution, with a special emphasis to the major pyroclastic events. *Journal of Volcanology and Geothermal Research* **100**, 139–163.

Carbonin, C., Negro, A.D., Ganeo, S., Piccirillo, E., 1991. Influence of magma composition and oxygen fugacity on the crystal structure of C2/c clinopyroxenes from a basalt-pantellerite suite. *Contributions to Mineralogy and Petrology* **108**, 34–42.

Carmichael, I.S., 2002. The andesite aqueduct: perspectives on the evolution of intermediate magmatism in west-central (105–99 W) Mexico. *Contributions to Mineralogy and Petrology* **143**, 641–663.

Carr, B.B., Clarke, A.B., Vitturi, M.d., 2020. Volcanic conduit controls on effusive-explosive transitions and the 2010 eruption of Merapi Volcano (Indonesia). *Journal of Volcanology and Geothermal Research* **392**, 106767.

Carr, B.B., Clarke, A.B., Vitturi, M.d., 2018. Earthquake induced variations in extrusion rate: A numerical modeling approach to the 2006 eruption of Merapi Volcano (Indonesia). *Earth and Planetary Science Letters* **482**, 377–387.

Carroll, M.R., Rutherford, M.J., 1987. The stability of igneous anhydrite: experimental results and implications for sulfur behavior in the 1982 El Chichon trachyandesite and

other evolved magmas. *Journal of Petrology* **28**, 781–801.

Carter, L.B., Dasgupta, R., 2018. Decarbonation in the Ca-Mg-Fe carbonate system at mid-crustal pressure as a function of temperature and assimilation with arc magmas–Implications for long-term climate. *Chemical Geology* **492**, 30–48.

Carter, L.B., Dasgupta, R., 2016. Effect of melt composition on crustal carbonate assimilation: Implications for the transition from calcite consumption to skarnification and associated $CO_2$ degassing. *Geochemistry, Geophysics, Geosystems* **17**, 3893–3916.

Carter, L.B., Dasgupta, R., 2015. Hydrous basalt–limestone interaction at crustal conditions: Implications for generation of ultracalcic melts and outflux of $CO_2$ at volcanic arcs. *Earth and Planetary Science Letters* **427**, 202–214.

Cashman, K.V., Sparks, R.S.J., Blundy, J.D., 2017. Vertically extensive and unstable magmatic systems: A unified view of igneous processes. *Science* **355**, eaag3055.

Castillo, P.R., 2012. Adakite petrogenesis. *Lithos* **134**, 304–316.

Cawthorn, R.G., O'Hara, M., 1976. Amphibole fractionation in calc-alkaline magma genesis. *American Journal of Science* **276**, 309–329.

Chacko, T., Mayeda, T.K., Clayton, R.N., Goldsmith, J.R., 1991. Oxygen and carbon isotope fractionations between $CO_2$ and calcite. *Geochimica et Cosmochimica Acta* **55**, 2867–2882.

Chadwick, J., 2008. Crustal processes in volcanic systems: case studies from Northern Ireland, New Zealand, and Indonesia (PhD thesis). Trinity College Dublin.

Chadwick, J.P., Troll, V.R., Ginibre, C., Morgan, D., Gertisser, R., Waight, T.E., Davidson, J.P., 2007. Carbonate assimilation at Merapi Volcano, Java, Indonesia: insights from crystal isotope stratigraphy. *Journal of Petrology* **48**, 1793–1812.

Chadwick, J.P., Troll, V.R., Waight, T.E., van der Zwan, F.M., Schwarzkopf, L.M., 2013. Petrology and geochemistry of igneous inclusions in recent Merapi deposits: a window into the sub-volcanic plumbing system. *Contributions to Mineralogy and Petrology* **165**, 259–282.

Chadwick, J., Troll, V., Schulz, B., Dallai, L., Freda, C., Schwarzkopf, L., Annersten, H., Skogby, H., 2010. The role of amphibole in Merapi arc magma petrogenesis: insights from petrology and geochemistry of lava hosted xenoliths and xenocrysts, in: EGU General Assembly Conference Abstracts. p. 15379.

Charlu, T.V., Newton, R.C., Kleppa, O.J., 1981. Thermochemistry of synthetic $Ca_2Al_2SiO_7$ (gehlenite)-$Ca_2MgSi_2O_7$ (åkermanite) melilites. *Geochimica et Cosmochimica Acta* **45**, 1609–1617.

Chiodini, G., Caliro, S., Aiuppa, A., Avino, R., Granieri, D., Moretti, R., Parello, F., 2011. First 13C/12C isotopic characterisation of volcanic plume $CO_2$. *Bulletin of Volcanology* **73**, 531–542.

Christensen, N.I., Mooney, W.D., 1995. Seismic velocity structure and composition of the continental crust: A global view. *Journal of Geophysical Research, Solid Earth* **100**, 9761–9788.

Chu, X., Lee, C.-T.A., Dasgupta, R., Cao, W., 2019. The contribution to exogenic $CO_2$ by contact metamorphism at continental arcs: A coupled model of fluid flux and metamorphic decarbonation. *American Journal of Science* **319**, 631–657.

Clarke, D.B., Henry, A.S., White, M.A., 1998. Exploding xenoliths and the absence of "elephants" graveyards' in granite batholiths. *Journal of Structural Geology* **20**, 1325–1343.

Clements, B., Hall, R., 2007. Cretaceous to Late Miocene stratigraphic and tectonic evolution of West Java. *Proceedings, Indonesian Petroleum Association. Thirty-first Annual Convention and Exhibition.*

Clements, B., Hall, R., Smyth, H.R., Cottam, M.A., 2009. Thrusting of a volcanic arc: a new structural model for Java. *Petroleum Geoscience* **15**, 159–174.

Clocchiatti, R., Joron, J.L., Kerinec, F., Treuil, M., 1982. Quelques données préliminaires sur la lave du dôme actuel du volcan Mérapi (Java, Indonésie) et sur ses enclaves. *CR Acad Sci Paris* **295**, 817–822.

Clocchiatti, R., Joron, J.-L., Treuil, M., 1986. Interaction entre le magma de l'Etna et son soubassement sédimentaire: arguments en faveur de la contamination sélective en alcalins des laves récentes. Centre national de la recherche scientifique.

Clocchiatti, R., Moro, A.D., Gioncada, A., Joron, J.L., Mosbah, M., Pinarelli, L., Sbrana, A., 1994. Assessment of a shallow magmatic system: the 1888–90 eruption, Vulcano Island, Italy. *Bulletin of Volcanology* **56**, 466–486.

Commer, M., Helwig, S.L., Hördt, A., Scholl, C., Tezkan, B., 2006. New results on the resistivity structure of Merapi Volcano (Indonesia), derived from three-dimensional restricted inversion of long-offset transient electromagnetic data. *Geophysical Journal International* **167**, 1172–1187.

Conte, A.M., Dolfi, D., Gaeta, M., Misiti, V., Mollo, S., Perinelli, C., 2009. Experimental constraints on evolution of leucite-basanite magma at 1 and 10-4GPa: implications for parental compositions of Roman high-potassium magmas. *European Journal of Mineralogy* **21**, 763–782.

Cooper, G.F., Davidson, J.P., Blundy, J.D., 2016. Plutonic xenoliths from Martinique, Lesser Antilles: evidence for open system processes and reactive melt flow in island arc crust. *Contributions to Mineralogy and Petrology* **171**, 1.

Cortés, J.A., Wilson, M., Condliffe, E., Francalanci, L., 2006. The occurrence of forsterite and highly oxidizing conditions in basaltic lavas from Stromboli volcano, Italy. *Journal of Petrology* **47**, 1345–1373.

Costa, F., Andreastuti, S., Maisonneuve, C.B. de, Pallister, J.S., 2013. Petrological insights into the storage conditions, and magmatic processes that yielded the centennial 2010 Merapi explosive eruption. *Journal of Volcanology and Geothermal Research* **261**, 209–235.

Costa, F., Dungan, M., 2005. Short time scales of magmatic assimilation from diffusion modeling of multiple elements in olivine. *Geology* **33**, 837–840.

Costa, F., Dungan, M., Singer, B., 2002. Hornblende-and phlogopite-bearing gabbroic xenoliths from Volcán San Pedro (36 S), Chilean Andes: evidence for melt and fluid migration

and reactions in subduction-related plutons. *Journal of Petrology* **43**, 219–241.

Cottrell, E., Gardner, J.E., Rutherford, M.J., 1999. Petrologic and experimental evidence for the movement and heating of the pre-eruptive Minoan rhyodacite (Santorini, Greece). *Contributions to Mineralogy and Petrology* **135**, 315–331.

Dallai, L., Freda, C., Gaeta, M., 2004. Oxygen isotope geochemistry of pyroclastic clinopyroxene monitors carbonate contributions to Roman-type ultrapotassic magmas. *Contributions to Mineralogy and Petrology* **148**, 247–263.

Daly, R.A., 1910. Origin of the alkaline rocks. *Geological Society of America Bulletin* **21**, 87–118.

Danyushevsky, L., Della-Pasqua, F., Sokolov, S., 2000. Re-equilibration of melt inclusions trapped by magnesian olivine phenocrysts from subduction-related magmas: petrological implications. *Contributions to Mineralogy and Petrology* **138**, 68–83.

Danyushevsky, L.V., 2001.. *Journal of Volcanology and Geothermal Research* **110**, 265–280.

Danyushevsky, L.V., Plechov, P., 2011. Petrolog3: Integrated software for modeling crystallization processes. *Geochemistry, Geophysics, Geosystems* **12**.

Davidson, J., 1985. Mechanisms of contamination in Lesser Antilles island arc magmas from radiogenic and oxygen isotope relationships. *Earth and Planetary Science Letters* **72**, 163–174.

Davidson, J.P., Hora, J.M., Garrison, J.M., Dungan, M.A., 2005. Crustal forensics in arc magmas. *Journal of Volcanology and Geothermal Research* **140**, 157–170.

Davidson, J.P., McMillan, N.J., Moorbath, S., Wörner, G., Harmon, R.S., Lopez-Escobar, L., 1990. The Nevados de Payachata volcanic region (18 S/69 W, N. Chile) II. Evidence for widespread crustal involvement in Andean magmatism. *Contributions to Mineralogy and Petrology* **105**, 412–432.

Davidson, J., Turner, S., Handley, H., Macpherson, C., Dosseto, A., 2007. Amphibole "sponge" in arc crust? *Geology* **35**, 787–790.

Davis, E., Bastas, C., 1978. Petrology and geochemistry of the metamorphic system of Santorini, in: Thera and the Aegean World. Cambridge University Press, p. 61.

Davis, E., Gartzos, E., Dietrich, V.J., 1998. Magmatic evolution of the Pleistocene Akrotiri volcanoes, in: Proceedings of the 2nd Workshop,"The European Laboratory Volcanoes", Santorini. pp. 2–4.

Debaille, V., Doucelance, R., Weis, D., Schiano, P., 2006. Multi-stage mixing in subduction zones: Application to Merapi volcano (Java island, Sunda arc). *Geochimica et Cosmochimica Acta* **70**, 723–741.

de Capitani, C., Petrakakis, K., 2010. The computation of equilibrium assemblage diagrams with Theriak/Domino software. *American Mineralogist* **95**, 1006–1016.

Deegan, F.M., Troll, V.R., Freda, C., Misiti, V., Chadwick, J.P., 2011. Fast and furious: crustal $CO_2$ release at Merapi volcano, Indonesia. *Geology Today* **27**, 63–64.

Deegan, F.M., Troll, V.R., Freda, C., Misiti, V., Chadwick, J.P., McLeod, C.L., Davidson, J.P., 2010. Magma–carbonate interaction processes and associated $CO_2$ release at Merapi Volcano, Indonesia: insights from experimental petrology. *Journal of Petrology* **51**, 1027–1051.

Deegan, F.M., Troll, V.R., Whitehouse, M.J., Jolis, E.M., Freda, C., 2016a. Boron isotope fractionation in magma via crustal carbonate dissolution. *Scientific Reports* **6**, 30774.

Deegan, F.M., Whitehouse, M.J., Troll, V.R., Budd, D.A., Harris, C., Geiger, H., Hålenius, U., 2016b. Pyroxene standards for SIMS oxygen isotope analysis and their application to Merapi volcano, Sunda arc, Indonesia. *Chemical Geology* **447**, 1–10.

Deer, W.A., Howie, R.A., Zussman, J., 1997. Rock-Forming Minerals. 2A, 2nd ed. Geological Society of London.

Deering, C.D., Bachmann, O., Vogel, T.A., 2011. The Ammonia Tanks Tuff: Erupting a melt-rich rhyolite cap and its remobilized crystal cumulate. *Earth and Planetary Science Letters* **310**, 518–525.

Del Gaudio, P., Ventura, G., 2008. Mechanical erosion of xenoliths by magmatic shear flow. *Geophysical Research Letters* **35**.

Del Moro, A., Fulignati, P., Marianelli, P., Sbrana, A., 2001. Magma contamination by direct wall rock interaction: constraints from xenoliths from the walls of a carbonate-hosted

magma chamber (Vesuvius 1944 eruption). *Journal of Volcanology and Geothermal Research* **112**, 15–24.

Del Moro, A., Gioncada, A., Pinarelli, L., Sbrana, A., Joron, J.L., 1998. Sr, Nd, and Pb isotope evidence for open system evolution at Vulcano, Aeolian Arc, Italy. *Lithos* **43**, 81–106.

Del Moro, S., Renzulli, A., Tribaudino, M., 2011. Pyrometamorphic processes at the magma–hydrothermal system interface of active volcanoes: Evidence from buchite ejecta of Stromboli (Aeolian Islands, Italy). *Journal of Petrology* **52**, 541–564.

DeMets, C., Gordon, R.G., Argus, D., Stein, S., 1990. Current plate motions. *Geophysical Journal International* **101**, 425–478.

Dempsey, S., 2013. Geochemistry of volcanic rocks from the Sunda Arc. *Durham E-Theses*.

DePaolo, D.J., 1981. Trace element and isotopic effects of combined wallrock assimilation and fractional crystallization. *Earth and Planetary Science Letters* **53**, 189–202.

Dessimoz, M., Müntener, O., Ulmer, P., 2012. A case for hornblende dominated fractionation of arc magmas: the Chelan Complex (Washington Cascades). *Contributions to Mineralogy and Petrology* **163**, 567–589.

Devine, J.D., Gardner, J.E., Brack, H.P., Laynet, G.D., Rutherford, M.J., 1995. Comparison of microanalytical methods for estimating $H_2O$ contents of silicic volcanic glasses. *American Mineralogist* **80**, 319–328.

Dietrich, V.J., Davis, E., Gartzos, E., 1998. Amphibole in rhyodacites and dacites from the Akrotiri volcanoes and the complexities of discontinuous fractional crystallization, in: Proceedings of the 2nd Workshop,"The European Laboratory Volcanoes", Santorini. pp. 2–4.

Di Martino, C., Forni, F., Frezzotti, M.L., Palmeri, R., Webster, J.D., Ayuso, R.A., Lucchi, F., Tranne, C.A., 2011. Formation of cordierite-bearing lavas during anatexis in the lower crust beneath Lipari Island (Aeolian arc, Italy). *Contributions to Mineralogy and Petrology* **162**, 1011–1030.

Di Martino, C., Frezzotti, M.L., Lucchi, F., Peccerillo, A., Tranne, C.A., Diamond, L.W., 2010. Magma storage and ascent at Lipari Island (Aeolian archipelago, Southern Italy) at 223–81 ka: the role of crustal processes and tectonic influence. *Bulletin of Volcanology* **72**, 1061–1076.

Di Paola, G.M., 1974. Volcanology and petrology of Nisyros Island (Dodecanese, Greece). *Bulletin Volcanologique* **38**, 944–987.

Di Rocco, T., Freda, C., Gaeta, M., Mollo, S., Dallai, L., 2012. Magma chambers emplaced in carbonate substrate: petrogenesis of skarn and cumulate rocks and implications for $CO_2$ degassing in volcanic areas. *Journal of Petrology* **53**, 2307–2332.

Donoghue, E., Troll, V.R., Schwarzkopf, L.M., Clayton, G., Goodhue, R., 2009. Organic block coatings in block-and-ash flow deposits at Merapi Volcano, central Java. *Geological Magazine* **146**, 113–120.

Droop, G., 1987. A general equation for estimating $Fe^{3+}$ concentrations in ferromagnesian silicates and oxides from microprobe analyses, using stoichiometric criteria. *Mineralogical Magazine* **51**, 431–435.

Druitt, T., 2014. New insights into the initiation and venting of the Bronze-Age eruption of Santorini (Greece), from component analysis. *Bulletin of Volcanology* **76**, 1–21.

Druitt, T., 1983. Explosive volcanism on santorini, greece (PhD thesis). University of Cambridge.

Druitt, T., Costa, F., Deloule, E., Dungan, M., Scaillet, B., 2012. Decadal to monthly timescales of magma transfer and reservoir growth at a caldera volcano. *Nature* **482**, 77–80.

Druitt, T., Francaviglia, V., 1992. Caldera formation on Santorini and the physiography of the islands in the late Bronze Age. *Bulletin of Volcanology* **54**, 484–493.

Druitt, T.H., Edwards, L., Mellors, R., Pyle, D., Sparks, R., Lanphere, M., Davies, M., Barreirio, B., 1999. Santorini volcano. *Geological Society Memoir* **19**.

Druitt, T.H., Pyle, D.M., Mather, T.A., 2019. Santorini volcano and its plumbing system. *Elements: An International Magazine of Mineralogy, Geochemistry, and Petrology* **15**,

177–184.

Druitt, T., Mellors, R., Pyle, D., Sparks, R., 1989. Explosive volcanism on Santorini, Greece. *Geological Magazine* **126**, 95–126.

Druitt, T., Mercier, M., Florentin, L., Deloule, E., Cluzel, N., Flaherty, T., Médard, E., Cadoux, A., 2016. Magma storage and extraction associated with plinian and interplinian activity at Santorini caldera (Greece). *Journal of Petrology* **57**, 461–494.

Ducea, M.N., Kidder, S., Zandt, G., 2003. Arc composition at mid-crustal depths: Insights from the Coast Ridge Belt, Santa Lucia Mountains, California. *Geophysical Research Letters* **30**, 36–1, 36–4.

Ducea, M., Saleeby, J., 1998. Crustal recycling beneath continental arcs: silica-rich glass inclusions in ultramafic xenoliths from the Sierra Nevada, California. *Earth and Planetary Science Letters* **156**, 101–116.

Dungan, M.A., 2005. Partial melting at the earth's surface: implications for assimilation rates and mechanisms in subvolcanic intrusions. *Journal of Volcanology and Geothermal Research* **140**, 193–203.

Dungan, M.A., Davidson, J., 2004. Partial assimilative recycling of the mafic plutonic roots of arc volcanoes: An example from the Chilean Andes. *Geology* **32**, 773–776.

Dunn, S., Bowman, J., 2003. Stable Isotopes in Contact Metamorphism of Carbonate Rocks. Teaching Petrology Workshop, Bozeman Montana, July 9-15, 2003.

Durand, C., Baumgartner, L.P., Marquer, D., 2015. Low melting temperature for calcite at 1000 bars on the join $CaCO_3$-$H_2O$–some geological implications. *Terra Nova* **27**, 364–369.

Durand, C., Boulvais, P., Marquer, D., Rossy, M., 2006. Stable isotope transfer in open and closed system across chemically contrasted boundaries: metacarbonate–granitoid contacts in the Quérigut magmatic complex (Eastern Pyrenees, France). *Journal of the Geological Society* **163**, 827–836.

Edwards, L., 1994. Magma cyclicity and isotopic variation on Santorini volcano, Aegean Sea, Greece. (PhD thesis). University of Bristol.

Eiler, J.M., 2001. Oxygen isotope variations of basaltic lavas and upper mantle rocks. *Reviews in mineralogy and geochemistry* **43**, 319–364.

Elburg, M.A., Smet, I., De Pelsmaeker, E., 2014. Influence of source materials and fractionating assemblage on magmatism along the Aegean Arc, and implications for crustal growth. *Geological Society, London, Special Publications* **385**, 137–160.

Ellam, R., Harmon, R., 1990. Oxygen isotope constraints on the crustal contribution to the subduction-related magmatism of the Aeolian Islands, southern Italy. *Journal of Volcanology and Geothermal Research* **44**, 105–122.

Ellis, B.S., Bachmann, O., Wolff, J.A., 2014. Cumulate fragments in silicic ignimbrites: The case of the Snake River Plain. *Geology* **42**, 431–434.

Erdmann, S., Martel, C., Pichavant, M., Bourdier, J.-L., Champallier, R., Komorowski, J.-C., Cholik, N., 2016. Constraints from phase equilibrium experiments on pre-eruptive storage conditions in mixed magma systems: a case study on crystal-rich basaltic andesites from Mount Merapi, Indonesia. *Journal of Petrology* **57**, 535–560.

Erdmann, S., Martel, C., Pichavant, M., Kushnir, A., 2014. Amphibole as an archivist of magmatic crystallization conditions: problems, potential, and implications for inferring magma storage prior to the paroxysmal 2010 eruption of Mount Merapi, Indonesia. *Contributions to Mineralogy and Petrology* **167**, 1016.

Fabbro, G., Druitt, T., Scaillet, S., 2013. Evolution of the crustal magma plumbing system during the build-up to the 22-ka caldera-forming eruption of Santorini (Greece). *Bulletin of Volcanology* **75**, 1–22.

Fabbro, G.N., Druitt, T.H., Costa, F., 2018. Storage and eruption of silicic magma across the transition from dominantly effusive to caldera-forming states at an arc volcano (Santorini, Greece). *Journal of Petrology* **58**, 2429–2464.

Federico, M., Peccerillo, A., Barbieri, M., Wu, T., 1994. Mineralogical and geochemical study of granular xenoliths from the Alban Hills volcano, Central Italy: bearing on evolutionary processes in potassic magma chambers. *Contributions to Mineralogy and Petrology* **115**, 384–401.

Feig, S.T., Koepke, J., Snow, J.E., 2010. Effect of oxygen fugacity and water on phase equilibria of a hydrous tholeiitic basalt. *Contributions to Mineralogy and Petrology* **160**, 551–568.

Feig, S.T., Koepke, J., Snow, J.E., 2006. Effect of water on tholeiitic basalt phase equilibria: an experimental study under oxidizing conditions. *Contributions to Mineralogy and Petrology* **152**, 611–638.

Fietzke, J., Frische, M., 2016. Experimental evaluation of elemental behavior during LA-ICP-MS: influences of plasma conditions and limits of plasma robustness. *Journal of Analytical Atomic Spectrometry* **31**, 234–244.

Flaherty, T., Druitt, T.H., Tuffen, H., Higgins, M.D., Costa, F., Cadoux, A., 2018. Multiple timescale constraints for high-flux magma chamber assembly prior to the Late Bronze Age eruption of Santorini (Greece). *Contributions to Mineralogy and Petrology* **173**, 75.

Foden, J., Green, D., 1992. Possible role of amphibole in the origin of andesite: some experimental and natural evidence. *Contributions to Mineralogy and Petrology* **109**, 479–493.

Ford, C., Russell, D., Groven, J., Fisk, M., 1983. Distribution coefficients of $Mg^{2+}$, $Fe^{2+}$, $Ca^{2+}$ and $Mn^{2+}$ between olivine and melt. *Journal of Petrology* **24**, 256–265.

Fornaseri, M., Turi, B., 1969. Carbon and oxygen isotopic composition of carbonates in lavas and ejectites from the Alban Hills, Italy. *Contributions to Mineralogy and Petrology* **23**, 244–256.

Forni, F., Ellis, B.S., Bachmann, O., Lucchi, F., Tranne, C.A., Agostini, S., Dallai, L., 2015. Erupted cumulate fragments in rhyolites from Lipari (Aeolian Islands). *Contributions to Mineralogy and Petrology* **170**, 1–18.

Forni, F., Petricca, E., Bachmann, O., Mollo, S., De Astis, G., Piochi, M., 2018. The role of magma mixing/mingling and cumulate melting in the Neapolitan Yellow Tuff caldera-forming eruption (Campi Flegrei, Southern Italy). *Contributions to Mineralogy and Petrology* **173**, 45.

Forster, M.A., Lister, G.S., 1999. Detachment faults in the Aegean core complex of Ios, Cyclades, Greece. *Geological Society of London Special Publications* **154**, 305–323.

Foumelis, M., Trasatti, E., Papageorgiou, E., Stramondo, S., Parcharidis, I., 2013. Monitoring Santorini volcano (Greece) breathing from space. *Geophysical Journal International* ggs135.

Fouqué, F.A., 1879. Santorini et ses éruptions. Masson et Cie, Paris.

Francalanci, L., Varekamp, J.C., Vougioukalakis, G., Delant, M.J., Innocenti, F., Manetti, P., 1995. Crystal retention, fractionation and crustal assimilation in a convecting magma chamber, Nisyros Volcano, Greece. *Bulletin of Volcanology* **56**, 601–620.

Francalanci, L., Zellmer, G.F., 2019. Magma genesis at the South Aegean volcanic arc. *Elements: An International Magazine of Mineralogy, Geochemistry, and Petrology* **15**, 165–170.

France, L., Ildefonse, B., Koepke, J., Bech, F., 2010. A new method to estimate the oxidation state of basaltic series from microprobe analyses. *Journal of Volcanology and Geothermal Research* **189**, 340–346.

Francis, D., Minarik, W., 2008. Aluminum-dependent trace element partitioning in clinopyroxene. *Contributions to Mineralogy and Petrology* **156**, 439–451.

Freda, C., Gaeta, M., Giaccio, B., Marra, F., Palladino, D.M., Scarlato, P., Sottili, G., 2011. $CO_2$-driven large mafic explosive eruptions: the Pozzolane Rosse case study from the Colli Albani Volcanic District (Italy). *Bulletin of Volcanology* **73**, 241–256.

Freda, C., Gaeta, M., Misiti, V., Mollo, S., Dolfi, D., Scarlato, P., 2008. Magma–carbonate interaction: An experimental study on ultrapotassic rocks from Alban Hills (Central Italy). *Lithos* **101**, 397–415.

Freise, M., Holtz, F., Nowak, M., Scoates, J.S., Strauss, H., 2009. Differentiation and crystallization conditions of basalts from the Kerguelen large igneous province: an experimental study. *Contributions to Mineralogy and Petrology* **158**, 505.

Frezzotti, M.-L., Andersen, T., Neumann, E.-R., Simonsen, S.L., 2002. Carbonatite melt–$CO_2$ fluid inclusions in mantle xenoliths from Tenerife, Canary Islands: a story of trapping, immiscibility and fluid–rock interaction in the upper mantle. *Lithos* **64**, 77–96.

Frezzotti, M.L., Peccerillo, A., Bonelli, R., 2003. Magma ascent rates and depths of crustal magma reservoirs beneath the Aeolian volcanic Arc (Italy): Inferences from fluid and melt inclusions in xenoliths. *Developments in Volcanology* **5**, 185–205.

Frezzotti, M.-L., Peccerillo, A., Zanon, V., Nikogosian, I., 2004. Silica-rich melts in quartz xenoliths from Vulcano Island and their bearing on processes of crustal anatexis and crust–magma interaction beneath the Aeolian Arc, Southern Italy. *Journal of Petrology* **45**, 3–26.

Friedrich, W.L., Kromer, B., Friedrich, M., Heinemeier, J., Pfeiffer, T., Talamo, S., 2006. Santorini eruption radiocarbon dated to 1627-1600 B.C. *Science* **312**, 548.

Frost, B.R., 1991. Introduction to oxygen fugacity and its petrologic importance. *Reviews in Mineralogy and Geochemistry* **25**, 1–9.

Fujita, S., Suzuki, K., Ohkawa, M., Shibasaki, Y., Mori, T., 2001. Reaction of hydrogrossular with hydrogen chloride gas at high temperature. *Chemistry of Materials* **13**, 2523–2527.

Fulignati, P., Kamenetsky, V.S., Marianelli, P., Sbrana, A., 2013. PIXE mapping on multiphase fluid inclusions in endoskarn xenoliths of AD 472 eruption of Vesuvius (Italy). *Periodico di Mineralogia* **82**, 291–297.

Fulignati, P., Kamenetsky, V.S., Marianelli, P., Sbrana, A., Mernagh, T.P., 2001. Melt inclusion record of immiscibility between silicate, hydrosaline, and carbonate melts: Applications to skarn genesis at Mount Vesuvius. *Geology* **29**, 1043–1046.

Fulignati, P., Marianelli, P., Santacroce, R., Sbrana, A., 2004. Probing the Vesuvius magma chamber–host rock interface through xenoliths. *Geological Magazine* **141**, 417–428.

Fulignati, P., Marianelli, P., Santacroce, R., Sbrana, A., 2000. The skarn shell of the 1944 Vesuvius magma chamber. Genesis and PTX conditions from melt and fluid inclusion data. *European Journal of Mineralogy* **12**, 1025–1039.

Fulignati, P., Panichi, C., Sbrana, A., Caliro, S., Gioncada, A., Moro, A.D., 2005. Skarn formation at the walls of the 79AD magma chamber of Vesuvius (Italy): Mineralogical and isotopic constraints. *Neues Jahrbuch fur Mineralogie, Abhandlungen* **181**, 53–66.

Furlong, K.P., Myers, J.D., 1985. Thermal-mechanical modeling of the role of thermal stresses and stoping in magma contamination. *Journal of Volcanology and Geothermal Research* **24**, 179–191.

Gaeta, M., Fabrizio, G., Cavarretta, G., 2000. F-phlogopites in the Alban Hills Volcanic District (Central Italy): indications regarding the role of volatiles in magmatic crystallisation. *Journal of Volcanology and Geothermal Research* **99**, 179–193.

Gaeta, M., Freda, C., Christensen, J.N., Dallai, L., Marra, F., Karner, D.B., Scarlato, P., 2006. Time-dependent geochemistry of clinopyroxene from the Alban Hills (Central Italy): clues to the source and evolution of ultrapotassic magmas. *Lithos* **86**, 330–346.

Gaeta, M., Rocco, T.D., Freda, C., 2009. Carbonate assimilation in open magmatic systems: the role of melt-bearing skarns and cumulate-forming processes. *Journal of Petrology* **50**, 361–385.

Gaetani, G.A., O'Leary, J.A., Shimizu, N., Bucholz, C.E., Newville, M., 2012. Rapid reequilibration of $H_2O$ and oxygen fugacity in olivine-hosted melt inclusions. *Geology* **40**, 915–918.

Galuskin, E.V., Galuskina, I.O., Bailau, R., Prusik, K., Gazeev, V.M., Zadov, A.E., Pertsev, N.N., Jeżak, L., Gurbanov, A.G., Dubrovinsky, L., 2013. Eltyubyuite, $Ca_{12}Fe^{3+}{}_{10}Si_4O_{32}Cl_6$– the $Fe^{3+}$ analogue of wadalite: a new mineral from the Northern Caucasus, Kabardino-Balkaria, Russia. *European Journal of Mineralogy* **25**, 221–229.

Galuskin, E.V., Gfeller, F., Galuskina, I.O., Armbruster, T., Bailau, R., Sharygin, V.V., 2015. Mayenite supergroup, part I: Recommended nomenclature. *European Journal of Mineralogy* **27**, 99–111.

Ganino, C., Arndt, N.T., Zhou, M.-F., Gaillard, F., Chauvel, C., 2008. Interaction of magma with sedimentary wall rock and magnetite ore genesis in the Panzhihua mafic intrusion, SW China. *Mineralium Deposita* **43**, 677.

Gasparon, M., Varne, R., 1998. Crustal assimilation versus subducted sediment input in west Sunda arc volcanics: an evaluation. *Mineralogy and Petrology* **64**, 89–117.

Genareau, K., Cronin, S.J., Lube, G., 2015. Effects of volatile behaviour on dome collapse and resultant pyroclastic surge dynamics: Gunung Merapi 2010 eruption. *Geological Society, London, Special Publications* **410**, 199–218.

Genevraye, P.D., Samuel, L., 1972. Geology of the Kendeng Zone (Central & East Java).

Genge, M.J., Price, G.D., Jones, A.P., 1995. Molecular dynamics simulations of $CaCO_3$ melts to mantle pressures and temperatures: implications for carbonatite magmas. *Earth and Planetary Science Letters* **131**, 225–238.

Gertisser, R., 2001. Gunung Merapi (Java, Indonesien): Eruptionsgeschichte und magmatische Evolution eines Hochrisiko-Vulkans (PhD thesis). University of Freiburg.

Gertisser, R., Charbonnier, S.J., Keller, J., Quidelleur, X., 2012. The geological evolution of Merapi volcano, Central Java, Indonesia. *Bulletin of Volcanology* **74**, 1213–1233.

Gertisser, R., Charbonnier, S.J., Troll, V.R., Keller, J., Preece, K., Chadwick, J., Barclay, J., Herd, R., 2011. Merapi (Java, Indonesia): anatomy of a killer volcano. *Geology Today* **27**, 57–62.

Gertisser, R., Keller, J., 2003a. Temporal variations in magma composition at Merapi Volcano (Central Java, Indonesia): magmatic cycles during the past 2000 years of explosive activity. *Journal of Volcanology and Geothermal Research* **123**, 1–23.

Gertisser, R., Keller, J., 2003b. Trace element and Sr, Nd, Pb and O isotope variations in medium-K and high-K volcanic rocks from Merapi Volcano, Central Java, Indonesia: evidence for the involvement of subducted sediments in Sunda arc magma genesis. *Journal of Petrology* **44**, 457–489.

Gertisser, R., Preece, K., Keller, J., 2009. The Plinian Lower Pumice 2 eruption, Santorini, Greece: magma evolution and volatile behaviour. *Journal of Volcanology and Geothermal Research* **186**, 387–406.

Ghiorso, M.S., 2016. Modeling carbonate assimilation into crustal magmas: Quantifying overpressure and eruption triggers, in: Goldschmidt Conference Abstracts. Yokohama,

Japan.

Ghiorso, M.S., Sack, R.O., 1995. Chemical mass transfer in magmatic processes IV. A revised and internally consistent thermodynamic model for the interpolation and extrapolation of liquid-solid equilibria in magmatic systems at elevated temperatures and pressures. *Contributions to Mineralogy and Petrology* **119**, 197–212.

Gilg, H., Lima, A., Somma, R., Belkin, H., Vivo, B.D., Ayuso, R., 2001. Isotope geochemistry and fluid inclusion study of skarns from Vesuvius. *Mineralogy and Petrology* **73**, 145–176.

Gill, J.B., 1981. Orogenic andesites and plate tectonics. Springer.

Glasser, F., 1995. Comments on wadalite, $Ca_6Al_5Si_2O_{16}Cl_3$, and the structures of garnet, mayenite and calcium chlorosilicate. Addendum. *Acta Crystallographica Section C: Crystal Structure Communications* **51**, 340–340.

Glazner, A.F., 2007. Thermal limitations on incorporation of wall rock into magma. *Geology* **35**, 319–322.

Glazner, A.F., 1994. Foundering of mafic plutons and density stratification of continental crust. *Geology* **22**, 435–438.

Glazner, A.F., Ussler, W., 1988. Trapping of magma at midcrustal density discontinuities. *Geophysical Research Letters* **15**, 673–675.

Goff, F., Love, S.P., Warren, R.G., Counce, D., Obenholzner, J., Siebe, C., Schmidt, S.C., 2001. Passive infrared remote sensing evidence for large, intermittent $CO_2$ emissions at Popocatépetl volcano, Mexico. *Chemical Geology* **177**, 133–156.

Goldstein, R.H., 2003. Petrographic analysis of fluid inclusions, in: Samson, I., Anderson, A., Marshall, D. (Eds.), Fluid Inclusions: Analysis and Interpretation, Mineral Association of Canada Short Course. Mineralogical Association of Canada Vancouver, pp. 9–53.

Good, D.J., Crocket J., H., Barnett R., L., 1997. A secondary clinopyroxene-chlorite-spinel assemblage in clinopyroxenite of the Mann complex, Abitibi Belt, Ontario: An unusual hydrothermal alteration suite. *Mineralogy and Petrology* **59**, 69–90.

Gordon, T. M., Greenwood, H.J., 1971. The Stability of Grossularite in $H_2O$-$CO_2$ Mixtures. *The American Mineralogist* **56**, 1674–1688.

Gorzkowska, I., Maciejewski, M., Rudnicki, R., 1988a. Thermal decomposition of $CaCO_3$ in the presence of calcium fluoride. *Journal of Thermal Analysis and Calorimetry* **33**, 983–990.

Gorzkowska, I., Maciejewski, M., Rudnicki, R., 1988b. Application of DTA and TG to studies of the $CaCO_3$-$CaF_2$ phase diagram. *Journal of Thermal Analysis and Calorimetry* **33**, 991–995.

Gozzi, F., Gaeta, M., Freda, C., Mollo, S., Rocco, T.D., Marra, F., Dallai, L., Pack, A., 2014. Primary magmatic calcite reveals origin from crustal carbonate. *Lithos* **190**–**191**, 191–203.

Grapes, R., 2010. Pyrometamorphism, 2nd ed. Springer.

Grapes, R.H., 1986. Melting and thermal reconstitution of pelitic xenoliths, Wehr volcano, East Eifel, West Germany. *Journal of Petrology* **27**, 343–396.

Greenwood, H., 1967. Wollastonite: stability in $H_2O$-$CO_2$ mixtures and occurrence in a contact-metamorphic aureole near Salmo. *British Columbia, Canada.American Mineralogist* **52**, 1669–1680.

Gregg, P., Silva, S. de, Grosfils, E., 2013. Thermomechanics of shallow magma chamber pressurization: Implications for the assessment of ground deformation data at active volcanoes. *Earth and Planetary Science Letters* **384**, 100–108.

Grew, E.S., Locock, A.J., Mills, S.J., Galuskina, I.O., Galuskin, E.V., Hålenius, U., 2013. Nomenclature of the garnet supergroup. *American Mineralogist* **98**, 785–811.

Grove, T., Kinzler, R., Baker, M., Donnelly-Nolan, J., Lesher, C., 1988. Assimilation of granite by basaltic magma at Burnt Lava flow, Medicine Lake volcano, northern California: decoupling of heat and mass transfer. *Contributions to Mineralogy and Petrology* **99**, 320–343.

Grove, T.L., Chatterjee, N., Parman, S.W., Médard, E., 2006. The influence of $H_2O$ on mantle wedge melting. *Earth and Planetary Science Letters* **249**, 74–89.

Grove, T.L., Till, C.B., Krawczynski, M.J., 2012. The role of $H_2O$ in subduction zone magmatism. *Annual Review of Earth and Planetary Sciences* **40**, 413–439.

Gualda, G.A., Ghiorso, M.S., Lemons, R.V., Carley, T.L., 2012. Rhyolite-MELTS: a modified calibration of MELTS optimized for silica-rich, fluid-bearing magmatic systems. *Journal of Petrology* **53**, 875–890.

Gualda, G.A.R., Gravley, D.M., Deering, C.D., Ghiorso, M.S., 2019. Magma extraction pressures and the architecture of volcanic plumbing systems. *Earth and Planetary Science Letters* **522**, 118–124.

Gustafson, W.I., 1974. The stability of andradite, hedenbergite, and related minerals in the system Ca-Fe-Si-O-H. *Journal of Petrology* **15**, 455–496.

Gutjahr, M., Ridgwell, A., Sexton, P.F., Anagnostou, E., Pearson, P.N., Pälike, H., Norris, R.D., Thomas, E., Foster, G.L., 2017. Very large release of mostly volcanic carbon during the Palaeocene-Eocene Thermal Maximum. *Nature* **548**, 573.

Hamada, M., Ushioda, M., Fujii, T., Takahashi, E., 2013. Hydrogen concentration in plagioclase as a hygrometer of arc basaltic melts: Approaches from melt inclusion analyses and hydrous melting experiments. *Earth and Planetary Science Letters* **365**, 253–262.

Hamilton, W.B., 1979. Tectonics of the Indonesian region. US Government Printing Office.

Hammer, J.E., 2006. Influence of fO2 and cooling rate on the kinetics and energetics of Fe-rich basalt crystallization. *Earth and Planetary Science Letters* **248**, 618–637.

Handley, H.K., Blichert-Toft, J., Gertisser, R., Macpherson, C.G., Turner, S.P., Zaennudin, A., Abdurrachman, M., 2014. Insights from Pb and O isotopes into along-arc variations in subduction inputs and crustal assimilation for volcanic rocks in Java, Sunda arc, Indonesia. *Geochimica et Cosmochimica Acta* **139**, 205–226.

Handley, H.K., Turner, S., Macpherson, C.G., Gertisser, R., Davidson, J.P., 2011. Hf–Nd isotope and trace element constraints on subduction inputs at island arcs: Limitations of Hf anomalies as sediment input indicators. *Earth and Planetary Science Letters* **304**, 212–223.

Handley, H., Reagan, M., Gertisser, R., Preece, K., Berlo, K., McGee, L., Barclay, J., Herd, R., 2018. Timescales of magma ascent and degassing and the role of crustal assimilation at Merapi volcano (2006–2010), Indonesia: Constraints from uranium-series and radiogenic isotopic compositions. *Geochimica et Cosmochimica Acta* **222**, 34–52.

Hansteen, T.H., Klügel, A., 2008. Fluid inclusion thermobarometry as a tracer for magmatic processes. *Reviews in Mineralogy and Geochemistry* **69**, 143–177.

Hansteen, T.H., Klügel, A., Schmincke, H.-U., 1998. Multi-stage magma ascent beneath the Canary Islands: evidence from fluid inclusions. *Contributions to Mineralogy and Petrology* **132**, 48–64.

Harlov, D., Renzulli, A., Ridolfi, F., 2006. Iron-bearing chlor-fluorapatites in crustal xenoliths from the Stromboli volcano (Aeolian Islands, Southern Italy) an indicator of fluid processes during contact metamorphism. *European Journal of Mineralogy* **18**, 233–241.

Harmon, R.S., Hoefs, J., 1995. Oxygen isotope heterogeneity of the mantle deduced from global $^{18}$O systematics of basalts from different geotectonic settings. *Contributions to Mineralogy and Petrology* **120**, 95–114.

Harris, C., Pronost, J.J.M., Ashwal, L.D., Cawthorn, R.G., 2004. Oxygen and hydrogen isotope stratigraphy of the Rustenburg Layered Suite, Bushveld Complex: constraints on crustal contamination. *Journal of Petrology* **46**, 579–601.

Hattori, K., 2018. Porphyry copper potential in Japan based on magmatic oxidation state. *Resource Geology* **68**, 126–137.

Hawthorne, F.C., Oberti, R., Harlow, G.E., Maresch, W.V., Martin, R.F., Schumacher, J.C., Welch, M.D., 2012. Nomenclature of the amphibole supergroup. *American Mineralogist* **97**, 2031–2048.

Heap, M., Mollo, S., Vinciguerra, S., Lavallée, Y., Hess, K.-U., Dingwell, D.B., Baud, P., Iezzi, G., 2013. Thermal weakening of the carbonate basement under Mt. Etna volcano (Italy): implications for volcano instability. *Journal of Volcanology and Geothermal Research* **250**, 42–60.

Heinrich, W., Hoffbauer, R., Hubberten, H.-W., 1995. Contrasting fluid flow patterns at the Bufa del Diente contact metamorphic aureole, north-east Mexico: evidence from stable isotopes. *Contributions to Mineralogy and Petrology* **119**, 362–376.

Henmi, C., Henmi, K., 1978. Synthesis of spurrite and tilleyite at low $CO_2$ partial pressure. *Mineralogical Journal* **9**, 106–110.

Hermes, O.D., Cornell, W.C., 1981. Quenched crystal mush and associated magma compositions as indicated by intercumulus glasses from Mt. Vesuvius, Italy. *Journal of Volcanology and Geothermal Research* **9**, 133–149.

Herzberg, C., Fyfe, W., Carr, M., 1983. Density constraints on the formation of the continental Moho and crust. *Contributions to Mineralogy and Petrology* **84**, 1–5.

Hickey-Vargas, R., Abdollahi, M.J., Parada, M.A., López-Escobar, L., Frey, F.A., 1995. Crustal xenoliths from Calbuco Volcano, Andean Southern Volcanic Zone: implications for crustal composition and magma-crust interaction. *Contributions to Mineralogy and Petrology* **119**, 331–344.

Higgins, M.D., 2006. Quantitative textural measurements in igneous and metamorphic petrology. Cambridge University Press.

Higgins, M.D., 2000. Measurement of crystal size distributions. *American Mineralogist* **85**, 1105–1116.

Hildner, E., Klügel, A., Hansteen, T.H., 2012. Barometry of lavas from the 1951 eruption of Fogo, Cape Verde Islands: Implications for historic and prehistoric magma plumbing systems. *Journal of Volcanology and Geothermal Research* **217**, 73–90.

Hildreth, W., 2004. Volcanological perspectives on Long Valley, Mammoth Mountain, and Mono Craters: several contiguous but discrete systems. *Journal of Volcanology and Geothermal Research* **136**, 169–198.

Hildreth, W., Moorbath, S., 1988. Crustal contributions to arc magmatism in the Andes of central Chile. *Contributions to Mineralogy and Petrology* **98**, 455–489.

Hill, E., Blundy, J.D., Wood, B.J., 2011. Clinopyroxene–melt trace element partitioning and the development of a predictive model for HFSE and Sc. *Contributions to Mineralogy*

*and Petrology* **161**, 423–438.

Hill, E., Wood, B.J., Blundy, J.D., 2000. The effect of Ca-Tschermaks component on trace element partitioning between clinopyroxene and silicate melt. *Lithos* **53**, 203–215.

Hirschmann, M., Ghiorso, M., Davis, F., Gordon, S., Mukherjee, S., Grove, T., Krawczynski, M., Medard, E., Till, C., 2008. Library of Experimental Phase Relations (LEPR): A database and Web portal for experimental magmatic phase equilibria data. *Geochemistry, Geophysics, Geosystems* **9**.

Holland, T., Blundy, J., 1994. Non-ideal interactions in calcic amphiboles and their bearing on amphibole-plagioclase thermometry. *Contributions to Mineralogy and Petrology* **116**, 433–447.

Holland, T.J.B., Powell, R., 1998. An internally consistent thermodynamic data set for phases of petrological interest. *Journal of Metamorphic Geology* **16**, 309–343.

Holloway, J.R., Blank, J.G., 1994. Application of experimental results to COH species in natural melts. *Reviews in Mineralogy* **30**, 187–187.

Holness, M.B., Cheadle, M.J., McKenzie, D., 2005a. On the use of changes in dihedral angle to decode late-stage textural evolution in cumulates. *Journal of Petrology* **46**, 1565–1583.

Holness, M.B., Tegner, C., Nielsen, T.F., Stripp, G., Morse, S.A., 2007. A textural record of solidification and cooling in the Skaergaard intrusion, East Greenland. *Journal of Petrology* **48**, 2359–2377.

Holness, M., Martin, V., Pyle, D., 2005b. Information about open-system magma chambers derived from textures in magmatic enclaves: the Kameni Islands, Santorini, Greece. *Geological Magazine* **142**, 637–649.

Honnorez, J., Keller, J., 1968. Xenolithe in vulkanischen Gesteinen der Äolischen Inseln (Sizilien). *Geologische Rundschau* **57**, 719–736.

Housh, T.B., Luhr, J.F., 1991. Plagioclase-melt equilibria in hydrous systems. *American Mineralogist* **76**, 477–492.

Huber, C., Bachmann, O., Manga, M., 2010. Two competing effects of volatiles on heat transfer in crystal-rich magmas: Thermal insulation vs defrosting. *Journal of Petrology*

**51**, 847–867.

Huckenholz, H., Lindhuber, W., Springer, J., 1974. The join $CaSiO_3$-$Al_2O_3$-$Fe_2O_3$ of the CaO-$Al_2O_3$-$Fe_2O_3$-$SiO_2$ quaternary system and its bearing on the formation of granditic garnets and fassaitic pyroxenes. *Neues Jahrbuch fur Mineralogie, Abhandlungen* **121**, 160–207.

Huijsmans, J.P., Barton, M., 1989. Polybaric geochemical evolution of two shield volcanoes from Santorini, Aegean Sea, Greece: evidence for zoned magma chambers from cyclic compositional variations. *Journal of Petrology* **30**, 583–625.

Huijsmans, J.P., Barton, M., Salters, V.J., 1988. Geochemistry and evolution of the calc-alkaline volcanic complex of Santorini, Aegean Sea, Greece. *Journal of Volcanology and Geothermal Research* **34**, 283–306.

Huijsmans, J.P.P., 1985. Calc-alkaline lavas from the volcanic complex of Santorini, Aegean Sea, Greece: a petrological, geochemical and stratigraphic study (PhD thesis). Instituut voor Aardwetenschappen Rijksuniversiteit Utrecht.

Hunter, R., 1996. Texture development in cumulate rocks. *Developments in Petrology* **15**, 77–101.

Iacono-Marziano, G., Gaillard, F., Pichavant, M., 2008. Limestone assimilation by basaltic magmas: an experimental re-assessment and application to Italian volcanoes. *Contributions to Mineralogy and Petrology* **155**, 719–738.

Iacono-Marziano, G., Gaillard, F., Pichavant, M., 2007. Limestone assimilation and the origin of $CO_2$ emissions at the Alban Hills (Central Italy): constraints from experimental petrology. *Journal of Volcanology and Geothermal Research* **166**, 91–105.

Iacono-Marziano, G., Gaillard, F., Scaillet, B., Pichavant, M., Chiodini, G., 2009. Role of non-mantle $CO_2$ in the dynamics of volcano degassing: The Mount Vesuvius example. *Geology* **37**, 319–322.

Innocenti, S., Marmol, M.-A. del, Voight, B., Andreastuti, S., Furman, T., 2013. Textural and mineral chemistry constraints on evolution of Merapi Volcano, Indonesia. *Journal of Volcanology and Geothermal Research* **261**, 20–37.

Irvine, T., 1982. Terminology for layered intrusions. *Journal of Petrology* **23**, 127–162.

Irving, A., 1974. Geochemical and high pressure experimental studies of garnet pyroxenite and pyroxene granulite xenoliths from the Delegate basaltic pipes, Australia. *Journal of Petrology* **15**, 1–40.

Ito, E., White, W.M., Göpel, C., 1987. The O, Sr, Nd and Pb isotope geochemistry of MORB. *Chemical Geology* **62**, 157–176.

Jackson, E., 1967. Ultramafic cumulates in the Stillwater, Great Dyke, and Bushveld intrusions, in: Ultramafic and Related Rocks. Wiley New York, pp. 20–38.

Jackson, E.D., 1961. Primary textures and mineral associations in the ultramafic zone of the Stillwater Complex, Montana (Professional Paper No. 358). US Government. Print. Office.

Jackson, J., 1994. Active tectonics of the Aegean region. *Annual Review of Earth and Planetary Sciences* **22**, 239–271.

Jago, B.C., Gittins, J., 1991. The role of fluorine in carbonatite magma evolution. *Nature* **349**, 56.

Jagoutz, O., 2014. Arc crustal differentiation mechanisms. *Earth and Planetary Science Letters* **396**, 267–277.

Jarrard, R.D., 1986. Relations Among Subduction Parameters. *Reviews of Geophysics* **24**, 217–284.

Jeffery, A.J., Gertisser, R., Troll, V.R., Jolis, E.M., Dahren, B., Harris, C., Tindle, A.G., Preece, K., O'Driscoll, B., Humaida, H., others, 2013. The pre-eruptive magma plumbing system of the 2007–2008 dome-forming eruption of Kelut volcano, East Java, Indonesia. *Contributions to Mineralogy and Petrology* **166**, 275–308.

Jégo, S., Pichavant, M., 2012. Gold solubility in arc magmas: Experimental determination of the effect of sulfur at 1000 C and 0.4 GPa. *Geochimica et Cosmochimica Acta* **84**, 560–592.

Jégo, S., Pichavant, M., Mavrogenes, J.A., 2010. Controls on gold solubility in arc magmas: An experimental study at 1000 C and 4 kbar. *Geochimica et Cosmochimica Acta* **74**,

2165–2189.

Joesten, R., 1974. Local equilibrium and metasomatic growth of zoned calc-silicate nodules from a contact aureole, Christmas Mountains, Big Bend region, Texas. *American Journal of Science* **274**, 876–901.

Jolis, E.M., Freda, C., Troll, V.R., Deegan, F.M., Blythe, L.S., McLeod, C.L., Davidson, J.P., 2013. Experimental simulation of magma–carbonate interaction beneath Mt. Vesuvius, Italy. *Contributions to Mineralogy and Petrology* **166**, 1335–1353.

Jolis, E., Troll, V., Harris, C., Freda, C., Gaeta, M., Orsi, G., Siebe, C., 2015. Skarn xenolith record crustal $CO_2$ liberation during Pompeii and Pollena eruptions, Vesuvius volcanic system, central Italy. *Chemical Geology* **415**, 17–36.

Jousset, P., Budi-Santoso, A., Jolly, A.D., Boichu, M., Dwiyono, S., Sumarti, S., Hidayati, S., Thierry, P., 2013. Signs of magma ascent in LP and VLP seismic events and link to degassing: An example from the 2010 explosive eruption at Merapi volcano, Indonesia. *Journal of Volcanology and Geothermal Research* **261**, 171–192.

Kadarusman, A., Massonne, H.-J., Roermund, H. van, Permana, H., Munasri, 2007. PT evolution of eclogites and blueschists from the Luk Ulo Complex of central Java, Indonesia. *International Geology Review* **49**, 329–356.

Kalamarides, R.I., 1986. High-temperature oxygen isotope fractionation among the phases of the Kiglapait intrusion, Labrador, Canada. *Chemical Geology* **58**, 303–310.

Karátson, D., Gertisser, R., Telbisz, T., Vereb, V., Quidelleur, X., Druitt, T., Nomikou, P., Kósik, S., 2018. Towards reconstruction of the lost Late Bronze Age intra-caldera island of Santorini, Greece. *Scientific reports* **8**, 7026.

Kelemen, P.B., Yogodzinski, G.M., Scholl, D.W., 2004. Along-strike variation in the Aleutian island arc: Genesis of high Mg# andesite and implications for continental crust. *Inside the subduction factory* **138**, 223–276.

Kent, A.J., 2008. Melt inclusions in basaltic and related volcanic rocks. *Reviews in Mineralogy and Geochemistry* **69**, 273–331.

Kerinec, F., 1982. Le Merapi, volcan actif d'arc insulaire (Java): Petrographie et geochimie des materiaux solides; implications geotectoniques (PhD thesis). Université Paris-Sud, Orsay, France.

Kerr, R.C., 2001. Thermal erosion by laminar lava flows. *Journal of Geophysical Research, Solid Earth* **106**, 26453–26465.

Kerrick, D., 1977. The genesis of zoned skarns in the Sierra Nevada, California. *Journal of Petrology* **18**, 144–181.

Kilgour, G.N., Saunders, K.E., Blundy, J.D., Cashman, K.V., Scott, B.J., Miller, C.A., 2014. Timescales of magmatic processes at Ruapehu volcano from diffusion chronometry and their comparison to monitoring data. *Journal of Volcanology and Geothermal Research* **288**, 62–75.

Kilias, A., Mountrakis, D., Tranos, M., Pavlides, S., 1998. The pre-volcanic metamorphic rocks of Santorini Island: Structural evolution and kinematics during the Tertiary (South Aegean, Greece), in: European Laboratory Volcanoes, Proc. 2nd Workshop on Europ. Lab. Volcanoes, Eds: R. Casale, M. Fytikas, G. Sigvaldasson and G. Vougioukalakis, Europ. Comm., Sci. Res. Develop. pp. 23–36.

Kilias, S.P., Nomikou, P., Papanikolaou, D., Polymenakou, P.N., Godelitsas, A., Argyraki, A., Carey, S., Gamaletsos, P., Mertzimekis, T.J., Stathopoulou, E., others, 2013. New insights into hydrothermal vent processes in the unique shallow-submarine arc-volcano, Kolumbo (Santorini), Greece. *Scientific reports* **3**, 2421.

Kimura, M., Mikouchi, T., Suzuki, A., Miyahara, M., Ohtani, E., Goresy, A.E., 2009. Kushiroite, CaAlAlSiO6: A new mineral of the pyroxene group from the ALH 85085 CH chondrite, and its genetic significance in refractory inclusions. *American Mineralogist* **94**, 1479–1482.

Kinman, W.S., Neal, C.R., 2006. Magma evolution revealed by anorthite-rich plagioclase cumulate xenoliths from the Ontong Java Plateau: insights into LIP magma dynamics and melt evolution. *Journal of Volcanology and Geothermal Research* **154**, 131–157.

Klaver, M., Blundy, J.D., Vroon, P.Z., 2018. Generation of arc rhyodacites through cumulate-melt reactions in a deep crustal hot zone: Evidence from Nisyros volcano. *Earth and Planetary Science Letters* **497**, 169–180.

Klaver, M., Carey, S., Nomikou, P., Smet, I., Godelitsas, A., Vroon, P., 2016. A distinct source and differentiation history for Kolumbo submarine volcano, Santorini volcanic field, Aegean arc. *Geochemistry, Geophysics, Geosystems* **17**, 3254–3273.

Klaver, M., Matveev, S., Berndt, J., Lissenberg, C.J., Vroon, P.Z., 2017. A mineral and cumulate perspective to magma differentiation at Nisyros volcano, Aegean arc. *Contributions to Mineralogy and Petrology* **172**, 1.

Kokh, M.A., Akinfiev, N.N., Pokrovski, G.S., Salvi, S., Guillaume, D., 2017. The role of carbon dioxide in the transport and fractionation of metals by geological fluids. *Geochimica et Cosmochimica Acta* **197**, 433–466.

Komorowski, J.-C., Jenkins, S., Baxter, P.J., Picquout, A., Lavigne, F., Charbonnier, S., Gertisser, R., Preece, K., Cholik, N., Budi-Santoso, A., 2013. Paroxysmal dome explosion during the Merapi 2010 eruption: processes and facies relationships of associated high-energy pyroclastic density currents. *Journal of Volcanology and Geothermal Research* **261**, 260–294.

Konstantinou, K., 2010. Crustal rheology of the Santorini–Amorgos zone: Implications for the nucleation depth and rupture extent of the 9 July 1956 Amorgos earthquake, southern Aegean. *Journal of Geodynamics* **50**, 400–409.

Konstantinou, K., Evangelidis, C., Liang, W.-T., Melis, N., Kalogeras, I., 2013. Seismicity, Vp/Vs and shear wave anisotropy variations during the 2011 unrest at Santorini caldera, southern Aegean. *Journal of Volcanology and Geothermal Research* **267**, 57–67.

Korzhiniskii, D., 1970. Theory of Metasomatic Zoning. Clarendon Press, Oxford.

Kouchi, A., Sugawara, Y., Kashima, K., Sunagawa, I., 1983. Laboratory growth of sector zoned clinopyroxenes in the system $CaMgSi_2O_6$-$CaTiAl_2O_6$. *Contributions to Mineralogy and Petrology* **83**, 177–184.

Krause, J., Brügmann, G.E., Pushkarev, E.V., 2007. Accessory and rock forming minerals monitoring the evolution of zoned mafic–ultramafic complexes in the Central Ural Mountains. *Lithos* **95**, 19–42.

Kténas, C., 1927. Les enclaves enallogénes et les laves endomorphisées de Fouqué-Kameni. *Compt. Rend.* **184**, 1012.

Kushiro, I., 1990. Partial melting of mantle wedge and evolution of island arc crust. *Journal of Geophysical Research, Solid Earth* **95**, 15929–15939.

Kyser, T.K., O'Neil, J.R., Carmichael, I.S.E., 1981. Oxygen isotope thermometry of basic lavas and mantle nodules. *Contributions to Mineralogy and Petrology* **77**, 11–23.

Lacroix, A., 1901. Sur deux nouveau groupes d'enclaves des roches eruptives. *Bulletin de la Société Française de Minéralogie* **24**, 488–504.

Lacroix, A., 1900. Sur les transformations endomorphiques de la andesite de Santorini sous l'influence d'enclaves enallogènes calcaires. *Comptes rendus hebdomadaires des séances de l'Académie des sciences* **130**, 272.

Lacroix, A., 1893. Les enclaves des roches volcaniques. Protat frères, imprimeurs.

Lacroix, B., Vennemann, T., 2015. Empirical calibration of the oxygen isotope fractionation between quartz and Fe–Mg-chlorite. *Geochimica et Cosmochimica Acta* **149**, 21–31.

Laiolo, M., Cigolini, C., 2006. Mafic and ultramafic xenoliths in San Bartolo lava field: New insights on the ascent and storage of Stromboli magmas. *Bulletin of Volcanology* **68**, 653–670.

LaMoreaux, P.E., 1995. Worldwide environmental impacts from the eruption of Thera. *Environmental Geology* **26**, 172–181.

Landtwing, M.R., Pettke, T., Halter, W.E., Heinrich, C.A., Redmond, P.B., Einaudi, M.T., Kunze, K., 2005. Copper deposition during quartz dissolution by cooling magmatic–hydrothermal fluids: the Bingham porphyry. *Earth and Planetary Science Letters* **235**, 229–243.

Lange, R.A., Frey, H.M., Hector, J., 2009. A thermodynamic model for the plagioclase-liquid hygrometer/thermometer. *American Mineralogist* **94**, 494–506.

Lavoie, D., 1995. Carbonate botryoids in Lower Devonian amygdaloidal basalts; evidence for precipitation of high-magnesium calcite from heated and volcanic $CO_2$-buffered marine waters. *Journal of Sedimentary Research* **65**, 541–546.

Lee, C.-T.A., Bachmann, O., 2014. How important is the role of crystal fractionation in making intermediate magmas? Insights from Zr and P systematics. *Earth and Planetary Science Letters* **393**, 266–274.

Lee, C.-T.A., Shen, B., Slotnick, B.S., Liao, K., Dickens, G.R., Yokoyama, Y., Lenardic, A., Dasgupta, R., Jellinek, M., Lackey, J.S., others, 2013. Continental arc–island arc fluctuations, growth of crustal carbonates, and long-term climate change. *Geosphere* **9**, 21–36.

Lentz, D.R., 1999. Carbonatite genesis: a reexamination of the role of intrusion-related pneumatolytic skarn processes in limestone melting. *Geology* **27**, 335–338.

Lepage, L.D., 2003. ILMAT: an excel worksheet for ilmenite–magnetite geothermometry and geobarometry. *Computers & Geosciences* **29**, 673–678.

Le Pichon, X., Angelier, J., 1979. The Hellenic arc and trench system: a key to the neotectonic evolution of the eastern Mediterranean area. *Tectonophysics* **60**, 1–42.

Levresse, G., Cervantes-de la Cruz, K.E., Aranda-Gómez, J.J., Dávalos-Elizondo, M.G., Jiménez-Sandoval, S., Rodríguez-Melgarejo, F., Alba-Aldave, L.A., 2016. CO 2 fluid inclusion barometry in mantle xenoliths from central Mexico: A detailed record of magma ascent. *Journal of Volcanology and Geothermal Research* **310**, 72–88.

Lindsley, D.H., 1983. Pyroxene thermometry. *American Mineralogist* **68**, 477–493.

Locock, A.J., 2014. An Excel spreadsheet to classify chemical analyses of amphiboles following the IMA 2012 recommendations. *Computers & Geosciences* **62**, 1–11.

Loucks, R.R., 1996. A precise olivine-augite Mg-Fe-exchange geothermometer. *Contributions to Mineralogy and Petrology* **125**, 140–150.

Lovering, J.F., White, A.J.R., 1969. Granulitic and eclogitic inclusions from basic pipes at Delegate, Australia. *Contributions to Mineralogy and Petrology* **21**, 9–52.

Lovering, T., 1937. Temperatures in a sinking xenolith. *EOS, Transactions American Geophysical Union* **18**, 263–263.

Lucchi, F., Gertisser, R., Keller, J., Forni, F., Astis, G.D., Tranne, C., 2013. Eruptive history and magmatic evolution of the island of Salina (central Aeolian archipelago). *Geological Society, London, Memoirs* **37**, 155–211.

Luce, J.V., 1969. The end of Atlantis: New light on an old legend (New Aspects of Antiquity). *London: Thames & Hudson.ISBN*.

Lucido, G., Nuccio, P.M., Leone, G., Longinelli, A., 1980. Amygdaloidal basalts: Isotopic and petrographic evidence for non-diagenetic crustal source of carbonate inclusions. *Tschermaks Mineralogische und Petrographische Mittlungen* **27**, 113–128.

Luhr, J.F., 2008. Primary igneous anhydrite: Progress since its recognition in the 1982 El Chichón trachyandesite. *Journal of Volcanology and Geothermal Research* **175**, 394–407.

Ma, C., Simon, S.B., Rossman, G.R., Grossman, L., 2009. Calcium Tschermak's pyroxene, $CaAlAlSiO_6$, from the Allende and Murray meteorites: EBSD and micro-Raman characterizations. *American Mineralogist* **94**, 1483–1486.

Macdonald, R., Belkin, H., Fitton, J., Rogers, N., Nejbert, K., Tindle, A., Marshall, A., 2008. The roles of fractional crystallization, magma mixing, crystal mush remobilization and volatile–melt interactions in the genesis of a young basalt–peralkaline rhyolite suite, the Greater Olkaria Volcanic Complex, Kenya rift valley. *Journal of Petrology* **49**, 1515–1547.

Macedonio, G., Dobran, F., Neri, A., 1994. Erosion processes in volcanic conduits and application to the AD 79 eruption of Vesuvius. *Earth and Planetary Science Letters* **121**, 137–152.

Macgregor, I.D., Carter, J., 1970. The chemistry of clinopyroxenes and garnets of eclogite and peridotite xenoliths from the Roberts Victor Mine, South Africa. *Physics of the Earth and Planetary Interiors* **3**, 391–397.

Manning, C.E., Bird, D.K., 1986. Hydrothermal clinopyroxenes of the Skaergaard intrusion. *Contributions to Mineralogy and Petrology* **92**, 437–447.

Markl, G., 2005. Mullite-corundum-spinel-cordierite-plagioclase xenoliths in the Skaergaard Marginal Border Group: multi-stage interaction between metasediments and basaltic magma. *Contributions to Mineralogy and Petrology* **149**, 196–215.

Marks, N., P., S., A., Z.R., H., F., Fridleifsson, G.Ó., 2010. Hydrothermal alteration in the Reykjanes geothermal system: Insights from Iceland deep drilling program well RN-17. *Journal of Volcanology and Geothermal Research* **189**, 172–190.

Marsh, B.D., 1998. On the interpretation of crystal size distributions in magmatic systems. *Journal of Petrology* **39**, 553–599.

Marsh, B.D., 1996. Solidification fronts and magmatic evolution. *Mineralogical Magazine* **60**, 5–40.

Marsh, B.D., 1988a. Crystal capture, sorting, and retention in convecting magma. *Geological Society of America Bulletin* **100**, 1720–1737.

Marsh, B.D., 1988b. Crystal size distribution (CSD) in rocks and the kinetics and dynamics of crystallization. *Contributions to Mineralogy and Petrology* **99**, 277–291.

Marsh, B.D., 1981. On the crystallinity, probability of occurrence, and rheology of lava and magma. *Contributions to Mineralogy and Petrology* **78**, 85–98.

Martin, V.M., Davidson, J.P., Morgan, D.J., Jerram, D.A., 2007. Constraints on the Rates of Replenishment, Magma Mixing, and Crystal Recycling at Santorini Volcano, Greece, in: American Geophysical Union, Fall Meeting 2007, Abstract #V41f-04.

Martin, V.M., Holness, M.B., Pyle, D.M., 2006a. Textural analysis of magmatic enclaves from the Kameni Islands, Santorini, Greece. *Journal of Volcanology and Geothermal Research* **154**, 89–102.

Martin, V.M., Pyle, D.M., Holness, M.B., 2006b. The role of crystal frameworks in the preservation of enclaves during magma mixing. *Earth and Planetary Science Letters* **248**, 787–799.

Martinez-Serrano, R.G., 2002. Chemical variations in hydrothermal minerals of the Los Humeros geothermal system, Mexico. *Geothermics* **31**, 579–612.

Mason, B., 1974. Aluminum-Titanium-Rich pyroxenes, with Special Reference to the Allende Meteorite. *American Mineralogist* **59**, 1198–1202.

Mason, E., Edmonds, M., Turchyn, A.V., 2017. Remobilization of crustal carbon may dominate volcanic arc emissions. *Science* **357**, 290–294.

Matthews, A., Schliestedt, M., 1984. Evolution of the blueschist and greenschist facies rocks of Sifnos, Cyclades, Greece. *Contributions to Mineralogy and Petrology* **88**, 150–163.

Matthews, S., Marquillas, R., Kemp, A., Grange, F., Gardeweg, M., 1996. Active skarn formation beneath Lascar Volcano, northern Chile: a petrographic and geochemical study of xenoliths in eruption products. *Journal of Metamorphic Geology* **14**, 509–530.

Mavrogenes, J., Blundy, J., 2017. Crustal sequestration of magmatic sulfur dioxide. *Geology* **45**, 211–214.

McBirney, A., 1969. Compositional variations in Cenozoic calc-alkaline suites of Central America, in: Proceedings of the Andesite Conference. State of Oregon Dept. Geol. Miner. Ind. Bull, pp. 185–189.

McBirney, A.R., Noyes, R.M., 1979. Crystallization and layering of the Skaergaard intrusion. *Journal of Petrology* **20**, 487–554.

McGee, L.E., McLeod, C., Davidson, J.P., 2015. A spectrum of disequilibrium melting preserved in lava-hosted, partially melted crustal xenoliths from the Wudalianchi volcanic field, NE China. *Chemical Geology* **417**, 184–199.

McGrath, A., Stouraiti, C., Windley, B., 2017. Geochemistry of mylonitic gneisses from the Cycladic Basement Unit (Paros and Serifos, Aegean Sea): implications for protoliths of the high-grade gneisses. *International Journal of Earth Sciences* **106**, 2067–2089.

McLeod, P., Sparks, R.S.J., 1998. The dynamics of xenolith assimilation. *Contributions to Mineralogy and Petrology* **132**, 21–33.

Meinert, L.D., 2005. World skarn deposits. *Economic Geolology 100$^{th}$ Aniversary Volume* 299–336.

Meinert, L.D., 1992. Skarns and skarn deposits. *Geoscience Canada* **19**, 145–162.

Melekhova, E., Blundy, J., Martin, R., Arculus, R., Pichavant, M., 2017. Petrological and experimental evidence for differentiation of water-rich magmas beneath St. Kitts, Lesser Antilles. *Contributions to Mineralogy and Petrology* **172**, 98.

Melekhova, E., Blundy, J., Robertson, R., Humphreys, M.C., 2015. Experimental evidence for polybaric differentiation of primitive arc basalt beneath St. Vincent, Lesser Antilles. *Journal of Petrology* **56**, 161–192.

Melekhova, E., Schlaphorst, D., Blundy, J., Kendall, J.-M., Connolly, C., McCarthy, A., Arculus, R., 2019. Lateral variation in crustal structure along the Lesser Antilles arc from petrology of crustal xenoliths and seismic receiver functions. *Earth and Planetary Science Letters* **516**, 12–24.

Mercier, J.L., Sorel, D., Vergely, P., Simeakis, K., 1989. Extensional tectonic regimes in the Aegean basins during the Cenozoic. *Basin Research* **2**, 49–71.

Michaud, V., 1995. Crustal xenoliths in recent hawaiites from Mount Etna, Italy: evidence for alkali exchanges during magma-wall rock interaction. *Chemical Geology* **122**, 21–42.

Michaud, V., Clocchiatti, R., Sbrana, S., 2000. The Minoan and post-Minoan eruptions, Santorini (Greece), in the light of melt inclusions: chlorine and sulphur behaviour. *Journal of Volcanology and Geothermal Research* **99**, 195–214.

Miller, S.A., Collettini, C., Chiaraluce, L., Cocco, M., Barchi, M., Kaus, B.J., 2004. Aftershocks driven by a high-pressure $CO_2$ source at depth. *Nature* **427**, 724–727.

Minster, J.B., Jordan, T.H., 1978. Present-day plate motions. *Journal of Geophysical Research, Solid Earth* **83**, 5331–5354.

Mollo, S., Blundy, J.D., Giacomoni, P., Nazzari, M., Scarlato, P., Coltorti, M., Langone, A., Andronico, D., 2017. Clinopyroxene-melt element partitioning during interaction between trachybasaltic magma and siliceous crust: Clues from quartzite enclaves at Mt. Etna volcano. *Lithos* **284**, 447–461.

Mollo, S., Del Gaudio, P., Ventura, G., Iezzi, G., Scarlato, P., 2010a. Dependence of clinopyroxene composition on cooling rate in basaltic magmas: implications for thermobarometry. *Lithos* **118**, 302–312.

Mollo, S., Gaeta, M., Freda, C., Di Rocco, T., Misiti, V., Scarlato, P., 2010b. Carbonate assimilation in magmas: a reappraisal based on experimental petrology. *Lithos* **114**, 503–514.

Mollo, S., Heap, M.J., Iezzi, G., Hess, K., Scarlato, P., Dingwell, D.B., 2012. Volcanic edifice weakening via decarbonation: A self-limiting process? *Geophysical Research Letters* **39**, L15307.

Mollo, S., Masotta, M., 2014. Optimizing pre-eruptive temperature estimates in thermally and chemically zoned magma chambers. *Chemical Geology* **368**, 97–103.

Mollo, S., Putirka, K., Iezzi, G., Del Gaudio, P., Scarlato, P., 2011. Plagioclase–melt (dis) equilibrium due to cooling dynamics: implications for thermometry, barometry and hygrometry. *Lithos* **125**, 221–235.

Mollo, S., Putirka, K., Misiti, V., Soligo, M., Scarlato, P., 2013. A new test for equilibrium based on clinopyroxene–melt pairs: clues on the solidification temperatures of Etnean alkaline melts at post-eruptive conditions. *Chemical Geology* **352**, 92–100.

Mollo, S., Vona, A., 2014. The geochemical evolution of clinopyroxene in the Roman Province: A window on decarbonation from wall-rocks to magma. *Lithos* **192**, 1–7.

Morimoto, N., 1988. Nomenclature of pyroxenes. *Mineralogy and Petrology* **39**, 55–76.

Morse, S.A., 1976. The lever rule with fractional crystallisation and fusion. *American Journal of Science* **276**, 330–346.

Mortazavi, M., Sparks, R., 2004. Origin of rhyolite and rhyodacite lavas and associated mafic inclusions of Cape Akrotiri, Santorini: the role of wet basalt in generating calcalkaline silicic magmas. *Contributions to Mineralogy and Petrology* **146**, 397–413.

Muhling, J.R., Griffin, B.J., 1991. On recasting garnet analyses into end-member molecules—revisited short note. *Computers & Geosciences* **17**, 161–170.

Murphy, M.D., Sparks, R.S.J., Barclay, J., Carroll, M.R., Brewer, T.S., 2000. Remobilization of andesite magma by intrusion of mafic magma at the Soufriere Hills Volcano, Montserrat, West Indies. *Journal of petrology* **41**, 21–42.

Müntener, O., Kelemen, P.B., Grove, T.L., 2001. The role of $H_2O$ during crystallization of primitive arc magmas under uppermost mantle conditions and genesis of igneous pyroxenites: an experimental study. *Contributions to Mineralogy and Petrology* **141**, 643–658.

Müntener, O., Ulmer, P., 2018. Arc crust formation and differentiation constrained by experimental petrology. *American Journal of Science* **318**, 64–89.

Nadeau, O., Stix, J., Williams-Jones, A.E., 2013a. The behavior of Cu, Zn and Pb during magmatic–hydrothermal activity at Merapi volcano, Indonesia. *Chemical Geology* **342**, 167–179.

Nadeau, O., Williams-Jones, A.E., Stix, J., 2013b. Magmatic-hydrothermal evolution and devolatilization beneath Merapi volcano, Indonesia. *Journal of Volcanology and Geothermal Research* **261**, 50–68.

Nadeau, O., Williams-Jones, A.E., Stix, J., 2010. Sulphide magma as a source of metals in arc-related magmatic hydrothermal ore fluids. *Nature Geoscience* **3**, 501.

Nakamura, M., 1995. Continuous mixing of crystal mush and replenished magma in the ongoing Unzen eruption. *Geology* **23**, 807–810.

Nakamura, M., Shimakita, S., 1998. Dissolution origin and syn-entrapment compositional change of melt inclusion in plagioclase. *Earth and Planetary Science Letters* **161**, 119–133.

Neave, D.A., Hartley, M.E., Maclennan, J., Edmonds, M., Thordarson, T., 2017. Volatile and light lithophile elements in high-anorthite plagioclase-hosted melt inclusions from Iceland. *Geochimica et Cosmochimica Acta* **205**, 100–118.

Neave, D.A., Passmore, E., Maclennan, J., Fitton, G., Thordarson, T., 2013. Crystal–melt relationships and the record of deep mixing and crystallization in the ad 1783 Laki Eruption, Iceland. *Journal of Petrology* **54**, 1661–1690.

Neave, D.A., Putirka, K., 2017. A new clinopyroxene-liquid barometer, and implications for magma storage pressures under Icelandic rift zones. *American Mineralogist* **102**, 777–794.

Newcomb, K., McCann, W., 1987. Seismic history and seismotectonics of the Sunda Arc. *Journal of Geophysical Research* **92**, 421–439.

Newhall, C., Bronto, S., Alloway, B., Banks, N., Bahar, I., Marmol, M.D., Hadisantono, R., Holcomb, R., McGeehin, J., Miksic, J., 2000. 10,000 Years of explosive eruptions of Merapi Volcano, Central Java: archaeological and modern implications. *Journal of Volcanology and Geothermal Research* **100**, 9–50.

Nicholls, I.A., 1971a. Santorini volcano, Greece—Tectonic and petrochemical relationships with volcanics of the Aegean Region. *Tectonophysics* **11**, 377–385.

Nicholls, I.A., 1971b. Calcareous inclusions in lavas and agglomerates of Santorini volcano. *Contributions to Mineralogy and Petrology* **30**, 261–276.

Nicholls, I.A., 1971c. Petrology of Santorini volcano, Cyclades, Greece. *Journal of Petrology* **12**, 67–119.

Nielsen, R.L., 2011. The effects of re-homogenization on plagioclase hosted melt inclusions. *Geochemistry, Geophysics, Geosystems* **12**.

Nielsen, R.L., Drake, M.J., 1979. Pyroxene-melt equilibria. *Geochimica et Cosmochimica Acta* **43**, 1259–1272.

Nimis, P., 1999. Clinopyroxene geobarometry of magmatic rocks. Part 2. Structural geobarometers for basic to acid, tholeiitic and mildly alkaline magmatic systems. *Contributions to Mineralogy and Petrology* **135**, 62–74.

Nimis, P., 1995. A clinopyroxene geobarometer for basaltic systems based on crystal-structure modeling. *Contributions to Mineralogy and Petrology* **121**, 115–125.

Nimis, P., Taylor, W.R., 2000. Single clinopyroxene thermobarometry for garnet peridotites. Part I. Calibration and testing of a Cr-in-Cpx barometer and an enstatite-in-Cpx thermometer. *Contributions to Mineralogy and Petrology* **139**, 541–554.

Nimis, P., Ulmer, P., 1998. Clinopyroxene geobarometry of magmatic rocks Part 1: An expanded structural geobarometer for anhydrous and hydrous, basic and ultrabasic systems. *Contributions to Mineralogy and Petrology* **133**, 122–135.

Nomikou, P., Hübscher, C., Carey, S., 2019. The Christiana–Santorini–Kolumbo Volcanic Field. *Elements: An International Magazine of Mineralogy, Geochemistry, and Petrology* **15**, 171–176.

Orlando, A., Massimo D'Orazio, P.A., Borrini, D., 2008. Experimental determination of plagioclase and clinopyroxene crystal growth rates in an anhydrous trachybasalt from Mt Etna (Italy). *European Journal of Mineralogy* **20**, 653–664.

Otamendi, J.E., Tiepolo, M., Walker, B.A., Cristofolini, E.A., Tibaldi, A.M., 2016. Trace elements in minerals from mafic and ultramafic cumulates of the central Sierra de Valle Fértil, Famatinian arc, Argentina. *Lithos* **240**, 355–370.

Palme, H., O'Neill, H., others, 2014. Cosmochemical estimates of mantle composition, in: Treatise on Geochemistry, 2nd Edition. Elsevier.

Pamukcu, A.S., Carley, T.L., Gualda, G.A., Miller, C.F., Ferguson, C.A., 2013. The evolution of the Peach Spring giant magma body: Evidence from accessory mineral textures and compositions, bulk pumice and glass geochemistry, and rhyolite-MELTS modeling. *Journal of Petrology* **54**, 1109–1148.

Panienka, S., 2012. The Concentration of Lithium in Plagioclase Crystals of the Minoan Tephra,(Santorini, Greece) (PhD thesis). Ruprecht-Karls-Universität, Heidelberg.

Papazachos, C.B., 2019. Deep structure and active tectonics of the South Aegean volcanic arc. *Elements: An International Magazine of Mineralogy, Geochemistry, and Petrology* **15**, 153–158.

Parat, F., Holtz, F., Streck, M.J., 2011. Sulfur-bearing magmatic accessory minerals. *Reviews in Mineralogy and Geochemistry* **73**, 285–314.

Parks, M.M., Biggs, J., England, P., Mather, T.A., Nomikou, P., Palamartchouk, K., Papanikolaou, X., Paradissis, D., Parsons, B., Pyle, D.M., 2012. Evolution of Santorini Volcano dominated by episodic and rapid fluxes of melt from depth. *Nature Geoscience* **5**, 749–754.

Parman, S.W., Grove, T.L., Kelley, K.A., Plank, T., 2010. Along-arc variations in the pre-eruptive H2O contents of Mariana arc magmas inferred from fractionation paths.

*Journal of Petrology* **52**, 257–278.

Pascal, M.-L., Di Muro, A., Fonteilles, M., Principe, C., 2009. Zirconolite and calzirtite in banded forsterite-spinel-calcite skarn ejecta from the 1631 eruption of Vesuvius: inferences for magma-wallrock interactions. *Mineralogical Magazine* **73**, 333–356.

Pascal, M.-L., Katona, I., Fonteilles, M., Verkaeren, J., 2005. Relics of high-temperature clinopyroxene on the join di–cats with up to 72 mol.% $Ca(Al,Fe^3)AlSiO_6$ in the skarns of Ciclova and Magureaua Vatei, Carpathians, Romania. *The Canadian Mineralogist* **43**, 857–881.

Passmore, E., Maclennan, J., Fitton, G., Thordarson, T., 2012. Mush Disaggregation in Basaltic Magma Chambers: Evidence from the AD 1783 Laki Eruption. *Journal of Petrology* **53**, 2593–2623.

Patchett, P.J., 1980. Thermal effects of basalt on continental crust and crustal contamination of magmas. *Nature* **283**, 559.

Peccerillo, A., Astis, G.D., Faraone, D., Forni, F., Frezzotti, M., 2013. Chapter 15: Compositional variations of magmas in the Aeolian arc: implications for petrogenesis and geodynamics. *The Aeolian Islands Volcanoes. Geological Society, London, Memoirs* **37**, 491–510.

Peccerillo, A., Dallai, L., Frezzotti, M.L., Kempton, P.D., 2004. Sr–Nd–Pb–O isotopic evidence for decreasing crustal contamination with ongoing magma evolution at Alicudi volcano (Aeolian arc, Italy): implications for style of magma-crust interaction and for mantle source compositions. *Lithos* **78**, 217–233.

Peccerillo, A., Wu, T., 1992. Evolution of calc-alkaline magmas in continental arc volcanoes: evidence from Alicudi, Aeolian arc (southern Tyrrhenian Sea, Italy). *Journal of Petrology* **33**, 1295–1315.

Pe-Piper, G., Piper, D., 2005. The South Aegean active volcanic arc: relationships between magmatism and tectonics. *Developments in Volcanology* **7**, 113–133.

Pe-Piper, G., Piper, D.J.W., Reynolds, P.H., 1983. Paleomagnetic stratigraphy and radiometric dating of the Pliocene volcanic rocks of Aegina, Greece. *Bulletin Volcanologique*

**46**, 1–7.

Perinelli, C., Mollo, S., Gaeta, M., De Cristofaro, S.P., Palladino, D.M., Armienti, P., Scarlato, P., Putirka, K., 2016. An improved clinopyroxene-based hygrometer for Etnean magmas and implications for eruption triggering mechanisms. *American Mineralogist* **101**, 2774–2777.

Pistone, M., Arzilli, F., Dobson, K.J., Cordonnier, B., Reusser, E., Ulmer, P., Marone, F., Whittington, A.G., Mancini, L., Fife, J.L., 2015. Gas-driven filter pressing in magmas: Insights into in-situ melt segregation from crystal mushes. *Geology* **43**, 699–702.

Povoden, E., Horacek, M., Abart, R., 2002. Contact metamorphism of siliceous dolomite and impure limestones from the Werfen formation in the eastern Monzoni contact aureole. *Mineralogy and Petrology* **76**, 99–120.

Praptisih, Siregar, M.S., 2002. Petrografi dan fasies batugamping Formasi Wonosari di daerah Bayat, Jawa Tengah, in Sumberdaya Geologi Daerah Istimewa Yogyakarta dan Jawa Tengah. *Ikatan Ahli Geologi Indonesia, Pengda DIY-Jateng* 32–40.

Preece, K., 2014. Transitions between effusive and explosive activity at Merapi volcano, Indonesia: a volcanological and petrological study of the 2006 and 2010 eruptions. (PhD thesis). University of East Anglia.

Preece, K., Gertisser, R., Barclay, J., Berlo, K., Herd, R.A., 2014. Pre-and syn-eruptive degassing and crystallisation processes of the 2010 and 2006 eruptions of Merapi volcano, Indonesia. *Contributions to Mineralogy and Petrology* **168**, 1–25.

Price, R.C., Smith, I.E., Stewart, R.B., Gamble, J.A., Gruender, K., Maas, R., 2015. High-K andesite petrogenesis and crustal evolution: Evidence from mafic and ultramafic xenoliths, Egmont Volcano (Mt. Taranaki) and comparisons with Ruapehu Volcano, North Island, New Zealand. *Geochimica et Cosmochimica Acta*.

Putirka, K., 2016. Amphibole thermometers and barometers for igneous systems and some implications for eruption mechanisms of felsic magmas at arc volcanoes. *American Mineralogist* **101**, 841–858.

Putirka, K., 2008. Thermometers and barometers for volcanic systems. *Reviews in Mineralogy and Geochemistry* **69**, 61–120.

Putirka, K., 1999. Clinopyroxene+liquid equilibria to 100 kbar and 2450 K. *Contributions to Mineralogy and Petrology* **135**, 151–163.

Putirka, K., Johnson, M., Kinzler, R., Longhi, J., Walker, D., 1996. Thermobarometry of mafic igneous rocks based on clinopyroxene-liquid equilibria, 0-30 kbar. *Contributions to Mineralogy and Petrology* **123**, 92–108.

Putirka, K., Mikaelian, H., Ryerson, F., Shaw, H., 2003. New clinopyroxene-liquid thermobarometers for mafic, evolved, and volatile-bearing lava compositions, with applications to lavas from Tibet and the Snake River Plain, Idaho. *American Mineralogist* **88**, 1542–1554.

Putlitz, B., Matthews, A., Valley, J.W., 2000. Oxygen and hydrogen isotope study of high-pressure metagabbros and metabasalts (Cyclades, Greece): implications for the subduction of oceanic crust. *Contributions to Mineralogy and Petrology* **138**, 114–126.

Pyle, D., Ivanovich, M., 1988. Crystal cannibalisation, crustal contamination and the petrogenesis of arc magmas. *Chemical Geology* **70**, 129.

Pyle, D.M., 1997. The global impact of the Minoan eruption of Santorini, Greece. *Environmental Geology* **30**, 59–61.

Reagan, M., Handley, H., Gertisser, R., Turner, M., Berlo, K., Preece, K., 2017. U-series evidence for ongoing skarnification beneath Merapi Volcano, Indonesia, in: IAVCEI 2017 Conference Abstracts. Portland, Oregan, Usa. p. 883.

Reck, H., 1936. Santorini: der Werdegang eines Inselvulkans und sein Ausbruch 1925-1928. Ergebnisse einer deutschgriechischen Arbeitsgemeinschaft. D. Reimer, Andrews & Steiner.

Reiners, P.W., Nelson, B.K., Ghiorso, M.S., 1995. Assimilation of felsic crust by basaltic magma: thermal limits and extents of crustal contamination of mantle-derived magmas. *Geology* **23**, 563–566.

Renzulli, A., Serri, G., Santi, P., Mattioli, M., Holm, P.M., 2001. Origin of high-silica liquids at Stromboli volcano (Aeolian Islands, Italy) inferred from crustal xenoliths. *Bulletin of Volcanology* **62**, 400–419.

Renzulli, A., Tribaudino, M., Salvioli-Mariani, E., SERRI, G., 2003. Cordierite-anorthoclase hornfels xenoliths in Stromboli lavas (Aeolian Islands, Sicily) an example of a fast cooled contact aureole. *European Journal of Mineralogy* **15**, 665–679.

Ridolfi, F., Renzulli, A., 2012. Calcic amphiboles in calc-alkaline and alkaline magmas: thermobarometric and chemometric empirical equations valid up to 1,130° C and 2.2 GPa. *Contributions to Mineralogy and Petrology* **163**, 877–895.

Rittmann, A., 1933. Die geologisch bedingte Evolution und Differentiation des Somma-Vesuv magmas. *Zeitschrift für Vulkanologie* **15**, 8–94.

Rizzo, A., Barberi, F., Carapezza, M., Piazza, A.D., Francalanci, L., Sortino, F., D'Alessandro, W., 2015. New mafic magma refilling a quiescent volcano: Evidence from He-Ne-Ar isotopes during the 2011–2012 unrest at Santorini, Greece. *Geochemistry, Geophysics, Geosystems* **16**, 798–814.

Roedder, E., 1984. Fluid Inclusions. Reviews in Mineralogy vol. 12. Mineralogical Society of America, Washington.

Rose, N.M., Bird, D.K., 1994. Hydrothermally altered dolerite dykes in East Greenland: implications for Ca-metasomatism of basaltic protoliths. *Contributions to Mineralogy and Petrology* **116**, 420–432.

Rubin, A.M., 1995. Propagation of magma-filled cracks. *Annual Review of Earth and Planetary Sciences* **23**, 287–336.

Rudnick, R.L., Fountain, D.M., 1995. Nature and composition of the continental crust: a lower crustal perspective. *Reviews of Geophysics* **33**, 267–309.

Rudnick, R.L., Gao, S., 2003. 3.01 - Composition of the Continental Crust, in: Turekian, H.D.H.K. (Ed.), Treatise on Geochemistry. Pergamon, Oxford, pp. 1–64.

Rutstein, M., 1971. Re-examination of wollastonite-hedenbergite ($CaSiO_3$-$CaFeSi_2O_6$) Equilibria. *American Mineralogist* **56**, 2040–2052.

Rutstein, M.S., White, W.B., 1971. Vibrational spectra of high-calcium pyroxenes and pyroxenoids. *American Mineralogist* **56**, 877–887.

Ryan, M.P., 1987. Neutral buoyancy and the mechanical evolution of magmatic systems, in: Magmatic Processes: Physicochemical Principles. Geochem. Soc. University Park, PA, pp. 259–287.

Saltogianni, V., Stiros, S.C., Newman, A.V., Flanagan, K., Moschas, F., 2014. Time-space modeling of the dynamics of Santorini volcano (Greece) during the 2011–2012 unrest. *Journal of Geophysical Research, Solid Earth* **119**, 8517–8537.

Salvioli-Mariani, E., Renzulli, A., Serri, G., Holm, P.M., Toscani, L., 2005. Glass-bearing crustal xenoliths (buchites) erupted during the recent activity of Stromboli (Aeolian Islands). *Lithos* **81**, 255–277.

Santo, A., 2005. Magmatic evolution processes as recorded in plagioclase phenocrysts of Nea Kameni rocks (Santorini Volcano, Greece), in: Developments in Volcanology. Elsevier, pp. 139–160.

Santo, A., Jacobsen, S., Baker, J., 2004. Evolution and genesis of calc-alkaline magmas at Filicudi Volcano, Aeolian Arc (southern Tyrrhenian Sea, Italy). *Lithos* **72**, 73–96.

Santo, A., Peccerillo, A., 2008. Oxygen Isotopic Variations in the Clinopyroxene from the Filicudi Volcanic Rocks (Aeolian Islands, Italy): Implications for Open-System Magma Evolution. *Open Mineralogy Journal* **2**, 22–33.

Scacchi, A., 1887. Catalogo dei minerali vesuviani con la notizia della loro composizione e del loro giacimento. R. stab. tipografico eorum Francesco Giannini & Figli.

Schliestedt, M., Altherr, R., Matthews, A., 1987. Evolution of the Cycladic crystalline complex: petrology, isotope geochemistry and geochronolgy, in: Chemical Transport in Metasomatic Processes. Springer, pp. 389–428.

Schwarzkopf, L., Schmincke, H.-U., Troll, V., 2001. Pseudotachylite on impact marks of block surfaces in block-and-ash flows at Merapi volcano, Central Java, Indonesia. *International Journal of Earth Sciences* **90**, 769–775.

Shaw, C.S., 2009. Caught in the act—the first few hours of xenolith assimilation preserved in lavas of the Rockeskyllerkopf volcano, West Eifel, Germany. *Lithos* **112**, 511–523.

Shaw, C.S., 2000. The effect of experiment geometry on the mechanism and rate of dissolution of quartz in basanite at 0.5 GPa and 1350 C. *Contributions to Mineralogy and Petrology* **139**, 509–525.

Shejwalkar, A., Coogan, L.A., 2013. Experimental calibration of the roles of temperature and composition in the Ca-in-olivine geothermometer at 0.1 MPa. *Lithos* **177**, 54–60.

Shimazaki, H., Shimizu, M., Nakano, T., 1986. Carbon and oxygen isotopes of calcites from Japanese skarn deposits. *Geochemical Journal* **20**, 297–310.

Shin, D., Lee, I., 2003. Evaluation of the volatilization and infiltration effects on the stable isotopic and mineralogical variations in the carbonate rocks adjacent to the Cretaceous Muamsa Granite, South Korea. *Journal of Asian Earth Sciences* **22**, 227–243.

Sigurdsson, H., Carey, S., Alexandri, M., Vougioukalakis, G., Croff, K., Roman, C., Sakellariou, D., Anagnostou, C., Rousakis, G., Ioakim, C., 2006. Marine investigations of Greece's Santorini volcanic field. *EOS, Transactions American Geophysical Union* **87**, 337–342.

Sillitoe, R.H., 2010. Porphyry copper systems. *Economic Geology* **105**, 3–41.

Simakin, A.G., Salova, T.P., Armienti, P., 2003. Kinetics of clinopyroxene growth from a hydrous hawaiite melt. *Geochemistry International* **41**, 1165–1175.

Simakin, A., Salova, T., Bondarenko, G., 2012. Experimental study of magmatic melt oxidation by $CO_2$. *Petrology* **20**, 593–606.

Simmons, J.M., Carey, R.J., Cas, R.A.F., Druitt, T.H., 2017. High magma decompression rates at the peak of a violent caldera-forming eruption (Lower Pumice 1 eruption, Santorini, Greece). *Bulletin of Volcanology* **79**, 1.

Siregar, M.S., 1996. Endapan pasang-surut dalam Formasi Wonosari. *Proceedings Indonesian Association of Geologists, the 25th Annual Convention.*

Sisson, T., Bacon, C., 1999. Gas-driven filter pressing in magmas. *Geology* **27**, 613–616.

Sisson, T., Grove, T., 1993. Experimental investigations of the role of $H_2O$ in calc-alkaline differentiation and subduction zone magmatism. *Contributions to Mineralogy and Petrology* **113**, 143–166.

Skarpelis, N., Liati, A., 1990. The prevolcanic basement of Thera at Athinios: metamorphism, plutonism and mineralization. *Thera and the Aegean World III* **2**, 172–182.

Sliwinski, J., Bachmann, O., Ellis, B., Dávila-Harris, P., Nelson, B., Dufek, J., 2015. Eruption of Shallow Crystal Cumulates during Explosive Phonolitic Eruptions on Tenerife, Canary Islands. *Journal of Petrology* **56**, 2173–2194.

Sliwinski, J.T., Bachmann, O., Dungan, M.A., Huber, C., Deering, C.D., Lipman, P.W., Martin, L.H.J., Liebske, C., 2017. Rapid pre-eruptive thermal rejuvenation in a large silicic magma body: the case of the Masonic Park Tuff, Southern Rocky Mountain volcanic field, CO, USA. *Contributions to Mineralogy and Petrology* **172**, 1.

Smith, D.J., 2014. Clinopyroxene precursors to amphibole sponge in arc crust. *Nature Communications* **5**.

Smyth, H., Hall, R., Hamilton, J., Kinny, P., 2005. East Java: Cenozoic basins, volcanoes and ancient basement.

Snyder, D., Carmichael, I.S.E., Wiebe, R.A., 1993. Experimental study of liquid evolution in an Fe-rich, layered mafic intrusion: constraints of Fe-Ti oxide precipitation on the T-fO2 and T-P paths of tholeiitic magmas. *Contributions to Mineralogy and Petrology* **113**, 73–86.

Sobolev, V.N., McCammon, C.A., Taylor, L.A., Snyder, G.A., Sobolev, N.V., 1999. Precise Moessbauer milliprobe determination of ferric iron in rock-forming minerals and limitations of electron microprobe analysis. *American Mineralogist* **84**, 78–85.

Span, R., Wagner, W., 1996. A new equation of state for carbon dioxide covering the fluid region from the triple-point temperature to 1100 K at pressures up to 800 MPa. *Journal of Physical and Chemical Reference Data* **25**, 1509–1596.

Spandler, C., Martin, L.H., Pettke, T., 2012. Carbonate assimilation during magma evolution at Nisyros (Greece), South Aegean Arc: Evidence from clinopyroxenite xenoliths.

*Lithos* **146**, 18–33.

Sparks, R.S.J., Huppert, H.E., Kerr, R., McKenzie, D., Tait, S.R., 1985. Postcumulus processes in layered intrusions. *Geological Magazine* **122**, 555–568.

Spera, F.J., Bohrson, W.A., 2001. Energy-constrained open-system magmatic processes I: general model and energy-constrained assimilation and fractional crystallization (EC-AFC) formulation. *Journal of Petrology* **42**, 999–1018.

Stamper, C., Blundy, J., Arculus, R., Melekhova, E., 2014. Petrology of Plutonic Xenoliths and Volcanic Rocks from Grenada, Lesser Antilles. *Journal of Petrology* **55**, 1353–1387.

Stern, R.J., 1979. On the origin of andesite in the northern Mariana island arc: Implications from Agrigan. *Contributions to Mineralogy and Petrology* **68**, 207–219.

Sterner, S.M., Pitzer, K.S., 1994. An equation of state for carbon dioxide valid from zero to extreme pressures. *Contributions to Mineralogy and Petrology* **117**, 362–374.

Stormer, J.C., Nicholls, J., 1978. XLFRAC: a program for the interactive testing of magmatic differentiation models. *Computers & Geosciences* **4**, 143–159.

Streck, M.J., 2014. Evaluation of crystal mush extraction models to explain crystal-poor rhyolites. *Journal of Volcanology and Geothermal Research* **284**, 79–94.

Streckeisen, A., 1974. Classification and nomenclature of plutonic rocks. *Geol.Rundsch* **63**, 773–786.

Sugawara, T., 2001. Ferric iron partitioning between plagioclase and silicate liquid: thermodynamics and petrological applications. *Contributions to Mineralogy and Petrology* **141**, 659–686.

Sun, C., Graff, M., Liang, Y., 2017. Trace element partitioning between plagioclase and silicate melt: The importance of temperature and plagioclase composition, with implications for terrestrial and lunar magmatism. *Geochimica et Cosmochimica Acta* **206**, 273–295.

Sun, C., Liang, Y., 2012. Distribution of REE between clinopyroxene and basaltic melt along a mantle adiabat: effects of major element composition, water, and temperature. *Contributions to Mineralogy and Petrology* **163**, 807–823.

Sun, W., Liang, H., Ling, M., Zhan, M., Ding, X., Zhang, H., Yang, X., Li, Y., Ireland, T.R., Wei, Q., Fan, W., 2013. The link between reduced porphyry copper deposits and oxidized magmas. *Geochimica et Cosmochimica Acta* **103**, 263–275.

Surono, M., Jousset, P., Pallister, J., Boichu, M., Fabrizia, M., Buongiorno, A.B., Rodriguez, F.C., Andreastuti, S., Prata, F., Schneider, D., 2012. The 2010 explosive eruption of Java's Merapi volcano-a '100-year'event. *Journal of Volcanology and Geothermal Research* **241**–**242**, 121–135.

Svensen, H., Planke, S., Malthe-Sørenssen, A., Jamtveit, B., Myklebust, R., Eidem, T.R., Rey, S.S., 2004. Release of methane from a volcanic basin as a mechanism for initial Eocene global warming. *Nature* **429**, 542–545.

Syracuse, E.M., Abers, G.A., 2006. Global compilation of variations in slab depth beneath arc volcanoes and implications. *Geochemistry, Geophysics, Geosystems* **7**, Q05017.

Szymanowski, D., Wotzlaw, J.-F., Ellis, B.S., Bachmann, O., Guillong, M., Quadt, A. von, 2017. Protracted near-solidus storage and pre-eruptive rejuvenation of large magma reservoirs. *Nature Geoscience* **10**, 1–8.

Taylor, B.E., Bucher-Nurminen, K., 1986. Oxygen and carbon isotope and cation geochemistry of metasomatic carbonates and fluids—Bergell aureole, Northern Italy. *Geochimica et Cosmochimica Acta* **50**, 1267–1279.

Taylor, S.R., 1967. The origin and growth of continents. *Tectonophysics* **4**, 17–34.

Taylor, S.R., McLennan, S.M., 1985. The continental crust: Its composition and evolution.

Thirlwall, M., Graham, A., Arculus, R., Harmon, R., Macpherson, C., 1996. Resolution of the effects of crustal assimilation, sediment subduction, and fluid transport in island arc magmas: Pb-Sr-Nd-O isotope geochemistry of Grenada, Lesser Antilles. *Geochimica et Cosmochimica Acta* **60**, 4785–4810.

Thompson, J., 1959. Local equilibrium in metasomatic processes. *Researches in geochemistry* **1**, 427–457.

Thompson, R., 1974. Some high-pressure pyroxenes. *Mineralogical Magazine* **39**, 768–787.

Thompson, R., Morrison, M., Hendry, G., Parry, S., Simpson, P., Hutchison, R., O'Hara, M., 1984. An Assessment of the relative roles of crust and mantle in magma genesis: An elemental approach [and Discussion]. *Philosophical Transactions of the Royal Society of London A: Mathematical, Physical and Engineering Sciences* **310**, 549–590.

Tiepolo, M., Langone, A., Morishita, T., Yuhara, M., 2012. On the recycling of amphibole-rich ultramafic intrusive rocks in the arc crust: evidence from Shikanoshima Island (Kyushu, Japan). *Journal of Petrology* **53**, 1255–1285.

Tilley, C., 1952. Some trends of basaltic magma in limestone syntexis. *American Journal of Science* **250**, 529–545.

Tilley, C., Harwood, H., 1931. The dolerite-chalk contact of Scawt Hill, Co. Antrim. The production of basic alkali-rocks by the assimilation of limestone by basaltic magma. *Mineralogical Magazine* **22**, 439–468.

Tilley, C., Vincent, H., 1938. Aluminous pyroxenes in metamorphosed limestones. *Geological Magazine* **75**, 81–86.

Tollan, P., Bindeman, I., Blundy, J., 2012. Cumulate xenoliths from St. Vincent, Lesser Antilles Island Arc: a window into upper crustal differentiation of mantle-derived basalts. *Contributions to Mineralogy and Petrology* **163**, 189–208.

Tollan, P., O'Neill, H.S.C., Hermann, J., Benedictus, A., Arculus, R., 2015. Frozen melt–rock reaction in a peridotite xenolith from sub-arc mantle recorded by diffusion of trace elements and water in olivine. *Earth and Planetary Science Letters* **422**, 169–181.

Toplis, M., 2005. The thermodynamics of iron and magnesium partitioning between olivine and liquid: criteria for assessing and predicting equilibrium in natural and experimental systems. *Contributions to Mineralogy and Petrology* **149**, 22–39.

Toutain, J.-P., Sortino, F., Baubron, J.-C., Richon, P., Surono, Sumarti, S., Nonell, A., 2009. Structure and $CO_2$ budget of Merapi volcano during inter-eruptive periods. *Bulletin of Volcanology* **71**, 815–826.

Tracy, R.J., Frost, B.R., 1991. Phase equilibria and thermobarometry of calcareous, ultramafic and mafic rocks, and iron formations, in: Kerrick, D.M. (Ed.), Rev. Mineral.

Geochem. Mineralogical Society of America, pp. 207–289.

Tregoning, P., Brunner, F., Bock, Y., Puntodewo, S., McCaffrey, R., Genrich, J., Calais, E., Rais, J., Subarya, C., 1994. First geodetic measurement of convergence across the Java Trench. *Geophysical Research Letters* **21**, 2135–2138.

Treiman, A.H., Essene, E.J., 1983. Phase equilibria in the system $CaO$-$SiO_2$-$CO_2$. *American Journal of Science* **283**, 97–120.

Trigila, R., 1995. The volcano of the Alban Hills. Tipografia Sgs.

Troll, V.R., Deegan, F.M., Jolis, E.M., Harris, C., Chadwick, J.P., Gertisser, R., Schwarzkopf, L.M., Borisova, A.Y., Bindeman, I.N., Sumarti, S., 2013. Magmatic differentiation processes at Merapi Volcano: inclusion petrology and oxygen isotopes. *Journal of Volcanology and Geothermal Research* **261**, 38–49.

Troll, V.R., Hilton, D.R., Jolis, E.M., Chadwick, J.P., Blythe, L.S., Deegan, F.M., Schwarzkopf, L.M., Zimmer, M., 2012. Crustal $CO_2$ liberation during the 2006 eruption and earthquake events at Merapi volcano, Indonesia. *Geophysical Research Letters* **39**, L11302.

Tuttle, O.F., Harker, R.I., 1957. Synthesis of spurrite and the reaction wollastonite+calcite $\rightleftharpoons$ spurrite+carbon dioxide. *American Journal of Science* **255**, 226–234.

Tyrrell, G., 1926. The Principles Of Petrology. Methuen And Co. Ltd.; London.

Ulmer, P., 2001. Partial melting in the mantle wedge—the role of H 2 O in the genesis of mantle-derived 'arc-related'magmas. *Physics of the Earth and Planetary Interiors* **127**, 215–232.

Untung, M., Sato, Y., Satou, Y., 1978. Gravity and Geological Studies in Java, Indonesia. Geological Survey of Japan.

Upton, B., Aspen, P., Hinton, R., 2001. Pyroxenite and granulite xenoliths from beneath the Scottish Northern Highlands Terrane: evidence for lower-crust/upper-mantle relationships. *Contributions to Mineralogy and Petrology* **142**, 178–197.

Upton, B.G.J., Semet, M.P., Joron, J.-L., 2000. Cumulate clasts in the Bellecombe Ash Member, Piton de la Fournaise, Réunion Island, and their bearing on cumulative processes in the petrogenesis of the Réunion lavas. *Journal of volcanology and geothermal*

*research* **104**, 297–318.

Vaggelli, G., Francalanci, L., Ruggieri, G., Testi, S., 2003. Persistent polybaric rests of calc-alkaline magmas at Stromboli volcano, Italy: pressure data from fluid inclusions in restitic quartzite nodules. *Bulletin of Volcanology* **65**, 385–404.

Vaggelli, G., Pellegrini, M., Vougioukalakis, G., Innocenti, S., Francalanci, L., 2009. Highly Sr radiogenic tholeiitic magmas in the latest inter-Plinian activity of Santorini volcano, Greece. *Journal of Geophysical Research, Solid Earth* **114**, B06201.

Valentine, G.A., Groves, K.R., 1996. Entrainment of country rock during basaltic eruptions of the Lucero volcanic field, New Mexico. *The Journal of Geology* **104**, 71–90.

Valley, T., John W, 1986. Stable isotope geochemistry of metamorphic rocks, in: Rev. Mineral. Geochem.: Stable Isotope Geochemistry, Rev. Mineral. Geochem. Mineralogical Society of America Washington, DC.

van Bemmelen, 1949. The Geology of Indonesia. Goverment Printing, The Hague.

van der Zwan, F., Chadwick, J.P., Troll, V.R., 2013. Textural history of recent basaltic-andesites and plutonic inclusions from Merapi volcano. *Contributions to Mineralogy and Petrology* **166**, 43–63.

van Hinsberg, V.J., Berlo, K., Migdisov, A.A., Williams-Jones, A.E., 2016. $CO_2$-fluxing collapses metal mobility in magmatic vapour. *Geochemical Perspectives Letters* **2**, 169–177.

Van Orman, J.A., Grove, T.L., Shimizu, N., 2001. Rare earth element diffusion in diopside: Influence of temperature, pressure, and ionic radius, and an elastic model for diffusion in silicates. *Contributions to Mineralogy and Petrology* **141**, 687–703.

Veizer, J., Hoefs, J., 1976. The nature of $O^{18}/O^{16}$ and $C^{13}/C^{12}$ secular trends in sedimentary carbonate rocks. *Geochimica et Cosmochimica Acta* **40**, 1387–1395.

Vespa, M., Keller, J., Gertisser, R., 2006. Interplinian explosive activity of Santorini volcano (Greece) during the past 150,000 years. *Journal of Volcanology and Geothermal Research* **153**, 262–286.

Vigneresse, J.L., Barbey, P., Cuney, M., 1996. Rheological transitions during partial melting and crystallization with application to felsic magma segregation and transfer. *Journal of Petrology* **37**, 1579–1600.

Voight, B., Constantine, E.K., Siswowidjoyo, S., Torley, R., 2000. Historical eruptions of Merapi volcano, central Java, Indonesia, 1768–1998. *Journal of Volcanology and Geothermal Research* **100**, 69–138.

Vollmer, R., 1975. Origin of alkaline rocks. *Nature* **257**, 116–117.

Vougioukalakis, G.E., Satow, C.G., Druitt, T.H., 2019. Volcanism of the South Aegean volcanic arc. *Elements: An International Magazine of Mineralogy, Geochemistry, and Petrology* **15**, 159–164.

Wager, L., Brown, G., Wadsworth, W., 1960. Types of igneous cumulates. *Journal of Petrology* **1**, 73–85.

Wakita, K., Bambang, W., 1994. Cretaceous radiolarians from the Luk-Ulo melange complex in the Karangsambung area, central Java, Indonesia. *Journal of Southeast Asian Earth Sciences* **9**, 29–43.

Waters, L.E., Lange, R.A., 2015. An updated calibration of the plagioclase-liquid hygrometer-thermometer applicable to basalts through rhyolites. *American Mineralogist* **100**, 2172–2184.

Watson, E.B., 1982. Basalt contamination by continental crust: some experiments and models. *Contributions to Mineralogy and Petrology* **80**, 73–87.

Weber, M.B., Tarney, J., Kempton, P.D., Kent, R.W., 2002. Crustal make-up of the northern Andes: evidence based on deep crustal xenolith suites, Mercaderes, SW Colombia. *Tectonophysics* **345**, 49–82.

Weis, F.A., Stalder, R., Skogby, H., 2016. Experimental hydration of natural volcanic clinopyroxene phenocrysts under hydrothermal pressures (0.5 - 3 kbar). *American Mineralogist* **101**, 2233–2247.

Wenzel, T., Baumgartner, L.P., Brügmann, G.E., Konnikov, E.G., Kislov, E.V., 2002. Partial melting and assimilation of dolomitic xenoliths by mafic magma: the Ioko-Dovyren

intrusion (North Baikal Region, Russia). *Journal of Petrology* **43**, 2049–2074.

Werner, C., Brantley, S., 2003. $CO_2$ emissions from the Yellowstone volcanic system. *Geochemistry, Geophysics, Geosystems* **4**, 1061.

Whitaker, M.L., Nekvasil, H., Lindsley, D.H., Di Francesco, N.J., 2007. The Role of Pressure in Producing Compositional Diversity in Intraplate Basaltic Magmas. *Journal of Petrology* **48**, 365–393.

White, S.M., Crisp, J.A., Spera, F.J., 2006. Long-term volumetric eruption rates and magma budgets. *Geochemistry, Geophysics, Geosystems* **7**, Q03010.

Whitley, S., Gertisser, R., Halama, R., Preece, K., Troll, V.R., Deegan, F.M., 2019. Crustal $CO_2$ contribution to subduction zone degassing recorded through calc-silicate xenoliths in arc lavas. *Scientific Reports* **9**, 8803.

Winpenny, B., Maclennan, J., 2011. A partial record of mixing of mantle melts preserved in Icelandic phenocrysts. *Journal of Petrology* **52**, 1791–1812.

Wolff, J.A., Ellis, B., Ramos, F.C., Starkel, W.A., Boroughs, S., Olin, P.H., Bachmann, O., 2015. Remelting of cumulates as a process for producing chemical zoning in silicic tuffs: A comparison of cool, wet and hot, dry rhyolitic magma systems. *Lithos* **236**, 275–286.

Wölbern, I., Rümpker, G., 2016. Crustal thickness beneath Central and East Java (Indonesia) inferred from P receiver functions. *Journal of Asian Earth Sciences* **115**, 69–79.

Wyers, G.P., 1987. Petrogenesis of calc-alkaline and alkaline magmas from the southern and eastern Aegean Sea, Greece (PhD thesis). The Ohio State University.

Wyllie, P.J., Haas Jr, J.L., 1965. The system $CaO$-$SiO_2$-$CO_2$-$H_2O$: 1. Melting relationships with excess vapor at 1 kilobar pressure. *Geochimica et Cosmochimica Acta* **29**, 871–892.

Xu, W.-C., Zhang, H.-F., Luo, B.-j., Guo, L., Yang, H., 2015. Adakite-like geochemical signature produced by amphibole-dominated fractionation of arc magmas: An example from the Late Cretaceous magmatism in Gangdese belt, south Tibet. *Lithos* **232**, 197–210.

Yanagida, Y., Nakamura, M., Yasuda, A., Kuritani, T., Nakagawa, M., Yoshida, T., 2018. Differentiation of a hydrous arc magma recorded in melt inclusions in deep crustal cumulate xenoliths from Ichinomegata Maar, NE Japan. *Geochemistry, Geophysics, Geosystems.*

Zambonini, F., 1910. Mineralogia vesuviana. Tipografia della r. accademia delle scienze fisiche e matematiche.

Zanon, V., Frezzotti, M., Peccerillo, A., 2003. Magmatic feeding system and crustal magma accumulation beneath Vulcano Island (Italy): evidence from $CO_2$ fluid inclusions in quartz xenoliths. *Journal of Geophysical Research, Solid Earth* **108**, 2298.

Zanon, V., Nikogosian, I., 2004. Evidence of crustal melting events below the island of Salina (Aeolian arc, southern Italy). *Geological Magazine* **141**, 525–540.

Zarayskiy, G.P., Zharikov, V.A., Stoyanovskaya, F.M., Balashov, V.N., 1987. The experimental study of bimetasomatic skarn formation. *International Geology Review* **29**, 629–758.

Zellmer, G., Annen, C., Charlier, B., George, R., Turner, S., Hawkesworth, C., 2005. Magma evolution and ascent at volcanic arcs: constraining petrogenetic processes through rates and chronologies. *Journal of Volcanology and Geothermal Research* **140**, 171–191.

Zellmer, G., Turner, S., Hawkesworth, C., 2000. Timescales of destructive plate margin magmatism: new insights from Santorini, Aegean volcanic arc. *Earth and Planetary Science Letters* **174**, 265–281.

Zhang, J., Davidson, J., Humphreys, M., Macpherson, C., Neill, I., 2015. Magmatic Enclaves and Andesitic Lavas from Mt. Lamington, Papua New Guinea: Implications for Recycling of Earlier-fractionated Minerals through Magma Recharge. *Journal of Petrology* **56**, 2223–2256.

Zhao, Z.-F., Zheng, Y.-F., 2003. Calculation of oxygen isotope fractionation in magmatic rocks. *Chemical Geology* **193**, 59–80.

Zharikov, V.A., 1969. High temperature mineral equilibria in the system $CaO$-$SiO_2$-$CO_2$. *Geochem. Internat.* **6**, 853–869.

Zheng, Y.-F., 2011. On the theoretical calculations of oxygen isotope fractionation factors for carbonate-water systems. *Geochemical Journal* **45**, 341–354.

Zheng, Y.-F., 1993. Calculation of oxygen isotope fractionation in anhydrous silicate minerals. *Geochimica et Cosmochimica Acta* **57**, 1079–1091.

# Appendices

# Appendix A

# Chapter 2 - Plutonic Xenoliths from Santorini Appendix

## A.1 Melt Inclusion Post-entrapment Modification

The effects of post entrapment crystallisation along the sidewalls of the melt inclusion and diffusive equilibration between the trapped melt and host crystal are well established (e.g. Danyushevsky *et al.*, 2000; Kent, 2008; Nielsen, 2011), and therefore care is required in establishing whether they represent representative melt compositions of the host magmatic system. In the following section we will assess the compositions of the melt inclusions relative to the liquid line of descent and apply corrections where needed to melt inclusions that appear to have been modified. These corrections assume the trapped melt was originally in equilibrium with the host mineral, and plot within the liquid line of descent for Santorini magmas (Figure 2.16).

### A.1.1 Olivine-hosted inclusions

Variation diagrams (FeO vs $SiO_2$, FeO vs MgO, CaO/Al2O3 vs MgO) show olivine hosted melt inclusions fall outside the liquid line of descent for Santorini, showing a strong elevation in CaO/Al2O3 and depletion in Fe (Fe loss: Danyushevsky *et al.*, 2000) (Figure A.1), coupled with $KD_{Fe-Mg}^{olivine-melt}$ values below the equilibrium range of 0.3 $\pm$ 0.03 (Toplis, 2005; Putirka, 2008). These melt inclusions were corrected for post entrapment modification using Petrolog (Danyushevsky and Plechov, 2011). The original melt FeO* is estimated based on the amount of FeO* required to bring the inclusions to back to the liquid line of descent, and comparision with clinopyroxene and plagioclase hosted melt inclusion compositions. Ford *et al.* (1983) was used as the olivine-melt model and fugacity was set at QFM (Gertisser *et al.*, 2009). PEC

corrections required 0.5 to 17.9% olivine addition.

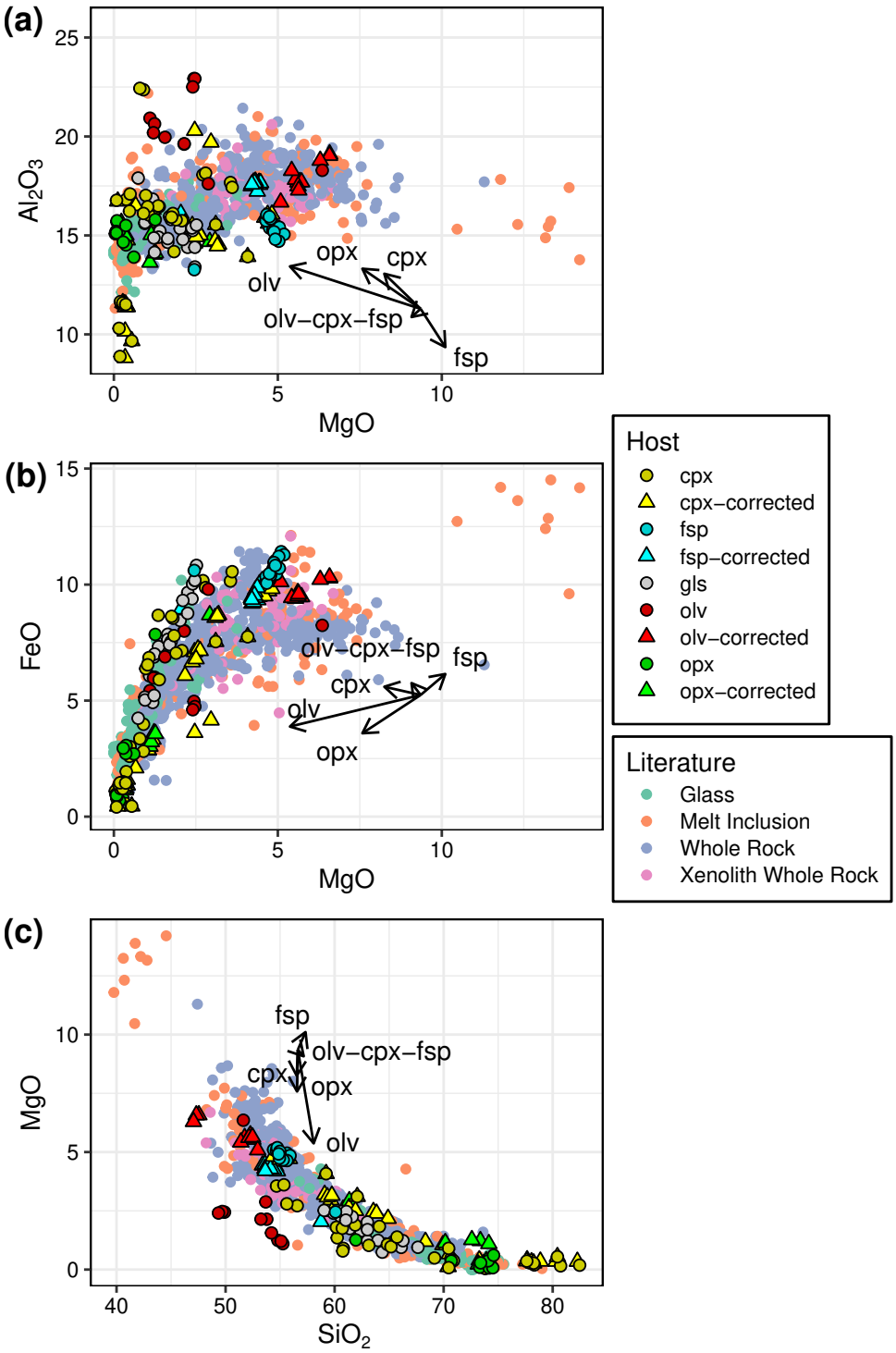


*Figure A.1: Melt inclusion compositions and corrections for post entrapment crystallisation (PEC). Fractionation vectors show the effect of 10% crystallisation of the host crystal on the melt inclusion composition, and the effect of olivine, clinopyroxene and plagioclase crystallisation in modal proportions similar to the olivine gabbro.*

### A.1.2 Clinopyroxene and Orthopyroxene Hosted Inclusions

There is no universally accepted method of correcting clinopyroxene-hosted melt inclusion compositions. A selection of methods were attempted (discussed below), which lead to heavily $Al_2O_3$ depleted compositions that lie far outside the liquid line of descent for Santorini. As the effect of post entrapment modification cannot be ruled out for these analyses, and methods to account for this produce exotic melt compositions, they are not used as potential liquids for thermobarometry.

Preece *et al.* (2014) corrected clinopyroxene melt inclusions by incrementally adding calulated equilibrium clinopyroxene compositions to the melt inclusion until the equilibrium clinopyroxene Mg# matched the host composition. Attempting this using the Nielsen and Drake (1979) equilibrium model used by Preece *et al.* (2014) produces unnatural clinopyroxene compositions, and additional testing using Danyushevsky (2001) both lead to strongly FeO and $Al_2O_3$ depleted melts relative to the liquid line of descent. Using the predicted component models of Putirka (1999), Mollo *et al.* (2013) and Neave and Putirka (2017) (new DiHd model found in the supplementary spreadsheet) with a fixed $KD_{Fe-Mg}^{cpx-melt} = 0.28$ (Putirka, 2008) to produce a predicted clinopyroxene compositions in equilibrium with the melt inclusion incrementally require significant >50% clinopyroxene addition to reach DiHd and EnFs equilibrium between melt inclusion and host, and to reach $KD_{Fe-Mg}^{cpx-melt} = 0.28$ equilibrium. A final attempt following Bali *et al.* (2018) by adding host clinopyroxene to the melt inclusion until $KD_{Fe-Mg}^{cpx-melt} = 0.28$ is achieved required plausible correction percentages (<20%) and $Al_2O_3$ concentrations at overlap the literature volcanic data and intercumulus glasses analysed in this study. Therefore this is the correction method used in this study. Orthopyroxene were corrected by adding the host orthopyroxene back to the inclusion until $KD_{Fe-Mg}^{opx-melt} = 0.29 \pm 0.06$ (Putirka, 2008) is approached, which produced plausible melt compositions that follow the liquid line of descent, overlapping interstitial glass analyses. This required less than 8% orthopyroxene addition.

### A.1.3 Plagioclase

PEC of plagioclase-hosted melt inclusions is evidenced by a fine micron-scale rim of lower An plagioclase around melt inclusion rims, and elements strongly compatible in plagioclase such as $Al_2O_3$ diverging from the liquid line of descent along a plagioclase crystallisation vector (Figure A.1), mirroring PEC trends identified by Nielsen (2011). These inclusions were corrected following the approach of Neave *et al.* (2017) and Bali *et al.* (2018), where the original melt inclusion composition is assumed to lie on the liquid line of decent. Host plagioclase composition is added back to the inclusion until the $Al_2O_3$ vs MgO concentration in the melt inclusion approximates that predicted by a linear regression through the literature volcanic whole rock and glass dataset used in Chapter 2. This results in 9 to 19% plagioclase addition. The corrected compositions all fall within the $KD^{pl-liq}_{Ab-An} = 0.1 \pm 0.05$ equilibrium test of Putirka (2008) for systems <1050°C, and are at the lower end of that predicted by the plagioclase-liquid equilibrium test derived in this study (Appendix section A.2.2). Comparison between temperatures predicted by plagioclase-liquid thermometry and liquid plagioclase saturation temperature (Putirka, 2008 equations 24a and 26) are <11°C, within the 36°C SEE of the thermometers, indicating equilibrium (c.f Putirka, 2008; Bali *et al.*, 2018). These corrections increase temperatures estimated by thermobarometric models of Putirka (2008) by 19-36°C, which are lower than the 36°C SEE of the Putirka (2008) thermometer.

## A.2 Thermobarometry model justification

### A.2.1 $H_2O$ estimates for thermobarometry

Most thermobarometric equations are $H_2O$ sensitive but most potential liquids in the database used for mineral melt thermobarometry lack water measurements. To address this, published FTIR and SIMS measured water contents (FTIR: Cottrell *et al.*, 1999; Gertisser *et al.*, 2009; SIMS: Panienka, 2012; Cadoux *et al.*, 2014; Druitt *et al.*, 2016) were used to develop a simple linear model to estimate water contents in the melt as a function of $SiO_2$ (Figure A.2). Although $K_2O$ is incompatible at Santorini and has been used as a differentiation index in previous studies

(e.g. Druitt *et al.*, 2016), Cadoux *et al.* (2014) does not report $K_2O$ values, therefore we use the larger $SiO_2$ dataset. Groundmass glass $H_2O$ measurements are not included in the regression due to potential $H_2O$ loss during degassing (c.f. Panienka, 2012). Water contents estimated by difference from 100 wt% (Anderson, 1973, 1974; Devine *et al.*, 1995) are additionally not used in the regression due to their inherent larger uncertainty, and systematically higher estimated $H_2O$ concentrations. Melt inclusions can rapidly lose $H_2O$ (e.g. Gaetani *et al.*, 2012), therefore melt inclusion measurements may represent minimum original $H_2O$ estimates. To mitigate this, we use a fit that by eye fits the majority of the higher $H_2O$ estimates. Compared to a calculated linear fit, using higher $H_2O$ estimates raises pressure estimates by 0.2-0.7 kbar for the clinopyroxene-only model (Putirka, 2008 equation 32b), and $<$ 0.1 kbar for clinopyroxene-melt models (Putirka, 2008 equations 30 and 31, @Neave2017), both of which are far lower than reported model uncertainty of ˜2.5 kbar (Putirka, 2008). Temperature estimates are reduced by $<$14°C, also lower than published model uncertainty of 35°C.

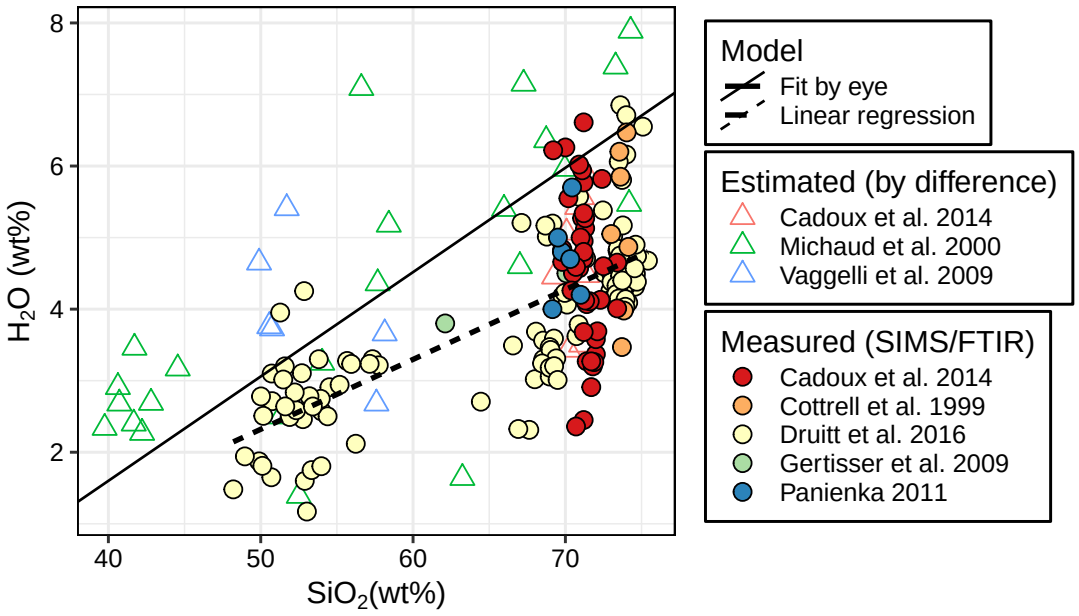


*Figure A.2: Linear regression (dashed) and high $H_2O$ fit by eye (solid) regression lines of published measured water contents used for thermobarometry. $H_2O$ values estimated by difference from 100 wt% are shown for comparison to the SIMS/FTIR measured data. Data from Cadoux* et al. *(2014), Michaud* et al. *(2000); Vaggelli* et al. *(2009), Cottrell* et al. *(1999), Druitt* et al. *(2016). Gertisser* et al. *(2009), Panienka (2012).*

### A.2.2 Equilibrium tests

Before applying any thermobarometric models to the Santorini data, mineral and liquid pairs need testing for chemical equilibrium. This section assesses mineral-liquid equilibrium tests to find the most accurate model for the Santorini data. In this section, and the following thermobarometric testing section, we show three experimental datasets. The LEPR dataset is the Library of Experimental Phase Relations (Hirschmann *et al.*, 2008) which provides the main dataset used to calibrate many of the equilibrium tests and thermobarometric models. The 'Additional experiments' dataset are a selection of experimental data for mostly arc volcanoes published after 2008 not found in the LEPR database, which additionally will not have been used to calibrate the Putirka (2008) models and the Neave and Putirka (2017) barometer. The final dataset are the Santorini experiments of Cadoux *et al.* (2014), Andújar *et al.* (2015) and Andújar *et al.* (2016), which are the most important for testing the validity of equilibrium testing models and thermobarometric models. These datasets are also not found in the calibration datasets for the equilibrium and thermobarometric models. All models in the following sections are performed iteratively, where a barometer is paired to a thermometer and solved simultaneously, to recreate the approach applied to the Santorini xenoliths.

#### Clinopyroxene

There are two different clinopyroxene equilibrium tests. First, tests based on partitioning of Fe and Mg between clinopyroxene and liquid (Putirka *et al.*, 1996; Putirka, 1999, 2008; Bédard, 2010), and secondly, comparing calculated clinopyroxene chemical components, such as DiHd, EnFs, CaTs, against the measured clinopyroxene components (Putirka, 1999, 2008; Mollo *et al.*, 2013; Neave and Putirka, 2017). As the former $KD_{cpx-melt}^{Fe-Mg}$ models have been shown to perform poorly compared to the component based tests when cooling rate varies (Putirka, 2008; Mollo *et al.*, 2012; Mollo and Masotta, 2014), we only consider the component based equilibrium tests for our thermobarometric assessment of the Santorini plutonic xenolith pressure and temperature conditions. Figure A.3 shows that the equilbrium model presented in the appendix spreadsheet of Neave and Putirka (2017) paired with the barometer of Neave and

Putirka (2017) and thermometer of Putirka (2008) equation 33 is the most accurate at predicting equilibrium clinopyroxene-liquid pairs. The barometer of Neave and Putirka (2017) itself is not the most accurate at predicting clinopyroxene crystallisation pressures for the datasets we have tested it with however and is not used for pressure estimates (Figures A.6, A.7).

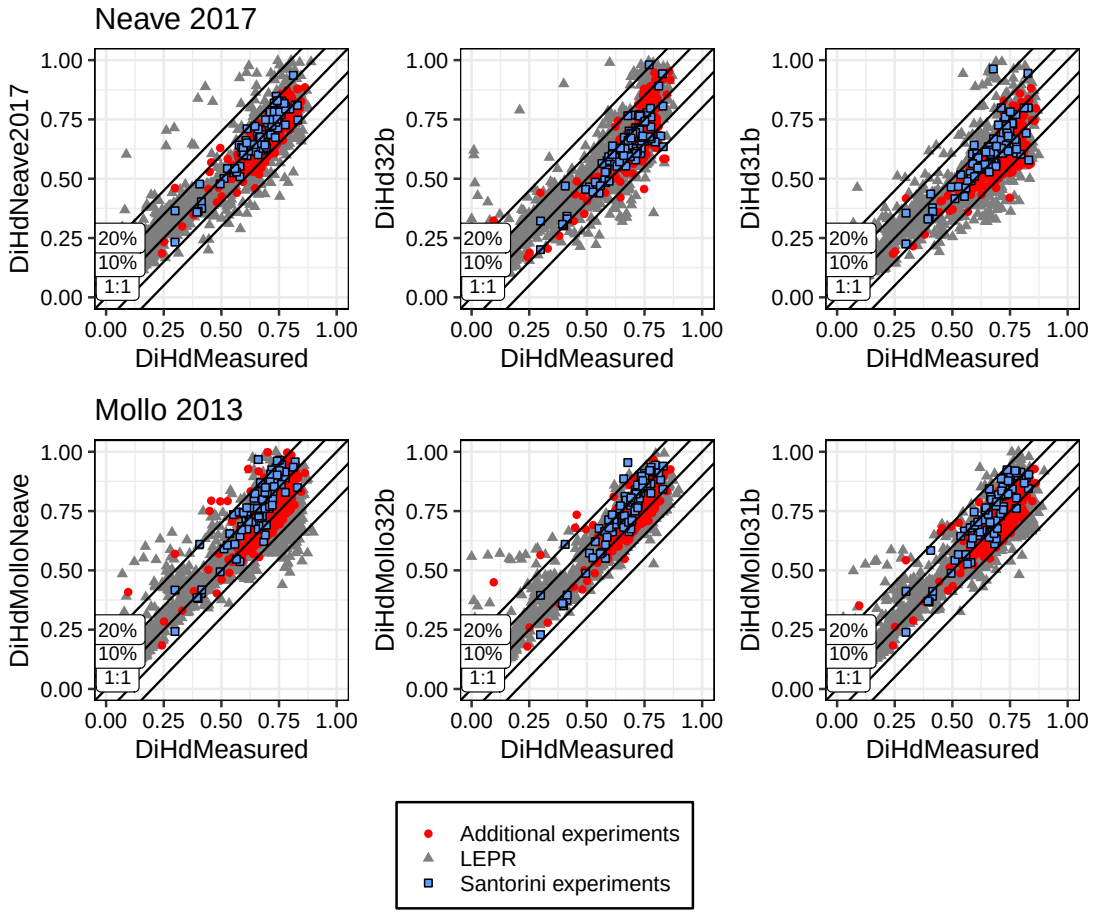


*Figure A.3: Clinopyroxene equilibrium tests tested with experimental data. All models are paired to Putirka (2008) equation 33 thermometer, and tested with three barometers: Putirka (2008) equations 31,32b and Neave and Putirka (2017). The lines represent the 1:1 line, +10% and +20% uncertainty. Published model uncertainties are around 0.07*

### Orthopyroxene

We next assess the accuracy of the two orthopyroxene-melt equilibrium tests of Bédard (2007) and Putirka (2008). Putirka (2008) showed that $KD_{Fe-Mg}^{opx-melt} = 0.29 \pm 0.06$, weakly correlated to $X_{Si}^{Melt}$. This melt dependent regression struggles to recover the $KD_{Fe-Mg}^{opx-melt}$ values at high $X_{Si}^{Melt}$, where many Santorini experimental data lie ($R^2 = 0.1$, SEE=0.08). The multiple

regression based on melt and orthopyroxene composition equation 7b of Bédard (2007) recovers the Santorini experimental data and global dataset more accurately ($R^2$=0.25, SEE=0.07).

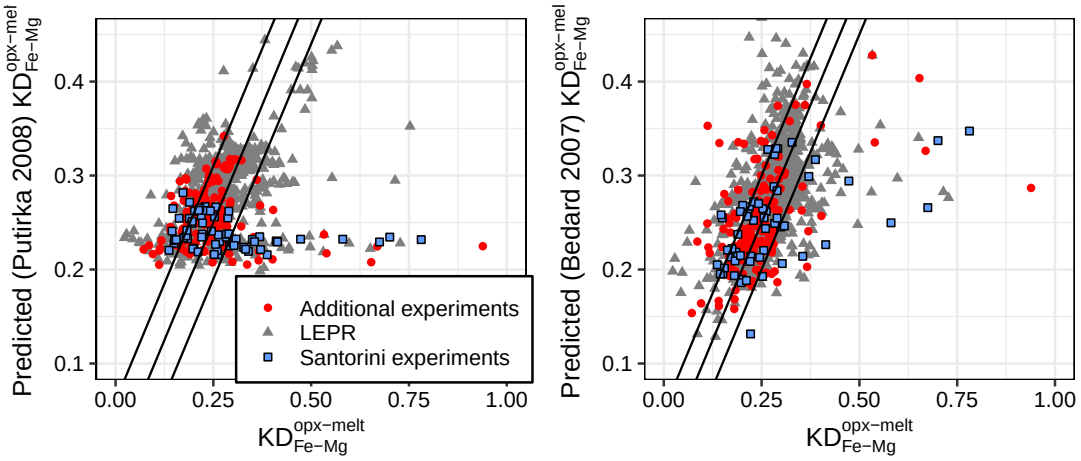


*Figure A.4: Orthopyroxene equilibrium tests, showing that the multiple linear regression model equation 7b of Bédard (2007) recovers the Santorini experimental data best. Axes are truncrated omitting some extreme outliers. Lines show the 1:1 line and reported model uncertainty (0.06) A) Putirka (2008). B) Bédard (2007) equation 7b.*

### New plagioclase equilibrium test

Putirka (2008) suggested a temperature sensitive equilibrium test for plagioclase based on albite-anorthite partitioning between plagioclase and liquid, where at T $<$ 1050°C equilibrium $KD^{Ab-An}_{Plagioclase-melt}$ is 0.1 $\pm$ 0.05 and T $>$ 1050°C $KD^{Ab-An}_{Plagioclase-melt}$ 0.25 $\pm$ 0.11. The post-2008 experimental dataset, including Santorini experiments (Cadoux *et al.*, 2014; Andújar *et al.*, 2015, 2016) help fill the temperature gap in the LEPR database (Hirschmann *et al.*, 2008) which defined the two temperature bracketsin the Putirka (2008) equilibrium test. Here we derive a model based on $X^{Si}_{liquid}$ (Figure A.5) to avoid the circularity of requiring a temperature to predict an equilibrium KD value for calculating temperatures. This model is calibrated on the global dataset, including Santorini experimnental data, and is therefore widely applicable to igneous systems. $X^{Si}_{liquid}$ is correlated with the natural logarithm of $KD^{Ab-An}_{Plagioclase-melt}$ ($R^2$=0.51 SEE=0.45), producing the following equation.

$$ln(KD^{Ab-An}_{Plagioclase-Liquid}) \pm 0.4541 = 1.26954 - 5.38702X^{Si}_{liquid}$$

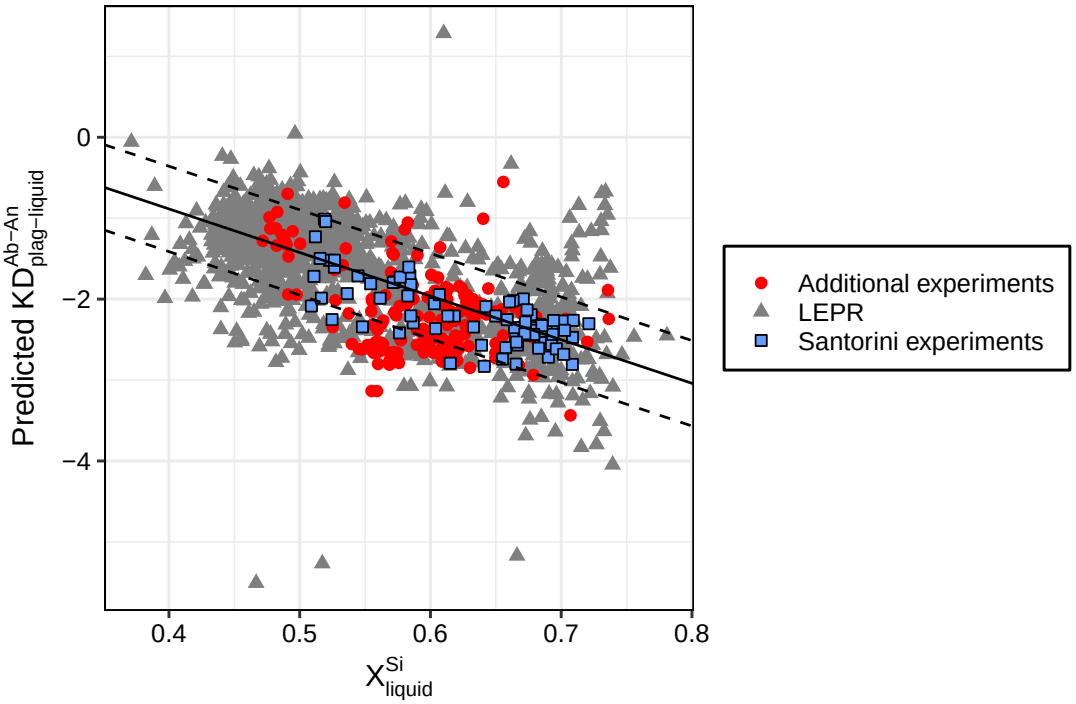


*Figure A.5: New plagioclase equilibrium test. Dashed lines show one standard deviation uncertainty.*

### A.2.3 Thermobarometer testing

Thermobarometric models (Nimis, 1995; Nimis and Taylor, 2000; Loucks, 1996; Putirka, 2008; Neave and Putirka, 2017) were tested using the LEPR database and additional experimental data from mostly arc volcanoes published post publication of Putirka (2008), including Santorini experiments (Cadoux *et al.*, 2014; Andújar *et al.*, 2015, 2016), to check their accuracy when calculated iteratively, and assess any systematic errors in temperature or pressure. The clinopyroxene-olivine thermometer of Loucks (1996) had no correlation to experimental temperature with the data of Stamper *et al.* (2014) and Andújar *et al.* (2015), and no improvement with an attempt at recalibration, therefore is not discussed further. The widely applied clinopyroxene-only barometer of Nimis (1995) and thermometer of Nimis and Taylor (2000) are additionally not considered due to their restricted calibration ranges, and not being suitable for calk-alkaline and hydrous systems.

The most accurate thermometer and barometer combination from the following tests is Putirka (2008) equation 33 (temperature) paired with 32b (pressure). This results in a $R^2$ of 0.93

with a SEE of 19°C for pressures <10 kbar when comparing averaged predicted temperatures for each experimental temperature (c.f. Putirka, 2008).

**Clinopyroxene thermometers paired with barometers**

**Clinopyroxene barometers paired with thermometer Putirka (2008) equation 33**

Overall the Putirka (2008) equation 32b barometer performs the most accurately, although with a small pressure overestimation for the Santorini data, not observed in the rest of the LEPR and post-2008 experimental datasets. Putirka (2008) equation 31 requires a pressure correction at low < 5kbar pressure. The Neave and Putirka (2017) barometer performs well at low pressures but has the largest pressure residual spread of the three barometers, reflecting the more restricted calibration dataset used. In this thesis, we apply a 2 kbar pressure correction to equation 31 to compensate for the overestimation.

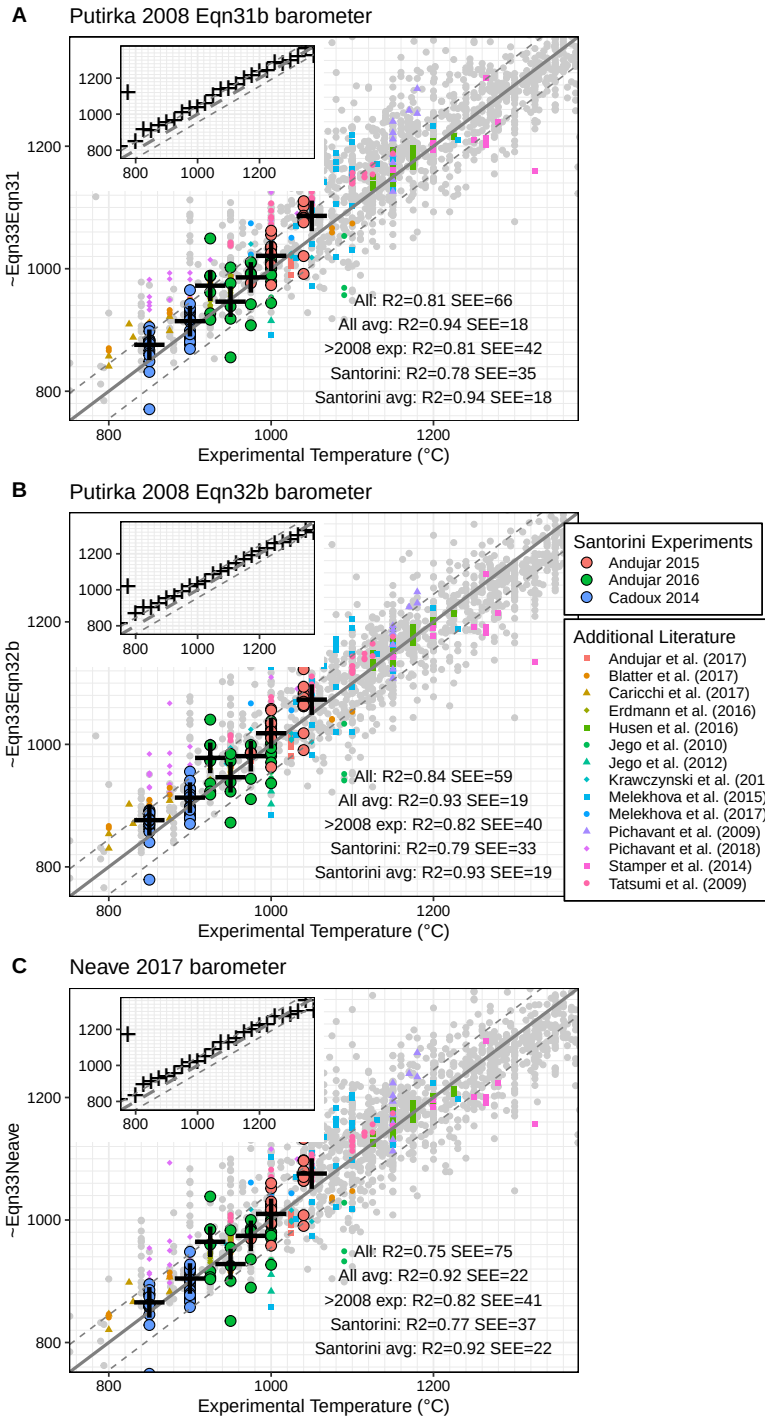


*Figure A.6: Clinopyroxene-melt iterative paired thermometer tests. Equation 33 (Putirka, 2008) is paired with three barometers. Thick black crosses are averages of Santorini experiments. Solid line is 1:1, dashed is published model error of 45°C. Inset shows results averaged by experimental temperatures rounded to nearest 25°C. Light grey points are the results from the LEPR database.*

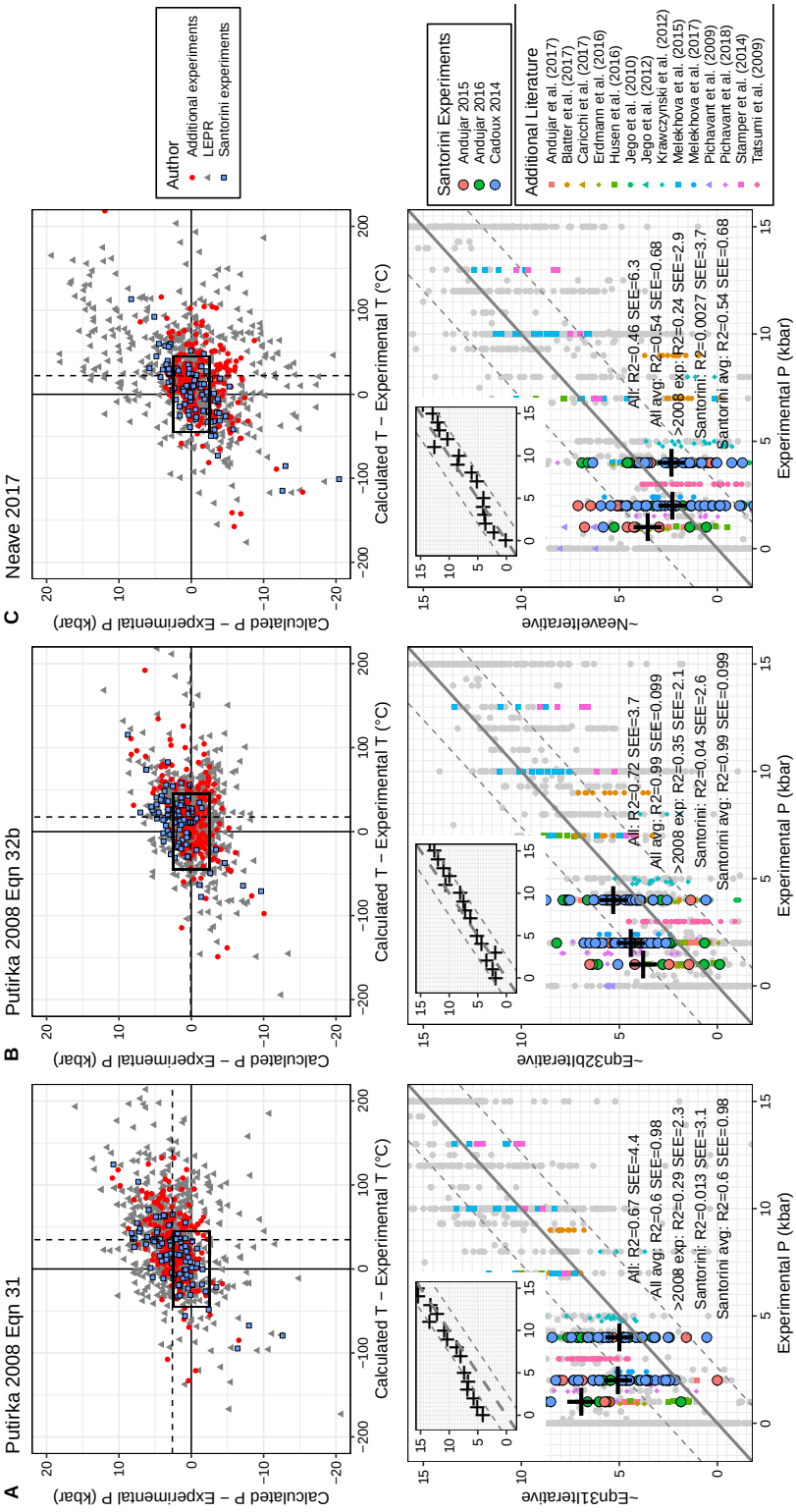


*Figure A.7: Clinopyroxene barometers. Experimental data are filtered for the top residual plot row between 800-1150°C and P < 10 kbar. Overall the Putirka (2008) equation 32b barometer performs the most accurate, although with a small pressure overestimation for the Santorini data, not seen in the rest of the LEPR (light grey) and post-2008 (red) experimental datasets. Putirka (2008) equation 31 requires a pressure correction at low < 5kbar pressure. The Neave and Putirka (2017) barometer performs well at low pressures but has the largest pressure residual spread of the three barometers, reflecting the smaller calibration dataset used.*

**Orthopyroxene thermobarometers**

Orthopyroxene thermobarometers (Putirka, 2008 equations 28, 29a, 29b) are shown in Figure A.8. Generally the thermometer performs well for experiments with Santorini compositions, but the barometer overestimates pressures in the $< 5$ kbar pressure range applicable to Santorini. A 2 kbar pressure correction is therefore applied to results from this barometer in the main text. For Santorini experiments, temperature estimates are within model error.

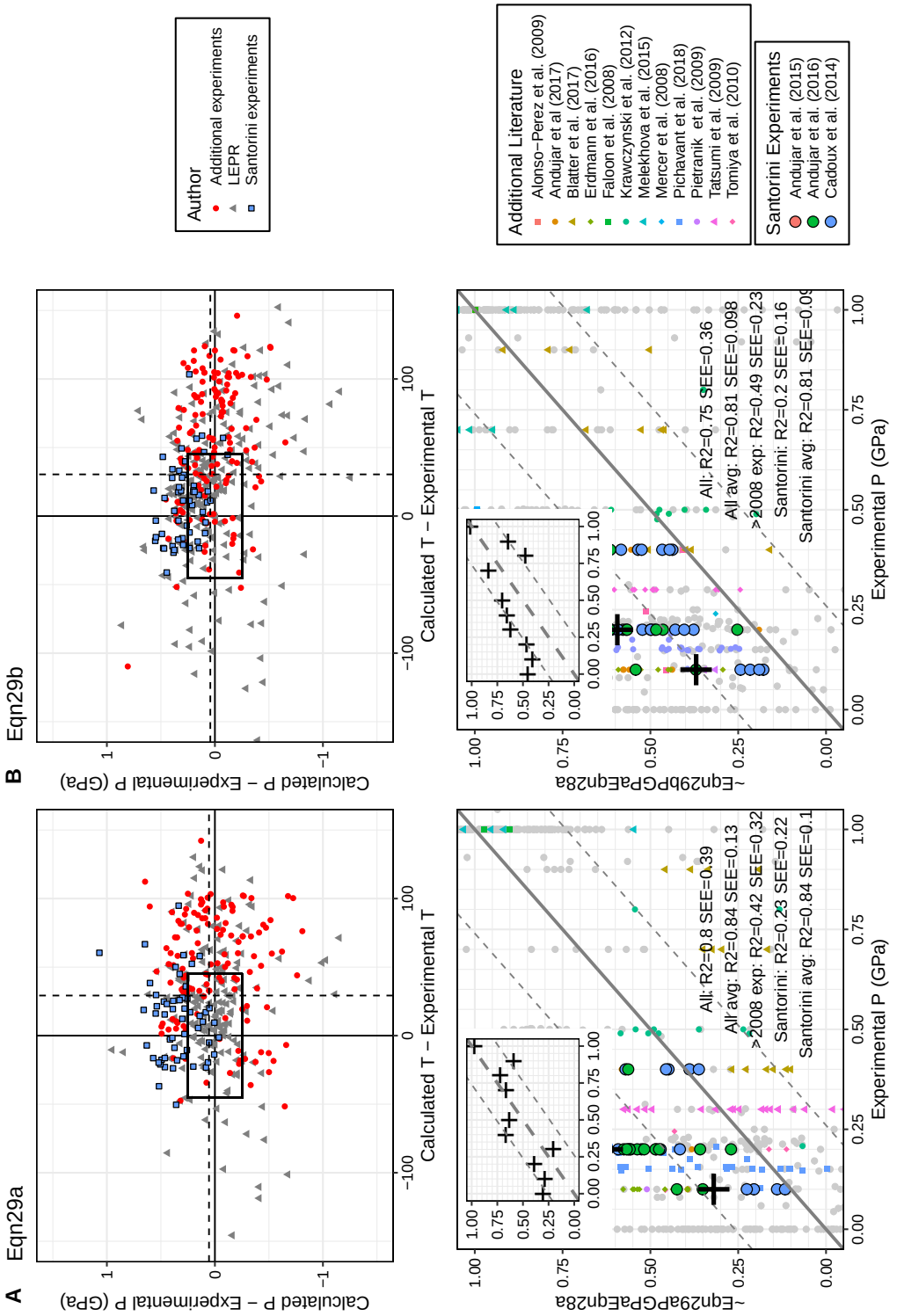


*Figure A.8: Orthopyroxene thermobarometer testing. Experimental data are filtered for the top residual plot row between 800-1150°C and $P < 10$ kbar.*

**Plagioclase-melt thermobarometry and hygrometry**

Plagioclase thermobarometers (Putirka, 2008) are shown in Figure A.9. Putirka (2008) noted that the barometer equation 25 should be used with caution, and the uncertainty with this barometer can be seen in Figure A.9. When the barometer and thermometer are paired using experimental $H_2O$ contents, the error in thermometry is substantial for the Santorini experiments. When the experimental conditions are used as pressure and temperature inputs the thermometry results have much smaller uncertainty, but the pressure estimates are not significantly improved. $H_2O$ estimates are within model uncertainty when using experimental conditions, and have larger uncertainty when the barometer is paired to the thermometer (Figure A.10). For this reason, we use the results from plagioclase thermometry and hygrometry paired with a constant value of 2 kbar, which is the average of results of barometry from clinopyroxene and orthopyroxene-melt calculations. Temperatures vary $<10$°C for each 1 kbar, which is insignificant compared to the published model uncertainty, and the 1-4 kbar range of pressures (Druitt *et al.*, 2016 and references therein).

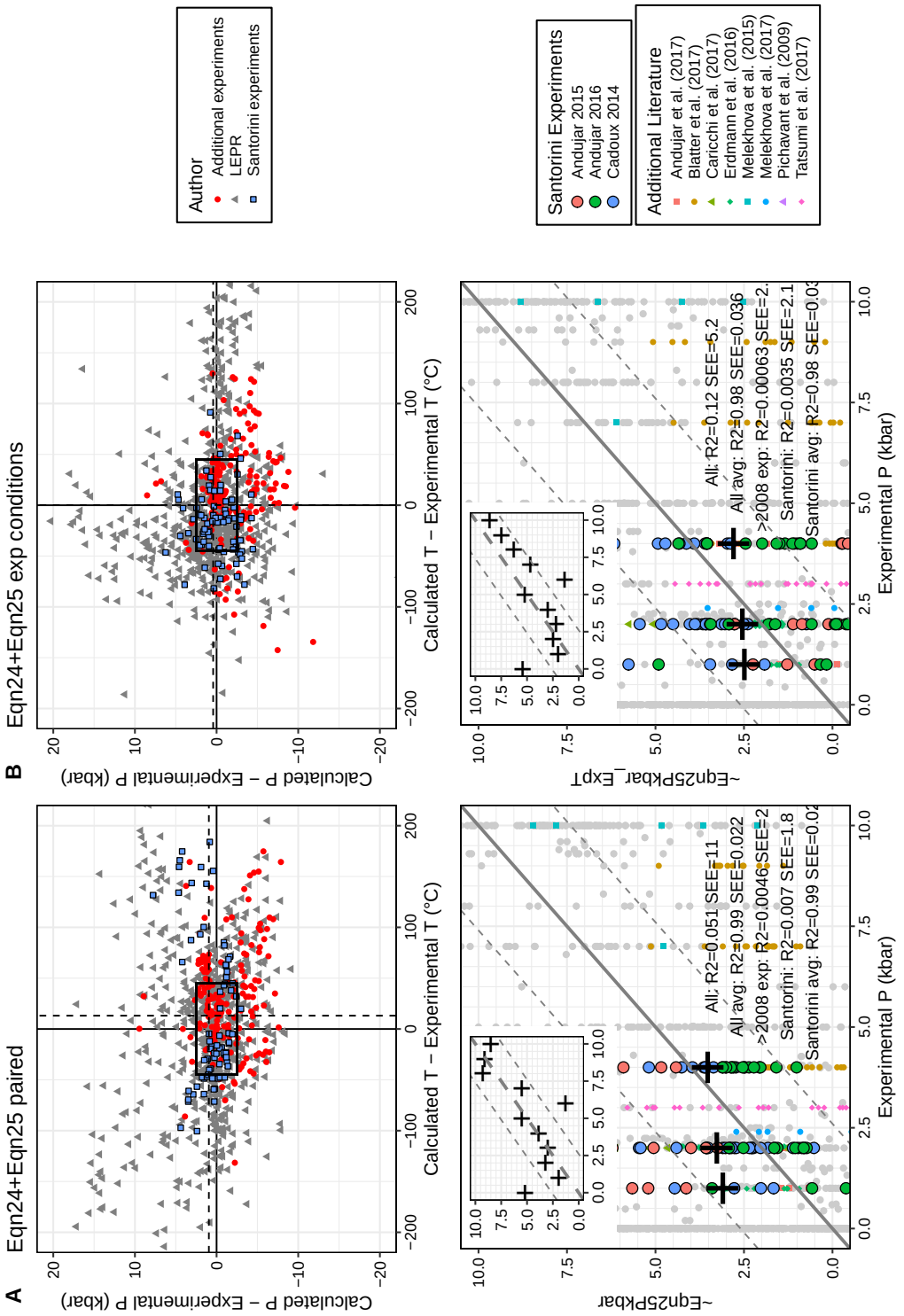


*Figure A.9: Plagioclase pressure and temperature model evaluation. Experimental T is filtered between 700-1150°C and P < 10kbar.*

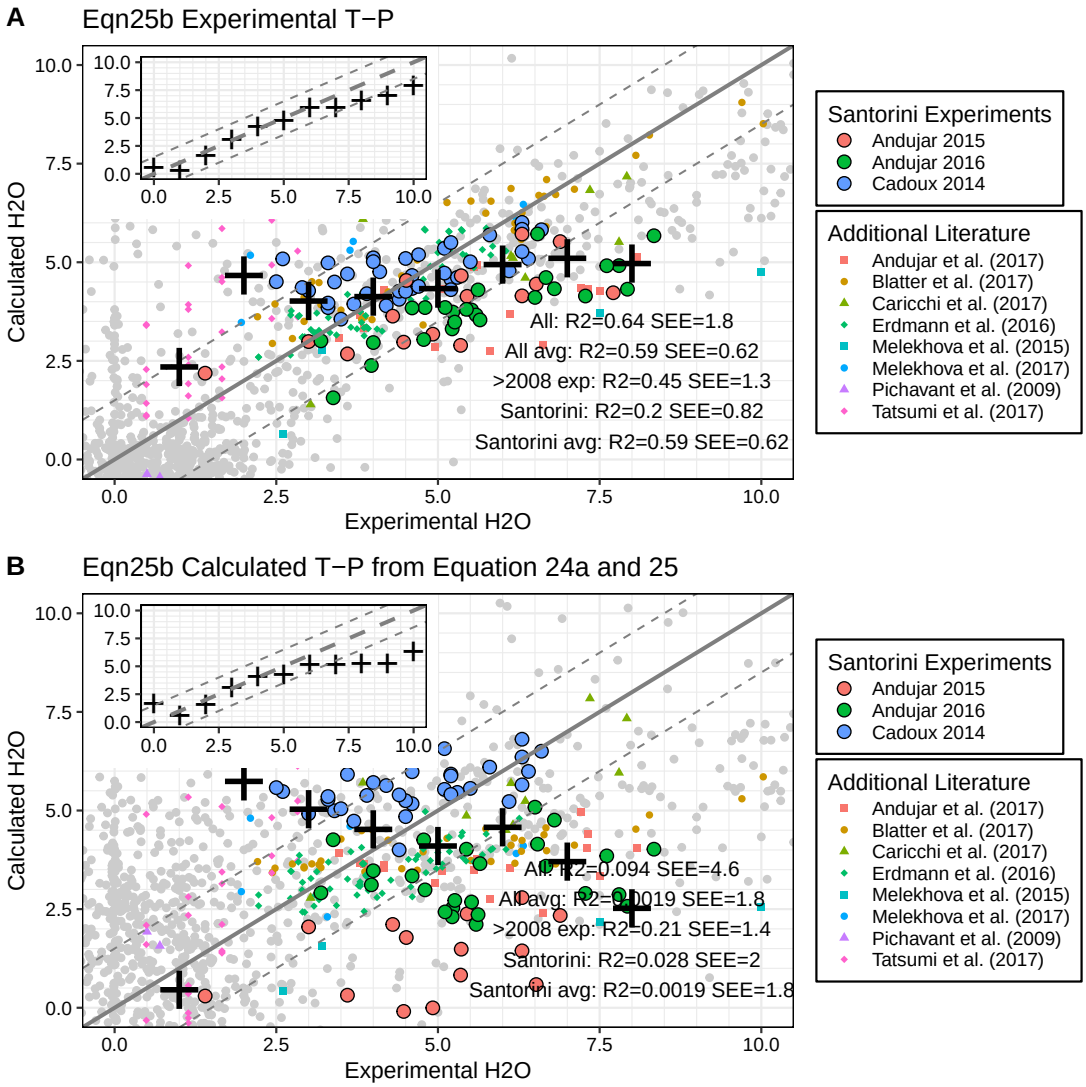


*Figure A.10: Plagioclase hygrometry using Putirka (2008) models. Both the results from the experimental conditions used as an input (a) and the thermometer and barometers equation 24 and 25 paired (b). Crosses show data averaged to the nearest 1 wt% experimental $H_2O$.*

## A.3 Mineral Partition Coefficients

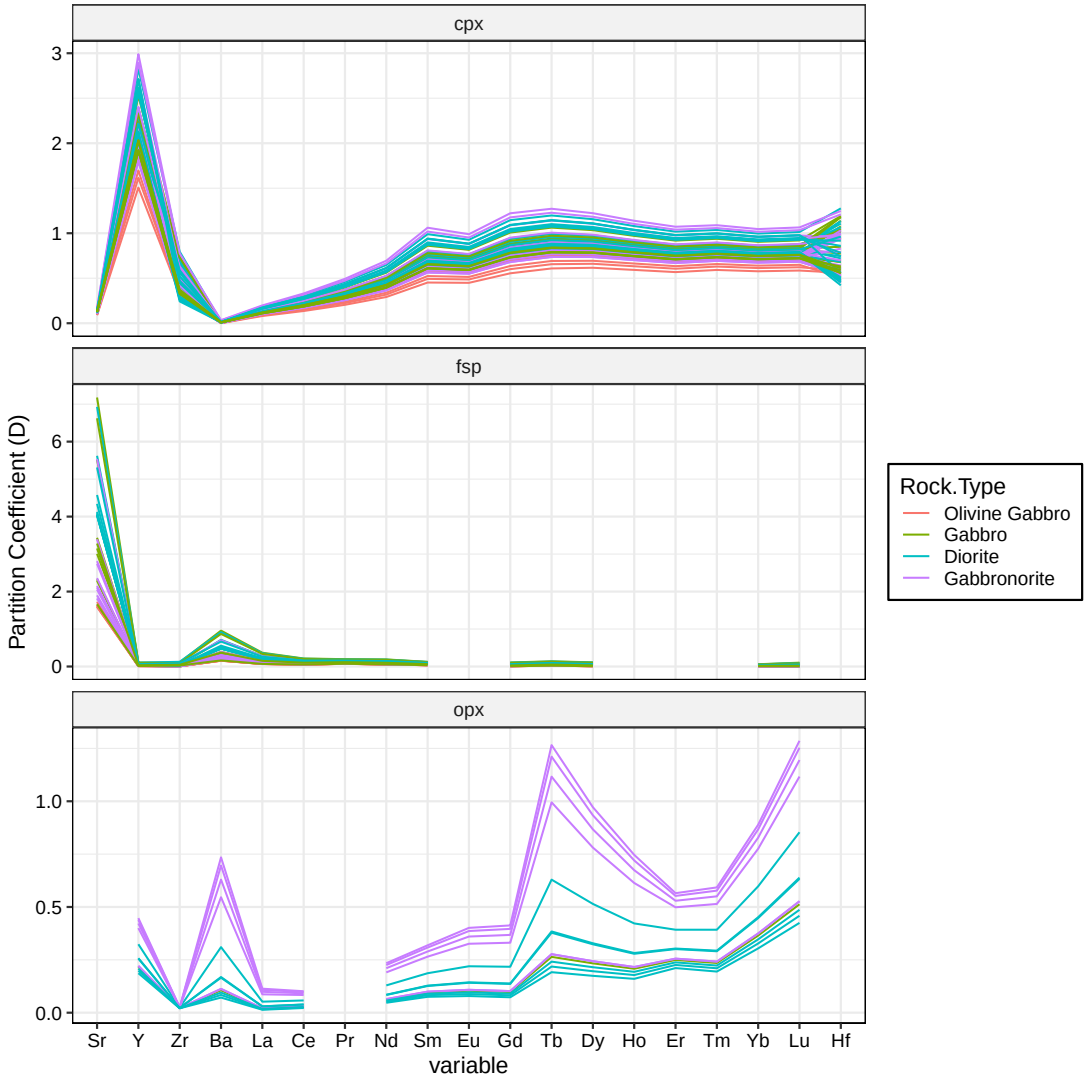


*Figure A.11: Partition coefficients used in this study. Calculated using the models described in section 2.3.4*

## A.4 Xenolith mineral compositions by eruption

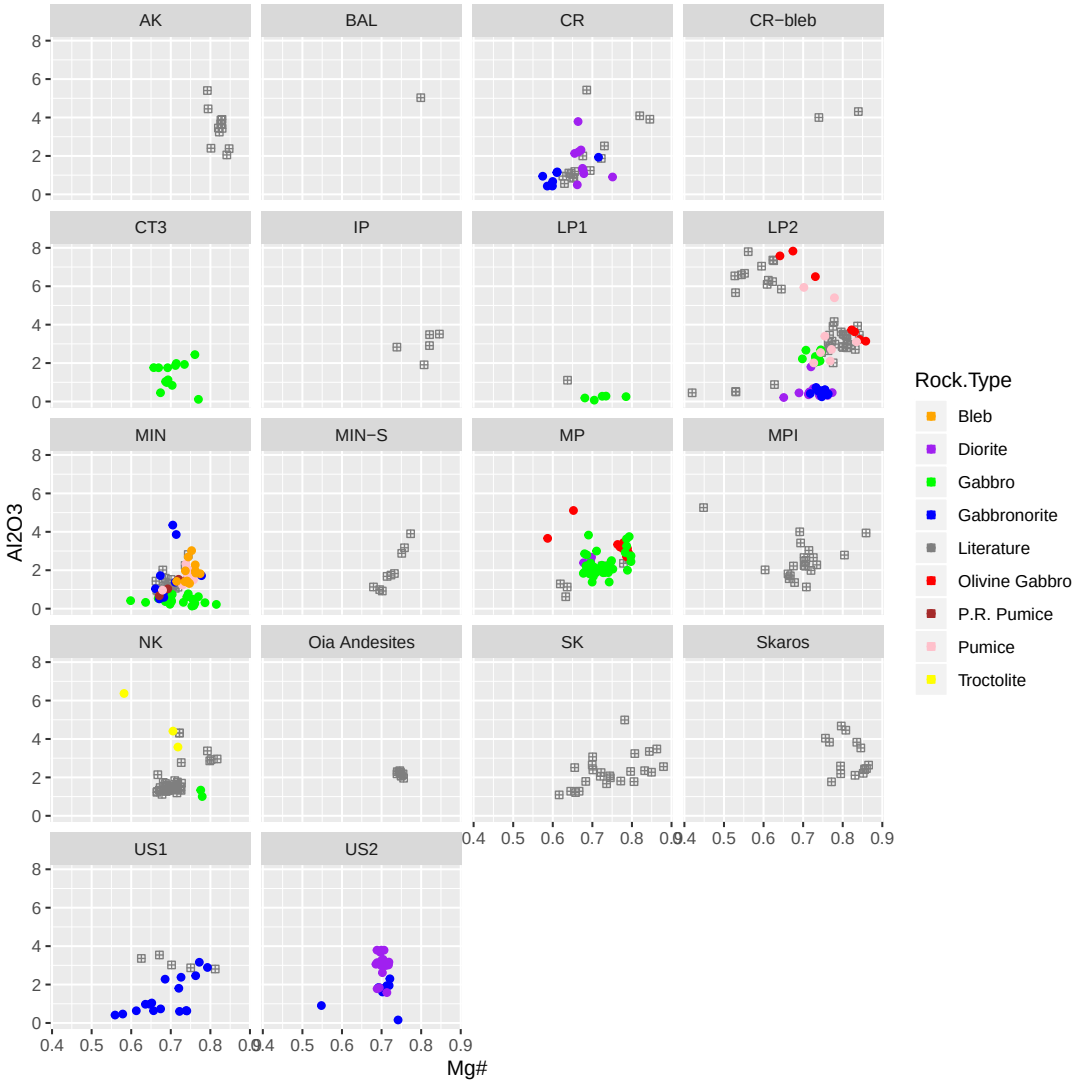


*Figure A.12: Xenolith clinopyroxene compared to volcanic clinopyroxene on an eruption by eruption basis. Literature data from Druitt (1983), Huijsmans (1985), Barton and Huijsmans (1986), Cottrell* et al. *(1999), Cabato (2007), Gertisser* et al. *(2009), Vaggelli* et al. *(2009), Panienka (2012), Cadoux* et al. *(2014), Andújar* et al. *(2015) and Druitt* et al. *(2016).*

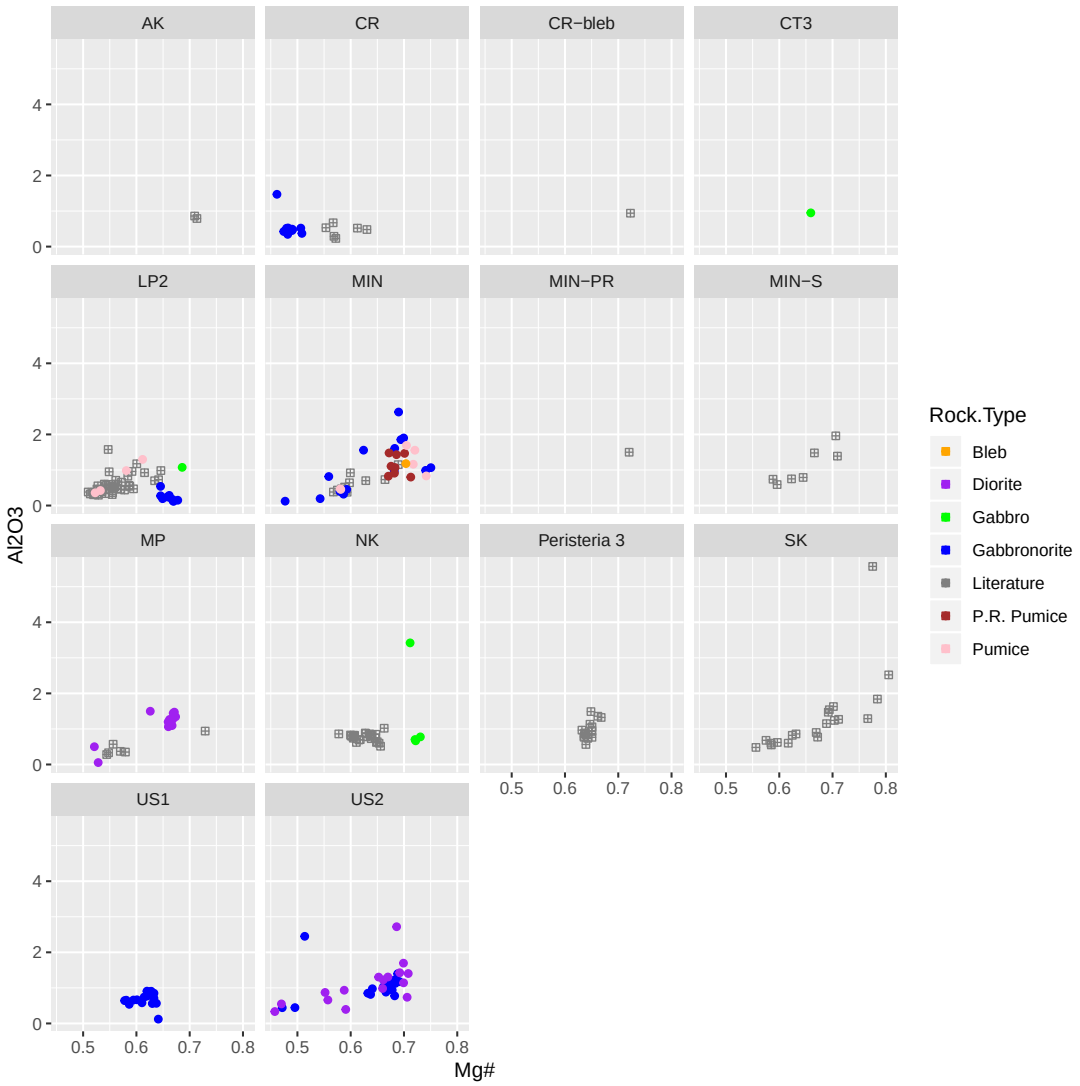


*Figure A.13: Xenolith orthopyroxene compared to volcanic clinopyroxene on an eruption by eruption basis. Literature data from Druitt (1983), Huijsmans (1985), Cabato (2007), Gertisser* et al. *(2009), Panienka (2012) and Druitt* et al. *(2016).*

## A.5 Sample List

*Table A.1: Sample list. Remaining sizes are VS very small (~5g), S small etc, VL: very large >1kg. Freshness VF: very fresh, essentially no alteration observable*

| Sample | Remaining | Unit | Type | Freshness | Probed | Laser |
|---|---|---|---|---|---|---|
| 2-8-3 | M | Akrotiri Lavas | Enclave | | | |
| 2-8-6 | M | Akrotiri Lavas | Enclave | | | |
| 8-1-1 | L | Akrotiri Lavas | Enclave | | | |
| 8-1-7-1 | M ? | Akrotiri Lavas | Enclave | | | |
| 8-1-7-1 | M ? | Akrotiri Lavas | Enclave | | | |
| 2-6 | ML | Akrotiri Phreato | syeno granite | | | |
| 2-6-1 | VS | Akrotiri Phreato | Enclave | | | |
| 2-6-5 | SM | Akrotiri Phreato | Lava | | | |
| 12-1-1 | L | CR | Crustal | | | |
| 12-1-3 | S | CR | Gabbro | | | |
| 12-1-3-2 | | CR | Crustal | | | |
| 12-1-5 | L | CR | Gabbronorite | M | Y | Y |
| 13-1-3-2 | M | CR | | | | |
| 5-3-1 | S | CR | Gabbro | | | |
| 5-3-10 | ML | CR | Gabbro | | | |
| 5-3-15 | S | CR | Gabbro | | | |
| 5-3-2 (1) | S | CR | Gabbro | | | |
| 5-3-2 (2) | VS | CR | Gabbro | | | |
| 5-3-22 | VL | CR | qtz gabbro | LM | | |
| 5-3-3 | M | CR | Gabbro | | | |
| 5-3-4 | ? | CR | Gabbro | | | |
| 5-3-4 (3) | VS | CR | Gabbro | | Y | Y |
| 6-3-1 | VL | CT3 | Gabbro | MH | Y | Y |
| 6-3-3 | SM | CT3 | Gabbro | LM | | |
| 6-3-5-1 | VL | CT3 | Gabbro | LM | | |
| 6-3-6-1 | M | CT3 | Crustal | | | |
| 6-3-6-2 | S | CT3 | Gabbro | | | |
| 6-3-6-3 | SM | CT3 | Gabbro | | | |
| 6-3-7 | VL | CT3 | Gabbro | LM | | |
| 6-4-1-1 | S | LP1 | Gabbro | L | | |
| 6-4-1-2 | M | LP1 | Granite | F | | |
| 6-4-2 | M | LP1-C | Gabbro | | Y | Y |
| 13-1-2-1 | M | LP2 | Gabbro | MH | N | N |
| 13-1-2-2 | ML | LP2 | Gabbro | M | | |
| 13-1-2c | S | LP2 | crustal | | | |
| 13-2-1 | S | LP2 | Gabbro | | | |
| 13-2-2 | S | LP2 | granite | | | |
| 13-2-3 | S | LP2 | granite | | | |
| 8-3-1 | S | LP2 | Gabbro | M | | |

| Sample | Remaining | Unit | Type | Freshness | Probed | Laser |
|---|---|---|---|---|---|---|
| 8-3-3 | S | LP2 | Gabbro | | | |
| 9-1-8-1 | S | LP2 | Olivine gabbro | F | | |
| 9-1-8-2 | S | LP2 | Olivine gabbro | | | |
| 9-1-8-3 | S | LP2 | Gabbro | VF | Y | Y |
| 13-1-1c | Y | LP2-A3 | Crustal | | | |
| 9-1-1-2 | VS | LP2-A3 | Gabbro | LM | | |
| 9-1-1-3 | VS | LP2-A3 | Gabbronorite | | Y | Y |
| 9-1-1-4 | VS | LP2-A3 | Marble | | | |
| 9-1-1-5 | SM | LP2-A3 | Gabbro | | | |
| 9-1-1-c | S | LP2-A3 | Marble-CS? | | | |
| 9-1-2 | S | LP2-A3 | Olivine gabbro | VF | | |
| 9-1-3 | L | LP2-A3 | Gabbro | | | |
| 9-1-4 | ML | LP2-A3 | Gabbro | F | | |
| 9-1-5 | L | LP2-A3 | Gabbro | | | |
| 9-1-6 | L | LP2-A3 | Gabbro | F | | |
| 8-3-5-1 | S | LP2-B2 | schist | | | |
| 6-7 | S | LP2-D | Crustal | | | |
| 6-7-2 | S | LP2-D | Gabbro | | | |
| 3-5-1 | S | Minoan A | Gabbronorite | | | |
| 3-5-2 | S | Minoan A | Gabbronorite | VF | | |
| 9-3 | M | Minoan A | Gabbronorite | F | N | N |
| 9-3-1 | S | Minoan A | Gabbronorite | F | N | N |
| 9-3-2 | L | Minoan A | Gabbronorite | H | Y | Y |
| 13-6-2 | M | Minoan A P1b | Gabbro | | | |
| 1-2-3 | S | Minoan B | P-rich pumice | | Y | N |
| 10-6 | M | Minoan C | Lava | | | |
| 10-6-6 | ? | Minoan C | Granite+carbonate | | | |
| 10-6-C1 | VS | Minoan C | Gabbro | M | | |
| 10-6-C2 | VS | Minoan C | Gabbro | | | |
| 13-6-3 C | M | Minoan C | Qtz Gabbro | F | | |
| 14-1-2 | L | Minoan C | Gabbronorite | | | |
| 4-4 C | S | Minoan C | Gabbro | M | Y | Y |
| 1-5-C | VS | Minoan D | Marble | | | |
| 12-3-1 | S | Minoan D | altered lava? | | | |
| 12-3-2 | S | Minoan D | Crustal | | | |
| 12-3-t | M | Minoan D | altered lava? | | | |
| 16-1-C | VS | Minoan D | Granite | | | |
| 11-1-1 | S | MP-A | Gabbronorite | F | | |
| 11-1-2 | S | MP-A | Gabbronorite | MH | | |
| 15-1- 3 | L | MP-A | Gabbro | | | |
| 15-1-1-1 | M | MP-A | Gabbro | L | | |
| 6-5-2-1 | SM | MP-A | Olivine gabbro | F | Y | Y |
| 6-5-2-2 | SM | MP-A | Melilite | | | |
| 6-5-3 | SM | MP-A | Gabbronorite | | Y | Y |
| 9-2-2 | L | MP-A | Gabbro | MF | Y | Y |
| 9-2-3 | L | MP-A | Gabbro (dolerite?) | F | | |
| 9-2-4-1 | M | MP-A | Gabbro | M | | |
| 11-2-1 (1) | ? | NK | Troctolite cluster | | | |
| 11-2-1 (2) | ? | NK | Troctolite cluster | | | |
| 11-2-1 (3) | ? | NK | Troctolite cluster | | | |
| 11-2-1 (4) | ? | NK | Troctolite cluster | | | |
| 11-2-1 (5) | Y | NK | CS (Basement?) | | | |

| Sample | Remaining | Unit | Type | Freshness | Probed | Laser |
|---|---|---|---|---|---|---|
| 11-2-1 (6) | Y | NK | Gabbronorite | | Y | N |
| 11-2-1 (7) | ? | NK | Pl pheno | | | |
| 11-2-1 (8) | ? | NK | CS (enclave?) | | | |
| 11-2-1 (9) | ? | NK | Enclave? | | | |
| 11-2-1 U (1) | Y | NK | Gabbro | | | |
| 11-2-1 U (2) | Y | NK | Pl pheno | | | |
| 11-2-2 U | Y | NK | Quartz | | | |
| 11-2-2 U (2) | ? | NK | Troctolite cluster | | | |
| 11-2-2 U (3) | ? | NK | Troctolite cluster | | | |
| 11-2-3 (1) | Y | NK | Enclave | | | |
| 11-2-3 (2) | Y | NK | Enclave, banded | | | |
| 11-2-3 U (3) | SM | NK | Lava | | | |
| 11-2-3 U (4) | ? | NK | ? | | | |
| 11-2-3 U (5) | ? | NK | Troctolite cluster | | | |
| 11-2-3 U (6) | VS | NK | Quartz | | | |
| 11-2-3U (1) | ? | NK | ? | | | |
| 11-2-3U (2) | VS | NK | Quartz | | | |
| 5-2-1 U | Y | NK | Troctolite cluster | | Y | N |
| 5-2-2 U | Y | NK | Quartz | | | |
| 5-2-3 U | Y | NK | ? | | | |
| 5-2-5 U | Y | NK | Quartz | | | |
| 14-5 | VS | SKAROS | Gabbro | F | | |
| 12-2-1 | ML | US1 | Gabbro (possible enclave though?) | | | |
| 12-2-2 | S | US1 | Gabbronorite | F | Y | Y |
| 13-5-1 | M | US1 | Gabbro | L | | |
| 13-5-2 | VS | US1 | Gabbro | L | N | N |
| 12-1-6-1 | S | US2 | Gabbro | L | | |
| 12-1-6-2 | M | US2 | Gabbro | L | | |
| 12-1-8-1 | VS | US2 | Gabbro | L | | |
| 12-1-8-2 | M | US2 | Gabbronorite | F | Y | Y |
| 14-1-1-3 | S | US2 | Gabbronorite | VF | Y | Y |
| 10-7-1-1 | VS | US2-D | Gabbro | | | |
| 10-7-1-2 | S | US2-D | Gabbro | | | |
| 10-7-1-3 | S | US2-D | Gabbro | | | |
| 10-7-2 | S | US2-D | enclave/old lava? | | | |
| 10-7-3 | S | US2-D | Lava | | | |
| 14-1-3-1 | Y | US2-D | schist | | | |
| 14-1-3-2 | S | US2-D | gabbro | | | |
| 14-1-3-4 | M | US2-D | Gabbro | M | | |
| 14-1-3-5 | S | US2-D | gabbro | M | | |
| 14-1-3-c | VS | US2-D | lava | | | |
| 14-2 | ? | US2-D | gabbro | | | |
| 14-20 (probably 14-2) | L | US2-D | ? prob crustal | | | |
| 14-3-1 | S | US2-D | gabbro | | | |
| 21D | | LP2 | Olivine gabbro | F | | |
| 23D | | LP2 | Olivine gabbro | F | | |
| 24D | | LP2 | Olivine gabbro | F | Y | Y |
| 25D | | LP2 | Olivine gabbro | F | | |
| 27D | | LP2 | Olivine gabbro | F | | |
| 28D | | LP2 | Gabbro | | Y | Y |
| 29D | | LP2 | Olivine gabbro | F | | |
| 2-1 | | MIN | Pumice | | Y | N |

| Sample | Remaining | Unit | Type | Freshness | Probed | Laser |
|---|---|---|---|---|---|---|
| 1-2 | | MIN | Bleb | | Y | N |
| 20 | | LP2 | Pumice | | Y | N |
| 30D | | LP2 | | | | |

# Appendix B

# Chapter 3 - Effects of Magma Carbonate Interaction at Merapi Appendix

# B.1 Sample List

*Table B.1: Merapi xenolith sample list and general mineralogy. M: magmatic xenolith. E: exoskarn xenolith. E-B: exoskarn B xenolith. O: major phase, X: abundant, +: minor phase*

| Sample | Assemblage | Cpx | CaTs cpx | Gn | Gh | Ti-Fe ox | Sp | Tit | Cal | Wo | Qtz | Plg | Ap/El | Amp | Gls | Anh | Zones |
|---|---|---|---|---|---|---|---|---|---|---|---|---|---|---|---|---|---|
| CS-1 | M | O | | | | X | | | + | O | | X | | | X | | R2, R3, R4 |
| CS-2 | M | X | | | | X | | + | | X | + | X | | | X | | R1, R2, R3, R4 |
| CS 3 | M | X | | | | | | | + | X | X | X | | | | | N |
| CS-4 | - | X | | | | | | | | | | O | + | X | | | N |
| CS-5 | M | X | | | | | | | | O | | O | | | | | R2 |
| CS-6 | M | X | | | | | | | | X | | O | | | | | R2 |
| CS-7 | M | X | | | | | | | + | X | | X | | | X | | R2, R3, R4 |
| CS-8 | M | X | | | | | | | | X | X | X | | | | | R2 |
| CS-9 | M | X | | | | + | | | + | X | | X | | | X | + | R2, R3, R4 |
| CS-10 | B | X | | | | | | + | | X | O | X | + | | | | R1 |
| CS-11 | E | X | | X | | | | | X | X | + | X | | | | | R2 |
| CS-12 | - | X | | | | | | | | x | X | + | | | | | NA |
| CS-13 (not cs) | - | O | | | | O | | | | | x | O | | | | | |
| CS 14 | B | X | | | | | | | | X | O | X | | | | | |
| CS-15 | - | X | | | | X | | | | | | X | | | | | R1,R2 |
| CS-16 | M | X | | + | | | | + | | X | | X | | | X | + | R1, R2, R3,R4 |
| CS-17 | M | O | X | O | | | | + | | O | | X | | | X | | R2, R3, R4 |
| CS-18 | M | X | | X | + | | | | + | O | + | X | | | X | | R1, R2, R3, R4 |
| CS-19 | M | X | X | X | | ? | | | + | X | | X | | | X | | Homogeneous glass, R2, R3b (gn) |
| MX-1 | M | X | X | X | + | X | | + | | O | | X | + | + | X | | R1, R2, R3, R3b,R4 |
| MX-2 | - | X | | | | X | | | | | O | X | | | | | R1 |
| MX-3 | M | X | | | | X | | + | + | O | + | + | + | | X | | R2, R3,R4 |
| MX-4 | M | X | | | | X | | + | | O | | O | | | X | | R1, R2, R3, R4 |
| MX-5 | M | O | | | | + | | | | O | X | X | + | | X | | R1, R2, R3, R4 |
| MX-6 | E | O | P | X | | | | + | | O | | + | ? | | | | NA |
| mx99-3s | E-B | X | O | O | O | + | X | | | + | | + | + | | X | | R1 |
| MX99-4 | M | X | | | | X | | + | | O | | X | + | | X | | R1-R4 |
| MX99-5s | E | X | X | X | + | X | | | | X | | X | x | | X | | R1,R2 |
| M13-24G | M | O | X | O | | + | | + | + | O | | O | | | X | + | Homogeneous glass at contact |
| M13-24G 1 | M | O | X | O | | + | | X | + | X | | X | | | X | + | Homogeneous glass at contac |
| M13-04C | B | | | | | | | + | | X | O | x | | | | | |
| M13-30 | M | + | | + | | | | | | O | | + | | | X | | |
| M13-10 | M | X | | X | | | | | + | O | | + | | | | | NA, R2, R3(gn) |
| M11-34 | M | X | | | | | | | | O | | X | | | | | NA, R2, R3 |
| M13-02 | E | X | | | | | | | O | X | X | + | | | | | |

## B.2 Supplementary Petrography

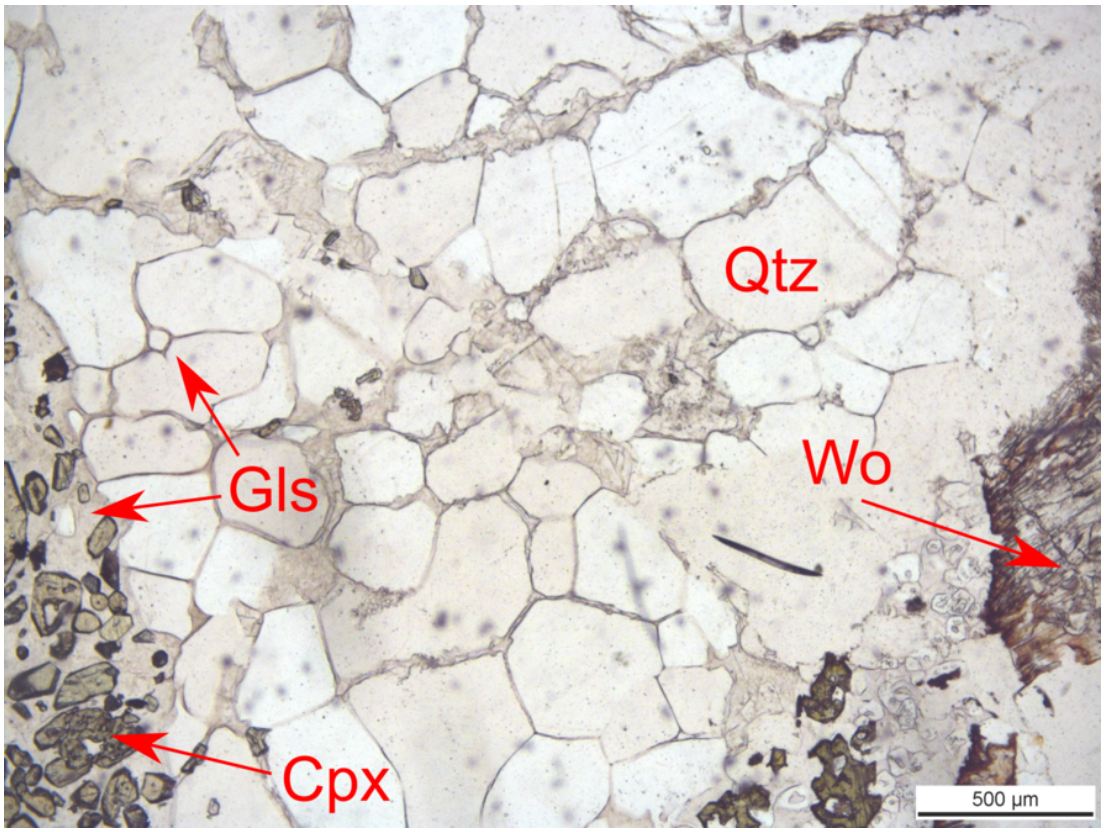


*Figure B.1: Photomicrograph of the buchite xenolith textures. Rounded quartz with interstitial glass in buchite sample CS14. Qtz = quartz, Wo = wollastonite, Cpx = clinopyroxene, Gls = glass.*

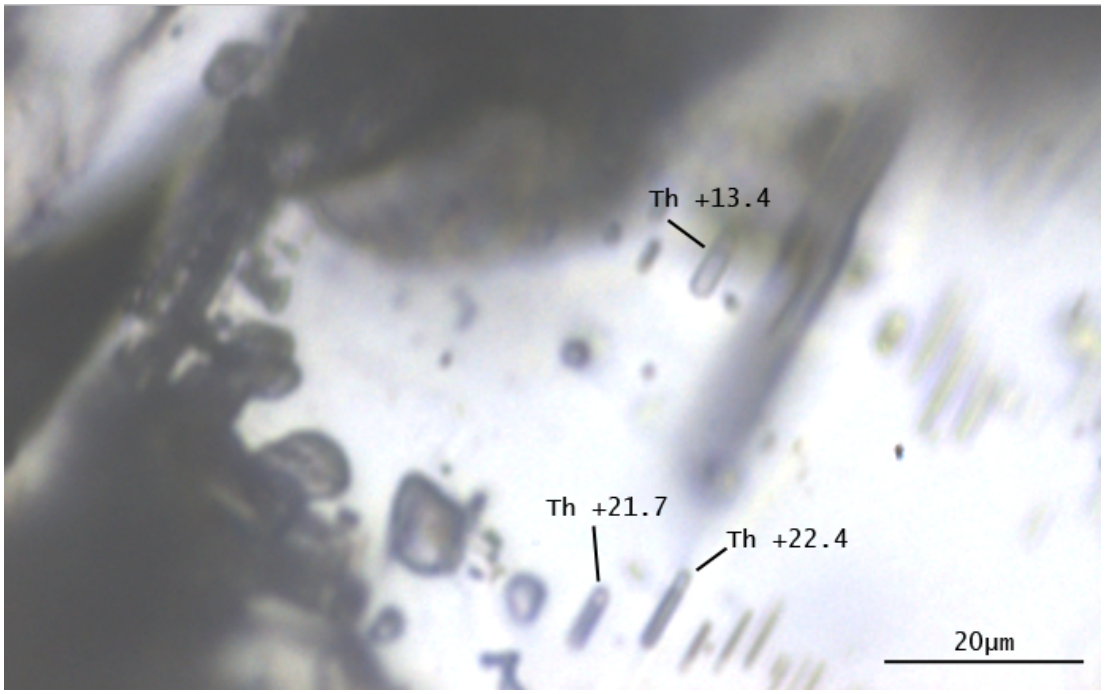


*Figure B.2: Photomicrograph of fluid + vapour CO2 fluid inclusions in sample MX3. Th: homogenisation temperature.*

## B.3 Supplementary Results

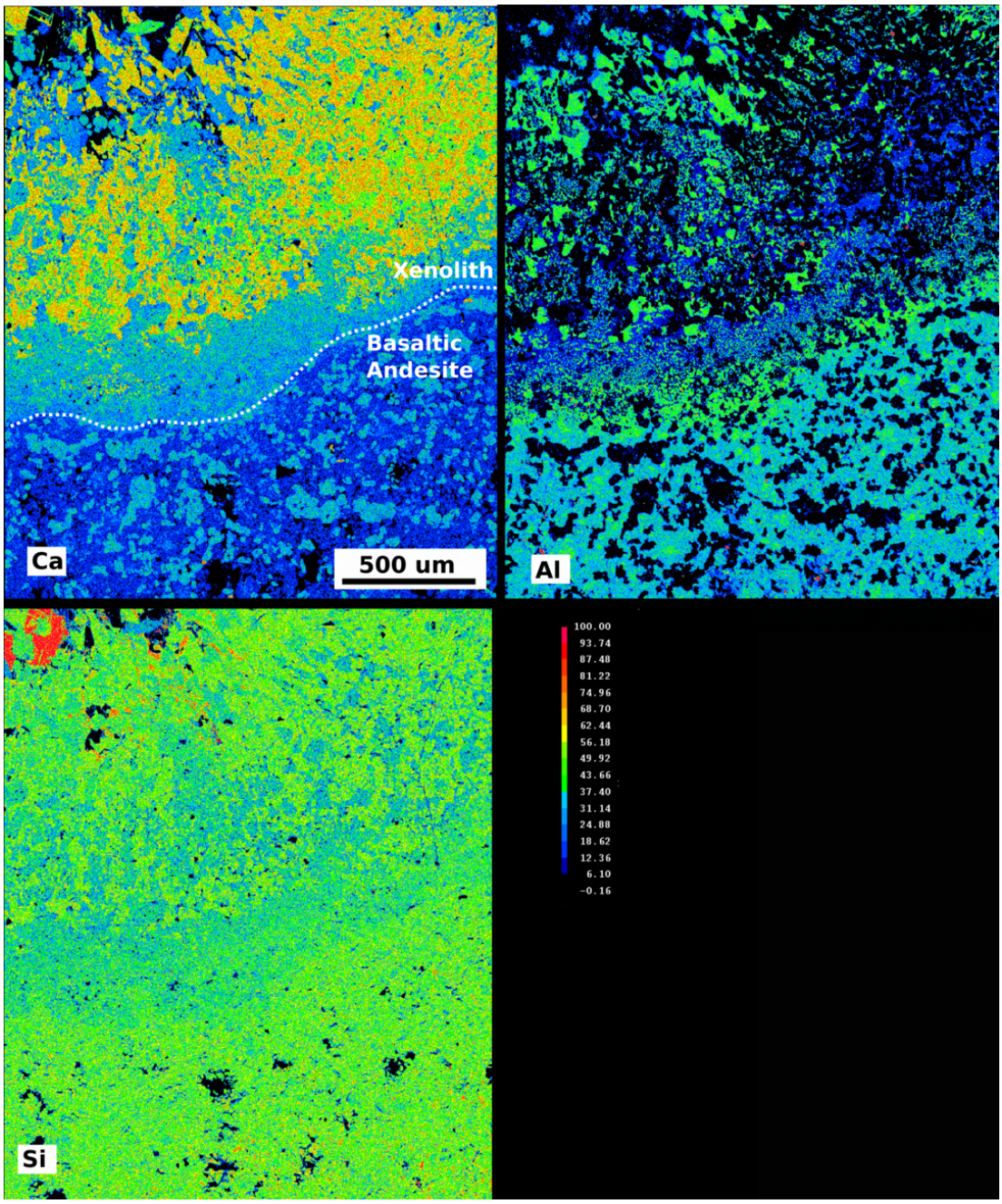


*Figure B.3: Ca, Al and Si chemical element maps of magmatic skarn xenolith sample MXCS-3*

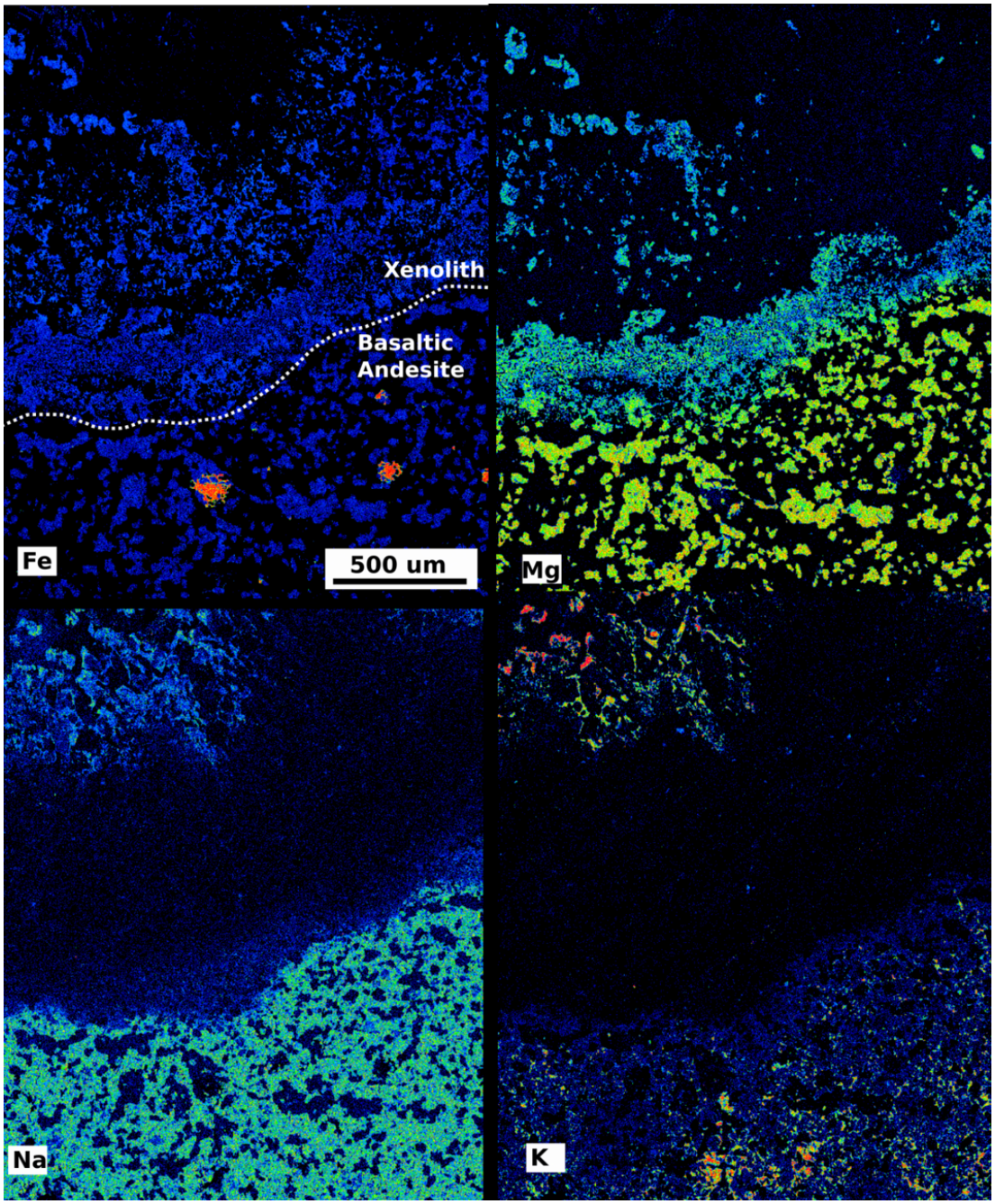


*Figure B.4: Fe, Mg, Na and K chemical element maps of magmatic skarn xenolith sample MXCS-3*

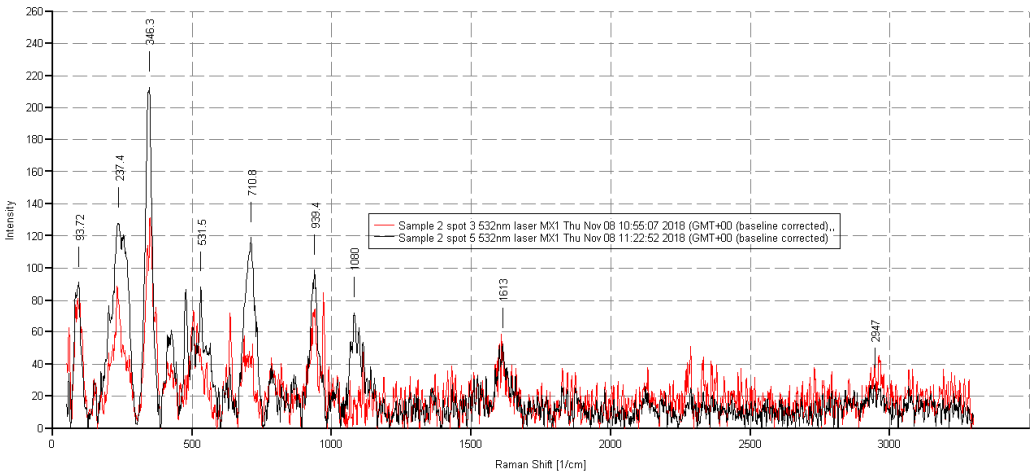


*Figure B.5: Raman spectra for the wadalite-like mineral in sample MX1. This trace mineral (< 50um crystal size) is in close association with wollastonite, garnet and calcite, therefore an analysis without overlap with these minerals was difficult.*

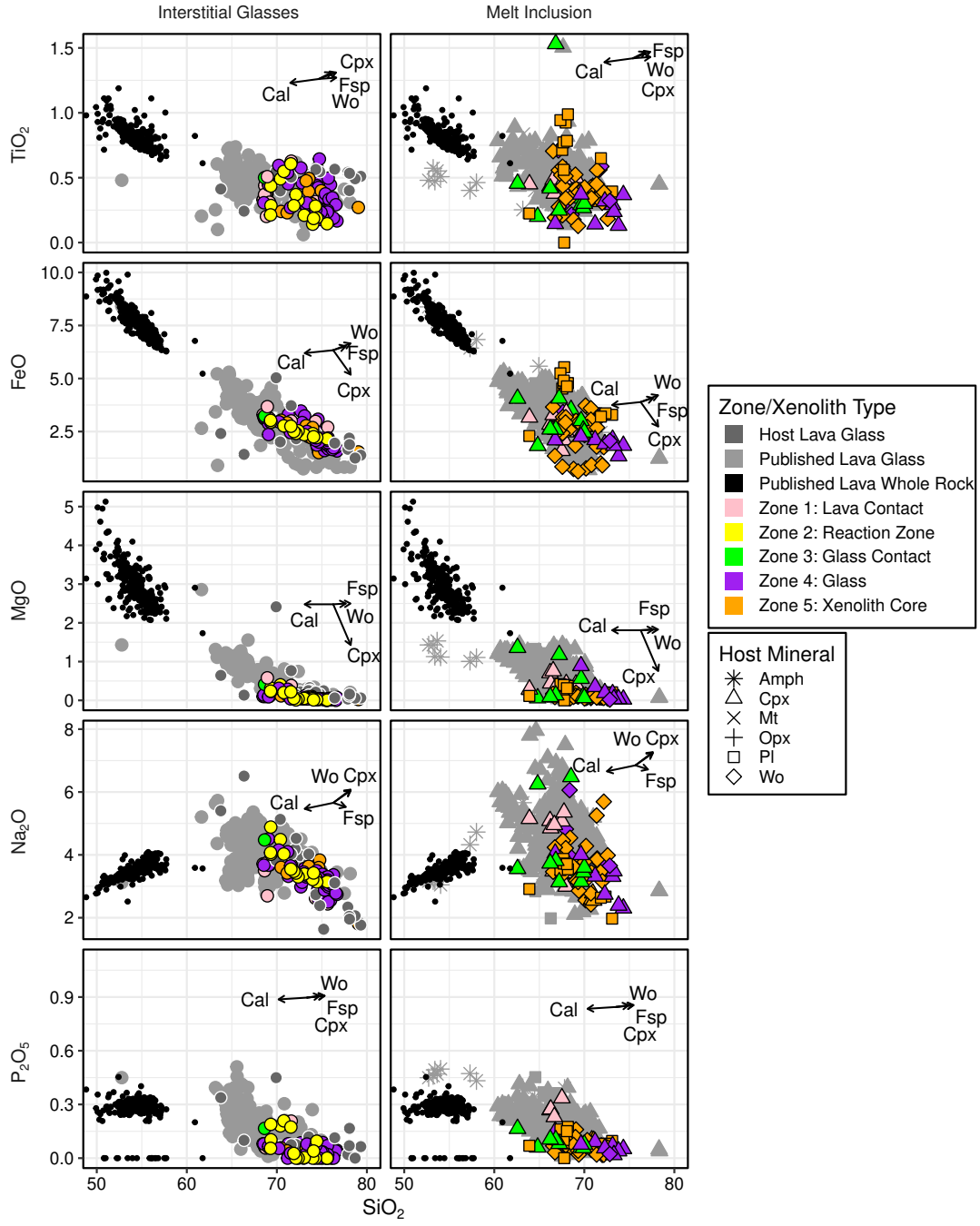


*Figure B.6: Harker diagrams of Merapi xenolith and lava glasses for major elements not shown in the main text*

## B.4 Preliminary Calcite LA-ICP-MS Trace Element Data

Trace elements in calcite were analysed at the GEOMAR Helmholtz Centre for Ocean Research Kiel using a Nu Instruments ATTOM HR-ICP-MS connected to a Coherent Lambda Physics GEOLAS pro 193 nm excimer laser ablation system. Measurements were made using a 2

mJ/cm 2 energy density for 300 pulses at a laser repetition rate of 10Hz with a 44 µm spot size, and a 50 s flush time. Measurements were made on the same polished sections used for EMPA to provide a robust internal standard using the sum of $^{29}$Si and $^{43}$Ca for normalisation. Calibration was undertaken on a NIST 610 reference glass and repeat measurements of basaltic glasses USGS BCR-2G and USGS BHVO-2G as secondary standards were repeated throughout each analytical session to check accuracy and precision. Measurements were made in blocks of 8 to minimise the effects of drift. Full details of the instrument setup is provided in Fietzke and Frische (2016).

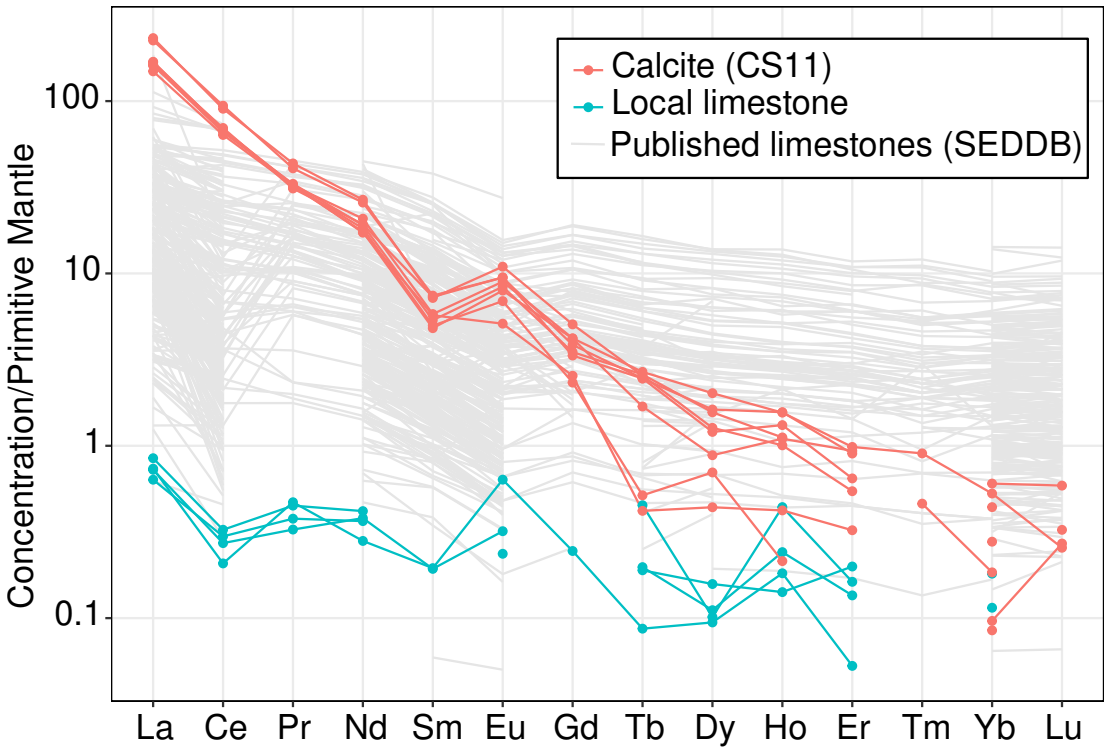


*Figure B.7: Preliminary calcite rare earth element data for Type E residual calcites in exoskarn sample CS11 (see Whitley* et al.*, 2019 for details). Data are normalised to primitive mantle using Palme* et al. *(2014). The local limestone is sampled from Parangtritis, ~60km from Merapi (see Figure C.1, Whitley* et al.*, 2019 supplementary figure). Light grey literature data for marine limestones from SEDDB (`https://www.earthchem.org/seddb`)*

*Table B.2: Trace element data for 4 calcites in sample CS11. These are Type E calcites in the main thesis text and Whitley* et al. *(2019).*

| Rock/Mineral | Limestone | Limestone | Limestone | Limestone | Cal | Cal | Cal | Cal |
|---|---|---|---|---|---|---|---|---|
| Sample | LMST-3 | LMST-3 | LMST-3 | LMST-3 | CS11 | CS11 | CS11 | CS11 |
| *ppm* | | | | | | | | |
| $^{7}$Li | 0.75 | <LOD | <LOD | 1.54 | <LOD | <LOD | <LOD | <LOD |
| $^{23}$Na | 58.90 | 62.18 | 49.99 | 41.12 | 12.86 | 19.12 | 6.75 | 6.64 |
| $^{24}$Mg | 1989.38 | 1777.17 | 1546.24 | 1875.14 | 249.21 | 305.23 | 242.54 | 246.23 |
| $^{27}$Al | 12.26 | 265.73 | 23.84 | 50.78 | 1.74 | 5.82 | 1.69 | <LOD |
| $^{45}$Sc | 0.48 | 0.29 | 0.71 | 0.40 | <LOD | <LOD | <LOD | 0.24 |
| $^{49}$Ti | 6.30 | <LOD | <LOD | <LOD | <LOD | 3.83 | <LOD | <LOD |
| $^{51}$V | 1.27 | 1.37 | 0.78 | 0.73 | <LOD | <LOD | <LOD | <LOD |
| $^{53}$Cr | 12.59 | 11.09 | 6.39 | 7.92 | <LOD | <LOD | <LOD | 1.12 |
| $^{55}$Mn | 4.83 | 15.41 | 6.98 | 11.05 | 246.90 | 278.30 | 1106.10 | 1109.40 |
| $^{59}$Co | <LOD | <LOD | <LOD | <LOD | 0.17 | <LOD | <LOD | <LOD |
| $^{61}$Ni | <LOD | <LOD | <LOD | <LOD | 28.73 | <LOD | 18.18 | 14.59 |
| $^{65}$Cu | <LOD | <LOD | <LOD | <LOD | <LOD | <LOD | <LOD | 1.39 |
| $^{66}$Zn | 1.65 | 1.98 | 2.74 | 1.17 | 1.87 | 1.41 | <LOD | <LOD |
| $^{85}$Rb | <LOD | <LOD | <LOD | 0.42 | <LOD | <LOD | <LOD | <LOD |
| $^{86}$Sr | 368.68 | 268.45 | 340.17 | 339.77 | 724.04 | 842.75 | 485.25 | 483.63 |
| $^{88}$Sr | 351.52 | 262.33 | 339.39 | 342.97 | 743.63 | 815.18 | 482.60 | 484.08 |
| $^{89}$Y | 1.18 | 1.33 | 1.66 | 1.29 | 4.77 | 1.45 | 8.00 | 8.02 |
| $^{90}$Zr | 0.36 | <LOD | <LOD | 0.29 | <LOD | <LOD | 0.33 | <LOD |
| $^{93}$Nb | 0.28 | <LOD | 0.32 | <LOD | <LOD | <LOD | <LOD | <LOD |
| $^{133}$Cs | <LOD | <LOD | <LOD | <LOD | <LOD | <LOD | <LOD | <LOD |
| $^{137}$Ba | 1.58 | 3.13 | 1.16 | 2.11 | 93.35 | 138.64 | 74.46 | 79.66 |
| $^{139}$La | 0.50 | 0.58 | 0.43 | 0.50 | 153.55 | 115.52 | 110.27 | 110.65 |
| $^{140}$Ce | 0.36 | 0.57 | 0.52 | 0.48 | 164.87 | 119.25 | 115.56 | 122.42 |
| $^{141}$Pr | 0.12 | 0.12 | 0.10 | 0.09 | 10.82 | 8.59 | 8.80 | 8.27 |
| $^{146}$Nd | 0.38 | 0.56 | 0.49 | 0.51 | 34.58 | 24.43 | 25.57 | 25.89 |
| $^{147}$Sm | 0.08 | <LOD | <LOD | 0.08 | 3.23 | 2.16 | 2.33 | 3.18 |
| $^{153}$Eu | 0.11 | 0.04 | <LOD | 0.05 | 1.58 | 1.15 | 1.39 | 1.58 |
| $^{157}$Gd | 0.14 | <LOD | <LOD | <LOD | 2.25 | 1.36 | 2.05 | 1.95 |
| $^{159}$Tb | 0.01 | 0.05 | 0.02 | 0.02 | 0.26 | 0.06 | 0.28 | 0.26 |
| $^{163}$Dy | 0.07 | 0.07 | 0.11 | 0.08 | 0.87 | 0.51 | 1.13 | 1.18 |
| $^{165}$Ho | 0.03 | 0.07 | 0.02 | 0.04 | 0.21 | 0.03 | 0.18 | 0.25 |
| $^{166}$Er | 0.02 | 0.08 | 0.09 | 0.06 | 0.30 | <LOD | <LOD | 0.42 |
| $^{169}$Tm | <LOD | <LOD | <LOD | <LOD | <LOD | 0.03 | <LOD | <LOD |
| $^{172}$Yb | <LOD | 0.05 | <LOD | 0.09 | 0.21 | 0.09 | 0.29 | 0.13 |
| $^{175}$Lu | <LOD | <LOD | <LOD | <LOD | <LOD | <LOD | 0.04 | <LOD |
| $^{178}$Hf | <LOD | 0.05 | <LOD | <LOD | <LOD | <LOD | <LOD | 0.03 |
| $^{181}$Ta | <LOD | <LOD | 0.14 | <LOD | 0.08 | <LOD | <LOD | 0.09 |
| $^{208}$Pb | 0.38 | 0.12 | 0.20 | 0.16 | 0.93 | 1.22 | 2.36 | 2.36 |
| $^{232}$Th | 0.09 | 0.10 | 0.07 | 0.08 | 0.06 | 0.01 | 0.01 | 0.03 |
| $^{238}$U | 0.73 | 1.52 | 0.80 | 0.71 | <LOD | <LOD | <LOD | <LOD |

## B.5 Supplementary Discussion: Thermobarometric Model Testing

The abundance of glass and common mineral phases (clinopyroxene, plagioclase) in the magmatic skarn xenoliths allows application of mineral-melt and melt-only thermobarometric models (e.g. Putirka, 2008; Neave and Putirka, 2017). Testing of these models on carbonate-bearing systems was first performed by Mollo *et al.* (2010b) on their experimental dataset covering a limited temperature range (1150-1300°C) and a fixed pressure of 500 MPa. We have collated data from eight carbonate assimilation experimental studies (see Figure B.8 for references) covering a wide range of P-T-$fO_2$ conditions (0-1000 MPa, 900-1200°C, NNO to air), variable proportions and compositions (calcite to dolomite) of carbonate and variable silicate magma

compositions (basalt to dacite) to further test the equilibrium and thermobarometric models of Putirka *et al.* (1996), Putirka *et al.* (2003), Putirka (2008) and Neave and Putirka (2017). We have focused on clinopyroxene-based thermobarometric models, as clinopyroxene is the second most abundant mineral phase in the xenoliths after wollastonite, has the most experimental data available, and can provide both temperature and pressure estimates (Figure B.8). This assessment has uncertainties due to authors' variable preferences for reporting data precision, $H_2O$ contents estimated 'by-difference' (Anderson, 1973, 1974; Devine *et al.*, 1995), and a due bias towards studies based on high temperature Italian potassic melts. We however believe our approach provides a first-order approximation of the accuracy of thermobarometric models over a wide range of carbonate-assimilating systems. We tested the models using reported experimental conditions, and iteratively solving thermometers paired with barometers, as would be undertaken on natural unknown samples.

Results from Putirka *et al.* (1996) (not shown) perform very poorly and are not considered further ($R^2 < 0.20$, residual standard error (RSE) $> 100$°C and 3 kbar respectively). The most accurate and precise temperatures derived from published models are from the models of Putirka (2008): glass-only clinopyroxene saturation thermometer (equation 34: $R^2 = 0.53$, RSE = ±46°C, Figures B.8A-B), clinopyroxene-melt thermometer (equation 33: $R^2 = 0.58$, RSE = ±59°C, Figures B.8C-E), and the clinopyroxene only barometer (equation 32b: $R^2 = 0.1$, RSE = ±2.6 kbar, Figures B.8F-H), both when tested with experimental conditions and iteratively calculated (Figures B.8). The low $R^2$ values for equation 32b are due to 1 atm experimental overestimates (discussed below). Our assessment of the most accurate models has similar results to that of Mollo *et al.* (2010b) testing these models on their dataset, however based on our larger collated dataset, we can not also recommend the use of the models of Putirka *et al.* (1996) and Putirka (2008) equation 32a. Mineral-melt thermometer equation 33 (Putirka, 2008) iteratively paired with clinopyroxene-only barometer 32b (Putirka, 2008) (Figure B.8D) and the clinopyroxene-melt barometer of Neave and Putirka (2017) (Figure B.8E) produces large temperature overestimations with increasing carbonate assimilation in higher temperature mafic melts. Most of these overestimations are related to the experiments of Mollo and Vona (2014), which produced highly aluminous clinopyroxenes (up to 12.24 wt% $Al_2O_3$) from equilibration at very high oxygen fugacities (up to air). The best barometric model is clinopyroxene-only equation 32b of Putirka (2008) paired with the clinopyroxene thermometer equation 34 (Figure B.8H), recovering a relative sense of pressure at lower pressures when taking the average of the experimental pressures, tending towards slight pressure underestimation. There is a large

pressure overestimation in 1 atm experiments, which is a known issue with some barometric models and some experimental setups (Putirka, 2008; Neave and Putirka, 2017). However, these are predominantly due to the inclusion of the experiments of Mollo and Vona (2014) which equilibrated clinopyroxenes at up to air oxygen fugacity conditions. This overestimation is much more exaggerated when equation 32b is paired with clinopyroxene-melt thermometer equation 33 (Figure B.8G), due to the higher temperature overestimates. Both the equation 32c (Figure B.8J) and the barometer of Neave and Putirka (2017) (Figure B.8I) produce severe pressure overestimates at pressures <500 MPa. Putirka (2008) equation 31 performs well when calculated with known experimental temperatures, but loses the relative sense of pressure below 5 kbar when iteratively calculated with a thermometer (Figure B.8K-L).

On the basis of this investigation, and clinopyroxene-interstitial glass pairs indicating disequilibrium ($KD_{Fe-Mg}^{cpx-melt}$ « 0.28), we have only used equations 34 (glass only) and 32b (cpx only) of Putirka (2008) for thermometry and barometry calculations, respectively.

Attempts were made to recalibrate the Putirka (2008) thermobarometers and additionally produce new models using the collated carbonate assimilation experimental dataset. A small improvement was made in thermometry of the > 1000°C experimental data, however the data below 1000°C strongly overestimate temperatures by > 100°C, which is likely a result of very few published experimental data existing in that temperature range. As this is the temperature region expected for our xenoliths (see discussion) we do not use the new model, although it is presented below for completeness. Recalibration of the barometers was not possible due to the limited experimental dataset not showing any correlated variables.

A new glass-only thermometer recovers the carbonate assimilation experimental dataset to ± 32°C, $R^2 = 0.64$, applicable to > 1000°C systems.

$$T(C) = 1279.55 + 38.44ln(X_{CaO}^{liq} X_{MgO}^{liq}) + 137.946 X_{SiO_2}^{liq}$$

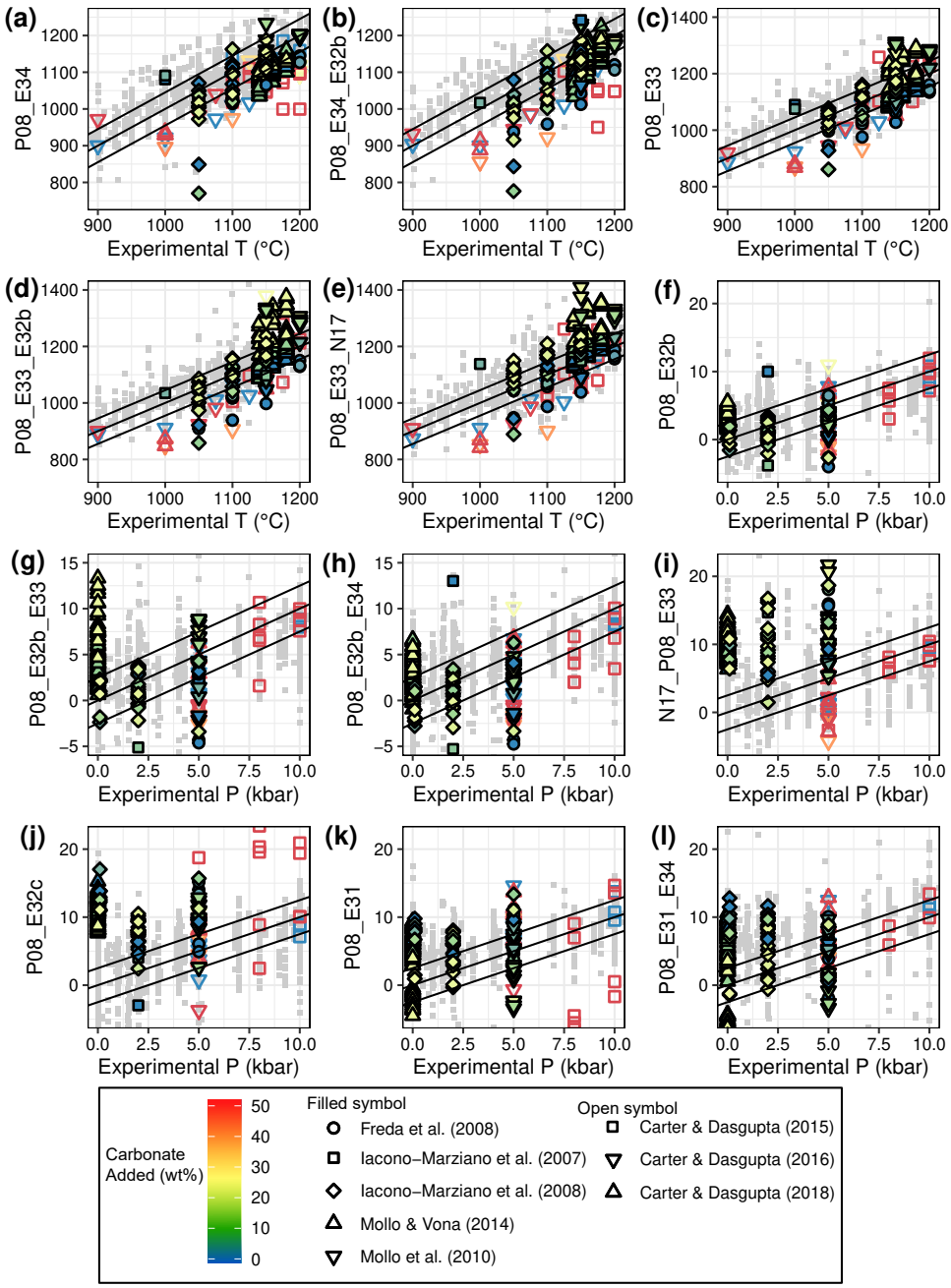


*Figure B.8: Selected thermobarometric model testing results. The axis labels are read as follows: P08 refers to equations from Putirka (2008), N17 refers to the barometric formulation from Neave and Putirka (2017). For instance, N17_P08_E33 is the barometer from Neave and Putirka (2017) paired with Putirka (2008) equation 33. Light grey symbols are modelling results for comparison derived from a global non-carbonate assimilation experimental dataset (Library of Experimental Phase Relations (LEPR Hirschmann* et al.*, 2008), and additional experimental data (Snyder* et al.*, 1993; Sugawara, 2001; Berndt* et al.*, 2005; Hammer, 2006; Whitaker* et al.*, 2007; Botcharnikov* et al.*, 2008; Freise* et al.*, 2009; Feig* et al.*, 2010; Jégo* et al.*, 2010; Jégo and Pichavant, 2012; Mollo and Vona, 2014; Cadoux* et al.*, 2014; Andújar* et al.*, 2015). Thermometer equation 34 and barometer 32b (Putirka, 2008) produce the most accurate estimates of the experimental conditions.*

# Appendix C

# Chapter 4 - Crustal volatile release at Merapi Appendix

*Table C.1: C and O isotopic compositions of calcite in calc-silicate xenoliths of Merapi volcano. 2σ errors are typically 0.4 ‰ for oxygen and 0.8 ‰ for carbon.*

| Sample | Calcite Type* | Rock Type | $\delta^{18}O$ (‰) | $\delta^{13}C$ (‰) |
|---|---|---|---|---|
| CS17 | A | Magmatic | +23.8 | -3.7 |
| CS17 | A | Magmatic | +22.7 | -4.2 |
| CS17 | A | Magmatic | +24 | +1.8 |
| CS17 | A | Magmatic | +21.4 | +1.8 |
| CS17 | A | Magmatic | +22.3 | +0.4 |
| CS17 | B | Magmatic | +21.6 | -6.8 |
| CS17 | B | Magmatic | +21.3 | -0.6 |
| CS17 | B | Magmatic | +20.5 | -6.4 |
| CS17 | B | Magmatic | +20.5 | -6.5 |
| CS17 | B | Magmatic | +24.3 | -13.5 |
| MX3 | B | Magmatic | +24.2 | -29.3 |
| MX3 | B | Magmatic | +23.5 | -29.1 |
| MX3 | B | Magmatic | +23.6 | -28.3 |
| MX3 | B | Magmatic | +24.1 | -28.3 |
| MX3 | B | Magmatic | n.a. | n.a. |
| MX3 | B | Magmatic | n.a. | n.a. |
| MX3 | B | Magmatic | +25.6 | -22.6 |
| MX3 | B | Magmatic | n.a. | n.a. |
| MX3 | B | Magmatic | n.a. | n.a. |
| MX3 | B | Magmatic | n.a. | n.a. |
| MX3 | B | Magmatic | n.a. | n.a. |
| MX3 | B | Magmatic | n.a. | n.a. |
| MX5 | B | Magmatic | +23.8 | -22.5 |
| MX5 | B | Magmatic | +20.5 | -14.9 |
| MX5 | B | Magmatic | +24.9 | -19.3 |
| MX5 | B | Magmatic | +24 | -18.8 |
| MX5 | B | Magmatic | +24 | -19.7 |
| MX5 | B | Magmatic | +23.5 | -21.5 |
| MX5 | B | Magmatic | +23.1 | -25.1 |
| MX5 | B | Magmatic | +22.9 | -22.5 |
| MX5 | B | Magmatic | +23.8 | -22.7 |
| MX1 | C | Magmatic | +20.1 | -13.6 |
| MX1 | C | Magmatic | +14 | -12.4 |
| MX1 | C | Magmatic | +21.5 | -8.1 |
| MX1 | C | Magmatic | +22 | -6.3 |

| Sample | Calcite Type* | Rock Type | $\delta^{18}O$ (‰) | $\delta^{13}C$ (‰) |
|---|---|---|---|---|
| MX1 | C | Magmatic | +23 | -0.1 |
| MX1 | C | Magmatic | +23.1 | -2.7 |
| MX1 | C | Magmatic | +19.3 | -3.5 |
| MX1 | C | Magmatic | +23 | -0.8 |
| MX1 | C | Magmatic | +19.9 | -8.7 |
| MX1 | C | Magmatic | +17.9 | -18.5 |
| MX1 | C | Magmatic | +19.6 | -0.1 |
| MX1 | C | Magmatic | +17.8 | +3.3 |
| MX1 | C | Magmatic | +18.9 | +3.5 |
| MX1 | C | Magmatic | +9.9 | -15.9 |
| MX1 | D | Magmatic | +17.9 | -4.4 |
| MX1 | D | Magmatic | +14.6 | -6.4 |
| MX1 | D | Magmatic | n.a. | n.a. |
| MX5 | D | Magmatic | +17.6 | -13.8 |
| MX5 | D | Magmatic | +17 | -14.9 |
| CS11 | E | Exoskarn | +15.7 | -12.9 |
| CS11 | E | Exoskarn | +15.5 | -14 |
| CS11 | E | Exoskarn | +19 | -8.3 |
| CS11 | E | Exoskarn | +18.6 | -8.4 |
| CS11 | E | Exoskarn | +18.6 | -7.8 |
| CS11 | E | Exoskarn | +18.6 | -7.8 |
| CS11 | E | Exoskarn | +18.7 | -7.4 |
| CS11 | E | Exoskarn | +15 | -9 |
| CS11 | E | Exoskarn | +15 | -11 |
| CS11 | E | Exoskarn | +14.9 | -8.5 |
| CS11 | E | Exoskarn | +15.2 | -9.8 |
| CS11 | E | Exoskarn | +15.1 | -9.1 |
| M13-02 | E | Exoskarn | +14 | -12.1 |
| M13-02 | E | Exoskarn | +13.9 | -11.7 |
| M13-02 | E | Exoskarn | +14 | -12.1 |
| M13-02 | E | Exoskarn | +14.3 | -11.8 |
| M13-02 | E | Exoskarn | +14.3 | -10.5 |
| M13-02 | E | Exoskarn | +16.5 | -4.9 |
| M13-02 | E | Exoskarn | +16.7 | -4.9 |
| M13-02 | E | Exoskarn | +16.5 | -4.6 |
| M13-02 | E | Exoskarn | +16.6 | -5 |
| M13-02 | E | Exoskarn | +16.8 | -4.7 |
| M13-02 | E | Exoskarn | +17 | -5.5 |
| M13-02 | E | Exoskarn | +17.2 | -5.1 |
| M13-02 | E | Exoskarn | +17 | -5.9 |
| M13-02 | E | Exoskarn | +18.4 | -5.6 |
| M13-02 | E | Exoskarn | +15.8 | -5.7 |

* Calcite type: A = Glass hosted; B = Interstitial; C = Melt-like; D = Inclusion; E = Residual

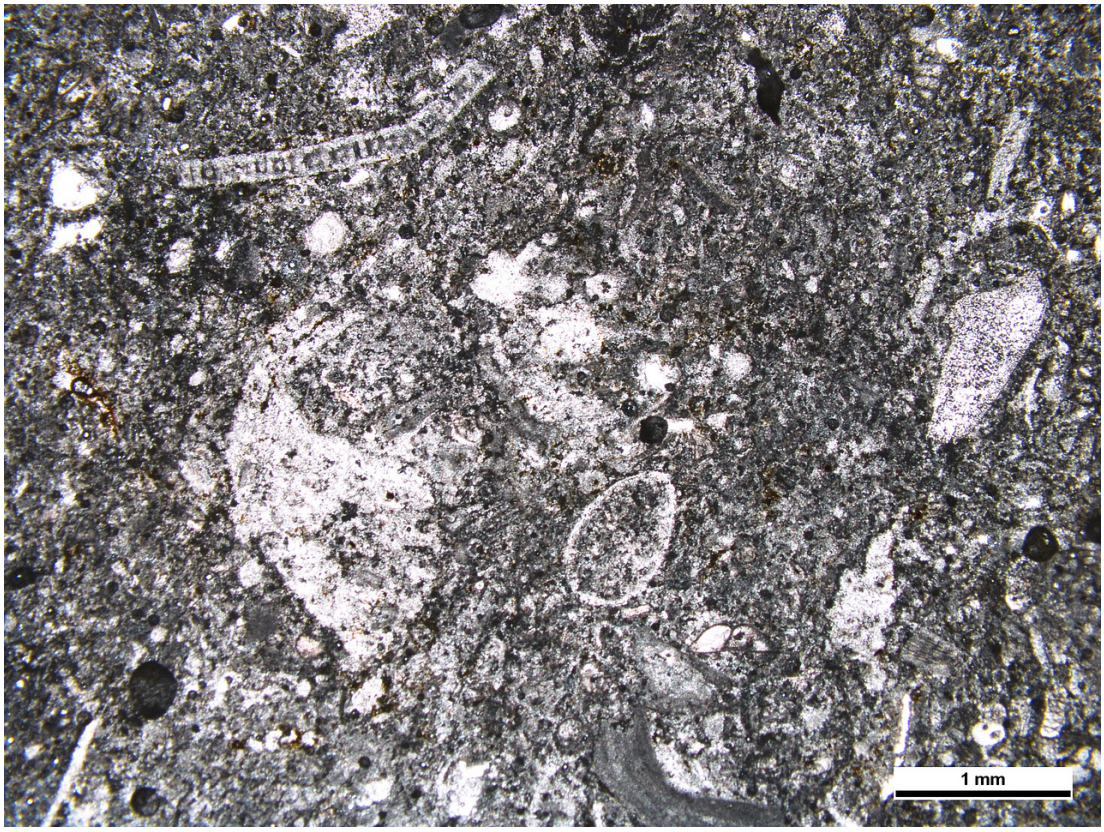


*Figure C.1: Local limestone sampled from Parangtritis. Thin section imaged in transmitted light. This limestone is from the Late Miocene to Early Pliocene Wonosari formation which comprises tidal-algal packstone, reef crest/front coral boundstone, upper-slope orbitoid-algal packstone and lower-slope packstone-wackestone (Siregar, 1996; Praptisih and Siregar, 2002).*

# Appendix D

# Chemical Datasets

All data produced within this thesis and collated from literature data to produce the figures is provided on an online supplement to this thesis and the associated published papers from this work.